Volume 98 Number 7 July 2017

BAMS

Bulletin of the American Meteorological Society

3D LASER SCANS OF HAIL

A FLOOD OF FLOOD DATA

CLIMATE IN 5,000 YEARS

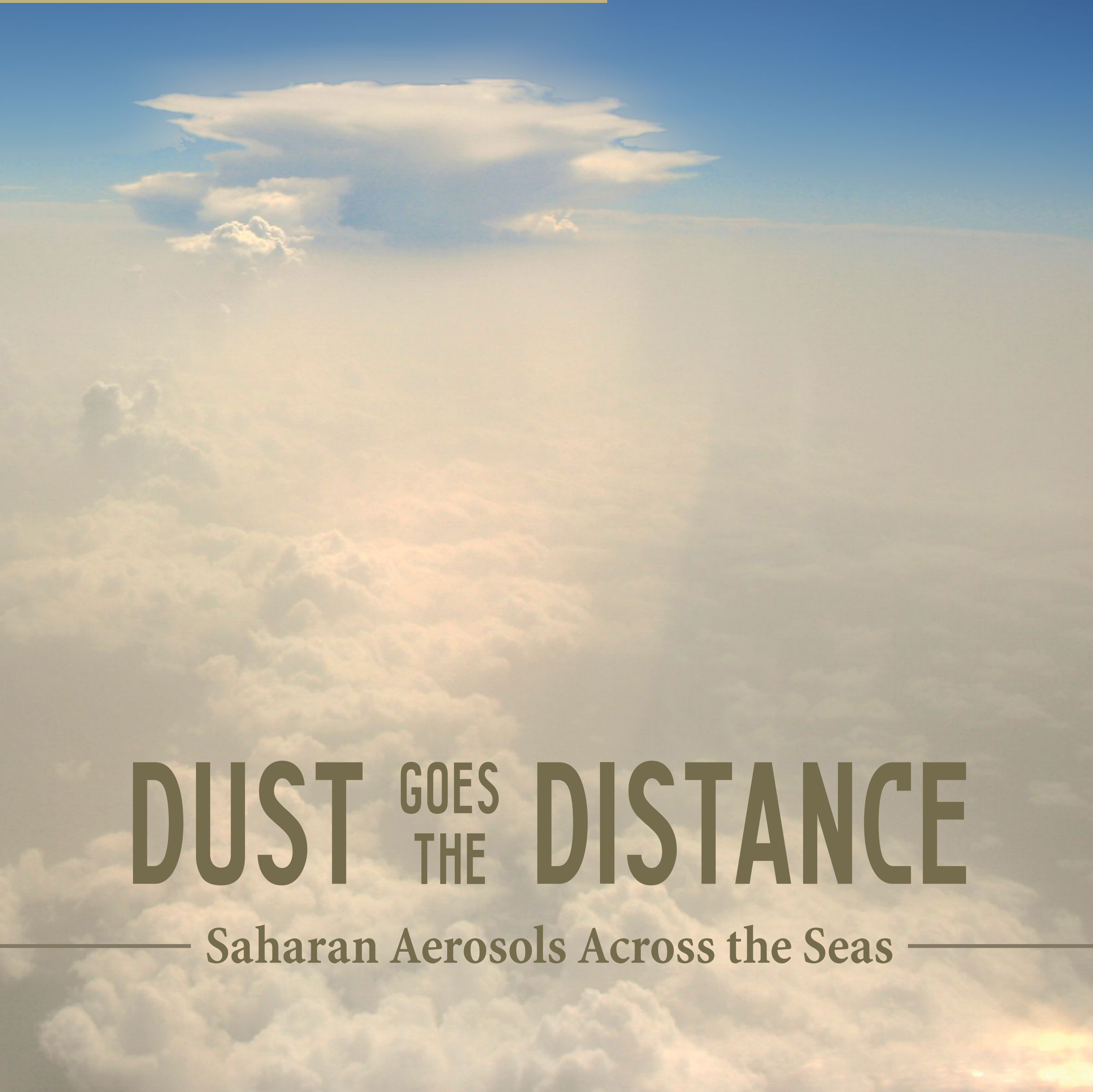

DUST GOES THE DISTANCE

Saharan Aerosols Across the Seas

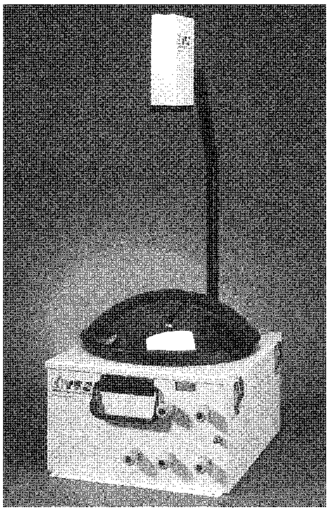

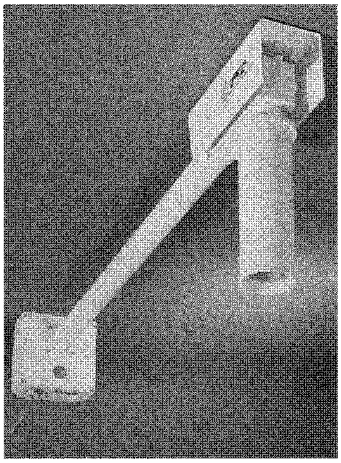

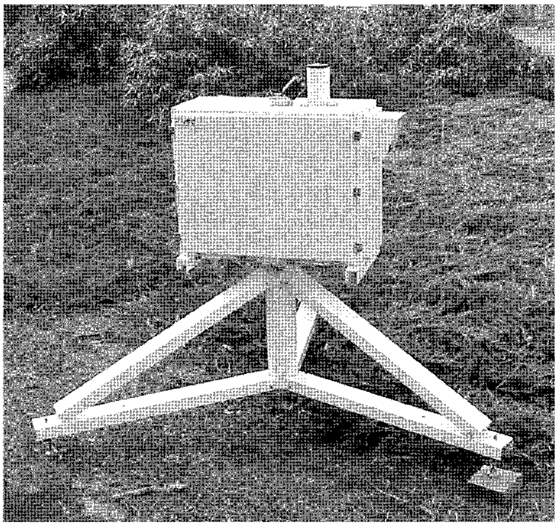

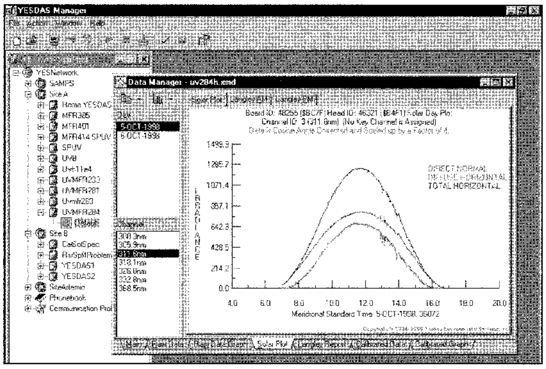
YESDAS Manager
File Action Window Help
YESNetwork
SAMPS
Site A
Home YESDAS
MFR385
MFR401
MFR414 SPUV
SPUV
UVB
Uvb11e4
UVMFR233
UVMFR281
Uvmfr283
UVMFR284
Default
Site B
CalSolSpec
RsrSpfProblem
YESDAS1
YESDAS2
SiteArtemic
Phonebook
Communication Prof
Data Manager - uv284h.xmd
Solar Plot
Langley AM
Langley PM
Day
5-OCT-1998
6-OCT-1998
Channel
300.3nm
305.9nm
311.6nm
318.1nm
326.0nm
332.8nm
368.5nm
Board ID: 48255 ($BC7F) Head ID: 46321 ($B4F1) Solar Day Plot
Channel ID: 3 (311.6nm) (No Key Channel is Assigned)
Data is Cosine Angle Corrected and Scaled up by a Factor of 4.
IRRADIANCE
1499.9
1285.7
1071.4
857.1
642.8
428.5
214.2
0.0
DIRECT NORMAL
DIFFUSE HORIZONTAL
TOTAL HORIZONTAL
4.0
6.0
8.0
10.0
12.0
14.0
16.0
18.0
20.0
Meridional Standard Time 5-OCT-1998, 36072
Main
Raw Data
Raw Data Graph
Solar Plot
Langley Report
Calibrated Data
Calibrated Graph


AMS
American Meteorological Society
AMS
American Meteorological Society
AMS
AMS
AMERICAN METEOROLOGICAL SOCIETY 1919
Hurricane Pioneer: Memoirs of Bob Simpson
Joseph P. Bassi
A SCIENTIFIC PEAK
THE THINKING PERSON'S GUIDE TO CLIMATE CHANGE
ROBERT HENSON
William H. Haggard
The America

BAMS
Bulletin of the American Meteorological Society

VOLUME 98, NUMBER 7, JULY 2017

IN BOX

ESSAY

ARTICLES

ON THE COVER

Dust layers over the Caribbean in summer 2013. The Saharan Aerosol Long-Range Transport and Aerosol–Cloud-Interaction Experiment (SALTRACE) studies the transport of African dust across the Atlantic and its impact on radiation and clouds in the Caribbean. For more information, see the article by Weinzierl et al., starting on p. 1427. Photo courtesy Bernadett Weinzierl/Universität Wien

Supplements (Ⓢ) and online content are available online at http://journals.ametsoc.org/toc/bams/98/7

PUBLISHER
Keith L. Seitter
EDITOR-IN-CHIEF
Jeffrey Rosenfeld
SENIOR EDITOR
Christopher Cappella
BAMS EDITORIAL BOARD
Chair
Jeff Waldstreicher
Aerosol and Cloud Physics
Cynthia Twohy
Atmospheric Chemistry/Air Quality
William R. Stockwell
Atmospheric Dynamics/Tropical Meteorology
Chris Landsea
Brian Mapes
Ed Zipser
Biometeorology
Peter Blanken
Climate/Climate Variability
Art DeGaetano
Bjorn Stevens
Climate Analysis
Mike Alexander
Education
Donna Charlevoix
History
James R. Fleming
Hydrology
Qingyun Duan
Numerical Analysis/Mesoscale Modeling
Brian Etherton
Observing Systems
Tammy Weckwerth
Oceanography
Mike McPhaden
Policy
Genene Fisher
Satellite Meteorology
Jeff Hawkins
Timothy J. Schmit
Society/Economic Impacts
Lisa Dilling
PRODUCTION STAFF
Managing Editor
Bryan Hanssen
News Editors
Rachel S. Thomas-Medwid
Matthew Gillespie
Production Editors
Denise M. Moy
Roger Wood
Meetings Editor
Claudia J. Gorski
Editorial Assistant
Melissa Fernau
Production Associate
Jillian G. Neustel
Senior Production Assistant
Christopher R. Faucher
Advertising
Kelly Garvey Savoie
DIRECTOR OF COMMUNICATIONS
Tom Champoux
COMMUNICATIONS STAFF
Digital Communications Manager
Brian Mardirosian
Communications Assistant
Sangjun Lee
DIRECTOR OF PUBLICATIONS
Kenneth F. Heideman
JOURNALS STAFF
Journals Production Manager
Michael Friedman
Managing Technical Editor
Mark E. Fernau
Managing Copy Editor
Jessica A. LaPointe
Technical Editors
Richard R. Brandt
John K. Creilson
Copy Editors
Brandon M. Crose
Jason Emmanuel
Gary Gorski
Ramesh Pillay
Nicole Rietmann
Jordan Stillman
Lesley A. Williams
Publications Coordinator
Gwendolyn Whittaker

CONTENTS

MEETING SUMMARIES

MESONETS
The importance of their near-surface weather and climate observations, in Mahmood et al. (p. 1349)

The *Bulletin of the American Meteorological Society* is the official organ of the Society, devoted to editorials, articles of interest to a large segment of the membership, professional and membership news, announcements, and Society activities. Editing and publishing are under the direction of Keith L. Seitter, executive director. Contributors are encouraged to send proposals to be considered for publication. For guidance on preparation and style, see the Authors' Resource Center online at www.ametsoc.org/pubs/arcindex.html.

AMS officers, councilors, and commissioners: president-elect (acting president), Roger Wakimoto; executive director, Keith L. Seitter; secretary–treasurer, Richard D. Rosen; past presidents, Alexander MacDonald and Frederick H. Carr; councilors, Philip E. Ardanuy, Elizabeth J. Austin, CCM, Andrea J. Bleistein, Carol Anne Clayson, John V. Cortinas, Jr., William E. Easterling, Tanja E. Fransen, Laura K. Furgione, David Gochis, Sue Ellen Haupt, James L. Kinter, Kevin R. Petty, Nicole Riemer, and Alan R. Sealls, CBM, Adam H. Sobel; commissioners, Donna Charlevoix, William P. Mahoney, Maureen McCann, CBM and CCM, Robert M. Rauber, Yvette Richardson, and Bruce Telfeyan.

The Bulletin of the American Meteorological Society (ISSN 0003-0007) is published monthly by the American Meteorological Society, 45 Beacon St., Boston, MA 02108-3693. Periodical postage paid at Boston, MA, and at additional mailing offices. Subscription price to members is included in annual dues. Subscription price to nonmembers is available on request; single issues are $12.50 each for members, $20 for nonmembers (prices incl. shipping and handling). Address all business communications to the Executive Director, AMS, 45 Beacon St., Boston, MA 02108-3693 (617-227-2425). POSTMASTER: Send address changes to Bulletin of the American Meteorological Society, 45 Beacon St., Boston, MA 02108-3693.

© Copyright 2017, American Meteorological Society (AMS). Permission to use figures, tables, and brief excerpts from this journal in scientific and educational work is hereby granted, provided source is acknowledged. Any use of the material in this journal that is considered to be "fair use" under Section 107 or that satisfies the conditions specified in Section 108 of the U.S. Copyright Law (17 USC, as revised by P.L. 94-553) does not require the Society's permission. Items that do not bear their own separate copyright notices either are in the public domain or are U.S. Government works for which copyright protection is not available. Republication, systematic reproduction, and any other use of any material in this journal, unless exempted by the above statements, requires written permission or license from the AMS. Additional details are provided in the AMS Copyright Policies, available from the AMS at 617-227-2425 or amspubs@ametsoc.org. "American Meteorological Society," the Seal of the American Meteorological Society, and the AMS Seal of Approval are registered trademarks of the American Meteorological Society.

NOWCAST

45 BEACON

DEPARTMENTS

3D HAIL MODELING

How laser scanning technology will lead to better hail detection, forecasting, and damage mitigation, in Giammanco et al. (p. 1341).

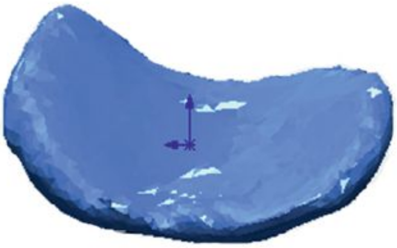

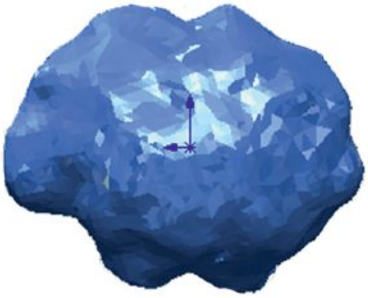

LETTER FROM THE EDITOR: BOILING POINT OF THE MIND

Some numbers are iconic. For a baseball fan, it might be 56, the number of games in Joe DiMaggio's untouchable hitting streak. For a traveling salesman, perhaps it's 53.5, the reimbursement rate in cents per mile of business driving.

For us, there are plenty of candidates. Maybe it's 9.8 (in °C per km, the dry adiabatic lapse rate), 23.5 (in degrees, the declination of Earth with respect to the orbital plane), or 26.5 (in °C, the sea surface temperature threshold for tropical cyclone formation).

None of them is better than plain 100, the °C boiling point of water. Maybe it doesn't come to mind first because it's so easy and so widely known. More significantly, maybe it's because the boiling point is a relative value, depending on atmospheric pressure. Not everyone lives at standard atmospheric pressure.

In fact, it's a lot harder to pin down the boiling point than most people realize. Sam Miller's article (p. 1485) shows that computing the boiling temperature of water at different atmospheric pressures using four different methods will yield four different results. The differences in bias and error are perhaps minor for practical purposes, but not for physical science.

That might be disturbing for those of us for whom numbers help isolate facts and order our experience. But numbers still abound in this issue—numbers that might set your mind aboil all the same. Here are a few that jumped out at me:

200: the number for the distance, in meters, that a surface observing station should be situated away from ordinary, 20-m-tall trees. There are a lot of places, particularly in the eastern United States, in which this distance is a truly limiting parameter for mesonets. Good locations for stations at 30 km or smaller intervals are not easy to find. Mahmood et al. (p. 1349) make clear that the miraculous growth of mesonets in the past few decades has depended on clearing innumerable scientific, fiscal, practical, and political hurdles.

212.7: the median number of hours of precipitation it took to trigger a flooding event in the database compiled by Shen et al. (p. 1493). The database covers the contiguous United States and combines U.S. Geological Survey stream gauge data with radar data tracking the precipitation. The total number of floods in the 11-year database is a mind-boggling 542,092.

20: the percent of NSF-funded field program principal investigators who had at least 30 years of experience since their Ph.D.'s. That's a distinguished set of people, but as Avallone and Baeuerle (p. 1333) show, there's a flip side to the increasing trend in experience level. In some ways it is more difficult than ever for early career scientists to serve as PIs in field programs. Likewise, this trend may be slowing the increase in the number of women who have been PIs (so far, only 24 out of the total 190).

For each reader, different numbers will rise to the top. They will fix ideas in your mind and, hopefully, transition you to a different phase of thinking.

—*Jeff Rosenfeld,* Editor-in-Chief

ABSTRACTS

A 20-YEAR HISTORY OF NSF-SUPPORTED ATMOSPHERIC SCIENCE FIELD CAMPAIGNS: STATISTICS AND DEMOGRAPHICS

Over the past two decades, the National Science Foundation's Division of Atmospheric and Geospace Sciences (AGS) has funded nearly 200 atmospheric science–related field campaigns that have included deployment of AGS-sponsored observing facilities. These projects have spanned the range from modest, single-investigator experiments to massive, multi-investigator, multiagency campaigns. They have occurred both domestically and abroad, on every continent and over most oceans. In this article, we present an analysis of some of the details about these campaigns, including such elements as deployment location and cost of the campaign, and of statistics related to the principal investigators (e.g., type and location of institution, gender, years since degree). In addition, we assess trends in field campaign cost. These results provide a retrospective view of atmospheric science field work that has been supported since 1992. (*Page 1333*)

USING 3D LASER SCANNING TECHNOLOGY TO CREATE DIGITAL MODELS OF HAILSTONES

The emergence of 3D scanning technologies has provided a new opportunity to explore the shape characteristics of hailstones in great detail. The ability to effectively map the shape of hailstones will improve assessments of hailstone aerodynamic properties, how their density relates to their strength, and how radar energy is scattered. Ultimately, 3D scanning of hailstones will contribute toward research in hail detection, forecasting,

and damage mitigation of severe hail, which accounts for well over $1 billion in annual insured losses.

The use of a handheld 3D laser scanner in a field setting was explored during field campaigns in 2015 and 2016. Hailstones were collected following thunderstorm passages and were measured, weighed, and scanned. The system was successful in capturing 3D models of more than 40 hailstones. A full scan takes approximately 3 minutes to complete, and data can be captured at a resolution of 0.008 cm. It is believed this is the first time such a system has been used to produce 3D digital hailstone models. Analysis of the model data has shown that hailstones depart from spherical shapes as they increase in diameter, and that bulk density and strength show little correlation. While the dataset presented here is small, the use of 3D scanners in the field is a practical method to obtain detailed datasets on hailstone characteristics. In addition, these data could be used to 3D-print hailstones to explore their aerodynamics, to produce cavity molds for ice impact tests, and for modeling radar scattering properties of natural hailstone shapes. (*Page 1341*)

MESONETS: MESOSCALE WEATHER AND CLIMATE OBSERVATIONS FOR THE UNITED STATES

Mesoscale in situ meteorological observations are essential for better understanding and forecasting the weather and climate and to aid in decision-making by a myriad of stakeholder communities. They include, for example, state environmental and emergency management agencies, the commercial sector, media, agriculture, and the general public. Over the last three decades, a number of mesoscale weather and climate observation networks have become operational. These networks are known as mesonets. Most are operated by universities and receive different levels of funding. It is important to communicate the current status and critical roles the mesonets play.

Most mesonets collect standard meteorological data and in many cases ancillary near-surface data within both soil and water bodies. Observations are made by a relatively spatially dense array of stations, mostly at subhourly time scales. Data are relayed via various means of communication to mesonet offices, with derived products typically distributed in tabular, graph, and map formats in near–real time via the World Wide Web. Observed data and detailed metadata are also carefully archived.

To ensure the highest-quality data, mesonets conduct regular testing and calibration of instruments and field technicians make site visits based on "maintenance tickets" and prescheduled frequencies. Most mesonets have developed close partnerships with a variety of local, state, and federal-level entities. The overall goal is to continue to maintain these networks for high-quality meteorological and climatological data collection, distribution, and decision-support tool development for the public good, education, and research. (*Page 1349*)

OBSERVING AND PREDICTING THE 2015/16 EL NIÑO

The El Niño of 2015/16 was among the strongest El Niño events observed since 1950 and took place almost two decades after the previous major event in 1997/98. Here, perspectives of the event are shared by scientists from three national meteorological or climate services that issue regular operational updates on the status and prediction of El Niño–Southern Oscillation (ENSO). Public advisories on the unfolding El Niño were issued in the first half of 2015. This was followed by significant growth in sea surface temperature (SST) anomalies, a peak during November 2015–January 2016, subsequent decay, and its demise during May 2016. The life cycle and magnitude of the 2015/16 El Niño was well predicted by most models used by national meteorological services, in contrast to the generally overexuberant model predictions made the previous year. The evolution of multiple atmospheric and oceanic measures demonstrates the rich complexity of ENSO, as a coupled ocean–atmosphere phenomenon with pronounced global impacts. While some aspects of the 2015/16 El Niño rivaled the events of 1982/83 and 1997/98, we show that it also differed in unique and important ways, with implications for the study and evaluation of past and future ENSO events. Unlike previous major El Niños, remarkably above-average SST anomalies occurred in the western and central equatorial Pacific but were milder near the coast of South America. While operational ENSO systems have progressed markedly over the past several decades, the 2015/16 El Niño highlights several challenges that will continue to test both the research and operational forecast communities. (*Page 1363*)

OVER 5,000 YEARS OF ENSEMBLE FUTURE CLIMATE SIMULATIONS BY 60-KM GLOBAL AND 20-KM REGIONAL ATMOSPHERIC MODELS

An unprecedentedly large ensemble of climate simulations with a 60-km atmospheric general circulation model and dynamical downscaling with a 20-km regional climate model has been performed to obtain probabilistic future projections of low-frequency local-scale events. The climate of the latter half of the twentieth century, the climate 4 K warmer than the preindustrial climate, and the climate of the latter half of the twentieth century without historical trends associated with the anthropogenic effect are each simulated for more than 5,000 years. From large ensemble simulations, probabilistic future changes in extreme events are available directly without using any statistical models. The atmospheric models are highly skillful in representing localized extreme events, such as heavy precipitation and tropical cyclones. Moreover, mean climate changes in the models are consistent with those in phase 5 of the Coupled Model Intercomparison Project (CMIP5) ensembles. Therefore, the results enable the assessment of probabilistic change in localized severe events that have large uncertainty from internal variability. The simulation outputs are open to the public as a database called "Database for Policy Decision Making for Future Climate Change" (d4PDF), which is intended to be utilized for impact assessment studies and adaptation planning for global warming. (*Page 1383*)

ARCTIC RADIATION-ICEBRIDGE SEA AND ICE EXPERIMENT (ARISE): THE ARCTIC RADIANT ENERGY SYSTEM DURING THE CRITICAL SEASONAL ICE TRANSITION

The National Aeronautics and Space Administration (NASA)'s Arctic Radiation-IceBridge Sea and Ice Experiment (ARISE) acquired unique aircraft data on atmospheric radiation and sea ice properties during the critical late summer to autumn sea ice minimum and commencement of refreezing. The C-130 aircraft flew 15 missions over the Beaufort Sea between 4 and 24 September 2014. ARISE deployed a shortwave and longwave broadband radiometer (BBR) system from the Naval Research Laboratory; a Solar Spectral Flux Radiometer (SSFR) from the University of Colorado Boulder; the Spectrometer for Sky-Scanning, Sun-Tracking Atmospheric Research (4STAR) from the NASA Ames Research Center; cloud microprobes from the NASA Langley Research Center; and the Land, Vegetation and Ice Sensor (LVIS) laser altimeter system from the NASA Goddard Space Flight Center. These instruments sampled the radiant energy exchange between clouds and a variety of sea ice scenarios, including prior to and after refreezing began. The most critical and unique aspect of ARISE mission planning was to coordinate the flight tracks with NASA Cloud and the Earth's Radiant Energy System (CERES) satellite sensor observations in such a way that satellite sensor angular dependence models and derived top-of-atmosphere fluxes could be validated against the aircraft data over large gridbox domains of order 100–200 km. This was accomplished over open ocean, over the marginal ice zone (MIZ), and over a region of heavy sea ice concentration, in cloudy and clear skies. ARISE data will be valuable to the community for providing better interpretation of satellite energy budget measurements in the Arctic and for process studies involving ice–cloud–atmosphere energy exchange during the sea ice transition period. (*Page 1399*)

THE SAHARAN AEROSOL LONG-RANGE TRANSPORT AND AEROSOL–CLOUD INTERACTION EXPERIMENT: OVERVIEW AND SELECTED HIGHLIGHTS

North Africa is the world's largest source of dust, a large part of which is transported across the Atlantic to the Caribbean and beyond where it can impact radiation and clouds. Many aspects of this transport and its climate effects remain speculative. The Saharan Aerosol Long-Range Transport and Aerosol–Cloud-Interaction Experiment (SALTRACE; www.pa.op.dlr.de/saltrace) linked ground-based and airborne measurements with remote sensing and modeling techniques to address these issues in a program that took place in 2013/14. Specific objectives were to 1) characterize the chemical, microphysical, and optical properties of dust in the Caribbean, 2) quantify the impact of physical and chemical changes ("aging") on the radiation budget and cloud microphysical processes, 3) investigate the meteorological context of transatlantic dust transport, and 4) assess the roles of removal processes during transport.

SALTRACE was a German-led initiative involving scientists from Europe, Cabo Verde, the Caribbean, and the United States. The Falcon research aircraft of the Deutsches Zentrum für Luft- und Raumfahrt (DLR), equipped with a comprehensive aerosol and wind lidar payload, played a central role. Several major dust outbreaks were studied with 86 h of flight time under different conditions, making it by far the most extensive investigation on long-range transported dust ever made.

This article presents an overview of SALTRACE and highlights selected results including data from transatlantic flights in coherent air masses separated by more than 4,000-km distance that enabled measurements of transport effects on dust properties. SALTRACE will improve our knowledge on the role of mineral dust in the climate system and provide data for studies on dust interactions with clouds, radiation, and health. (*Page 1427*)

DIURNAL VARIATION OF TRMM/LIS LIGHTNING FLASH RADIANCES

This study provides, for the first time, an analysis of the climatological diurnal variations in the lightning flash radiance data product ε from the Tropical Rainfall Measuring Mission Lightning Imaging Sensor (TRMM/LIS). The ε values over 13 years (2002–14), and over a global scale (~38°S–38°N), reveal novel and remarkably consistent regional and seasonal patterns as a function of the local solar time (LST). In particular, the diurnal variation of ε (over both continental and oceanic regions) is characterized by a monotonic increase from late afternoon (~2000 LST), attaining a maximum around 0900 LST, followed by a decreasing trend. The continental (oceanic) ε values reach a broader minimum spanning from ~1500 to 1900 LST (~1800 to 2000). The relative diurnal amplitude variation in continental ε is about 45%, compared to about 15% for oceanic ε. This study confirms that the results are not affected by diurnal biases associated with instrument detection or other statistical artifacts. Notable agreement is shown between the diurnal variations of ε and the global-scale (~38°S–38°N) mesoscale convective system areal extent. Comparisons with recently published diurnal variations of cloud-to-ground lightning peak current over the United States also exhibit a marked similarity. Given the novelty of these findings, a few tentative hypotheses about the underlying physical mechanism(s) are discussed. (*Page 1453*)

RECENT ADVANCES IN SATELLITE DATA RESCUE

To better understand the impacts of climate change, environmental monitoring capabilities must be enhanced by deploying additional and more accurate satellite- and ground-based (including in situ) sensors. In addition, reanalysis of observations collected decades ago

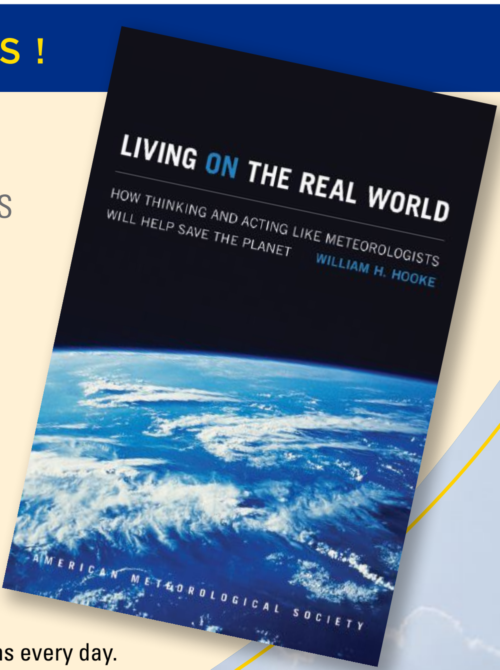

but long forgotten can unlock precious information about the recent past. Historical, in situ observations mainly cover densely inhabited areas and frequently traveled routes. In contrast, large selections of early meteorological satellite data, waiting to be exploited today, provide information about remote areas unavailable from any other source. When initially collected, these satellite data posed great challenges to transmission and archiving facilities. As a result, data access was limited to the main teams of scientific investigators associated with the instruments. As archive media have aged, so have the mission scientists and other pioneers of satellite meteorology, who sometimes retired in possession of unique and unpublished information.

This paper presents examples of recently recovered satellite data records, including satellite imagery, early infrared hyperspectral soundings, and early microwave humidity soundings. Their value for climate applications today can be realized using methods and techniques that were not yet available when the data were first collected, including efficient and accurate observation simulators and data assimilation into reanalyses. Modern technical infrastructure allows serving entire mission datasets online, enabling easy access and exploration by a broad range of users, including new and old generations of climate scientists. (*Page 1471*)

METHODS FOR COMPUTING THE BOILING TEMPERATURE OF WATER AT VARYING PRESSURES

Boiling is an extreme form of evaporation that occurs when the saturation vapor pressure is equal to the total atmospheric pressure. This paper computes boiling temperature by four different methods and compares the results to data provided in the *CRC Handbook of Physics and Chemistry.* The first method utilizes a constant value for the latent heat of vaporization (l_v) in the Clausius–Clapeyron equation, and the second method uses a previously published temperature-dependent linear function for l_v. A third method is suggested that begins by deriving a new second-order function for l_v, and then applies this function in an error-reduction loop to determine boiling temperature as a function of pressure. This method for computing boiling temperature shows a mean bias of 0.31°C between mean sea level pressure and 100 hPa and a mean error of less than a tenth of a percent, which is a significant improvement over both of the first two methods. The fourth method uses a fifth-order polynomial, eliminating l_v and making pressure the independent variable, which is used to compute boiling temperature with a mean bias of 0.25°C and a mean error of 0.09% for pressures between mean sea level pressure and 100 hPa. (*Page 1485*)

A COMPREHENSIVE DATABASE OF FLOOD EVENTS IN THE CONTIGUOUS UNITED STATES FROM 2002 TO 2013

Notwithstanding the rich record of hydrometric observations compiled by the U.S. Geological Survey (USGS) across the contiguous United States (CONUS), flood event catalogs are sparse and incomplete. Available databases or inventories are mostly survey- or report-based, impact oriented, or limited to flash floods. These data do not represent the full range of flood events occurring in CONUS in terms of geographical locations, severity, triggering weather, or basin morphometry. This study describes a comprehensive dataset consisting of more than half a million flood events extracted from 6,301 USGS flow records and radar-rainfall fields from 2002 to 2013, using the characteristic point method. The database features event duration; first- (mass center) and second- (spreading) order moments of both precipitation and flow, flow peak and percentile, event runoff coefficient, base flow, and information on the basin geomorphology. It can support flood modeling, geomorphological and geophysical impact studies, and instantaneous unit hydrograph and risk analyses, among other investigations. Preliminary data analysis conducted in this study shows that the spatial pattern of flood events affected by snowmelt correlates well with the mean annual snowfall accumulation pattern across CONUS, the basin morphometry affects the number of flood events and peak flows, and the concentration time and spreadness of the flood events can be related to the precipitation first- and second-order moments. (*Page 1493*)

CORRECTION

In the May issue of *BAMS,* the time period reported in the AMS Giving Program Donor Roster was incorrect. The roster recognizes those who supported the AMS Giving Program from January 1, 2016, through December 31, 2016.

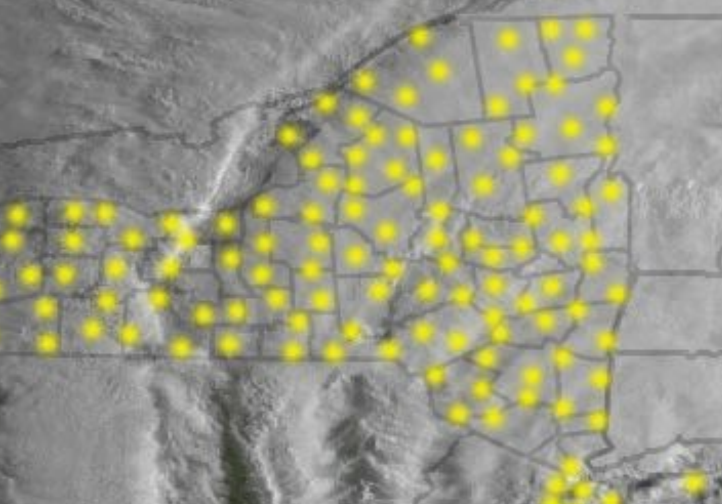

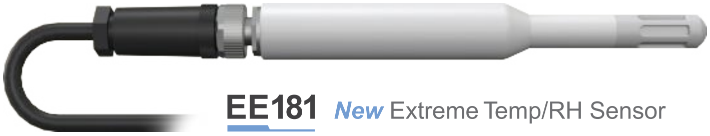

NOWCAST

NEWS AND NOTES

Do Changing Atlantic Ocean Temperatures Affect Pacific Cyclones?

Two years ago, Christina Patricola, Ping Chang, and R. Saravanan of Texas A&M University determined that sea surface temperatures (SSTs) in parts of the Pacific Ocean could suppress Atlantic Ocean hurricane activity by as much as 50%. More recently, the same researchers decided to look into a reverse effect, and they discovered that Atlantic SSTs are in fact influencing Pacific storms, as well. Those findings were recently published in *Geophysical Research Letters*.

The scientists utilized cyclone data for the years 1950–2015 as well as simulations of idealized climate cycles using the Weather Research and Forecasting Model in a tropical channel mode. They found that warming Atlantic SSTs lead to fewer and less powerful tropical cyclones in the eastern Pacific, while cooler SSTs in the Atlantic lead to more eastern Pacific cyclone activity and stronger storms.

The researchers determined that these dynamics are driven by the Atlantic meridional mode (AMM) with its pattern of increasing and decreasing SSTs in the Atlantic Ocean. In its positive phase, the AMM generates uncommonly warm SSTs in the northern tropics and lower midlatitudes and cool SSTs in the southern tropics, strengthening Atlantic hurricanes; the negative phase, with cool SSTs in the north and warmer waters in the south, stifles cyclones. The new study reveals that the AMM can have similar—but opposite—effects in the eastern Pacific basin, quashing cyclone seasons during positive phases and fueling them during negative phases. The authors discovered in both their simulations and observations that vertical wind shear in the eastern Pacific increased during the AMM's positive phase, suppressing cyclones there. This is similar to the effect of warm SSTs in the tropical Pacific, which increase wind shear over the Atlantic and cut down hurricane formation there.

The researchers note that the new study could help to improve the accuracy of seasonal tropical cyclone forecasting.

Seafloor Topography Influences Deep Ocean Circulation

In 1966, noted oceanographer Walter Munk theorized that deep ocean water is brought back to the surface by small-scale ocean turbulence in the form of internal gravity waves breaking beneath the ocean's

FOR CLOUD RESEARCH, JUST POINT AND CLICK

What's the best way to see into a cloud? Most of our knowledge about cloud properties comes from satellite observations, but the information these provide can be limited, since they are unable to show slight differences in cloud thickness and extent—which can influence how much light the clouds reflect. This is especially true for cumulus humilis—or "fair weather"—clouds, which form and disperse rapidly and often are very small and difficult to detect. A new study published in the *Journal of Geophysical Research: Atmospheres* has found a simple solution to the problem of cloud observations: a digital camera. Researchers used a commercially available camera to take images of cumulus humilis and other optically thin clouds over north-central Oklahoma in a period of 7 minutes. They created a time series of photos, taken from a distance of about 2 kilometers, enabling a resolution of 4 centimeters, which is 3–5 orders of magnitude finer than satellites can produce. A pixel-by-pixel analysis of the images was able to reveal significant variations in the structure of the clouds, including their radiance and optical depth. Since those measurements indicate how much light the clouds scatter as well as how much they allow to pass through, respectively, this new technique of looking at clouds could lead scientists to a better understanding of cloud physics, which in turn could help improve climate models.

surface and moving among different density layers in the water. The amount of water transported is tremendous—approximately 107 cubic meters per second—and the mixing power created by the breaking internal gravity waves that would be necessary to push that deep water back to the surface would be equivalent to about 10 incandescent light bulbs per cubic kilometer of ocean. So what parts of the ocean generate that kind of turbulence? In a new study published in *Nature Geoscience,* researchers believe underwater topography is the key.

The study dates back to 2009 in the Southern Ocean, when the scientists "released a blob of dye, like a drop of milk in a coffee cup, and let the ocean mix it around," explains study coauthor Raffaele Ferrari of MIT. They sampled this tracer over a two-year period to learn more about ocean water mixing, and discovered that very little mixing—or turbulence—occurred where the ocean had few topographic features. But when the tracer encountered seamounts and ridges, "all of a sudden, it started to spread in the vertical quite fast, at three times the rate predicted by Munk," Ferrari explains.

To uncover the source of this mixing, the researchers created a numerical model that incorporated all the external forces in the Southern Ocean region, including wind patterns, solar heating, evaporation, and precipitation. After adding data from their tracer research, they modeled the turbulence for the entire ocean region while accounting for the undersea topography—an enormous challenge, as they were uncertain the model's resolution would be sufficient to describe the comparatively miniscule tracer's motions in such a vast body of seawater.

"I did some preliminary calculations, back of the envelope estimates, and realized we would have just enough resolution to be able to do it," recalls MIT postdoctoral student Ali Mashayek, the study's lead author.

Their modeled tracer mimicked the movement of the tracer they observed, spreading vertically at a similar rate as the real tracer. In the model, the tracer became entrapped in areas with rough topography that included features like seamounts and ridges, mixing vertically before eventually swirling through calmer waters to the surface.

"In the abyssal ocean, you have 4,000-meter sea mountains and very deep troughs, up and down, and these topographic features help create turbulence," Ferrari explains. "What seems to be emerging is that water comes back up from the abyss by spending a lot of time in these places where turbulence is really strong."

According to the researchers, over extended periods all of this turbulence may equal the amount of mixing predicted by Munk, and as a result may explain how deep ocean waters rise to the surface. A better understanding of this process can help researchers calculate how long carbon is stored deep in the ocean before coming back to the surface and being reintroduced to the atmosphere.

"The general understanding is that abyssal waters take [a] few to several thousand years to resurface," Mashayek says. "If a considerable amount of such upwelling occurs rapidly along sloped boundaries, continental margins, and midocean ridges, then the time scale of recycling of abyssal waters can be shorter." [Source: MIT]

New Study Finds Droughts Can Migrate

While most might think of droughts as being stationary, new research published in *Geophysical Research Letters* reveals that some droughts actually migrate thousands of kilometers, "like a slow-motion hurricane on a time scale of months to years instead of days to weeks," says the study's lead author, Princeton University graduate student Julio Herrera-Estrada. The finding could aid in planning for future droughts by improving the forecast of their development and endurance.

Researchers utilized the Climate Forecast System Reanalysis model to study soil moisture from around the world for the years 1979–2009. They identified more than 1,400 droughts and located "hotspots" where multiple droughts followed similar paths (for example, from south to north in the southwestern United States). They found that about 10% of the droughts they analyzed traveled between 1,400 and 3,100 kilometers, and that "the droughts that travel the farthest are amongst the ones that last the longest, which in turn, tend to be the most intense ones," Herrera-Estrada explains.

The researchers discovered that droughts moved at different speeds depending on the continent, and in some cases stopped completely for a period of time before starting to move again. They found that North American droughts that do migrate travel about 500 miles in 16 months. The most recent migrating drought they found started in 2008 in Russia and Ukraine and moved 1,700 kilometers to the northeast over almost a year, traveling through parts of Kazakhstan before stalling in northwest Russia.

"People haven't really thought of droughts in this way," Herrera-Estrada notes.

The scientists plan more research to determine the reason for the movement of droughts, although they speculate that a land–atmosphere feedback mechanism could be responsible: A drought-afflicted region has less water available for evaporation, which leads to less precipitation falling downwind from the drought area, thus producing drought conditions in the downwind region. An additional possible explanation is the slight shifting of a weather pattern such as a high pressure system, which could "pull" a drought along with it as it moves. [Sources: International Institute for Applied Systems Analysis, weather.com, Thomson Reuters]

Freshwater Contributes to Hurricane Intensification

While traveling over the ocean, tropical storms often encounter swirling bands of warm water known as eddies, which can give a hurricane extra strength through enhanced and sustained heat and moisture fluxes. A new study has found that freshwater deposited by rivers into the ocean can affect the dynamics of these eddies and make them even more effective in intensifying storms. The findings were published in the *Journal of Geophysical Research: Oceans*.

A group of scientists used 55 oceanic profilers during a 2014 aircraft study to measure a large warm core eddy and the Caribbean Current in the eastern Caribbean Sea, as well as instrumented airborne tubes to measure near-surface atmospheric conditions above the eddy. The oceanic data collected included temperature and salinity of the eddy and background flow, upper-ocean stratification, velocity structure, and characteristics of the water mass and a residing barrier layer within the eddy.

They discovered that brackish water flowed out from the Amazon and Orinoco rivers and created a freshwater barricade known as a barrier layer that settled within the eddy. Normally, a tropical storm passing over an eddy would cause cooler water to be pulled up toward the surface, but according to lead author Johna Rudzin, a Ph.D. student at the University of Miami, "the unique part about the barrier layer is it reduces the efficiency of bringing that cooler water to the surface. When the hurricane tries to mix the upper ocean, it would be much more difficult because of the freshwater input."


The Weather and Climate of Texas
weatherwise
PHOTO CONTEST
The East Coast Blizzard of 2016
weatherwise
DOES LIGHTNING GO DOWN OR UP?
Sitting Down with AccuWeather's Joel Myers

This results in even more ideal conditions for the growth of the hurricane passing over the eddy. Last year, Hurricane Matthew rapidly intensified after passing near a warm ocean eddy located near where the measurements for this study were taken. Rudzin noted that it's possible a barrier layer could have played a role in that storm's growth, although more observations are necessary to be certain.

"We've seen barrier layers elsewhere like [in] the western Pacific and in the tropical Atlantic, but what's striking here is how the barrier layer tends to arrest mixing, much the same way that strong currents inhibit mixing processes," says coauthor Nick Shay of the University of Miami. "There is not much sea surface temperature cooling."

The researchers believe their study represents the first observations of a barrier layer within a warm core eddy. [SOURCE: *The Palm Beach Post*]

CONFERENCE NOTEBOOK

HOUSTON FLOODS—HOW ARE PEOPLE DYING, AND WHAT CAN WE DO ABOUT IT?

Flooding continues to be the most deadly weather hazard in and around Houston. This became quite evident from May 2015 through May 2016 when 19 people died from flooding, mostly during two separate flash flood emergencies. Despite the accurate and timely warnings, all but one of these deaths were directly related to vehicles. To better understand how the weather enterprise could improve its life-safety mission, a thorough examination of flood deaths around the Houston area since 1994 was conducted.

Between 1994 and 2016, there were 61 flood-related fatalities in the Houston metropolitan area, including 56 drownings, 2 heart attacks, and 3 electrocutions. Most of the fatalities occurred in cars, with 39 of the 56 drownings related to vehicles, followed by 11 people walking in or moving around on flooded water. Since Tropical Storm Allison in 2001, all but one known flood death in Houston possibly could have been avoided had the person stayed where they were located when the flooding began. This study suggests the normal messaging of *"move to* *higher ground"* and *"turn around, don't drown"* (TADD) may not adequately combat the flood deaths in the nation's fourth largest city. Most of the vehicle deaths occurred in underpasses, after dark, when the depth of water at the bottom of an underpass is most difficult to discern while driving. In addition, the terrain is flat with very few areas of true "higher ground."

Using these data, the NWS is working with a team of media, emergency managers, public safety officials, and transportation decision-makers in formulating a multitiered messaging campaign to combat flood deaths in the Houston area. While TADD remains an important message for those already on the roads, the lack of terrain and very few deaths occurring in homes or businesses suggest people would be much safer staying in place. Therefore we are exploring other messaging, such as *"stay put, stay dry, stay alive–unless told to leave."* We are also exploring messaging and education efforts on escaping a rapidly sinking car as several drownings occurred because people stayed in their cars. Finally, given the large variance in flooding around Houston, the team is examining the utility to decision-makers and the media of a 5-tiered flood warning system.—Jeffry Evans (NOAA/NWS), L. Wood, D. Reilly, and J. Lindner, "Houston floods— How are people dying, and what can we do about it?" presented at the Fifth Symposium on Building a Weather-Ready Nation: Enhancing Our Nation's Readiness, Responsiveness, and Resilience to High Impact Weather Events, 22-26 January 2017, Seattle, Washington.

Tropical Cyclone Prediction and Predictability: Advances and Challenges

Of all the scientific predictions that are made, hurricane forecasts are probably the most consequential. Lives and livelihoods are saved or lost depending on the quality of the forecasts. Consequently, much effort has been expended to improve hurricane prediction and, as a result, errors in forecasts of hurricane tracks have decreased over the past four-and-a-half decades. This success can be traced to improvements in observations, hurricane models, methods of incorporating observations into models, and also to the increasing skill with which the flow near hurricanes is forecast.

In stark contrast to hurricane track forecasts, predictions of

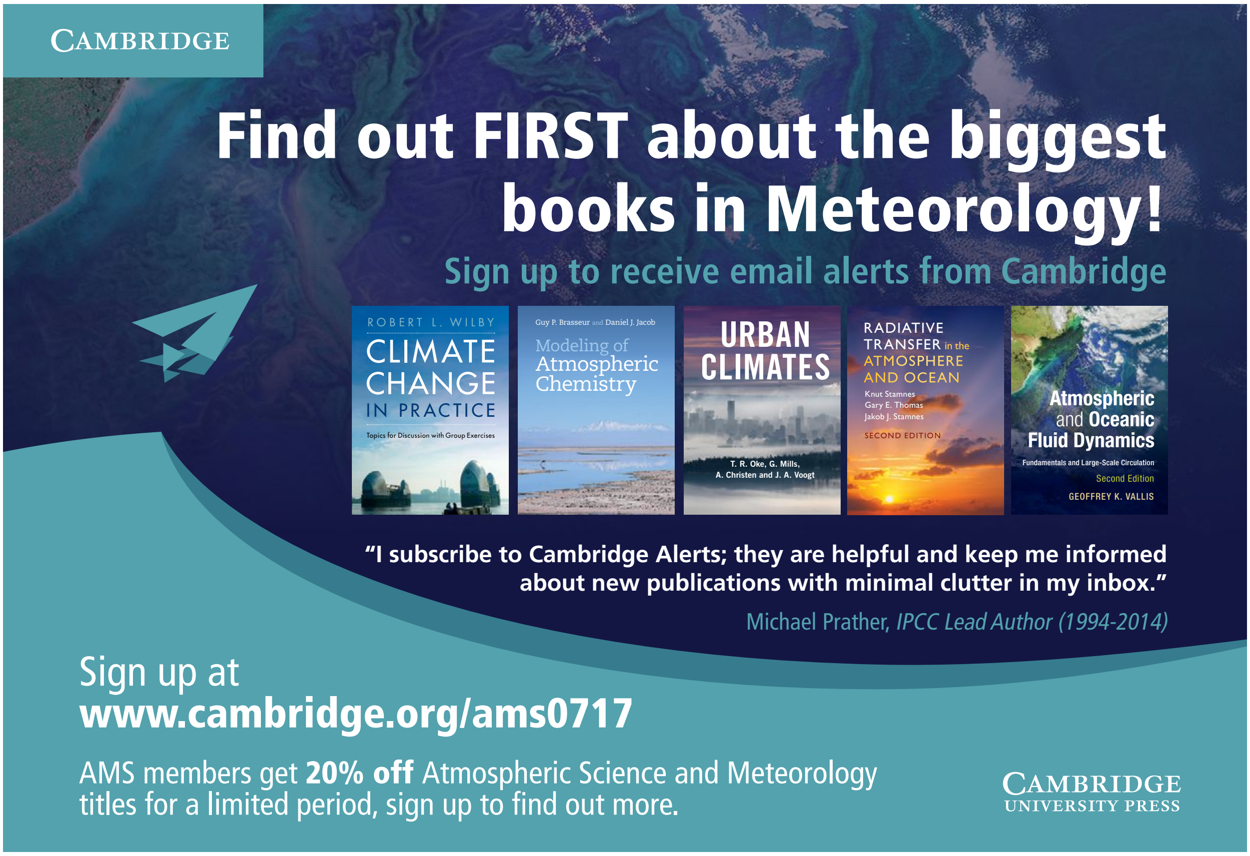

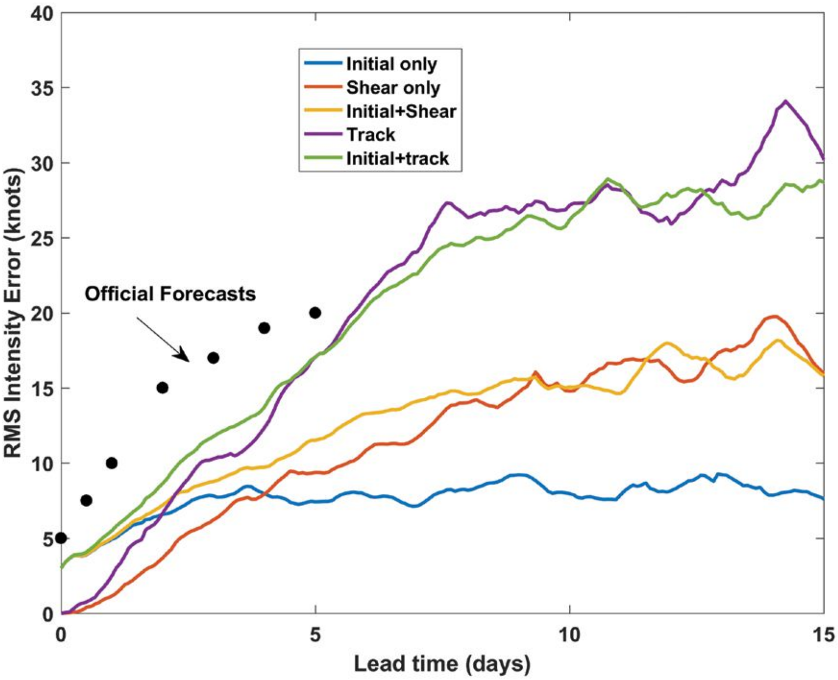

Growth of hurricane wind speed errors (in knots) as a function of forecast time in days. The blue curve shows what happens when the only error is a 3-knot error in the initial hurricane wind speed; the red curve shows errors resulting from errors in forecast wind shear along the hurricane's path; the yellow curve shows what happens when both of the above errors are considered; the purple curve shows errors due only to errors in forecasts of the hurricane's path; and the green curve shows errors due to all of the above. This last, green curve shows our best estimate of what we could do today if our hurricane models were perfect but we still had imperfect measurements and forecasts of large-scale atmospheric conditions. The black dots show current errors in official National Hurricane Center forecasts.

hurricane wind speeds have shown little improvement since records began more than 45 years ago. Why? Our research focused on three sources of error: Inaccurate specification of the initial state of the atmosphere including the hurricane, errors in forecasting the environment through which the hurricane is forecast to move, and errors in forecasting the track of the storm. We assumed that the hurricane model itself is perfect, giving us an estimate of how well we could do if we had better models.

We found that errors in wind speed forecasts out to 3 days are due mostly to incorrect specification of the hurricane itself, including its wind structure and the moisture content of its eyewall. The eyewall moisture is particularly challenging because it is difficult to measure, but we showed that it can be indirectly inferred from careful measurements of the rate of intensification of the hurricane.

Beyond 3 days, intensity errors result mostly from errors in the forecast of the hurricane track and the environment through which it moves.

Our most important result is that there is still a wide gap between the skill with which we could forecast hurricane winds, given the current quality of observations and forecasts of the large-scale atmospheric and oceanic environment, and the actual skill of current forecasts. Thus by improving hurricane models, and the methods by which we incorporate observations into those models, we could make big improvement in hurricane wind forecasts, even if we did not continue to improve observations and forecasts of the hurricane environment. Doing all three might yield greatly improved hurricane forecasts out to 5 days and beyond.—Kerry Emanuel (MIT), and F. Zhang, "Tropical cyclone prediction and predictability: Advances and challenges," presented at the Second Symposium on Multi-scale Atmospheric Predictability, 22-26 January 2017, Seattle, Washington.

Source Attribution of Black Carbon and its Radiative Forcing in China

When wood or coal is burned, black carbon (BC, a.k.a. soot) is one of the by-products. Though soot particles can be fine and powdery, they can have a large effect on the environment. Local and nonlocal sources of soot have different influences on radiative forcing—changing the Earth's energy balance—in its destination region. In China, for example, air quality becomes poor because of an increase in tiny atmospheric particles from rapid urban and economic growth in recent years. When more cars hit the road or people use more appliances (powered by coal-generated electricity), more of these particles are released into the atmosphere. But just how much influence these particles from one region have on the air quality of neighboring areas has been uncertain, until now.

Our research used simulations of the Community Earth System Model with emissions for the years 2010–14 and a BC source-tagging technique to quantify the source attribution for mass concentration, haze formation, transport of BC, and its direct radiative forcing in China. They found that in regions with high emissions (e.g., northern and southern China), local emissions predominantly contributed to BC concentrations, while nonlocal emissions more strongly influenced BC over central and western China, which have lower emissions.

The study showed that during polluted days, nonlocal sources played an important role in increasing regional BC concentrations. In the winter haze season, more than 50% of surface BC in China originated from emissions in north China, which contributed more than 90% to local BC and a substantial amount to south, southwest, and central-west China.

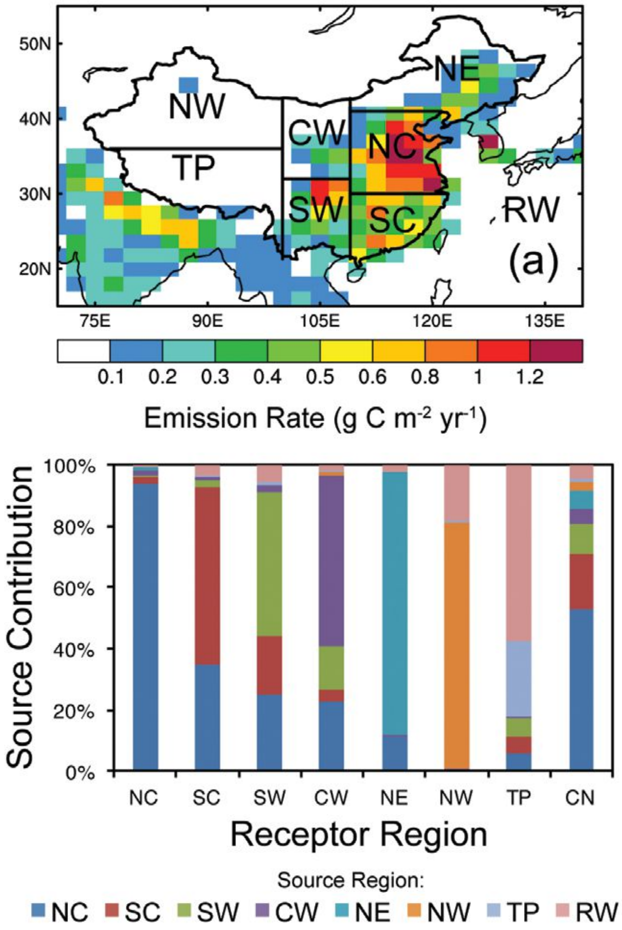

***Top:* Spatial distribution of BC emissions averaged over the years 2010–14 and the defined source regions (NC: north China, SC: south China, SW: southwest China, CW: central-west China, NE: northeast China, NW: northwest China, TP: Tibetan Plateau, and RW: rest of the world).**

***Bottom:* Source attribution of wintertime BC surface concentration in China (CN) and the seven smaller regions.**

The study also showed that local emissions accounted for 65% of BC direct radiative forcing (i.e., atmospheric heating) in China, while emissions from inside and outside China are equally important for BC outflow from East Asia that affects BC over the Pacific Ocean and the western United States. Emissions from China accounted for 8% of BC concentration and 29% of the total air column load of BC in the western United States in spring.

Due to its warming effect in the climate system, BC is potentially important for climate mitigation, and its source attribution is equally important to understand its impacts locally and regionally.—Yang Yang (Pacific Northwest National Laboratory), H. Wang, S. J. Smith, P.-L. Ma, and P. J. Rasch, "Source attribution of black carbon and its direct radiative forcing in China," presented at the 19th Conference on Atmospheric Chemistry, 22-26 January 2017, Seattle, Washington.


AccuWeather
esri
Scintec
CKHEED MARTIN
NORTH
AMS
600
50
INEERING

PAPERS OF NOTE

MECHANISMS CONTRIBUTING TO THE TUG HILL LAKE-EFFECT SNOWFALL MAXIMUM

The Tug Hill Plateau (hereafter Tug Hill), which rises ~500 meters above the eastern shore of Lake Ontario, is well known as one of the snowiest locations in the eastern United States and as a hub for winter recreation. Much of this distinction is rooted in its location east of Lake Ontario, which generates frequent lake-effect snowstorms that extend downstream, producing some of the most intense snowstorms in the world. Tug Hill receives the brunt of this snowfall, with accumulations more than twice as high as the surrounding lowlands. Heavy lake-effect snowfall inundated Tug Hill on 11–12 December 2013, producing 101.5 centimeters (40 inches) of snow over the upper plateau in just 24 hours—a snowstorm intensely observed during the Ontario Winter Lake-effect Systems (OWLeS) field project. Our study uses observations collected during this event, in conjunction with Weather Research and Forecasting (WRF) Model simulations, to examine the nonorographic and orographic mechanisms responsible for the Tug Hill precipitation maximum.

A key contributor to precipitation enhancement over Tug Hill was a land-breeze front that formed along Lake Ontario's southeastern shoreline and extended obliquely across the lake-effect system. The land-breeze front separated warmer, lake-modified air from cooler, continental air that passed through the lowlands south of Lake Ontario, avoiding lake modification. Localized ascent along this boundary contributed to an inland precipitation maximum even in simulations in which Tug Hill was removed, and contributed to a shift in the orientation of the banded lake-effect precipitation maximum as the band extended inland across Tug Hill and into the western Adirondacks. Orographic effects still contributed to enhanced precipitation, however, as flow impinging on the convex windward slope of Tug Hill intensified and broadened the ascent region, increasing parameterized depositional and accretional hydrometeor growth, and reducing sublimational losses over the high terrain.

To our knowledge, the contribution of the land-breeze front to precipitation enhancement over Tug Hill has not been recognized previously. Prior studies over the Great Lakes highlight the role of land-breeze convergence in the initiation and organization of lake-effect convection, but do not describe the complex configuration of land-breeze fronts produced by the unique shoreline geometry of Lake Ontario, and their impacts inland over Tug Hill. Given that most lake-effect events over Tug Hill feature broadly similar large-scale conditions, it is likely that land-breeze fronts similar to those discussed in our study contribute to precipitation enhancement in other events over Tug Hill, while the orographic effects identified may contribute to a broader

FLYING THE UNFRIENDLY SKIES WITH A CHANGING CLIMATE

As if air travel isn't uncomfortable enough already, new research has found that increasing atmospheric CO_2 levels could cause more severe turbulence in the North Atlantic flight corridor. Focusing on an area at an elevation of about 39,000 feet over the North Atlantic that has heavy air traffic, and limiting the study to wintertime (when turbulence is strongest), Paul Williams of the University of Reading ran two climate model simulations—one with preindustrial levels of CO_2, and the second with twice that amount. To determine turbulence frequency, he examined 21 indicators of air turbulence levels related to wind—such as air flow direction and wind speed—and compared the results for each simulation. He discovered that all degrees of turbulence increased along with the CO_2 levels, from a 59% upsurge in light turbulence to, more notably, a 149% increase in the more harmful severe turbulence. "We're particularly interested in severe turbulence, because that's the kind of turbulence that's strong enough to hospitalize people," Williams says. The study, which was published in *Advances in Atmospheric Sciences*, expands upon 2013 research that Williams coauthored, and attributes the increase in bumpiness to changes in the jet stream due to rising amounts of CO_2. Warming temperatures near Earth's surface are expected to change the atmospheric slope between the equator and the poles, which would then lead to a stronger jet stream and a subsequent increase in wind patterns that cause turbulence. Williams plans to study other flight routes in future research. [SOURCE: *The Washington Post*]

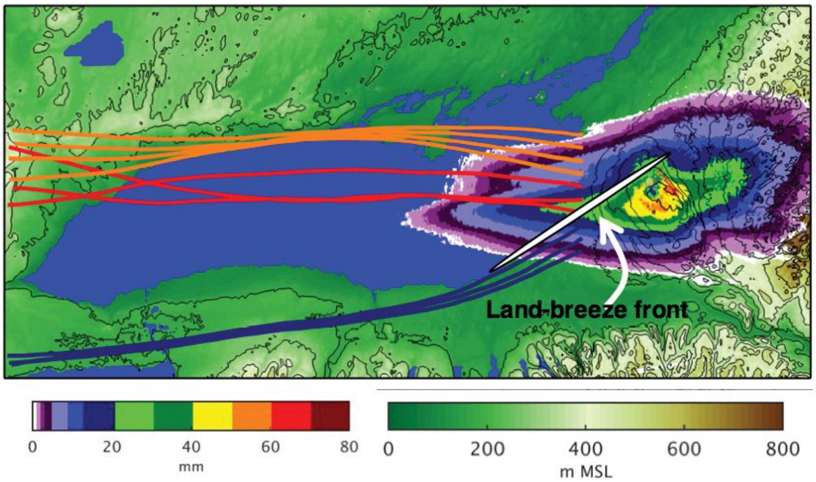

Schematic diagram of the land-breeze front (white line), superimposed on the radar-derived precipitation accumulations from 0300–2200 UTC 11 Dec 2013 (shaded following the color bar at the bottom left). Colored lines depict air parcel trajectories ending on the lowest model level at 1800 UTC 11 Dec. Trajectory color represents the amount of warming the parcel undergoes (blue=least, red=most, orange=moderate). Terrain is shaded following the color bar at the bottom right and is contoured at 100-meter intervals.

spectrum of events with and without land-breeze fronts.

Future work should extend this analysis to other events and utilize idealized simulations to better understand the interplay between land-breeze and orographic forcings during lake-effect events over Lake Ontario and other bodies of water.—Leah S. Campbell (University of Utah), and W. J. Steenburgh, "The OWLeS IOP2b lake-effect snowstorm: Mechanisms contributing to the Tug Hill precipitation maximum," in the July *Monthly Weather Review.*

QUANTIFYING THE DEPENDENCE OF SATELLITE CLOUD RETRIEVALS ON INSTRUMENT UNCERTAINTY

Clouds significantly affect Earth's radiation budget, having a net

Why aren't you using it?

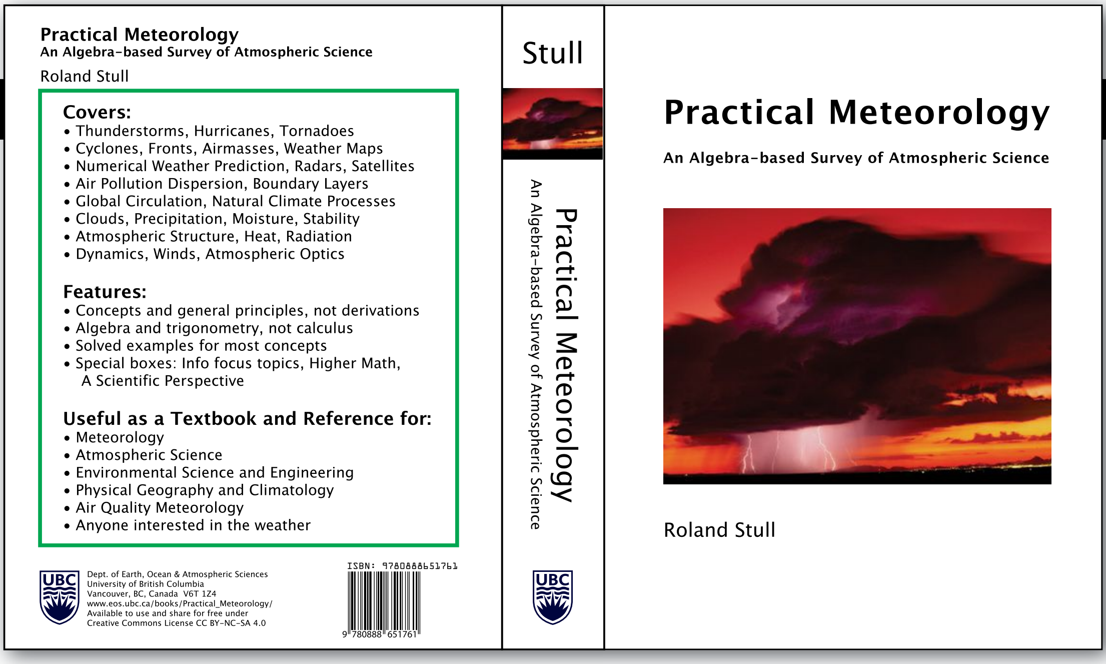

Practical Meteorology
An Algebra-based Survey of Atmospheric Science
Roland Stull

Covers:
- Thunderstorms, Hurricanes, Tornadoes
- Cyclones, Fronts, Airmasses, Weather Maps
- Numerical Weather Prediction, Radars, Satellites
- Air Pollution Dispersion, Boundary Layers
- Global Circulation, Natural Climate Processes
- Clouds, Precipitation, Moisture, Stability
- Atmospheric Structure, Heat, Radiation
- Dynamics, Winds, Atmospheric Optics

Features:
- Concepts and general principles, not derivations
- Algebra and trigonometry, not calculus
- Solved examples for most concepts
- Special boxes: Info focus topics, Higher Math, A Scientific Perspective

Useful as a Textbook and Reference for:
- Meteorology
- Atmospheric Science
- Environmental Science and Engineering
- Physical Geography and Climatology
- Air Quality Meteorology
- Anyone interested in the weather

Dept. of Earth, Ocean & Atmospheric Sciences
University of British Columbia
Vancouver, BC, Canada V6T 1Z4
www.eos.ubc.ca/books/Practical_Meteorology/
Available to use and share for free under
Creative Commons License CC BY-NC-SA 4.0

ISBN: 9780888651761

Stull
Practical Meteorology
An Algebra-based Survey of Atmospheric Science

Practical Meteorology
An Algebra-based Survey of Atmospheric Science
Roland Stull

It is free online for everyone worldwide, with no advertising. Find it here:
https://www.eoas.ubc.ca/books/Practical_Meteorology/
Over 28,000 downloads of chapter pdfs by students, instructors & professionals from 113 countries last year.
Written by Prof. R. Stull, Certified Consulting Meteorologist, Fellow of the AMS, Fellow of CMOS, CFII.

cooling effect on the climate system. But cloud response to Earth's warming climate is one of the largest sources of uncertainty among global climate model projections. Our research focused on how more stringent instrument calibration requirements reduce the time needed to constrain cloud property uncertainties and, in turn, uncertainties in cloud feedback and anthropogenic radiative forcing. Climate models generally agree that the net cloud feedback is positive but disagree on its magnitude.

We estimated relationships among global, decadal trends in cloud properties (cloud fraction, optical thickness, and effective temperature), equilibrium climate sensitivity (ECS), and shortwave and longwave cloud feedback. In doing so our analysis provided the first direct link between satellite instrument calibration requirements and their impact on constraints on ECS and detection times of global cloud properties. We also related trends in water cloud effective radius to trends in radiative forcing (ERFaci) to demonstrate how more accurate instrument calibration could reduce the uncertainty in aerosol indirect effect several decades sooner than operational instruments.

We used cloud properties retrieved by the Clouds and the Earth's Radiant Energy System (CERES) Cloud Property Retrieval System, which uses measurements from the Moderate Resolution Imaging Spectroradiometer (MODIS). Detecting trends in climate variables on decadal scales requires highly accurate, stable measurements and retrieval algorithms. Trend detection time depends on the trend magnitude, natural variability, and instrument and retrieval algorithm uncertainty, the relationship among which is represented by a climate uncertainty framework used in this study. This framework was used to demonstrate how more accurate reflected solar and infrared satellite measurements shorten the time it takes to constrain cloud property trend uncertainties by several decades, particularly for total cloud optical thickness, effective temperature, and water cloud effective radius.

Different cloud types have varied radiative impacts on the climate system depending on several attributes, such as their thermodynamic phase, altitude, and optical thickness. Therefore, conducting these studies by cloud types would be a valuable extension of this work. Combining the trend uncertainty analysis with the radiative impact of different cloud types would help to prioritize among requirements for future satellite sensors and understanding the climate detection capabilities of existing sensors. Additionally, time varying algorithm uncertainties and biases may also contribute to climate change–scale cloud property trend uncertainties and can extend trend detection times. Such uncertainties should also be estimated and, if possible, reduced. Such studies will become increasingly important within the current U.S. and global challenge to appropriate sufficient resources for climate change monitoring.—Yolanda L. Shea (NASA Langley Research Center), B. A. Wielicki, S. Sun-Mack, and P. Minnis, "Quantifying the dependence of satellite cloud retrievals on instrument uncertainty," in a forthcoming issue of the *Journal of Climate.*

Contribution of Urban Surface Expansion to Regional Warming in Beijing

Beijing, the capital of China, is located in one of three city clusters in eastern China that have high economic vitality. With the rapid economic development and population explosion, marked urban surface expansion occurred in Beijing between the 1980s and 2010s. The contribution of urban surface expansion to regional warming as detected from meteorological observational station data may vary with considerable uncertainty because of the spatial heterogeneity of such data—a situation that promotes a requirement for numerical model-based investigations. Satellite-based images from 1980 to 2016 that have fine resolution over the three city clusters and show the urban surface expansion in China from rapid economic development and anthropogenic activity were used to perform a 37-year nested dynamical downscaling using the Weather Research and Forecasting (WRF) Model to quantify this contribution to regional warming.

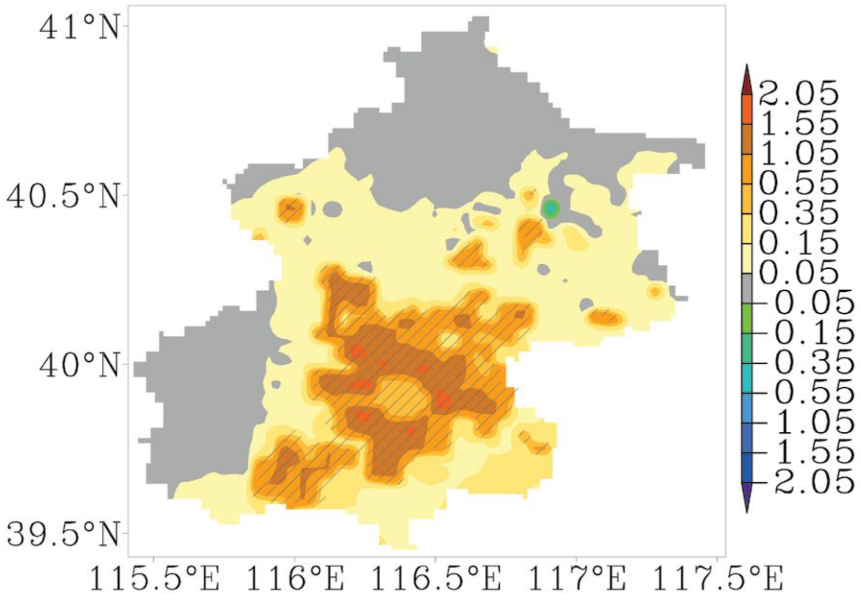

Spatial distributions of annual averaged urban-related warming (°C) between 1980 and 2016 in Beijing. Shaded areas passed the 90% confidence-level *t* test.

The 37-year area-averaged annual urban-related warming across the whole Beijing area was 0.25°C. The contribution of land-use changes to the globally averaged surface air temperature (SAT) trend is unlikely to be more than 10%. However, the contribution of urban surface expansion to regional warming was approximately 22% of the overall warming in Beijing. The diurnal temperature range (DTR) in Beijing in summer decreased by −0.27°C.

The contributions to land-use grids that changed from nonurban (in 1980) to urban (in 2016; N2U) were much stronger than those to grids that were classified as urban in both time periods (U2U), which were closer to the values of urban areas (including N2U and U2U) because of the intense increase in urban surface areas. Urban-related warming expressed marked annual variation and was greater in the warm seasons and lesser in the cold seasons. The greater increase in SAT minimum and the weaker SAT maximum accounted for the decreased DTR.

Because of the special geographic characteristics for the plains areas of Beijing in the southeastern region and surrounding mountain areas in the northwestern region, respectively accounting for approximately 62% and 38% of the total area, urban-related warming was mainly concentrated in the plains areas. The 37-year area-averaged annual urban-related warming in the plains areas of Beijing was 0.52°C. The contribution of urban surface expansion to regional warming was approximately 42% in the plains areas of Beijing. The DTR in summer there decreased by −0.71°C.

In addition to urban surface expansion, other aspects, such as building density and height, aerosol emissions, and anthropogenic heat release, are not covered in our study because of the difficulties in monitoring as well as large uncertainties. Therefore more studies are necessary.—Deming Zhao (Chinese Academy of Sciences), and J. Wu, "Contribution of urban surface expansion to regional warming in Beijing, China," in the June *Journal of Applied Meteorology and Climatology.*

A 20-Year History of NSF-Supported Atmospheric Science Field Campaigns

Statistics and Demographics

Linnea M. Avallone and Brigitte Baeuerle

Over the past two decades, programs in the National Science Foundation (NSF) Division of Atmospheric and Geospace Sciences (AGS) have funded nearly 200 atmospheric science-related field campaigns that have included deployment of AGS-supported observing facilities. These projects have spanned the range from modest, single-investigator experiments to massive, multi-investigator, multi-agency campaigns. They have occurred both domestically and abroad, on every continent and over most oceans. In this article, we present an analysis of some aspects of these campaigns as well as statistics related to principal investigator demographics.

The data presented here were compiled from historical records maintained by the various facility managers that included dates and locations of field campaigns as well as information about the facilities deployed. Details of funding, both in support of the facilities used for the field campaign and the science associated with it, were obtained from NSF's internal records. Only proposals funded for participation in a field activity were considered; proposals funded subsequent to a campaign (e.g., for data analysis or synthesis, modeling) were not included. Typically, these proposals were three-year awards that covered preparation for the field campaign, execution of the field phase, and initial data quality control and analysis. All costs have been normalized to 2009 dollars, based on Office of Management and Budget tables.[1] Demographic data on principal investigators (gender, year of highest degree) were determined from information in the public domain, such as an individual's professional web page, professional society sites, or LinkedIn.

AFFILIATIONS: Avallone—Division of Atmospheric and Geospace Sciences, National Science Foundation, Arlington, Virginia; Baeuerle—Earth Observing Laboratory, National Center for Atmospheric Research, Boulder, Colorado
CORRESPONDING AUTHOR: Linnea Avallone, lavallon@nsf.gov

DOI:10.1175/BAMS-D-15-00222.1

OBSERVING FACILITIES AND DEPLOYMENTS. The Lower Atmosphere Observing Facilities (LAOF) supported by NSF AGS between 1992 and 2015 are listed in Table 1. Note that few of these facilities were available for the entire period discussed in this article; some have been acquired or added, while others have been retired. This evolution of the deployable assets reflects both the natural life cycle of facilities and the changing needs of the observations community.

Since 1992, NSF AGS has supported, all or in part, 199 field projects. Complete funding data were available for all but seven of these campaigns. The vast majority of projects were funded by the Physical and Dynamic Meteorology (PDM) program or its predecessors (91), with an additional 30 supported by the Atmospheric Chemistry program. The remainder were distributed among Climate and Large-Scale Dynamics, Aeronomy, Solar-Terrestrial Physics, Ocean Sciences, Polar Programs, and various special initiatives.

The maps in Figs. 1 and 2 illustrate the deployment locations, domestic and international, respectively, associated with these field campaigns. Only the primary base of operations for each project is noted, not regions covered by aircraft flights or mobile ground-based campaigns. While deployment sites are

---

[1] Table 10.1, available at https://obamawhitehouse.archives.gov/sites/default/files/omb/budget/fy2017/assets/hist10z1.xls.

Table 1. NSF AGS–supported facilities, 1992–2015.

Facility	Operator	Dates as a facility	# of uses (1992–2015)
Radar			
CHILL[a]	Colorado State University	1990–present	29
S-band Dual Polarization Doppler Radar (S-Pol)	NCAR/EOL[b]	1995–present	16
Doppler on Wheels (DOW)	Center for Severe Weather Research	2008–present	15
CP-2, CP-3, CP-4	NCAR/EOL	1975–95	3
Electra Doppler Radar (ELDORA)[c]	NCAR/EOL	1992–2012	14
Wyoming Cloud Radar (WCR)[d]	University of Wyoming	2004–present	15
HIAPER Cloud Radar (HCR)	NCAR/EOL	2015–present	3
Aircraft			
Lockheed C-130Q	NCAR/EOL	1993–present	38
Lockheed Electra L-188	NCAR/EOL	1975–99	18
Gulfstream V[e]	NCAR/EOL	2005–present	27
Beechcraft King Air B200T	NCAR/EOL	1982–92	8
Beechcraft King Air B200T	University of Wyoming	1987–present	49
North American Sabreliner NA-265–60	NCAR/EOL	1968–92	3
T-28	South Dakota School of Mines and Technology	1987–2004	12
WB-57F	NCAR/EOL	1995–97	1

reasonably well-distributed throughout the United States, there are some areas of concentration that reflect the predominant locations for certain types of phenomena under study. For example, the U.S. Central Plains is frequently chosen for experiments involving severe weather, while the California coast allows access to the marine environment. International deployments have been concentrated in the Western Hemisphere, with a smattering in Europe and Asia. Generally speaking, this is related to ease and safety of deployment, rather than about the presence or lack of interesting phenomena to study. NSF-funded field campaigns in Africa are notably lacking. Although several have been proposed in recent years, logistical complexity, high cost, and safety concerns have prevented these projects from being selected.

FIELD CAMPAIGN COSTS. Figure 3 (left) shows the combined total cost of each funded field campaign since fiscal year 1992. These values include the costs of both deploying the supported facilities and those that are directly associated with the science of the field campaign, borne by the science programs. All values have been normalized to 2009 dollars, as noted above. These same data are shown as a histogram in Fig. 3 (right) to illustrate that the majority of campaigns (~62%) cost less than one million dollars ($1M). Nonetheless, slightly more than 10% of funded campaigns in this time period cost in excess of $5M and 1.5% exceeded $10M. The most expensive study carried out in the 1992–2015 time frame was Tropical Ocean and Global Atmosphere Coupled Ocean–Atmosphere Response Experiment (TOGA COARE); the remainder of the "top 10 list" is presented in Table 2.

There is a sense among NSF program officers and LAOF facility managers that atmospheric science field campaigns have grown more complex and more expensive over time. While it is difficult to objectively assess "complexity," which can include factors such as number of participants or facilities, deployment location, number of funding agencies involved,

TABLE 1. (continued)

Facility	Operator	Dates as a facility	# of uses (1992–2015)
Aircraft Instrumentation			
GPS dropsondes[f]	NCAR/EOL	1995–present	28
HIAPER Airborne Instrumentation Suite (HAIS)[g]	NCAR/EOL	2005–present	24
Wyoming Cloud Lidar (WCL)	University of Wyoming	2010–present	9
Surface, Sounding and Profiling Systems			
Atmosphere Surface Turbulence Exchange Research (ASTER)[h]	NCAR/EOL	1990–98	5
GPS Advanced Upper Air Soundings (GAUS)[i]	NCAR/EOL	1999–2014	45
Integrated Surface Flux System (ISFS)	NCAR/EOL	2000–present	22
Integrated Sounding System (ISS)	NCAR/EOL	1992–present	45
Portable Automated Mesonet (PAM I, II, III)[j]	NCAR/EOL	1976–99	13
Tethered Atmospheric Observing System (TAOS)	NCAR/EOL	2000–04	1

[a] Can be requested as a facility through 2017.

[b] National Center for Atmospheric Research Earth Observing Laboratory; formerly Atmospheric Technology Division.

[c] Originally flown on NCAR Electra, then on NRL P-3.

[d] On either University of Wyoming King Air or C-130.

[e] Also known as High Performance Instrumented Airborne Platform for Environmental Research (HIAPER).

[f] Now under the name Airborne Vertical Atmospheric Profiling System (AVAPS).

[g] A suite of 14 instruments built in conjunction with the acquisition of the Gulfstream V aircraft; used on both the G-V and C-130 aircraft.

[h] Capabilities now part of Integrated Surface Flux System.

[i] Previously known as CLASS; can no longer be requested as a facility.

[j] Capabilities now part of Integrated Surface Flux System.

number of scientific objectives, etc., the normalized cost data do allow us to look at the expense of projects. The median cost of field campaigns for each fiscal year was computed and is plotted in Fig. 4, along with a linear fit line ($r^2 = 0.34$) that indicates growth in cost of approximately $61,000 per year, resulting in nearly a quintupling of the median cost over 20 years. The high median costs in a few years skew this trend, but they do not necessarily correlate with years in which the most expensive field campaigns were supported; rather, there is an absence of low-cost (<$100,000) studies. Removing the values for the five highest-cost years results in a trend ($r^2 = 0.32$) of $25,000 per year. By comparison, a linear fit to the annual mean of field campaign funding over time (not shown here) yields an increase of about $62,500 per year ($r^2 = 0.25$), similar to the value obtained from the median. This suggests that occasional very expensive campaigns are not making a large contribution to the calculated trend. Nonetheless, the interannual variability is quite large, so any conclusions about the magnitude of the increased cost of field campaigns over time are difficult to draw.

PRINCIPAL INVESTIGATORS. Demographic data were compiled for the people listed as principal investigators (PIs) on each of the 199 field projects. Most projects had more than one PI or lead scientist, identified through their coordination of the lead scientific proposal, science planning document, or lead author of the main campaign publication. PIs of individual grant proposals associated with projects

Fig. 1. U.S. deployments of NSF AGS observing facilities, 1992–2015.

Fig. 2. International deployments of NSF AGS facilities, 1992–2015.

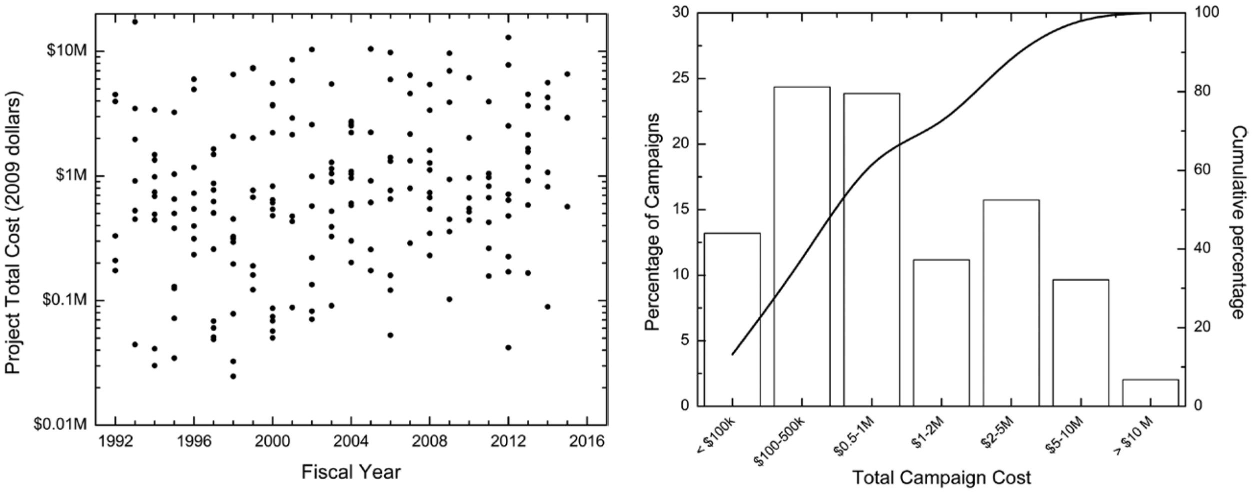

Fig. 3. (left) Total field campaign cost (science plus deployment), adjusted to 2009 dollars. Note logarithmic cost scale. (right) Distribution of field campaign costs.

Table 2. Top 10 most expensive field campaigns, 1992–2015.

Name	Year	Program[a]	Cost in 2009 dollars
Tropical Ocean and Global Atmosphere Coupled Ocean–Atmosphere Response Experiment (TOGA COARE)	1992	CLD, OCE	$17,253,233
Dynamics of the Madden–Julian Oscillation (DYNAMO)	2012	CLD, OCE	$12,931,861
Rain in Cumulus over the Ocean (RICO)	2005	PDM	$10,460,807
International H_2O Project 2002 (IHOP_2002)	2002	PDM	$10,335,917
Megacities Impact on Regional and Global Environment (MIRAGE)	2006	ATC	$9,799,864
VAMOS Ocean-Cloud-Atmosphere-Land Study (VOCALS)	2009	CLD	$9,656,752
Verification of the Origins of Rotation in Tornadoes Experiment (VORTEX2)	2009	PDM	$9,648,119
Asian Pacific Regional Aerosol Characterization Experiment (ACE-ASIA)	2001	ATC, OCE	$8,573,218
Southern Oxidant and Aerosol Study (SOAS)	2013	ATC	$8,059,815
Deep Convective Clouds and Chemistry (DC3)	2012	ATC, PDM	$7,776,950

[a] ATC = Atmospheric Chemistry; CLD = Climate and Large-Scale Dynamics;
PDM = Physical and Dynamic Meteorology; OCE = Ocean Sciences (not including ship time costs).

were not enumerated. Among the 327 PIs, there were 190 unique investigators; of these, only 24 were female. It was not possible to reliably determine race or ethnicity based on the data available, so minority status is not reported here. PIs were distributed across 70 different institutions or organizations. Not surprisingly, the majority (51) of these were doctoral institutions (40 R1 and 11 R2).[2] The remainder came from four master's schools (3 M1 and 1 M3), three baccalaureate colleges, seven small businesses, one Federally Funded Research and Development Center (FFRDC), two U.S. Government laboratories, one

---

[2] According to the Carnegie Classification of Institutions of Higher Education—see http://carnegieclassifications.iu.edu/classification_descriptions/basic.php.

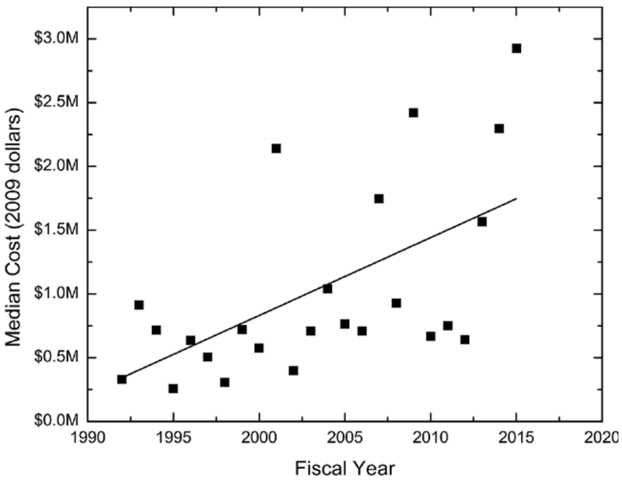

Fig. 4. Median field campaign cost (in 2009 dollars) per fiscal year. The linear fit suggests an increase of approximately $61,000 per year in costs.

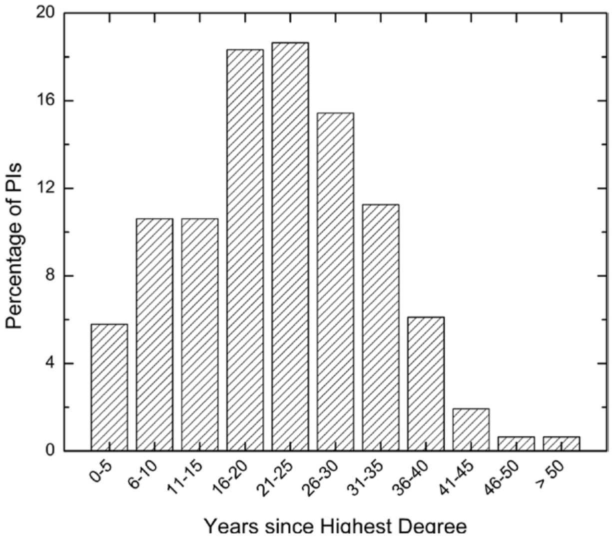

Fig. 5. Distribution of PI experience for 311 PIs.

nonprofit, and one four-year engineering-focus school. However, more than half of PIs represent just 11 institutions: National Center for Atmospheric Research (NCAR, 42 PIs); University of Colorado (10); University of Washington (9); University of Wyoming (8); University of Oklahoma (7); Colorado State University (6); University of Utah (6); University of Nevada, Reno/Desert Research Institute (5); The Pennsylvania State University (5); University of Illinois (5); and University of Miami (5). The western U.S. university focus is curious, but we do not know the reason for it. The presence of three facility provider institutions in this list (NCAR, University of Wyoming, and Colorado State University) reflects both the leading role that scientists from those organizations play in their fields and also the funding of numerous test or small exploratory campaigns originating from facility-affiliated scientists.

A long-standing concern in the atmospheric and related sciences that there is a shortage of researchers trained in observational science prompted us to look at the experience level of scientists proposing successful field campaigns, based on years since highest degree (generally the Ph.D.). Figure 5 shows a histogram of the distribution of PI experience, binned in 5-yr increments. Only about 16% of PIs can be considered early career (≤10 years since degree), while nearly 20% have more than 30 years of experience since receiving their degrees. The relatively small number of early career PIs is not surprising, given that leadership of field campaigns can be a high-risk activity that is discouraged in the pre-tenure years. If, instead, the average PI experience (that is, the average of the experience of all PIs on a campaign) is distributed, the shape of the histogram is quite similar, with 12% of campaigns having a PI team with an average of 10 years' experience or less. This suggests that partnering of junior PIs with more senior ones is not very common, even though that might be a way to reduce the risk to an early career scientist and for less experienced researchers to gain valuable mentoring.

In Fig. 6, the data from Fig. 5 are broken down by gender. The distribution of experience among the female PIs is much more compact than that of male PIs, most likely reflecting the more recent entry of substantial numbers of women into the atmospheric sciences (see data in Hartten and LeMone 2010). Interestingly, though, substantially higher percentages of younger women than men have successfully led field campaigns in the past two decades.

Finally, we look at whether there is a trend in PI experience with time. Figure 7 shows the average years since degree of PIs for field campaigns conducted since 1993. Although the correlation is not terribly strong ($r^2 = 0.58$), there does appear to be a trend of increasing years of experience with time. This might be attributed to the idea that, once successful, PIs successfully propose further in later years. However, this increasing experience with time runs somewhat counter to expectations, given that more, collectively less experienced, women are entering the field. Recalling the trend toward more expensive (and perhaps more complex) field campaigns, we note that

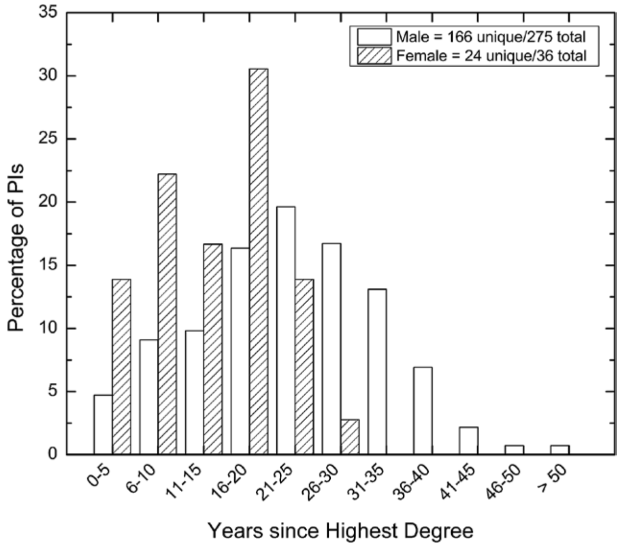

Fig. 6. Distribution of PI experience by gender. The numbers in the legend indicate the number of unique and total PIs; the total sample size is the same as in Fig. 5.

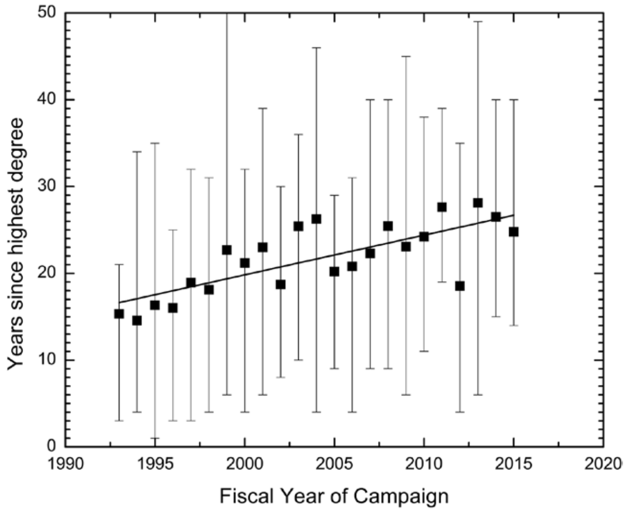

Fig 7. PI experience over time. The fit line implies an increase of experience of 0.5 years per year, or slightly more than 10 years over the 1992–2015 time period. Error bars indicate the range of PI experience for campaigns in each year.

there is no correlation between campaign cost and PI experience (not shown). While it is hard to know what the root cause of this trend is, it is worrisome that the population of field campaign PIs is aging.

In this short article, we have presented an analysis of some aspects of the past twenty years of NSF AGS-supported atmospheric science field campaigns to illustrate both general characteristics and possible trends. We have not attempted to quantify the results of these field campaigns in terms of publications or other outcomes; while interesting and valuable, that type of analysis is beyond our current data-gathering capabilities. It is important for the reader, and especially for anyone who might be planning to propose a field campaign, to realize that nothing presented here is intended as a guideline or constraint. Rather, we encourage early and direct communication with NSF program managers and LAOF providers to obtain advice about what is feasible. In particular, we note that many successful field campaigns have been funded only after revision and resubmission, building on feedback from the NSF merit review process and the facility request review conducted by the Observing Facilities Assessment Panel (OFAP). We anticipate that the creative and enterprising atmospheric sciences community will continue to execute exciting field campaigns well into the future.

ACKNOWLEDGMENTS. Disclaimer: Any opinions, findings, and conclusions or recommendations expressed in this material are those of the author(s) and do not necessarily reflect the views of the National Science Foundation.

FOR FURTHER READING

Hartten, L. M. and M. A. LeMone, 2010: The evolution and current state of the atmospheric sciences "pipeline." *Bull. Amer. Meteor. Soc.*, **91,** 942–956, doi:10.1175/2010BAMS2537.1.


Weather
STUDIES
Photo: Anupa Asokan


Ocean
STUDIES
Photo: Anupa Asokan


Climate
STUDIES
Photo: Jean-Baptiste Dodane


READ
IT
ON
ANY
DEVICE

Using 3D Laser Scanning Technology to Create Digital Models of Hailstones

Ian M. Giammanco, Benjamin R. Maiden, Heather E. Estes, Tanya M. Brown-Giammanco

3D LASER SCANNING AND HAIL. Hailstorms account for more than $1 billion in annual insured property losses, and their increasing trend seen over the past two decades has outpaced advances in observation, forecasting, and mitigation of hail damage (Changnon et al. 2009; Roeder 2012; Kunkel et al. 2013). In 2012, the Insurance Institute for Business and Home Safety (IBHS) began a comprehensive research program with the overarching goal to help mitigate property losses from severe hail. A component of this initiative included determining the properties of hailstones that must be accounted for in laboratory material impact tests such that the results of these standardized test methods would be reasonably predictive of real-world performance of building materials. Subsequently, this led to a field campaign to measure the physical and material properties of hail, and to explore emerging technologies to aid in this effort.

It is well known that hailstones are found in a variety of nonhomogeneous shapes and can have large protuberances, which makes characterizing their true shape difficult using conventional means (i.e., caliper or ruler). Obtaining an accurate volume through physical measurements is also difficult, even when measuring multiple dimensions. In the past, record-breaking hailstones were kept in cold storage so a cast could be made of the hailstone. The impact craters of giant hailstones have also been examined and molds made of their shapes, as well (Knight and Knight 2001). While the process is effective in capturing the hailstone shape, it is cumbersome and time-consuming. A method was needed that provided accurate 3D measurement data without substantial contamination or melting of the hailstone prior to strength testing. The finescale, nonhomogeneous nature of hailstones provided the motivation to investigate how 3D laser scanners could be applied toward hail research.

The emergence of 3D scanning technology has led to new research opportunities across a wide range of fields (e.g., medical, mechanical and civil engineering, archaeology, etc.) but with little application within physical meteorology. In the atmospheric sciences, measurement systems such as lidar, particle imagers, laser disdrometers, scintillometers, optical rain gauges, and visibility sensors come to mind when considering laser-based applications. These systems are focused on in situ measurement of atmospheric particles or rely on backscattered energy from these particles. For 3D laser scanners, most atmospheric particles are too small and their in situ collection is too difficult for a manually operated laser scanning system to be of use to map their shape. However, hailstones are large enough and their shape is complex enough for laser scans and the 3D models that are produced to be scientifically beneficial. Three-dimensional laser scanners are also efficient for collecting sizeable datasets to evaluate the complex shapes of hailstones. During field campaigns in 2015 and 2016, a handheld 3D laser scanner was used successfully by IBHS to collect full digital 3D models of hailstones. It is believed this is the first time this technology has been used in this manner.

AFFILIATIONS: Giammanco, Maiden, Estes, and Brown-Giammanco—Insurance Institute for Business and Home Safety, Richburg, South Carolina
CORRESPONDING AUTHOR: Ian M. Giammanco, igiammanco@ibhs.org

DOI:10.1175/BAMS-D-15-00314.1

EVOLUTION OF 3D SCANNER TECHNOLOGY. The development of scanning technology to obtain accurate and precise measurements of objects began in the 1960s with advances in computer technology. Optical methods proved to be much faster, did not require direct physical contact with specimens, and were well-suited for complex shapes. The foundational research that integrated both passive photogrammetric and active laser techniques was pioneered by the National Research Council of Canada (Mayer 1999). Modern systems apply an active laser and passive photogrammetric components to capture point-cloud data to produce the digitized 3D model. At each data point, the distance and angle from the object to the system is recorded in a scanner-relative coordinate system. For large objects, several footprints of data are needed to stitch together the full 3D shape. Processing algorithms assimilate these footprints and remove duplicate data. Most current systems connect the point-cloud data by applying a nonuniform rational basis (NURB) spline fit. The result is faceted polygons (typically triangles), which produces the 3D surface. With advancements in reducing the size and cost of electronic components, small, single-operator, handheld units have become less cost-prohibitive for a wide range of research projects, including field studies and commercial applications.

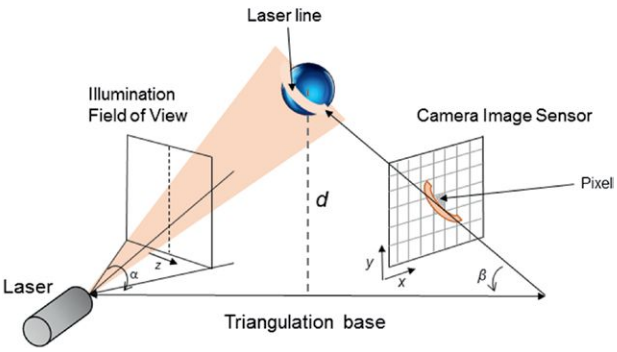

Fig. 1. Conceptual diagram of the laser, single-camera configuration, and triangulation coordinate system for a typical 3D laser scanning system, where *d* is the distance between the object and the scanner unit. Note that multiple cameras are used in hand-held systems, and the figure describes the configuration of one camera unit relative to the laser.

CAPABILITY SCOPING. The system selected to explore 3D scanning of natural hailstones was a handheld HandySCAN EXAscan system, manufactured by Creaform Inc. The system is a noncontact active scanner that employs a class II eye-safe laser to project a beam on a target. An array of cameras tracks the projected laser location, as shown in the conceptual diagram in Fig. 1. Its relatively small size, low weight (~1.5 kg), and simple operation by a single person made it ideal for use in a field vehicle, under

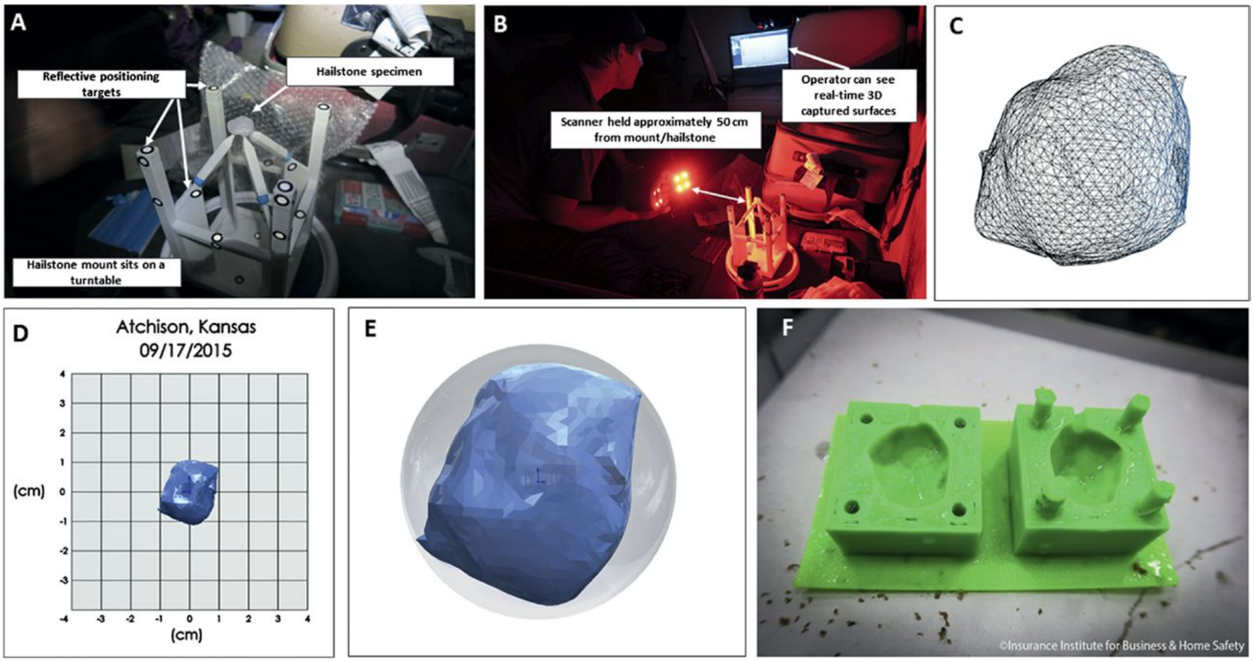

Fig. 2. (a and b) Photographs of the scanner in operation. The positioning targets, hailstone mount, and turntable are annotated; (c) the 3D faceted surface created by processing the collected point-cloud data; (d) the full 3D model of the first hailstone captured with this system; (e) comparison with a sphere of the same maximum diameter; and (f) the 3D-printed cavity mold of this hailstone.

nonoptimal conditions (Fig. 2a,b). To operate the unit, information must be simultaneously collected on the unit's position while it is scanning the specimen. Additionally, the unit must be calibrated prior to operation periods. The scanner is calibrated by using a plate with a grid of reflective targets, supplied by the manufacturer (reflective targets are identified in Fig. 2a,b). The precise dimensions and target locations of the plate are stored in the operating software, which is able to identify and adjust for any small bias errors. Small errors may result from temperature changes and the expansion and contraction of hardware components such that calibration is recommended prior to scanning sessions. The reflective positioning targets are also used to define the coordinate system with respect to the specimen being scanned. Targets are scanned separately (only one time) prior to data collection. The information is stored by the operating software and applied when scanning of the specimen is underway. The targets are adhered either to the specimen itself or to a mounting system such that the unit always has several positioning targets in its field of view (HandySCAN EXAscan requires at least three). If the minimum number of targets is not detected during data collection, the software will cease logging until they are identified to automatically avoid data gaps due to user error. The system has a trigger that toggles the laser projection, camera operation, and data collection.

The unit has a maximum configurable resolution of 0.008 cm, an accuracy of ±0.004 cm, and a maximum sampling rate of 25 kHz. It is tethered to a laptop computer running Creaform's VXelements software package to operate the scanner, view ongoing scans in real time, and store the data. The NURB spline-based polygon-mesh approach is used by VXelements to capture, process, and display the 3D data. The processed dataset can then be quality controlled to synthetically fill in missing data, remove other objects that may have been in the field of view, and filter spurious returns. Once the data have been processed, additional analyses can be performed on the digital model to extract more information on the characteristics of the hailstone. Data can also be exported in a .STL file format for use in standard CAD packages or other computational analysis tools.

LABORATORY ICE TESTING.

The EXAscan system's ability to detect and map ice surfaces was tested using ice spheres made with pure distilled water (very clear ice) and water with diffused carbon dioxide gas (bubble-filled, opaque ice). The ice spheres were then chipped or deformed to introduce small shape changes to evaluate the scanner's ability to detect these deformations. It was quickly discovered during initial testing that ice surfaces are difficult mediums to effectively scan. Clear ice surfaces and ice surfaces coated with a large amount of liquid water scattered the projected laser such that it was not well defined on the object surface. Subsequently, the photogrammetric camera tracking functionality could not resolve the true location of the projected laser. This resulted in large gaps in the digitized model. Performance was improved when opaque, bubble-filled ice was tested, but this required long scanning durations and revisiting scanned areas to capture a complete model. To reduce the amount of scatter, a light dusting of a fine powder (i.e., athlete's foot spray) was used, enabling the system to adequately track the projected beam and map the ice surfaces. At times, compressed air was also used to help remove any liquid water on the surface of the hailstone. Although this introduces a foreign substance onto the hailstone similar to an immersion test, compressive strength testing yielded no detectable influence between coated and uncoated laboratory ice spheres. The method is still more practical than immersion testing in a field setting, especially when considering substances used in past research (i.e., liquid mercury). During this initial testing, it was also determined that full scans can be completed in less than 1 min at low sampling resolutions, while higher resolution scans can take 2–3 min to complete. The length of time needed for a complete scan was determined to be suitable for a pilot field application to help mitigate the melting of stones while they were being scanned.

SCANNING HAILSTONES IN THE FIELD.

The scanner system was pilot tested in the field for the first time in 2015 to determine if it would be effective for use during the 2016 field measurement program. Calibration was performed after the target storm was selected but prior to data collection. This helped mitigate any measurement errors from temperature changes and possible expansion and contraction of hardware components during transit. Hailstones were collected from a target thunderstorm following its passage across an identified roadway. Liquid water present on the surface of the hailstone was quickly wiped clean or blown off using compressed air prior to the powder application.

To allow the operator to quickly scan the full volume, a custom mount was designed and 3D-printed to support the stone. The acrylonitrile butadiene styrene (ABS) plastic material helped reduce melting resulting from the direct contact between the hailstone and the supports. The mount used three points of contact to support the stone with as little interference as possible. Reflective positioning targets were permanently fixed to the mount to calibrate the scanner position relative to the mount and allow for the mount to be placed on a turntable. The reflective targets allow the unit to "know" its relative position in three-dimensional space. The turntable allowed the hailstone to be rotated so that the sides of the stones could be scanned without the operator needing to move frequently within the vehicle. The mount also allowed enough space between supports so the bottom of a hailstone could be captured by the operator simply turning the unit to allow the laser to pass across the underside of the hailstone. The support mount is detected during scanning, but is removed in data processing, leaving just the 3D model of the hailstone. An example of a hailstone being scanned in the field and the resulting 3D model can be seen at https://vimeo.com/167924554. Before a hailstone was scanned, specimens were photographed, measured with a caliper, and weighed.

2015 PILOT FIELD TESTING. The system was first deployed during a period of active severe weather in the Central Plains on 15–18 September 2015. The field team intercepted a supercell thunderstorm near Atchison, Kansas, on 17 September 2015, which produced a relatively high bulk concentration of small hail (<2 cm). Attempts to collect a full scan of small hailstones (<1 cm) were unsuccessful due to the original design of the prototype mount (corrected in a later version). The hailstones were too small to effectively support as they began to melt. Fortunately, a larger hailstone (2.5 cm in diameter) was gathered, and a successful scan was made. The data were processed to remove scanner interference, synthetically fill any small data gaps, and produce the full 3D model (Fig. 2c,d). It is believed that this was the first successful 3D laser scan of a hailstone. The scan of this particular hailstone was completed in approximately 3 min at a resolution of 0.008 cm and used a maximum sampling rate of 25 kHz. The fully scanned hailstone had a mass of 2.50 g, and a maximum diameter of 2.504 cm. The diameter was defined as the longest straight line between two points, which passed through the center of the hailstone model. The volume, determined from the model, was 3.654 cm^3, which was 54% less than a sphere of the same diameter (Fig. 2e). The volume coupled with the measured mass yielded a bulk density of 0.68 g cm^{-3}. The digitized 3D model was used to 3D-print a cavity mold based upon the highly detailed hailstone shape (Fig. 2f), and demonstrated the linkage between 3D scanning and printing technology. The success of integrating the digital hail model into a CAD design application and 3D-printing a model highlighted the ability to duplicate natural hailstone shapes and their intricate details in a laboratory setting. This, coupled with exploration of diffused gas ice mixtures, could lead to the re-creation of laboratory hailstones that match the physical and material properties of hailstones observed in the field.

2016 FIELD MEASUREMENT PROGRAM AND ANALYSIS. The 2016 field measurement program focused on obtaining 3D models of hailstones and performing corresponding compressive strength tests. The efforts produced 42 digital hailstone models collected primarily from supercell thunderstorms in the Southern Great Plains of the United States in May and June of 2016. A subset of scanned hailstones, showing the variety of shapes that were captured, is shown in Fig. 3. The high-resolution models allowed for an accurate volume estimate to be obtained for each hailstone. It is acknowledged that some melting may have occurred prior to collection, and/or liquid water contained within small cavities in the hailstone may have drained, resulting in a small bias. It is also possible that protuberances may have been rounded off because of melting or impact with the ground. When compared with hailstone densities estimated using physical measurements and shape assumptions, the errors are expected to be reduced.

Throughout historical literature, summarized by Knight and Knight (2001), hailstones are commonly referred to as "hard" or "soft" with no quantification of their strength. It is frequently assumed that hailstone strength and their damage potential scales with bulk density (Knight et al. 2008). The true relationship between density and strength is unknown at this time. The use of 3D-scanned hailstones combined with recent advances in the ability to test hailstones for their compressive strength can help clarify the relationship and determine if laboratory impact tests must replicate it in order to accurately produce a true correlation with real-world performance of building materials.

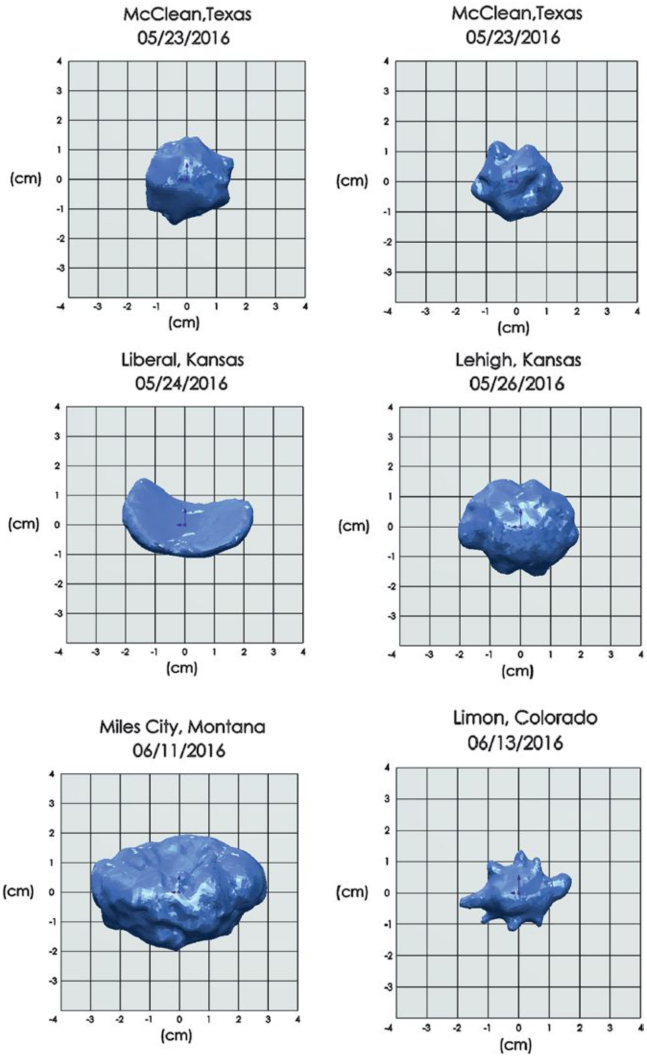

Fig. 3. Collection of several hailstone models showing the variety of shapes captured during the 2016 field program. The date and general location are provided for each hailstone.

The 3D-scanned hailstones were subjected to compressive strength testing, which applies an increasing compressive force with a strain rate on the order of 10^{-1} s^{-1} to the hailstone until it fractures. The peak force at the time of fracture is captured and then scaled by the cross-sectional area (i.e., plane) in which the force was exerted to produce an estimate of uniaxial compressive stress. The compressive stress was used as a proxy to represent the hardness property of the hailstone (Giammanco et al. 2015). These stones were also examined with respect to the diameter-to-mass relationship, bulk density, their volume normalized by that of a sphere with the same maximum diameter, and their compressive strength (Fig. 4). The observations also showed that hailstone densities trend closer to pure ice (0.9 g cm^{-3}) as they get larger. Three hailstones exhibited a density greater than 0.9 g cm^{-3} and were characterized by nearly all clear ice with no visible layering structure. The hailstones also had notable protuberances. The high density of these stones raises the question of whether "super" density ice occurs in hailstones or if this was the result of a measurement error. It is possible that some mass loss between measurement and scanning occurred such that the density estimate contained an error; however, the maximum diameter measured using a caliper was within 0.04 cm for all three hailstones when compared to the scanner-based diameter. The scale used has a precision of 0.01 g, but any shaking or movement of the scale could have introduced some source of measurement error. The use of this system in the field will help improve the understanding of hailstone bulk density distributions and determine if high-density and/or low-density hailstones are more prevalent than historical literature would suggest. It was clear that the measured hailstones departed from spherical shapes with increasing diameter, which is in agreement with recent field observations (Heymsfield et al. 2014) (Fig. 4c).

Throughout historical literature, low-density hailstones were often associated with being soft and of low strength. There has been little quantitative analysis to substantiate this expectation or to investigate a potentially different relationship. The datasets collected through 3D scanning and compressive strength testing allowed for a preliminary examination of how the two variables may be related. The relationship between the measured peak forces showed a general linear trend, with a larger force required for higher densities (not shown). However, the peak force must be scaled by the area of the plane in which the force was applied to produce an appropriate measure of strength. As shown in Fig. 4d, the slight linear trend was toward weaker hailstones with higher bulk densities. It is noted that the sample size shown here is only 42 hailstones, and larger datasets are needed. The ability to evaluate these properties is a notable advance that will foster new research toward understanding hailstone characteristics and determining their properties that affect damage potential.

RESEARCH APPLICATIONS OF 3D HAILSTONE MODELS. The first effort to 3D-scan hailstones was successful in proving the system could be operated efficiently in the field, collect a

FIG. 4. Observations of 3D-scanned hailstones derived from the digital models and physical measurements for (a) mass as a function of maximum diameter and the curve for an ice sphere with a density of 0.9 g cm^{-3} (solid orange); (b) bulk density as a function of maximum diameter; (c) ratio of the hailstone volume to the volume of a sphere of the same maximum diameter; and (d) compressive stress (used as a proxy for strength/hardness) as a function of bulk density.

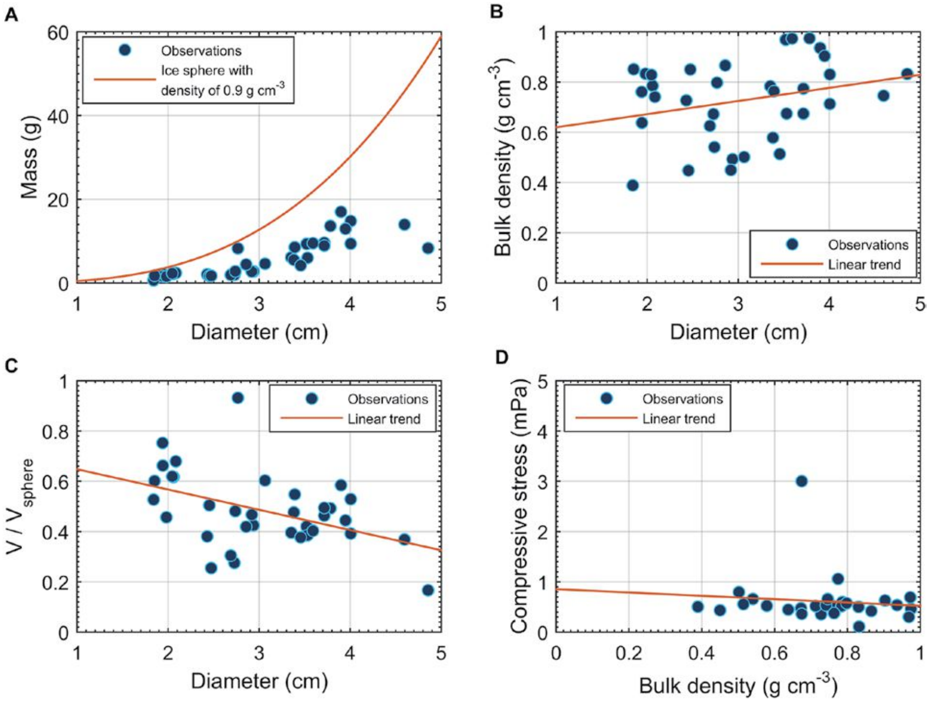

quality number of 3D models, and allow for further strength testing. The ability to collect these digital representations of natural hailstones will open the door to new investigations of their shapes and material properties. By eliminating the need for contact or immersion methods of determining hailstone densities, quantifying the relationship between bulk density and hailstone strength was possible. This capability will help improve ice-based laboratory impact test methods to ensure they are representing the necessary properties of natural hail. Cavity molds can also be used to determine if hailstone shape influences the type of damage for different materials.

The aerodynamics of hailstones is an area that could also benefit from 3D hail model datasets. Digitized hail shapes could also be leveraged to explore the aerodynamic drag characteristics of hail through experimental and computational methods, which are vital to ensuring that proper kinetic energies are used in material impact tests. Current test standards use impact kinetic energies determined through assumptions that drag coefficients for spherical shapes can be used for natural hailstones (Heymsfield et al. 2014). Assumptions regarding hailstone drag, terminal velocities, and kinetic energies are also made within hydrometeor parameterization schemes for numerical weather prediction models (Morrison et al. 2015). The aerodynamic applications described here could be leveraged to improve the hail-related portions of these schemes. Experiments could also shed light on the tumbling of hailstones, which can complicate radar detection, especially for dual-polarimetric radars (Straka et al. 2000). An improved understanding of this effect may provide the ability to extract more detailed hydrometeor information (i.e., mean shape, concentration) from the dual-polarimetric moments.

The use of 3D laser scanning systems continues to grow rapidly across a wide range of fields. Until now, their use in the atmospheric sciences has been limited. The pilot investigation presented here has shown how the technology can be used effectively to understand the characteristics of hail beyond what is considered in historical studies. These data will foster new research into the aerodynamics of hailstone shapes, the relationship between strength and density, radar hail detection, and hail damage severity. Each of these applications rely on the accurate representation of hail, and can be used to improve material impact-testing practices, improve hailstorm postevent characterizations, and develop new risk assessment methods through numerical modeling efforts. Each will ultimately aid in mitigating the large amount of property loss that occurs each year from severe hail.

ACKNOWLEDGMENTS. Funding for the field program and analysis efforts are provided by the Insurance Institute for Business and Home Safety through the annual operating budget. We would like to acknowledge Kevin

Outz from Matrix CAD Design, Inc. for his invaluable assistance in proof-of-concept testing of 3D scanners for this application.

FOR FURTHER READING

American Society for Testing of Materials, 2010: Standard test method for hail impact resistance of aerospace transparent enclosures. ASTM, 8 pp. [Available at www.astm.org/Standards/F320.htm.]

Beraldin, J.-A., F. Blais, L. Cournoyer, M. Rioux, S. H. El-Hakim, R. Rodella, F. Bernier, and N. Harrison, 1999: 3D Digital Imaging and Modeling, *Proc. Second International Conf. on 3D Digital Imaging and Modelling,* Ottawa, Canada, 34–43.

Besl, P. J., 1988: Range Imaging Sensors. *Mach. Vis. Appl.,* **1,** 127–152, doi:10.1007/BF01212277.

Changnon, S. A., D. Changnon, and S. D. Hilberg, 2009: *Hailstorms across the Nation: An Atlas about Hail and Its Damages.* Illinois State Water Survey, 95 pp.

FM Approvals, 2005: Specification test standard for impact resistance testing of rigid roofing materials by impacting with freezer ice balls (FM 4473). FM Approvals, 8 pp. [Available online at www.fmapprovals.com/approval-standards?filter=0.]

Giammanco, I. M., T. M. Brown, R. G. Grant, D. L. Dewey, J. D. Hodel, and R. A. Stumpf, 2015: Evaluating the hardness characteristics of hail through compressive strength measurements. *J. Atmos. Oceanic Technol.,* **32,** 2100–2112, doi:10.1175/JTECH-D-15-0081.1.

Heymsfield, A. J., I. M. Giammanco, and R. L. Wright, 2014: Terminal velocities and kinetic energies of natural hailstones. *Geophys. Res. Lett.,* **41,** 8666–8672, doi:10.1002/2014GL062324.

Kim, H., and J. N. Keune, 2007: Compressive strength of ice at impact strain rates. *J. Mater. Sci.,* **42,** 2802–2806, doi:10.1007/s10853-006-1376-x.

Knight, C. A., and N. C. Knight, 2001: Hailstorms. *Severe Convective Storms.* C. A. Doswell III, Ed., AMS, 223–254.

——, P. T. Schlatter, and T. W. Schlatter, 2008: An unusual hailstorm on 24 June 2006 in Boulder, Colorado. Part II: Low density growth of hail. *Mon. Wea. Rev.,* **136,** 2833–2848, doi:10.1175/2008MWR2338.1.

Knight, N. C., 1986: Hailstone shape factor and its relationship to radar interpretation of hail. *J. Climate Appl. Meteor.,* **25,** 1956–1958, doi:10.1175/1520-0450(1986)025<1956:HSFAIR>2.0.CO;2.

Kunkel, K., and Coauthors, 2013: Monitoring and understanding trends in extreme storms. *Bull. Amer. Meteor. Soc.,* **94,** 499–514, doi:10.1175/BAMS-D-11-00262.1.

Laurie, J. A. P., 1960: Hail and its effects on buildings. Council for Scientific and Industrial Research Rep. 176, 12 pp.

Mayer, R., 1999: *Scientific Canadian: Invention and Innovation From Canada's National Research Council.* Raincoast Books, 192 pp.

Morrison, H., A. Morales, and C. Villanueva-Birriel, 2015: Concurrent sensitivities of an idealized deep convective storm to parameterization of microphysics, horizontal grid resolution, and environmental static stability. *Mon. Wea. Rev.,* **143,** 2082–2104, doi:10.1175/MWR-D-14-00271.1.

Roeder, P., Ed., 2012: Severe weather in North America: Perils, risks, and insurance. Knowledge Series: Natural Hazards, Munich RE Rep., 274 pp.

Straka, J. M., D. S. Zrnic, and A. V. Ryzhkov, 2000: Bulk hydrometeor classification and quantification using polarimetric radar data: Synthesis of relations. *J. Appl. Meteor.,* **39,** 1341–1372, doi:10.1175/1520-0450(2000)039<1341:BHCAQU>2.0.CO;2.

MESONETS

Mesoscale Weather and Climate Observations for the United States

Rezaul Mahmood, Ryan Boyles, Kevin Brinson, Christopher Fiebrich,
Stuart Foster, Ken Hubbard, David Robinson, Jeff Andresen, and Dan Leathers

Mesonets play a critical role in near-surface weather and climate observations. It is essential that we continue to maintain, operate, and expand these networks.

Mesoscale in situ meteorological observations, roughly spanning a 30-km (~20 mi) radius or grid box around a given location, are essential to better foster weather and climate forecasting and decision-making by a myriad of stakeholder communities. The latter include, for example, state environmental and emergency management agencies, water managers, farmers, energy producers and distributors, the transportation sector, the commercial sector, media, and the general public. To meet these needs, the past three decades have seen a growth in the number of mesoscale weather and climate observation networks over various regions of the United States. These networks are known as mesonets (short for mesoscale network) and are largely a result of efforts at the state level (Fig. 1). In addition, these mesonets are playing a key role in fulfilling the objectives of the weather and climate observation community as identified by two recent National Research Council (NRC) reports (NRC 2009, 2012).

Most of these networks are operated by universities, reflecting a commitment to research, service, and outreach, and focus on observation quality and integrity. Levels of funding to support mesonets vary widely, reflecting a range of institutional and state priorities. As technological advances and societal needs for weather and climate information grow, mesonets continue to undergo an evolution from the formative age of mesonet development to a period of growth and integration. Hence, it is important to communicate the significant development and current status of these valuable means of environmental monitoring.

In this paper, we will discuss a brief history and context that provided the impetus to develop these networks, types of data mesonets collect, data

AFFILIATIONS: Mahmood and Foster—Department of Geography and Geology, and Kentucky Climate Center, Western Kentucky University, Bowling Green, Kentucky; Boyles—North Carolina State Climate Office, North Carolina State University, Raleigh, North Carolina; Brinson—Delaware Environmental Observing System, Department of Geography, University of Delaware, Newark, Delaware; Fiebrich—Oklahoma Climatological Survey, School of Meteorology, University of Oklahoma, Norman, Oklahoma; Hubbard—High Plains Regional Climate Center, School of Natural Resources, University of Nebraska–Lincoln, Lincoln, Nebraska; Robinson—Department of Geography, Rutgers, The State University of New Jersey, Piscataway, New Jersey; Andresen—Department of Geography, Michigan State University, East Lansing, Michigan; Leathers—Department of Geography, University of Delaware, Newark, Delaware
CORRESPONDING AUTHOR: Rezaul Mahmood, rezaul.mahmood@wku.edu

The abstract for this article can be found in this issue, following the table of contents.
DOI:10.1175/BAMS-D-15-00258.1

In final form 18 September 2016

collection frequency and dissemination approaches, site selection, station exposure, instrumentation, station maintenance, metadata, research applications, decision-support tools based on the mesonet data, funding issues, and future challenges and opportunities.

BRIEF HISTORY. Surface weather observations in the United States began on the East Coast in the late seventeenth century (Fiebrich 2009). Weather observations remained sparse and sometimes sporadic until agencies including the Surgeon General, army, and General Land Office began requesting regular observations at widespread locations. The Smithsonian Institution was responsible for organizing the first large "network" of volunteer weather observers across the nation. These observers became the foundation for today's National Weather Service Cooperative Observing Program (COOP). In the 1970s, improvements in electronics (miniaturization) and increased dependability of storage devices led to improved sensors and to multiple-function data processors at remote sites. This made it possible to automate weather data collection (Hubbard et al. 1983). Applications of weather data continued to grow and users sought the data for near-real-time decisions. This led to the development and growth of automated weather networks in the latter part of the twentieth century through present. An important aspect of this growth was the development of spatially dense networks with subhourly (with resolution up to 5 min) observations in the 1980s and 1990s. Two examples of networks that led the way are the Nebraska Mesonet (Hubbard et al. 1983; Hubbard 2001) and Oklahoma Mesonet (McPherson et al. 2007). Since these networks were developed with high spatial density (e.g., up to every

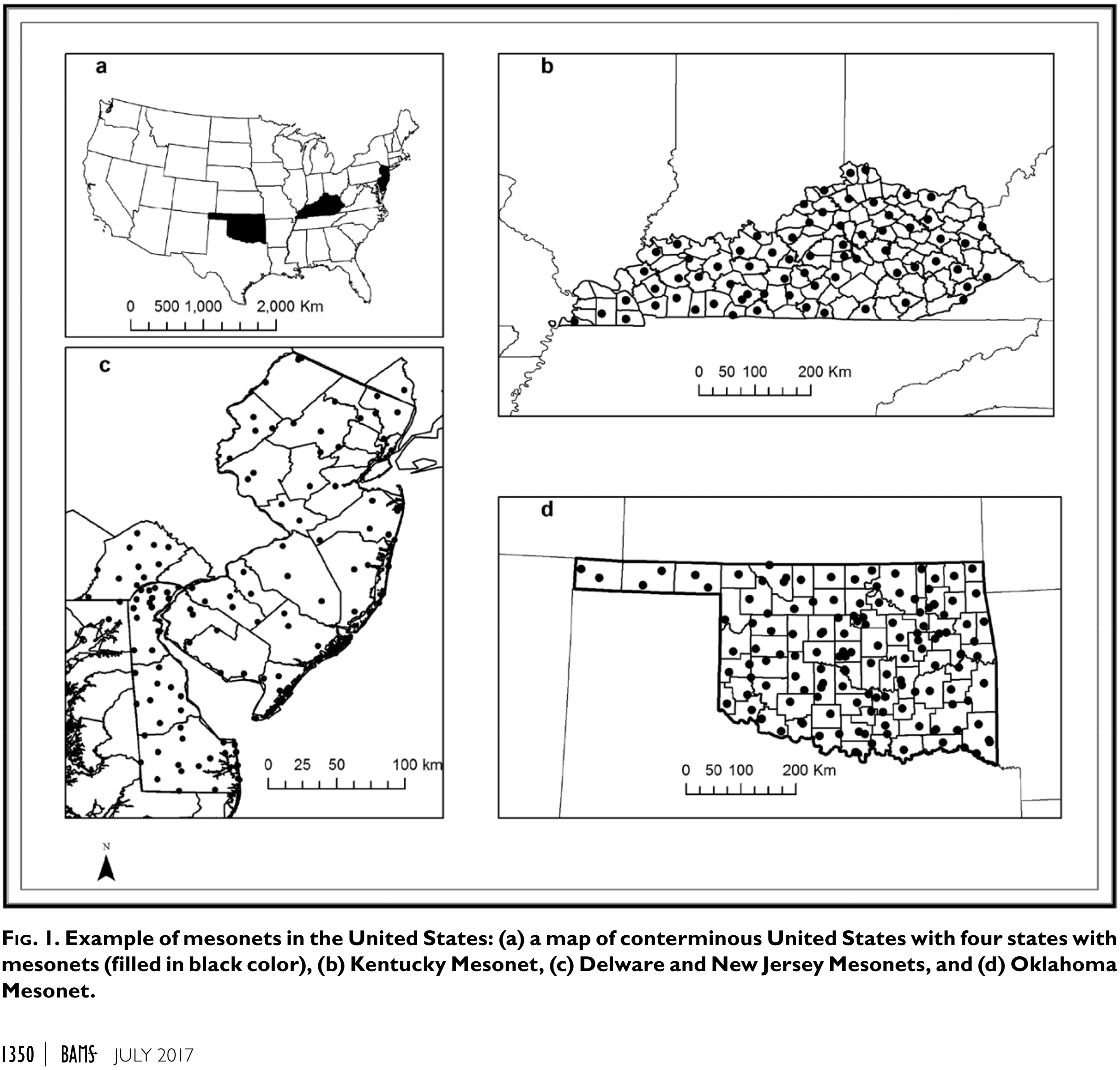

Fig. 1. Example of mesonets in the United States: (a) a map of conterminous United States with four states with mesonets (filled in black color), (b) Kentucky Mesonet, (c) Delware and New Jersey Mesonets, and (d) Oklahoma Mesonet.

32 km), the term mesonet was coined to describe the new observation networks. The Oklahoma Mesonet was built with an injection of state funding, while the Nebraska Mesonet was built more "bottom up" with local funding sources. These two mesonets represent alternative models for funding and development, and this is an important point to the evolution of mesonets elsewhere. Further information on the development of weather observations in the United States can be found in Fiebrich (2009).

Table 1 contains a list of statewide networks. The two networks from Alabama and the networks from west Texas and Louisiana are not truly statewide mesonet because they focus on particular regions of their respective states. On the other hand, networks from Illinois, Iowa, Minnesota, and New Mexico are quite sparsely distributed. There are many smaller public networks, but these do not have the following qualities: i) nonfederal, ii) statewide coverage, and iii) weather and climate focused. The third item is important because it helps to distinguish many mesonets from, for example, transportation networks [i.e., Road Weather Information Systems (RWIS)], which many states operate. Many mesonets (not all) are maintained not only for real-time use, but are also managed or strive to maintain "climate" standards. Most of these networks are operated by universities and are collocated with State Climate Offices.

INSTRUMENTATION AND VARIABLES OBSERVED. Many mesonets across the United States utilize research-grade instrumentation

Table 1. Statewide mesonets.

State	Network	Total number of real-time stations
Alabama	North Alabama Climate Network	22
Alabama	University of South Alabama Mesonet (CHILI)	25
Arizona	Arizona Meteorological Network	21
Arkansas	Arkansas State Plant Board Weather Network	50
California	California Irrigation Management Information System	152
Colorado	Colorado Agricultural Meteorological Network	75
Delaware	Delaware Environmental Observing System	57
Florida	Florida Automated Weather Network	42
Georgia	Georgia Automated Weather Network	82
Illinois	Illinois Climate Network	19
Iowa	Iowa Environmental Mesonet	17
Kansas	Kansas Mesonet	51
Kentucky	Kentucky Mesonet	66
Louisiana	Lousiana Agroclimatic Information System	9
Michigan	Enviroweather	82
Minnesota	Minnesota Mesonet	8
Missouri	Missouri Mesonet	24
Nebraska	Nebraska Mesonet	68
New Jersey	New Jersey Weather and Climate Network	61
New Mexico	New Mexico Climate Network	6
New York	New York Mesonet	101
North Carolina	North Carolina ECONet	40
North Dakota	North Dakota Agricultural Weather Network	90
Oklahoma	Oklahoma Mesonet	120
South Dakota	South Dakota Mesonet	25
Texas	West Texas Mesonet	98
Utah	Utah Agricultural Weather Network	32
Washington	Washington AgWeatherNet	176
	Total	**1,619**

to measure a number of important environmental parameters, as maintaining a highly reliable network with accurate data is central to the mission of every mesonet. The typical instrumentation suite used by mesonets today was highly influenced by earlier mesonets, which were commonly based around, at least in part, agriculture–climate-related applications (Hubbard et al. 1983; Brock et al. 1995). The suite of meteorological instrumentation incorporated in these early networks had a focus on providing a better understanding of the water balance through the estimation of reference evapotranspiration and automated, remote measurements of precipitation. Table 2 shows a list of typical instruments used in current mesonets across the United States.

Table 2. Typical set of instruments used on U.S. mesonet meteorological stations.

Instrument	Parameter measured
Platinum resistance thermometers	Air temperature
Capacitive hygrometer	Relative humidity
Propeller anemometer	Wind speed
Potentiometer wind vane	Wind direction
Silicon photovoltaic pyranometer	Solar radiation
Tipping-bucket rain gauge	Rainfall/precipitation
Capacitive barometer	Barometric pressure
Soil moisture sensors (widely varies)	Soil moisture

In the context of limited funding for the mesonets, these types of instruments have the advantage of being quite accurate, robust, and somewhat affordable to acquire and maintain. Depending on the local stakeholder needs and availability of funding, mesonet operators provide data from networks with as few as a dozen stations, for example, the South Alabama Mesonet, to well over a hundred stations, like the Oklahoma Mesonet. Instrument acquisition and maintenance costs are critical to the long-term viability of all mesonets, since fiscal support is typically limited and may be highly variable from year to year. Differences in instrumentation among networks are driven by a combination of local stakeholder needs, science goals of the network, and the availability of funding to support the network. For instance, since 2007 the Delaware Environmental Observing System (DEOS) has added 26 sonic snow depth sensors to its network to serve the Delaware Department of Transportation's snow removal reimbursement program.

Some networks differ based on their deployment strategies. The Kentucky Mesonet and Oklahoma Mesonet utilize aspirators on their air temperature sensors to improve the quality of their air temperature data. Some mesonets use heating elements on their tipping-bucket rain gauges, while others use weighing rain gauges winterized with antifreeze to melt frozen precipitation and obtain liquid equivalent precipitation. Meanwhile, some mesonets do not attempt to measure frozen precipitation at all. Soil sensors are another common feature of mesonets across the United States. Most networks measure volumetric water content (VWC) and soil temperature at one or all of the World Meteorological Organization's (WMO) soil sensor depth specifications (5, 10, 20, 50, and 100 cm). This is typically done using soil water reflectometers for VWC and encapsulated thermistors for soil temperature. Meanwhile, other networks measure soil water matric potential using a thermocouple encased in a porous ceramic block (Illston et al. 2008).

Most networks' meteorological stations take multiple samples (3- to 5-s sampling is the most common) from sensors every observation period, depending on sensor response coefficients, station power consumption constraints, and the intrinsic variability of the parameter being measured. Hence, the sampling and observation interval varies from network to network. However, as indicated above, nearly all mesonets have subhourly observation intervals, commonly at a 5-min increment. Given highly reliable and robust measurement systems, U.S. mesonets are thus able to provide quality, high temporal and spatial resolution data to many stakeholders for real-time weather and climate applications.

STATION EXPOSURE AND SITE SELECTION. The majority of mesonet stations consist of sensors wired directly into central datalogging and microprocessing units. Sensors, datalogger, power, and communications subsystems are mounted onto tripods or towers with small horizontal footprints of between 1 and 3 m. With all sensors effectively collocated, sensor exposure is chosen based on a number of siting criteria and operational requirements. While each sensor performs best under different exposures, stations are often placed in locations that best achieve the following objectives (AASC 1985; Bennett et al. 1987; WMO 1983, 2008; Leroy 2010):

1) Maximize airflow for naturally aspirated temperature, humidity, and pressure sensors.
2) Minimize nearby obstructions to ensure accurate radiation measurements.

3) Minimize wind flow around the precipitation gauge.
4) Ensure soils are representative of the surrounding region.
5) Maximize distance from tall obstructions (e.g., buildings and trees) to ensure accurate wind measurements that are often recorded at 2, 3, 5, and/or 10 m above ground. One rule of thumb is that the minimum desired distance between a tall object and a station is about 10 times the height of the object.
6) Maximize long-term stability of surrounding land cover.
7) Maximize site host's ability to support the station over the long term.

Radiation, temperature, humidity, wind, and pressure sensors typically require open exposure, with no obstruction to incoming radiation or airflow.

Station siting requirements also must consider needs for power and communications. Some mesonet stations require access to AC power, particularly to meet the power demands of aspirated temperature shields and sensors with heating elements. However, many mesonet stations use only solar panels to power sensors (including aspirated shields), datalogger, and communication subsystems. In either case, mesonet stations typically use power sources interfaced with trickle-charge batteries, providing stored energy capacity. Also, as wireless cellular communications networks become more pervasive and cost effective, many mesonets make siting decisions based on access to these networks.

An example of a mesonet station is shown in Figs. 2 and 3. With constrained energy storage capacity, many mesonet stations with solar panels use a naturally aspirated temperature shield, often a Gill radiation shield. Figure 4 shows (Fig. 4a) an aspirated radiation shield and (Fig. 4b) a nonaspirated Gill radiation shield. In the latter case, sensors inside the Gill radiation shields perform best when the background wind consistently moves ambient air across the sensors. However, as noted above, other mesonets use aspirated temperature shields throughout their network.

Figures 5a,b show differences in temperature for nonaspirated and aspirated shields from Christian County site in western Kentucky where temperatures measured by nonaspirated (naturally ventilated) shields are typically higher for all months for both maximum and minimum temperatures. However, it is also apparent that these biases are higher during the summer months for maximum temperatures when solar radiation loadings are higher and wind speeds are lower. Figures 6a–c shows noticeably higher temperature in the early morning hours when wind speeds and solar angle are low. As wind speed increases in the afternoon, these differences declined. Detailed analysis of the influence of wind speed and solar radiation on temperature measurement can also be found in Hubbard et al. (2004, 2005).

In contrast, precipitation sensors perform best under calm wind conditions (Rodda 1973; Sevruk 1989; Yang et al. 1998; Duchon and Essenberg 2001). Wind can create turbulence around the rim of accumulation-based precipitation gauges, causing

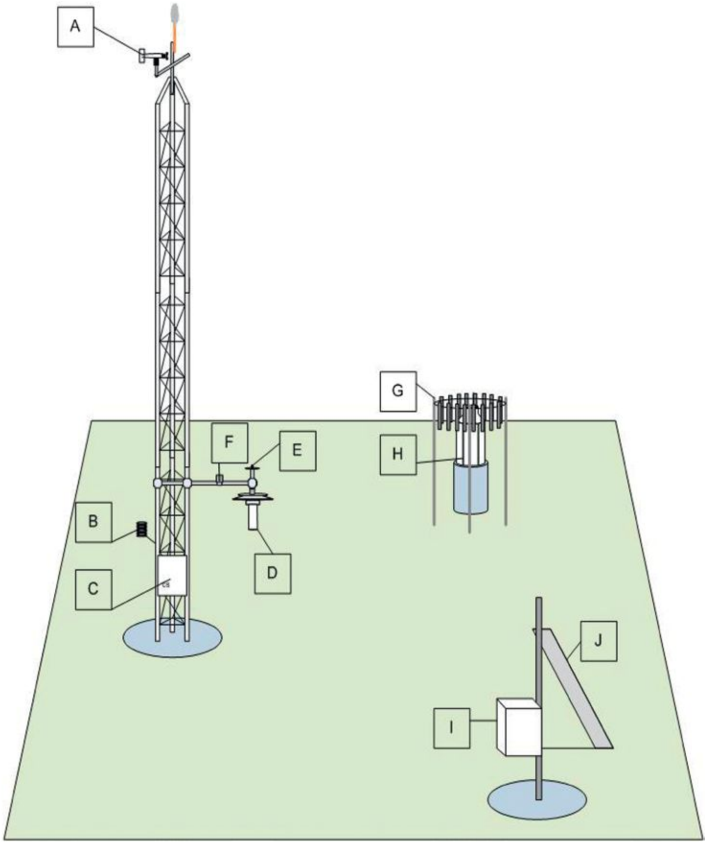

Fig. 2. Instrumentation and layout of a mesonet station. Instrumentations are A: wind monitor, B: relative humidity sensor, C: datalogger enclosure, D: temperature sensors, E: pyranometer, F: wetness sensor, G: single alter shield, H: precipitation gauge, I: battery enclosure, and J: solar panel. Soil moisture and temperature sensors and guy wires not shown and drawing not to scale.

Fig. 3. A mesonet station in Kentucky with good exposure.

undercatchment of both liquid and, especially, frozen precipitation. While many mesonets deploy wind screens to reduce wind near the rim of the gauge, this undercatch cannot be completely eliminated in locations with steady or high winds. A majority of the mesonets use tipping-bucket rain gauges, while weighing bucket gauges are also used by the mesonets that receive substantial frozen precipitation. Weighing bucket gauges reduce the magnitude of undercatch during intense rainstorms (Duchon and Biddle 2010). However, the costs of purchase and maintenance are also significantly higher compared to tipping buckets.

In the eastern United States, where forested landscapes are relatively common, stations are often selected to ensure adequate exposure and fetch for the wind sensors, which are typically located at 2, 3, 5, or 10 m above ground level. While achieving this objective can be relatively easy in more arid regions of the central and western United States, in the east this is often the most challenging siting requirement to meet. The WMO and EPA standard is to ensure that the horizontal distance between the sensor and any substantial obstruction is at least 10 times the height of the obstruction. For a station with nearby trees of 20 m (~60 ft), this means the wind sensor should ideally be at least 200 m (~600 ft) away from those trees. For many locations in the eastern United States, this becomes quite challenging or impossible (Fig. 7). Only large pastures, cropland, and grassland often meet this requirement.

Another factor that often drives station site selection is the ability of the site host to support the station for years to come. Often, this means that the host (public or private) must agree to the location of the station. The sensors cannot interfere with other activities at the location, such as crop management (planting, irrigation, harvest protocols, and equipment), airport flight operations, or water treatment. Occasionally, mesonet stations must also meet aesthetic requirements of the host, as not all potential site hosts find these stations visually pleasing.

Regardless of instrumentation, the quality and utility of observations collected by a mesonet station depend upon the quality of the site. Siting criteria typically favor stations located in flat, open, grassy areas, far removed from the influences of sources of anthropogenic forcing. More importantly, stations are located to ensure the data recorded are reliable and representative of the weather and climate of the area, not just recording the microclimate of the small footprint of the base. In practice, however, station siting is one of the greatest challenges that mesonets face. Site hosts often want a tripod mounted or tower installed near a building, on a rooftop, or along the edge of property lines—locations generally thought to be "out of view." This creates a conflict with the scientific objectives for sensor exposure that demand the siting of sensors in open areas away from buildings, trees, and rooflines. Mesonet managers sometimes work with potential hosts for months or even years to

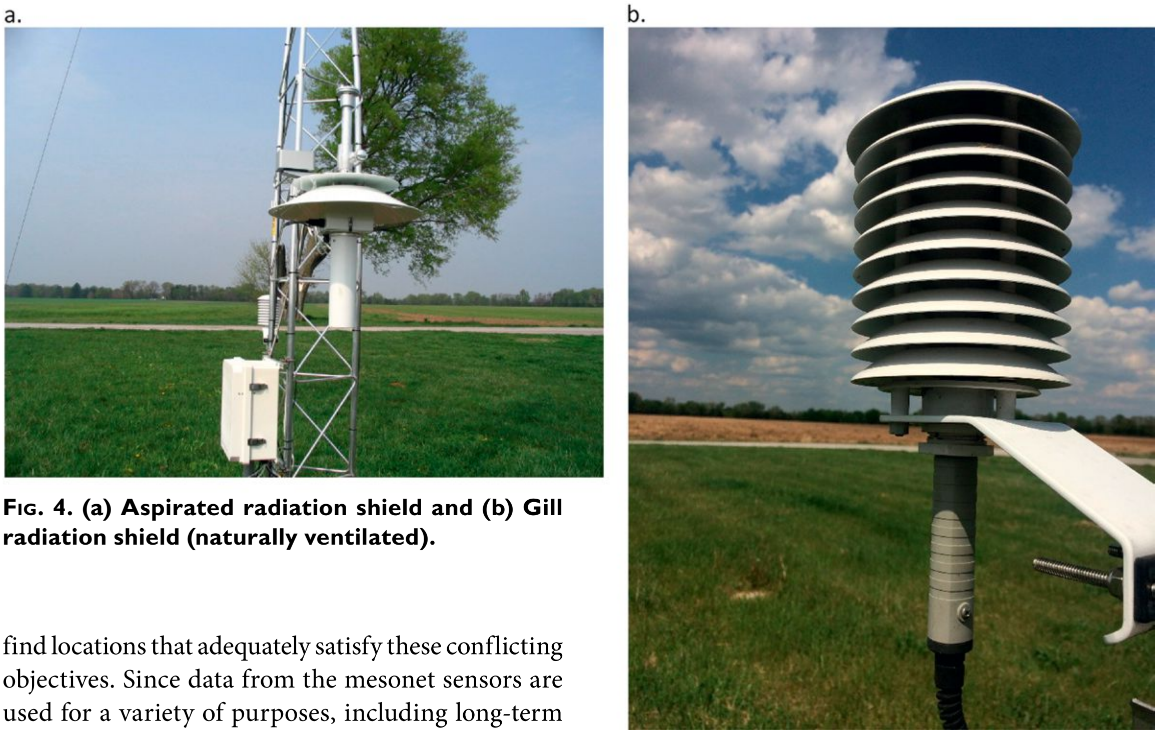

Fig. 4. (a) Aspirated radiation shield and (b) Gill radiation shield (naturally ventilated).

find locations that adequately satisfy these conflicting objectives. Since data from the mesonet sensors are used for a variety of purposes, including long-term climate monitoring, mesonet managers try to select locations that will not be exposed to land use and land cover change for decades to come. Each potential station move to accommodate changes in host's needs introduces a discontinuity in the climatic data record and limits the ability for scientists to use the data record for long-term studies. Occasionally, exposure for some sensors is compromised because no other suitable site is available in the area (Fig. 5).

Availability of wireless communication also plays an important role in the final selection of sites. As noted previously, many mesonets provide data for near-real-time emergency management and other time-sensitive decision-making. Hence, wireless infrastructure to enable reliable communication and data transmission from a mesonet site is critical. Situations are sometimes encountered where a site meets all the scientific criteria and has a willing land-owner host but lacks reliable communication infrastructure nearby. As the reach of wireless infrastructure expands, more high-quality sites for weather and climate monitoring become available.

As noted above, it is desirable that mesonet stations are located approximately every 30 km. However, in many cases it is difficult to achieve this objective. Several factors influence the ability of a mesonet to achieve spatial uniformity. These include, among others, the ability to secure local funding commitments to cover station installation and operating costs. Hence, stations are more likely to be placed on public lands where host agencies have a specific requirement for weather and climate data or in municipalities that desire to have weather information for a myriad of uses.

TRANSMISSION OF DATA FROM REMOTE STATIONS TO A CENTRAL INGEST AND PROCESSING FACILITY. The majority of stations in various mesonets rely on wireless transmission of data and these data get relayed in near–real time to computer servers located at the home institution. Most of the mesonets apply near-real-time automated quality assurance (QA) and quality control (QC) procedures (further discussion is provided in the following section) before disseminating data to specific users or to the general public. QA/QC procedures are developed based on known science related to the physical behavior of the near-surface atmosphere. While commonalities exist, mesonets have typically developed their own automated QA/QC procedures. Some of the more established mesonets have developed robust QA/QC procedures, while others have developed more rudimentary ones, again often a function of available funding. In either case, the goal is to identify and flag problematic data. These data can then be further investigated by a QA/QC operator and, if warranted, a maintenance ticket may be issued and a technician sent to the site to further investigate and resolve the issues. Additional details regarding QA/QC are provided in the next section.

Data transmission and distribution can be challenging. Disruptions of service sometime occur when commercial wireless providers perform maintenance on their communication networks or when station communication devices in the field fail or become unstable. In some cases, these disruptions may simultaneously impact multiple mesonet stations. Normally, data from mesonet stations are not lost, as they are temporarily stored in the datalogger, often for at least a month. When communication with the station is reestablished, data are retrieved from storage. While mesonets increasingly benefit from outsourcing their communications to wireless providers, they have no influence over the operation of those private networks beyond access to available technical support services. Further, in order to maintain seamless data transmission, mesonets must plan appropriately in order to be prepared to upgrade modems and related communications protocols when communication providers introduce next-generation technologies.

DATA QA/QC AND SITE MAINTENANCE.

Quality control of the data is necessary to maintain the credibility of the datasets. Mesoscale meteorological data can become inaccurate for a variety of reasons (Fiebrich et al. 2010). For measurements, the first line of defense against erroneous observations is the calibration of sensors against primary or secondary standards. When a sensor to be deployed in a mesonet is evaluated alongside a standard sensor, the resulting signal from the mesonet sensor can be calibrated against the standard (e.g., Aceves-Navarro et al. 1988). Employing statistics for the calibration can estimate the error associated with the mesonet sensor (e.g., the standard error of estimate). Sensors should be calibrated on a frequency appropriate for the stability of the sensor as determined by testing the change in calibrations over time. This may be as frequent as every 18–36 months for sensors such as hygrometers and pyranometers or as long as 48 to 60 months for more stable sensors such as thermistors and anemometers (Fiebrich et al. 2006). In any case, the calibration leads to an estimate of the systematic error to be expected from the sensors.

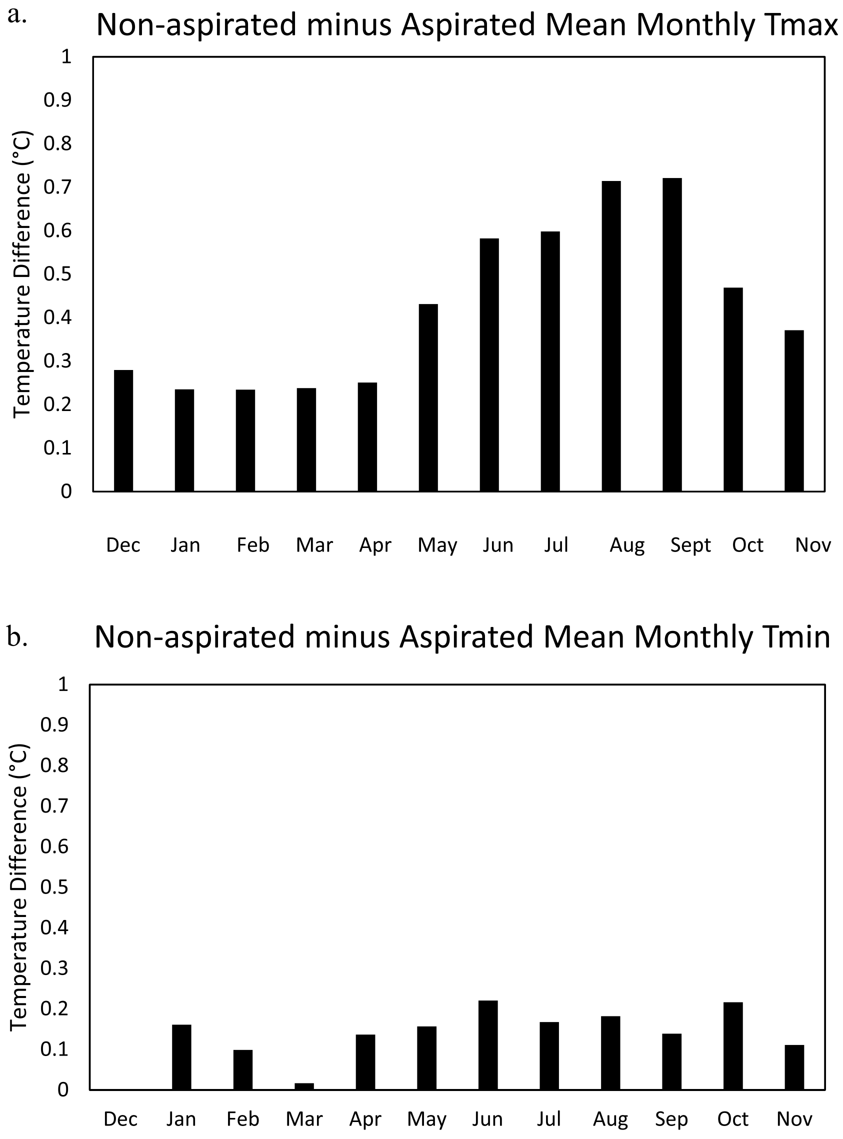

Fig. 5. Differences of temperatures between nonaspirated and aspirated radiation shield: (a) mean monthly maximum temperature and (b) mean monthly minimum temperature. Positive differences suggest warmer temperature under nonaspirated shield. Data are from Christian County station of Kentucky Mesonet and from Dec 2012 through Nov 2013.

A multitude of automated and manual quality control tests have been developed for mesoscale meteorological data. The techniques range from general sensor and climatological range tests to more sophisticated temporal, spatial, and sensor-specific ones. Fiebrich et al. (2010) provided a detailed review of the various techniques commonly used for QA/QC. Daily evaluation of the flagged data will provide early identification of sensors that may be drifting or malfunctioning and thus lead to an overall improvement in the data quality.

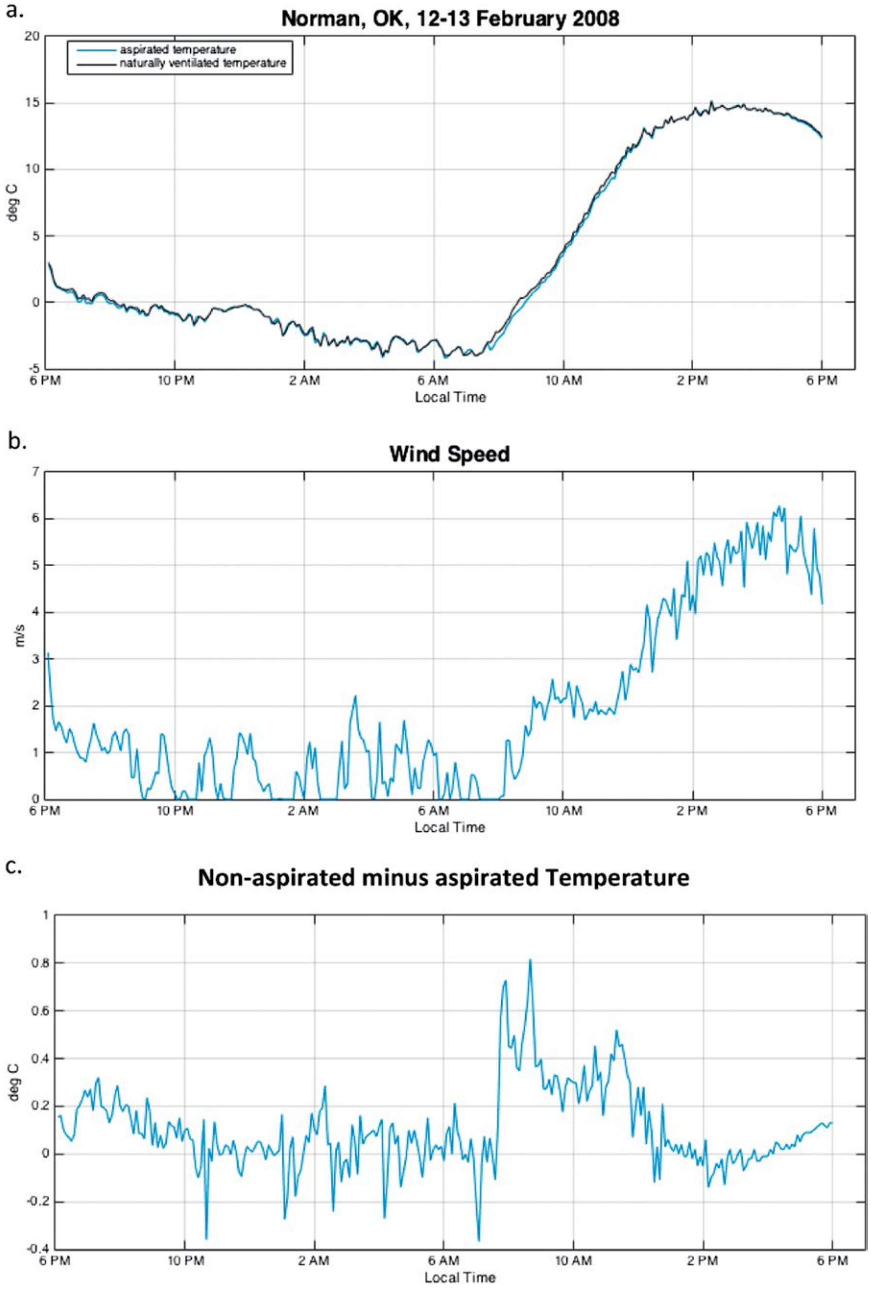

Fig. 6. (a) Time series plot of the air temperature at Norman, Oklahoma, on 12–13 Feb 2008. The blue line shows measurements made by an aspirated temperature sensor, while the black line shows measurements made by a nonaspirated (naturally ventilated) temperature sensor. (b) Wind speed. (c) Difference between the temperature observations made by the nonaspirated (naturally ventilated) temperature sensor and the aspirated temperature sensor. Differences were greatest in the late morning hours when both sun angle and wind speed was low (1 m s^{-1}).

Routine site maintenance plays an important role in ensuring quality data from a mesonet (Fiebrich et al. 2006). The frequency of site maintenance varies from every month (at least for part of the year) to seasonal to annual, depending on environmental factors (e.g., vegetation growth), sensor performance, and availability of resources (e.g., funding). Vegetation conditions can have a significant effect on measurements of soil temperature and moisture, as well as a notable effect on air temperature, humidity, and wind speeds. In general, the goal of vegetation maintenance is to minimize the microscale influences of the station location. Routine site visits also permit technicians to periodically inspect, level, clean, test, and rotate the sensors at a station. Each site visit is also an opportunity to collect valuable metadata (e.g., periodic station photographs and sensor inventories). Note that most mesonets have detailed databases where they archive detailed metadata regarding status of the site (e.g., photographs, technician notes during their site visits), sensor make and model, sensor calibration information, and timing of sensor deployment, among others. These metadata are extremely valuable during analysis of data for a variety of meteorological and climatological studies.

Fig. 7. A mesonet station in North Carolina with nearby obstructions (trees).

DECISION-SUPPORT TOOLS FOR USERS.

An important aspect of development and usage of mesonet data is their wide variety of applications in emergency management decision-making in near–real time or on day-to-day or longer time scales. The "local scale" of mesonet observations intrinsically allows forecasters to pinpoint the locations of fronts and other boundaries for convective initiation and wind shifts. The mesonet observations also provide precise identification of the freezing line at the surface for predicting winter precipitation type. Most mesonets have developed additional decision-support tools for farmers, agriculture concerns, emergency managers, foresters, water managers, weather forecasters, K–12 educators, and many others. In most cases, these tools are available free of charge through the World Wide Web. Recently, mesonets have begun to develop smart phone–based applications that are available for free or for a small fee. Specific examples include decision tools for irrigation scheduling, evapotranspiration calculation, pest management, planting date determination, severe weather warnings, forest fire forecasts, and drought monitoring, to name a few. Decision tool development, sophistication, and availability to users generally depend on funding availability. Overall, the practical and economic impacts of such information can be significant. For example, Michigan State University's Enviroweather Project provides information to support agricultural and natural resource–related decision-making in Michigan, based on the input data from an 83-site mesonet. In a recent survey of cherry and apple growers across the state, mesonet data users reported significant reductions in their use of pesticides (relative to nonusers), increases in both crop yield and quality, and an estimated collective yearly economic beneficial impact of more than $1.7 million (U.S. dollars) associated with the use of web-based information (Andresen et al. 2012).

PARTNERSHIPS. A distinguishing aspect of mesonets represented in this paper is that they operate as not-for-profit entities, and most involve strong grassroots efforts. Thus, mesonets have developed strong collaborative partnerships with their users. These partners include individual citizens (e.g., a site host who provided access to their land for a station tower), state and local government entities (e.g., emergency management, county fiscal court, local school board, etc.), and private industry and local businesses (sponsoring a station by making predetermined annual contribution for station maintenance). In some cases, these local-level entities also bear the cost of the station purchase and installation and contribute toward recurring annual costs of communication and maintenance. Success in building and sustaining local-level partnerships requires a substantial engagement and persistence on the part of mesonet operators. But these local-level partnerships constitute an invaluable foundation of support, as they facilitate the exchange of information and ideas that help mesonet operators better meet the needs of diverse user communities. Through time, state and local partners develop a greater appreciation of the value of locally accurate and timely weather and climate data from perspectives including public safety and economic benefit. In addition, through these long-term partnerships, local and state entities come to value the local expertise available at institutions that operate these mesonets.

State and federal partnerships are also key elements of mesonets. In many cases, mesonets receive funding from state agencies in return for defined deliverables, normally relating to public safety and emergency response. Regionally, some mesonets share data with Regional Climate Centers funded by the National Oceanic and Atmospheric Administration. A number of mesonets have been providing data for various federal entities over many years; most often these exchanges are free of charge. However, there are cases where a federal partner provides limited funding for the data. Increasingly, mesonets are contributing near-real-time data and metadata through the federally supported National Mesonet Program (Dahlia 2013). These data support a variety of National Weather Service (NWS) activities tied to weather forecasting. Independent of this effort, many mesonets make data available directly to local NWS offices for their forecasting and alerting activities as a public service to local residents. Indeed, many local NWS offices are among the strongest partners of the mesonets.

FUNDING CHALLENGES. Public availability of weather and climate data helps to enhance public health and safety, promote economic development, and further environmental awareness and education. Recognition of these societal benefits creates an expectation that observing networks should be publicly funded and that data should be freely available. However, public funding is scarce and within this context, mesonet operators face ongoing challenges to secure financial resources necessary to develop, operate, and maintain networks that collect and ensure data that support research and high-value decision-making.

Various funding models have been implemented, as each mesonet has developed from a unique set of circumstances. Some have a strong top-down structure, relying heavily on startup and recurring annual operating funding from a single or small number of sources at the level of state government. The target markets for data and information provided by mesonets are often dictated by the funding sources. Mesonets that are funded by and serve agricultural interests can be found at some land-grant universities. Other mesonets emphasize public safety and emergency management, with funding channeled through corresponding state agencies. Still, when funding is provided through a single or small number of entities, mesonets can be vulnerable to sizeable budget cuts during economic downturns or when administrative priorities change.

On the other hand, in an effort to develop agility and resilience, mesonets may also strive to build a bottom-up funding model based on funding at the local level tied to development and operation of individual monitoring stations. Agility enables a mesonet to identify and pursue opportunities to expand network coverage on a station-by-station basis. Bottom-up funding also creates resilience by diversifying funding streams. However, some downsides to a bottom-up approach include high administrative overhead and investment of significant staff time to acquire and maintain funding. Additionally, individual mesonets may pursue opportunities to leverage their networks through research and development projects, including public–private partnerships. Ultimately, the sustainability and growth of mesonets are enhanced through successful efforts to develop funding streams through partnership building at the local, state, and federal levels, while providing value to partners at each level.

FUTURE DIRECTION. In situ weather and climate observations collected by mesonets provide "ground truth" of near-surface atmospheric and surface conditions. They are increasingly used to advance understanding of land surface–atmosphere interactions and the evolution of meteorological events, to initialize and validate forecast models, and to improve weather forecasting. On a longer time scale they enable insights into climate variability and climate change. Near-real-time availability of data also makes them valuable in emergency management and response situations. Data from mesonets are used in applications associated with agriculture (irrigation, crop planting, fertilizer and pesticide applications, freeze protection, insurance), water management, drought, public health, air quality, renewable energy generation, and transportation. Through various applications, they inform societally relevant policy and decision-making.

We hold that these mesonets are vital assets contributing to their states and to society at large. Based at and operated by universities, those operating these networks share a commitment to develop, operate, and maintain environmental monitoring that provides research-grade information. Though some mesonets are well established and have been in operation for decades, we note that the collective development of mesonets is still in the formative stage. This is evident in the diversity of operational and funding models. While this represents a strength resulting from the diverse range of experiential and expert knowledge collectively provided by these mesonets, we envision a future stage of development that will lead to greater commonality in the structure of mesonets, though each will remain unique.

Therein, we make the following recommendations:

1) Network operation, maintenance, and expansion: In situ observation networks should continue to be operated and maintained. Reliable streams of operating funding should be provided to support and more fully leverage the value of these networks. Funding mechanisms need to be developed to facilitate the expansion of networks

such that greater geographic coverage, at times at a high density, be provided in areas where needed observations are unavailable.

2) New observation capabilities: We recognize that advances in technology and improved budgetary conditions are likely to enable mesonets to expand the array of environmental measurements that they record. This could include adding temperature and wind measurements at different levels, flux measurements for land–atmosphere interactions, incorporation of atmospheric profilers or unmanned aerial vehicles (UAVs) to better monitor the boundary layer, expanding soil monitoring, adding cameras to capture images and video, and otherwise developing more intelligent monitoring networks. These and other advances are likely to result through expanding partnerships, both in the public and private sectors.
3) Network upgrade: The authors appreciate that availability of funding for maintaining and upgrading existing observational infrastructure is limited. However, we hope we have illustrated that the societal value, including direct social and economic benefit of these networks, far outweighs (by many fold) the investment. Funding should also be directed in such a way that a currently operating network can continue to upgrade its instrumentation and exposure so that it can further meet scientific requirements for data quality. For instance, a network could switch from 3- to 10-m towers for better wind monitoring and possible relocation of stations for better exposure. In addition, funding can go to add any missing but critical observations (hence, instrumentation) for any particular network.

These recommendations are not all encompassing. We suggest that they offer a foundational basis for the mesonets to play an important role in weather and climate observation and continue to provide valuable scientific and societally relevant information.

ACKNOWLEDGMENTS. The authors thank Dolly Na-Yemeh for preparation of Fig. 1. Thanks also go to two anonymous reviewers for their valuable comments and suggestions.

REFERENCES

AASC, 1985: Heights and exposure standards for sensors on automated weather stations. The State Climatologist, Vol. 9, No. 4, National Climatic Data Center, Asheville, NC. [Available online at www.stateclimate.org/sites/default/files/upload/pdf/state-climatologist/00000029.pdf.]

Aceves-Navarro, L. A., K. G. Hubbard, and J. J. Schmidt, 1988: Group calibration of silicon cell pyranometers for use in an automated network. *J. Atmos. Oceanic Technol.*, 5, 875–879, doi:10.1175/1520-0426(1988)005<0875:GCOSCP>2.0.CO;2.

Andresen, J., and Coauthors, 2012: "Enviro-weather: A Weather-based Information System for Pest, Natural Resource, and Agricultural Production Management in Michigan." *The Climate Observer* (July 2012), 1-3. [Available online at http://mrcc.isws.illinois.edu/cliwatch/eNews/observer_201206_full.html.]

Bennett, E., and Coauthors, 1987: On-site meteorological program guidance for regulatory modeling applications. EPA-450/4-87-013, 187 pp. [Available from EPA Office of Air Quality Planning and Standards, Research Triangle Parks, NC 27711.]

Brock, F. V., K. C. Crawford, R. L. Elliott, G. W. Cuperus, S. J. Stadler, H. L. Johnson, and M. D. Eilts, 1995: The Oklahoma mesonet: A technical overview. *J. Atmos. Oceanic Technol.*, **12**, 5–19, doi:10.1175/1520-0426(1995)012<0005:TOMATO>2.0.CO;2.

Dahlia, J., 2013: The National Mesonet Pilot Program: Filling in the gaps. *Weatherwise*, **66**, 26–33, doi:10.1080/00431672.2013.800418.

Duchon, C. E., and G. R. Essenberg, 2001: Comparative rainfall observations from pit and aboveground rain gauges with and without wind shields. *Water Resour. Res.*, **37**, 3253–3263, doi:10.1029/2001WR000541.

——, and C. J. Biddle, 2010: Undercatch of tipping-bucket gauges in high rain rate events. *Adv. Geosci.*, **25**, 11–15, doi:10.5194/adgeo-25-11-2010.

Fiebrich, C. A., 2009: History of surface weather observations in the United States. *Earth Sci. Rev.*, **93**, 77–84, doi:10.1016/j.earscirev.2009.01.001.

——, D. L. Grimsley, R. A. McPherson, K. A. Kesler, and G. R. Essenberg, 2006: The value of routine site visits in managing and maintaining quality data from the Oklahoma Mesonet. *J. Atmos. Oceanic Technol.*, **23**, 406–416, doi:10.1175/JTECH1852.1.

——, C. R. Morgan, A. G. McCombs, P. K. Hall Jr., and R. A. McPherson, 2010: Quality assurance procedures for mesoscale meteorological data. *J. Atmos. Oceanic Technol.*, **27**, 1565–1582, doi:10.1175/2010JTECHA1433.1.

Hubbard, K. G., 2001: The Nebraska and High Plains regional experience with automated weather stations. *Automated Weather Stations for Applications in Agriculture and Water Resources Management: Current Use and Future Perspectives*, K. G. Hubbard and M. V. K. Sivakumar, Eds., High Plains Climate

Center and World Meteorological Organization, 219–227.

——, N. J. Rosenberg, and D. C. Nielsen, 1983: Automated weather data network for agriculture. *J. Water Resour. Plann. Manage.*, **109**, 213–222, doi:10.1061/(ASCE)0733-9496(1983)109:3(213).

——, X. Lin, C. B. Baker, and B. Sun, 2004: Air temperature comparison between the MMTS and the USCRN temperature systems. *J. Atmos. Oceanic Technol.*, **21**, 1590–1597, doi:10.1175/1520-0426(2004)021<1590:ATCBTM>2.0.CO;2.

——, ——, and ——, 2005: On the USCRN temperature system. *J. Atmos. Oceanic Technol.*, **22**, 1095–1100, doi:10.1175/JTECH1715.1.

Illston, B. G., J. B. Basara, D. K. Fisher, R. Elliot, C. A. Fiebrich, K. C. Crawford, K. Humes, and E. Hunt, 2008: Mesoscale monitoring of a soil moisture across a statewide network. *J. Atmos. Oceanic Technol.*, **25**, 167–182, doi:10.1175/2007JTECHA993.1.

Leroy, M., 2010: Siting classification for surface observing stations on land. *Workshop on Quality Management in Surface, Climate and Upper-Air Observations in RA II (Asia)*, Tokyo, Japan, JMA/WMO, 47–66. [Available online at www.jma.go.jp/jma/en/Activities/qmws_2010/CountryReport/CS202_Leroy.pdf.]

McPherson, R. A., and Coauthors, 2007: Statewide monitoring of the mesoscale environment: A technical update on the Oklahoma Mesonet. *J. Atmos. Oceanic Technol.*, **24**, 301–321, doi:10.1175/JTECH1976.1.

NRC, 2009: *Observing Weather and Climate from the Ground Up: A Nationwide Network of Networks*. The National Academies Press, 250 pp.

——, 2012: *Weather Services for the Nation: Becoming Second to None*. The National Academies Press, 86 pp.

Rodda, J. C., 1973: Annotated bibliography on precipitation measurement instruments. WMO/IHD Projects Rep. 17, No. 343, 278 pp.

Sevruk, B., 1989: Wind-induced measurement error for high-intensity rains. *Proc. Int. Workshop on Precipitation Measurement*, WMO Tech. Document 328, 199–204.

WMO, 1983: *Guide to meteorological instruments and methods of observation*. 5th ed. World Meteorological Organization WMO-8, 483 pp.

——, 2008: *Guide to meteorological instruments and methods of observation*. 7th ed. World Meteorological Organization WMO-8, 681 pp.

Yang, D., B. E. Goodison, J. R. Metcalfe, V. S. Golubev, R. Bates, T. Pangburn, and C. L. Hanson, 1998: Accuracy of NWS 8" standard nonrecording precipitation gauge: Results and application of WMO intercomparison. *J. Atmos. Oceanic Technol.*, **15**, 54–68, doi:10.1175/1520-0426(1998)015<0054:AONSNP>2.0.CO;2.

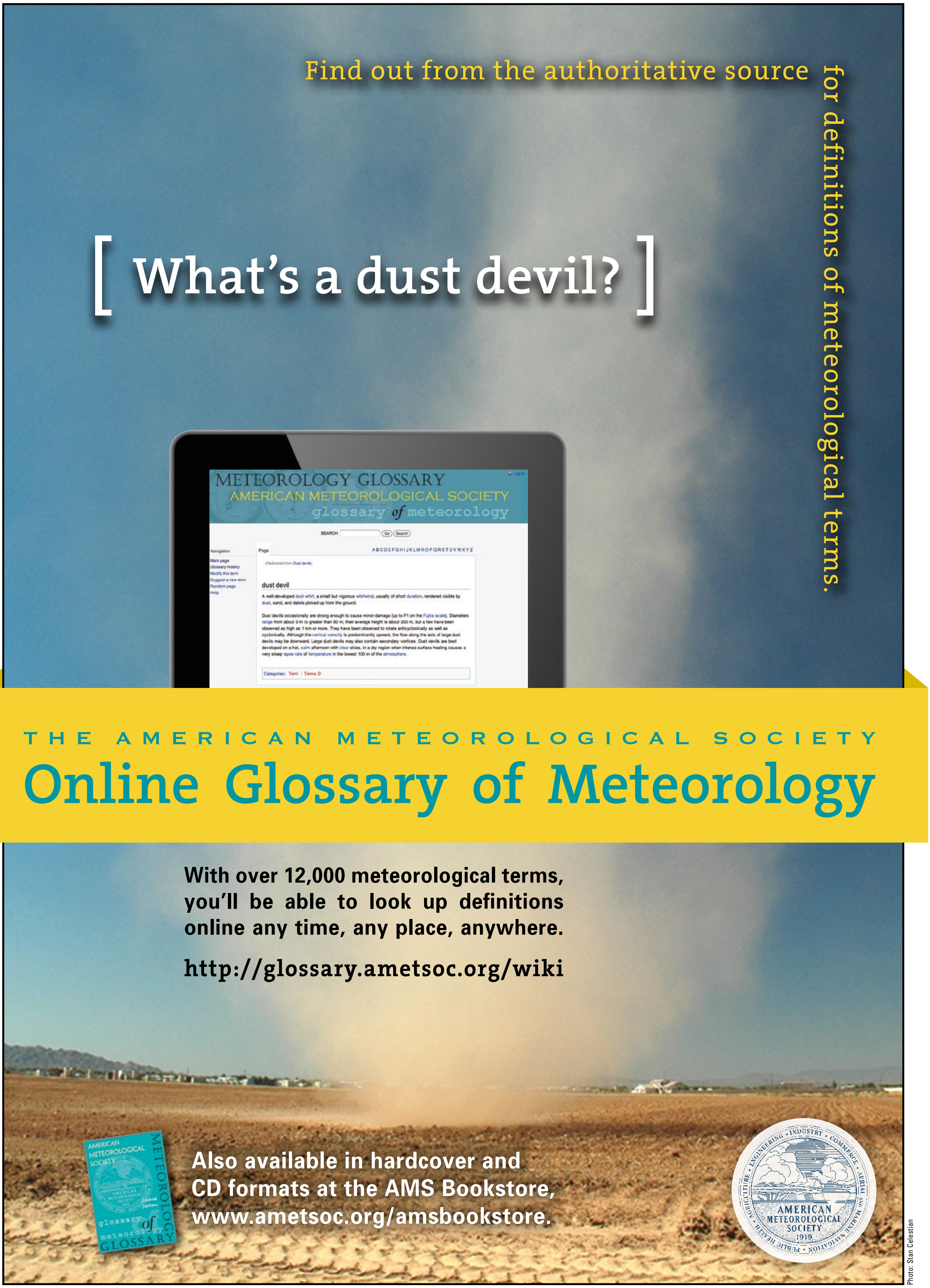

Find out from the authoritative source for definitions of meteorological terms.

[What's a dust devil?]

METEOROLOGY GLOSSARY
AMERICAN METEOROLOGICAL SOCIETY
glossary *of* meteorology

SEARCH Go Search

Navigation
Main page
Glossary History
Modify this term
Suggest a new term
Random page
Help

Page
A B C D E F G H I J K L M N O P Q R S T U V W X Y Z

(Redirected from Dust devils)

dust devil

A well-developed dust whirl; a small but vigorous whirlwind, usually of short duration, rendered visible by dust, sand, and debris picked up from the ground.

Dust devils occasionally are strong enough to cause minor damage (up to F1 on the Fujita scale). Diameters range from about 3 m to greater than 30 m; their average height is about 200 m, but a few have been observed as high as 1 km or more. They have been observed to rotate anticyclonically as well as cyclonically. Although the vertical velocity is predominantly upward, the flow along the axis of large dust devils may be downward. Large dust devils may also contain secondary vortices. Dust devils are best developed on a hot, calm afternoon with clear skies, in a dry region when intense surface heating causes a very steep lapse rate of temperature in the lowest 100 m of the atmosphere.

Categories: Term | Terms D

THE AMERICAN METEOROLOGICAL SOCIETY

Online Glossary of Meteorology

With over 12,000 meteorological terms, you'll be able to look up definitions online any time, any place, anywhere.

http://glossary.ametsoc.org/wiki

Also available in hardcover and CD formats at the AMS Bookstore, www.ametsoc.org/amsbookstore.

Photo: Stan Celestian

OBSERVING AND PREDICTING THE 2015/16 EL NIÑO

Michelle L. L'Heureux, Ken Takahashi, Andrew B. Watkins, Anthony G. Barnston, Emily J. Becker, Tom E. Di Liberto, Felicity Gamble, Jon Gottschalck, Michael S. Halpert, Boyin Huang, Kobi Mosquera-Vásquez, and Andrew T. Wittenberg

The El Niño of 2015/16 rivaled the major El Niño events of 1982/83 and 1997/98, showcasing advancements in operational observing and prediction systems, while offering challenges for the future.

The 2015/16 El Niño was likely the most widely anticipated El Niño–Southern Oscillation (ENSO) event ever, and it was preceded by nearly four decades of advancements in observing and prediction systems. Unlike the previous major El Niño event of 1997/98 (e.g., McPhaden 1999), the most recent El Niño was embedded within the fabric of the Internet and social media, with arguably more frequent updates and pathways to convey information than ever before. By mid-2015, operational forecast centers around the world were nearly unanimous: this El Niño was very likely to be strong, with the potential of rivaling previous major El Niño events in 1982/83 and 1997/98. Given the widespread coverage of these ENSO outlooks and the comparisons made to other similarly strong El Niño events, there was considerable concern about significant global impacts. While the El Niño phenomenon itself was well predicted in 2015/16, climate impacts near El Niño's peak matched historical patterns in some areas (e.g., Ropelewski and Halpert 1987; Halpert and Ropelewski 1992), but in other regions, additional climate factors clearly played a role.

Because the ENSO cycle, with its warm (El Niño) and cool (La Niña) phases, is a leading source of seasonal climate variability and predictability, it is closely monitored by many national and international organizations. The authorship on this paper is composed of individuals associated with three national-level assessments on ENSO from the National Oceanic and Atmospheric Administration (NOAA) in the United States, the Bureau of Meteorology (BoM) in Australia, and one of the agencies that composes the

AFFILIATIONS: L'Heureux, Gottschalck, and Halpert—NOAA/NWS/NCEP/Climate Prediction Center, College Park, Maryland; Takahashi and Mosquera-Vásquez—Instituto Geofísico del Perú, Lima, Peru; Watkins and Gamble—Australian Bureau of Meteorology, Melbourne, Victoria, Australia; Barnston—International Research Institute for Climate and Society, Columbia University, New York, New York; Becker and Di Liberto—NOAA/NWS/NCEP/Climate Prediction Center/Innovim, College Park, Maryland; Huang—NOAA/National Centers for Environmental Information, Asheville, North Carolina; Wittenberg—NOAA/Geophysical Fluid Dynamics Laboratory, Princeton, New Jersey
CORRESPONDING AUTHOR: Michelle L'Heureux, michelle.lheureux@noaa.gov

The abstract for this article can be found in this issue, following the table of contents.
DOI:10.1175/BAMS-D-16-0009.1

A supplement to this article is available online (10.1175/BAMS-D-16-0009.2)

In final form 26 October 2016

Multisectoral Committee of the National Study of El Niño (ENFEN) in Peru. All provide operational, or regularly updated, ENSO assessments, in part because these countries are known to have climates—and indeed economies and societies—significantly influenced by ENSO. These three agencies also happen to be geographically complementary, spanning the Pacific Ocean basin. They go beyond the automatic generation of observational and model output to provide summary-level information of the progress of ENSO and its forecast, which is aimed at a diverse set of users among the general public, whose knowledge ranges from technically savvy to novice.

ENSO is a sprawling and multifaceted coupled ocean–atmosphere climate phenomenon that affects every country in a different manner. Table 1 summarizes the current El Niño definitions and watch/alert/warning systems in association with the national-level ENSO updates. As in past years, the timing of El Niño status updates and declarations varied during 2015/16 because of differences in datasets and ENSO criteria and thresholds, which are governed by differing regional impacts. For example, Peru issues forecasts for a "coastal El Niño" because the amount of coastal rainfall they receive is very sensitive to how warm sea surface temperatures (SST) adjacent to South America become (e.g., Takahashi 2004). Ultimately, though, every agency examines a broad range of oceanic and atmospheric anomalies to inform their updates. Internationally, the Niño-3.4 SST region (thin red box in Fig. 6), in the east-central equatorial Pacific Ocean, is perhaps the most common measure of ENSO because this region is strongly coupled with the overlying atmosphere (e.g., Barnston et al. 1997) and to global teleconnections. This index also tends to be the focus of operational model displays.

These operational updates have evolved over past decades as a result of lessons learned from previous ENSO events and user demands placed on them. The 2015/16 El Niño not only showcased the latest generation of ENSO climate services, but this knowledge was disseminated and interpreted across a wide variety of media platforms, ranging from traditional mainstream outlets to social media—a vastly different communication environment compared to the last major El Niño event of 1997/98. This came with its own set of advantages, such as exposure to far broader audiences, and disadvantages, such as the sometimes-questionable interpretation of datasets and forecast outlooks, which differed from official assessments. While the ENSO assessments and dissemination processes vary by national agency, the following sections of this paper summarize our collective experience in tracking the observational evolution, verifying the model forecasts, and documenting the global climate anomalies associated with the historic 2015/16 El Niño.

DATASETS AND METHODS. Since the major El Niño of 1997/98, many observational reconstructions and reanalysis datasets have been created or improved. Unlike station-based data or point "in situ" observations (e.g., a buoy), these gridded datasets are complete both spatially and temporally and, for the statistical reconstructions of SST, extend as far back as the late 1800s. Several operationally oriented centers update datasets in near–real time, which allows scientists to monitor the tropical Pacific. Given the interest in the 2015/16 El Niño and its potential impacts, these real-time datasets were popular with users, many of whom were interested in the strength of the event and its ranking relative to past El Niño events.

Complicating this assessment, however, each center relies on a set of core observational datasets for its ENSO updates, so the exact values for a given variable (e.g., Niño-3.4 SST) will vary depending on which dataset is examined. These differences between datasets primarily arise because of structural reasons, such as the choice of the dynamical model or the statistical method used to infill between available observations. The disparities are particularly evident across the tropical Pacific Ocean, which contains large regions that are not covered by point measurements (e.g., buoys, ships). Many centers additionally rely on datasets that ingest not only buoy or ship data, but also satellite information. However, the modern satellite record began in the late 1970s, which prevents the use of these datasets for historical rankings going further back in time. Moreover, satellite estimates have biases (due to issues like varying equatorial crossing times), which need to be corrected by in situ surface observations, and these corrections can vary over time and space as new satellites are incorporated (e.g., Huang et al. 2015a). Some datasets like the NOAA Extended Reconstructed SST (ERSST) opt to not include satellite information in order to preserve the consistency, or homogeneity, of the record. But, for purposes outside of historical comparisons and to provide more real-time ENSO updates, these satellite-based datasets are strongly relied upon both to get an overall sense of the ENSO evolution and as the initial conditions for many forecast models.

Because of the interest in how the 2015/16 event compares with other major El Niño events, we prioritize datasets that are routinely updated and, when possible, datasets that were constructed with the intent of providing a consistent, homogenous climate record. Individually, none of these datasets represent "the truth" or perfect measurements over the entire tropical Pacific Ocean. For that reason, in addition to showing the individual datasets, we also display the average of multiple datasets to compare events, which we hypothesize can reduce the structural error associated with the observational datasets, analogous to the reduction of error through multimodel averaging (e.g., DelSole et al. 2014).

To compare historical strength, we focus on the SST statistical reconstructions: two versions of ERSST (v3b and v4; Smith et al. 2008; Huang et al. 2015b), the Hadley Centre SST (HadISST; Rayner et al. 2003), and the Centennial In Situ Observation-Based Estimates (COBE) SST dataset (Ishii et al. 2005), which extend back to the late 1800s. All Niño index regions (shown in Fig. 6) are computed to provide a sense of how the events varied by location. These indices span the equatorial Pacific Ocean and are used to summarize the breadth of the SST anomalies and where they are largest. Thus, these regions are also used to provide information on the "El Niño flavor," a term popularized in recent years to describe the continuum of different spatial patterns of SST anomalies that result from ENSO (Capotondi et al. 2015).

To evaluate the tropical Pacific atmosphere, we feature the zonal gradient of 1000-hPa geopotential height between Indonesia and the eastern equatorial Pacific, the equatorial Southern Oscillation index (EQSOI), and the more traditional, station-based Tahiti minus Darwin Southern Oscillation index (SOI). To compare the former, we use seven reanalysis datasets that extend back to at least 1979 (see caption of Fig. 5). We also examine three satellite-based outgoing longwave radiation (OLR) records, a proxy for tropical convection, which compared to precipitation, is better monitored over the tropical Pacific Ocean and therefore more stable in time and space. Data are based on the Advanced Very High Resolution Radiometer (AVHRR; Liebmann and Smith 1996) and the High Resolution Infrared Radiation Sounder (HIRS) v2r2 and v2r7 (Lee et al. 2007).

To describe the within-event evolution of the 2015/16 El Niño and how similar it was to past major events, we make use of the daily depth of the 20°C

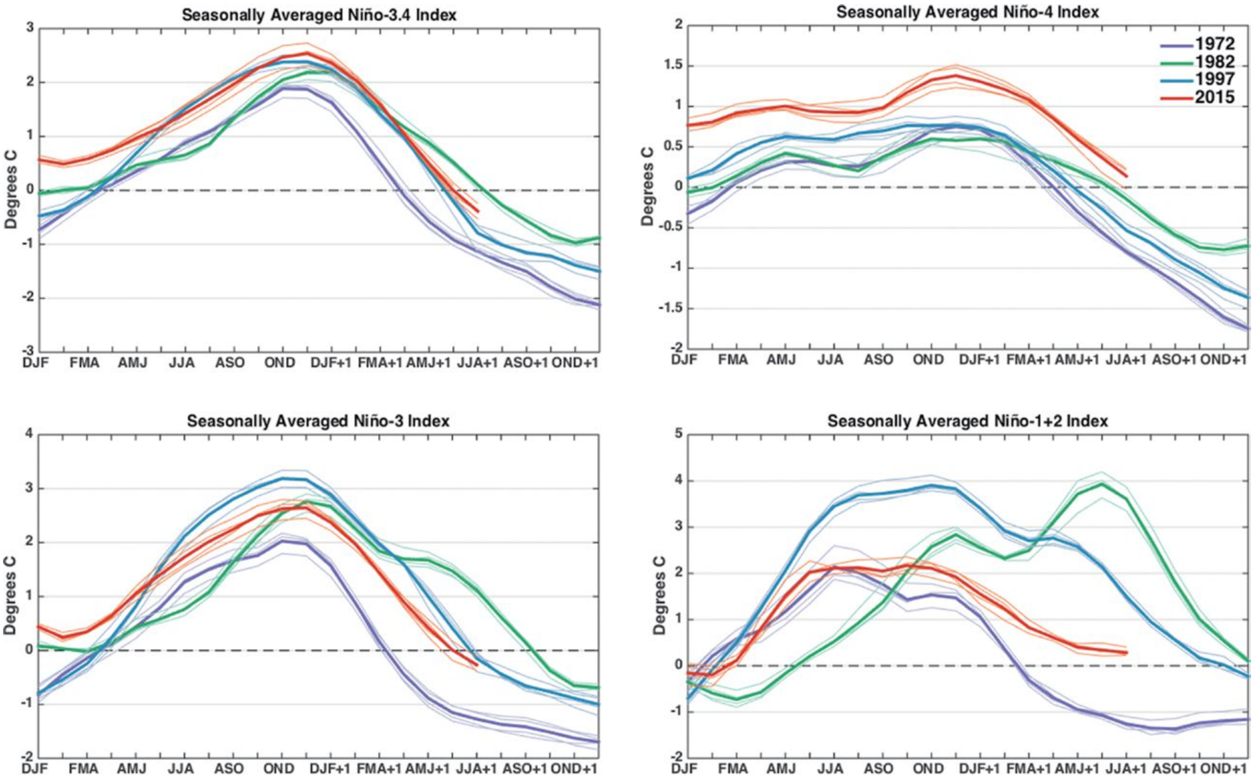

Fig. 1. Evolution of seasonal (3 month) averaged values of the (top left) Niño-3.4, (top right) Niño-4, (bottom left) Niño-3, and (bottom right) Niño-1+2 SST indices during 2015/16 (red), 1997/98 (blue), 1982/83 (green), and 1972/73 (purple). The Niño-3.4 region covers 5°N–5°S, 170°–120°W; the Niño-4 region covers 5°N–5°S, 150°–160°E; the Niño-3 region covers 5°N–5°S, 150°–90°W; and the Niño-1+2 region covers 0°–10°S, 90°–80°W (regions displayed in Fig. 6). Thin lines correspond to the ERSSTv3b, ERSSTv4, COBE, and HadISST datasets and the thicker line is the average of all datasets. Departures are formed by removing monthly means during 1981–2010.

Table 1. Current ENSO systems for Australia, Peru, and the United States.

Australian Bureau of Meteorology
El Niño/La Niña watch: The chance of an El Niño developing in the coming season has increased. When these criteria have been met in the past, El Niño/La Niña conditions have developed around 50% of the time. The following criteria are used: 1) ENSO phase is currently neutral or La Niña/El Niño is declining. 2) Either of the following conditions apply: of the closest 20 analog years (based on SOI), 4 or more have shown El Niño/La Niña characteristics or significant subsurface warming (El Niño) or cooling (La Niña) has been observed in the western or central equatorial Pacific Ocean. 3) One-third or more of the surveyed climate models show SSTs at least 0.8°C above average (El Niño) or below average (La Niña) in the Niño-3 or Niño-3.4 regions by late winter or spring.
El Niño/La Niña alert: The chance of an El Niño/La Niña developing in the coming season has increased. When these criteria have been met in the past, El Niño/La Niña has developed around 70% of the time. The following three criteria need to be met: 1) A clear warming (El Niño) or cooling (La Niña) trend has been observed in the Niño-3 or Niño-3.4 regions during the past 3–6 months. 2) Trade winds have been weaker (El Niño) or stronger (La Niña) than average in the western or central equatorial Pacific Ocean during any 2 of the last 3 months. 3) The 2-month average SOI is −7 or lower (El Niño) or +7 or higher (La Niña). 4) A majority of surveyed climate models show SSTs at least 0.8°C above average (El Niño) or below average (La Niña) in the Niño-3 or Niño-3.4 regions by the late winter or spring.
El Niño/La Niña: An El Niño/La Niña has been declared and is under way. Any three of the following criteria need to be met: 1) Temperatures in the Niño-3 or Niño-3.4 regions are 0.8°C warmer (El Niño) or cooler (La Niña) than average. 2) Trade winds have been weaker (El Niño) or stronger (La Niña) than average in the western or central equatorial Pacific Ocean during any 3 of the last 4 months. 3) The 3-month average SOI is −7 or lower (El Niño) or +7 or higher (La Niña). 4) A majority of surveyed climate models show SSTs remaining at least 0.8°C above average (El Niño) or below average (La Niña) in the Niño-3 or Niño-3.4 regions of the Pacific until the end of the year.
Updated as part of the ENSO Wrap-Up: www.bom.gov.au/climate/enso/
Comité encargado del Estudio Nacional del Fenómeno El Niño (ENFEN Committee, Peru)
ENFEN monitors and predicts El Niño/La Niña in two regions: • The first is the "coastal" El Niño (La Niña), when the Índice Costero El Niño (ICEN; 3-month running-mean Niño-1+2 SST index, www.met.igp.gob.pe/datos/icen.txt) is above (below) 0.4°C (−1.0°C) for three or more consecutive months. The overall strength of the event is determined by the three largest ICEN values in the event, according to preestablished thresholds. In the Northern Hemisphere winter/spring, warming can produce heavy rain over the arid coast. • The second region is the "central Pacific" El Niño/La Niña, which is based on the Niño-3.4 SST index using a threshold of ±0.5°C. This impacts the Peruvian Andes and the Amazon through teleconnections.
The following are the alert system states for the coastal El Niño/La Niña: • Coastal El Niño/La Niña watch, when there is a higher expectation that El Niño/La Niña will occur than not. • Coastal El Niño/La Niña alert, when the El Niño/La Niña is believed to have started based on observed ocean–atmosphere conditions and/or if the ICEN qualifies. • Inactive, when neutral conditions are present or El Niño/La Niña conditions are expected to end.
Updated as part of ENFEN's official statements: www.imarpe.pe/imarpe/lista.php?id_seccion=I016602000000000000000

isotherm from the Tropical Atmosphere Ocean (TAO; McPhaden et al. 2010) buoys and Argo floats (e.g., Roemmich and Gilson 2009), weekly SST results from the Optimal Interpolation SST dataset (OISSTv2; Reynolds et al. 2002), and daily 10-m winds from the European Centre for Medium-Range Weather Forecasts (ECMWF) interim reanalysis (ERA-Interim) (Dee et al. 2011). To evaluate the combined multimodel forecasts made by the International Research Institute for Climate and Society (IRI) and Climate Prediction Center (CPC) during 2014–16, the newer, higher-resolution (0.25° × 0.25°) daily OISST product is used to compute seasonal mean Niño-3.4 index values (Reynolds et al. 2007). While most models are not initialized with the same SST data, the dynamical models use higher-resolution analyses like the daily OISST.

To examine the 500-hPa geopotential height anomalies over the globe during the Northern Hemisphere winter, we make use of monthly data from the National Centers for Environmental Prediction (NCEP)–National Center for Atmospheric Research (NCAR) reanalysis (Kalnay et al. 1996). Observed surface air temperature data are obtained from the 2.5° × 2.5° gridded GHCN+CAMS temperature dataset (Fan and Van den Dool 2008), a combination

TABLE 1. Continued.

National Oceanic and Atmospheric Administration (NOAA)/Climate Prediction Center, United States
El Niño/La Niña watch: When oceanic and atmospheric conditions across the tropical Pacific are favorable for the onset of El Niño–La Niña within the next 6 months.
El Niño/La Niña advisory, when El Niño/La Niña conditions are present as measured by the following three criteria:
El Niño advisory: 1) 1-month Niño-3.4 SST index value that is at or in excess of +0.5°C, 2) atmospheric conditions are consistent with El Niño (i.e., weaker low-level trade winds, enhanced convection over the central or eastern Pacific Ocean), and 3) The expectation that El Niño will persist as measured by at least five overlapping seasonal (3-month average) Niño-3.4 SST index values at or in excess of +0.5°C.
La Niña advisory: 1) 1-month Niño-3.4 SST index value that is equal to or less than −0.5°C, 2) atmospheric conditions are consistent with La Niña (i.e., stronger low-level trade winds, suppressed convection over the central Pacific Ocean), and 3) the expectation that La Niña will persist as measured by at least five overlapping seasonal (3-month average) Niño-3.4 SST index values at or less than −0.5°C.
Final El Niño/La Niña advisory, when the El Niño/La Niña has ended.
Not active (NA), when the ENSO alert system is not active.
Updated as part of the ENSO Diagnostics Discussion: www.cpc.ncep.noaa.gov/products/analysis_monitoring/enso_advisory/index.shtml

of two large station datasets, the Global Historical Climate Network (GHCN) and the Climate Anomaly Monitoring System (CAMS). Global precipitation data are from the 2.5° × 2.5° gridded Precipitation Reconstruction Dataset (PREC; Chen et al. 2002), which is also based on gauge observations from GHCN and CAMS.

Unless clearly specified otherwise, anomalies are calculated as departures from a 1981–2010 monthly mean climatology or, for submonthly data, a climatology that is based on the first four harmonics of the seasonal cycle. Because of this fixed 30-yr base period, longer decadal or secular trends are likely to be incorporated into the anomalies (e.g., L'Heureux et al. 2013).

EVOLUTION OF TROPICAL PACIFIC OCEANIC AND ATMOSPHERIC ANOMALIES.

During the 2015/16 El Niño, all of the Niño SST indices registered values that were at least among the top three in the historical record, reinforcing its categorization as one of the strongest El Niño events on record extending at least back to 1950. Figure 1 presents the evolution of the seasonal (3 month) average values of the Niño SST indices during 2015/16 relative to 1972/73, 1982/83, and 1997/98. Overlapping seasonal index values are presented because ENSO is a climate phenomenon, typically identified on seasonal-to-interannual time scales. With the exception of Niño-1+2, the Niño indices were nearly +0.5°C above average at the beginning of 2015. This was warmer than at the start of 1997 and 1982 and likely the remnants of a borderline El Niño-neutral situation in 2014 (McPhaden 2015). Positive SST anomalies were largest near the international date line through March 2015 (Fig. 2, left). Beneath the surface, temperature anomalies were also warm in the western and central equatorial Pacific (Fig. 3, left). As in 1997, a series of westerly wind bursts during the first quarter of 2015 (Fig. 4, left) resulted in the eastward progression of a downwelling oceanic Kelvin wave (Fig. 3, left). As the thermocline deepened in the eastern Pacific, positive SST anomalies significantly strengthened near South America where the Niño-1+2 and Niño-3 indices reached +1.5°C by May–July (MJJ) 2015 (Fig. 1, bottom row).

The region of the largest positive SST anomalies expanded westward from May through November 2015, which was also similar to the evolution during 1997 (Fig. 2). Primarily because of the increase of the thermocline depth and surface temperatures anomalies, NOAA, BoM, and ENFEN all declared the onset of El Niño conditions by mid-May 2015. Most Niño regions closely tracked the evolution of the 1997/98 El Niño through July 2015, which, alongside model forecasts, was factored into the outlooks as corroborating information that this event would likely peak as a strong event based on warming in the Niño-3.4 and the Niño-1+2 indices. In accordance with this outlook, the Niño-3.4 and Niño-3 indices grew monotonically during the rest of 2015, peaking near +2.5°C during November–January (NDJ)

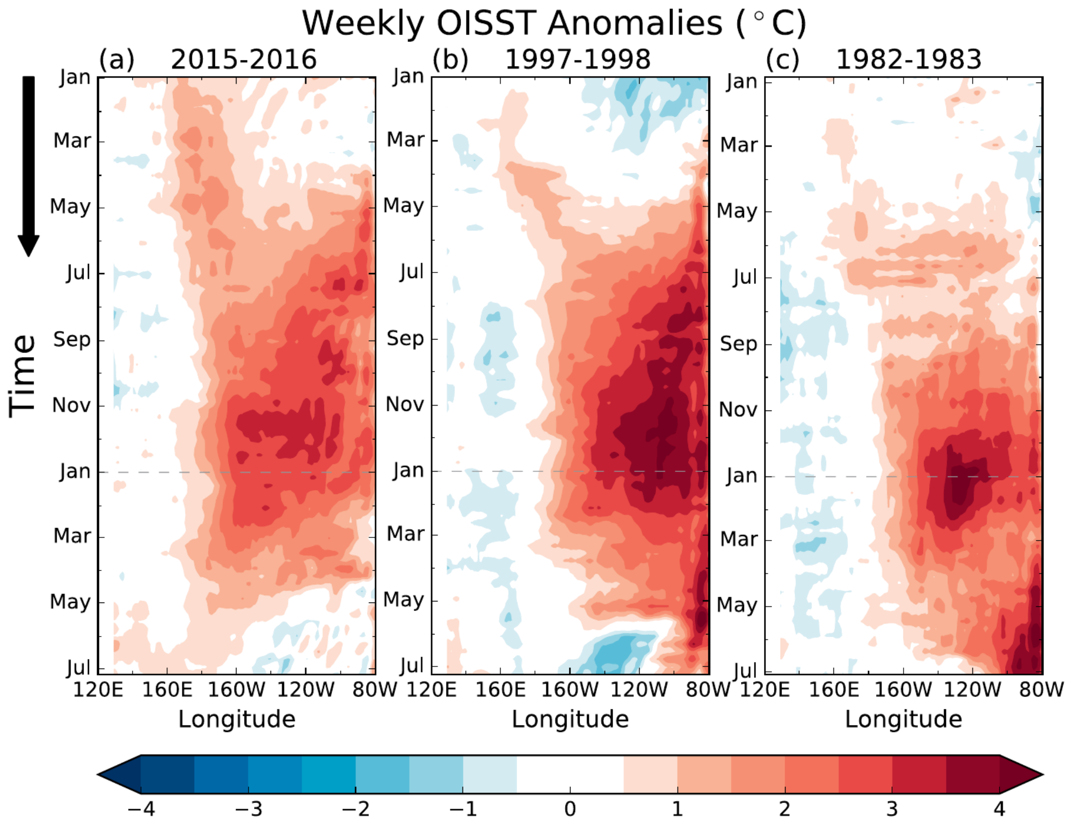

Fig. 2. Longitude–time (Hovmöller) diagram of weekly SST anomalies across the equatorial Pacific Ocean (5°S–5°N) from 120°E to 80°W during (a) 2015/16, (b) 1997/98, and (c) 1982/83. Departures are formed by removing the first four harmonics of interpolated from daily data during 1981–2010. Data are based on weekly OISSTv2.

2015/16 (Fig. 1). However, across the eastern Pacific, the thermocline depth anomalies during NDJ 2015/16 were not as deep as 1997/98.

Going back to at least 1950, seasonal Niño-3.4 index values were near record at the peak of the event, but the spread among different datasets (Fig. 1) and the uncertainty as documented in ERSSTv4 by Huang et al. (2016) precludes clear designation as a record. The westernmost Niño-4 index values were particularly remarkable compared to the previous events, with seasonal values near +1.0°C through most of 2015, and a peak just shy of 1.5°C during NDJ 2015/16. In contrast, the other significant El Niño events failed to reach +1°C. Interestingly, the 2015/16 warming in the Niño-4 region was comparable to that of the 2009/10 El Niño, which was not a major event, but had record warming in this region (Lee and McPhaden 2010).

After the midpoint of 2015, the growth in the Niño-1+2 and Niño-3 SST indices noticeably slowed relative to the 1997/98 El Niño (Fig. 1). In fact, the easternmost Niño-1+2 index did not perceptibly strengthen beyond the MJJ 2015 value of +2°C, which clearly fell short of the nearly +4°C maximum achieved during the 1997/98 and 1982/83 events. While there were roughly the same number of downwelling Kelvin waves as in 1997/98, they did not have as much of an influence on the amplitude of the subsurface temperature anomalies in the eastern Pacific (Fig. 3), consistent with the smaller eastward extent, and weaker magnitude, of the westerly wind anomalies (Fig. 4). This may be tied to cooling related to the decadal shift toward stronger trade winds (e.g., Hu et al. 2013) or possibly related to the nonlinear convective feedback across the eastern Pacific Ocean (e.g., Takahashi and Dewitte 2016).

Indices that measure the atmospheric component of ENSO over the tropical Pacific (e.g., pressure and convection) were also indicative of an impressive El Niño in 2015/16, albeit not a record-setting one. Figure 5 (top) shows that the traditional SOI, based on the difference in sea level pressure between Tahiti minus Darwin stations (dashed lines), and the equatorial SOI (solid lines) were both substantially negative, reflecting the weakening of the Pacific Walker circulation that is typical of El Niño. During 2015/16, the SOI minimum was nearly 2 standard deviations below the 1981–2010 mean, and the minimum EQSOI value

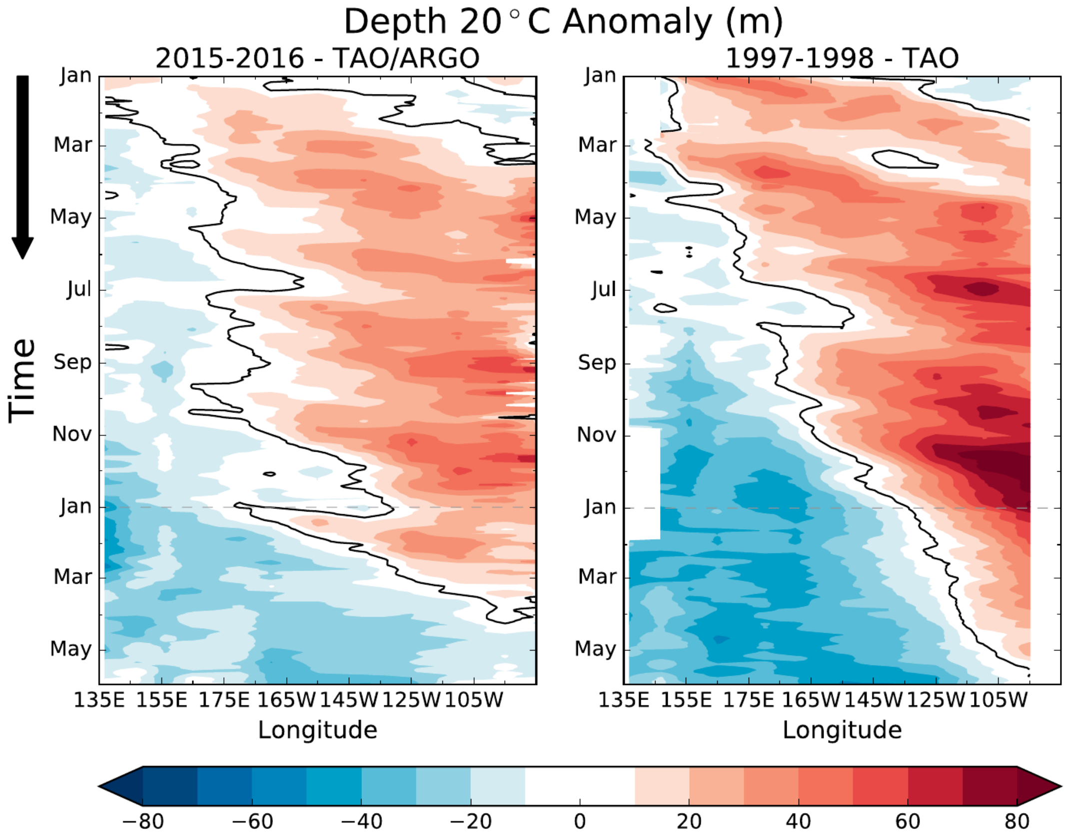

Fig. 3. Longitude–time (Hovmöller) diagram of 5-day running averages of the 20°C isotherm depth (m) across the equatorial Pacific (2°S–2°N) from 135°E to 75°W during (left) 2015/16 and (right) 1997/98. Data are based on the TAO moored buoys from 11 transects and Argo floats near 85°W. A 5-day running mean was applied and spatial interpolation is based on Python contourf. The data were processed by the Instituto Geofisico del Peru using the 1981–2010 climatology obtained from NCEP Global Ocean Data Assimilation System (GODAS).

was approximately –2.5 standard deviations using the mean of the reanalyses, with noticeable spread among the individual datasets. The 2015/16 values were not as low as in 1982/83 (the historical record for both the SOI and EQSOI) and also fell short of 1997/98 values.

The OLR indices over the eastern and central tropical Pacific Ocean were also quite negative, indicating increased convection and rainfall over the areas of above-average SST (Fig. 5, middle and bottom panels; Chiodi and Harrison 2013; L'Heureux et al. 2015). The eastern Pacific OLR index is strongly skewed compared to the central Pacific index, reflecting nonlinearity in SSTs (e.g., Takahashi and Dewitte 2016), so the differences in evolution with 1997/98 and 1982/83 are more dramatic. However, seasonal values in both indices were among the top three most significant events.

As is typical with the evolution of ENSO events, all ENSO indices weakened after the Northern Hemisphere winter of 2015/16. As the event decayed, there was a steeper dropoff in the eastern regions of Niño-1+2 and Niño-3 compared to 1982/83 and in Niño-1+2 compared to 1997/98 (Fig. 1). The Niño-1+2 region was most similar to the trajectory of 1972/73, which was in stark contrast to the 1982/83 event that maximized during May–July of the second year and the 1997/98 event. During the latter two events, the anomalous westerly winds across the eastern Pacific helped to maintain larger positive SST anomalies (Vecchi and Harrison 2006), which were absent in 2015/16 (Fig. 4). After April–June (AMJ) 2016, the Niño regions returned to values reflective of ENSO-neutral conditions, though the decrease in Niño-4 lagged the other El Niño events because it achieved higher SST anomalies at its peak.

Overall, one of the more distinct aspects of the 2015/16 El Niño, compared to 1997/98 and 1982/83, was the cooler SST anomalies in the east and warmer SST anomalies in the west; this was especially noticeable at the maximum in November and December 2015 (Fig. 2). Consistent with the Bjerknes feedback (coupling between SST and wind anomalies), Fig. 4 shows that the westerly wind anomalies from August through December 2015 were not as strong as in the

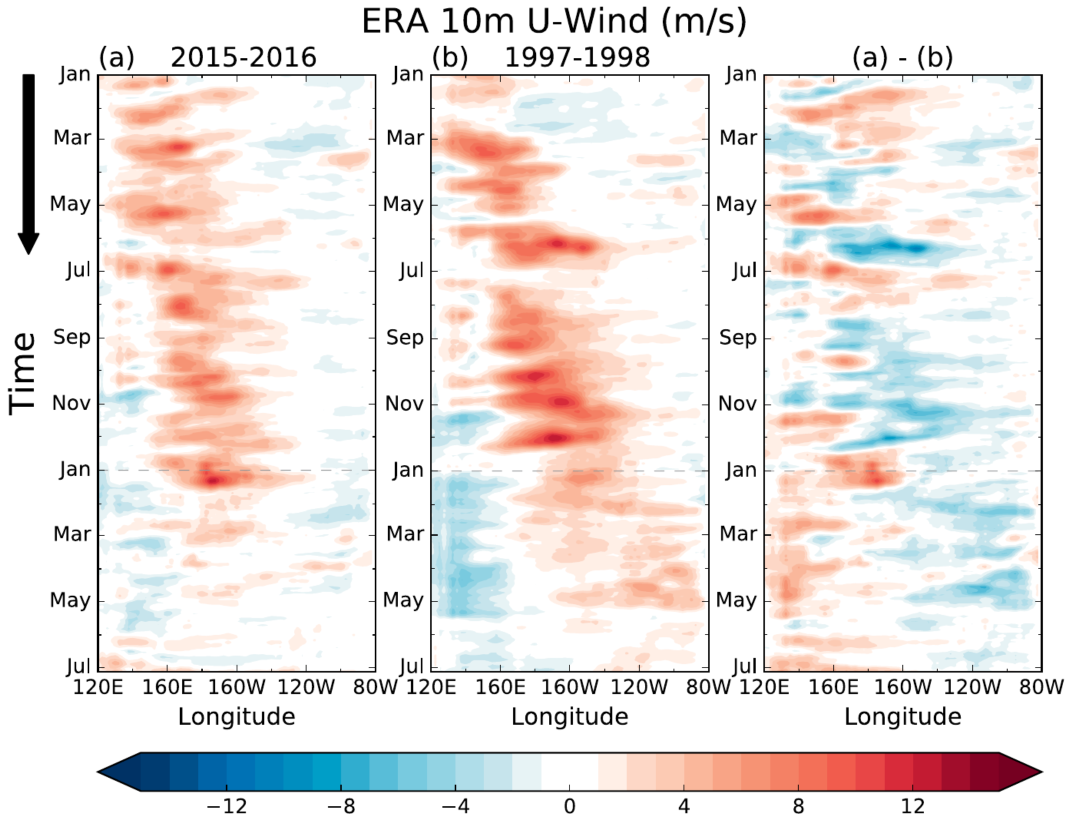

Fig. 4. Longitude–time (Hovmöller) diagram of daily 10-m zonal wind anomalies across the equatorial Pacific Ocean (5°S–5°N) from 120°E to 80°W during (a) 2015/16 and (b) 1997/98, and (c) the difference between 2015/16 and 1997/98. Departures are formed by removing the first four harmonics of interpolated daily data during 1981–2010. Data are based on ERA-Interim.

same months in 1997 over the central and eastern equatorial Pacific Ocean [this is also replicated using NCEP Climate Forecast System Reanalysis (CFSR) 10-m winds; not shown]. Hence, relative to the *anomalies* of the last major El Niño, the zonal or east–west differences in anomalous SST, subsurface temperatures, winds, and pressure during the last half of 2015 were not as pronounced across the equatorial Pacific Ocean.

Figures ES1 and ES2 in the online supplement to this article (http://journals.ametsoc.org/doi/10.1175/BAMS-D-16-0009.2) also indicate that the anomalous meridional SST gradient was more relaxed during 2015/16 relative to 1997/98 and 1982/83. Typically, during El Niño, SSTs are above average on the equator and then taper to smaller values off the equator. During 2015/16, across the eastern Pacific (150°–90°W), the anomalous SSTs were relatively warmer just to the north of the equator (5°–10°N) and cooler immediately along the equator (2.5°S–2.5°N). Figure ES2 suggests that the weakening of the typical anomalous El Niño meridional gradient was associated with a corresponding dearth of enhanced convection across the central and eastern Pacific Ocean (also see Fig. 5).

The exceptional Niño-4 SST index values reflect the enhanced westward extension of positive SST anomalies during 2015/16. While one could define this pattern as a major El Niño event with a bit of a "central Pacific" flavor in a relative sense compared to the other major events, we would be remiss not to point out the broad stretch of above-average SSTs extending across the central and eastern equatorial Pacific. In fact, the SST anomalies with the largest amplitudes occurred within the east-central Pacific and, in particular, within the Niño-3.4 region (Fig. 1). Figure 6 shows that the observed SST anomalies spatially correlate very well onto the pattern that results from regressing SST anomalies onto the Niño-3.4 index. At its peak in November–January, the pattern of SST anomalies extended farther westward and projected better onto the Niño-3.4 index than in previous major El Niño events (Fig. ES1).

In addition to the most recent El Niño projecting well onto the Niño-3.4 index relative to past years between 1982 and 2016 (cf. individual black dots in the bottom panels of Fig. 6), the 2015/16 boreal winter also was associated with nearly equal weights

▸ Fig. 5. Evolution of (top) seasonal (3 month) averaged values of the traditional Tahiti–Darwin station-based SOI (dashed lines) and EQSOI (solid lines), (middle) central Pacific OLR index, and (bottom) eastern Pacific OLR index during 2015/16 (red), 1997/98 (blue), and 1982/83 (green). The EQSOI is based on the difference between the 5°N–5°S, 80°–130°W and 5°N–5°S, 90°–140°E regions. CP OLR is based on the 5°S–5°N, 170°E–140°W region and the EP OLR region covers 5°S–5°N, 160°–110°W. Thin solid lines in the top panel correspond to the NCEP CFSR (Saha et al. 2010), NCEP–NCAR reanalysis (Kalnay et al. 1996), NCEP–Department of Energy (DOE) Atmospheric Model Intercomparison Project (AMIP) II reanalysis (Kanamitsu et al. 2002), ERA-Interim (Dee et al. 2011), Japanese 55-year Reanalysis (JRA-55) (Kobayashi et al. 2015), and NASA Modern-Era Retrospective Analysis for Research and Applications (MERRA1) and MERRA2 (Rienecker et al. 2011). Thin solid lines in (middle) and (bottom) are from AVHRR and the HIRS v2r2 and v2r7. The thick solid line in all panels is the average of individual datasets. All indices are standardized using monthly means and standard deviations during 1981–2010.

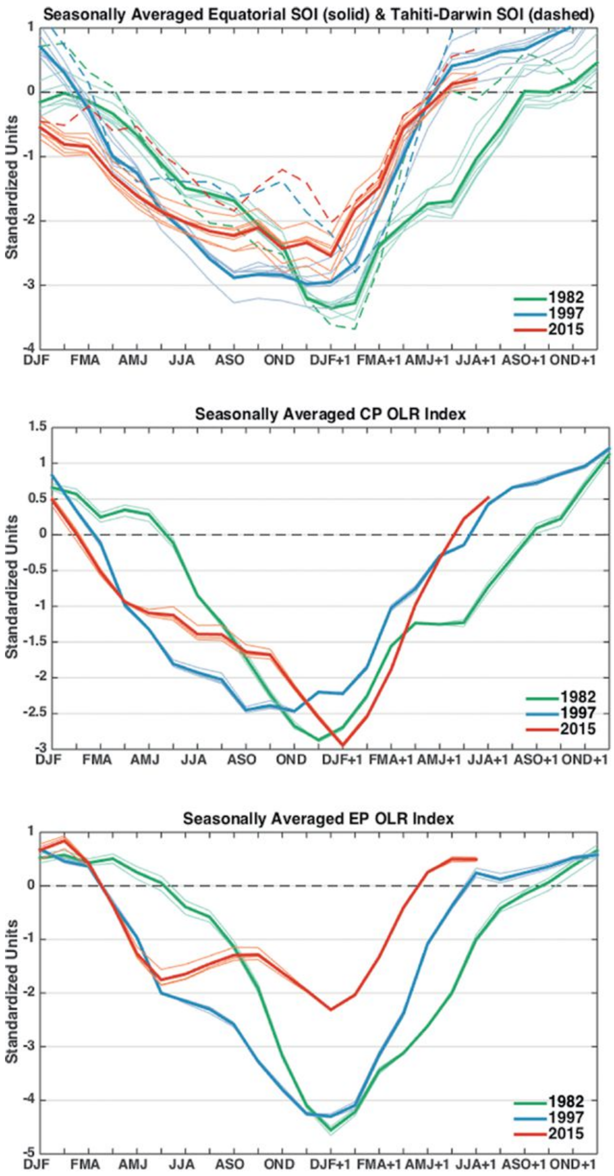

(~2 standard deviation values) in the so-called E and C indices of Takahashi et al. (2011). While there are many different indices available for evaluating ENSO flavors, the E and C indices isolate SST anomalies in the eastern and central equatorial Pacific Ocean, respectively. For example, the 1982/83 and 1997/98 El Niño had strongly projected onto the E index relative to 2015/16, while the previous El Niño in 2009/10 was well captured by the C index. Therefore, the most recent event was approximately in the middle of the ENSO continuum (Capotondi et al. 2015), with less intensification in the far eastern Pacific Ocean.

MODEL FORECASTS OF THE NIÑO-3.4 SEA SURFACE TEMPERATURE INDEX.

Operational forecast centers consider their own in-house climate models and a number of model plumes, which display members and/or ensemble means from an assortment of different models. The IRI/CPC multimodel plume of Niño-3.4 SST forecasts is perhaps the longest-running, operational collection of various models, which includes both dynamical and statistical models. Once a month, agencies around the world provide ensemble-average, overlapping seasonal Niño-3.4 SST index values going out to 9 months. The exact dates of initialization, number of members in the ensemble mean, and mean bias correction is left up to the model providers.

An average of the multimodel ensemble (MME) of just over 15 "dynamical" and nearly 10 "statistical" models is displayed in the latest updates of the IRI/CPC plume.[1] However, embedded within the dynamical category are a set of about five models called intermediate-complexity coupled models (ICMs) that are not comprehensive like the state-of-the-art dynamical models and rely more heavily on statistical methods. Over the last couple of years, in general, the skill scores associated with the dynamical average improve when the ICM results are excluded, and the ICM-only average is not an improvement upon the

---

[1] Dynamical models typically require supercomputing resources, involve data assimilation systems, and explicitly calculate the future state based on the physics of the atmosphere, land, ice, and oceans, and their interactions. Statistical models can be run on a desktop computer and rely upon historical relationships in the observational record and assume these relationships will hold into the future.

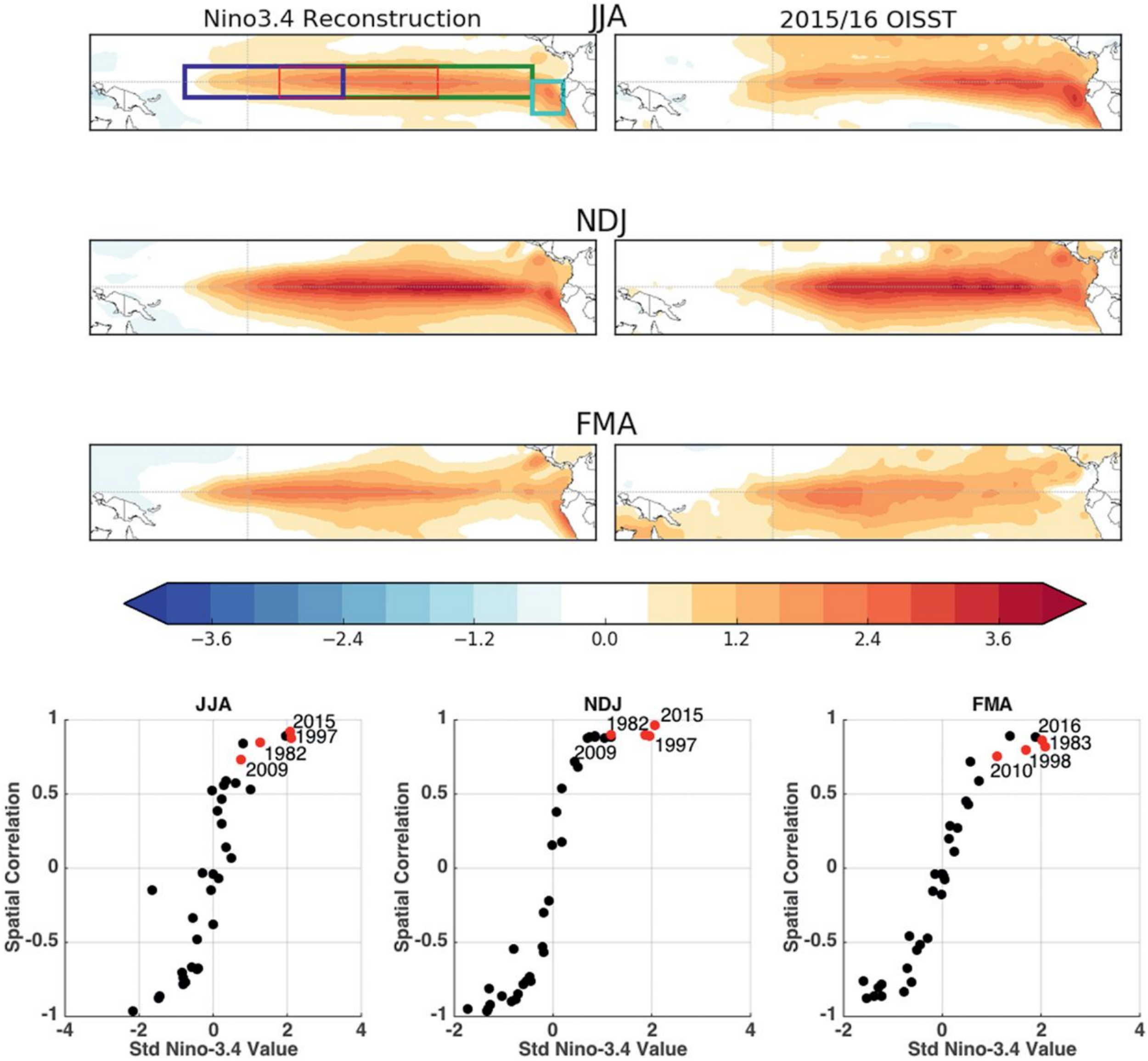

Fig. 6. SST anomaly reconstruction based on the weighted regression map of (top left) the Niño-3.4 index and (top right) the observed SST anomalies during 2015/16 for seasonal averages during JJA, NDJ, and FMA. (bottom) The spatial correlation between the reconstruction and observations is shown along the ordinate and the seasonal average Niño-3.4 index value is shown along the abscissa. Each dot represents a single year between 1982 and 2016. The red dots indicate the 2015/16 El Niño, two other strong El Niños in 1997/98 and 1982/83, and the 2009/10 El Niño, which is the El Niño prior to the 2015/16 event. The top-left panel displays the Niño-4 region (blue), Niño-3.4 region (thin red), Niño-3 region (green), and Niño-1+2 region (aqua). Departures are formed by removing monthly means during 1981–2010. Data are based on weekly OISSTv2.

statistical model average (see Figs. ES3–ES5 in the online supplement to this paper).

Figure 7 illustrates, in grayscale, every individual model forecast made for targets during December–February (DJF) 2013/14 through February–April (FMA) 2015/16 for the dynamical (top panel), which include the ICMs, and statistical models (bottom panel). The solid blue and red lines lie within the spread of the gray lines because they represent the MME average of the individual models. Generally, the MME mean tends to be more skillful than any individual model because the averaging helps to cancel out model errors (Palmer et al. 2004; Kirtman et al. 2014). However, a single observation will be a result of some predictable signal (e.g., ENSO dynamics) and unpredictable, random noise, while averaging in the MME is designed to suppress the unpredictable noise in order to enhance the signal. ENSO events are forecast opportunities when the role of the predictable signal becomes greater than the typical level of noise (e.g., Vecchi et al. 2006; Kumar and Hu 2014).

The 2015/16 predictions of the Niño-3.4 SST index were successful, especially when juxtaposed with the low ENSO predictability of the previous decade (Barnston et al. 2012) and the predictions of an El Niño in 2014/15 that did not grow as expected (McPhaden 2015). For target periods during 2014, the statistical MME average anomalies (blue lines) were closer to the observed anomalies (black line), while the dynamical MME average (red lines) largely overforecasted the amount of warming in Niño-3.4. But, after mid-2014, the forecasts improved and were generally closer to the modest warming (Niño-3.4 near +0.5°C) observed for several seasons in 2014/15.

Coming out of the 2014/15 Northern Hemisphere winter, a number of dynamical and statistical models were predicting a decrease in the Niño-3.4 index. Once the observational data showed warming in early 2015, many dynamical and statistical models began to forecast a more significant El Niño. However, both MME averages underestimated the peak strength of the episode, not catching onto the possibility of a +2°C-sized event until mid-July 2015 for the dynamical and mid-August 2015 for the statistical models.

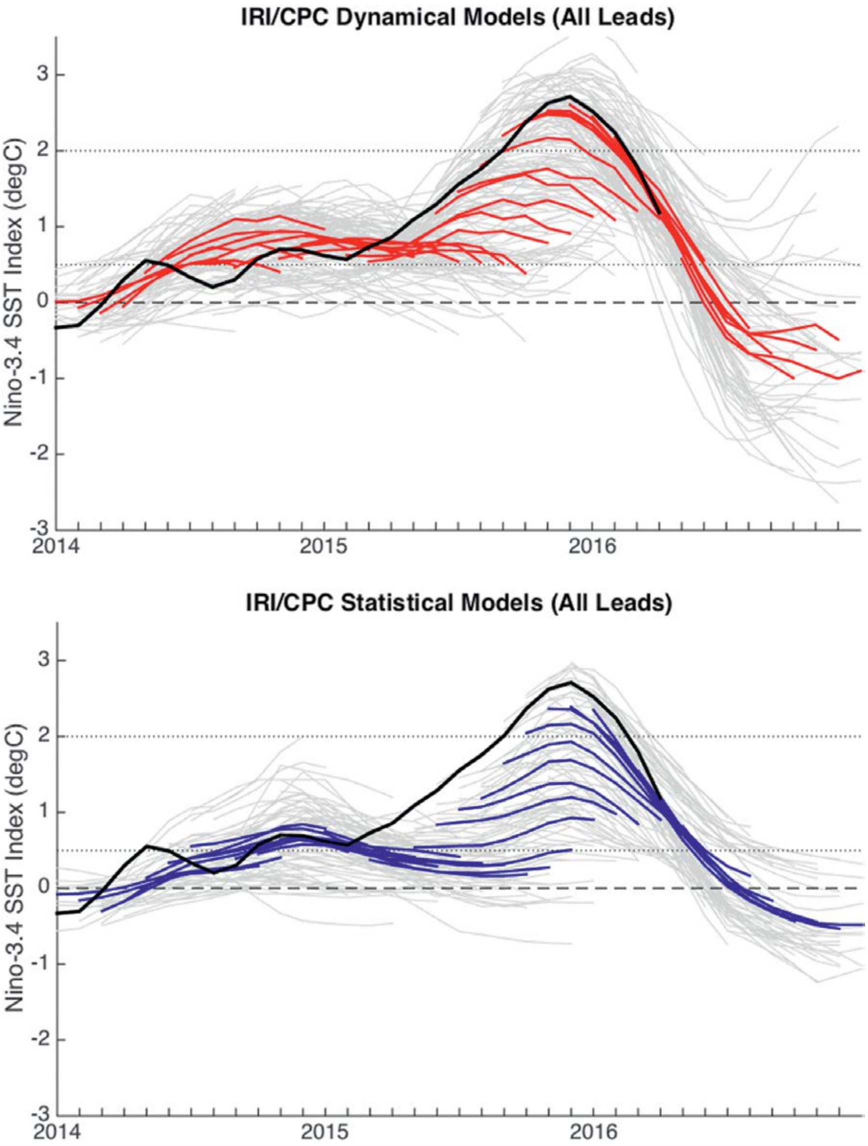

Fig. 7. Predictions of the Niño-3.4 index for overlapping, seasonal target periods from DJF 2013/14 to FMA 2016 for the (top) dynamical and (bottom) statistical models drawn from the IRI/CPC plume. Gray lines show every individual model forecast and the red and blue lines show the dynamical and statistical multimodel averages, respectively. The thick black line shows the observational databased on seasonal averages of daily OISST data.

By August 2015, official ENSO outlooks were more assertively playing up the potential of a historically strong event. At this time, public communications explicitly favored an event rivaling the peak amplitudes of past major El Niños. As far back as May 2015, BoM noted that the dynamical model averages from the World Meteorological Organization (WMO) Global Producing Center of Long Range Forecasts (a subset of models in the IRI/CPC plume) were in excess of +2°C for the upcoming fall/winter seasons. ENFEN also noted that Niño-1+2 forecasts created using the North American Multimodel Ensemble (Kirtman et al. 2014) approached the strength predicted for 1997/98.

Statistical models largely lagged the growth rate seen in the dynamical models in 2015 and never foresaw the peak amplitude of the event as well as the dynamical models. This disparity is consistent with past ENSO forecasts; in general, the statistical models often lag the dynamical models because they are

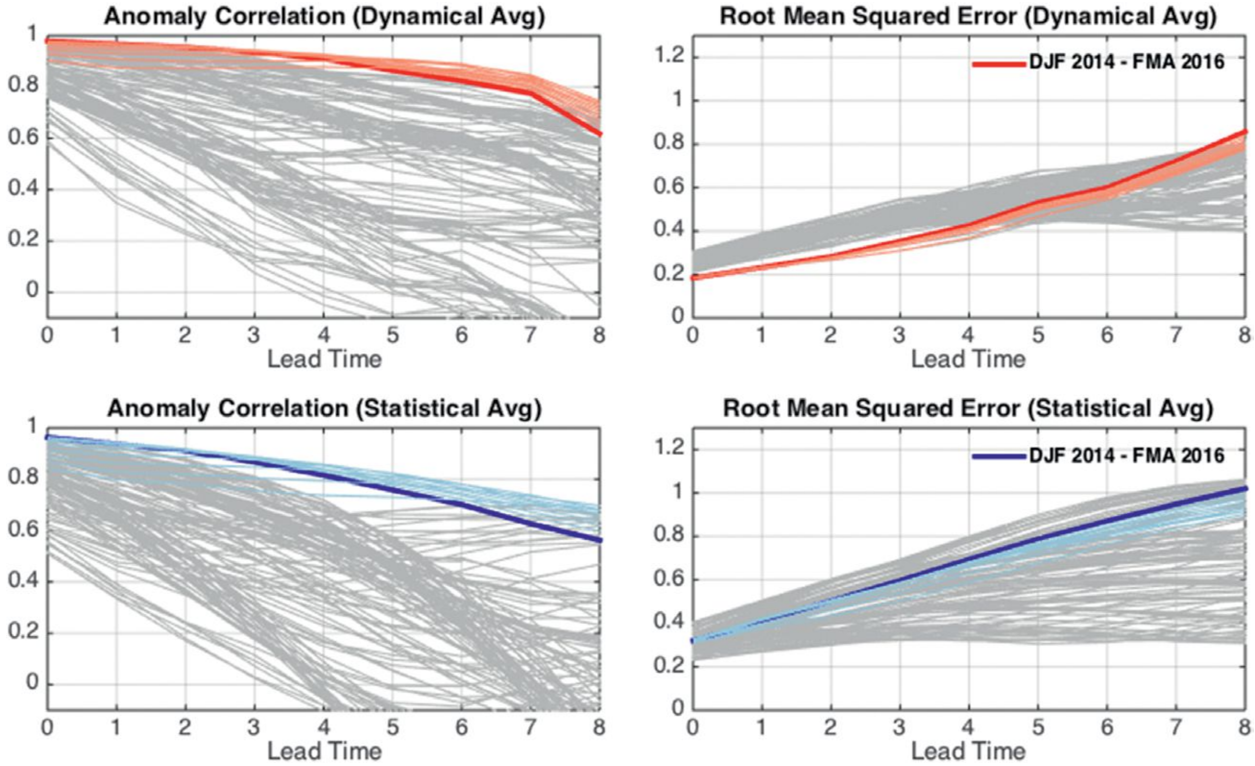

Fig. 8. The (left) ACs and (right) RMSEs between the observations and multimodel averages of the (top) dynamical and (bottom) statistical forecasts of the Niño-3.4 index. The thick blue and red lines show the skill for targets from DJF 2013/14 to FMA 2016. The gray lines are the skill of past windows of 26 consecutive overlapping seasons, each sliding by one season, with thin blue and red lines showing windows that overlap with the DJF 2013/14–FMA 2016 period. Forecast data are verified against seasonal averages of daily OISST data.

not configured to take advantage of the most recent changes in the observational evolution (e.g., Barnston et al. 2012). Many statistical models are trained on monthly or seasonal averages, so they cannot resolve the short-term changes (e.g., westerly wind bursts) that the dynamical models are initialized with. Thus, the statistical model "success" during 2014 may be due to the fact they were not equipped to react to conditions that the dynamical models saw as important precursors or amplifiers of El Niño growth.

Evaluating skill using the temporal anomaly correlation (AC) within a ~2-yr sliding interval, the dynamical and statistical MME average forecasts were the highest for the most recent event since the IRI/CPC model plume was created in 2002 (see the appendix for details on the forecast verification metrics). Figure 8 (left column) shows that targets during DJF 2014–FMA 2016 (thick red and blue lines) had the largest AC results compared to equivalent length time ranges going back to 2002 (gray lines are past windows of 26 consecutive overlapping seasons, each sliding by one season). The thinner red and blue lines correspond to ranges that are strongly associated with the recent period [e.g., from NDJ 2013 to January–March (JFM) 2016]. The ACs were in excess of 0.6 going out to lead-8 for both model types, with dynamical models demonstrating slightly more skill for lead-0 to lead-7. The dynamical MME average had an AC greater than 0.9 going out to lead-4, while the statistical MME average only did so going out to lead-2. The AC metric rewards a good fit between the forecast and observational time series during a larger event (relative to a good fit during a smaller event) and, so, the greater AC results were partially due to the fact that this event was, by far, the largest in the model record (2002–16) and was well forecasted.

Compared to the AC, the root-mean-square error (RMSE) was generally not as skillful relative to past IRI/CPC model forecasts of the Niño-3.4 index (Fig. 8, right column). For the statistical MME, the RMSEs were roughly 0.8°–1.0°C past lead-4, while they were 0.5°–0.8°C for the dynamical MME. For the longest leads, the statistical and dynamical models had among the largest errors going back to 2002. Conversely, for the shorter lead times (lead-0 to lead-4), the dynamical MME average had among the smallest errors in the IRI/CPC plume history. Beyond lead-1, the statistical model RMSE remained roughly in the

▸ FIG. 9. Scatterplots of observed Niño-3.4 index values (plotted along the abscissa) against (top) lead-0, (middle) lead-4, and (bottom) lead-8 forecasts based on the (left) dynamical and (right) statistical multimodel averages (plotted along the ordinate) for all seasonal (3 month) averages dating back to the beginning of the model plume in Feb 2002. The color shading shows the year of the target season, and the numeral highlights the location of the NDJ target season and year (displaying last two digits between 2002 and 2015). The *r* value in the top-left corner is the correlation between the observations and forecasts made between February 2002 and April 2016. Forecast data are verified against seasonal averages of daily OISST data.

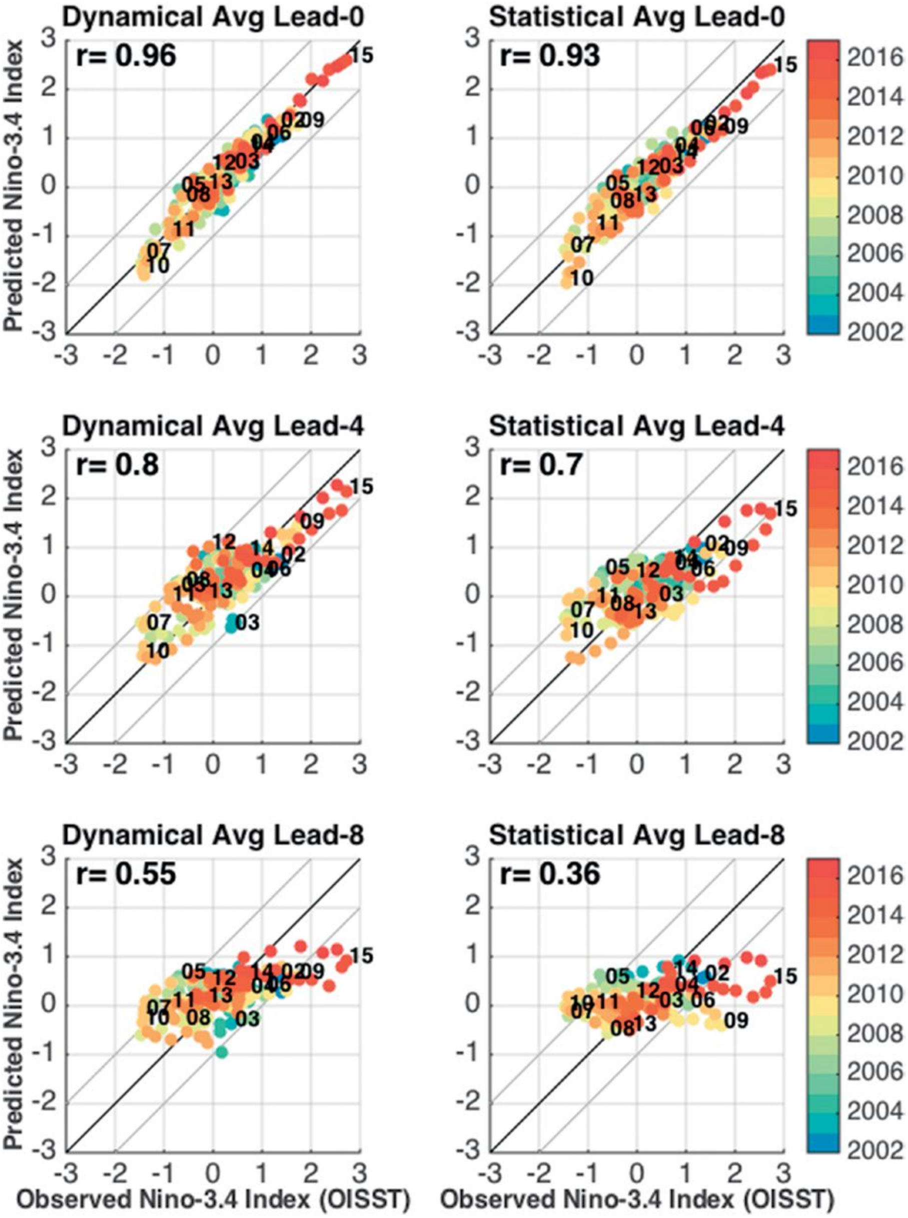

upper quartile of the historical error spread, while improving to the midpoint of the spread for the very shortest leads. Figure 9 indicates that all multimodel averages tend to underestimate the observed values the stronger the event becomes and the longer the lead time (for both El Niño and La Niña). This result may be unsurprising for a large-amplitude event, but the low errors (0.2°–0.3°C) in the dynamical models at short lead times were rather exceptional.

There are other multimodel plumes, such as the North American Multimodel Ensemble (Kirtman et al. 2014) and the European Multimodel Seasonal-to-Interannual Prediction project (EUROSIP; Palmer et al. 2004), that are increasingly relied upon by forecasters who regularly comment on the probability of ENSO events. The advantage of these plumes is that they additionally display the individual ensemble members, which capture the intrinsic "noise" or uncertainty associated with climate forecasts. Probabilistic verification metrics also need to be applied to evaluate whether observations were within the spread of outcomes. It is also worth testing whether the spread of model forecasts reflects the real-world uncertainty because it is generally thought most models are underdispersive or tend to be overly confident (e.g., Shi et al. 2015).

Not only is there uncertainty associated with the models, but there is uncertainty among the observational data used as verification (e.g., Goddard et al. 2009). In general, the prevailing trend is toward the development of higher-resolution products, so daily OISST was selected herein as the basis for model verification. But, undoubtedly, statistical models, with their generally coarser inputs and outputs, are at an inherent disadvantage when compared against a high-resolution

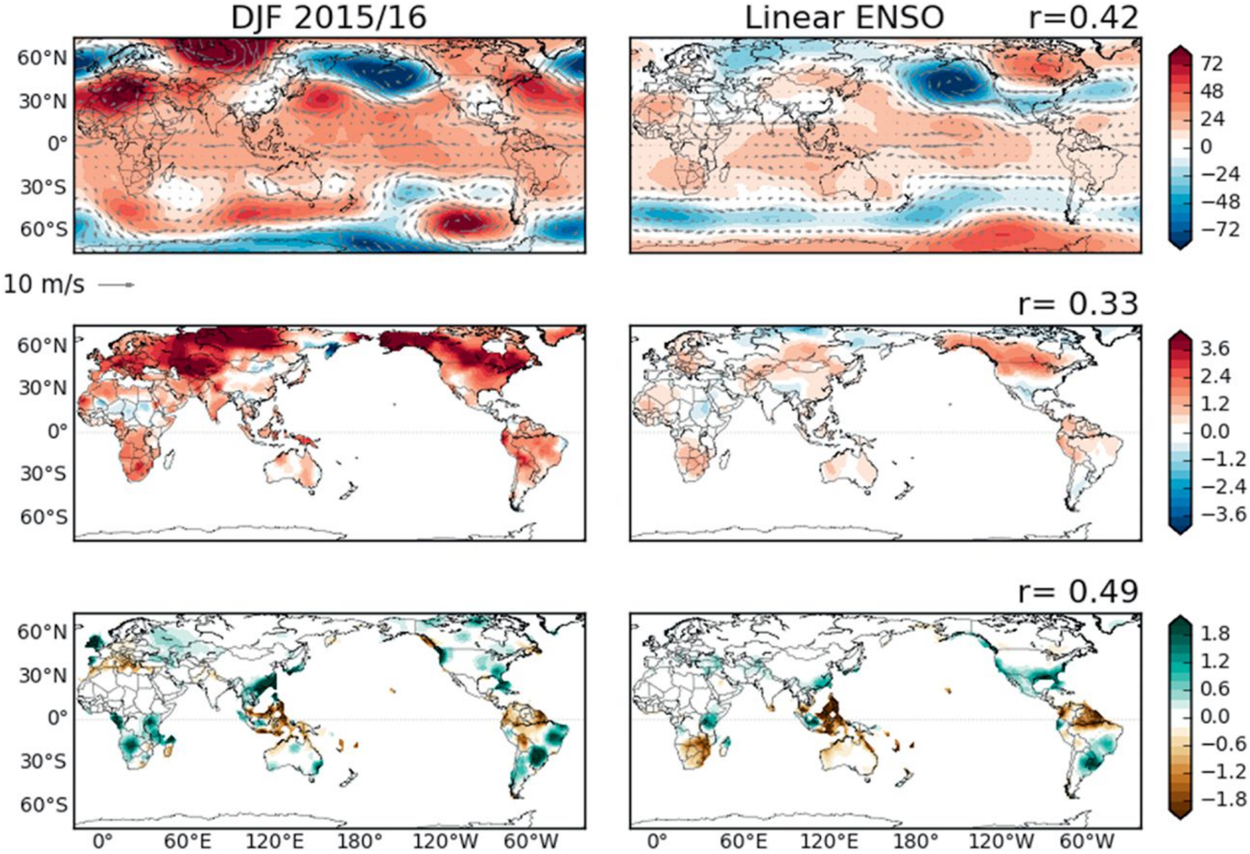

Fig. 10. DJF 2015/16 anomalies of (top) 500-hPa geopotential height and winds, (middle) surface temperature, and (bottom) precipitation. (left) The observational data, and (right) the reconstruction for 2015/16 (weighted regression map of the Niño-3.4 index). The *r* values show the spatial correlation coefficient between the observational and the reconstructed anomalies (cosine weighted by latitude). Geopotential height and wind data are from the NCEP–NCAR reanalysis, the temperature is from the gridded GHCN+CAMS dataset, and precipitation data are from the gridded PREC dataset. Departures are formed by removing monthly means during 1981–2010.

observational dataset. Because statistical models are often built and trained with data from statistical reconstructions (because of the longer records they provide), it may be worthwhile to develop new strategies to increase the resolution of these datasets.

GLOBAL ANOMALIES DURING DECEMBER–FEBRUARY. The strength of El Niño is usually greatest during the Northern Hemisphere winter and its impacts generally widespread, with pronounced changes in the Walker circulation across the global tropics and anomalous wave trains that extend into the extratropical latitudes of both hemispheres (Bjerknes 1969; Horel and Wallace 1981). At mid- to high latitudes, changes to the long-wave pattern interact with synoptic-scale eddies, resulting in the persistence and recurrence of storms and other synoptic events over certain regions. As a result, the influence of El Niño is often identified in seasonal averages and not in shorter time averages.

During DJF 2015/16, above-average 500-hPa geopotential heights dominated the tropical latitudes and the midlatitudes of both hemispheres, with a large anticyclonic anomaly over Siberia during DJF 2015/16 (Fig. 10, top row). Associated with this pattern, strongly above-average temperatures prevailed over most of the globe, with particularly significant positive anomalies over the mid- to high latitudes of the Northern Hemisphere (Fig. 10, middle row). The most significant regions of increased precipitation were located over the northwestern and southeastern United States, southern and eastern South America, southeast China, and just south of the equator in eastern Africa (Fig. 10, bottom row). Drier conditions were prominent over northern South America and around Indonesia. So, how well did this observed pattern relate to El Niño?

One way to quantify the match is to compute the spatial correlation coefficient between the observed pattern and a typical El Niño pattern. To estimate the latter, detrended DJF climate anomalies are regressed onto standardized and detrended values of the DJF Niño-3.4 index from 1979 to 2014. The regression map is then weighted with the observed DJF 2015/16 Niño-3.4 index value in order to obtain the same units as the observational data (Fig. 10, right column). Thus, the analysis shown here is assuming a linear response to Niño-3.4 SST anomalies and will exclude nonlinear relationships. For all three variables in Fig. 10, the spatial correlation coefficients between the observations and the linear ENSO pattern are between 0.3 and 0.5, which means roughly 10%–25% of the spatial variance was explained by ENSO during DJF 2015/16. While significant, this is not very large, and indicates that there were other sources of variability during the Northern Hemisphere winter that were not well described by this linear estimate of El Niño.

The aspects of the circulation that were perhaps most consistent with El Niño were the distinctive wave trains tracing a great-circle route across the North and South Pacific Oceans. Anomalous cyclonic flow was observed in the Gulf of Alaska and middle latitudes of the South Pacific Ocean, with anomalous anticyclones poleward and east of the anomalous troughs over Canada and closer to West Antarctica. However, the cyclonic anomaly in the Gulf of Alaska and the anticyclonic anomaly near West Antarctica were shifted northward compared to the typical El Niño response. Over North America, the anomalous warmth projected well onto the El Niño pattern, but the observed anomalies were more intense and widespread than otherwise expected with El Niño. The anticipated pattern of below-average temperatures and heights over the southern tier of the United States did not emerge. Globally, many of the regions that typically experience warmer conditions during El Niño were also above average in 2015/16, and these anomalies were more prominent.

Relative to the temperature anomalies, precipitation was more consistent with El Niño during DJF 2015/16. However, there were some notable exceptions from the El Niño pattern, such as the lack of increased precipitation over the southwestern and south-central United States. Likewise, southernmost Africa was not as dry as one might expect from an El Niño during DJF–though dry conditions over southern Africa were more prominent during August–October (ASO) through October–December (OND) 2015 (not shown). In northern Australia, December brought significantly more rainfall than normal, though both January and February were very much below the median—more in line with El Niño expectations. During the 1982/83 and 1997/98 events, devastating rainfall impacted Ecuador and coastal Peru during boreal winter/spring, but this was much weaker in 2015/16. However, the expected drier conditions in the Andean region did prevail during the recent event [see Fig. ES6, which because of low station coverage provides a comparison with Tropical Rainfall Measuring Mission (TRMM) data].

To examine longer-term changes, the ~35-yr linear trend was computed (with its start point at the beginning of the modern satellite era). Interestingly, this simple estimate nearly rivals the ENSO anomalies as a descriptor in the 500-hPa geopotential height anomalies, with a spatial correlation coefficient of 0.37 during DJF 2015/16 (Fig. ES7). Upon inspection, this is found to be largely due to the Southern Hemisphere trend toward lower heights over Antarctica and higher heights spanning the middle latitudes, which matches well with the observed anomalies. Neither the DJF linear trends in temperature nor precipitation anomalies correlate significantly with the observed pattern (Fig. ES7).

To estimate the portion of the observed DJF 2015/16 variability that was not related to either the linear trend or linear ENSO, the summed maps are subtracted from the observations (Fig. 11). The resulting so-called residual pattern will still include nonlinearity in ENSO or any other variability that is not well described by the linear trend or linear ENSO. The stochastic nature of the atmosphere will also result in event-to-event differences. We find that the residual anomalies are highly correlated to the observed pattern with spatial correlation coefficients between 0.5 and 0.8. The linear removal clearly does an adequate job of removing the elevated heights in the tropics and the typical anomalous wave trains that span the extratropical North and South Pacific during El Niño. What remains are zonal bands of above-average heights encircling the middle latitudes of both hemispheres, with below-average heights located poleward (the only notable exception being the large anticyclonic anomaly near Siberia). Thus, the residual identifies a nearly global, poleward shift in the midlatitude westerly wind anomalies or jet streams. Accompanying this shift in the Northern Hemisphere, the residual of precipitation is strikingly La Niña–like over the contiguous United States, with rainfall enhanced over the Pacific Northwest and suppressed along the southern tier. Western Europe is also wetter than average, likely because of anomalous westerly flow. Similarly, in the Southern Hemisphere, an anomalous increase in precipitation is evident over southeastern Australia and southern Africa, perhaps due in part to the easterly wind

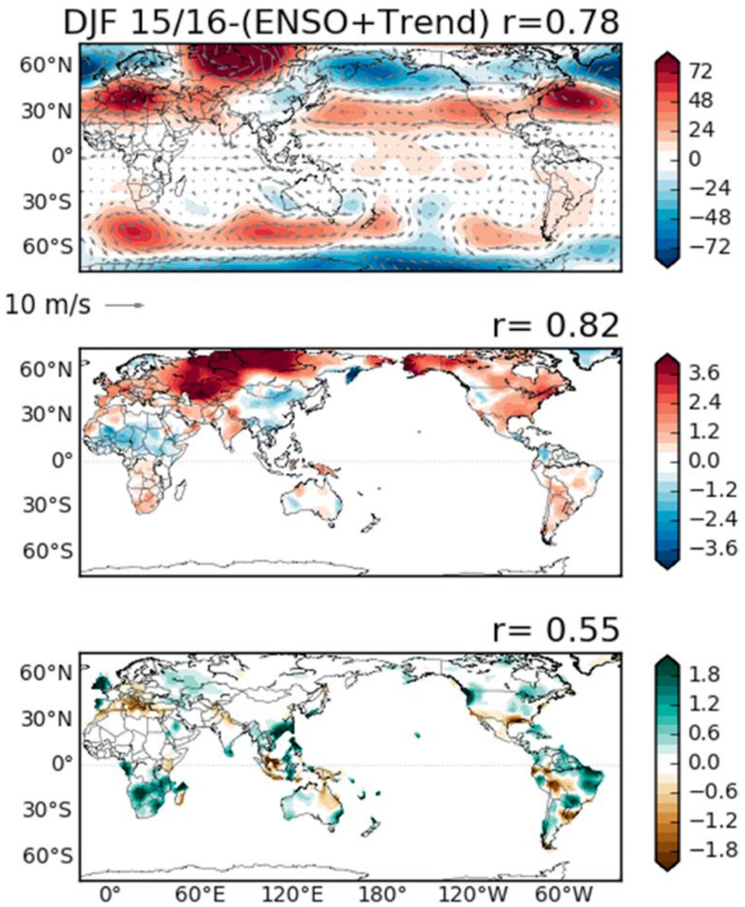

Fig. 11. As in Fig. 10, but showing the residual anomalies formed from subtracting the trend plus ENSO reconstruction from the observational data. The *r* values show the spatial correlation coefficient between the observational and the residual anomalies.

anomalies off the ocean on the equatorward side of the anomalous ridges. The northward shift of the jet (more midlatitude ridging) and strong anomalous anticyclone near Siberia also overlaps with the strongly above-average temperatures across the Northern Hemisphere extratropics.

Despite the fact the observed and residual circulation anomalies have a distinctive annular appearance in the Northern Hemisphere, the DJF 2015/16 Arctic Oscillation (AO) index value was near zero when standardized relative to DJF seasons over 1979–2016. In the Southern Hemisphere, the DJF Antarctic Oscillation (AAO) index was more significant with a positive value of 0.8 standardized units. This outcome was somewhat surprising given El Niño is often associated with negative values of the AAO during November–February (e.g., L'Heureux and Thompson 2006). Instead, increased rainfall over portions of southeastern Australia during DJF 2015/16 appears consistent with the overall positive trend in the AAO (also reflected in Fig. ES7; Hendon et al. 2007; Murphy and Timbal 2008; Thomas et al. 2015).

Overall, it appears that El Niño coupled with a poleward shift in the jet streams significantly influenced the global climate during December–February 2015/16. It is possible that nonlinearity in El Niño (e.g., the specific location of the strongest SST anomalies) contributed to the departures from the classically linear anomalies across the globe. Also differences from the linear pattern can be expected to occur simply because of sampling variability, with event-to-event differences naturally arising because of the limited record. It is interesting that a nearly hemispheric structure in the residual circulation was uncovered, which suggests an origin that was not simply isolated to the Pacific sector. The zonal structure may have arisen from random extratropical internal atmospheric variability, aided by feedbacks between eddies and the zonal mean flow (e.g., Limpasuvan and Hartmann 2000). Also, positive temperature anomalies throughout the tropical troposphere may have contributed to the poleward shift in the jet (Butler et al. 2010; Lim et al. 2016). A final possibility for the departure from the linear ENSO estimate is the potential influence of subseasonal activity across the global tropics (e.g., Kelvin waves, Madden–Julian oscillation), which exerted an influence on tropical rainfall and was aliased into the seasonal averages. We leave it to others to provide a more exhaustive attribution of the possible drivers of the 2015/16 climate anomalies, including exploring other seasons, which can have a greater influence on certain countries (e.g., Australian impacts are largest during the Southern Hemisphere spring).

SUMMARY AND FUTURE CONSIDERATIONS. Most atmospheric and oceanic indices suggest the 2015/16 El Niño was among the top three strongest El Niño events in the historical record dating back to 1950. While it was not unequivocally a record, there were several ways in which this El Niño differed from previous major events in 1982/83 and 1997/98. The west-central Pacific subsurface and surface temperature anomalies were much warmer, while the eastern Pacific was comparatively cooler. As expected during El Niño, the trade winds were weaker, but not as weak during the last half of 2015 as during previous significant events. Related to this, the pressure differences across the tropical Pacific, as measured by the two Southern Oscillation indices, suggest the 2015/16 El Niño had less amplitude relative to the other events. The two OLR indices were both among the top three going back to 1979 but lagged the other two events in the eastern Pacific.

In some aspects, the operational model forecasts for the Niño-3.4 index were among the most skillful going back to at least 2002. However, this should not suggest complacency as seen during the borderline El Niño-neutral situation during 2014/15 when the dynamical models, in particular, largely overestimated the degree of warming. The longest-lead predictions in the dynamical, intermediate, and statistical models contain relatively large errors (0.5°C past lead-4), which make predictions of ENSO strength an ongoing challenge. Also, the ensemble average of the multimodel ensemble lagged the initial increases in Niño-3.4 during early 2015, especially for the statistical models, and underpredicted strength beyond the more immediate leads. Statistical models appear to be hampered by their inability to respond to submonthly factors that portend ENSO growth, though this may have paradoxically been to their advantage during 2014. While forecast improvements should be sought, an important challenge is to communicate that a portion of the forecast uncertainty is irreducible: there will always be error in the initial conditions, boundary forcing, and through the use of imperfect models.

Given the historical stature of the 2015/16 El Niño, it is clear that it will be an event that will be vigorously dissected. From an operational perspective, however, there are a couple of areas worth examining further. One fundamental challenge is to better understand the influence of trends in the real-time observational data. The WMO recommends that the most recent 30-yr base period be used to define anomalies [currently, 1981–2010; Arguez et al. (2012)], but it is likely that some part of the ENSO indices is not related purely to ENSO dynamics, but climate change and warming trends. So, how do we best quantify the portion of the anomalies related to ENSO versus the portion related to decadal, multidecadal, or secular variability? And how important is it to diagnose the role of trends when it comes to El Niño monitoring and prediction on a monthly or seasonal basis? For example, what are the consequences of a +2.3°C seasonal Niño-3.4 index value that is revised to +2.1°C after trends are removed? Overall, how substantial is the effect of long-term variability on seasonal ENSO characteristics, dynamics, and predictability?

While our scientific understanding of climate change and its consequences has progressed markedly since 1997/98, there are still challenges to quantifying and communicating its role on the shorter time scales. While the statistical decomposition in the previous section on global anomalies during DJF is offered as a first estimate, there are certainly other methods of extracting the role of various components of the climate system (e.g., Bonfils et al. 2015). Given the tremendous interest from the public to understand the drivers of recent climate anomalies, it remains worthwhile to fine-tune methods and test their applicability to a real-time environment.

The 2015/16 event was the first major "24–7 El Niño" coming within a vastly different media setting, with a fast and diverse network (e.g., mobile devices) that did not exist during the last major event of 1997/98. The forecast centers approached this in a variety of ways, using social media, videos and infographics, and blogs (e.g., ENSO blog: www.climate.gov/news-features/department/enso-blog) to provide additional information beyond that provided in routine operational assessments, typically issued at biweekly to monthly intervals. However, the constant coverage and frequent media updates remained surprising, as ENSO is a slow, seasonally evolving phenomenon that helps set the background flow and increases the chances for certain weather events to reoccur over certain areas but does not directly cause any weather event.

Thus, there was a visible disconnect between the demands of "here and now" coverage and the pace of useful updates that could be provided by the centers on ENSO. For example, while daily or weekly averaged data provide a useful snapshot of tendencies across the tropical Pacific Ocean, they are not currently designed to provide a long, continuous, stable record for historical comparison. Daily and weekly data can also be influenced by a variety of factors outside of ENSO [e.g., tropical cyclones, the Madden–Julian oscillation, and a number of other intraseasonal phenomena; Hendon and Glick (1997)]. Yet, despite these caveats, some users relied on these real-time data records to publicize frequent updates on the strength or rank of El Niño. Also, when certain precipitation impacts began to occur, these weather events were sometimes labeled as El Niño storms even though El Niño does not directly cause storms but, rather, sets the overall background for them.

Additionally, there were signs that the forecast for El Niño itself was conflated with the forecasts for its associated impacts. At the major national forecast centers, operations related to forecasting ENSO and operations related to creating outlooks of temperature and precipitation may be closely related, but they remain separate endeavors. ENSO is a leading predictor over certain countries and therefore strongly influences the seasonal climate outlook, but it is clearly not the only factor in the models considered by forecasters. The signal-to-noise ratio becomes smaller as one moves away from the tropical Pacific Ocean (e.g., Kumar et al. 2000), and so, for most parts of the world, the confidence in an upcoming ENSO event is likely to be higher than the chance of its related impacts.

To clarify some of these service and communication issues, climate services aimed at bridging the provider–user gaps may be helpful. These can range from supporting studies of how users interpret and apply products, to buttressing science communication efforts, such as building easy-to-navigate, clearly described webpages supported by an authoritative social media presence. The role of "learning by doing" also cannot be overstated. With the occurrence of each El Niño event, there are opportunities to learn and apply those lessons to future events. The 2015/16 event was no different in this regard and will, hopefully, have provided many users with a greater appreciation of the probabilistic nature of impacts related to El Niño, which needs to be explicitly recognized and factored into their risk analysis and decision-making.

ACKNOWLEDGMENTS. We thank Leigh Zhang (NOAA/CPC) for updating several reanalysis datasets on our behalf. ML, EB, TD, and AB are grateful for support from the NOAA Climate Programs Office (CPO)/Climate.gov for the ENSO Blog. AB also acknowledges NOAA CPO/MAPP Grant NA12OAR4310082. KT and KM acknowledge the PP068 program and colleagues at the ENFEN Committee. KT also appreciates the support of the U.S. Embassy in Peru, the Peruvian Embassy in the United States, and Min. J. M. Benites.

APPENDIX: VERIFICATION METRICS. In this paper, the anomaly correlation (AC) coefficient is computed as

$$\mathrm{AC} = \frac{\overline{x'y'}}{\sigma_x \sigma_y}, \tag{A1}$$

where x and y are the observational and forecast time series, primes denote anomalies from the time mean, the overbar indicates the average over time, and the sigmas are the standard deviation of x and y. The numerator represents the covariance between x and y.

The values associated with the AC lie between −1 and 1 and are dimensionless. Negative values indicate an inverse linear relations between x and y, while positive values indicate a direct linear relations. Values near zero indicate a poor fit between x and y, and values at 1 or −1 reflect a perfect fit or match between the variability in x and y.

The root-mean-square error (RMSE) is calculated as

$$\mathrm{RMSE} = \sqrt{\frac{\sum (x-y)^2}{n}}, \tag{A2}$$

where n is the sample size. The RMSE is the square root of the average of the squares of the error, or the difference between x and y. Larger RMSE values indicate larger differences either of the same sign (bias) or of both signs between the observational and forecast time series. Smaller RMSEs indicate smaller differences between the time series.

REFERENCES

Arguez, A., I. Durre, S. Applequist, R. S. Vose, M. F. Squires, X. Yin, R. R. Heim Jr., and T. W. Owen, 2012: NOAA's 1981–2010 U.S. climate normals: An overview. *Bull. Amer. Meteor. Soc.*, **93**, 1687–1697, doi:10.1175/BAMS-D-11-00197.1.

Barnston, A. G., M. Chelliah, and S. B. Goldenberg, 1997: Documentation of a highly ENSO-related SST region in the equatorial Pacific: Research note. *Atmos.–Ocean*, **35**, 367–383, doi:10.1080/07055900.1997.9649597.

——, M. K. Tippett, M. L. L'Heureux, S. Li, and D. G. DeWitt, 2012: Skill of real-time seasonal ENSO model predictions during 2002–11: Is our capability increasing? *Bull. Amer. Meteor. Soc.*, **93**, 631–651, doi:10.1175/BAMS-D-11-00111.1.

Bjerknes, J., 1969: Atmospheric teleconnections from the equatorial Pacific. *Mon. Wea. Rev.*, **97**, 163–172, doi:10.1175/1520-0493(1969)097<0163:ATFTEP>2.3.CO;2.

Bonfils, C. J. W., B. D. Santer, T. J. Phillips, K. Marvel, L. R. Leung, C. Doutriaux, and A. Capotondi, 2015: Relative contributions of mean-state shifts and ENSO-driven variability to precipitation changes in a warming climate. *J. Climate*, **28**, 9997–10 013, doi:10.1175/JCLI-D-15-0341.1.

Butler, A. H., D. W. J. Thompson, and R. Heikes, 2010: The steady-state atmospheric circulation response to climate change–like thermal forcings in a simple general circulation model. *J. Climate*, **23**, 3474–3496, doi:10.1175/2010JCLI3228.1.

Capotondi, A., and Coauthors, 2015: Understanding ENSO diversity. *Bull. Amer. Meteor. Soc.*, **96**, 921–938, doi:10.1175/BAMS-D-13-00117.1.

Chen, M., P. Xie, J. E. Janowiak, and P. A. Arkin, 2002: Global land precipitation: A 50-yr monthly analysis based on gauge observations. *J. Hydrometeor.*, **3**, 249–266, doi:10.1175/1525-7541(2002)003<0249:GLPAYM>2.0.CO;2.

Chiodi, A. M., and D. E. Harrison, 2013: El Niño impacts on seasonal U.S. atmospheric circulation, temperature, and precipitation anomalies: The OLR-event perspective. *J. Climate*, **26**, 822–837, doi:10.1175/JCLI-D-12-00097.1.

Dee, D. P., and Coauthors, 2011: The ERA-Interim reanalysis: Configuration and performance of the data assimilation system. *Quart. J. Roy. Meteor. Soc.*, **137**, 553–597, doi:10.1002/qj.828.

DelSole, T., J. Nattala, and M. K. Tippett, 2014: Skill improvement from increased ensemble size and model diversity. *Geophys. Res. Lett.*, **41**, 7331–7342, doi:10.1002/2014GL060133.

Fan, Y., and H. Van den Dool, 2008: A global monthly land surface air temperature analysis for 1948–present. *J. Geophys. Res.*, **113**, D01103, doi:10.1029/2007JD008470.

Goddard, L., D. G. DeWitt, and R. W. Reynolds, 2009: Practical implications of uncertainty in observed SSTs. *Geophys. Res. Lett.*, **36**, L09710, doi:10.1029/2009GL037703.

Halpert, M. S., and C. F. Ropelewski, 1992: Surface temperature patterns associated with the Southern Oscillation. *J. Climate*, **5**, 577–593, doi:10.1175/1520-0442(1992)005<0577:STPAWT>2.0.CO;2.

Hendon, H. H., and J. Glick, 1997: Intraseasonal air–sea interaction in the tropical Indian and Pacific Oceans. *J. Climate*, **10**, 647–661, doi:10.1175/1520-0442(1997)010<0647:IASIIT>2.0.CO;2.

——, D. W. J. Thompson, and M. C. Wheeler, 2007: Australian rainfall and surface temperature variations associated with the Southern Hemisphere annular mode. *J. Climate*, **20**, 2452–2467, doi:10.1175/JCLI4134.1.

Horel, J. D., and J. M. Wallace, 1981: Planetary-scale atmospheric phenomena associated with the Southern Oscillation. *Mon. Wea. Rev.*, **109**, 813–829, doi:10.1175/1520-0493(1981)109<0813:PSAPAW>2.0.CO;2.

Hu, Z.-Z., A. Kumar, H.-L. Ren, H. Wang, M. L. Heureux, and F.-F. Jin, 2013: Weakened interannual variability in the tropical Pacific Ocean since 2000. *J. Climate*, **26**, 2601–2613, doi:10.1175/JCLI-D-12-00265.1.

Huang, B., W. Wang, C. Liu, V. Banzon, H.-M. Zhang, and J. Lawrimore, 2015a: Bias adjustment of AVHRR SST and its impacts on two SST analyses. *J. Atmos. Oceanic Technol.*, **32**, 372–387, doi:10.1175/JTECH-D-14-00121.1.

——, and Coauthors, 2015b: Extended Reconstructed Sea Surface Temperature version 4 (ERSST.v4). Part I: Upgrades and intercomparisons. *J. Climate*, **28**, 911–930, doi:10.1175/JCLI-D-14-00006.1.

——, M. L'Heureux, Z.-Z. Hu, and H.-M. Zhang, 2016: Ranking the strongest ENSO events while incorporating SST uncertainty. *Geophys. Res. Lett.*, **43**, 9165–9172, doi:10.1002/2016GL070888.

Ishii, M., A. Shouji, S. Sugimoto, and T. Matsumoto, 2005: Objective analyses of sea-surface temperature and marine meteorological variables for the 20th century using ICOADS and the Kobe collection. *Int. J. Climatol.*, **25**, 865–879, doi:10.1002/joc.1169.

Kalnay, E., and Coauthors, 1996: The NCEP/NCAR 40-Year Reanalysis Project. *Bull. Amer. Meteor. Soc.*, **77**, 437–471, doi:10.1175/1520-0477(1996)077<0437:TNYRP>2.0.CO;2.

Kanamitsu, M., W. Ebisuzaki, J. Woollen, S.-K. Yang, J. J. Hnilo, M. Fiorino, and G. L. Potter, 2002: NCEP–DOE AMIP-II reanalysis (R-2). *Bull. Amer. Meteor. Soc.*, **83**, 1631–1643, doi:10.1175/BAMS-83-11-1631.

Kirtman, B. P., and Coauthors, 2014: The North American Multimodel Ensemble: Phase-1 seasonal-to-interannual prediction; phase-2 toward developing intraseasonal prediction. *Bull. Amer. Meteor. Soc.*, **95**, 585–601, doi:10.1175/BAMS-D-12-00050.1.

Kobayashi, S., and Coauthors, 2015: The JRA-55 reanalysis: General specifications and basic characteristics. *J. Meteor. Soc. Japan*, **93**, 5–48, doi:10.2151/jmsj.2015-001.

Kumar, A., and Z.-Z. Hu, 2014: How variable is the uncertainty in ENSO sea surface temperature prediction? *J. Climate*, **27**, 2779–2788, doi:10.1175/JCLI-D-13-00576.1.

——, A. G. Barnston, P. Peng, M. P. Hoerling, and L. Goddard, 2000: Changes in the spread of the variability of the seasonal mean atmospheric states associated with ENSO. *J. Climate*, **13**, 3139–3151, doi:10.1175/1520-0442(2000)013<3139:CITSOT>2.0.CO;2.

Lee, H.-T., A. Gruber, R. G. Ellingson, and I. Laszlo, 2007: Development of the HIRS outgoing longwave radiation climate dataset. *J. Atmos. Oceanic Technol.*, **24**, 2029–2047, doi:10.1175/2007JTECHA989.1.

Lee, T., and M. J. McPhaden, 2010: Increasing intensity of El Niño in the central-equatorial Pacific. *Geophys. Res. Lett.*, **37**, L14603, doi:10.1029/2010GL044007.

L'Heureux, M. L., and D. W. J. Thompson, 2006: Observed relationships between the El Niño–Southern Oscillation and the extratropical zonal-mean circulation. *J. Climate*, **19**, 276–287, doi:10.1175/JCLI3617.1.

——, D. C. Collins, and Z.-Z. Hu, 2013: Linear trends in sea surface temperature of the tropical Pacific Ocean and implications for the El Niño–Southern Oscillation. *Climate Dyn.*, **40**, 1223–1236, doi:10.1007/s00382-012-1331-2.

——, M. K. Tippett, and A. G. Barnston, 2015: Characterizing ENSO coupled variability and its impact on North American seasonal precipitation and temperature. *J. Climate*, **28**, 4231–4245, doi:10.1175/JCLI-D-14-00508.1.

Liebmann, B., and C. A. Smith, 1996: Description of a complete (interpolated) outgoing longwave radiation dataset. *Bull. Amer. Meteor. Soc.*, **77**, 1275–1277.

Lim, E.-P., H. H. Hendon, J. M. Arblaster, C. Chung, A. F. Moise, P. Hope, G. Young, and M. Zhao, 2016: Interaction of the recent 50 year SST trend and La Niña 2010: Amplification of the Southern Annular Mode and Australian springtime rainfall. *Climate Dyn.*, **47**, 2273–2291, doi:10.1007/s00382-015-2963-9.

Limpasuvan, V., and D. L. Hartmann, 2000: Wave-maintained annular modes of climate variability. *J. Climate*, **13**, 4414–4429, doi:10.1175/1520-0442(2000)013<4414:WMAMOC>2.0.CO;2.

McPhaden, M. J., 1999: Genesis and evolution of the 1997–98 El Niño. *Science*, **283**, 950–954, doi:10.1126/science.283.5404.950.

——, 2015: Playing hide and seek with El Niño. *Nat. Climate Change*, **5**, 791–795, doi:10.1038/nclimate2775.

——, A. Busalacchi, and D. Anderson, 2010: A TOGA retrospective. *Oceanography*, **23**, 86–103, doi:10.5670/oceanog.2010.26.

Murphy, B. F., and B. Timbal, 2008: A review of recent climate variability and climate change in southeastern Australia. *Int. J. Climatol.*, **28**, 859–879, doi:10.1002/joc.1627.

Palmer, T. N., and Coauthors, 2004: Development of a European Multimodel Ensemble System for Seasonal-to-Interannual Prediction (DEMETER). *Bull. Amer. Meteor. Soc.*, **85**, 853–872, doi:10.1175/BAMS-85-6-853.

Rayner, N. A., D. E. Parker, E. B. Horton, C. K. Folland, L. V. Alexander, D. P. Rowell, E. C. Kent, and A. Kaplan, 2003: Global analyses of sea surface temperature, sea ice, and night marine air temperature since the late nineteenth century. *J. Geophys. Res.*, **108**, 4407, doi:10.1029/2002JD002670.

Reynolds, R. W., N. A. Rayner, T. M. Smith, D. C. Stokes, and W. Wang, 2002: An improved in situ and satellite SST analysis for climate. *J. Climate*, **15**, 1609–1625, doi:10.1175/1520-0442(2002)015<1609:AIISAS>2.0.CO;2.

——, T. M. Smith, C. Liu, D. B. Chelton, K. S. Casey, and M. G. Schlax, 2007: Daily high-resolution-blended analyses for sea surface temperature. *J. Climate*, **20**, 5473–5496, doi:10.1175/2007JCLI1824.1.

Rienecker, M. M., and Coauthors, 2011: MERRA: NASA's Modern-Era Retrospective Analysis for Research and Applications. *J. Climate*, **24**, 3624–3648, doi:10.1175/JCLI-D-11-00015.1.

Roemmich, D., and J. Gilson, 2009: The 2004–2008 mean and annual cycle of temperature, salinity, and steric height in the global ocean from the Argo program. *Prog. Oceanogr.*, **82**, 81–100, doi:10.1016/j.pocean.2009.03.004.

Ropelewski, C. F., and M. S. Halpert, 1987: Global and regional scale precipitation patterns associated with the El Niño/Southern Oscillation. *Mon. Wea. Rev.*, **115**, 1606–1626, doi:10.1175/1520-0493(1987)115<1606:GARSPP>2.0.CO;2.

Saha, S., and Coauthors, 2010: The NCEP Climate Forecast System Reanalysis. *Bull. Amer. Meteor. Soc.*, **91**, 1015–1057, doi:10.1175/2010BAMS3001.1.

Shi, W., N. Schaller, D. MacLeod, T. N. Palmer, and A. Weisheimer, 2015: Impact of hindcast length on estimates of seasonal climate predictability. *Geophys. Res. Lett.*, **42**, 1554–1559, doi:10.1002/2014GL062829.

Smith, T. M., R. W. Reynolds, T. C. Peterson, and J. Lawrimore, 2008: Improvements to NOAA's historical merged land–ocean surface temperature analysis (1880–2006). *J. Climate*, **21**, 2283–2296, doi:10.1175/2007JCLI2100.1.

Takahashi, K., 2004: The atmospheric circulation associated with extreme rainfall events in Piura, Peru, during the 1997–1998 and 2002 El Niño events. *Ann. Geophys.*, **22**, 3917–3926, doi:10.5194/angeo-22-3917-2004.

——, and B. Dewitte, 2016: Strong and moderate nonlinear El Niño regimes. *Climate Dyn.*, **46**, 1627–1645, doi:10.1007/s00382-015-2665-3.

——, A. Montecinos, K. Goubanova, and B. Dewitte, 2011: ENSO regimes: Reinterpreting the canonical and Modoki El Niño. *Geophys. Res. Lett.*, **38**, L10704, doi:10.1029/2011GL047364.

Thomas, J. L., D. W. Waugh, and A. Gnanadesikan, 2015: Southern Hemisphere extratropical circulation: Recent trends and natural variability. *Geophys. Res. Lett.*, **42**, 5508–5515, doi:10.1002/2015GL064521.

Vecchi, G. A., and D. E. Harrison, 2006: The termination of the 1997–1998 El Niño. Part I: Mechanisms of oceanic change. *J. Climate*, **19**, 2633–2646, doi:10.1175/JCLI3776.1.

——, A. T. Wittenberg, and A. Rosati, 2006: Reassessing the role of stochastic forcing in the 1997–1998 El Niño. *Geophys. Res. Lett.*, **33**, L01706, doi:10.1029/2005GL024738.

OVER 5,000 YEARS OF ENSEMBLE FUTURE CLIMATE SIMULATIONS BY 60-KM GLOBAL AND 20-KM REGIONAL ATMOSPHERIC MODELS

Ryo Mizuta, Akihiko Murata, Masayoshi Ishii, Hideo Shiogama, Kenshi Hibino,
Nobuhito Mori, Osamu Arakawa, Yukiko Imada, Kohei Yoshida, Toshinori Aoyagi,
Hiroaki Kawase, Masato Mori, Yasuko Okada, Tomoya Shimura, Toshiharu Nagatomo,
Mikiko Ikeda, Hirokazu Endo, Masaya Nosaka, Miki Arai, Chiharu Takahashi, Kenji Tanaka,
Tetsuya Takemi, Yasuto Tachikawa, Khujanazarov Temur, Youichi Kamae, Masahiro Watanabe,
Hidetaka Sasaki, Akio Kitoh, Izuru Takayabu, Eiichi Nakakita, and Masahide Kimoto

An unprecedentedly large ensemble of climate simulations with high-resolution atmospheric models enables the assessment of probabilistic change by global warming in low-frequency local-scale severe events.

Planning of adaptation to global warming is ready to start at the national level, presuming that warming of the climate system is unequivocal and that continued emissions of greenhouse gases will cause further warming and changes in all components of the climate system (IPCC 2013). Planning for adaptation will be based on impact assessments of disasters, agriculture, water resources, ecosystems, human health, and so on, in each region. For each impact assessment, detailed projections of extreme events, such as heavy rainfall, heat wave, drought, and strong wind, are required at the regional scale as well as projections of climatological temperature and precipitation.

AFFILIATIONS: Mizuta, Murata, Ishii, Imada, Yoshida, Aoyagi, Kawase, Endo, Nosaka, Sasaki, and Takayabu—Meteorological Research Institute, Tsukuba, Ibaraki, Japan; Shiogama—National Institute for Environmental Studies, Tsukuba, Ibaraki, Japan; Hibino, Arakawa, Nagatomo, Kamae, and Kitoh—University of Tsukuba, Tsukuba, Ibaraki, Japan; Mori, Okada, Shimura, Tanaka, Takemi, Temur, and Nakakita—Disaster Prevention Research Institute, Kyoto University, Uji, Kyoto, Japan; Mori, Arai, Takahashi, Watanabe, and Kimoto—Atmosphere and Ocean Research Institute, University of Tokyo, Kashiwa, Chiba, Japan; Ikeda—Japan Agency for Marine-Earth Science and Technology, Yokohama, Kanagawa, Japan; Tachikawa—Graduate School of Engineering, Kyoto University, Kyoto, Japan

CORRESPONDING AUTHOR: Ryo Mizuta, rmizuta@mri-jma.go.jp

The abstract for this article can be found in this issue, following the table of contents.

DOI:10.1175/BAMS-D-16-0099.1

In final form 16 November 2016

However, the uncertainty of the change is still large, even for the global-mean surface temperature change. Uncertainties become larger as the spatial scale considered is reduced, for example, when examining the regional distribution of change. There is greater uncertainty in temporally variable components than temporal-mean values. Furthermore, rare events have much larger uncertainty, although such events can have the most significant impacts on human activity (Collins et al. 2013).

The major sources of these uncertainties are uncertainties in the emission scenarios of greenhouse gases and in climate models. These are considered by phase 5 of the Coupled Model Intercomparison Project (CMIP5) experiments, in which multiple emission scenarios are applied to multiple climate models, providing information for evaluating the uncertainties in large-scale phenomena (e.g., Hawkins and Sutton 2009).

In addition, uncertainty from internal variability is expected to be more important for less frequent anomalous weather and climate extremes (Deser et al. 2012; Xie et al. 2015). Internal variability includes decadal variations in the ocean, interannual variability in the extratropical atmosphere, intraseasonal variation in the tropics, and so on. Kay et al. (2015) emphasized the importance of uncertainties in climate projections arising from internal variability by conducting a large ensemble climate simulation. Large ensemble simulations yield the probability density functions of variables such as temperature and precipitation, and allow us to discuss their changes in a warming climate, and the function tails as the climate extremes.

Large ensemble simulations are also useful for understanding human influences on past changes in extreme events, by using an approach termed probabilistic event attribution (PEA). The approach evaluates the degree to which human influence has affected the probability and magnitude of individual extreme events rather than long-term trends (Allen 2003), through comparing results from atmospheric general circulation models (AGCMs) with and without anthropogenic changes in boundary conditions during a single season or a few years (Pall et al. 2011; Christidis and Stott 2014; Mori et al. 2014; Shiogama et al. 2014). The AGCM-based PEA generally benefits from much larger initial-condition ensembles (≥100) than the traditional detection and attribution studies using atmosphere–ocean coupled models (AOGCMs) (<10).

Currently, however, suites of climate change simulations by AOGCMs are conducted with an atmospheric resolution coarser than 100 km (Collins et al. 2013), and a similar resolution in the large ensemble simulations. These resolutions are not fine enough for regional impact assessment studies related to small-scale climate extremes affected by local topography, and low-resolution models are not suitable for phenomena such as tropical cyclones, the East Asian monsoon, and blocking (e.g., Fowler et al. 2007). In Asia in particular, since the monsoon and tropical cyclones are major causes of natural hazards and also water sources, changes in these phenomena are the key issues for regional impact assessment. Direct dynamical downscaling to regional climate models (RCMs) can include the effects of regional-scale topography, but it cannot include phenomena that are not simulated in the parent GCMs (Xie et al. 2015).

To overcome these problems, we have been employing a high-resolution AGCM (Kitoh et al. 2016). Simulations of a warmer climate using an AGCM with 20-km resolution were performed (e.g., Murakami et al. 2012a), in which sea surface temperature (SST) changes from CMIP climate models are prescribed as the lower boundary conditions. In addition, finer-scale projections have been performed over the Japanese region by downscaling to a regional climate model with 5-km resolution (Kanada et al. 2012; Nakano et al. 2013). Furthermore, uncertainties from different SST changes, cumulus parameterization schemes, and emission scenarios have been examined using ensemble simulations using 60-km AGCM (Endo et al. 2012; Murakami et al. 2012b; Kitoh et al. 2016). The results of these simulations are now being used in various impact assessment studies for natural disasters, including river discharge/flooding (Duong et al. 2014), storm surge (Yasuda et al. 2014), and ocean waves (Mori et al. 2010; Shimura et al. 2015), as well as water resources, agriculture, ecosystems, and human health.

In this study, this approach using a high-resolution AGCM is applied to the evaluation of uncertainty arising from internal variability. The 60-km AGCM, which is capable of representing tropical cyclones, combined with dynamical downscaling using the 20-km RCM, which gives finer-scale heavy precipitation and topographical effects, are used to perform a large ensemble simulation. We performed 100-member simulations of the period 1951–2010 and 90-member simulations for 60 years of a warmer climate using the AGCM, and a large part of the results are downscaled with the RCM. In addition, 100-member AGCM simulations were performed for 1951–2010 without historical long-term warming trends. These large-size and long-term ensembles of the high-resolution models facilitate analyses of long-term trends and future changes in localized rare events that cannot be represented by coarse-resolution models and small-size ensembles, although the uncertainty of the ocean internal variability cannot be examined. The simulation results are freely available for the community as a database named "Database for Policy Decision Making for Future Climate Change" (d4PDF), which is intended to be utilized for impact assessment studies.

MODELS AND METHODS. *Models*. The d4PDF consists of outputs from global warming simulations by a global atmospheric model with horizontal grid spacing of 60 km (AGCM) and from regional downscaling simulations covering the Japan area by a regional climate model with 20-km grid spacing (RCM).

The AGCM used here is the Meteorological Research Institute AGCM, version 3.2 (MRI-AGCM3.2). This model was developed based on a version of the numerical weather prediction model used operationally at the Japan Meteorological Agency (JMA 2007). We use the model with 60-km resolution, which has 640 × 320 grid cells, corresponding to a triangular truncation of 319 with a linear Gaussian grid (TL319) in the horizontal. The number of vertical levels is 64 (top at 0.01 hPa). The model is exactly the same as the MRI-AGCM3.2 with high resolution (MRI-AGCM3.2H) listed in the CMIP5 archive. Further details of the model and its performance can be found in Mizuta et al. (2012). Previous studies have shown that the AGCM has high skill in simulating regional-scale climate such as the geographical distribution of tropical cyclones (Murakami et al. 2012a,b) and monsoon precipitation (Endo et al. 2012), including intense rainfall associated with the East Asian summer monsoon (Kusunoki and Mizuta 2013), as well as the global-scale climate (Mizuta et al. 2012).

The RCM downscaling simulations are performed by the Meteorological Research Institute Nonhydrostatic Regional Climate Model (NHRCM). The horizontal grid size is 211 × 175, covering Japan, the Korean Peninsula, and the eastern part of the Asian continent. The NHRCM has 40 layers in the vertical. Detailed specifications of the model have been reported by Sasaki et al. (2011) and Murata et al. (2013).

Experimental settings. Three sets of experiments are performed by the AGCM: a historical climate simulation, a +4-K future climate simulation, and a nonwarming simulation. The SST, sea ice concentration (SIC), and sea ice thickness (SIT) are prescribed as the lower boundary conditions, and global-mean concentrations of greenhouse gases and three-dimensional distributions of ozone and aerosols as the external forcing. The duration of each experiment is 60 years. Each set of experiments has 90–100 ensemble members, for which the initial conditions and the lower boundary conditions are perturbed. The settings of the experiments are summarized in Table 1.

The past historical climate from 1951 to 2010 is simulated with 100 ensemble members. The observed monthly mean SST and SIC [Centennial Observation-Based Estimates of SST, version 2 (COBE-SST2); Hirahara et al. 2014] and climatological monthly SIT from Bourke and Garrett (1987) are used as the lower boundary conditions. In addition to using different initial conditions, small perturbations of SST (δSSTs) based on SST analysis error are added to COBE-SST2 for the ensemble experiments. The details of these perturbations are described in the appendix. Global-mean concentrations of greenhouse gases [CO_2, CH_4, N_2O, and chlorofluorocarbons (CFCs)]

Table 1. Duration (yr), ensemble size, and prescribed boundary conditions of the three simulations.

	Historical simulation	+4-K future simulation	Nonwarming simulation
Duration	**60 (1951–2010)**	**60**	**60 (1951–2010)**
Members (GCM)	100	6 × 15	100
Members (RCM)	50	6 × 15	—
Greenhouse gases	Observed	Values at 2090 of RCP8.5	Values at 1850
Aerosols	Monthly output from MRI-CGCM	2090 output from MRI-CGCM	Sulfate, black carbon, organic carbon: values at 1850; mineral dust, sea salt: same as historical simulation
Ozone	Monthly output from MRI-CCM	2090 output from MRI-CCM	1961 output from MRI-CCM

are set to the observational values for each year. Three-dimensional distributions of ozone from the MRI Chemistry–Climate Model (MRI-CCM; Deushi and Shibata 2011) and aerosols from the MRI Coupled Atmosphere–Ocean General Circulation Model, version 3 (MRI-CGCM3; Yukimoto et al. 2012), are used.

The future climate in which the global-mean surface air temperature becomes 4 K warmer than the preindustrial climate is simulated, corresponding to that around the end of the twenty-first century under the representative concentration pathway 8.5 (RCP8.5) scenario of CMIP5. In this simulation, the amplitude of the warming is kept constant throughout the 60-yr integration. This is a different experimental setting from the so-called emission scenario simulations in which the stage of global warming is changing during the simulation period. With this experiment, we can obtain a large sample size under the same specified stage of global warming.

For the use of the +4-K simulation, climatological SST warming patterns (ΔSSTs) are added to the observational SST after removing the long-term trend component, as shown in Fig. 1. The trend component in the observations is derived as the leading empirical orthogonal function (EOF) computed from the 5-yr mean during 1951–2010, which explains most of the observational trend. The ΔSSTs are the difference between 1991–2010 and 2080–99 in the historical and RCP8.5 experiments by the CMIP5 models. Six CMIP5 models were selected based on a cluster analysis of geographical patterns of SST changes (Mizuta et al. 2014) so that the six patterns cover the most part of the uncertainty of the patterns in all the CMIP5 models. Each pattern is multiplied by a scaling factor so as to give a global-mean surface air temperature warming of 4 K. The six models and the corresponding factors are listed in Table 2, and the six ΔSSTs are shown in Figs. 2a–f.

For each of the six ΔSSTs, 15-member ensemble experiments are conducted using different initial conditions and different δSSTs, giving a total of 90 members. The δSSTs are the same as those for the historical simulation. The greenhouse gases are set to the value in 2090 of the RCP8.5 scenario. The ozone and aerosol distributions are the average from 2088 to 2092 in the extended experiments with the same models as used in the historical simulation.

We also performed a nonwarming simulation, assuming that global warming has not taken place since the preindustrial climate. The same boundary conditions as the historical simulation are given, except that the long-term trend is removed. This simulation is intended for comparison with the historical simulation for attribution studies of historical climate change. Since it also has no warming trend, it can be used for comparison with the +4-K simulation for analyses in which the effect of the warming trend within the historical simulation cannot be ignored, for example, the future change in the amplitude of the interannual temperature variability. The number of ensemble members is 100, using the same initial and boundary perturbations as the historical simulation. The baseline of the detrended SST is the average from 1900 to 1919 in which the SST warming since the preindustrial climate was not clearly observed. Greenhouse gases are set to the estimated

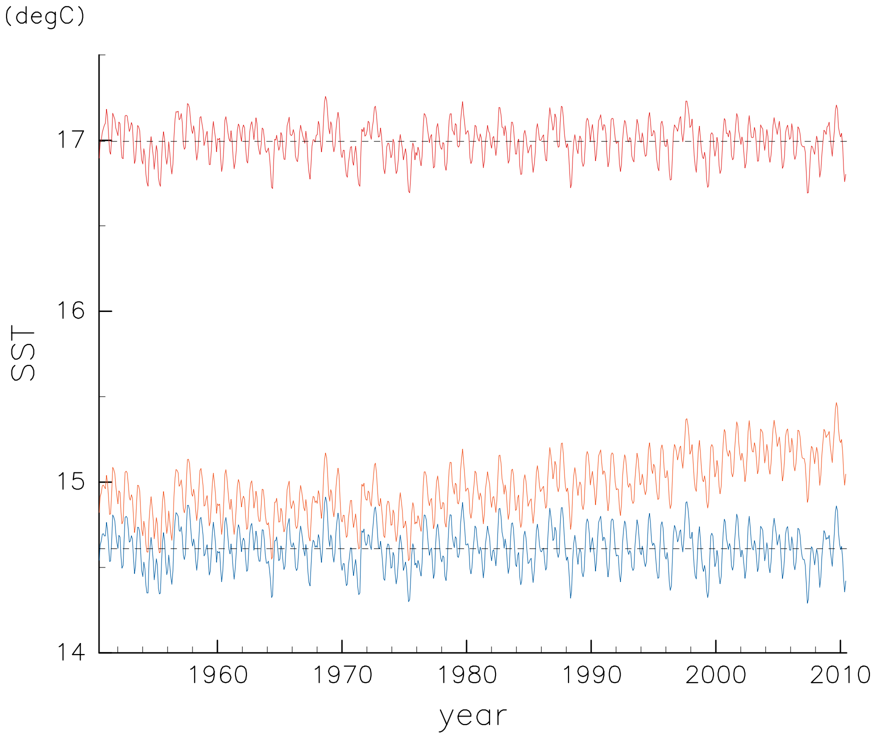

Fig. 1. Monthly mean SST averaged over 60°S–60°N prescribed for the historical climate simulation (orange line), the +4-K climate simulation (red line), and the nonwarming simulation (blue line).

Table 2. CMIP5 models used for obtaining SST changes, and the scaling factor multiplied by the SST difference for 1991–2010 and 2080–99. AORI = Atmosphere and Ocean Research Institute. NIES = National Institute for Environmental Studies. JAMSTEC = Japan Agency for Marine-Earth Science and Technology.

Model	Institution (Country)	Scaling factor
CCSM4	National Center for Atmospheric Research (United States)	1.10981
GFDL CM3	National Oceanic and Atmospheric Administration (NOAA) GFDL (United States)	0.75166
HadGEM2-AO	Met Office Hadley Centre (United Kingdom)	0.902224
MIROC5	AORI, NIES, JAMSTEC (Japan)	1.06162
MPI-ESM-MR	Max Planck Institute for Meteorology (Germany)	1.01852
MRI-CGCM3	Meteorological Research Institute (Japan)	1.13509

value in 1850. The ozone distribution is fixed to the average from 1960 to 1962 in the same experiment as used in the historical simulation. The aerosol is from the experiment in which the sulfate, black carbon, and organic carbon emissions are set to preindustrial values. As we cannot show much about the results of the nonwarming simulation, see Shiogama et al. (2016) for more details and the first results.

The dynamical downscaling simulations by the RCM are conducted for 50 members of the historical simulation and for 90 members of the +4-K simulation. Simulations for only 50 members are conducted for the historical case due to the limitation of the computational resource. Time integrations are split to each year; the simulation starts on 20 July and terminates on 31 August of the following year. The first 40 days of integration is the spinup, and output from 1 September to 31 August of the following year is available for diagnosis.

Climatological change and its dispersion in the results. The global-mean change in the prescribed SST from the historical simulation to the +4-K future simulation (Fig. 1) is 2.61 K. In the results of the AGCM experiments, we obtain global-mean surface air temperature change from the historical simulation to the +4-K simulation of 3.64 K. Since the observed warming from the preindustrial climate to the duration of the historical simulation (1951–2010) is 0.45 K, the warming from the preindustrial to the +4-K simulation is about 4.1 K. The error of about 0.1 K comes from the difference in land surface warming between the six CMIP5 models and the AGCM.

Figures 2g–r compare the changes in the annual-mean precipitation from the outputs of the six CMIP5 models and those from the AGCM results for the six ΔSST ensemble experiments. While all CMIP5 models (Figs. 2g–l) have precipitation increasing in the tropics and extratropics and decreasing in the subtropics, there are differences between the models associated with the differences in the SST changes. The differences are large in the tropics, especially around the Maritime Continent. These intermodel differences are also represented in the results of the 60-km AGCM (Figs. 2m–r), showing that a certain component of the uncertainties from different climate models is covered by the six ΔSST ensemble experiments: precipitation increases more over the central to eastern equatorial Pacific and less over the Maritime Continent region in the Hadley Centre Global Environment Model, version 2—Atmosphere and Ocean (HadGEM2-AO); the Max Planck Institute Earth System Model, medium resolution (MPI-ESM-MR); and the Meteorological Research Institute Coupled Atmosphere–Ocean General Circulation Model, version 3 (MRI-CGCM3; Figs. 2i,k,l,o,q,r). This result is consistent with the El Niño–like pattern of SST change (Figs. 2c,e,f). In contrast, SST warming in the western Pacific is comparable to that in the eastern equatorial Pacific in the Community Climate System Model, version 4 (CCSM4); the Geophysical Fluid Dynamics Laboratory Climate Model, version 3 (GFDL CM3); and the Model for Interdisciplinary Research on Climate, version 5 (MIROC5; Figs. 2g,h,j,m,n,p), resulting in a more zonally uniform change in precipitation. Differences between the models are also found around the Atlantic Ocean, the Indian Ocean, the Amazon, and the South Pacific convergence zone.

BENEFITS OF THE HIGH-RESOLUTION LARGE ENSEMBLE: GCM. The high-resolution large ensemble results enable us to assess the statistical change in very rare precipitation events. Figure 3a shows the frequency distribution of daily precipitation in the historical simulation for the grid square including Tokyo, Japan, compared with the observational station data at Tokyo, without bias correction. The observational data lie within the ensemble spread of single-member results (blue lines), showing that the model simulates extreme precipitation events very well. Since the data length is limited, in both the observations and the single-member experiment the error becomes large at a frequency lower than about 0.1% (once in 3 years). However, the frequency distribution from 10 members (green lines) can represent frequencies for a range from 0.03% (once in 10 years) to 0.003% (once in 100 years), and the frequency distribution from the total 100 members (red line) shows reasonable frequencies around 0.001% (once in 300 years).

Figure 3b shows the change as the ratio between the historical simulation and +4-K future simulations

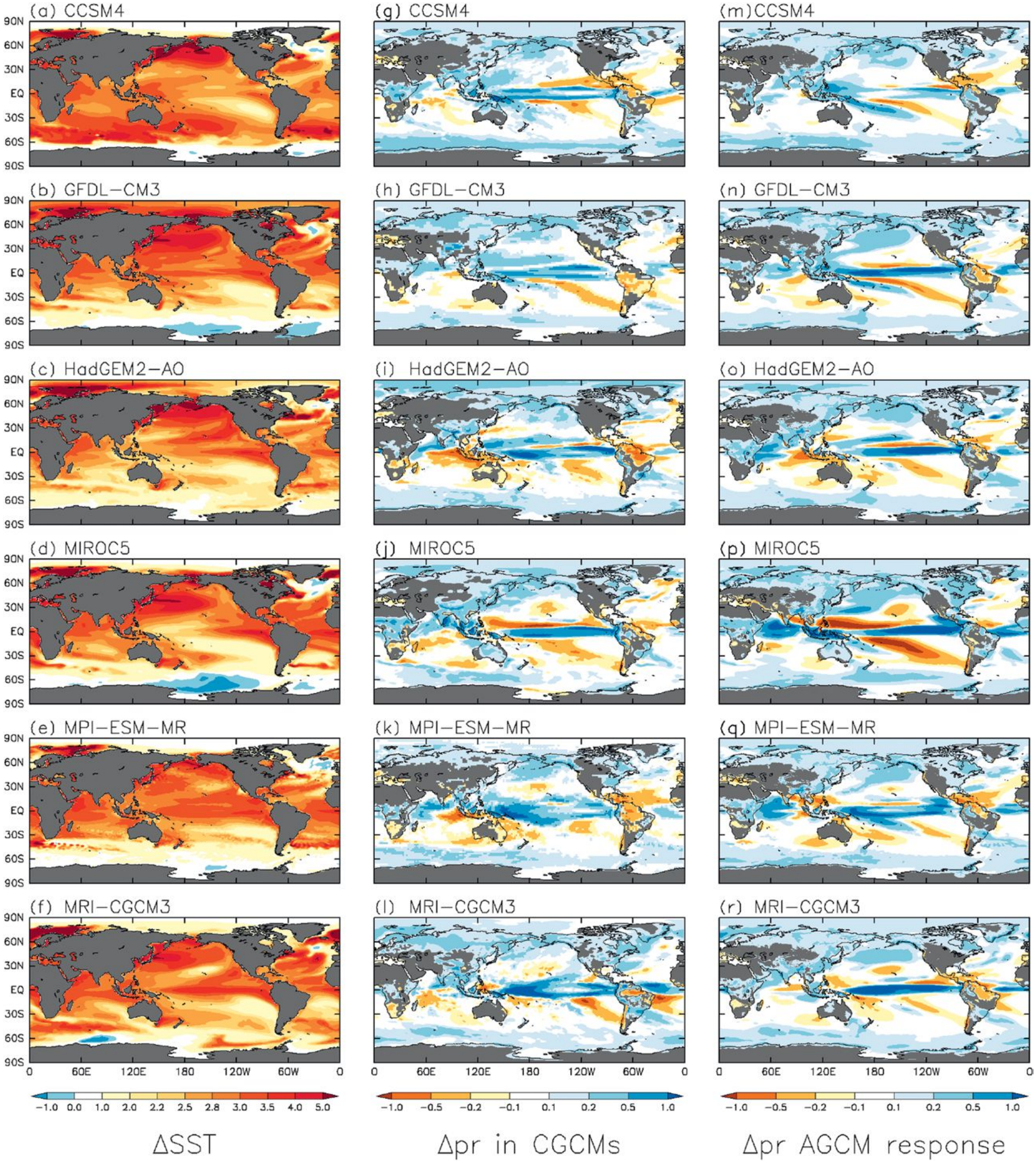

Fig. 2. Annual-mean horizontal distributions of (a)–(f) SST changes (K) for the six ΔSST ensemble experiments, (g)–(l) precipitation changes normalized by the global-mean SST change (mm day^{-1} K^{-1}) from the historical experiments to the RCP8.5 experiments of the six CMIP5 model outputs, and (m)–(r) those from the historical simulation to the +4-K ensemble AGCM simulation using the six different ΔSST.

of the occurrences of each precipitation rate. While the change is relatively small at weaker precipitation rates, it is positive for heavy precipitation above 70 mm day^{-1}. Moreover, the increase is larger with higher precipitation rates. Although the rates of increase depend on the prescribed SST change patterns, the increase is common to all the SST change patterns.

These results are not localized to Tokyo. Figure 4 shows the global distribution of the 10-yr return value of daily precipitation in the historical simulation and the change in the +4-K future simulation, calculated from the 90th-percentile value of the annual maximum daily precipitation. The results from a single member of the historical simulation (Fig. 4a) can capture only the large-scale features, and small-scale characteristics are masked by the noise due to the limited sample size. The change ratio obtained with a single member (Fig. 4c) consists of a mixture of regions of increasing and decreasing precipitation over most of the land. In contrast, clear and smooth images are obtained by using 90 ensemble members for each of the historical and +4-K simulations (Figs. 4b,d). The 10-yr return value of daily precipitation is over 200 mm day^{-1} in central India, the northwestern and southwestern Pacific Ocean, and the southwestern Indian Ocean. Regions of future increase are found over most of the world, and regions of future decrease are limited to the subtropics in the Atlantic and eastern Pacific oceans. The large-scale geographical patterns of the historical simulation and the change in the warmer climate are comparable to those estimated from the CMIP5 multimodel median (Kharin et al. 2013), except for the increase over the driest regions like northern Africa and a slight decrease over the Philippines. A decrease of climatological-mean heavy precipitation over the Philippines Sea is associated with a decrease of tropical cyclone number in the future climate (Kitoh and Endo 2016). Previous studies, including Kharin et al. (2013), used fitting to extreme value distributions for estimating such extreme values, which requires assuming distribution parameters. However, the use of a large ensemble enables us to estimate extreme values without any assumptions of their distributions. The change in the global average of the return value is +32.8%. The rate of increase per 1-K warming (11.5% K^{-1}) is larger than the result from the CMIP5 multimodel median (about 5.8% K^{-1}; Kharin et al. 2013), although it is within its intermodel dispersion. This could be associated with the horizontal resolution of the model (Sugiyama et al. 2010).

Figure 5a shows an unbiased estimate of the standard deviation σ_{tot} between the 90 ensemble members for the change ratio in the 10-yr return value of daily precipitation. The σ_{tot} value is ~30% in the subtropics and ~15% in the midlatitudes. The blue line in Fig. 6 is the zonal-mean ratio of the 95% confidence interval of the change (~1.96σ) to the change itself

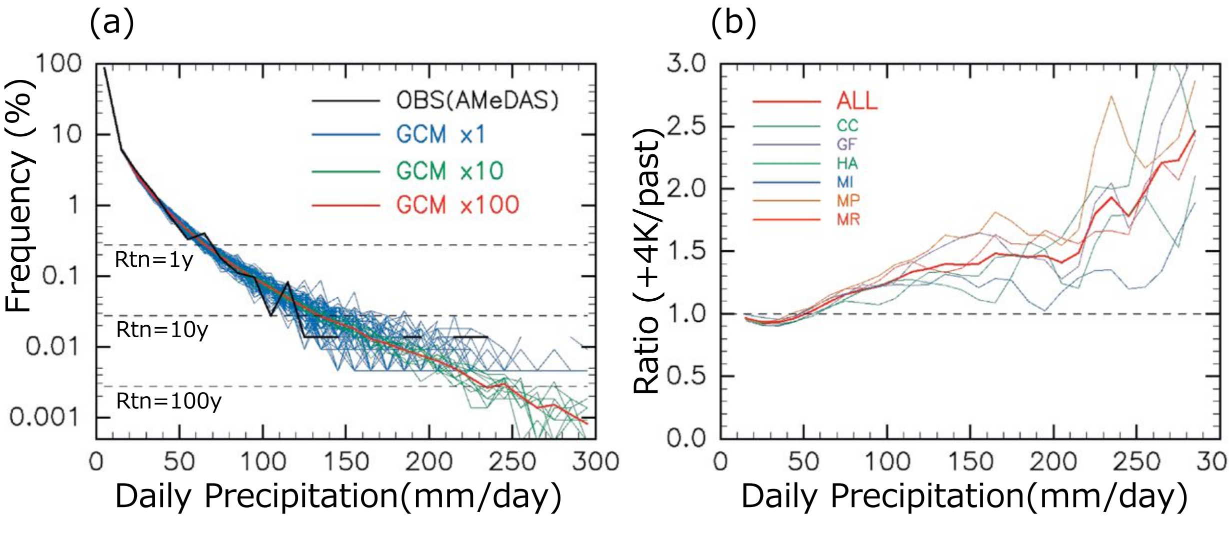

Fig. 3. (a) Frequency distributions of daily precipitation on the grid square including Tokyo for the historical simulation. The black line indicates distributions from the station observations at Tokyo from 1980 to 1999, the blue lines indicate distributions from each of the 100 ensemble members, the green lines are 10-member averages, and the red line indicates distributions from the 100 members. (b) Ratio between the historical and +4-K simulations of the occurrences of each precipitation rate on the grid square including Tokyo. The six thin lines correspond to the six ΔSST patterns, and the thick red line is from all members.

(Fig. 4d). The ratio is larger than 1 at all latitudes; that is, the confidence interval is larger than the change, meaning that uncertainty exists even regarding the sign of change. The other lines in Fig. 6 show how the statistical confidence interval of the ensemble-mean change becomes narrower as the ensemble number increases. The confidence interval for *N* members is calculated from 90 samples of an *N*-member ensemble chosen by the bootstrap method. If we use 10 members, then the sign of the change becomes confident except over the subtropics. Furthermore, the ratio decreases to less than 0.5 when the number of ensemble members is increased to 90.

The total variance σ^2_{tot} in Fig. 5a can be decomposed into the variance due to the difference in ΔSST patterns $\sigma^2_{\Delta\mathrm{SST}}$ (Fig. 5b) and the internal variability seen in the 15 δSST ensemble σ^2_{int} (Fig. 5c) by using a statistical method based on a concept of the analysis of variance (ANOVA) applied by Rowell et al. (1995) and Endo et al. (2016). The result shows that $\sigma_{\Delta\mathrm{SST}}$ is small in the extratropics (Fig. 5b), suggesting that the patterns of SST warming have less influence on this aspect of the change in the extratropics. In the equatorial Pacific and Atlantic Oceans, in contrast, the change depends mainly on the SST warming pattern. The $\sigma_{\Delta\mathrm{SST}}$ and σ_{int} are comparable in the subtropics, showing that the combination of the two different kinds of ensemble experiments is able to cover a wide range of uncertainty in the change.

We can also examine extreme temperature events. While such events occur more widely than extreme precipitation events, there could be some benefit in performing the high-resolution simulations around the regions affected by orography with a scale of ~100 km.

Figure 7a shows the global distribution of the 20-yr return value of the maximum surface air temperature in the latter half of the historical simulation. Note that this is calculated from the 95th-percentile value of annual maximum temperature, so at most one hot day is counted for each heat wave event. The values over the ocean are masked, as the day-to-day variability is smaller than in the real world due to the prescribed monthly SST. Very high temperature events over inland areas are represented. The change from the historical simulation to the +4-K simulation is shown in Fig. 7b. A large-scale distribution consistent with the CMIP5

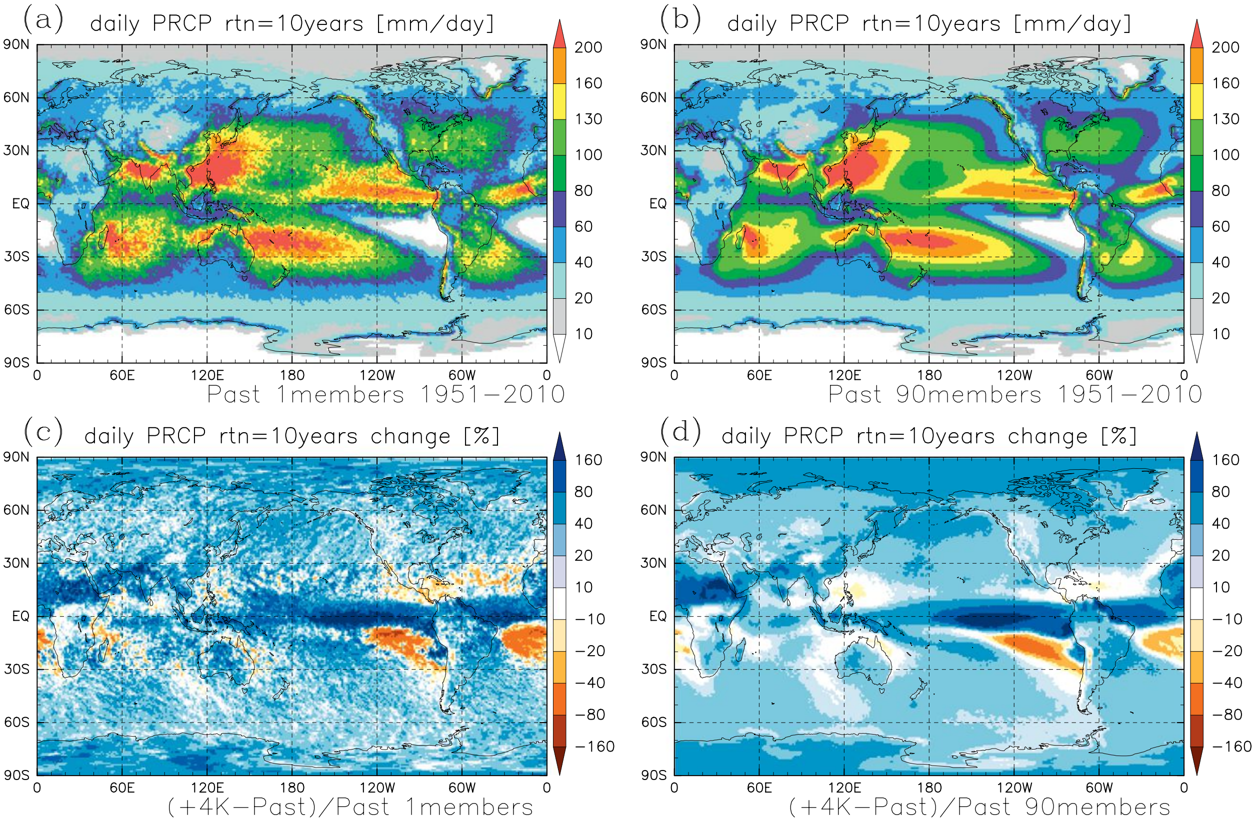

Fig. 4. The 10-yr return value of daily precipitation (a),(b) in the historical simulation and (c),(d) in the change ratio from the historical simulation to the +4-K simulation. (a),(c) The results from a single member and (b),(d) the ensemble mean of 90 members.

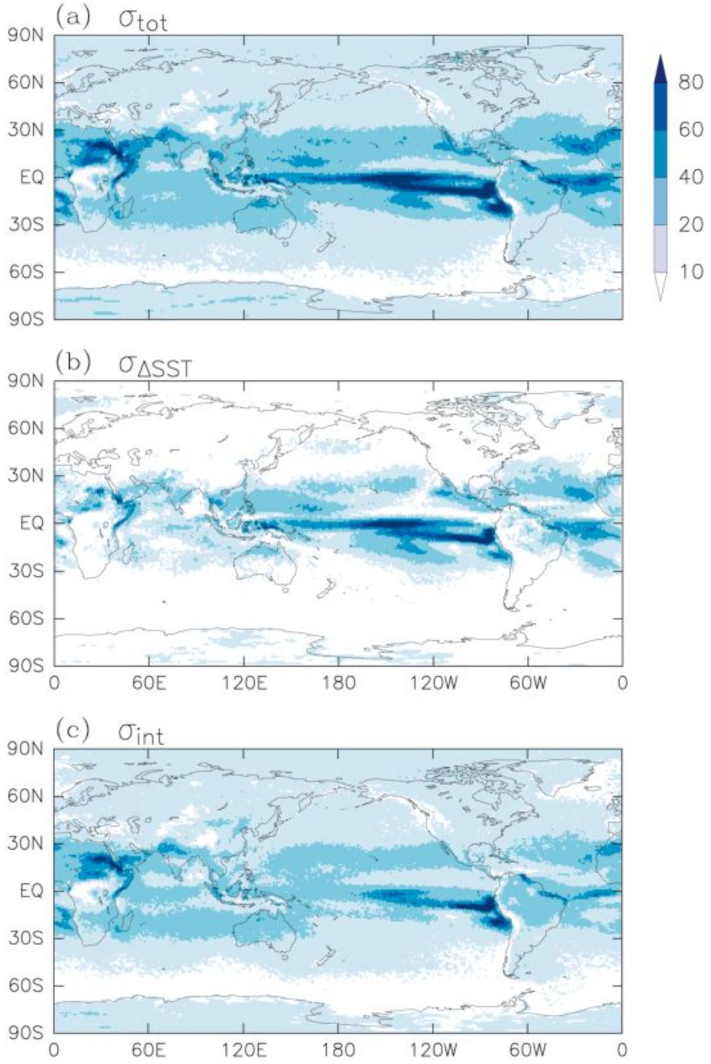

Fig. 5. Standard deviation σ_{tot} (%) of the differences between the historical and +4-K simulations in the 10-yr return value of daily precipitation for (a) all ensemble members, and components of σ_{tot} due to (b) the difference in ΔSST patterns $\sigma_{\Delta SST}$ and (c) the internal variability seen in the 15 δSST ensembles σ_{int}, using ANOVA without replication.

multimodel results (Collins et al. 2013; Kharin et al. 2013) is obtained over land, accompanied by a finer-scale distribution. A comparison with the seasonal-mean surface temperature warming (Figs. 7c,d) shows that the change in extremely high temperatures is almost the same as the change in the mean temperatures during the warm season over large areas of the land, with the difference being within 1 K. However, there are some exceptional areas around central Europe, southern Brazil, southern China, and the polar region, where the difference between the mean temperature warming and the extremely high temperature increase is more than 2 K. The difference in Europe is also found in an ensemble of 15 regional climate simulations over Europe (Vautard et al. 2014).

Figure 8 shows the probability distribution functions (PDFs) of annual maximum surface temperature for four representative locations. Over most of the world, the shape of the PDF does not change between the three simulations, as in Denver, Colorado (Fig. 8a). On the other hand, around central Europe and southern Brazil, as in Munich, Germany (Fig. 8b), and Rio de Janeiro, Brazil (Fig. 8c), the PDFs in the +4-K simulation are much broader than those in the historical simulation. Since the mean increase in annual maximum temperature is not so different from the increase in seasonal-mean temperature, the difference between the mean temperature warming and the extremely high temperature increase is attributed to a change in the shape of the PDFs. More elaborate analysis is needed to examine the mechanism associated with these extremely high temperature events and whether this projection is realistic. There are also some regions, such as Fairbanks, Alaska (Fig. 8d), where the shape of the PDF narrows slightly.

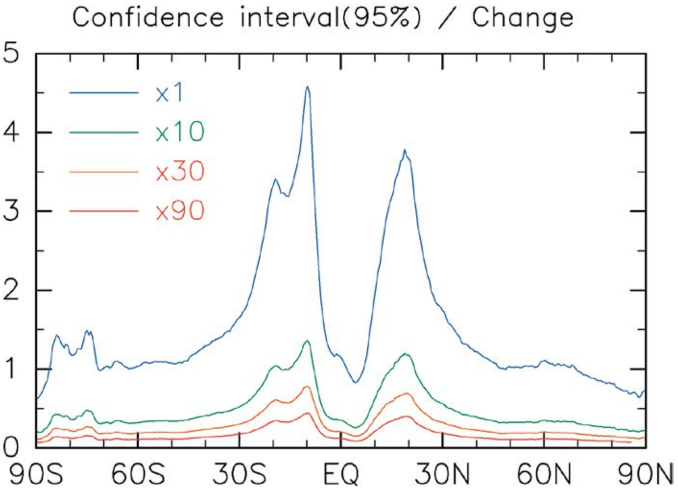

Fig. 6. Ratio of the zonal-mean 95% confidence interval of change to the zonal-mean change, for the 10-yr return value of daily precipitation. The confidence interval for *N* members is calculated from 90 sets of *N*-member ensembles chosen by the bootstrap method.

Such information on regional changes in extreme weather and climate events can be used to evaluate the impacts on natural disasters, agriculture, water resources, ecosystems, human health, and so on. In particular, very rare events with a return period of more than several decades must be evaluated for adaptation planning for flooding, sediment disasters, or high tides, since infrastructure such as dams and banks along rivers and coasts are constructed to prevent disasters caused by rare events. Figure 9 shows the 50-yr return value of surface wind speed. This return value is used for evaluating extremely high tide events. The distribution from the historical simulation (Fig. 9b) is smoother than that estimated from reanalysis data (Fig. 9a), which itself is useful for evaluating the distribution under the present climate. The change from the historical simulation to the +4-K simulation (Fig. 9c) shows an increase in the midlatitudes from 20° to 40°. A large part of the change is associated with the changes in the track and strength of tropical cyclones, which will also be reported in another publication.

BENEFITS OF THE HIGH-RESOLUTION LARGE ENSEMBLE: RCM. Extreme daily precipitation is projected using RCM simulations, which enable analyses of the detailed spatial distribution of extreme precipitation. Figure 10a shows the distribution of the 50-yr return value of daily precipitation around the main Japanese islands estimated from observational data. The return value is calculated using the maximum likelihood fitting for the generalized extreme value (GEV) distribution with the annual maximum daily precipitation (R1d) data. The results of the observational station data are interpolated onto the model land grid points. The value in the historical simulation is calculated in the same way to compare with that of the observation and is shown in Fig. 10b. The spatial distributions of the extreme precipitation in the model and observational results are similar to each other, with larger values on the coast of the Pacific Ocean. This is due to the high horizontal resolution of the RCM.

The future change is presented in Fig. 10c. Basic patterns of the changes are similar to the value in the

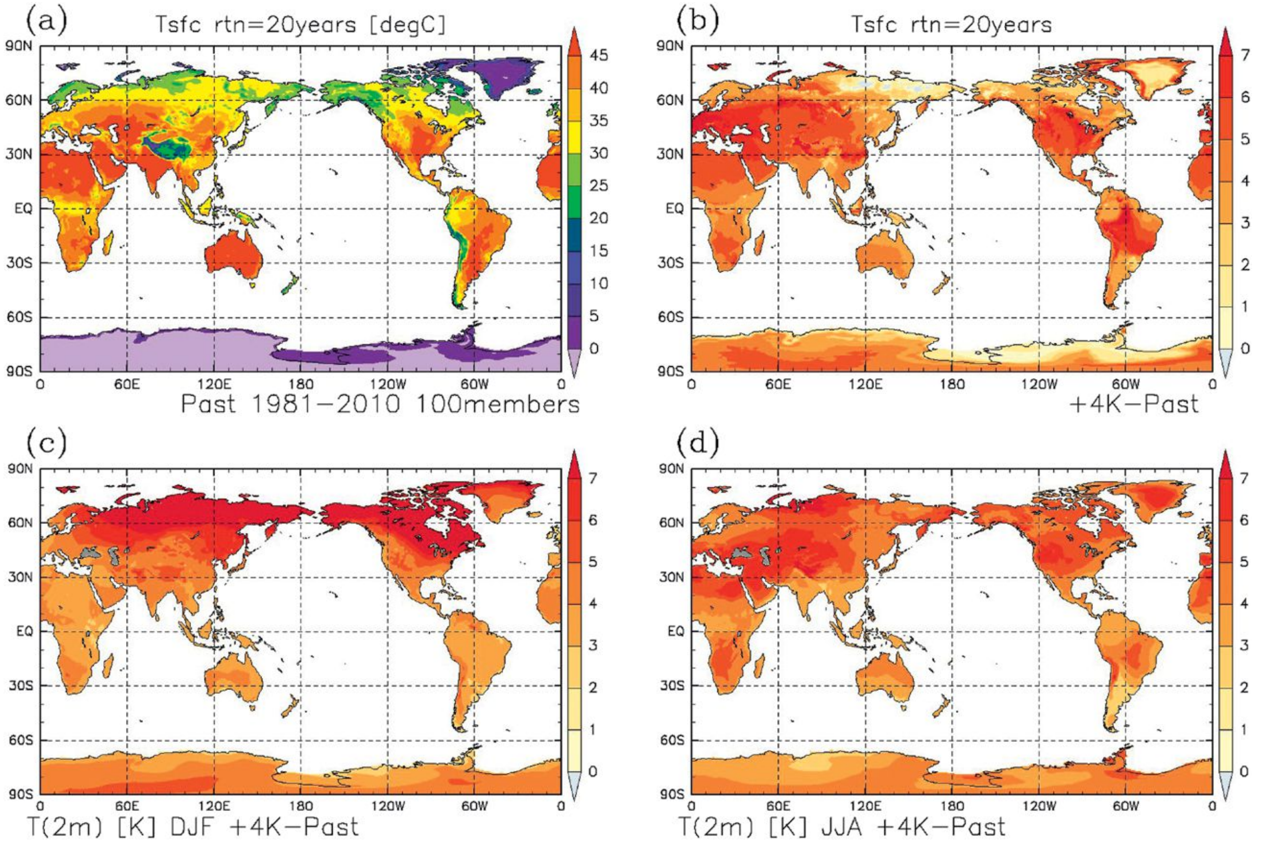

Fig. 7. (top) The 20-yr return value of maximum surface air temperature for (a) the latter half of the historical simulation and (b) the change in the +4-K simulation. These 20-yr return values are calculated from the 95th-percentile value of annual maximum of daily maximum temperature. (bottom) Seasonal-mean surface temperature change (c) from Dec to Feb and (d) from Jun to Aug.

historical simulation in Fig. 10b, which means the change relative to the value in the historical simulation has a larger spatial scale, especially along the coast of the Pacific Ocean (not shown). Whether the change in extreme precipitation is significant depends on the absolute values of the changes and their confidence intervals. Figure 10d shows the distribution of the 95% confidence intervals of the 50-yr-return-value estimation; these confidence intervals are the mean values of the historical and future simulations. The confidence intervals (Fig. 10d) are sufficiently smaller than the future changes (Fig. 10c) to conclude the significance of the future changes in most regions without a rigorous statistical test. This significance is due to the large number of samples, on the order of thousands, which reduces the confidence intervals and improves the reliability of estimations of extreme precipitation.

Next, extremely heavy precipitation in terms of annually accumulated precipitation is investigated. Annual amounts of precipitation are spatially averaged over each of the six regions of Japan shown in Fig. 11a and are sorted for each simulation. Then, the change in precipitation amount from the historical simulation to the +4-K simulation for each percentile is calculated. In this way, the dependence of changes in precipitation on percentile values is examined.

The change in the annually accumulated precipitation increases as the precipitation becomes heavier (Fig. 11b). For example, in the northern Japan (NJ) region the change ranges from 1.5% at the 5th percentile to 5.4% at the 95th percentile. This means that the amplitude of the variability increases in the future climate. This result is robust for the six regions of

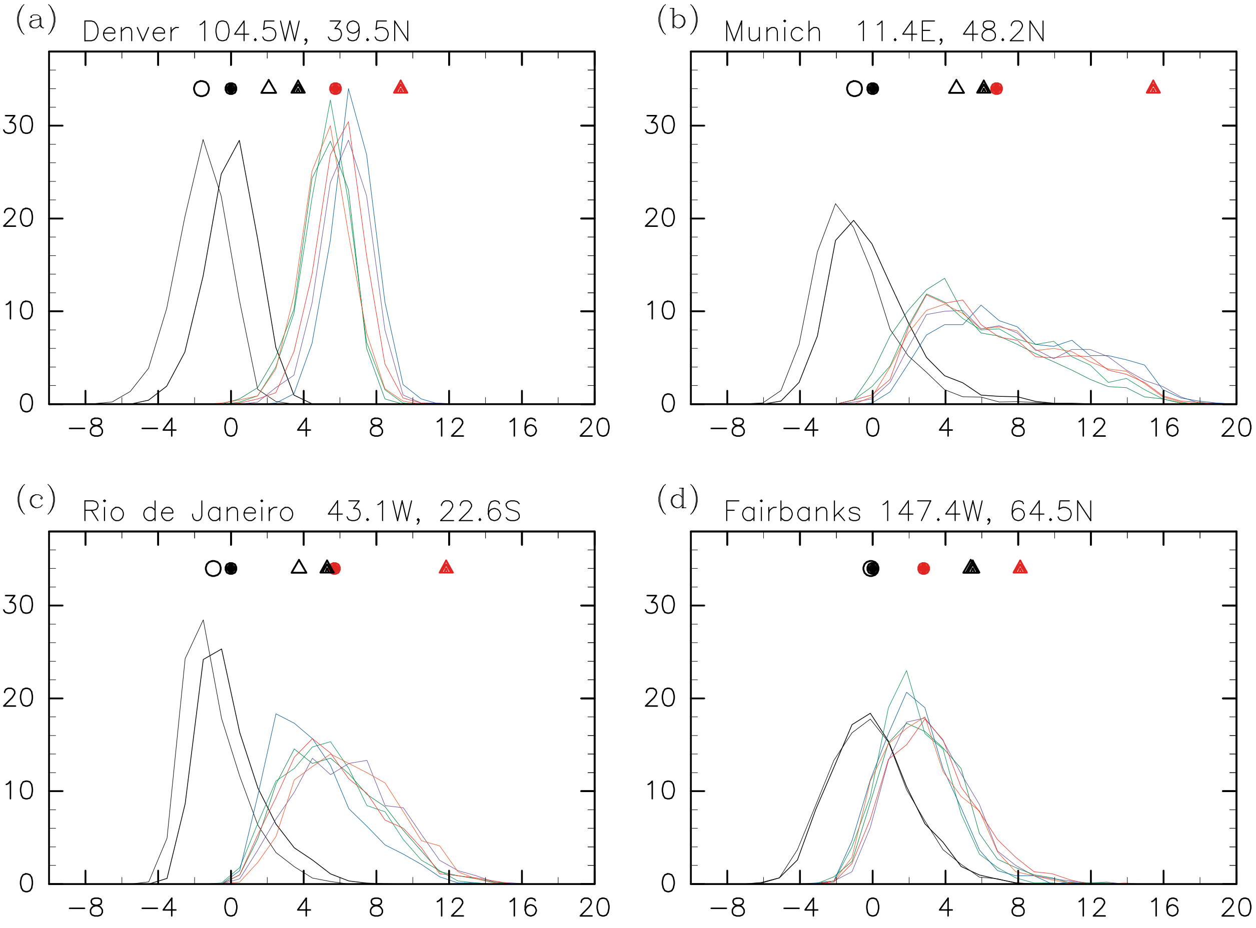

Fig. 8. Frequency distributions of annual maximum surface temperature for four representative points: (a) Denver (39.5°N, 104.5°W), (b) Munich (48.2°N, 11.4°E), (c) Rio de Janeiro (22.6°S, 43.1°W), and (d) Fairbanks (64.5°N, 147.4°W). The thick black line is from the latter half of the historical simulation, the thin black line is from the latter half of the nonwarming simulation, and color lines correspond to the six SST change patterns of the +4-K experiment. Bin size is 1 K, and the horizontal axis is the deviation from the average (K) in the latter half of the historical simulation. Circles and triangles are the averages and 20-yr return values, respectively, for the historical (black), nonwarming (open symbols), and +4-K (red) simulations.

Japan, except for below the 5th percentile and above the 95th percentile. The change tends to be negative for a range of lower percentiles in some regions. In the eastern (EJ) and western Japan (WJ) regions, the changes have negative values below about the 80th and 70th percentiles, respectively. Nevertheless, higher categories of the precipitation amount, such as the 90th percentile, increase even in those regions. Thus, the increase in heavy precipitation, in the annually accumulated sense, is seen more broadly than the increase in mean precipitation.

DISCUSSION AND CONCLUDING REMARKS. Results of high-resolution large ensemble simulations with a 60-km global atmospheric model and a 20-km regional climate model have been made publicly available as a database that enables us to discuss the uncertainty arising from internal variability in the future change in extreme weather and climate events. Using more than 5,000 years of data from the 60-km global model, extreme daily precipitation events with a return period of several decades can be calculated without any assumption of distribution functions. The increase in daily precipitation in the future simulation is greater for higher precipitation rates. Over central Europe and some other regions, the 20-yr return value of maximum surface temperature shows a greater increase than the mean temperature increase of the warm season. Using the downscaled results with the 20-km regional climate model, we obtain a more detailed spatial distribution associated with small topography.

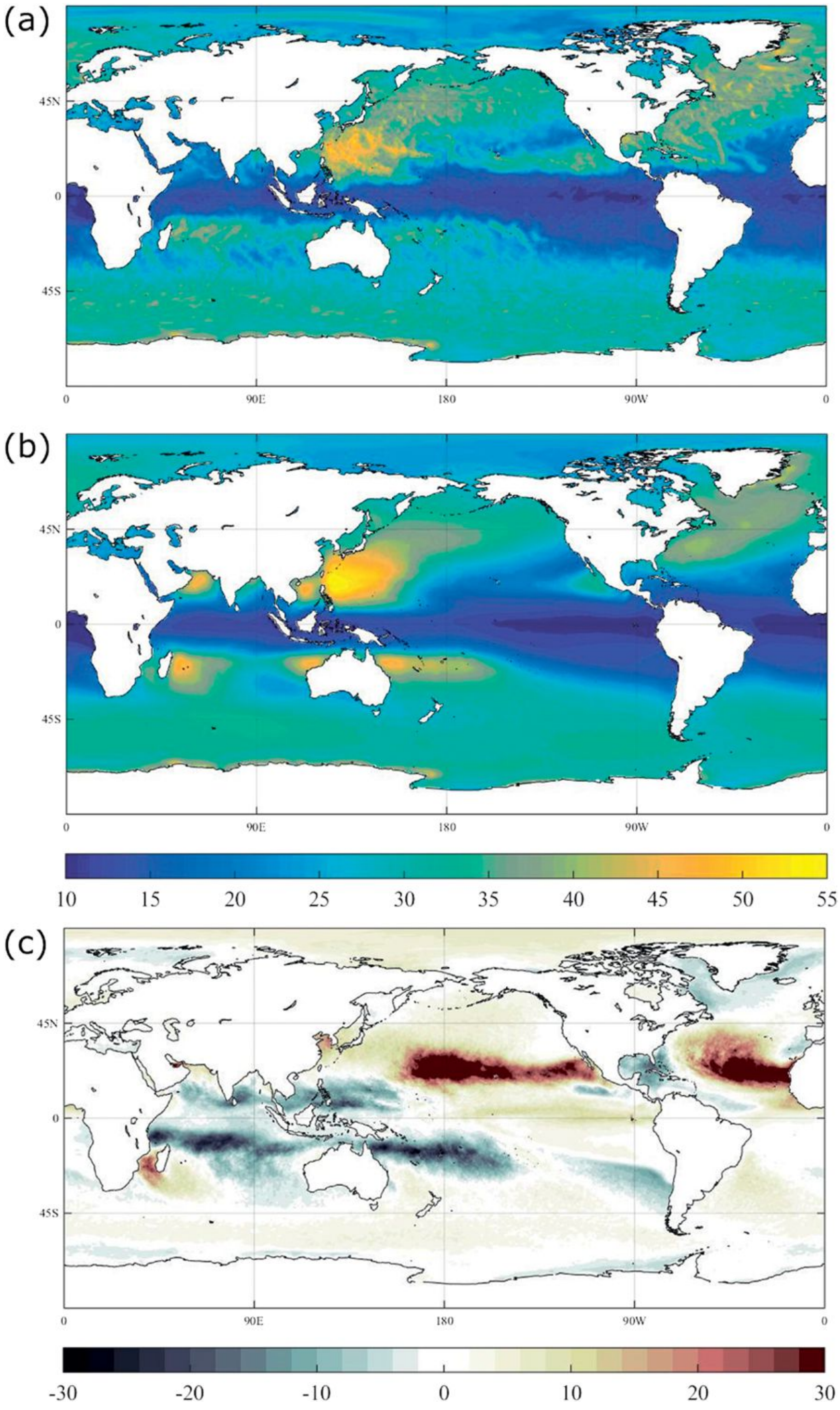

Fig. 9. Spatial distribution of the 50-yr return value of surface wind speed for (a) estimates from Japanese 55-year Reanalysis (JRA-55) data from 1958 to 2012 (m s^{-1}), (b) the historical simulation (m s^{-1}), and (c) the change from the historical simulation to the +4-K simulation (%).

The 60-km global model simulates realistic tropical cyclones in terms of their global frequency distribution (Murakami et al. 2012b). Changes in, for instance, the spatial distribution of tropical cyclone frequency can be identified and will be reported in another paper. While intense tropical cyclones are not well represented due to the lack of horizontal resolution, their change can also be estimated by applying a bias correction.

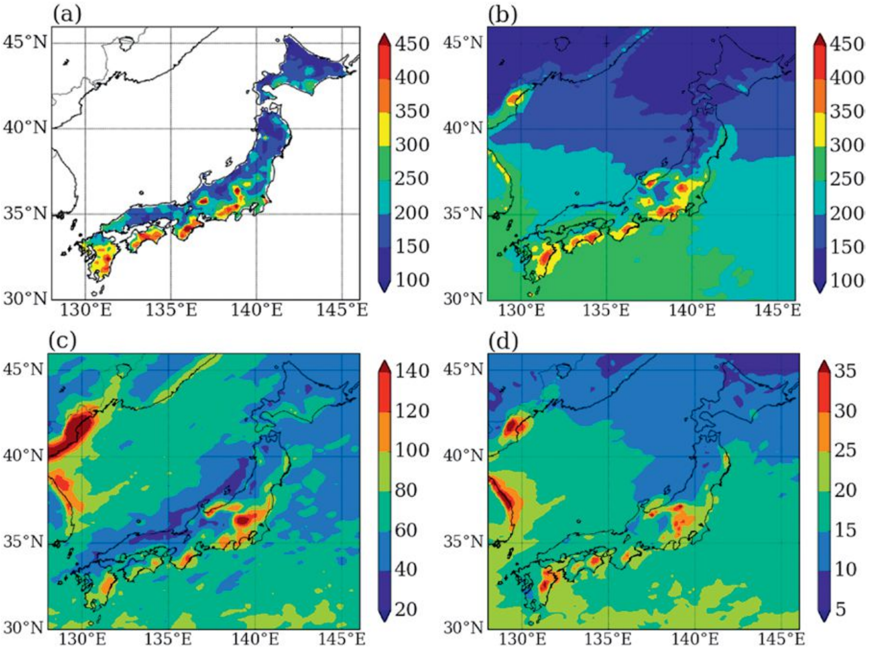

Fig. 10. Spatial distribution around the main Japanese islands of 50-yr return values of daily precipitation from (a) the historical climate model and (b) observational data [Automated Meteorological Data Acquisition System (AMeDAS) from 1980 to 1999], (c) difference between the historical and +4-K simulations, and (d) the average of the 95% confidence intervals in the historical and +4-K simulations.

The future experiment in the present study simulates the climate when the global-mean surface temperature becomes 4 K warmer than the preindustrial climate. The climate on the way to the 4-K warming is thought to be somewhere between the present climate and the +4-K climate. Whether "pattern scaling" can be applied, in which the change is estimated by linear interpolation of the global-mean surface temperature warming, would depend on the variables (Harris et al. 2013). We are planning to perform another experiment simulating a +2-K climate, which would enable us to estimate what variables are appropriate for pattern scaling.

Uncertainty in future change arising from the climate models is still large. For instance, the sign of the change in mean precipitation over the Maritime Continent region, which is related to patterns of SST change, depends on the climate models (Mizuta et al. 2014). In the present study, we are trying to consider the uncertainty by using different SST warming patterns from six different climate models. By doing so, we obtain different precipitation change patterns similar to those in the different climate models (Fig. 2). However, our results show a common distinctive pattern of change in summer precipitation over the northwestern Pacific different from the multimodel ensemble mean of the CMIP5 models. This is a limitation that arises from using the single MRI-AGCM. When similar high-resolution large ensemble simulations are performed by other models, an intercomparison would enable us to obtain more robust information on the probability of climate change. As an important step, outcomes from the High Resolution Model Intercomparison Project (HighResMIP; Haarsma et al. 2016) would provide a chance to estimate the intermodel spread of the high-resolution simulations.

ACKNOWLEDGMENTS. The Earth Simulator supercomputer was used in this study under the "Strategic Project with Special Support" of JAMSTEC. The study was also supported by the Program for Risk Information on Climate Change (SOUSEI) and the Data Integration and Analysis System (DIAS), both of which are sponsored by the Ministry of Education, Culture, Sports, Science and Technology of Japan. Extreme values by the GEV method were calculated using the extRemes R package (Gilleland and Katz 2011). We thank two anonymous reviewers for the useful comments. The simulation results are available online (via http://search.diasjp.net/search?lang=en&k=d4PDF).

APPENDIX: PERTURBATIONS FOR THE ENSEMBLE EXPERIMENTS. To obtain larger spreads of internal climate variability, perturbations of the lower boundary conditions are added for the ensemble simulations with the AGCM and the RCM, in addition to the use of different initial conditions. The initial conditions of the AGCM are

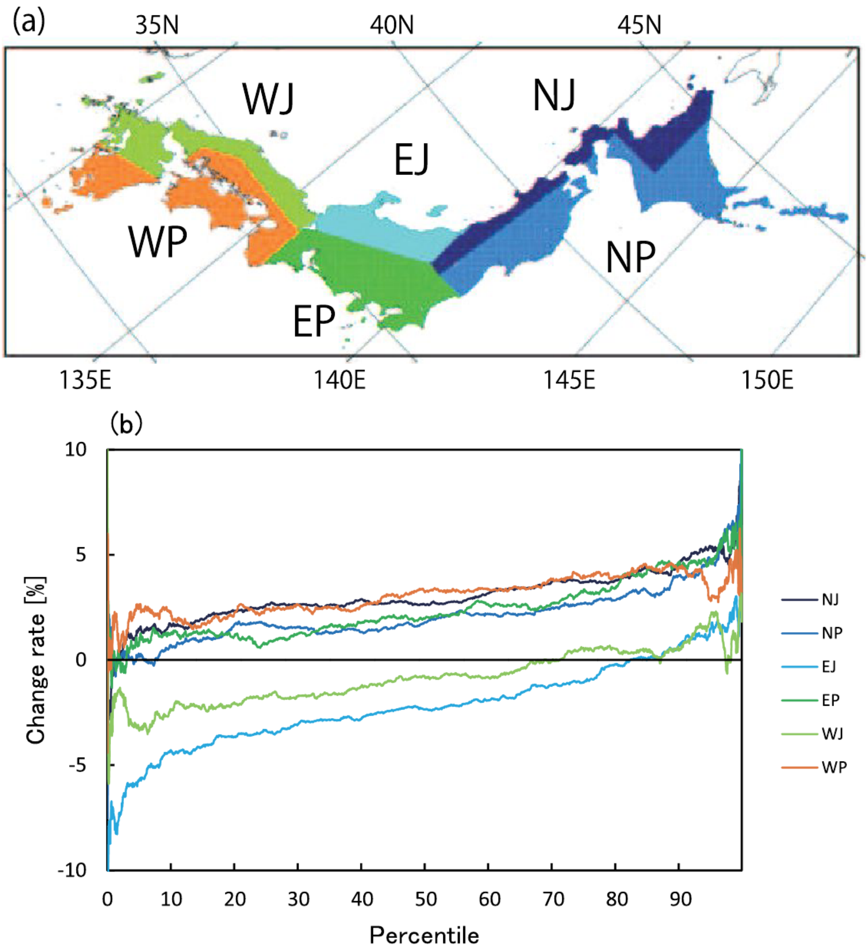

Fig. 11. (a) Map of Japan showing the regions used for analyses: Sea of Japan side of northern Japan (NJ), Pacific Ocean side of northern Japan (NP), Sea of Japan side of eastern Japan (EJ), Pacific Ocean side of eastern Japan (EP), Sea of Japan side of western Japan (WJ), and Pacific Ocean side of western Japan (WP). (b) Change in the annually accumulated precipitation averaged over each of the six regions. Data from 48 members for each simulation are used.

from snapshots on different dates in previous experiments with the same model, with 1 year of spinup. The perturbations of SST (δSSTs) are constructed by using EOFs representing the interannual variations in SST. The EOFs are the same as those used for reconstructing historical SSTs (Hirahara et al. 2014). Here we assume that the true SST is completely represented by the EOFs and that the uncertainty in COBE-SST2 results solely from the sampling of SST observations. The time series of each EOF component for δSST are randomly generated with an autoregressive moving-average model, assuming that the periodicity of each component is the same as that of the observations. The magnitude of the uncertainty should be proportional to the analysis errors that vary in space and time; however, this is set to be 30% of the standard deviation of the interannual variability of SST uniformly in space and time so that historical changes in the observational network are removed from consideration when analyzing the model simulation outputs. The value of 30% has been used as a typical magnitude of SST uncertainty in recent decades. In addition, SST variations due to mesoscale oceanic eddy activity, which are not represented by the EOFs, are overlain on the abovementioned perturbed SST. The magnitude of the eddy contribution is defined as the root-mean-square difference between COBE-SST2 and a satellite SST analysis, the latter of which is included in the COBE-SST2 products. Eddy observations are available only in the satellite era, and hence artificial eddies are substituted using Gaussian noise smoothed on scales of 200 km in space and 30 days in time (Chelton et al. 2007).

The perturbations for SIC and SIT are also applied to the ensemble simulations, which are constructed consistently with δSST. Using the relationship whereby SST is represented by quadratic functions of SIC (Hirahara et al. 2014), the SIC perturbation is inversely computed from δSST. The coefficients of the functions vary with basin and season. Horizontal patterns of the SIC in the future simulations are calculated from the future SST using different coefficients, constructed from the future SST and SIC of the multimodel ensemble mean of 36 CMIP5 models for the period from 2080 to 2099. The equations satisfy the condition that the total sea ice extent in each hemisphere computed from the future climatological SSTs is the same as that of the future climatological SIC in the CMIP5 models. Different coefficients are used for the six ΔSSTs. This ensures that the total sea ice extent is close to that in the multimodel ensemble mean.

Also note that the perturbation of SIC is realized through the quadratic equations. The observed SIT climatology is multiplied by a constant factor for each hemisphere for the future SIT so that the hemispheric sea ice volume change is the same as that of the CMIP5 multimodel ensemble. Zero SIT is specified at a grid point where there is no sea ice.

It is confirmed that the ensemble AGCM experiments with the perturbed SST, SIC, and SIT show similar sizes of ensemble spread in the atmosphere to those by the experiments with only initial-value perturbations, except for atmospheric variables near the sea surface, which are highly correlated with the SST variations.

REFERENCES

Allen, M. R., 2003: Liability for climate change. *Nature*, **421**, 891–892, doi:10.1038/421891a.

Bourke, R. H., and R. P. Garrett, 1987: Sea ice thickness distribution in the Arctic Ocean. *Cold Reg. Sci. Technol.*, **13**, 259–280, doi:10.1016/0165-232X(87)90007-3.

Chelton, D. B., M. G. Schlax, R. M. Samelsom, and R. A. de Szoeke, 2007: Global observations of large oceanic eddies. *Geophys. Res. Lett.*, **34**, L15606, doi:10.1029/2007GL030812.

Christidis, N., and P. A. Stott, 2014: Change in the odds of warm years and seasons due to anthropogenic influence on the climate. *J. Climate*, **27**, 2607–2621, doi:10.1175/JCLI-D-13-00563.1.

Collins, M., and Coauthors, 2013: Long-term climate change: Projections, commitments and irreversibility. *Climate Change 2013: The Physical Science Basis*, T. F. Stocker et al., Eds., Cambridge University Press, 1029–1136.

Deser, C., A. Phillips, V. Bourdette, and H. Teng, 2012: Uncertainty in climate change projections: The role of internal variability. *Climate Dyn.*, **38**, 527–546, doi:10.1007/s00382-010-0977-x.

Deushi, M., and K. Shibata, 2011: Development of a Meteorological Research Institute Chemistry-Climate Model version 2 for the study of tropospheric and stratospheric chemistry. *Pap. Meteor. Geophys.*, **62**, 1–46, doi:10.2467/mripapers.62.1.

Duong, D. T., Y. Tachikawa, and K. Yorozu, 2014: Changes in river discharge in the Indochina Peninsula region projected using MRI-AGCM and MIROC5 datasets. *J. Japan. Soc. Civil Eng. Ser. B1*, **70**, I_115–I_120.

Endo, H., A. Kitoh, T. Ose, R. Mizuta, and S. Kusunoki, 2012: Future changes and uncertainties in Asian precipitation simulated by multiphysics and multi–sea surface temperature ensemble experiments with high-resolution Meteorological Research Institute atmospheric general circulation models (MRI-AGCMs). *J. Geophys. Res.*, **117**, D16118, doi:10.1029/2012JD017874.

——, ——, R. Mizuta, and M. Ishii, 2017: Future changes in precipitation extremes in East Asia and their uncertainty based on large ensemble simulations with a high-resolution AGCM. *SOLA*, **13**, 7–12, doi:10.2151/sola.2017-002.

Fowler, H., M. Ekstrom, S. Blenkinsop, and A. Smith, 2007: Estimating change in extreme European precipitation using a multimodel ensemble. *J. Geophys. Res.*, **112**, D18104, doi:10.1029/2007JD008619.

Gilleland, E., and R. W. Katz, 2011: New software to analyze how extremes change over time. *Eos, Trans. Amer. Geophys. Union*, **92**, 13–14, doi:10.1029/2011EO020001.

Haarsma, R. J., and Coauthors, 2016: High Resolution Model Intercomparison Project (HighResMIP v1.0) for CMIP6. *Geosci. Model Dev.*, **9**, 4185–4208, doi:10.5194/gmd-9-4185-2016.

Harris, G. R., D. M. H. Sexton, B. B. Booth, M. Collins, and J. M. Murphy, 2013: Probabilistic projections of transient climate change. *Climate Dyn.*, **40**, 2937–2972, doi:10.1007/s00382-012-1647-y.

Hawkins, E., and R. Sutton, 2009: The potential to narrow uncertainty in regional climate predictions. *Bull. Amer. Meteor. Soc.*, **90**, 1095–1107, doi:10.1175/2009BAMS2607.1.

Hirahara, S., M. Ishii, and Y. Fukuda, 2014: Centennial-scale sea surface temperature analysis and its uncertainty. *J. Climate*, **27**, 57–75, doi:10.1175/JCLI-D-12-00837.1.

IPCC, 2013: *Climate Change 2013: The Physical Science Basis*. Cambridge University Press, 1535 pp.

JMA, 2007: Outline of the operational numerical weather prediction at the Japan Meteorological Agency; Appendix to WMO technical progress report. Japan Meteorological Agency, 194 pp. [Available online at www.jma.go.jp/jma/jma-eng/jma-center/nwp/outline-nwp/index.htm.]

Kanada, S., M. Nakano, and T. Kato, 2012: Projections of future changes in precipitation and the vertical structure of the frontal zone during the Baiu season in the vicinity of Japan using a 5-km-mesh regional climate model. *J. Meteor. Soc. Japan*, **90A**, 65–86, doi:10.2151/jmsj.2012-A03.

Kay, J. E., and Coauthors, 2015: The Community Earth System Model (CESM) Large Ensemble project: A community resource for studying climate change in the presence of internal climate variability. *Bull. Amer. Meteor. Soc.*, **96**, 1333–1349, doi:10.1175/BAMS-D-13-00255.1.

Kharin, V. V., F. W. Zwiers, X. Zhang, and M. Wehner, 2013: Changes in temperature and precipitation extremes in the CMIP5 ensemble. *Climatic Change*, **119**, 345–357, doi:10.1007/s10584-013-0705-8.

Kitoh, A., and H. Endo, 2016: Future changes in rainfall extremes associated with El Niño projected by a global 20-km mesh atmospheric model. *SOLA*, **12A**, 1–6, doi:10.2151/sola.12A-001.

——, T. Ose, and I. Takayabu, 2016: Dynamical downscaling for climate projection with high-resolution MRI AGCM-RCM. *J. Meteor. Soc. Japan*, **94A**, 1–16, doi:10.2151/jmsj.2015-022.

Kusunoki, S., and R. Mizuta, 2013: Changes in precipitation intensity over East Asia during the 20th and 21st centuries simulated by a global atmospheric model with a 60 km grid size. *J. Geophys. Res. Atmos.*, **118**, 11 007–11 016, doi:10.1002/jgrd.50877.

Mizuta, R., and Coauthors, 2012: Climate simulations using MRI-AGCM3.2 with 20-km grid. *J. Meteor. Soc. Japan*, **90A**, 233–258, doi:10.2151/jmsj.2012-A12.

——, O. Arakawa, T. Ose, S. Kusunoki, H. Endo, and A. Kitoh, 2014: Classification of CMIP5 future climate responses by the tropical sea surface temperature changes. *SOLA*, **10**, 167–171, doi:10.2151/sola.2014-035.

Mori, M., M. Watanabe, H. Shiogama, J. Inoue, and M. Kimoto, 2014: Robust Arctic sea-ice influence on the frequent Eurasian cold winters in past decades. *Nat. Geosci.*, **7**, 869–873, doi:10.1038/ngeo2277.

Mori, N., T. Yasuda, H. Mase, T. Tom, and Y. Oku, 2010: Projection of extreme wave climate change under the global warming. *Hydrol. Res. Lett.*, **4**, 15–19, doi:10.3178/hrl.4.15.

Murakami, H., and Coauthors, 2012a: Future changes in tropical cyclone activity projected by the new high-resolution MRI-AGCM. *J. Climate*, **25**, 3237–3260, doi:10.1175/JCLI-D-11-00415.1.

——, R. Mizuta, and E. Shindo, 2012b: Future changes in tropical cyclone activity projected by multi-physics and multi-SST ensemble experiments using the 60-km-mesh MRI-AGCM. *Climate Dyn.*, **39**, 2569–2584, doi:10.1007/s00382-011-1223-x.

Murata, A., H. Sasaki, M. Hanafusa, and K. Kurihara, 2013: Estimation of urban heat island intensity using biases in surface air temperature simulated by a nonhydrostatic regional climate model. *Theor. Appl. Climatol.*, **112**, 351–361, doi:10.1007/s00704-012-0739-2.

Nakano, M., M. Matsueda, and M. Sugi, 2013: Future projections of heat waves around Japan simulated by CMIP3 and high-resolution Meteorological Research Institute atmospheric climate models. *J. Geophys. Res. Oceans*, **118**, 5461–5488, doi:10.1002/jgrc.20375.

Pall, P., T. Aina, D. A. Stone, P. A. Stott, T. Nozawa, A. G. J. Hilberts, D. Lohmann, and M. R. Allen, 2011: Anthropogenic greenhouse gas contribution to flood risk in England and Wales in autumn 2000. *Nature*, **470**, 382–385, doi:10.1038/nature09762.

Rowell, D. P., C. K. Folland, K. Maskell, and M. N. Ward, 1995: Variability of summer rainfall over tropical North Africa (1906–92): Observations and modelling. *Quart. J. Roy. Meteor. Soc.*, **121**, 669–704, doi:10.1002/qj.49712152311.

Sasaki, H., A. Murata, M. Hanafusa, M. Oh'izumi, and K. Kurihara, 2011: Reproducibility of present climate in a non-hydrostatic regional climate model nested within an atmosphere general circulation model. *SOLA*, **7**, 173–176, doi:10.2151/sola.2011-044.

Shimura, T., N. Mori, and H. Mase, 2015: Future projection of ocean wave climate: Analysis of SST impacts on wave climate changes in the western North Pacific. *J. Climate*, **28**, 3171–3190, doi:10.1175/JCLI-D-14-00187.1.

Shiogama, H., M. Watanabe, Y. Imada, M. Mori, Y. Kamae, M. Ishii, and M. Kimoto, 2014: Attribution of the June-July 2013 heat wave in the southwestern United States. *SOLA*, **10**, 122–126, doi:10.2151/sola.2014-025.

Sugiyama, M., H. Shiogama, and S. Emori, 2010: Precipitation extreme changes exceeding moisture content increases in MIROC and IPCC climate models. *Proc. Natl. Acad. Sci. USA*, **107**, 571–575, doi:10.1073/pnas.0903186107.

Vautard, R., and Coauthors, 2014: The European climate under a 2°C global warming. *Environ. Res. Lett.*, **9**, 034006, doi:10.1088/1748-9326/9/3/034006.

Xie, S.-P., and Coauthors, 2015: Towards predictive understanding of regional climate change. *Nat. Climate Change*, **5**, 921–930, doi:10.1038/nclimate2689.

Yasuda, T., S. Nakajo, S. Kim, H. Mase, N. Mori, and K. Horsburgh, 2014: Evaluation of future storm surge risk in East Asia based on state-of-the-art climate change projection. *Coastal Eng.*, **83**, 65–71, doi:10.1016/j.coastaleng.2013.10.003.

Yukimoto, S., and Coauthors, 2012: A new global climate model of the Meteorological Research Institute: MRI-CGCM3—Model description and basic performance. *J. Meteor. Soc. Japan*, **90A**, 23–64, doi:10.2151/jmsj.2012-A02.

ARCTIC RADIATION-ICEBRIDGE SEA AND ICE EXPERIMENT

The Arctic Radiant Energy System during the Critical Seasonal Ice Transition

William L. Smith Jr., Christy Hansen, Anthony Bucholtz, Bruce E. Anderson, Matthew Beckley, Joseph G. Corbett, Richard I. Cullather, Keith M. Hines, Michelle Hofton, Seiji Kato, Dan Lubin, Richard H. Moore, Michal Segal Rosenhaimer, Jens Redemann, Sebastian Schmidt, Ryan Scott, Shi Song, John D. Barrick, J. Bryan Blair, David H. Bromwich, Colleen Brooks, Gao Chen, Helen Cornejo, Chelsea A. Corr, Seung-Hee Ham, A. Scott Kittelman, Scott Knappmiller, Samuel LeBlanc, Norman G. Loeb, Colin Miller, Louis Nguyen, Rabindra Palikonda, David Rabine, Elizabeth A. Reid, Jacqueline A. Richter-Menge, Peter Pilewskie, Yohei Shinozuka, Douglas Spangenberg, Paul Stackhouse, Patrick Taylor, K. Lee Thornhill, David van Gilst, and Edward Winstead

Through ARISE, NASA acquired unique aircraft data on clouds, atmospheric radiation and sea ice properties during the critical period between the sea ice minimum in late summer and autumn and the commencement of refreezing.

Arctic sea ice decline is one of the most profound manifestations of contemporary climate change, and the loss has been accelerating in recent years as seen by regular extreme September minima and lengthening of the melt season by 5 days decade^{-1} (Stroeve et al. 2012, 2014). This overall decline, combined with a shift toward entirely seasonal ice (Perovich and Polashenski 2012), implies the action of numerous feedbacks involving thinner and darker ice, changing cloud cover, and increasing energy input to the upper water column. Radiation feedbacks are a necessary mechanism to drive this decline (Perovich et al. 2008), although anomalous winds and preconditioning also play a major role in both trends and variability (Zhang et al. 2008). At the same time, it is expected that this large-scale decrease in Arctic sea ice will drive circulation anomalies throughout the troposphere (Cassano et al. 2014). There is a need to diagnose these changes empirically, and to validate climate model simulations, on a pan-Arctic basis.

Ultimately, this need is most satisfactorily addressed with well-characterized satellite remote sensing data. Several sensors from the National Aeronautics and Space Administration (NASA)'s *Terra* and *Aqua* spacecraft and A-Train constellation (https://atrain.gsfc.nasa.gov/) have provided observations of key components of the Arctic climate system for more than a decade, including atmospheric structure, cloud optical properties, and sea ice concentration (sea ice being available in the passive microwave satellite record going back to 1979). Concurrently, the Cloud and the Earth's Radiant Energy System (CERES) sensors, and their predecessors from the Earth Radiation Budget Experiment (ERBE), retrieve the net shortwave and longwave fluxes that reveal the combined action of the radiative and dynamical feedbacks involving Arctic sea ice. Hartmann and Ceppi (2014) use CERES data to show that every 10^6 km^2 decrease in September Arctic sea ice in recent years corresponds to an annual-mean increase in absorbed shortwave radiation of

---

Publisher's Note: On 18 July 2017 this article was revised to correct Fig. 12, which was omitted from the original publication.

2.5 W m^{-2} between 75° and 90°N. Further progress in our understanding of the whole Arctic climate system requires understanding how the individual components of the Arctic ocean–atmosphere system manifest in the CERES-measured fluxes and how well they are retrieved by other satellite sensors.

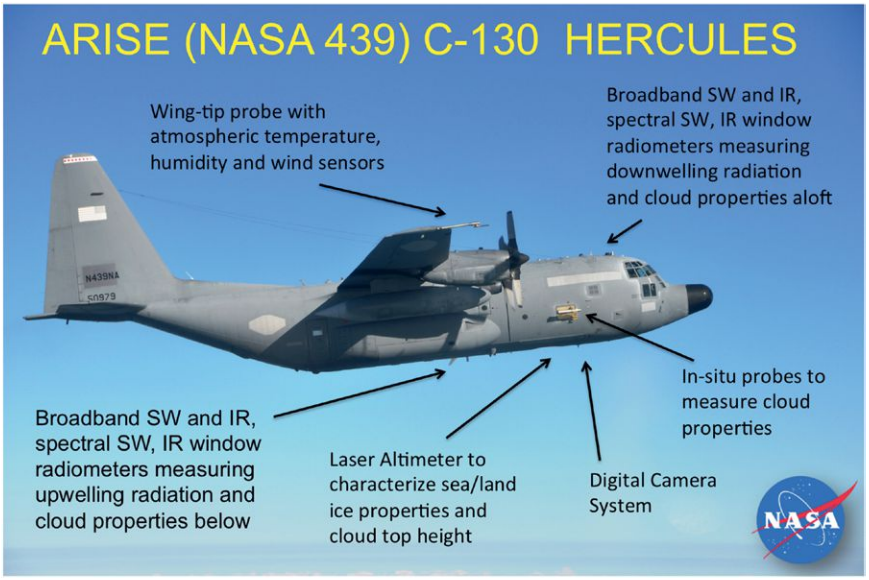

Fig. 1. The NASA C-130 research aircraft as configured for ARISE, showing the location of each instrument described in Table 1.

In addition, high-quality spectral and broadband radiometric data from above sea ice, and below, within, and above Arctic stratiform clouds, can provide a valuable resource for testing the overall effectiveness of parameterizations for cloud and sea ice evolution in climate models. For example, if a regional model is initialized with the meteorological conditions pertaining to a given flight mission, then the simulated energy fluxes at the surface and below, within, and above cloud can be compared with the data to note where agreement or discrepancies occur. If general model–data agreement appears in the microphysics, for example, then discrepancies in measured irradiance may be related to the radiative transfer parameterization (e.g., three-dimensional effects vs a plane-parallel model). Comparison of Arctic surface radiation measurements with climate model simulations has proven valuable (Tjernström et al. 2008); however, to date most Arctic aircraft studies related to climate model parameterizations have concentrated on cloud microphysics (e.g., Fridlind et al. 2007, 2012). Here we describe a unique aircraft campaign focused on cloud properties and radiative effects that can benefit both the remote sensing and climate modeling approaches to the study of Arctic change.

EXPERIMENT DESIGN AND EXECUTION.

One remarkable aspect of the Arctic Radiation-IceBridge Sea and Ice Experiment (ARISE) is the short timeline from experiment conception to successful execution in September 2014. NASA funding became

AFFILIATIONS: Smith, Anderson, Kato, Moore, Barrick, Chen, Loeb, Nguyen, Stackhouse, and Taylor—NASA Langley Research Center, Hampton, Virginia; Hansen, Cullather, Blair, and Rabine—NASA Goddard Space Flight Center, Greenbelt, Maryland; Bucholtz and Reid—Naval Research Laboratory, Monterey, California; Beckley and Cornejo—SGT, Lanham, Maryland; Corbett, Ham, Palikonda, Spangenberg, Thornhill, and Winstead—SSAI, Hampton, Virginia; Hines and Bromwich—Byrd Polar and Climate Research Center, The Ohio State University, Columbus, Ohio; Hofton and Kittleman—University of Maryland, College Park, College Park, Maryland; Lubin and Scott—Scripps Institution of Oceanography, University of California, San Diego, La Jolla, California; Segal Rosenhaimer and Shinozuka—Bay Area Environmental Research Institute, Petaluma, California; Redemann—NASA Ames Research Center, Moffett Field, California; Schmidt, Song, and Pilewskie—Department of Atmospheric and Oceanic Sciences, and Laboratory for Astrophysics and Space Physics, University of Colorado Boulder, Boulder, Colorado; Brooks—SSAI, Greenbelt, Maryland; Corr—Oak Ridge Associated Universities, Oak Ridge, Tennessee, and NASA Langley Research Center, Hampton, Virginia; Knappmiller and Miller—Laboratory for Astrophysics and Space Physics, University of Colorado Boulder, Boulder, Colorado; LeBlanc—Oak Ridge Associated Universities, Oak Ridge, Tennessee, and NASA Ames Research Center, Moffett Field, California; Richter-Menge—Cold Regions Research and Engineering Laboratory, U.S. Army Corps of Engineers, Hanover, New Hampshire; Van Gilst—National Suborbital Education and Research Center, University of North Dakota, Grand Forks, North Dakota
CORRESPONDING AUTHOR: William Smith, william.l.smith@nasa.gov

The abstract for this article can be found in this issue, following the table of contents.
DOI:10.1175/BAMS-D-14-00277.1

In final form 6 October 2016

Table 1. Parameters measured from the C-130 (NASA 439) during ARISE. NRL = Naval Research Laboratory. NSERC = Natural Sciences and Engineering Research Council of Canada. GSFC = Goddard Space Flight Center. LaRC = Langley Research Center.

Parameters	Instrument	Manufacturer (mentor)	Range (accuracy)
Broadband SW radiative flux, upwelling and downwelling	Pyranometer	Kipp & Zonen, modified CM22 (NRL BBR suite)	0.2–3.6 μm (3%)
Broadband LW radiative flux, upwelling and downwelling	Pyrgeometer	Kipp & Zonen, modified CG4 (NRL BBR)	4.5–42 μm (3%)
Global, direct, and diffuse SW radiative flux, downwelling	Sunshine pyranometer	Delta-T Devices SPN-1 (NRL BBR)	0.4–2.7 μm (5%)
Spectral SW radiance, downwelling	4STAR	(NASA Ames Research Center)	380–1700 nm, 6–12-nm resolution (3%)
Spectral SW irradiance, upwelling and downwelling	SSFR	(University of Colorado Boulder)	350–2150 nm, 6–12-nm resolution (3%–5%)
Cloud and surface temperature, up- and downlooking	Pyrometer	Heitronics KT-19.85 series II (NSERC and NRL)	9.6–11.5 μm (0.5°C)
Surface topography, vertical extent and structure	LVIS	(NASA GSFC)	1064 nm (10-cm vertical and 1-m horizontal precision)
IWC, LWC	WCM-2000	SEA, Inc. (NASA LaRC)	Water contents 0–10 g m^{-3}
Cloud droplet size distribution	CDP	DMT, Inc (NASA LaRC)	Sizes 2–50 μm
Liquid water path (LWP), precipitable water vapor	GVR (183 ghz)	ProSensing, Inc.	LWP 0–300 g m^{-2} (20 g m^{-2})
Location, attitude, meteorological variables [precipitation P, temperature T, relative humidity (RH), winds u and v]	Digital air data probes	Aventech ARIM200, Rosemount package, EdgeTech Vigilant (NSERC)	Static P (0.25 hPa), dynamic P (0.5 hPa), static T (0.2°C), RH (5%), u, v (1 m s^{-1})
Video and imagery, forward and nadir looking	Digital cameras	(NSERC and NASA GSFC)	1080 pixels

available in March of 2014 to supplement Operation IceBridge (OIB) with sea ice observations during the September transition in the Beaufort–Chukchi Seas, and a C-130 aircraft (N439NA) was also available that was capable of carrying advanced instrumentation for cloud and atmospheric energy budget observations during a time frame that is relatively undersampled in the high Arctic compared with spring and midsummer. OIB is an ongoing airborne science campaign to characterize sea ice, glaciers, and ice sheets in unprecedented detail while bridging the gap in polar observations between NASA's Ice, Cloud, and Land Elevation Satellite (ICESat) missions. The sea ice, radiation, cloud microprobe, and meteorological instruments are listed in Table 1, and their aircraft installation is depicted in Fig. 1. Because of the unusually short planning timeline, much of the instrument selection was based on proven track records and uncomplicated installation in the C-130. Nevertheless, the instrument suite was comprehensive and advanced, yielding a timely dataset, preliminary results of which are presented here.

While NASA satellites are making routine observations, an accurate interpretation of the data required to track Arctic climate change can be difficult. Uncertainties in atmospheric temperature and humidity, heterogeneity in surface conditions (including sea ice properties), and difficulties detecting and characterizing clouds over sea ice all contribute to the uncertainty associated with the CERES-derived irradiances, which is currently larger over sea ice than any other scene type (Su et al. 2015b). Thus, the evaluation of CERES top-of-atmosphere (TOA) and surface (SFC) radiative fluxes over the Arctic with data from the C-130 payload is a unique and important ARISE scientific objective. A number of ARISE flight plans were designed specifically to accomplish this objective over a wide range of conditions. Other flight plans were designed to characterize the composition of low-level clouds and their radiative effects over various sea ice conditions and to support OIB with sea and land ice characterizations. Recent work has shown that heterogeneity and small-scale interactions are important to consider, particularly in leads and over open water adjacent to sea ice (Vihma et al. 2014). The high time resolution of both the radiometric suite and surface remote sensors provides direct observation of heterogeneity.

ARISE was based at Eielson Air Force Base (AFB) near Fairbanks, Alaska. Weather prediction and regional modeling resources were used on-site for flight planning. Aircraft mission planning fell into three major categories: 1) CERES collocation and validation, 2) sea ice observation, and 3) cloud sampling. The missions that were accomplished are detailed in Table 2, and the associated flight tracks are illustrated in Fig. 2. Figure 3, obtained from the nadir and forward-looking cameras, shows examples of the wide variety of sea ice conditions sampled during ARISE, including thick multiyear ice, a wide range of broken and scattered ice conditions, melt ponds, and frazil and black ice upon refreezing.

The dates for the CERES experiments were fixed in advance, based on the known intersection of several satellite overpasses sufficiently within the range of the aircraft to allow for extensive gridbox flight patterns over the Beaufort Sea. Outside of those dates, sea ice and cloud radiation sampling missions were organized in near–real time based on the comprehensive weather data and forecasting available in the field. There was some advance planning given to within-cloud stacked transects, but due to the dynamic nature of the cloud cover,

TABLE 2. ARISE mission summary: select satellite overpass times (*A*: *Aqua*, *C*: *Cryosat-2*, *T*: *Terra*, S: *Suomi National Polar-Orbiting Partnership*), dominant surface type, and flight description. KWAL = Wallops Flight Facility, Wallops Island, VA. KTCM = McChord AFB, Tacoma, WA. PAEI = Eielson AFB. SCT = scattered. BKN = broken.

Start date (focal location)	Satellite overpasses (UTC)	Surface type	Takeoff (UTC)	Land (UTC)	Flight description
1 Sep 2014 (KWAL to KTCM)	—	Land	1415	2257	Transit from NASA Wallops to McChord AFB. LVIS canopy measurements.
2 Sep 2014 (KTCM to PAEI)	—	Land	1600	2235	Transit from McChord AFB to Eileson AFB. Southern Alaska glacier mapping
4 Sep 2014 (72.8°–75°N, 142°–159°W)	*A*: 2035, 2214 *T*: 2013, 2155 *S*: 2013, 2147	Ocean, sea ice (sct)	1815	0050[a]	Arctic Ocean survey near ice edge, low-cloud profiling
5 Sep 2014 (70.5°–80°N, 140°W)	*A*: 2119, 2258 *T*: 2136, 2317 *S*: 2054, 2230	Sea ice	2015	0320[a]	140°W sea ice survey from 70.5° to 80°N
6 Sep 2014 (72.5°–74.5°N, 135°–140°W)	*A*: 2023, 2202, 2341 *T*: 1935, 2117, 2258 *S*: 2001, 2134, 2313	Sea ice	1910	0215[a]	MIZ survey, radiative flux profiles, ML cloud characterization
7 Sep 2014 (74.1°–76.5°N, 140°–148°W)	*A*: 1927, 2106, 2245 *T*: 1916, 2058, 2239 *S*: 2042, 2218, 2357	Ocean	1815	0240[a]	CERES TOA gridbox experiment, full column profiles, low-cloud characterization
9 Sep 2014 (73.5°–75.2°N, 138°–145°W)	*A*: 1915, 2054, 2233 *T*: 2019, 2201, 2342 *S*: 2031, 2205, 2344	Sea ice (bkn)	1820	0200[a]	CERES SFC gridbox experiment, full column profiles, low-cloud characterization
10 Sep 2014 (75.2°–76.5°N, 134°–140°W)	*A*: 1958, 2137, 2316 *T*: 2000, 2142, 2323 *S*: 1936, 2112, 2249	Sea ice	1710	0155[a]	MIZ survey, low-cloud characterization and radiative fluxes along ice edge
11 Sep 2014 (72.2°–74.5°N, 130°–136.5°W)	*A*: 2042, 2221, 2359 *T*: 1941, 2123, 2304 *S*: 2019, 2153, 2332	Sea ice	1835	0205[a]	CERES TOA gridbox experiment, full column profiles, low-cloud characterization
13 Sep 2014 (72.7°–74.5°N, 130°–137°W)	*A*: 2029, 2208, 2347 *T*: 1903, 2045, 2226 *S*: 2007, 2141, 2320	Sea ice	1705	0125[a]	CERES SFC gridbox experiment, full column profiles, sea ice albedo and low-cloud characterization

[a] Flight completed following day.

the cloud radiation missions more often adapted to the conditions on the spot. On these occasions, satellite meteorology observations and updated forecasts were transmitted to the aircraft en route to the Beaufort Sea, to help vector the mission to the most interesting scenes.

METEOROLOGICAL CONDITIONS. Supporting weather forecasts for the ARISE flights were conducted with the NASA Goddard Earth Observing System Model, version 5 (GEOS-5; Molod et al. 2015), and Polar Weather Research and Forecasting (WRF) Model, version 3.5.1 (http://polarmet.osu.edu/PWRF/; Hines et al. 2015). Output fields from the forecasts are used here along with atmospheric reanalyses to represent synoptic meteorological conditions during the field program. Meteorology during ARISE may be categorized by two distinct regimes. During the first seven flights over the Arctic Ocean (4–11 September), the meteorological state was dominated by a surface high pressure over the southern Chukchi and/or Beaufort Seas. Figure 4 shows a composite set of 21-h Polar WRF forecasts valid at 1300 Alaska daylight time (AKDT), roughly at the midtimes of the C-130 flights. This resulted in northeasterly low-level flow over the Arctic coast and northern and central Alaska. There was considerable low-level cloudiness over the southern Beaufort Sea, consistent with the seasonal climatology (e.g., Intrieri et al. 2002). However midlevel and precipitating clouds were not extensive. Temperatures over central Alaska were mild with limited cloud cover—as indicated by the GEOS-5 cloud fraction (Fig. 5a), providing excellent flying weather.

A key synoptic shift occurred near 13 September that accompanied a northward advance and deepening of low pressure over Bristol Bay. Surface pressures fell over Alaska and the southern Beaufort Sea.

TABLE 2. Continued.

Start date (focal location)	Satellite overpasses (UTC)	Surface type	Takeoff (UTC)	Land (UTC)	Flight description
15 Sep 2014 (72.5°–76.5°N, 149°–159°W)	*A*: 2017, 2156, 2335 *T*: 2006, 2148, 2329 *S*: 1955, 2129, 2307	Ocean	1748	0156[a]	CERES TOA gridbox experiment, full column profiles, ML cloud characterization
16 Sep 2014 (74.7°–77°N, 136.5°–141°W)	*A*: 1921, 2100, 2239 *T*: 1947, 2129, 2310 *S*: 2037, 2212, 2350	Sea ice	1719	0135[a]	Low-cloud radiative closure experiment, diffuse and clear-sky albedo measurements
17 Sep 2014 (73.2°–74.8°N, 150.5°–156°W)	*A*: 2005, 2143, 2322 *T*: 1928, 2110, 2251 *S*: 1942, 2117, 2255	Ocean, sea ice (bkn)	1815	0127[a]	CERES SFC gridbox experiment, low-cloud characterization, ML cloud sampling
18 Sep 2014 (75.5°–77.5°N, 137°–149°W)	*A*: 1909, 2048, 2227 *T*: 1909, 2051, 2232 *S*: 2025, 2159, 2338 *C*: 1852	Sea ice	1655	0130[a]	*Cryosat-2* underflight, characterization of sea ice and surface albedo, MIZ repeat line, low-cloud profiling
19 Sep 2014 (71.8°–73.2°N, 128°–137°W)	*A*: 1952, 2131, 2310 *T*: 2032, 2213, 2355 *S*: 1930, 2106, 2242	Sea ice, ocean	1653	0111[a]	Low-cloud radiative closure experiment, cloud and surface characterization across sea ice edge
21 Sep 2014 (73°–76.5°N, 125°–131°W)	*A*: 1940, 2119, 2258 *T*: 1953, 2135, 2316 *S*: 1918, 2054, 2230	Sea ice	1650	0100[a]	MIZ sea ice characterization, low ML cloud profiling
24 Sep 2014 (73°–75°N, 128°–133.5°W)	*A*: 2011, 2150, 2329 *T*: 2038, 2219 *S*: 1948, 2123, 2301	Sea ice	1952	0208[a]	MIZ sea ice characterization, low-cloud profiling
2 Oct 2014 (southwest Alaska, Bristol Bay)	—	Land, ocean	2127	0602[a]	Alaskan glacier mapping, radiometer calibration maneuvers
4 Oct 2014 (PAEI to KTCM)	—	Land	0838	1814	Return transit to KWAL

[a] Flight completed following day.

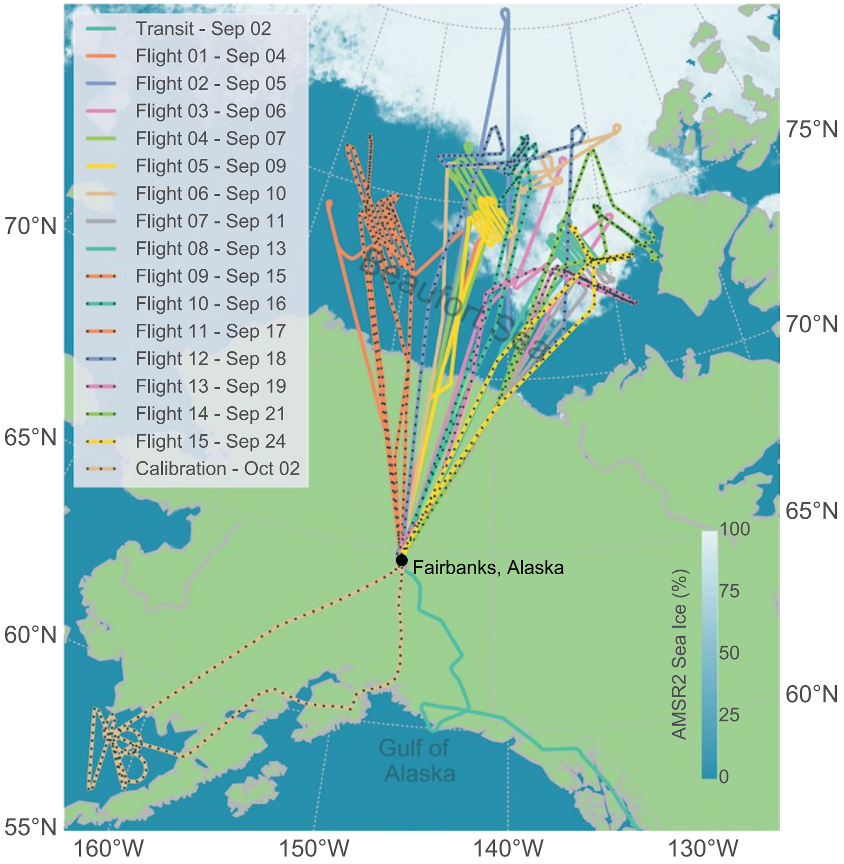

Fig. 2. Map of the ARISE mission flight tracks as described in Table 2.

During this second regime of 13–21 September, the region of surface high pressure was now located several hundred kilometers farther north over the Arctic Ocean (Fig. 4b). This resulted in east-northeasterly low-level flow over the flight target regions of the Arctic Ocean originating from a cold source region over sea ice. Simulated surface temperatures over the sea ice suggest surface freezing and thickening of the ice pack, consistent with reports from the C-130 staff (Fig. 4b). A weak time-averaged minimum pressure was located over the northwest corner of Alaska, as a series of weak mesoscale lows propagated eastward through the region. This is consistent with increased cloud cover over the North Slope of Alaska and the southern Beaufort Sea (Fig. 5b). Increased cloud cover and some light precipitation occurred in central Alaska during the second regime, and daily average temperatures dropped from near 15°C at Eielson on 13 September to 5°C on 21 September. During the later stages of this regime, dense fog occasionally appeared in the morning over central Alaska, limiting the C-130 flights from Eielson. Time series of Polar WRF low-level temperature over open ocean and sea ice in the Beaufort Sea indicate fluctuations on mesoscale and fast synoptic time scales between cold periods of strong low-level static instability and warmer periods of near-neutral low-level static stability (Fig. 6). Low-level temperatures were several degrees colder over sea ice than over open water. Moreover, the Polar WRF simulations show that during the ARISE field program faster net seasonal cooling occurred over sea ice than over open water.

The Polar Meteorology Group at The Ohio State University has done extensive Arctic testing of Polar WRF, including in the northern Alaska and Beaufort Sea regions. Specific to the ARISE campaign, we compared a Polar WRF, version 3.6, run against near-surface observations from Barrow, Nome, Prudhoe, and Red Dog in Alaska, and buoys in the Chukchi Sea. Polar WRF was run on a 283 × 312 cell grid with 70 vertical levels and 8-km horizontal resolution. Table 3 shows that the model reasonably produces the near-surface air temperature, wind speed, wind direction, and surface pressure during September 2014. The multiday sea level pressure averages for regime 1 and regime 2, shown by Figs. 4a and 4b, respectively, are highly consistent with the summer and fall seasonal low-level wind climatologies near northern Alaska as shown by Figs. 3c and 3d in Zhang et al. (2016), respectively. Early analysis of the Polar WRF simulations suggest that ARISE meteorology during September 2014 yielded less low cloud liquid water and more cloud ice than during the August–September 2008 Arctic Summer Cloud Ocean Study (ASCOS; Tjernström et al. 2012).

PRELIMINARY RESULTS. *CERES.* CERES is a key component of the Earth Observing System (EOS) and *Suomi National Polar-Orbiting Partnership* (*SNPP*) observatory. During ARISE, four CERES instrument flight models (FM) were fully functional on the EOS *Terra* (FM1 and FM2), *Aqua* (FM3), and the *SNPP* (FM5) satellites. The CERES program strives for consistent instrument performance, calibration, and data products across satellite platforms to the

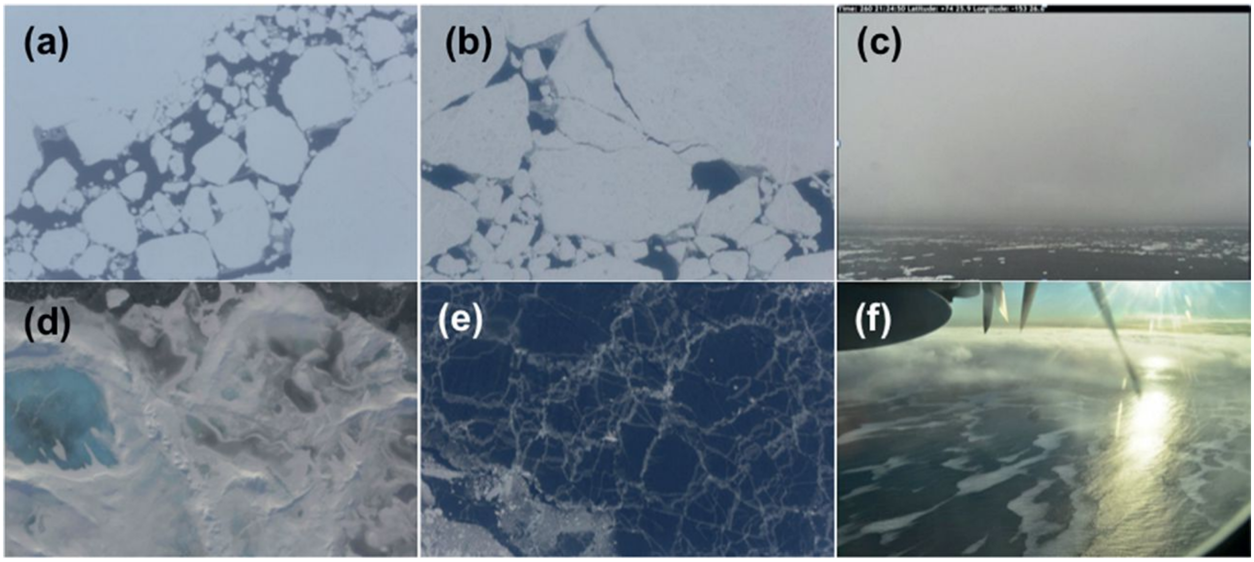

Fig. 3. Surface conditions during the 2014 sea ice transition period over the Beaufort Sea photographed from the ARISE aircraft using the nadir camera. (a) 5 Sep, 80°N, 140°W; (b) 10 Sep, 77°N, 128°W; (c) 17 Sep, 74°N, 152°W; (d) 16 Sep, 77°N, 143°W; (e) 16 Sep, 76°N, 141°W; and (f) 24 Sep, 73°N, 129°W.

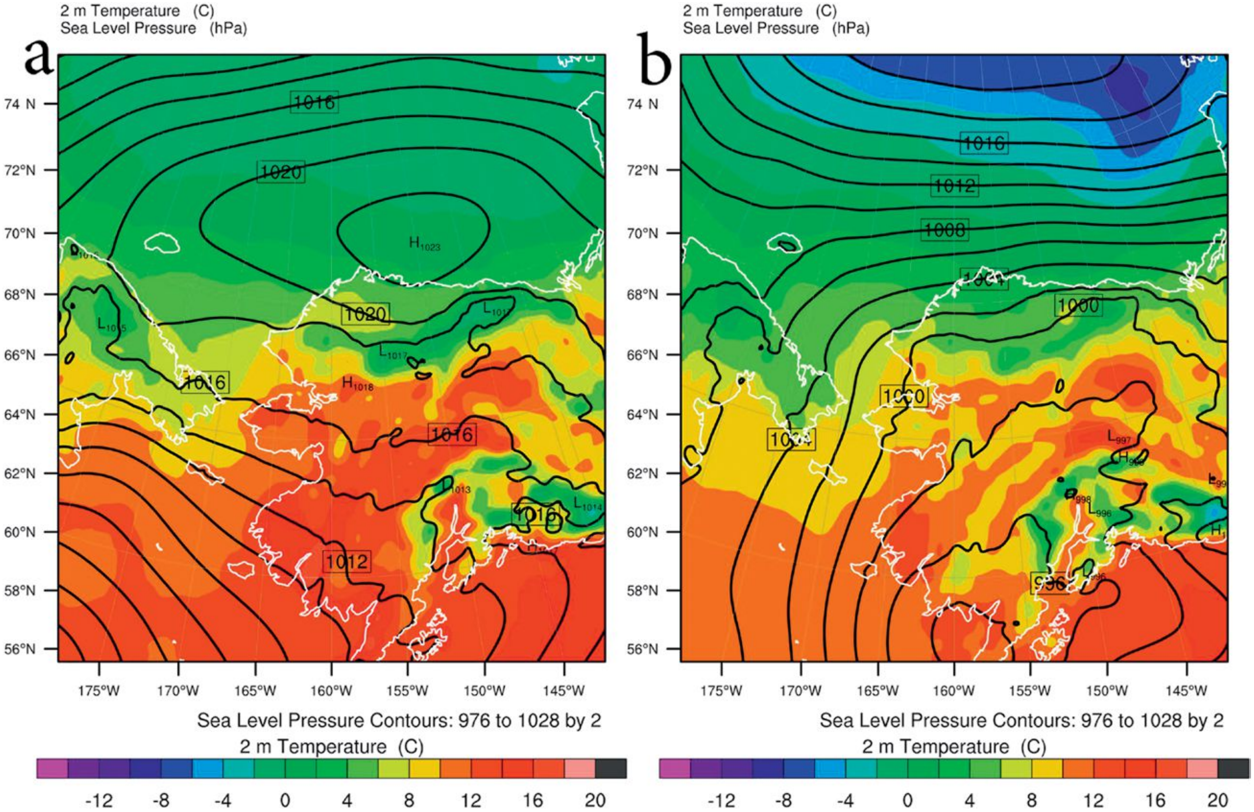

Fig. 4. Average sea level pressure (contours, interval 2 hPa) and 2-m temperature (°C; shaded) from Polar WRF 21-h forecasts (1300 AKDT) for (a) the first seven flights (4–11 Sep 2014) and (b) the next seven flights (13–21 Sep 2014).

extent possible. CERES products provide the most accurate spatially complete depiction of radiant energy exchanges in the Arctic. However, the uncertainty associated with the CERES-derived irradiances is currently larger over sea ice than any other scene type (Su et al. 2015b). The CERES Science Team provides instantaneous satellite footprint (level 2) and the hourly gridded mean (level 3) TOA and surface

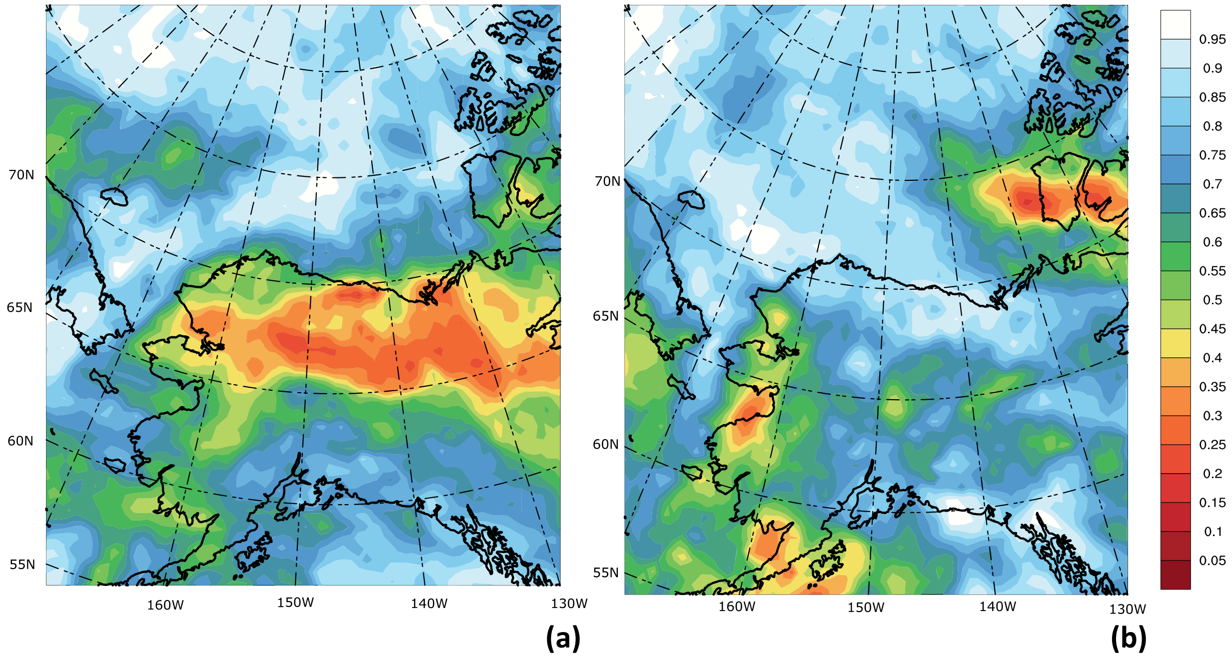

Fig. 5. Total cloud fraction from NASA's Modern-Era Retrospective Analysis for Research and Applications, version 2 (MERRA-2), for 2200 UTC, averaged for (a) 4–11 Sep and (b) 13–21 Sep 2014.

irradiance data products. ARISE observations provide an opportunity to evaluate irradiances for both of these products over the Arctic. Two CERES objectives are 1) to evaluate the level 2 CERES-derived top-of-atmosphere irradiance over areas with different sea ice conditions and 2) to evaluate hourly gridded mean irradiances in the level 3 CERES radiative flux data products.

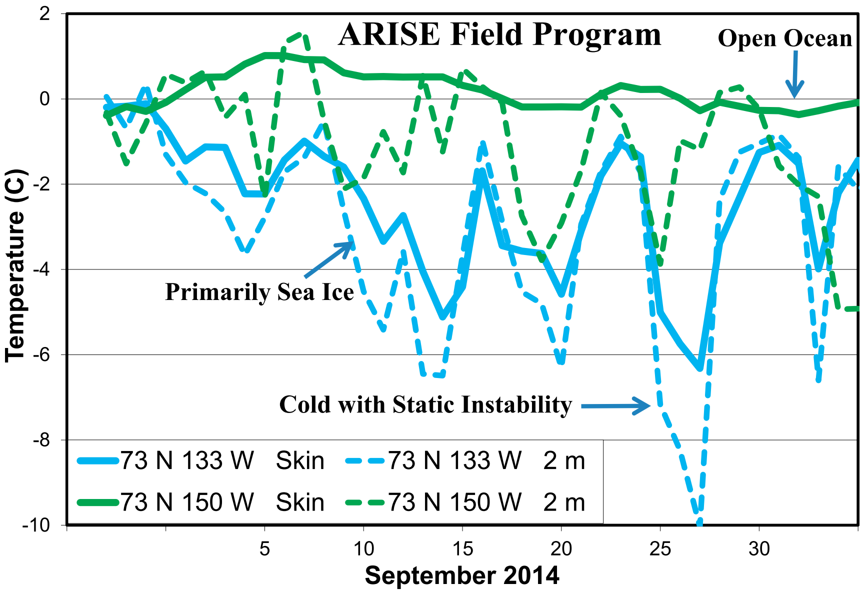

Fig. 6. Time series of skin temperature (solid lines) and 2-m temperature (dashed) for Polar WRF grid points at 73°N, 133°W (blue) and 73°N, 150°W (green). Temperatures are 21-h forecasts valid at 1300 AKDT, near the center times of ARISE flights.

The CERES instrument measures reflected and emitted shortwave (SW; 0.2–5 μm) and longwave (LW; 5–50 μm) radiances at a footprint size of ~20×20 km at nadir. Loeb et al. (2012) demonstrate excellent stability of the CERES instrument to better than 0.3 W m^{-2} decade^{-1} and an absolute accuracy (2σ) of the CERES TOA fluxes of 2% in the SW and 1% in the LW (Loeb et al. 2009). After properly accounting for the spectral response of the radiometric filters (Loeb et al. 2001), the CERES radiances are converted to irradiances using angular distribution models (ADMs; Su et al. 2015a; Loeb et al. 2005). An ADM is a set of anisotropic factors that relates the radiance measured at a certain viewing geometry to a radiant flux. The anisotropy of the radiation field varies significantly under different surface types and cloud conditions. Thus, ADMs vary with scene type, especially for the

Table 3. Demonstration of monthly mean Polar WRF (<PWRF>), version 3.6, simulation agreement with Alaska and Chukchi Sea monthly mean observations (<Obs>) of near-surface temperature (°C), wind speed (m s^{-1}), wind direction (°), and mean sea level pressure (MSLP, hPa), for Sep 2014. The surface observation stations are Prudhoe Bay (70.40°N, 148.53°W), Nome (64.50°N, 165.43°W), Klondike buoy (70.87°N, 168.25°W), Red Dog Dock (67.58°N, 164.07°W), Burger buoy (71.50°N, 164.13°W), and Barrow (71.29°N, 156.79°W).

Station variable	Correlation	rmse	Bias	<Obs>	<PWRF>
Prudhoe Bay buoy temperature	0.7726	1.307	−0.213	1.528	1.315
Nome temperature	0.9256	2.058	−1.485	8.330	6.845
Klondike buoy temperature	0.7938	0.771	0.112	2.738	2.850
Red Dog Dock temperature	0.8694	1.923	0.054	6.668	6.722
Burger buoy temperature	0.7391	1.068	0.790	1.299	2.089
Barrow 2-m temperature	0.8650	1.415	−1.055	2.019	0.965
Barrow 10-m temperature	0.8295	1.122	−0.445	1.385	0.940
Prudhoe Bay buoy wind speed	0.8904	3.054	−1.982	9.100	7.118
Nome wind speed	0.7359	2.062	−0.648	4.434	3.787
Klondike buoy wind speed	0.9044	1.352	0.276	8.040	8.317
Red Dog Dock wind speed	0.7989	2.149	0.197	5.349	5.546
Burger buoy wind speed	0.8773	1.807	1.056	7.018	8.073
Barrow 10-m wind speed	0.8372	1.984	−1.201	6.695	5.494
Prudhoe Bay buoy wind direction	0.7834	37.34	−1.13	150.04	148.91
Nome wind direction	0.5065	66.69	−20.35	170.97	150.62
Klondike buoy wind direction	0.8377	34.72	17.45	142.17	159.62
Red Dog Dock wind direction	0.6904	55.48	0.08	175.46	175.54
Burger buoy wind direction	0.8059	39.77	8.60	149.16	157.76
Barrow 10-m wind direction	0.9072	25.24	−10.52	167.67	157.15
Prudhoe Bay buoy MSLP	0.9983	0.56	−0.01	1,010.13	1,010.12
Nome MSLP	0.9978	0.66	−0.33	1,009.45	1,009.13
Klondike buoy MSLP	0.9927	1.49	1.11	1,010.92	1,009.81
Red Dog Dock MSLP	0.9965	0.76	0.29	1,008.91	1,009.19
Burger buoy MSLP	0.9976	1.11	−0.92	1,010.98	1,010.05
Barrow 2-m RH	0.6732	10.87	−7.29	90.65	83.36

shortwave, and accurate scene type identification is critical. The scene properties of each footprint are determined using a combination of satellite imager–derived cloud and surface properties (Minnis et al. 2011) and microwave-derived sea ice information. Temperature and humidity profiles required for the cloud retrievals are obtained from the NASA Global Modeling and Assimilation Office (GMAO) data assimilations system (Rienecker et al. 2008). Scene types in the Arctic are complex due to widely variable surface (e.g., Fig. 3) and cloud conditions.

To better evaluate the ADM performance and associated uncertainties in the instantaneous fluxes, one of the two CERES instruments on the *Terra* satellite—FM2—was placed in programmable azimuthal plane (PAP) scan mode during the ARISE campaign. The PAP mode was set to rotate FM2 for continuous targeting of a specific area as *Terra* passed over the region. This mode significantly increases the CERES sampling density and provides irradiance estimates over a wider range of viewing geometries in the area of interest. The other CERES instrument on *Terra*—FM1—was set to scan in the nominal cross-track direction. The difference in the spatial and angular sampling patterns for the FM1 and FM2 instruments is illustrated in Fig. 7. FM1 samples the broader area with a narrower viewing geometry, while FM2 samples over a more limited area but with a wider range of viewing geometries. This combination of coincident information from the PAP and cross-track scan modes, along with the aircraft measurements, provides a unique capability to test the CERES

ADMs and thus evaluate the uncertainties associated with CERES level 2 TOA data products.

Collocated aircraft measurements with level 2 satellite observations have been previously used to evaluate instantaneous irradiances and retrievals from satellite instruments. However, these occur only over a short time window for a given satellite overpass, leading to a small sample size and significant noise in the comparisons. Even under a best-case scenario, where instantaneous satellite-derived irradiances are found to agree with aircraft measurements, the corresponding uncertainty for hourly 1° × 1° gridded radiant fluxes is not clear. Thus, the direct evaluation of level 3 TOA and surface irradiances is a major goal and a unique concept of the ARISE mission.

To create the level 3 data products, the level 2 CERES fluxes are aggregated to construct hourly 1° × 1° gridded mean TOA radiant fluxes (Doelling et al. 2013). The CERES Synoptic (SYN) level 3 data (CERES level 3) also contain hourly 1° × 1° gridbox-mean surface irradiances (Rutan et al. 2015). CERES level 3 atmospheric and surface irradiances are computed hourly. Surface radiant fluxes are evaluated using radiant flux measurements at surface sites (Rutan et al. 2015; Kato et al. 2013). Uncertainty in level 3 surface radiant fluxes is described in Kato et al. (2013). Over the Arctic Ocean, conventional observations of the surface and atmosphere are scarce and there are few opportunities to evaluate irradiances. Furthermore, the characterization of cloud and atmospheric conditions required for CERES irradiance computations is more uncertain over the Arctic than over other regions of the world. Thus, larger errors in CERES surface irradiances are also likely. ARISE observations enable an evaluation of CERES input datasets and the subsequent TOA and surface level 3 irradiances, which are extensively used in model evaluation (e.g., Pincus et al. 2008; Wang and Su 2013; Itterly and Taylor 2014; English et al. 2014).

To acquire the necessary data, the NASA C-130 flew "lawn mower" patterns (Fig. 2) over ~200 km × 100 km or ~100 km × 100 km grid boxes at a nearly constant altitude, either ~6 km (TOA experiment) or near the surface (surface experiment), for 2–3 h. TOA ex-

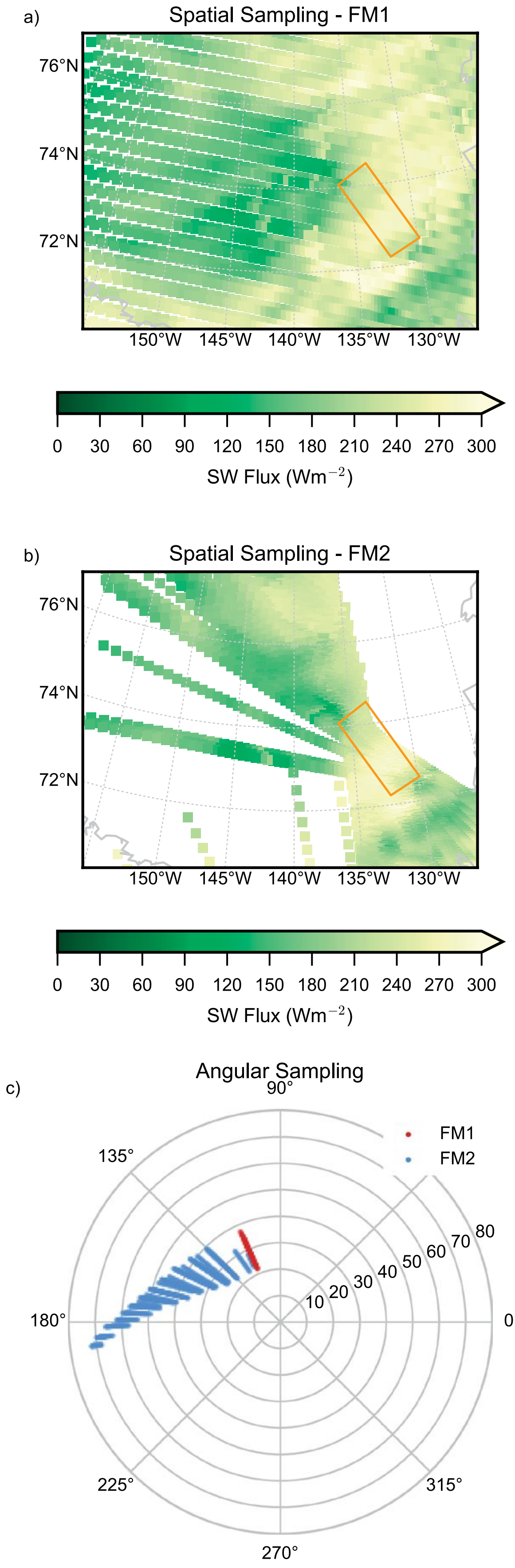

Fig. 7. (a) TOA SW irradiance derived from the CERES FM1 instrument (operated in the cross-track mode) on *Terra*. The orange box indicates the area where the TOA gridbox experiment took place on 11 Sep 2014. (b) As in (a), but for the FM2 instrument on *Terra* that was operated in a programmable azimuthal-plane mode. (c) Viewing zenith and relative azimuth angles of CERES FM1 (red) and FM2 (blue) measurements inside the orange grid box in (a) and (b).

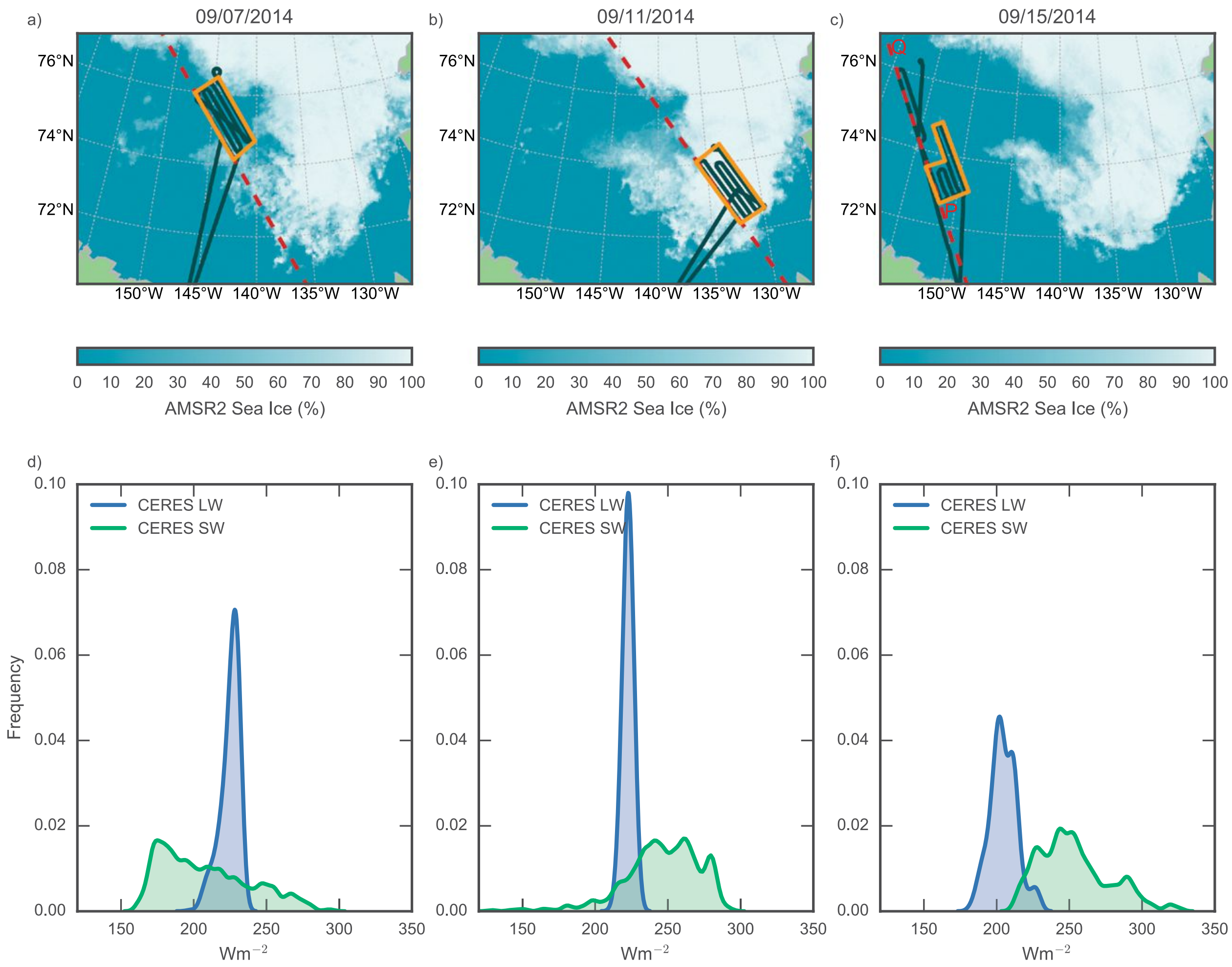

Fig. 8. (a)–(c) Sea ice cover derived from Advanced Microwave Scanning Radiometer 2 (AMSR2) [Arctic Radiation and Turbulence Interaction Study (ARTIST) sea ice (ASI) algorithm] with NASA C-130 flight-track overlays on 3 days when TOA gridbox experiments were conducted. The *CALIPSO* ground track is indicated by the dashed red lines. The P and Q markers in (c) correspond to the P and Q points, respectively, in Fig. 9. (d)–(f) Distribution of CERES-derived LW and SW irradiances over the grid box encompassed by the orange solid lines shown in (a)–(c), respectively.

periment flight paths consisted of five legs of 200-km length, spaced 20 km apart. The surface flight paths consisted of seven 100-km-length legs, spaced 15 km apart. The flight paths corresponding to the TOA experiments are shown in Figs. 8a–c. TOA and surface experiments were conducted in pairs over a particular region, separated by 2 days. This pairing strategy allowed ARISE to capture aircraft measurements of TOA and surface irradiances along with other data over similar surface conditions, and with the most optimal coincidence with CERES and other satellite overpasses.

One advantage of the Arctic compared to lower-latitude areas is the high frequency of polar-orbiting satellite overpasses that occur over a given region since the satellite orbits spatially converge. For ARISE, three "gridbox" locations were selected based upon the expected sea ice conditions and the most coincident satellite overpass times for the following spacecraft: *Terra*, *Aqua*, *SNPP*, *Cloud–Aerosol Lidar and Infrared Pathfinder Satellite Observations* (*CALIPSO*), and *CloudSat*. One flight leg of the lawn-mower pattern was always aligned with the *CALIPSO*/*CloudSat* ground track (Fig. 7, dashed red line). These active sensor observations, collocated with the aircraft data, provide detailed vertical profiles of clouds (Fig. 9) that are important to the evaluation of CERES irradiances, Moderate Resolution Imaging Spectroradiometer (MODIS) cloud retrievals, and the attribution of irradiance errors. For example, the MODIS cloud-top heights shown in Fig. 9d are retrieved with a single-layer assumption, which leads to underestimates when compared to *CloudSat*/*CALIPSO* retrievals in multilayered conditions. The MODIS cloud optical properties are also more uncertain over snow and ice for thinner clouds. Kato et al.

(2011) demonstrate improvements in surface radiation budget estimates over polar regions when combining cloud properties from *CALIPSO* and *CloudSat* with MODIS data. More detailed analyses to determine how MODIS cloud retrieval errors contribute to the surface irradiance uncertainties, particularly when active sensor data are not available, remain as future work. Multilayer retrieval methods (e.g., demonstrated later in Fig. 14) and other improvements in MODIS cloud retrievals are being developed and evaluated with ARISE and A-train data.

Each of the three sets of CERES level 3 evaluation experiments were performed over different surface conditions: over open ocean (15 and 17 September), over the marginal ice zone (MIZ; 7 and 9 September), and over an area of high sea ice concentration (11 and 13 September). All three regions were well sampled, with at least four satellite overpasses (from a combination of *Terra*, *Aqua*, and *SNPP*) during each 2.5–3-h aircraft flight. Figures 7d–f show the distribution of instantaneous CERES-derived SW and LW irradiances at TOA from within each of the orange grid boxes that bound the flight pattern. The distributions of LW and SW irradiances are noticeably different for each of the days. The differences can largely be understood by the cloud and surface conditions present in each of the grid boxes. On 7 September, the surface consisted of marginal ice and open ocean with a very low and quite optically thin overcast cloud layer. This results in a SW irradiance distribution that is skewed toward lower values with the long tail toward higher values due to the marginal sea ice and some cloud optical depth variability. Because the cloud tops were so low, there is little variation in the emission height, resulting in a narrow LW irradiance distribution. On 11 September, the surface consisted of high sea ice concentration with a combination of clear sky and low thin clouds. This creates a bright scene and correspondingly higher SW fluxes. The low cloud tops and cold sea ice results in a narrow LW irradiance distribution. While the surface on 15 September was open ocean, the cloud conditions were overcast, high, and very optically thick (see Fig. 9). This results in the comparatively high SW and low LW fluxes shown in Fig. 8f. These

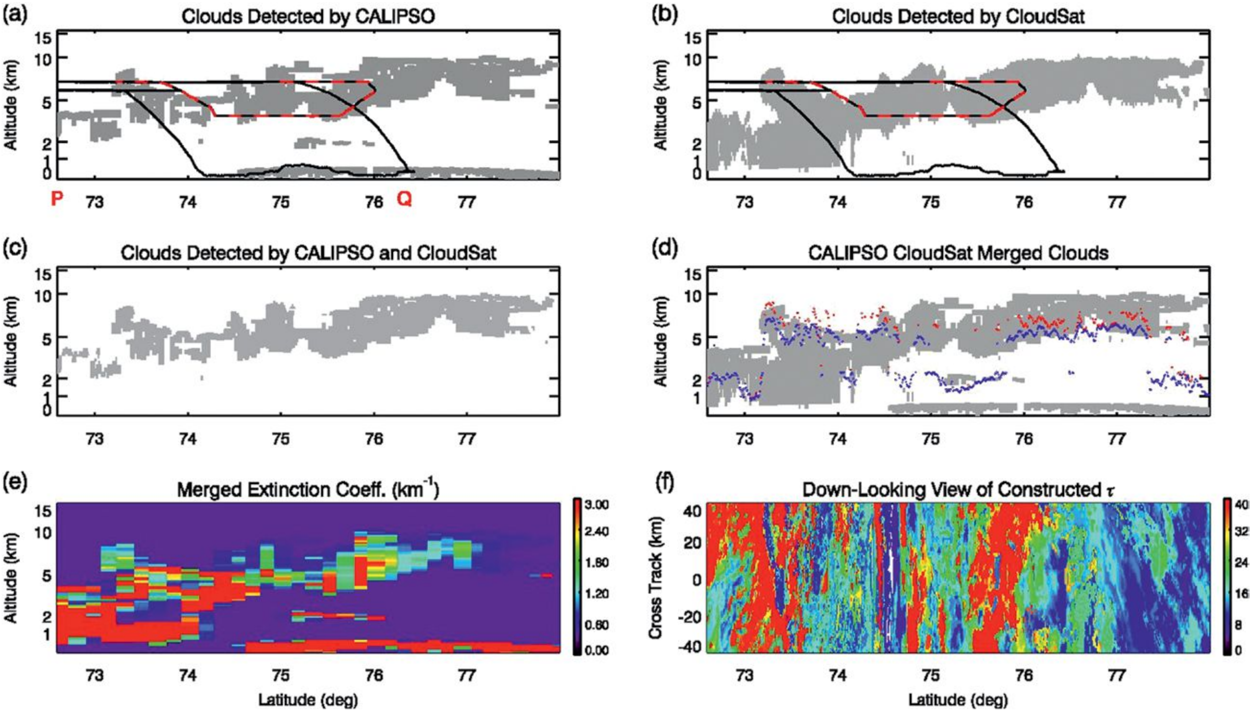

Fig. 9. Cloud-layer mask derived on 15 Sep 2014 from (a) *CALIPSO* vertical feature mask (VFM), (b) *CloudSat* 2B-CLDCLASS, (c) clouds detected by both *CALIPSO* and *CloudSat*, and (d) merged clouds, that is, clouds detected by *CALIPSO* or *CloudSat*. (e) CERES–*CALIPSO*–*CloudSat*–MODIS (CCCM)-merged 0.64-μm cloud extinction profiles derived at the CERES footprint scale (~20 km). (f) A downlooking view of 0.64-μm COT constructed with the method described in Barker et al. (2011). The C-130 flight track is shown in (a) and (b) by the black lines for the entire pattern and by the dashed red line for the period collocated to CERES observations with a time difference <30 min and a distance <20 km. MODIS-derived cloud-top and effective heights are shown in (d) by red and blue dots, respectively. The P and Q markers in (a) correspond to the locations shown of 15 Sep in Fig. 7c.

distributions will be compared with the broadband radiometer (BBR) irradiance measurements obtained from the C-130 (with suitable atmospheric correction). BBR irradiances taken near the surface will be compared with computed irradiances from the SYN product. The spectral surface albedo derived from the Solar Spectral Flux Radiometer (SSFR) will be used to evaluate the surface albedo used in the computations.

BBR. BBRs were mounted on the top and bottom of the aircraft to measure the down- and upwelling global solar (SW) irradiance (0.2–3.6 μm); the downwelling global, direct, and diffuse SW irradiance (0.4–42 μm); and the down- and upwelling infrared (LW) irradiance (4.5–42 μm; see Table 1). Kipp & Zonen pyranometers (Kipp & Zonen 2004) and pyrgeometers (Kipp & Zonen 2001), modified to make them better suited for use on an aircraft, measured the SW and LW irradiances. Modifications included new hermetically sealed back housings with the connector on the bottom that prevented condensation and freezing inside the domes and simplified the mounting of the sensors to the aircraft. The front-end optics and electronics of the original instruments were retained but an amplifier was added right below the sensors and the instruments were operated in current loop mode, a well-established technique to minimize electronic noise.

A Delta-T Devices sunshine pyranometer (SPN-1) was mounted on top of the aircraft to measure the downwelling global, direct, and diffuse SW irradiance. To accomplish this, the SPN-1 has a custom-designed hemispheric "shadowmask" that lies just under the protective glass dome that covers the instrument's seven thermopile sensors, each topped with a cosine-corrected diffuser and each with a spectral bandpass of 0.4–2.7 μm. The shadowmask is designed to ensure that at least one sensor is always exposed to the direct solar radiation, and at least one sensor is always shaded from the direct beam, independent of the orientation of the instrument to the sun. The global, direct, and diffuse SW irradiances are then derived from these maximum and minimum readings (Delta-T Devices 2007). Although there is some uncertainty regarding the absolute accuracy of the SPN-1 (Badosa et al. 2014), these data are particularly useful to obtain the direct–diffuse ratio needed to correct the downwelling SW irradiances for the attitude of the aircraft (Long et al. 2010; Bucholtz et al. 2008).

The SW radiometers were calibrated using the standard alternating sun–shade method (ASTM 2005), where the given sensor is compared to the true direct solar irradiance measured by an Eppley automatic Hickey–Frieden (AHF) absolute cavity radiometer. The sensitivities for the SW radiometers from pre- and postmission calibrations agreed to within 1%. The LW radiometers were calibrated by comparison of the measured signals to the irradiance of a blackbody immersed in a variable temperature alcohol bath. The calibration coefficients for the LW radiometers from pre- and postmission calibrations agreed to within 2%. Thus, the stability of the SW and LW radiometers during ARISE was excellent. For the SPN-1 the calibration from the manufacturer was used (8% estimated accuracy). This is sufficient here, since the SPN-1 measurements will be mainly used to correct the downwelling BBR SW irradiances for the attitude of the aircraft, which requires only the relative values of the global, direct, and diffuse SW irradiance.

Figures 10a and 10b show the CERES lawn-mower pattern flown on 7 September overlaid on the *NOAA-19* red–green–blue (RGB) and IR satellite images taken during the flight at 2150 UTC. A uniform, optically thin low-level cloud deck blanketed the area. The pinker area, apparent in the RGB image of the southeastern half of the pattern, indicates heavy concentrations of sea ice, while the darker areas in the northwestern half of the box indicate mostly open ocean beneath the clouds. The infrared image (Fig. 10b) indicates that the area was mostly clear of high clouds, although some thin scattered cirrus are seen in the northwestern portion of the box. These conditions were confirmed by the onboard flight scientist's notes and the forward video on the aircraft. Figure 10c is an image grab from the forward video taken at approximately the midpoint of the first leg of the pattern, showing the mostly clear skies aloft and a uniform low-level cloud deck. Figure 10d shows the order in which the lawn-mower pattern was flown. This flight is a good case for comparisons between the CERES and BBR SW and LW irradiances because, while there was some variation in the cloud and surface properties within the box, they remained nearly constant while the aircraft sampled the area. In fact, a particular advantage in conducting this type of experiment in the Arctic in late summer/early fall is that the sun, though low in the sky, remains at a nearly constant elevation angle and thus the incoming solar irradiance at the TOA is nearly constant for a long time during the day. Figure 10e shows that the solar zenith angle θ_o remained nearly constant (average $\theta_o = 69.75° \pm 0.62°$) during the entire pattern. This simplifies the interpretation of the aircraft irradiances, which take about 2 h to survey over the region, when compared to the nearly instantaneous CERES satellite measurements.

The corresponding BBR LW and SW irradiances are shown in Fig. 11. Figure 11a shows the measured down- and upwelling LW irradiances. The data during turns has been removed. Little variation in the down- or upwelling LW irradiances from leg to leg is apparent during the pattern. The mean downwelling LW for is 70.17 ± 5.74 W m^{-2}, while the average upwelling LW is 251.90 ± 4.60 W m^{-2}, confirming the uniformity of the conditions with respect to LW irradiance. Figure 11b shows the measured down- and upwelling SW irradiances. The downwelling SW fluxes require correction for the

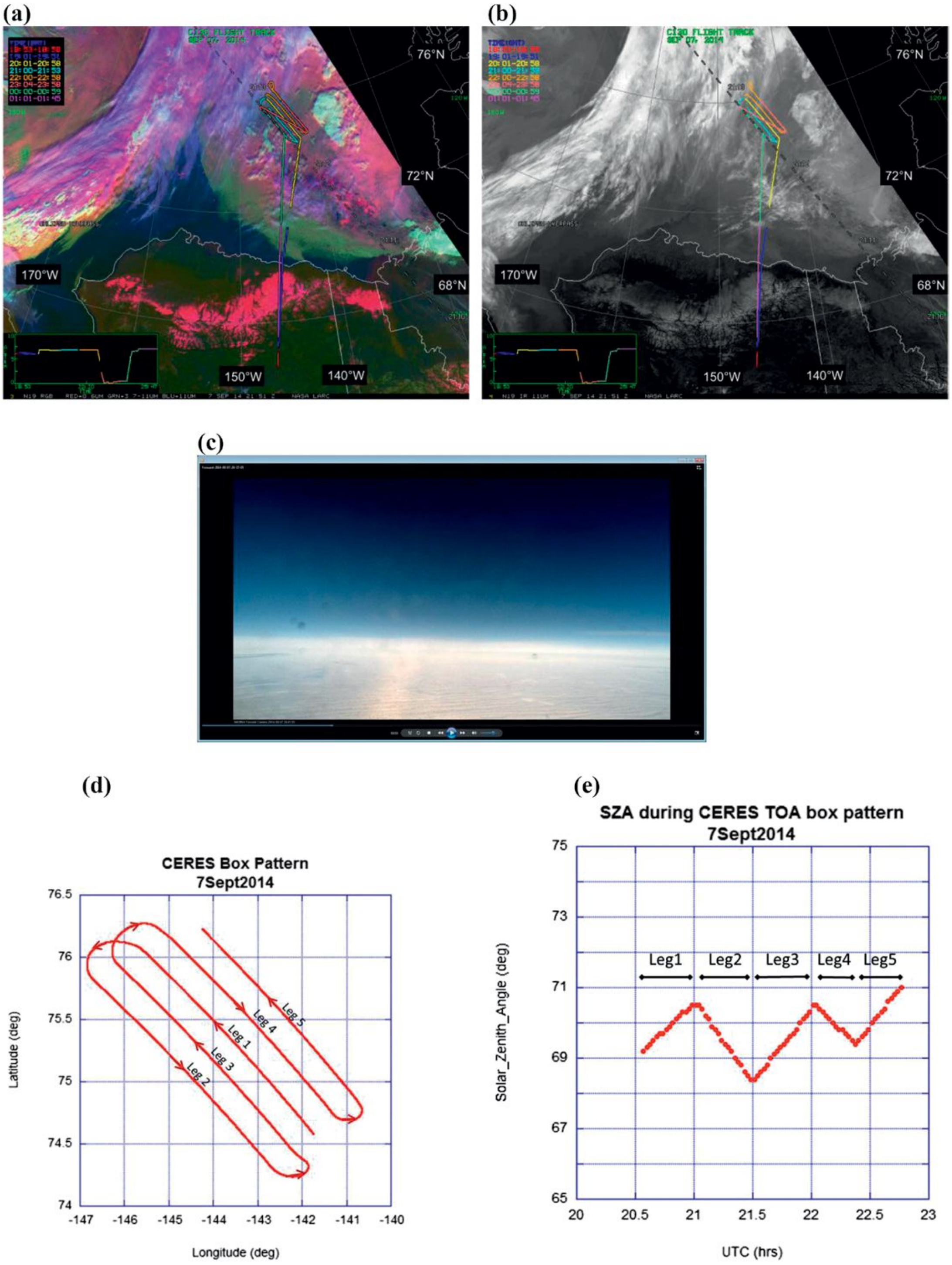

Fig. 10. Example of BBR data collection parameters on 7 Sep 2014. Aircraft flight pattern overlaid on the *NOAA-19* satellite (a) RGB and (b) IR images from 2150 UTC, (c) an image from the forward video camera, (d) the order of the lawn mower flight pattern, and (e) SZA.

attitude of the aircraft because changes in the pitch, roll, or heading of the aircraft can cause changes in the zenith angle of the sun with respect to the SW radiometer on top of the aircraft. This causes artificial offsets in the downwelling SW measurements (Bucholtz et al. 2008). This can be seen in Fig. 11b for the uncorrected downwelling SW irradiances shown in black. Dramatic shifts in the data are seen from one leg to the next as the aircraft changes heading. Using the pitch, roll, and heading from the aircraft's navigational system, the downwelling SW fluxes are corrected back to the true solar zenith angle and are found also to remain fairly constant during the flight, as shown in red in Fig. 11b. In this case, the SW irradiances are normalized to the mean solar zenith angle during the pattern ($\theta_o = 69.75°$) to make the SW measurements consistent throughout the flight pattern. In future analyses, other solar zenith angle (SZA) normalization strategies will be employed (e.g., to the CERES observation time). Most of the variability in downwelling SW is attributed to the scattered thin cirrus that occasionally occurred overhead. The mean downwelling SW irradiance is 399.35 ± 16.87 W m^{-2}. The upwelling SW irradiances show more variation, with increases or decreases within a given leg. This is attributed to the change in the sea surface conditions beneath the low-cloud deck. For example, the upwelling SW irradiances shown in Fig. 11b are smaller at the northwestern end of each leg because of the darker ocean compared to the brighter surfaces found over the southeastern end, where there was much more sea ice. The average upwelling SW irradiance for the entire pattern was 207.33 ± 32.48 W m^{-2}. The upwelling SW and LW irradiances are consistent with earlier Arctic aircraft campaigns (Curry and Herman 1985; Herman and Curry 1984; Pinto 1998; Curry et al. 2000), while the downwelling LW irradiance is smaller due to the aircraft's higher altitude during this particular flight pattern. This initial analysis is encouraging and supports the sampling strategy devised and employed during ARISE for evaluating CERES TOA and surface irradiances over the Arctic with aircraft measurements. More detailed analyses and comparisons between BBR and CERES are planned for all of the ARISE gridbox experiments.

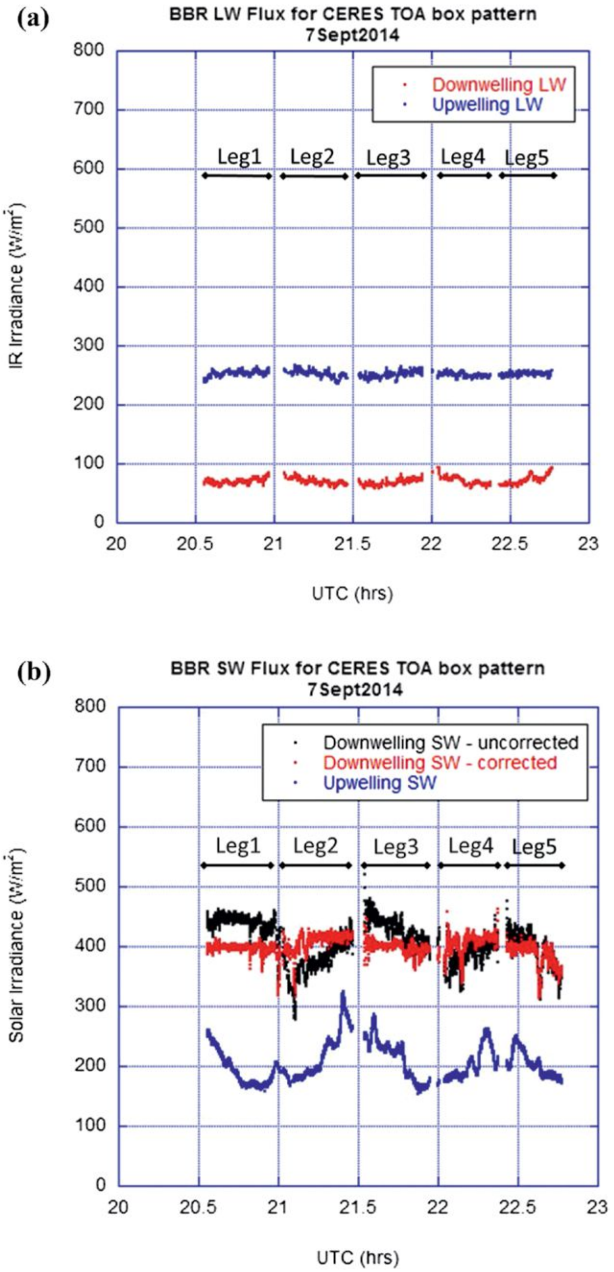

Fig. 11. BBR (a) LW and (b) SW fluxes from the flight tracks in Fig. 10.

SSFR. The SSFR (Pilewskie et al. 2003) measures downwelling (zenith: $F_\lambda^\downarrow$) and upwelling (nadir: $F_\lambda^\uparrow$) SW spectral irradiance from 350 to 2150 nm with a spectral resolution of 6–12 nm. Since its development, it has been used for deriving the radiative effect of cloud and aerosols, and for determining their properties in conjunction with remote sensing and in situ instruments (e.g., Schmidt and Pilewskie 2012). The SSFR has been used to validate satellite data (e.g., Coddington et al. 2008, 2010) and to develop cloud retrievals based on relative spectral information (McBride et al. 2012; Coddington et al. 2013; LeBlanc et al. 2015).

The instrument consists of two light collectors at the top and bottom of the aircraft fuselage, as well as a rack-mounted radiometer unit that is connected to the light collectors through fiber-optic bundles. For ARISE, the zenith light collector was mounted on an active leveling platform to keep the receiving plane of the light collectors aligned with the horizon during attitude changes of the airplane. The radiometer box contains two identical pairs of grating spectrometers covering the spectral range: (a) 350–1000 nm (Zeiss grating spectrometer with silicon linear diode array) and (b) 950–2200 nm (Zeiss grating spectrometer with InGaAs linear diode array). More instrument details can be found in Wendisch et al. (2013, chapter 7). The radiometric and angular responses were determined in the laboratory before and after the field deployment; the drift of the radiometric calibration was tracked with a portable field calibrator over the course of the mission (accuracy of 3%), and the horizontal alignment of the leveling platform was adjusted before each flight (accuracy of 0.2°). Because of the low sun elevation in the Arctic, minor misalignments of the instrument with respect to the horizon increase the absolute uncertainty (Wendisch et al. 2001) and low signal levels lead to elevated noise. In addition, reflections and obstructions from the aircraft itself or other instruments affect the measurements under these conditions. Overall, the absolute uncertainty was increased to about 7% for $\theta_o < 75°$.

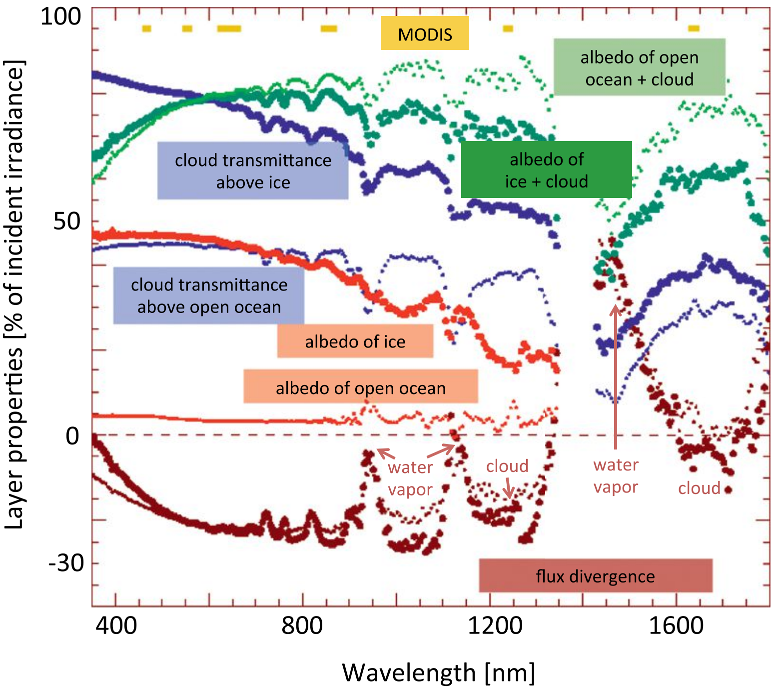

FIG. 12. SSFR-derived cloud properties for a case on 19 Sep 2015: A cloud field across the MIZ from open to ice covered (small and large symbols, respectively). Green: cloud albedo ($F^{\uparrow}/F^{\downarrow}$ above the cloud); red: surface albedo ($F^{\uparrow}/F^{\downarrow}$ below the cloud); blue: transmittance ($F^{\downarrow}_{\text{below}}/F^{\downarrow}_{\text{above}}$); and brown: flux divergence {apparent absorptance $[(F^{\downarrow}_{\text{above}}/F^{\uparrow}_{\text{above}}) - (F^{\downarrow}_{\text{below}}/F^{\uparrow}_{\text{below}})]/F^{\downarrow}_{\text{above}}$}. The channels of MODIS are shown in yellow.

Collocated legs above and below a cloud field can be used to derive reflected, transmitted, and absorbed radiation above the open ocean and ice, providing "ground truth" to satellite-derived estimates of these quantities. The aircraft platform is the only way to get the perspectives from "above," "below," and "within" a cloud almost all at once. Figure 12 demonstrates this for a case from 19 September, where a cloud field in the MIZ was sampled above both a clear area and an ice-covered area. It shows that the albedo [green spectra: $(F_{\lambda}^{\uparrow}/F_{\lambda}^{\downarrow}) \times 100\%$], derived from a high-level leg, is almost identical for the cloud above ice (large symbols) and the one above open ocean (small symbols), even though the surface albedo (red), derived from a low-level leg, is very different. The small differences of the albedo spectra can be explained by different cloud properties (optical thickness and effective radius) for the two cases. On the other hand, the cloud transmittance [blue: $(F_{\lambda}^{\downarrow,\text{below}}/F_{\lambda}^{\downarrow,\text{above}}) \times 100\%$] is substantially higher above ice than over open ocean because part of the enhanced upwelling radiation over ice is reflected down by the cloud. The distinct spectral shape in the albedo (decreasing toward the shortest wavelengths) is mirrored by the apparent absorptance (flux divergence), the difference between net irradiances above and below the layer normalized by incident irradiance

$$\left(\text{brown: } \left\{\left[\left(F_{\lambda}^{\downarrow} - F_{\lambda}^{\uparrow}\right)^{\text{above}} - \left(F_{\lambda}^{\downarrow} - F_{\lambda}^{\uparrow}\right)^{\text{below}}\right] F_{\lambda}^{\downarrow,\text{above}}\right\} \times 100\%\right).$$

This is indicative of the presence of horizontal transport of radiation (Schmidt et al. 2010; Song et al. 2016). In this case, the clouds act as net recipients of radiation from surrounding areas, which results in higher transmittance (and/or reflectance) than predicted by one-dimensional radiative transfer. Studies for reconciling measured in situ microphysics profiles with the corresponding irradiances above the contrasting surface types are underway and will be published separately.

This example begs the question whether such three-dimensional cloud effects remain significant when averaging over larger domains. A further interesting question concerns the relative magnitude of cloud and water vapor absorption for different types of clouds (thermodynamic phase and altitude) above different surface types. In our example, the water vapor absorption features (relative to the negative baseline caused by horizontal photon transport) are much more prominent than the weak cloud absorption features. For high clouds, the situation may be reverse. This will be quantified in future work, using spectral partitioning of the absorption by constituents (Kindel et al. 2011).

SSFR data will provide spectral surface albedo as a boundary condition for satellite and airborne remote sensing—a first example is shown in Fig. 12. From the measured albedo, transmittance, and absorptance spectra, cloud properties (optical thickness, thermodynamic phase, effective radius) can be derived that are averaged over the SSFR hemispherical footprint. These can be compared with satellite retrievals. The collection of aircraft and satellite cloud retrievals, in situ measurements, and spectral and broadband irradiances is expected to lead to a deeper understanding of the radiative effects of clouds in the MIZ.

4STAR. The Spectrometer for Sky-Scanning, Sun-Tracking Atmospheric Research (4STAR) instrument combines airborne sun tracking and sky scanning with spectroscopy by incorporating a sun-tracking–sky-scanning–zenith-pointing head with fiber-optic signal transmission to rack-mounted grating spectrometers (Dunagan et al. 2013) that cover the ultraviolet–visible (210–995 nm, spectrometer I) and SW infrared (950–1703 nm, spectrometer II) spectral regions, with a spectra acquisition rate of 1 Hz. During ARISE, 4STAR was operated in its three operation modes: sun tracking, sky scanning, and zenith pointing. The 4STAR tracking head was installed in a modified escape hatch in the zenith port at flight station 220 on the NASA C-130. The data acquisition, motion control, and spectrometers were installed further aft at a flight operator station.

In sun-tracking mode, two motors and a quadrant photodiode detector provide active tracking of the solar disk for measurements of direct solar beam transmittance. Dark counts are measured every 20 min with a shutter mechanism. Atmospheric transmittance is derived by dividing the dark-subtracted photon counts by a TOA reference spectrum, accounting for measurement integration time. The TOA reference spectrum is determined by the refined Langley plot method (Shinozuka et al. 2013). In ARISE, we obtained the 4STAR TOA calibration spectrum (Segal Rosenhaimer et al. 2014) using measurements from a dedicated high-altitude flight on 2 October. Direct sun products include aerosol optical depth (AOD; Shinozuka et al. 2013), total column water vapor (CWV), O_3, and NO_2 (Segal Rosenhaimer et al. 2014) under clear sky and cirrus optical depth under thin cirrus cases (Segal Rosenhaimer et al. 2013).

In sky-scanning mode, 4STAR measures the diffuse sky radiance at prescribed scattering angles from the sun in the almucantar or principal plane to retrieve aerosol properties (single-scattering albedo, size distribution, and refractive index; see Kassianov et al. 2012). In ARISE, a special modification of this mode was applied under cloudy scenes, with the goal of extracting scattering phase function properties from the various cloud types.

In the zenith mode, the instrument points in the zenith direction and measures diffuse radiances, for the retrieval of cloud phase, optical depth, and effective radii, following the method of LeBlanc et al. (2015). This mode is used under cloudy skies and accounts for 18% of the data collected by 4STAR during ARISE. Figure 13 shows an example illustrating the sensitivity to the zenith radiances to

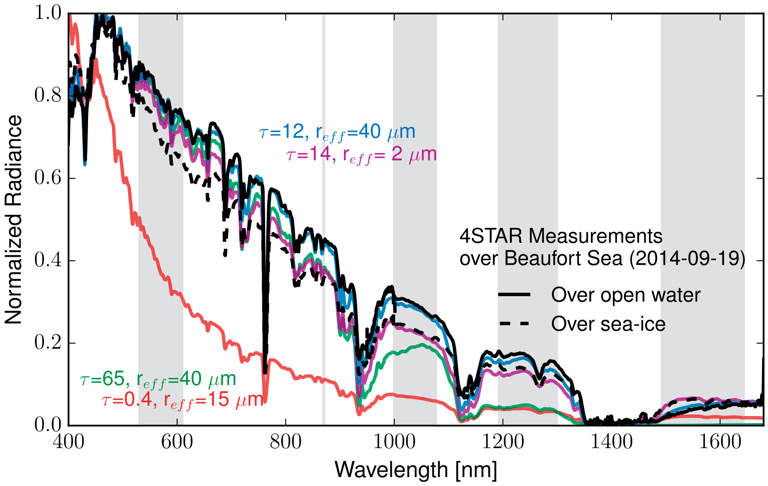

Fig. 13. 4STAR spectra of zenith radiance transmitted through cloud over open water and over sea ice (black) on 19 Sep 2014 compared with radiative transfer model simulations for various single-phase clouds (colors). Radiative transfer calculations used the scattering phase functions for ice particles described by Baum et al. (2011) and flight-level spectral albedo measured by SSFR. The green and red curves show the extremes of considered cloud properties, while blue and purple curves represent modeled radiances matching closely measured radiances. Gray areas indicate wavelength regions where the spectral shape can be used to retrieve cloud properties (optical depth, effective particle radius, thermodynamic phase).

cloud optical properties. Modeled radiances closely match the two example measured spectra, with small differences owing to the possible inclusion of cloud particles of mixed phase. The sky radiance measurements were calibrated before and after the 4STAR ARISE deployment to a National Institute of Standards and Technology (NIST)-traceable integrating sphere at the NASA Ames Research Center, and throughout the deployment with a field-portable 15.24-cm-diameter integrating sphere referenced against the same NIST-traceable source.

Cirrus cloud optical thickness (COT) was calculated based on the method detailed in Segal Rosenhaimer et al. (2013). This retrieval approach is based on the generation of lookup tables (LUTs) of total transmittance for the sun photometer's field of view (FOV) due to the direct and scattered irradiance over the spectral range measured, for a range of cirrus COT (0–4), and a range of ice cloud effective diameters (10–120 μm) by using explicit cirrus optical property models from Baum et al. (2011). To calculate the total transmittance seen by the instrument, which

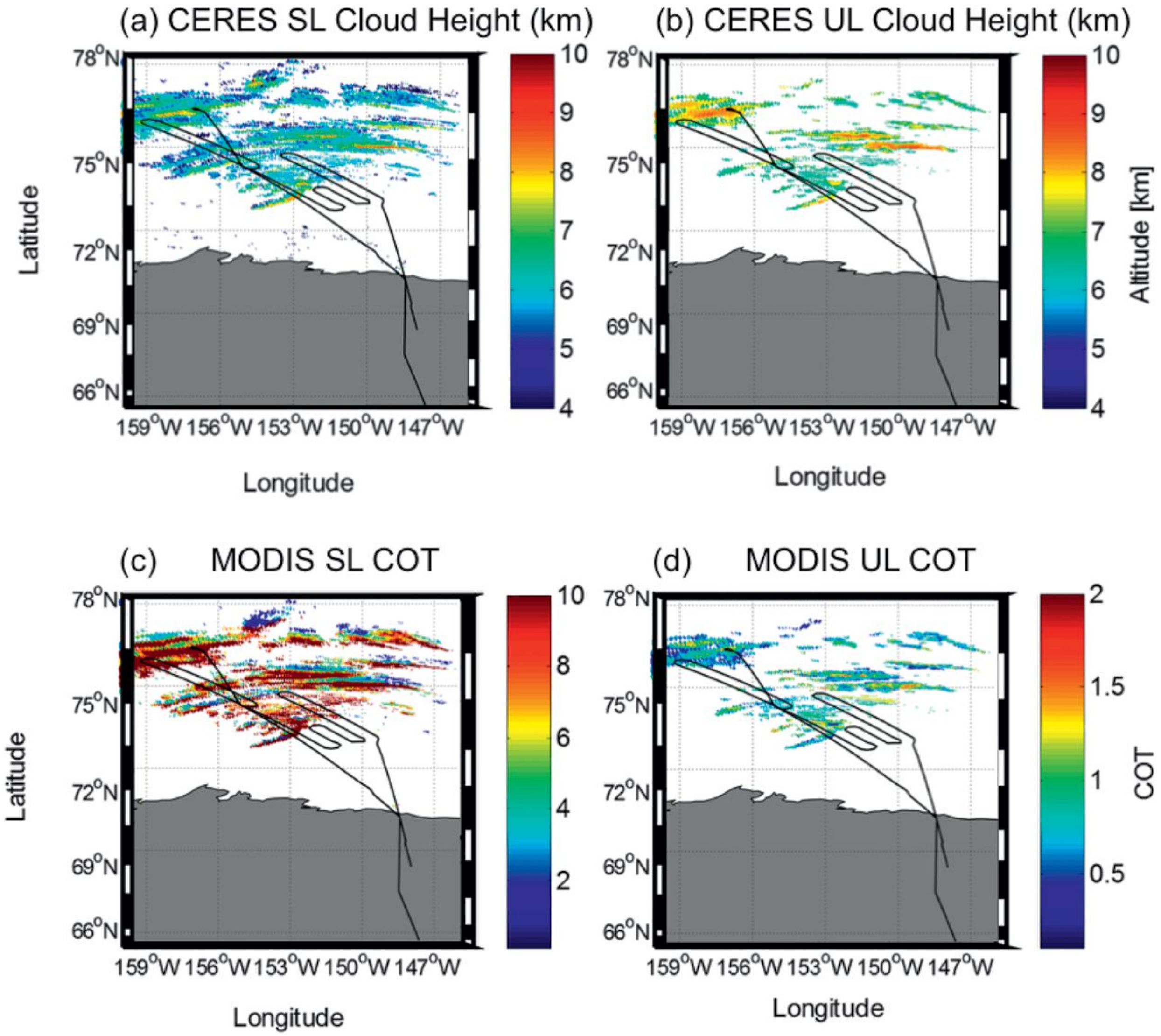

Fig. 14. 4STAR retrievals of cirrus COT on 15 Sep 2014 compared with MODIS retrievals from the nearest satellite overpass. (a) All ice clouds' top heights derived by CERES, overlaid by aircraft altitude (open circles). (b) Top-layer cloud height of ML clouds, derived by CERES, overlaid by aircraft altitude (open circles) for 15 Sep flight. (c) COT for all ML ice clouds with top above 5-km height derived by CERES (solid circles), overlaid by direct sun cirrus retrievals [based on procedure developed in Segal-Rosenheimer et al. (2013)] from the 4STAR instrument on board C-130 (open circles). (d) COT for only upper-layer clouds, as derived by CERES, overlaid by direct sun cirrus retrievals from 4STAR (open circles) for 15 Sep flight. Note the different color bar scales for (c) and (d).

includes both the direct and forward-scattered components, we use a function suggested by Shiobara and Asano (1994), generated by a three-dimensional (3D) Monte Carlo radiative transfer model. Our measurements are then corrected for the appropriate gas absorption and solar zenith angle at the time of measurement and compared to the modeled values over a range of wavelengths, spanning both visible and infrared spectrometers, and are chosen by the best-fit approach. Cirrus locations were adjusted from aircraft coordinates, since the 4STAR tracks the sun and does not view the clouds in zenith directly above the aircraft. The new location was calculated based on distance derived by the estimated cirrus height, the solar zenith angle, and the sun azimuth. Cirrus top height was approximated from MODIS and was ~9 km (300 mb for cirrus top height). The latter adjusted cirrus location is about 8 km from the aircraft coordinates.

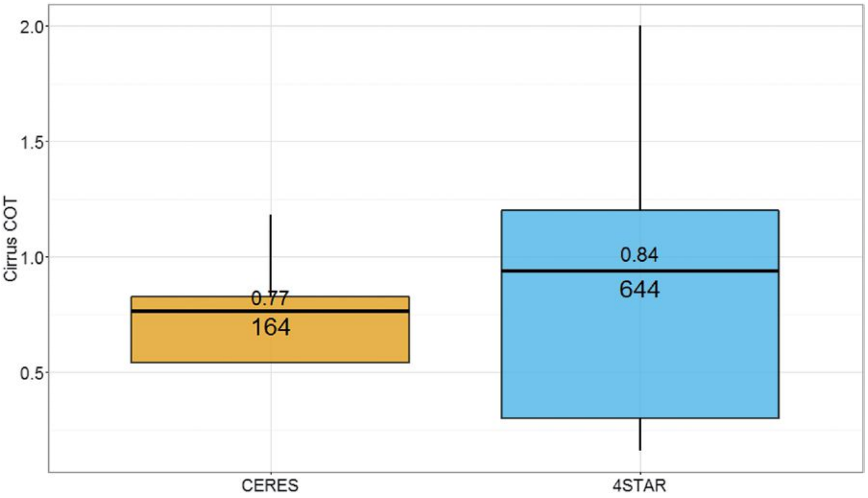

Fig. 15. Cirrus COT statistics from CERES–MODIS upper-layer cloud retrievals (yellow) and those derived from 4STAR (blue) using data taken on 15 Sep 2014 along the C-130 flight track shown in Fig. 14. Solid black lines indicate the median values, while the top and bottom numerical values indicate the mean values and the number of samples, respectively.

The 4STAR cirrus retrievals will not only aid the interpretation of the aircraft irradiance measurements but also be useful for validating satellite cloud property retrievals, such as COT (by direct comparison), and cloud-top height (CTH; indirectly). For example, Fig. 14 shows the CTH derived from the MODIS imager on *Terra* at 2140 UTC 15 September 2014. Two sets of MODIS CTH retrievals are shown. The first, shown in Fig. 14a, is based on a single-layer (SL) cloud assumption for all ice-phase clouds (Minnis et al. 2011), which often underestimates CTH (Chang et al. 2010a, and references therein). The second is based on a multilayer (ML) cloud algorithm (Chang et al. 2010b) and shown in Fig. 14b for the upper layer (Fig. 14b). While the satellite CTH estimates from the SL method are near or below the altitude of the aircraft, the upper-level CTHs determined from the ML algorithm are consistently higher than the aircraft, which is corroborated by numerous 4STAR observations of overhead cirrus. Figure 14c shows the total column COT derived from the MODIS SL method. For areas with clouds beneath the aircraft these retrievals are not comparable to 4STAR, since 4STAR is pointing at the overhead sun. However, the MODIS ML COT retrieval for the upper-level cloud should be more comparable to the 4STAR retrievals of cirrus above the aircraft. This statistical comparison is shown in Fig. 15. The CERES–MODIS upper-layer COTs, derived from the 2140 UTC *Terra* overpass, were spatially interpolated to match the 4STAR cirrus locations (found between 2100 and 2200 UTC). While the overall mean and median values of COT along the flight track are found to agree quite well as shown in Fig. 15 (0.84 and 0.77 for 4STAR and MODIS, respectively), the 4STAR data suggest more widespread cirrus may have been occurring than were detected with the CERES–MODIS method. Only 164 valid CERES points were found in comparison to 664 from 4STAR. One possible contributing factor to this difference is the relatively large 4STAR instrument FOV (compared to MODIS), which spans about 2°, allowing for coverage of the entire solar disk plus about 0.5° from each side. Thus, as the box plots indicate, 4STAR appears to be more sensitive to the optically thinner cirrus clouds, which are difficult to detect from MODIS. A comparison between only the coincident positive cirrus COT retrievals (not shown) indicates that the MODIS mean value of 0.77 is considerably lower than the mean value of 1.3 found from the corresponding 4STAR points. This is useful information that can be used to improve the skill of the satellite method. Table 4 describes the full range of 4STAR data products that will be available from ARISE.

LARGE cloud probes. Cloud droplet microphysical properties were measured in situ by the C-130 using multiple probes operated by the NASA Langley Aerosol Research Group (LARGE). The probes were mounted on the starboard side of the aircraft just forward of the propeller line (Fig. 1).

The multielement water content system (WCM-2000; SEA Inc.) is a three-wire probe based on commonly used and proven technologies that are combined to measure the total and liquid water content (TWC and LWC, respectively) simultaneously. The ice water content (IWC) is inferred from the difference between TWC and LWC. During ARISE, most of the mass measured with this instrument was liquid. Typically the ratio LWC/TWC is on the order of 90%–95%, and this is consistent with an earlier aircraft study of autumnal Arctic clouds sampled approximately a month later in the season (Pinto 1998). Uncertainties of 20% have been found across different Johnson–Williams LWC probes in a wind tunnel testing (Strapp and Schemenauer 1982), which lend support to the premise that these are supercooled liquid rather than ice clouds. In our preliminary inspection of the dataset, there does not seem to be a dependence of LWC/TWC across surface types.

Cloud droplet number and size distribution (2–50-μm diameter) are measured with a cloud droplet probe [CDP; Droplet Measurement Technologies (DMT)]. The CDP measures the forward-scattered light from cloud particles that pass through a laser beam. The intensity of the scattered light is related to the cloud particle size assuming spherical particles and is verified using NIST-traceable glass spheres (Thermo Fisher Scientific, Inc.). Liquid water and water vapor path above the aircraft are measured using a G-band (183 GHz) water vapor radiometer (GVR; ProSensing, Inc.). The GVR measures the brightness temperature of four receiver channels centered on the water vapor absorption line at 183.31 ± 1, ±3, ±7, and ±14 GHz. Two internal references (i.e., hot and warm targets at 333 and 293K, respectively) are used to calibrate the receivers once every 10 s during flight.

Low-level Arctic stratus clouds were sampled in situ during each of the ARISE science flights and were consistently observed within the shallow boundary layers spanning 0–350 m in altitude. An example of this vertical structure is shown in Fig. 16 for the research flight on 15 September. For this flight, the C-130 initially transited northwest toward the sea ice edge at approximately 7000 m before descending to the surface to profile three cloud layers centered at approximately 5500, 4000, and 300 m. The aircraft then ascended and descended through the low-cloud layer, for which vertical profiles are shown in Fig. 16, indicating that the cloud layer extended from 30 to 90 m at cloud base up to 490–550 m at cloud top. Mean droplet number concentrations were observed to be relatively constant throughout the cloud layer at approximately 100 cm^{-3}, while both droplet mean diameters and liquid water content increased with altitude (from 4 to 14–16 μm and from 0.15 to 0.4–0.5 g m^{-3}, respectively). Despite being near the monthly mean sea ice extent for September 2014, it was noted at the time that these aircraft maneuvers were conducted over a mostly sea ice–free surface with only the occasional patch of broken sea ice below.

This low-cloud structure contrasts that seen for a cloud sampling pattern carried out on 19 September considerably to the east of that on 15 September, where the aircraft flew vertically stacked legs across the sea ice edge from approximately 136° to 129°W longitude. As shown in the top-left panel of Fig. 17, the aircraft initially ascended from west to east while skirting the ever-increasing top of the cloud layer

Table 4. 4STAR data products during ARISE.

Product name	Description	Data level	Accuracy	4STAR mode
Aerosol optical depth	Total column AOD above the aircraft at 14 discrete wavelengths[a]	2	±0.02	Direct sun
Column water vapor	Total column water vapor above the aircraft	2	±0.05	Direct sun
Ozone	Total column ozone above the aircraft	2	1%	Direct sun
Zenith cloud radiances	Zenith cloud radiances at 24 discrete wavelengths	1	3%–5%	Zenith
Sky radiances	Sky radiances at four wavelengths (440, 673, 873, and 1020 nm) for selected cases	1	3%–5%	Sky scanning
Cloud properties	Cloud phase, cloud optical depth, and effective radius	2[b]	—	Zenith
Cirrus properties	Thin cirrus (0.01–4) optical depths	2[b]	±0.05	Direct sun

[a] These 14 wavelengths were chosen for window regions from the hyperspectral AOD measured.

[b] These products are still under development and are being processed for selected cases.

(black trace), then retraced its transect from east to west in a descending/ascending porpoise maneuver (red, blue, gold), and finally turned back west to east for a low-level horizontal leg through the lowest portion of the cloud. The western portion of the low-cloud layer (gold traces in Fig. 17) spanned 150–1200 m altitude, while the eastern portion (red traces) was shifted higher (600–2100 m). Despite these differences, typical droplet number concentrations, mean droplet diameter, and liquid water content were of similar magnitude across all three profiles.

In addition to the vertical cloud structure, level flight legs (green and cyan in Fig. 17) show a marked amount of horizontal variability. The cloud droplet number concentration and LWC traces in the top-right panel of Fig. 17 show an alternating pattern of cloud and cloud-free air as both LWC and the cloud droplet number concentration (CDNC) drop quickly to zero for brief periods of time. This cloud structure was clearly visible from the aircraft during this (and other) flight—the ocean surface could be discerned when looking at angles near nadir, while the view at lower angles was entirely opaque. Finally, we note the strong increase in cloud droplet number and corresponding decreases in both LWC and mean droplet diameter as the aircraft passed over the ice

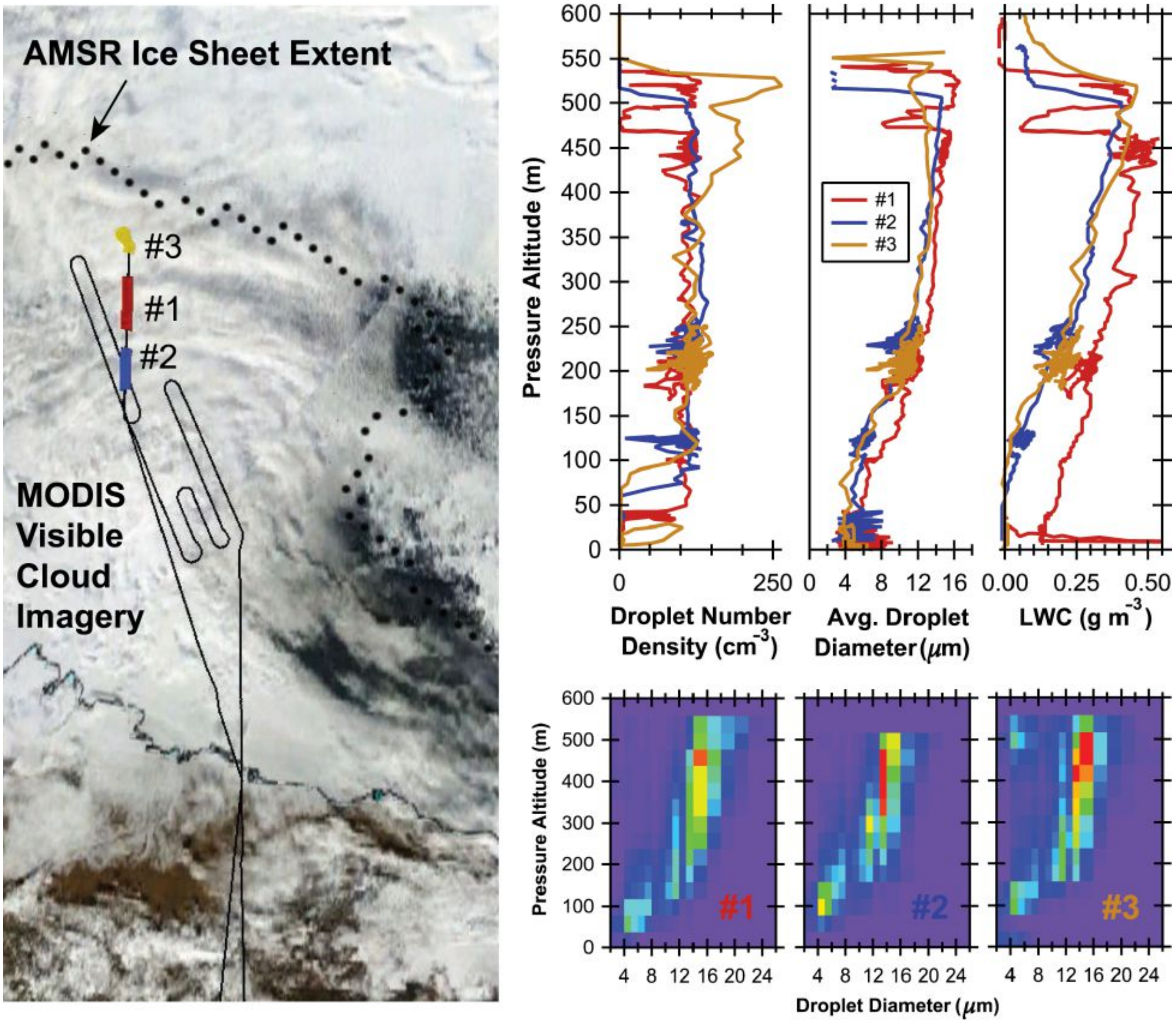

Fig. 16. Vertical profiles of cloud microphysical properties for three cloud penetrations on 15 Sep 2014. (left) The location of each profile is highlighted (red: 75.60°N, 156.04°W, blue: 74.82°N, 155.43°W, gold: 76.33°N, 156.83°W). The complete flight track is shown in black, the National Snow and Ice Data Center (NSIDC) monthly mean sea ice extent is shown as solid white, and the MODIS visible imagery is shown for the non-ice region. (top right) Traces of droplet number density, mean droplet size, and LWC at 1-Hz resolution during each profile. (bottom right) Droplet number size distributions binned by altitude.

sheet edge. This transition may be explained by a shift in the dynamics controlling these clouds or, possibly, by an increase in cloud condensation nuclei over the open waters.

LVIS. NASA's Land, Vegetation and Ice Sensor (LVIS) is a wide-swath scanning laser altimeter (lidar) system that digitally records the shapes of the outgoing and reflected laser pulses (Blair et al. 1999). Information extracted from the laser waveforms is combined postflight with precise laser pointing, scanning, and positioning data to precisely and accurately measure surface elevation and 3D surface structure relative to a reference surface, such as the World Geodetic System 1984 (WGS-84) reference ellipsoid (Hofton et al. 2008). Operating at a wavelength of 1064 nm and at a data rate of 1500 Hz, typical data precision and accuracy are at the 10-cm level over ice surfaces (Hofton et al. 2008). The sensor is used to collect data for cryospheric, ecological, biodiversity, and solid-Earth applications, providing a characterization of the three-dimensional nature of overflown surfaces. An atmospheric channel, implemented for the first time for the ARISE mission, provided a record of the returns at 1064 nm along the full laser path from the airplane to the ground. During data processing, these waveforms were combined over 1-s intervals within a common elevation range to provide the vertical distribution of reflected surfaces between the laser and the ground.

During ARISE, the sensor operated in two principal configurations that defined the data swath width. From medium to high flight altitudes, the full laser swath width was used. For example, from a 7-km flight altitude the laser swath was ~1400 m wide with an 18-m-wide footprint. From lower altitudes, in order to prevent overstressing of system components, an 80-mrad-wide laser

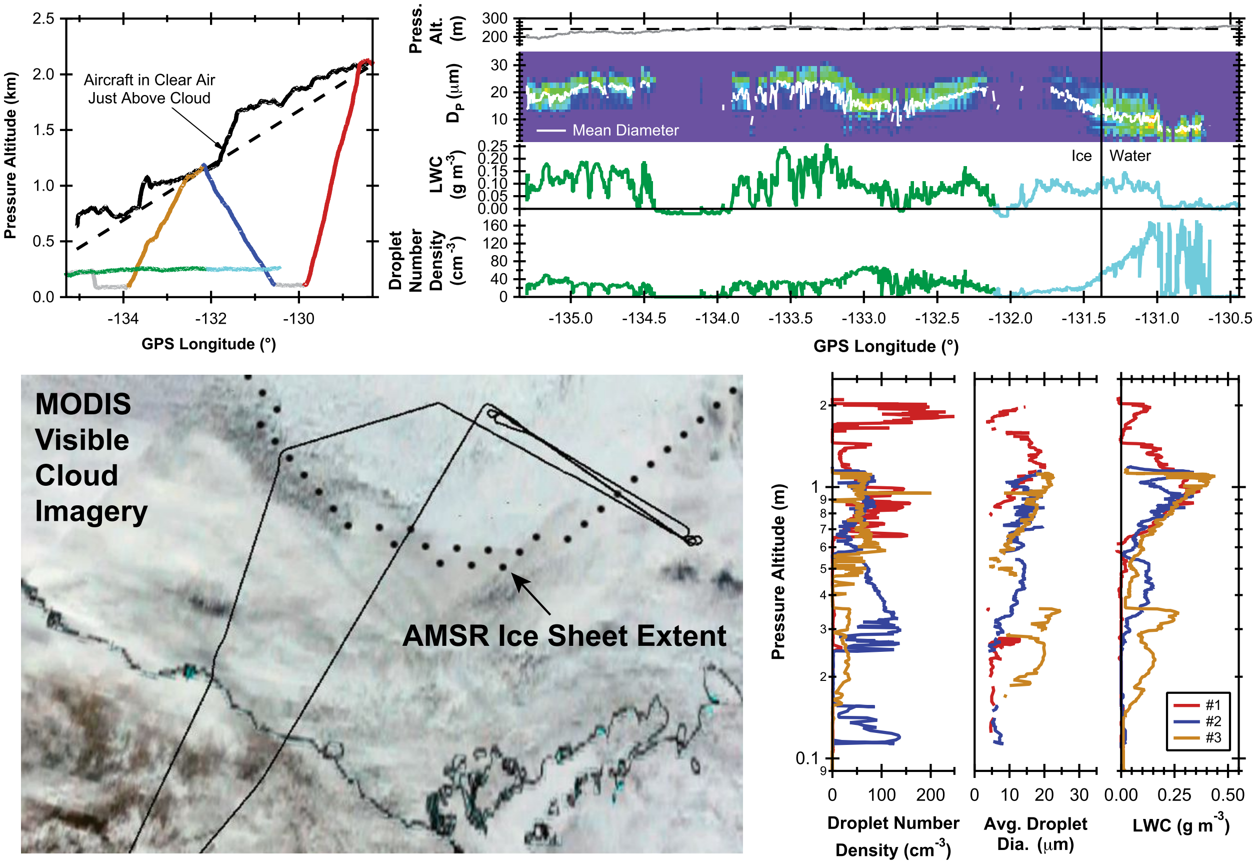

Fig. 17. Sampling of cloud properties across the ice edge centered near 72.3°N, 133.5°W on 19 Sep 2014. (top left) The altitude vs longitude trace shows the aircraft sampling strategy along (bottom left) the parallel tracks. Initially, the aircraft ascended from west to east following just above the cloud top (black trace). Then, three vertical profiles were carried out to map the vertical extent of the clouds (red, blue, gold). The vertical profile of droplet number density, mean diameter and LWC are shown in the lower right. Finally, a series of horizontal legs was performed at 800 ft (~245 m) along the same track. The cloud properties along one of these legs is shown in the upper right. Green (cyan) denotes the underflight of the gold (blue) profiles at 800 ft.

swath was used (e.g., from a 0.45-km flight altitude, the laser swath was ~4.5 m wide with eight ~1-m-wide footprints). Data products include the geolocated return laser waveform, defining the vertical distribution of the reflecting surfaces within the laser footprint relative to the reference ellipsoid (level 1B), and elevation data products extracted from the level 1B laser waveform using standard waveform interpretation algorithms, in this case the locations of the lowest and highest reflecting surfaces with the laser footprint (level 2).

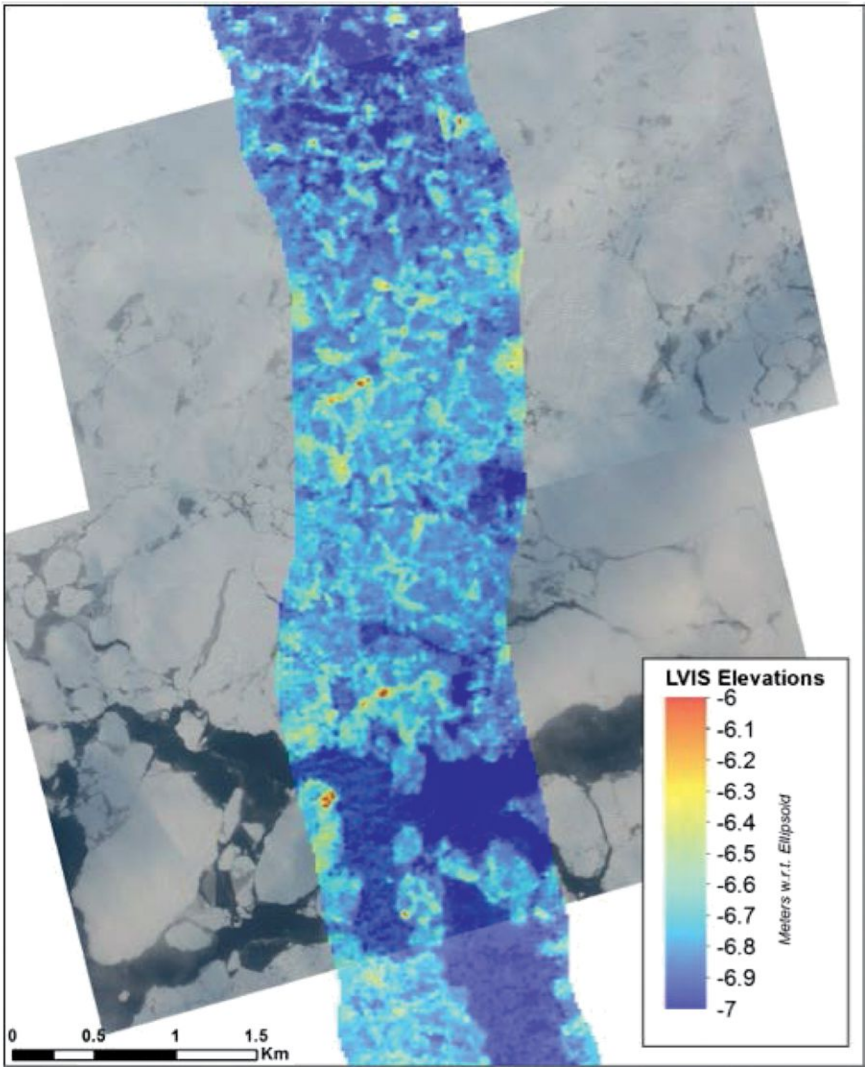

Fig. 18. Surface elevation data derived from the scanning LVIS superimposed on digital camera imagery taken near 76.4°N, 140°W on 5 Sep 2014 to help characterize sea ice properties and variability.

Data were typically collected throughout each ARISE flight even if the surface was not discernible through clouds in order to enable both radiation and ice target objectives to be met. Mission highlights included a 1,000-km-long transect from open water to sea ice along the 140°W longitude line (Fig. 18); a 600-km-long transect of an orbit track of the European Space Agency (ESA)'s *Cryosat-2* with the satellite passing directly overhead at the start of the line; repeated passes over the MIZ throughout the ARISE campaign over the time of the sea ice minimum; data swaths along several Alaskan glaciers, including the Columbia, Portage, Spencer, Trail, and Wolverine glaciers; and characterization of cloud-top heights throughout each flight to interpret the radiation measurements (Fig. 19). The LVIS team is developing a cloud-top height product based on the laser returns. As long as the laser beam is not fully attenuated, there is information on the top height of multiple cloud layers.

SUMMARY AND FUTURE WORK. ARISE was a uniquely successful experiment in three respects. First, the experiment collected advanced radiometric, laser altimeter, and in situ atmospheric data during the critical period of late summer and early autumn sea ice transition in the Beaufort Sea. Second, the aircraft measurements were effectively coordinated with multiple intersecting satellite overpasses, allowing for thorough validation of CERES climate data record products plus a greater understanding of the subgrid-scale variability that influences satellite products at high northern latitudes. Third, the experiment was conceived, planned, and executed in a remarkably short time—6 months from concept to flight missions, whereas many other experiments of this complexity often take several years to realize. This third success also entails a challenge for the ARISE Science Team: our expertise is almost exclusively within the domains of the flight instruments and

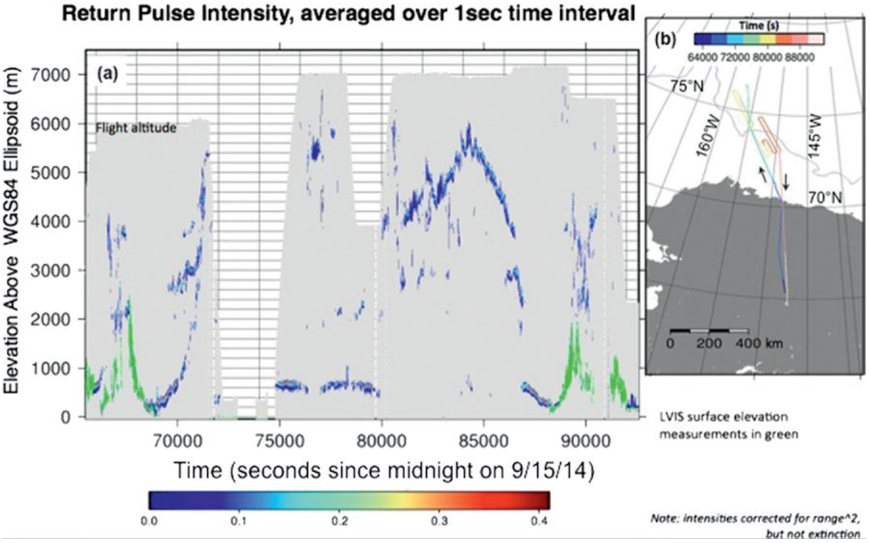

Fig. 19. LVIS return pulse intensity (a) along the C-130 flight track and (b) on 15 Sep 2014, depicting surface and cloud-top altitudes. An LVIS level 2 cloud altitude product is in development to complement and help interpret the cloudy-sky radiative flux measurements obtained during ARISE.

data interpretation specific to the instruments and satellite remote sensing. We therefore invite and encourage as wide a collaboration as possible with the broader community, particularly researchers interested in 1) applying the resulting well-tested CERES data products to global and regional climate modeling and climate change studies and 2) applying the combination of spectrally resolved and radiometric data and sea ice structure data to process studies involving radiant ice–ocean–atmosphere energy exchange during the sea ice transition. Already we have noticed one potentially important aspect of the clouds sampled throughout ARISE: there is a pronounced tendency toward liquid water in lower- and midtropospheric clouds, with relatively little radiative influence of cloud ice particles as compared with the geometrically extensive mixed-phase clouds observed over the region later in autumn (Verlinde et al. 2007). In this sense the cloud cover during the critical sea ice transition may be more typical of summer (e.g., Tjernström et al. 2012) than autumn. This merits further investigation because ice water content in Arctic mixed-phase clouds exerts a significantly contrasting radiative forcing compared with clouds that are almost entirely liquid water (Lubin and Vogelmann 2011). At the same time, the apparent simplicity of a cloud possibly dominated by a single thermodynamic phase may be offset by the 3D radiative transfer effects noted above (Fig. 12), and the high-time-resolution spectral radiometric data from ARISE can address these complexities.

The ARISE data, which are available at the NASA Langley Atmospheric Science Data Center and in the NASA OIB archive, contain a wealth of information on the Arctic sea ice transition from in situ process to satellite spatial scales. In addition to data analysis from the campaign itself, ARISE can help motivate future work. The average September Arctic sea ice extent exhibits large interannual variability of approximately 1,000,000 km^2, in addition to the pronounced downward trend over the past three decades (Stroeve et al. 2012). Additional missions during this transition season with similar instrumentation could provide insight into the precise radiative and thermodynamic precursors for onset of seasonal ice recovery. Stroeve et al. (2014) show that the timing of the melt onset impacts the amount of insolation absorbed during summer, which in turn influences the timing of the autumn ice recovery. Similar attention, perhaps an additional campaign, should focus on the springtime melt onset in the Beaufort Sea. Finally, for both the satellite and in situ objectives presented here, a follow-on aircraft mission would benefit from additional active sensors, such as polarized cloud lidar and cloud radar; a more complete cloud microprobe suite, including aerosol composition and microphysics; and dropsondes, to provide measurements of atmospheric thermodynamic structure specifically over ice of varying concentrations versus open water during a given mission. ARISE has demonstrated what is possible from long-range research aircraft; over the next decade, enhancements to instrumentation combined with a focus on timing of sea ice melt onset and autumn recovery can provide a foundation for thorough understanding of mechanisms for Arctic sea ice trends.

ACKNOWLEDGMENTS. ARISE was sponsored and supported by the Earth Science Division of NASA's Science Mission Directorate. We thank the program managers at NASA headquarters: Jack Kaye, Hal Maring, Bruce Tagg, and Tom Wagner. Their support and inspiration were critical in the planning and successful execution of ARISE given the urgency for the mission and the short time frame to accomplish it. We are grateful to the personnel at the NASA Wallops Flight Facility, who provided support for the C-130. We thank the C-130 flight crew and integration engineers for their support and significant accomplishes in readying and maintaining the aircraft. We particularly thank the pilots of the C-130—John Long and Jeff Chandler—for their expertise and genuine interest in helping us to accomplish our science objectives. We also thank the NASA Ames Earth Science Project Office for a number of contributions, including logistics support; the National Suborbital Education and Research Center (NSERC) for its support of the aircraft data system; Aaron Duley and his colleagues at the NASA Ames Research Center for configuring and maintaining the NASA Mission Tools Suite; and Nathan Eckstein and his colleagues at the Alaska Aviation Weather Unit for providing valuable meteorological support. Finally, we are grateful to the staff members at Eielson Air Force Base for all of their support in hosting the C-130 and the ARISE experiment team.

REFERENCES

ASTM, 2005: Standard test method for calibration of a pyranometer using a pyrheliometer. ASTM G167-05, ASTM International, 21 pp, doi:10.1520/G0167-05.

Badosa, J., J. Wood, P. Blanc, C. N. Long, L. Vuilleumier, D. Demengel, and M. Haeffelin, 2014: Solar irradiances measured using SPN1 radiometers: Uncertainties and clues for development. *Atmos. Meas. Tech.*, **7**, 4267–4283, doi:10.5194/amt-7-4267-2014.

Barker, H. W., M. P. Jerg, T. Wehr, S. Kato, D. P. Donovan, R. J. Hogan, 2011: A 3D cloud-construction algorithm for the EarthCARE satellite mission. *Q. J. R. Meteor. Soc.*, **137**, 1042–1058, doi:10.1002/qj.824.

Baum, B. A., P. Yang, A. J. Heymsfield, C. G. Schmitt, Y. Xie, A. Bansemer, Y. X. Hu, and Z. Zhang, 2011: Improvements in shortwave bulk scattering and absorption models for the remote sensing of ice clouds. *J. Appl. Meteor. Climatol.*, **50**, 1037–1056, doi:10.1175/2010JAMC2608.1.

Blair, J. B., D. L. Rabine, and M. A. Hofton, 1999: The Laser Vegetation Imaging Sensor (LVIS): A medium-altitude, digitization-only, airborne laser altimeter for mapping vegetation and topography. *ISPRS J. Photogramm. Remote Sens.*, **54**, 115–122, doi:10.1016/S0924-2716(99)00002-7.

Bucholtz, A., R. T. Bluth, B. Kelly, S. Taylor, K. Batson, A. W. Sarto, T. P. Tooman, and R. F. McCoy Jr., 2008: The Stabilized Radiometer Platform (STRAP)—An actively stabilized horizontally level platform for improved aircraft irradiance measurements. *J. Atmos. Oceanic Technol.*, **25**, 2161–2175, doi:10.1175/2008JTECHA1085.1.

Cassano, E. N., J. J. Cassano, M. E. Higgins, and M. C. Serreze, 2014: Atmospheric impacts of an Arctic sea ice minimum as seen in the Community Atmosphere Model. *Int. J. Climatol.*, **34**, 766–779, doi:10.1002/joc.3723.

Chang, F.-L., P. Minnis, B. Lin, M. Khaiyer, R. Palikonda, and D. Spangenberg, 2010a: A modified method for inferring upper troposphere cloud top height using the GOES 12 imager 10.7 and 13.3 μm data. *J. Geophys. Res.*, **115**, D06208, doi:10.1029/2009JD012304.

——, ——, J. K. Ayers, M. J. McGill, R. Palikonda, D. A. Spangenberg, W. L. Smith Jr., and C. R. Yost, 2010b: Evaluation of satellite-based upper troposphere cloud top height retrievals in multilayer cloud conditions during TC4. *J. Geophys. Res.*, **115**, D00J065, doi:10.1029/2009JD013305.

Coddington, O. M., and Coauthors, 2008: Aircraft measurements of spectral surface albedo and its consistency with ground-based and space-borne observations. *J. Geophys. Res.*, **113**, D17209, doi:10.1029/2008JD010089.

——, and Coauthors, 2010: Examining the impact of overlying aerosols on the retrieval of cloud optical properties from passive remote sensing. *J. Geophys. Res.*, **115**, D10211, doi:10.1029/2009JD012829.

——, P. Pilewskie, K. S. Schmidt, P. J. McBride, and T. Vukicevic, 2013: Characterizing a new surface-based shortwave cloud retrieval technique, based on transmitted radiance for soil and vegetated surface types. *Atmosphere*, **4**, 48–71, doi:10.3390/atmos4010048.

Curry, J. A., and G. F. Herman, 1985: Infrared radiative properties of summertime Arctic stratus clouds. *J. Climate Appl. Meteor.*, **24**, 525–538, doi:10.1175/1520-0450(1985)024<0525:IRPOSA>2.0.CO;2.

——, and Coauthors, 2000: FIRE Arctic Clouds Experiment. *Bull. Amer. Meteor. Soc.*, **81**, 5–29, doi:10.1175/1520-0477(2000)081<0005:FACE>2.3.CO;2.

Delta-T Devices, 2007: User manual for the Sunshine pyranometer, type SPN-1. 43 pp. [Available online at ftp://ftp.dynamax.com/manuals/SPN1_Manual.pdf.]

Doelling, D. R., and Coauthors, 2013: Geostationary enhanced temporal interpolation for CERES flux products. *J. Atmos. Oceanic Technol.*, **30**, 1072–1090, doi:10.1175/JTECH-D-12-00136.1.

Dunagan, S. E., and Coauthors, 2013: Spectrometer for Sky-Scanning Sun-Tracking Atmospheric Research (4STAR): Instrument technology. *Remote Sens.*, **5**, 3872–3895, doi:10.3390/rs5083872.

English, J. M., J. E. Kay, A. Gettelman, X. Liu, Y. Wang, Y. Zhang, and H. Chepfer, 2014: Contribution of clouds, surface albedos and mixed-phase ice nucleation schemes to Arctic radiation biases in CAM5. *J. Climate*, **27**, 5174–5197, doi:10.1175/JCLI-D-13-00608.1.

Fridlind, A. M., A. S. Ackerman, G. McFarquhar, G. Zhang, M. R. Poellot, P. J. DeMott, A. J. Prenni, and A. J. Heymsfield, 2007: Ice properties of single-layer stratocumulus during the Mixed-Phase Arctic Cloud Experiment: 2. Model results. *J. Geophys. Res.*, **112**, D24202, doi:10.1029/2007JD008646.

——, B. van Diedenhoven, A. S. Ackerman, A. Avramov, A. Mrowiec, H. Morrison, P. Zuidema, and M. D. Shupe, 2012: A FIRE-ACE/SHEBA case study of mixed-phase Arctic boundary layer clouds: Entrainment rate limitations on rapid primary ice nucleation processes. *J. Atmos. Sci.*, **69**, 365–389, doi:10.1175/JAS-D-11-052.1.

Hartmann, D. L., and P. Ceppi, 2014: Trends in the CERES dataset, 2000–13: The effect of sea ice and jet shifts and comparison to climate models. *J. Climate*, **27**, 2444–2456, doi:10.1175/JCLI-D-13-00411.1.

Herman, G. F., and J. A. Curry, 1984: Observational and theoretical studies of solar radiation in Arctic stratus clouds. *J. Climate Appl. Meteor.*, **23**, 5–24, doi:10.1175/1520-0450(1984)023<0005:OATSOS>2.0.CO;2.

Hines, K. M., D. H. Bromwich, L. Bai, C. M. Bitz, J. G. Powers, and K. W. Manning, 2015: Sea ice enhancements to Polar WRF. *Mon. Wea. Rev.*, **143**, 2363–2385, doi:10.1175/MWR-D-14-00344.1.

Hofton, M. A., J. B. Blair, S. B. Luthcke, and D. L. Rabine, 2008: Assessing the performance of 20–25 m footprint waveform lidar data collected in ICESat data corridors in Greenland. *Geophys. Res. Lett.*, **35**, L24501, doi:10.1029/2008GL035774.

Intrieri, J. M., C. W. Fairall, M. D. Shupe, P. O. G. Persson, E. L Andreas, P. S. Guest, and R. E. Moritz, 2002: An annual cycle of Arctic surface cloud forcing at SHEBA. *J. Geophys. Res.*, **107**, 8039, doi:10.1029/2000JC000439.

Itterly, K., and P. C. Taylor, 2014: Evaluation of the tropical TOA flux diurnal cycle in MERRA and ERA-Interim retrospective analyses. *J. Climate*, **27**, 4781–4796, doi:10.1175/JCLI-D-13-00737.1.

Kassianov, E., C. Flynn, J. Redemann, B. Schmid, P. B. Russell, and A. Sinyuk, 2012: Initial assessment of the Spectrometer for Sky-Scanning, Sun-Tracking Atmospheric Research (4STAR)-based aerosol retrieval: Sensitivity study. *Atmosphere*, **3**, 495–521, doi:10.3390/atmos3040495.

Kato, S., and Coauthors, 2011: Improvements of top-of-atmosphere and surface irradiance computations with CALIPSO-, CloudSat-, and MODIS-derived cloud and aerosol properties. *J. Geophys. Res.*, **116**, D19209, doi:10.1029/2011JD016050.

——, N. G. Loeb, F. G. Rose, D. R. Doelling, D. A. Rutan, T. E. Caldwell, L. Yu, and R. A. Weller, 2013: Surface irradiances consistent with CERES-derived top-of-atmosphere shortwave and longwave irradiances. *J. Climate*, **26**, 2719–2740, doi:10.1175/JCLI-D-12-00436.1.

Kindel, B. C., P. Pilewskie, K. S. Schmidt, O. Coddington, and M. D. King, 2011: Solar spectral absorption by marine stratus clouds: Measurements and modeling. *J. Geophys. Res.*, **116**, D10203, doi:10.1029/2010JD015071.

Kipp & Zonen, 2001: CG4 pyrgeometer: Instruction manual. 64 pp. [Available online at www.kippzonen.com/Download/33/CG-4-Manual.]

——, 2004: CM22 precision pyranometer: Instruction manual. 65 pp. [Available online at www.kippzonen.com/Download/55/CM-22-Pyranometer-Manual.]

LeBlanc, S. E., P. Pilewskie, K. S. Schmidt, and O. Coddington, 2015: A spectral method for discriminating thermodynamic phase and retrieving cloud optical thickness and effective radius using transmitted solar radiance spectra. *Atmos. Meas. Tech.*, **8**, 1361–1383, doi:10.5194/amt-8-1361-2015.

Loeb, N. G., K. J. Priestley, D. P. Kratz, E. B. Geier, R. N. Green, B. A. Wielicki, P. O'Rawe Hinton, and S. K. Nolan, 2001: Determination of unfiltered radiances from the Clouds and the Earth's Radiant Energy System instrument. *J. Appl. Meteor.*, **40**, 822–835, doi:10.1175/1520-0450(2001)040<0822:DOURFT>2.0.CO;2.

——, S. Kato, K. Loukachine, and N. Manalo-Smith, 2005: Angular distribution models for top-of-atmosphere radiative flux estimation from the Clouds and the Earth's Radiant Energy System instrument on the *Terra* satellite. Part I: Methodology. *J. Atmos. Oceanic Technol.*, **22**, 338, doi:10.1175/JTECH1712.1.

——, B. A. Wielicki, D. R. Doelling, G. L. Smith, D. F. Keyes, S. Kato, N. Manalo-Smith, and T. Wong, 2009: Toward optimal closure of the Earth's top-of-atmosphere radiation budget. *J. Climate*, **22**, 748–766, doi:10.1175/2008JCLI2637.1.

——, S. Kato, W. Su, T. Wong, F. G. Rose, D. R. Doelling, J. R. Norris, and X. Huang, 2012: Advances in understanding top-of-atmosphere radiation variability from satellite observations. *Surv. Geophys.*, **33**, 359–385, doi:10.1007/s10712-012-9175-1.

Long, C. N., A. Bucholtz, H. Jonsson, B. Schmid, A. Vogelmann, and J. Wood, 2010: A method of correcting for tilt from horizontal in downwelling shortwave irradiance measurements on moving platforms. *Open Atmos. Sci. J.*, **4**, 78–87, doi:10.2174/1874282301004010078.

Lubin, D., and A. M. Vogelmann, 2011: The influence of mixed-phase clouds on surface shortwave irradiance during the Arctic spring. *J. Geophys. Res.*, **116**, D00T05, doi:10.1029/2011JD015761.

McBride, P. J., K. S. Schmidt, P. Pilewskie, A. Walther, A. K. Heidinger, D. E. Wolfe, C. W. Fairall, and S. Lance, 2012: CalNex cloud properties retrieved from a ship-based spectrometer and comparisons with satellite and aircraft retrieved cloud properties. *J. Geophys. Res.*, **117**, D00V23, doi:10.1029/2012JD017624.

Minnis, P., and Coauthors, 2011: CERES Edition-2 cloud property retrievals using TRMM VIRS and Terra and Aqua MODIS data—Part I: Algorithms. *IEEE Trans. Geosci. Remote Sens.*, **49**, 4374–4400, doi:10.1109/TGRS.2011.2144601.

Molod, A. M., L. L. Takacs, M. Suarez, and J. Bacmeister, 2015: Development of the GEOS-5 atmospheric general circulation model: Evolution from MERRA to MERRA2. *Geosci. Model Dev.*, **8**, 1339–1356, doi:10.5194/gmd-8-1339-2015.

Perovich, D. K., and C. Polashenski, 2012: Albedo evolution of seasonal Arctic sea ice. *Geophys. Res. Lett.*, **39**, L08501, doi:10.1029/2012GL051432.

——, J. A. Richter-Menge, K. F. Jones, and B. Light, 2008: Sunlight, water, and ice: Extreme Arctic sea ice melt during the summer of 2007. *Geophys. Res. Lett.*, **35**, L11501, doi:10.1029/2008GL034007.

Pilewskie, P. J., and Coauthors, 2003: Solar spectral radiative forcing during the Southern African Regional Science Initiative. *J. Geophys. Res.*, **108**, 8486, doi:10.1029/2002JD002411.

Pincus, R., C. P. Batstone, R. J. P. Hofmann, K. E. Taylor, and P. J. Glecker, 2008: Evaluating the present-day simulation of clouds, precipitation, and radiation in climate models. *J. Geophys. Res.*, **113**, D14209, doi:10.1029/2007JD009334.

Pinto, J. O., 1998: Autumnal mixed-phase cloudy boundary layers in the Arctic. *J. Atmos. Sci.*, **55**, 2016–2038, doi:10.1175/1520-0469(1998)055<2016:AMPCBL>2.0.CO;2.

Rienecker, M. M., and Coauthors, 2008: The GOES-5 data assimilation system—Documentation of versions 5.0.1, 5.1.0, and 5.2.0. M. J. Suarez, Ed., Technical Report Series on Global Modeling and Data Assimilation, Vol. 27, NASA Tech. Memo. NASA/TM-2008-104606, 101 pp. [Available online at https://ntrs.nasa.gov/archive/nasa/casi.ntrs.nasa.gov/20120011955.pdf.]

Rutan, D. A., S. Kato, D. R. Doelling, F. G. Rose, L. T. Nguyen, T. E. Caldwell, and N. G. Loeb, 2015: CERES synoptic product: Methodology and validation of surface radiant flux. *J. Atmos. Oceanic Technol.*, **32**, 1121–1143, doi:10.1175/JTECH-D-14-00165.1.

Schmidt, K. S., and P. Pilewskie, 2012: Airborne measurements of spectral shortwave radiation in cloud and aerosol remote sensing and energy budget studies. *Light Scattering Reviews 6: Light Scattering and Remote Sensing of Atmosphere and Surface*, A. A. Kokhanovsky, Ed., Springer, 239–288, doi:10.1007/978-3-642-15531-4_6.

Schmidt, K. S., and Coauthors, 2010: Apparent absorption of solar spectral irradiance in heterogeneous ice clouds. *J. Geophys. Res.*, **115**, D00J22, doi:10.1029/2009JD013124.

Segal Rosenhaimer, M., P. B. Russell, J. M. Livingston, S. Ramachandran, J. Redemann, and B. A. Baum, 2013: Retrieval of cirrus properties by Sun photometry: A new perspective on an old issue. *J. Geophys. Res. Atmos.*, **118**, 4503–4520, doi:10.1002/jgrd.50185.

——, and Coauthors, 2014: Tracking elevated pollution layers with a newly developed hyperspectral Sun/Sky spectrometer (4STAR): Results from the TCAP 2012 and 2013 campaigns. *J. Geophys. Res. Atmos.*, **119**, 2611–2628, doi:10.1002/2013JD020884.

Shinozuka, Y., and Coauthors, 2013: Hyperspectral aerosol optical depths from TCAP flights. *J. Geophys. Res.*, **118**, 12 180–12 194, doi:10.1002/2013JD020596.

Shiobara, M., and S. Asano, 1994: Estimation of cirrus optical thickness from sun photometer measurements. *J. Appl. Meteor.*, **33**, 672–681, doi:10.1175/1520-0450(1994)033<0672:EOCOTF>2.0.CO;2.

Song, S., and Coauthors, 2016: The spectral signature of cloud spatial structure in shortwave irradiance. *Atmos. Chem. Phys.*, **16**, 13 791–13 806, doi:10.5194/acp-16-13791-2016.

Strapp, J. W., and R. S. Schemenauer, 1982: Calibrations of Johnson-Williams liquid water content meters in a high-speed icing tunnel. *J. Appl. Meteor.*, **21**, 98–108, doi:10.1175/1520-0450(1982)021<0098:COJWLW>2.0.CO;2.

Stroeve, J. C., M. C. Serreze, M. M. Holland, J. E. Kay, J. Maslanik, and A. P. Barrett, 2012: The Arctic's rapidly shrinking sea ice cover: A research synthesis. *Climatic Change*, **11**, 1005–1027, doi:10.1007/s10584-011-0101-1.

——, T. Markus, L. Boisvert, J. Miller, and A. Barrett, 2014: Changes in Arctic melt season and implications for sea ice loss. *Geophys. Res. Lett.*, **41**, 1216–1225, doi:10.1002/2013GL058951.

Su, W., J. Corbett, Z. Eitzen, and L. Liang, 2015a: Next-generation angular distribution models for top-of-atmosphere radiative flux calculation from CERES instruments: Methodology. *Atmos. Meas. Tech.*, **8**, 611–632, doi:10.5194/amt-8-611-2015.

——, ——, ——, and ——, 2015b: Next-generation angular distribution models for top-of-atmosphere radiative flux calculation from the CERES instruments: Validation. *Atmos. Meas. Tech.*, **8**, 3297–3313, doi:10.5194/amt-8-3297-2015.

Tjernström, M., J. Sedlar, and M. D. Shupe, 2008: How well do regional climate models reproduce radiation and clouds in the Arctic? An evaluation of ARCMIP simulations. *J. Appl. Meteor. Climatol.*, **47**, 2405–2422, doi:10.1175/2008JAMC1845.1.

——, and Coauthors, 2012: Meteorological conditions in the central Arctic summer during the Arctic Summer Cloud Ocean Study (ASCOS). *Atmos. Chem. Phys.*, **12**, 6863–6889, doi:10.5194/acp-12-6863-2012.

Verlinde, J., and Coauthors, 2007: The Mixed-Phase Arctic Cloud Experiment. *Bull. Amer. Meteor. Soc.*, **88**, 205–221, doi:10.1175/BAMS-88-2-205.

Vihma, T., and Coauthors, 2014: Advances in understanding and parameterization of small-scale physical processes in the marine Arctic climate system: A review. *Atmos. Chem. Phys.*, **14**, 9403–9450, doi:10.5194/acp-14-9403-2014.

Wang, H., and W. Su, 2013: Evaluating and understanding top of the atmosphere cloud radiative effects in Intergovernmental Panel on Climate Change (IPCC) Fifth Assessment Report (AR5) Coupled Model Intercomparison Project Phase 5 (CMIP5) models using satellite observations. *J. Geophys. Res. Atmos.*, **118**, 683–699, doi:10.1029/2012JD018619.

Wendisch, M., D. Müller, D. Schell, and J. Heintzenberg, 2001: An airborne spectral albedometer with active horizontal stabilization. *J. Atmos. Oceanic Technol.*, **18**, 1856–1866, doi:10.1175/1520-0426(2001)018<1856:AASAWA>2.0.CO;2.

——, and Coauthors, 2013: Atmospheric radiation measurements. *Airborne Measurements for Environmental Research: Methods and Instruments*, M. Wendisch and J.-L. Brenguier, Eds., Wiley, 343–412.

Zhang, J., R. Lindsay, M. Steele, and A. Schweiger, 2008: What drove the dramatic retreat of arctic sea ice during summer 2007? *Geophys. Res. Lett.*, **35**, L11505, doi:10.1029/2008GL034005.

Zhang, J.-L., F. Liu, W. Tao, J. Krieger, M. Shulski, and X. Zhang, 2016: Mesoscale climatology and variation of surface winds over the Chukchi–Beaufort coastal areas. *J. Climate*, **29**, 2721–2739, doi:10.1175/JCLI-D-15-0436.1.

THE SAHARAN AEROSOL LONG-RANGE TRANSPORT AND AEROSOL–CLOUD-INTERACTION EXPERIMENT

Overview and Selected Highlights

Bernadett Weinzierl, A. Ansmann, J. M. Prospero, D. Althausen, N. Benker, F. Chouza, M. Dollner, D. Farrell, W. K. Fomba, V. Freudenthaler, J. Gasteiger, S. Groß, M. Haarig, B. Heinold, K. Kandler, T. B. Kristensen, O. L. Mayol-Bracero, T. Müller, O. Reitebuch, D. Sauer, A. Schäfler, K. Schepanski, A. Spanu, I. Tegen, C. Toledano, and A. Walser

The aircraft and ground-based SALTRACE campaign in the tropical Atlantic in 2013/14 characterized the large-scale transport of African dust, dust "aging" during transit, and its impact on radiation and cloud microphysics.

Although substantial effort has been undertaken in the last decades to improve our knowledge about the role of aerosols in the climate system, aerosols and clouds still pose the largest uncertainty to estimates and interpretations of Earth's changing energy budget (IPCC 2013). Among aerosols, mineral dust particles (herein, simply "dust particles" or "dust") are of key importance because they contribute to about half of the global annual particle emissions by mass (Hinds 1999; Huneeus et al. 2011); significantly impact the radiation budget of Earth by scattering, absorption, and emission of solar and terrestrial radiation (Sokolik et al. 2001; Tegen 2003; Balkanski et al. 2007); act as cloud condensation nuclei (CCN); and have been identified as effective ice nucleating particles (INP; Hoose and Möhler 2012). Deposited dust can be a significant nutrient to the ocean (Jickells et al. 2005; Maher et al. 2010; Niedermeier et al. 2014). In addition, dust may have a severe impact on aviation by causing poor visibility (Weinzierl et al. 2012) affecting the takeoff and landing of aircraft. Last but not least, there is increasing evidence that dust might be a human health concern (Goudie 2014; Morman and Plumlee 2014).

The major dust source regions are located in the Northern Hemisphere and extend from the west coast of North Africa, through the Middle East, to Central Asia and China. Aerosol Comparisons between Observations and Models (AeroCom) simulations estimate that North Africa including the Sahara emits about 200–3,000 Tg of dust every year, thereby contributing about 70% to the total global dust emission (Huneeus et al. 2011). African dust is regularly transported westward across the Atlantic Ocean to the Caribbean (e.g., Prospero 1999; Prospero and Lamb 2003; Stevens et al. 2016), the southern United States (Prospero 1999), and northeastern South America (Swap et al. 1992; Prospero et al. 2014).

Publisher's Note: On 25 July 2017 this article was revised to correct an in-text citation for Walser et al. (2017).

During the summer months the main dust transport takes place in the Saharan air layer (SAL), a hot, dry, elevated layer that has its origins over the Sahara Desert (Carlson and Prospero 1972; Prospero and Carlson 1972). The SAL often covers large parts of the tropical Atlantic Ocean and can be easily tracked by satellite observations of aerosol optical depth (AOD) and lidar (e.g., Liu et al. 2008; Chouza et al. 2016a). Presently, the SAL is attracting great interest because it is suspected to influence tropical cyclone activity (e.g., Dunion and Velden 2004; Braun 2010; Evan et al. 2011; Peng et al. 2012; Brammer and Thorncroft 2015; Hankes et al. 2015). However, the details of this influence are not yet understood.

In the past decade several comprehensive airborne dust field experiments including the Saharan Mineral Dust Experiment (SAMUM-1, Heintzenberg 2009; SAMUM-2, Ansmann et al. 2011) were performed in the vicinity of the Sahara and in the outflow region of African dust in the Cabo Verde area. Table 1 and references therein give an overview over major airborne dust field experiments over Africa, the Atlantic Ocean, and in the Caribbean. Although a few airborne dust campaigns focused on the Caribbean, most of these previous measurements in the Caribbean only covered altitudes below 3 km, and they lacked the extensive instrumentation available to us in the Saharan Aerosol Long-Range Transport and Aerosol–Cloud-Interaction Experiment (SALTRACE). Recent ground-based measurements at the Caribbean island of Puerto Rico studied African dust size distribution, optical properties, dust-cloud impacts (Spiegel et al. 2014; Raga et al. 2016), and chemical composition (Gioda et al. 2013; Denjean et al. 2015; Fitzgerald et al. 2015; Denjean et al. 2016; Valle-Diaz et al. 2016).

Despite substantial progress, many questions concerning the role of dust in the climate system remain open (e.g., Ansmann et al. 2011; Ryder et al. 2015). For example, the uncertainty of Intergovernmental Panel on Climate Change (IPCC) Assessment Report 5 estimates for global average direct radiative forcing by anthropogenic mineral dust aerosol that is assumed to be 20% of total dust is [−0.3; +0.1] Wm^{-2} (Table 8.4 in Myhre et al. 2013). This range has not changed since the previous IPCC report in 2007, indicating further research needs.

A critical parameter for the derivation of radiative forcing estimates is the particle size distribution that is set at emission (Mahowald et al. 2014), but changes during long-range transport. For example, preferably large supermicron dust particles are lost through gravitational settling and efficient particle aging occurs when particles act as CCN and INP (Pöschl 2005). Cloud processing is one possible pathway producing sulfate-coated dust particles and changing the aerosol size spectrum (e.g., Levin et al. 1996; Wurzler et al. 2000), thus changing the probability of rain formation and influencing wet deposition of dust. Recent laboratory measurements indicate that dust particles may become better CCN after cloud processing (Kumar et al. 2011). Understanding the very complex interaction between aerosols, clouds, and precipitation is challenging and requires comprehensive, coordinated, and long-term measurements and state-of-the-art modeling (Stevens and Feingold 2009). Many models have attempted to simulate the effects of aging (e.g., Abdelkader et al. 2015), but it is difficult to assess the validity of these results because of the absence of data with which to test the effect.

AFFILIATIONS: Weinzierl and Spanu—Universität Wien (UNIVIE), Fakultät für Physik, Aerosolphysik und Umweltphysik, Wien, Austria, and Institut für Physik der Atmosphäre, Deutsches Zentrum für Luft- und Raumfahrt (DLR), Oberpfaffenhofen, Germany; Ansmann, Althausen, Fomba, Haarig, Heinold, Kristensen, Müller, Schepanski, and Tegen—Leibniz Institute for Tropospheric Research (TROPOS), Leipzig, Germany; Prospero—University of Miami, Miami, Florida; Benker and Kandler—Institut für Angewandte Geowissenschaften, Technische Universität Darmstadt, Darmstadt, Germany; Chouza, Groß, Reitebuch, Sauer, and Schäfler— Institut für Physik der Atmosphäre, Deutsches Zentrum für Luft- und Raumfahrt (DLR), Oberpfaffenhofen, Germany; Dollner and Gasteiger—Universität Wien (UNIVIE), Fakultät für Physik, Aerosolphysik und Umweltphysik, Wien, Austria, and Ludwig-Maximilians-Universität (LMU), Meteorologisches Institut, München, Germany; Farrell—Caribbean Institute for Meteorology and Hydrology (CIMH), Bridgetown, Barbados; Freudenthaler—Ludwig-Maximilians-Universität (LMU), Meteorologisches Institut, München, Germany; Mayol-Bracero—Department of Environmental Science, University of Puerto Rico, San Juan, Puerto Rico; Toledano—Grupo de Óptica Atmosférica, Universidad de Valladolid, Valladolid, Spain; Walser—Ludwig-Maximilians-Universität (LMU), Meteorologisches Institut, München, and Institut für Physik der Atmosphäre, Deutsches Zentrum für Luft- und Raumfahrt (DLR), Oberpfaffenhofen, Germany

CORRESPONDING AUTHOR: Bernadett Weinzierl, bernadett.weinzierl@univie.ac.at

The abstract for this article can be found in this issue, following the table of contents.
DOI:10.1175/BAMS-D-15-00142.1

A supplement to this article is available online (10.1175/BAMS-D-15-00142.2)

In final form 21 November 2016

In a recent review, Mahowald et al. (2014) concluded that new measurements of dust size distributions agree roughly within the size range between 0.1- and 5-μm particle diameters, but below and above this size range, the dust size distribution is not well understood. In particular, it is not clear why in situ observations generally lead to considerably larger mean particle sizes than retrievals from remote sensing instruments (Reid et al. 2003a; Müller et al. 2010; Toledano et al. 2011). This is particularly important for radiative forcing estimates, as the coarse mode size distribution has a strong impact on the radiative budget and can even switch the sign of the radiative forcing from a net cooling to heating (Otto et al. 2007).

These various studies demonstrate that dust is associated with a significant climate effect and may have a substantial impact on cloud processes and, furthermore, that particle aging might enhance these effects. We lack the understanding of the processes that lead to mixing of dust with other aerosols and of the factors that affect dust deposition.

In SALTRACE we collected a unique dataset that provides new insights into these processes. This article presents an overview of the SALTRACE program and highlights important results. In "Overview of the SALTRACE project," we introduce the SALTRACE measurement sites, intensive observation periods, and instrumentation. The remaining sections respectively evaluate the SALTRACE measurements in the context of the 50-yr Barbados dust record, describe the dust source activity during SALTRACE and follow with the conceptual "big picture" of transatlantic dust transport, and highlight selected SALTRACE results including the modification of dust during transatlantic transport, the passage of Tropical Storm Chantal and its impact on the dust layer structure, and dust as a reservoir/source for CCN and INP.

OVERVIEW OF THE SALTRACE PROJECT.

SALTRACE (www.pa.op.dlr.de/saltrace) was conducted from spring 2013 through summer 2014. Table 2 gives an overview of activities performed within the SALTRACE framework. The core of the SALTRACE program was an atmospheric column closure experiment[1] in June and July 2013 involving ground-based and airborne in situ and remote sensing observations in Barbados (main supersite), Puerto Rico, and Cabo Verde. For the airborne SALTRACE measurements, the Deutsches Zentrum für Luft- und Raumfahrt (DLR) research aircraft Falcon was equipped with a suite of in situ instruments for the determination of microphysical and optical aerosol properties, and with sampling devices for offline particle analysis, a nadir-looking 2-μm wind lidar, dropsondes, and instruments for standard meteorological parameters. Details about the instrumentation at the main supersite in Barbados and on the research aircraft as well as accompanied modeling activities at large-eddy and regional scale are given in Table ES1 of the supplemental material (http://dx.doi.org/10.1175/BAMS-D-15-00142.2). Before the measurements in June and July 2013, a cruise of the Research Vessel *Meteor* between Guadeloupe and Cabo Verde took place in April and May 2013 (Kanitz et al. 2014). Later, in February and March 2014 (SALTRACE-2) and June and July 2014 (SALTRACE-3), additional intensive ground-based lidar and sun photometer observations followed to cover the annual variability of dust flow into the Caribbean (Table 2).

Figure 1 sketches the airborne SALTRACE observations in summer 2013 including flight tracks (red lines). Figure 2 shows the Falcon base at Grantley International Airport together with the measurement locations of the in situ and remote sensing measurements on Barbados. In total, 31 research flights were performed. The DLR research aircraft Falcon spent more than 86 of a total of 110 flight hours studying dust from several dust outbreaks under a variety of atmospheric conditions between Senegal, Cabo Verde, the Caribbean, and Florida.

A detailed list of SALTRACE flights including takeoff time, landing time, and objective is provided in the supplemental material (Table ES2). The flights in the Cabo Verde region (11–17 June 2013) aimed to characterize dust close to the source region and are also used for comparison with data from SAMUM-2 measurements (January and February 2008) in the Cabo Verde area (Ansmann et al. 2011; Weinzierl et al. 2011; references therein). The first part of the research flights in the Caribbean (20–26 June 2013) studied the horizontal variability of dust properties with extended east–west and north–south sampling flights and included the transatlantic dust sampling of the same air mass on both sides of the Atlantic (17 and 22 June 2013). The flights on 30 June and 1 July were intended to investigate the variability of dust properties between Barbados, Antigua, and Puerto Rico and to study the wet deposition of dust. The second half of the measurements (5–12 July 2013) focused on extended vertical profiling over the Atlantic east of Barbados, over the lidar and

---

[1] Atmospheric column closure experiments aim to characterize the same parameters of a system with different, independent methods and models to minimize the measurement uncertainties through comparison of the derived values.

Table 1. Overview of airborne mineral dust field experiments near the dust sources over Africa, the Atlantic Ocean, and in the Caribbean mainly focusing on the past two decades. AMMA-SOP0: African Monsoon Multidisciplinary Analysis–Special Observation Period 0; BACEX: Barbados Aerosol Cloud Experiment; BOMEX: Barbados Oceanic and Meteorological Experiment; CARRIBA: Cloud, Aerosol, Radiation and Turbulence in the Trade Wind Regime over Barbados; CRYSTAL-FACE: Cirrus Regional Study of Tropical Anvils and Cirrus Layers—Florida-Area Cirrus Experiment; DABEX: Dust and Biomass-Burning Experiment; DODO: Dust Outflow and Deposition to the Ocean; Fennec: not an acronym; GERBILS: Geostationary Earth Radiation Budget Intercomparison of Longwave and Shortwave Radiation; ICE-D: Ice in Cloud Experiments—Dust; NAMMA: NASA AMMA; PRIDE: Puerto Rico Dust Experiment; SAMUM: Saharan Mineral Dust Experiment; SHADE: Saharan Dust Experiment.

Campaign acronym	Time span	Region	Objective/science focus	Overview
Field experiments near the dust sources/Africa				
SAMUM-1	May and Jun 2006	Southern Morocco	Characterize Saharan aerosol near the source region and quantify dust-related radiative effects	Heintzenberg (2009)
AMMA-SOP0	Jan and Feb 2006	West Africa	Characterize Saharan aerosol and biomass-burning aerosols from West Africa	Redelsperger et al. (2006)
DABEX	Jan and Feb 2006	Niger	Same topic as AMMA-SOP0	Haywood et al. (2008)
DODO	Feb and Aug 2006	West Africa	Characterize Saharan dust in two seasons, constrain model simulations, quantify deposition of iron to the North Atlantic Ocean	McConnell et al. (2008)
GERBILS	Jun 2007	North Africa	Geographic distribution and physical and optical properties of Saharan dust, impact on radiation, validation of satellite retrievals and numerical weather prediction models	Haywood et al. (2011)
FENNEC	Apr and Jun 2011, Jun 2012	Algeria and Mauritania	Improve understanding of the Saharan climate system through a synergy of observations and modeling	Washington et al. (2012); Ryder et al. (2015)
Atlantic Ocean off the coast of Africa				
SHADE	Sep 2000	Cabo Verde	Investigation of aerosol parameters relevant for the determination of the direct radiative effect	Tanré et al. (2003)
NAMMA	Aug–Sep 2006	Cabo Verde	Improve understanding of the relationship between the African easterly waves, the SAL, and tropical cyclogenesis	Zipser et al. (2009)
SAMUM-2	Jan and Feb 2008	Cabo Verde	Characterize Saharan aerosol and biomass-burning aerosol over the eastern Atlantic	Ansmann et al. (2011)
SAMUM-2b	May and Jun 2008	Cabo Verde	Same as SAMUM-2, but summer measurements	Ansmann et al. (2011)
SALTRACE	Apr–Jul 2013, see Table 2	Cabo Verde	Characterize dust properties before long-range transport with the same instrumentation as over the Caribbean	This study
ICE-D	Aug 2015	Cabo Verde	Study influence of mineral dust on clouds and improve representation of dust-produced INP and CCN in models	Cotton (2016)
Caribbean				
BOMEX	May–Jul 1969	Barbados	Measure vertical distribution of Saharan dust in the Caribbean and quantify dust transport over Atlantic	Prospero and Carlson (1972)
PRIDE	Jun and Jul 2000	Caribbean	Understand the issues of dust transport and radiative forcing in the subtropical North Atlantic Ocean	Reid et al. (2003b)
CRYSTAL-FACE	Jul 2002	Southern Florida	Investigate ice nucleation potential of long-range transported Saharan dust	Sassen et al. (2003)
BACEX	Mar and Apr 2010	Barbados	Observe cloud–aerosol interactions	Jung et al. (2013)

CARIBBA	Nov 2010 and Apr 2011	Barbados	High-resolution and collocated measurements of trade wind cumuli and aerosol to characterize aerosol–cloud interactions	Siebert et al. (2013)
SALTRACE	2013/14, see Table 2	Barbados and Caribbean	Characterize properties of aged dust in the Caribbean, quantify the impact of "aging" on the radiation budget and cloud microphysical processes, investigate the meteorological context of transatlantic dust transport, and assess the roles of removal processes during transport	This study

ground sites on Barbados, and west of the Caribbean islands to study downwind transport from Barbados and island effects (Chouza et al. 2016b; Jähn et al. 2016). Furthermore, we had the unique opportunity to make measurements before, during, and after the passage of Tropical Storm Chantal (8–10 July 2013). To our knowledge, these are the first measurements of dust conditions in the vicinity of such a storm ever made with an extensive aerosol instrument package. A second sequence of dust sampling flights was performed toward Puerto Rico and into the Bahamas–Florida area (11–13 July 2013). The flight program culminated with a route that took the Falcon along the East Coast of the United States, across the high-latitude North Atlantic, and back to our home base in Germany. During the flights back to Germany, the Falcon encountered thick smoke layers where refractory black carbon mass mixing ratios reached values as high as 100–380 ng kg^{-1}, higher than the values around 270 ng kg^{-1} observed in an intense smoke layer in the upper troposphere over Germany originating from the pyroconvective Pagami Creek fire (Minnesota, United States) (Dahlkötter et al. 2014).

SALTRACE IN THE CONTEXT OF THE 50-YR BARBADOS DUST RECORD. Barbados was chosen as main supersite for SALTRACE because it is the easternmost island of the Caribbean which enables measurements of undisturbed African dust layers after they transit the Atlantic. Furthermore, Barbados has the world's longest record of ground-based dust measurements, which started in 1965 and continues today (Prospero and Lamb 2003; Prospero et al. 2014), allowing us to evaluate the SALTRACE data in long-term context.

Dust transport follows a pronounced seasonal cycle with a minimum in winter and a maximum in summer peaking in June–August (Doherty et al. 2008; Prospero et al. 2014). Figure 3 depicts average summer (June–August) dust mass concentration values measured at Ragged Point, Barbados, between 1965 and 2013. The years of the SAMUM and SALTRACE measurements are indicated in red. Average summer dust mass concentrations vary from less than 10 to around 50 μg m^{-3} from year to year. The periods of high dust concentrations in the early 1970s and in the mid-1980s were linked to drought conditions in Africa (Prospero and Lamb 2003; Prospero et al. 2014), and the variability of the winds over the Sahara has been shown to impact in the dust load over the Atlantic (Wang et al. 2015; Evan et al. 2016). The causes of the variation in dust transport since the 1980s are still a subject of research and numerous efforts have been made to relate the Barbados dust record to various climate indices—for example, El Niño–Southern Oscillation (ENSO) (Prospero and Lamb 2003; DeFlorio et al. 2016), North Atlantic Oscillation (NAO) (Ginoux et al. 2004; Evan et al. 2006), and Atlantic Multidecadal Oscillation (AMO) (Evan et al. 2011; Wang et al. 2012; DeFlorio et al. 2016). Of these the AMO seems to have played a particularly strong role. However, it is notable that high concentrations in 1997/98 were coincident with an exceptionally strong El Niño. Since about 1970, excepting the periods of high concentration in summer, low summer-mean values seem to fall between 15 and 20 μg m^{-3}, which might be thought of as a "background" value range. The mean value of 21 μg m^{-3} during SALTRACE is slightly above in this range. Thus, measurements made during SALTRACE could be regarded as being representative of "normal" dust conditions.

Figure 4 shows time series of AOD (black crosses) measured with Aerosol Robotic Network (AERONET; http://aeronet.gsfc.nasa.gov/) sun photometers at Cabo Verde, Barbados, and Puerto Rico throughout the main SALTRACE period. It illustrates the dust layer at Barbados with a time–height cross section of volume linear depolarization ratio (VLDR; for details, see discussion of Fig. 6). Maximum AOD (500 nm) detected with the sun photometers reached values of 0.85 at Cabo Verde, 0.61 at Barbados, and 0.56 at Puerto Rico during SALTRACE. The ground-based lidar measurements at Barbados showed that mineral dust contributed about 50%–70% of the total AOD at 532 nm (Groß et al. 2015). The red triangles in Fig. 4 indicate the median AOD (500 nm) during the 3–4-h duration of the individual Falcon flights, which fell into the ranges 0.5–0.8 for flights in the Cabo Verde area and 0.1–0.5 for flights in the Caribbean. The Ångström exponent of the AOD at the Barbados site (not shown) was around 0.2 on most days except for very clean (dust free) days where it increased to 0.5.

Most Falcon flights were performed during high-dust-concentration conditions, but some flights also focused on low-dust conditions. Figure 4 shows surface-level dust mass concentration at Ragged Point (blue dots) [see Kristensen et al. (2016) for more details on ground-based measurements during SALTRACE]. The dust mass concentration was derived from spectral absorption coefficients measured with a spectral optical absorption photometer (SOAP; Müller et al. 2009) by fitting spectral mass absorption coefficients between wavelengths 425 and 675 nm to the measurements following a reanalysis of data from Müller et al. (2009) and Schladitz et al. (2009).

The temporal trends of AOD and dust concentration at the ground agree well indicating that 1) dust makes a major contribution to the AOD in the Caribbean, 2) dust transported at higher altitudes into the Caribbean in the SAL is effectively mixed down into the boundary layer over Barbados, and 3) we can expect good comparability between ground-based,

Table 2. Airborne, ground-based, and shipborne measurements in the context of SALTRACE.

Activity	Time	Observations, location	Aerosol layering
METEOR-cruise	29 Apr–23 May 2013	Shipborne lidar, Guadeloupe–Cabo Verde	Dust above marine
SALTRACE	10 Jun–15 Jul 2013	SALTRACE column experiment (ground-based and airborne in situ and remote sensing observations); for measurement locations see Fig. 1	Dust above marine
SALTRACE-2	15 Feb–8 Mar 2014	Ground-based lidar and sun photometers, Barbados	Smoke/dust above marine
SALTRACE-3	19 Jun–12 Jul 2014	Ground-based lidar and sun photometers, Barbados	Dust above marine

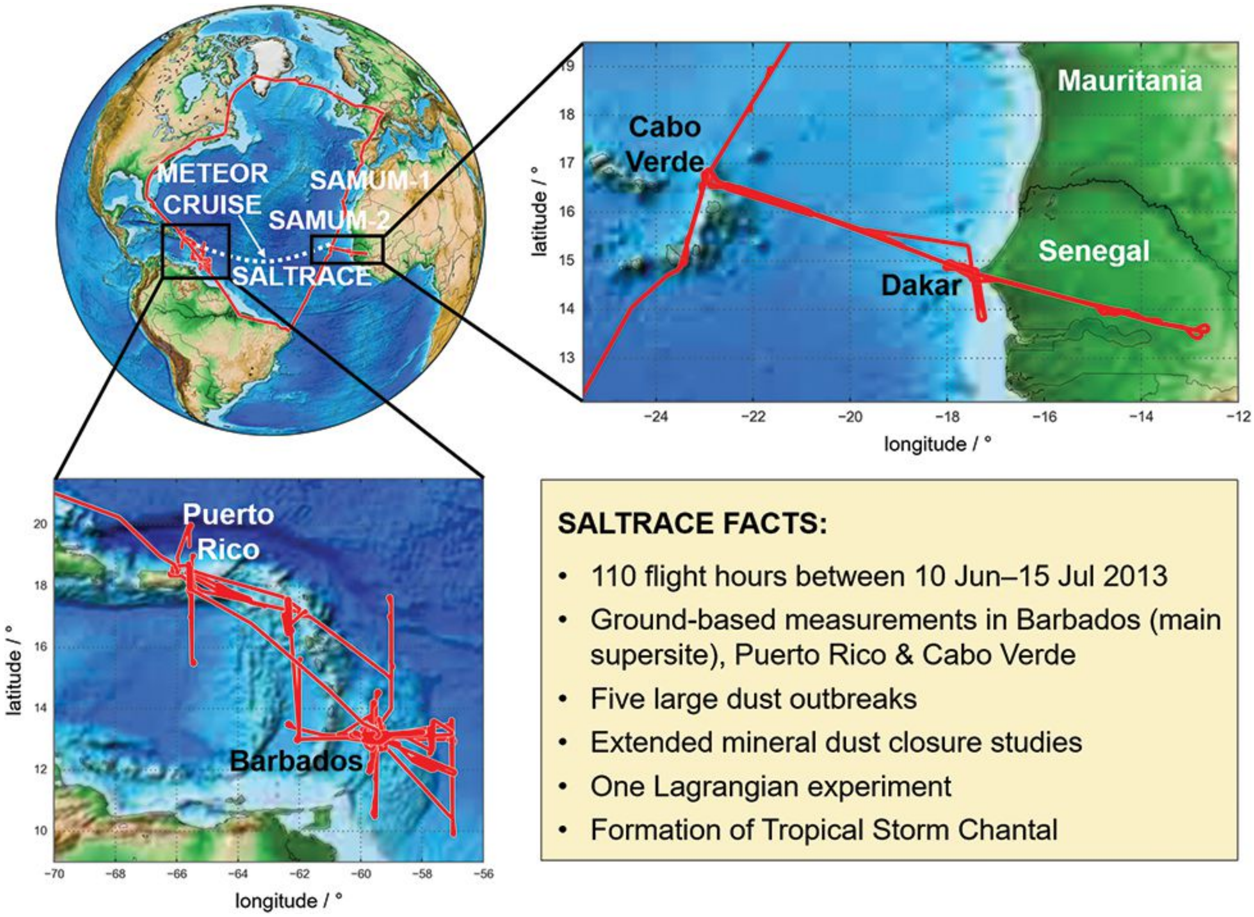

SALTRACE FACTS:

- 110 flight hours between 10 Jun–15 Jul 2013
- Ground-based measurements in Barbados (main supersite), Puerto Rico & Cabo Verde
- Five large dust outbreaks
- Extended mineral dust closure studies
- One Lagrangian experiment
- Formation of Tropical Storm Chantal

Fig. 1. Flight tracks (red lines) of the airborne SALTRACE observations (note: no data are available in Brazilian airspace) in summer 2013 with the ground sites in Barbados (main supersite), Cabo Verde, and Puerto Rico indicated. Furthermore, the locations of the SAMUM measurements in Morocco (2006) and Cabo Verde (2008) are shown.

airborne, and remote sensing observations (see also Fig. 12). Previously, Smirnov et al. (2000) had shown that monthly means of AOD and ground-based dust concentrations were highly correlated at Barbados. Our results show a good correlation on a daily basis.

DUST SOURCE ACTIVITY DURING SALTRACE. Various sources across North Africa contribute to the dust load in the Caribbean. Figure 5 summarizes the most active dust sources for SALTRACE, SAMUM-1, and SAMUM-2. The dust source activity (DSA) was inferred from infrared dust index images calculated from brightness temperature measurements by the Spinning Enhanced Visible and Infrared Imager (SEVIRI) on board the Meteosat Second Generation (MSG) satellite

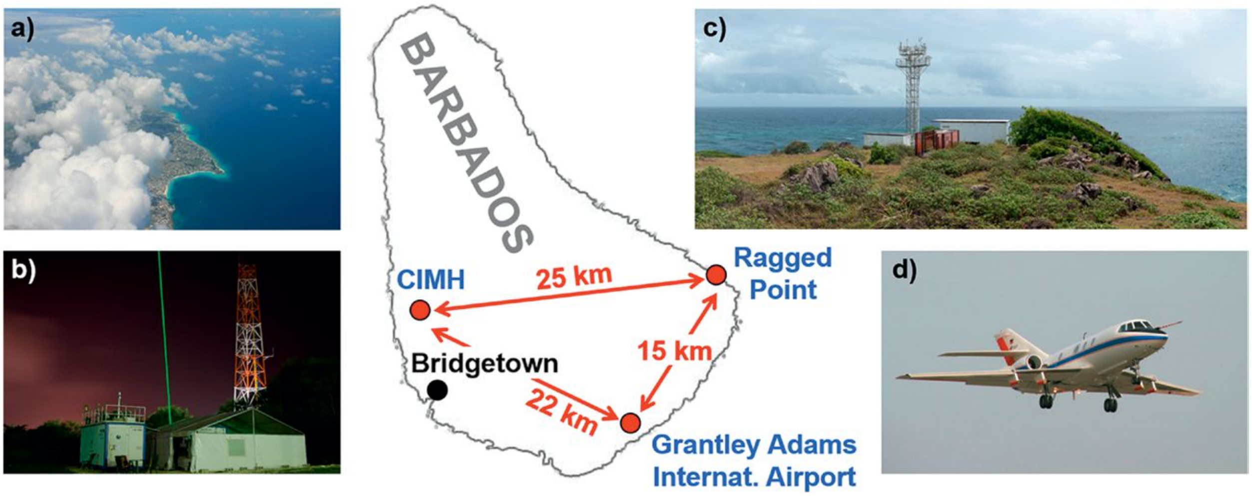

Fig. 2. Map with SALTRACE measurement locations on Barbados. (a) Photograph of trade wind cumuli over Barbados that were frequently observed. (b) Lidar and sun photometer container at Caribbean Institute for Hydrology and Meteorology, Barbados (13°8′55″N, 59°37′29″W). The green line is the laser beam from the TROPOS lidar instrument. (c) Measurement tower with the ground-based in situ measurements at Ragged Point (13°09′54″N, 59°25′56″W). (d) The DLR Falcon research aircraft taking off at Barbados (13°4′32″N, 59°29′30″W) on 20 Jun 2013.

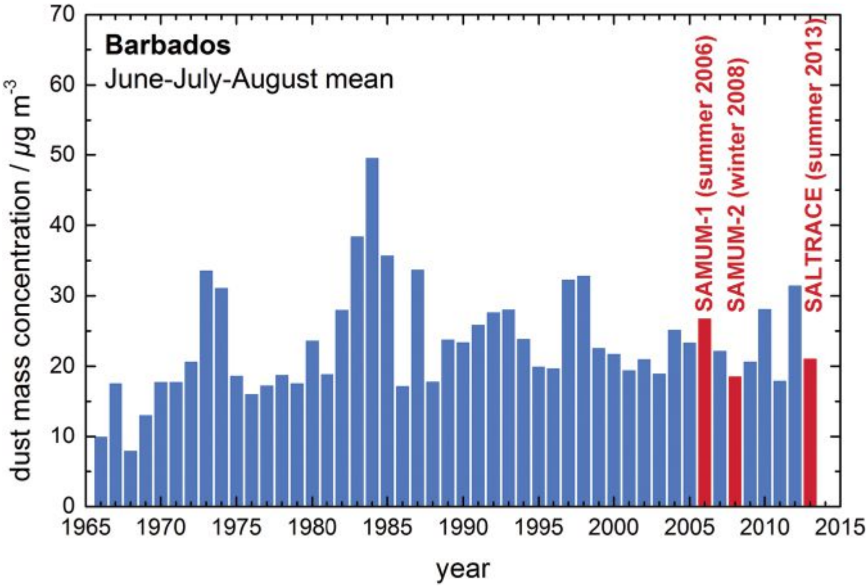

Fig. 3. Summer (Jun–Aug)-mean dust concentrations at Barbados from 1965 to 2013 with the years of the airborne field experiments SAMUM and SALTRACE indicated.

(Schepanski et al. 2007, 2009, 2012). For each of the three field campaigns, daily maps of DSA were summarized and occurrence frequencies of DSA were calculated (Fig. 5). Areas showing a DSA frequency above the 97th percentile for the corresponding time period were colored. The gray-shaded areas indicate all source regions that were active during SALTRACE. Although seasonal and thus campaign-

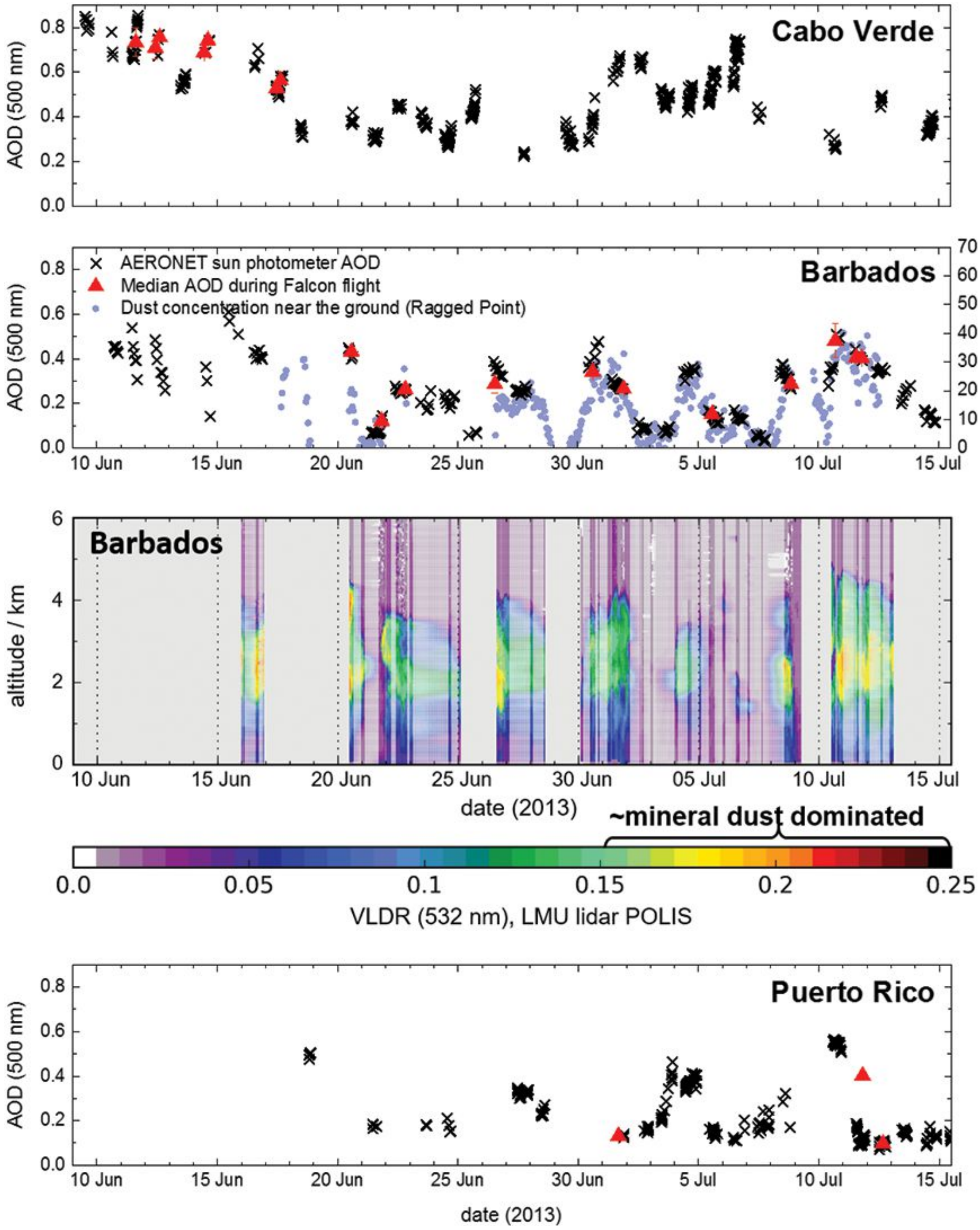

Fig. 4. AOD (500 nm) throughout SALTRACE at Cabo Verde, Barbados, and Puerto Rico together with a time–height cross section of VLDR (532 nm) illustrating the dust layer at Barbados. The red triangles in the three time series indicate the median AOD during the duration of the Falcon flights. For Barbados, also the dust mass concentration near the ground at Ragged Point is shown (blue circles). Lidar sequences in which clouds shielded the dust layer were removed. To better visualize the time evolution of the dust layer, the lidar data were linearly interpolated in periods without data. Interpolation was only performed if AOD time series suggested that no major changes were taking place. White-shaded areas mark interpolated sequences.

related differences in the pattern distribution of frequent DSA are apparent, dust sources located in the Adrar–Hoggar–Aïr mountain region as well as the Bodélé Depression region were predominantly active throughout all three campaigns. Dust source hot spots over the northern part of the Sahara and the Maghreb region were predominantly active during SAMUM-1 (May and June) and SALTRACE (June and July), suggesting that these regions are of additional importance in late spring and early summer.

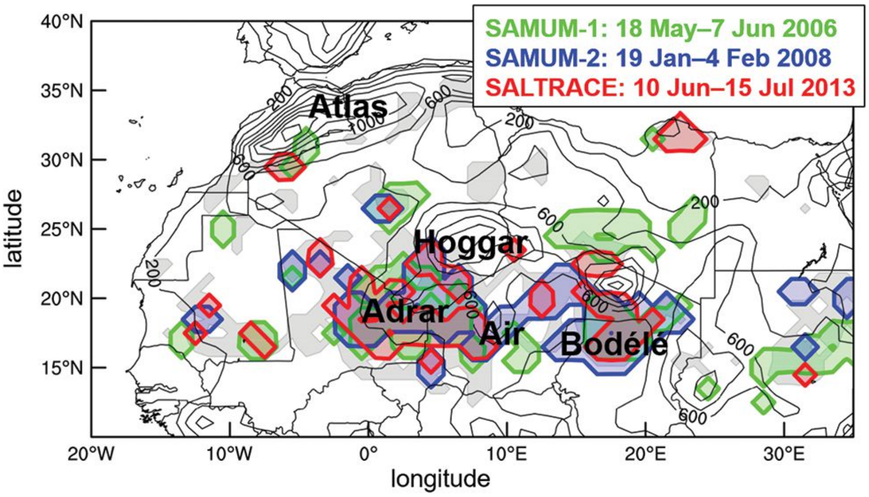

Fig. 5. Regions of most active dust sources during SALTRACE (red contours), SAMUM-1 (green contours), and SAMUM-2 (blue contours). The gray-shaded areas indicate all source regions active during SALTRACE regardless of their emission intensity and activation frequency. Solid contour lines represent the orography with altitudes (m above sea level) indicated.

Dust from the most active sources during SALTRACE identified in Fig. 5 is expected to have a high kaolinite and low illite abundance, as well as low calcium and high total iron contents (Scheuvens et al. 2013; Nousiainen and Kandler 2015). The ratio of oxide to total iron is estimated to be higher for Bodélé and Hoggar than for Mali sources (Formenti et al. 2014). In contrast, the less active sources in the northern Sahara would be dominated by illite and exhibit higher calcite contents. Except for Bodélé, the most active sources have a generally high iron oxide content. The dust therefore is expected to contribute considerably to shortwave radiation absorption. It is particularly expected to dominate absorption for supermicron particles (Müller et al. 2009). Furthermore, their comparatively high feldspar content (Nickovic et al. 2012) might influence the specific ice nucleation ability (Atkinson et al. 2013).

THE BIG PICTURE: MINERAL TRANSPORT FROM AFRICA INTO THE CARIBBEAN.

The large-scale features of dust transport from Africa across the Atlantic were initially described in the early 1970s (Prospero et al. 1970; Carlson and Prospero 1972; Schütz 1980), but the modification of dust properties during long-range transport is still an open question. After emission over Africa, the warm, dry, and dust-containing SAL leaves the African continent and travels westward at a speed of about 1,000 km day^{-1}, crossing to Barbados in about 5 days (e.g., Huang et al. 2010). Within the course of the year, the main transport corridor for the dust outflow from Africa exhibits a south–north migration related to the seasonal displacement of the Hadley cell in general and the cycle of the complex West African circulation in particular, in which the African easterly jet and its disturbances, so-called African easterly waves (AEWs), play an important role (e.g., Thorncroft and Blackburn 1999; Kiladis et al. 2006; Knippertz and Todd 2010). In June and July, the center of the dust corridor and the largest AOD is found between 15° and 20°N transporting mineral dust into the Caribbean and toward Florida, whereas in winter, the dust corridor is centered between 5° and 10°N and the dust extends to South America (Schütz 1980; Huang et al. 2010; Yu et al. 2015).

As visible in Fig. 4, dust concentrations in Barbados have a pulsating nature that is connected to the passage of AEWs (Carlson and Prospero 1972), which periodically interrupt the dust flow into the Caribbean and occasionally intensify into tropical cyclones (Zipser et al. 2009). The passage of AEWs is associated with moist air, cloudiness, and precipitation. Dust events appear to follow behind AEWs (Karyampudi and Carlson 1988).

The structure and vertical distribution of the mineral dust layer changes during transit. Figure 6 (top) shows these changes by means of cross sections of backscatter from the airborne wind lidar system on board the Falcon (Chouza et al. 2015; Chouza et al. 2016a). The bottom panel of Fig. 6 sketches the changes in dust layer structure and also the processes modifying the size distribution of the dust aerosol. Over West Africa, dust extends from the surface to 6–7-km altitude (e.g., Schütz 1980; Weinzierl et al. 2009). When leaving the African continent, the dust-containing continental outflow overrides the cool dust-free trade winds to form the elevated SAL (Weinzierl et al. 2009, 2011; Khan et al. 2015). In the Cabo Verde region, the lidar shows a homogenous dust layer extending above the trade wind inversion from about 1.5- to 6–7-km altitude (Fig. 6, top). During transit, the top of the SAL descends from 6–7 km over West Africa to 4–5 km in the Caribbean with an average of ~0.4–0.6 km day^{-1}. Dust is transferred from the SAL to the marine boundary layer by entrainment at the top of the marine boundary layer, via turbulent and convective downward mixing, and by gravitational settling of mainly supermicron particles leading to changes in the dust size distribution. In addition, cloud processing, dilution, and wet deposition are expected to modify aerosol properties in the SAL in the course of transport.

The vertical layering described in Fig. 6 is typical for summer. Figure 7 illustrates the variability and seasonal differences in vertical structure based on ground-based lidar observations with the Backscatter Extinction Lidar-Ratio Temperature Humidity Profiling Apparatus (BERTHA) (Haarig et al. 2016; Haarig et al. 2017, manuscript submitted to *Atmos. Chem. Phys.*) from the Leibniz Institute for Tropospheric Research (TROPOS) at three different locations between Africa and the Caribbean in summer 2006, 2008, 2013, and 2014 and in winter 2008 and 2014. The six panels depict time–altitude cross sections of the VLDR at wavelengths of 710 and 1,064 nm, respectively. The VLDR is derived from the ratio of the measured cross-polarized to copolarized component in the backscattered light when linearly polarized light is emitted by the laser. This quantity includes the contribution from both, molecules and particles. From the VLDR, the linear depolarization ratio of particles (PLDR) can be derived, which serves to identify aerosol types (e.g., Tesche et al. 2009, 2011; Weinzierl et al. 2011; Burton et al. 2012; Groß et al. 2013). Regions with predominantly aspherical particles of pure dust (PLDR of 31% ± 3% at 532 nm; Freudenthaler et al. 2009) appear in red. Marine aerosol with mostly spherical particles (PLDR of 2% ± 1% at 532 nm for relative humidities greater than 50%; Groß et al. 2011) are shown in blue. Mixtures of dust particles with spherical particles (e.g., marine aerosol at high relative humidity but also biomass particles) appear as yellow-greenish colors (Tesche et al. 2009).

In all cases, the aerosol layers extend from the ground up to altitudes between 3 and 5 km. However, the layer structures change with season because of variations in aerosol types and meteorological conditions, notably the south–north migration of the main transport corridor for the dust and biomass-burning outflow from Africa. In winter, dust is

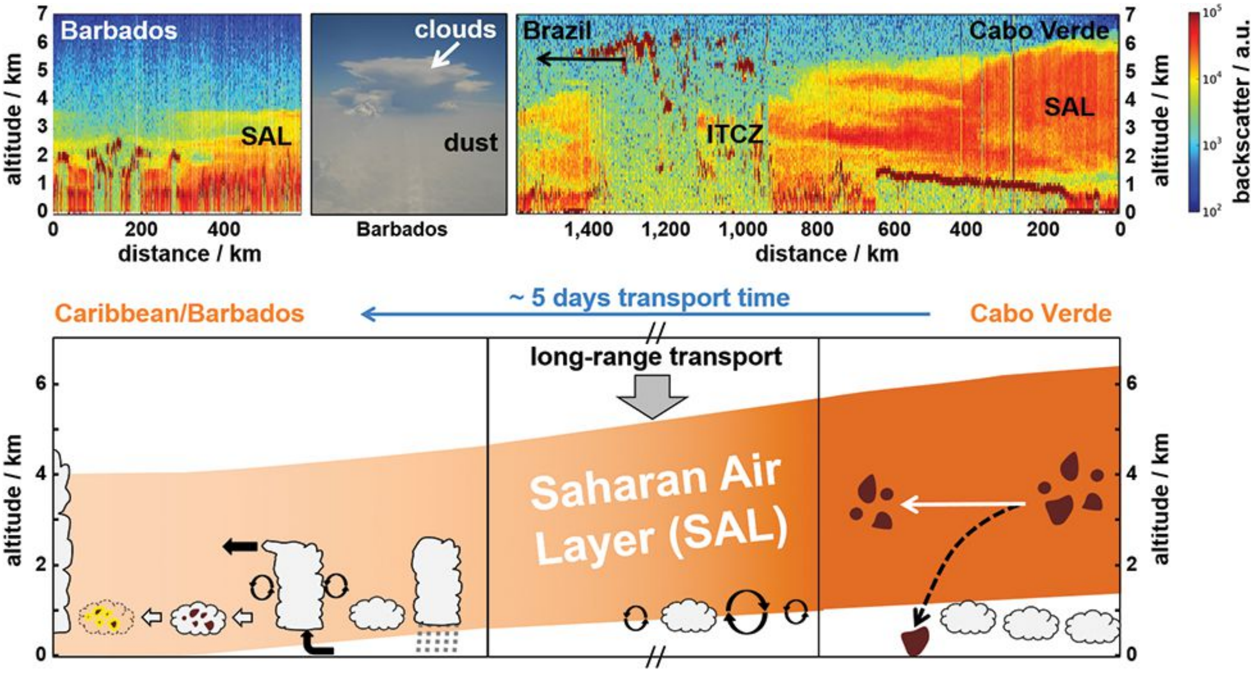

Fig. 6. (top) Lidar cross sections of dust-layer structure in (right) the Cabo Verde region and (left) Barbados together with (center) a photograph of dust layers in the Caribbean during SALTRACE in summer 2013. (bottom) Schematics of dust "aging" processes during transport from Africa into the Caribbean.

typically transported below 2-km altitude while biomass-burning dust mixtures are carried aloft; transport is primarily in latitudes south of Barbados which receives little aerosol during that time of year. In summer, the vertical aerosol distribution over Barbados shows three layers with different aerosol properties: 1) the boundary layer from the surface up to about 700 m where marine aerosols dominate; 2) above that, a layer of mixed mineral dust and marine aerosols reaching up to 1.5–2.5 km—this also is the height range where (mainly) trade wind cumulus clouds are present; and 3) the top layer extends from 1.5–2.5 to typically 4–5 km and is characterized by relatively pure Saharan dust. This layer contributes about half of the total optical depth at 532 nm (Groß et al. 2015).

Although we describe the transatlantic dust transport in simple terms, it should be clear that the processes are quite complex. Note, for example, that at Cabo Verde during summer, when transport to the Caribbean is at a maximum, there is very little dust in the marine boundary layer, which is dominated by the low-level northeasterly trade wind flow. Transport takes place in the SAL above the measurement site. Similarly at Barbados in summer, the VLDR product would suggest that there is little dust in the boundary layer despite the fact that about 10–40 μg m^{-3} of dust (Fig. 4) are present [for comparison: 50 μg m^{-3} is the limit value for 24-h exposure to fine particulate matter (PM10) in the EU; http://ec.europa.eu/environment/air/quality/standards.htm]. This is a consequence of the boundary layer being heavily loaded with sea salt aerosol thus lowering the dust contribution to the total aerosol volume to about 30%–40% (Groß et al. 2016) and thereby decreasing the PLDR impact of dust.

HIGHLIGHTED SALTRACE RESULTS. In this section, we highlight three results from SALTRACE: The first example investigates the modification of mineral dust during transatlantic transport on the basis of a Lagrangian dust sampling experiment between Cabo Verde and Barbados. The second example presents the SALTRACE measurements

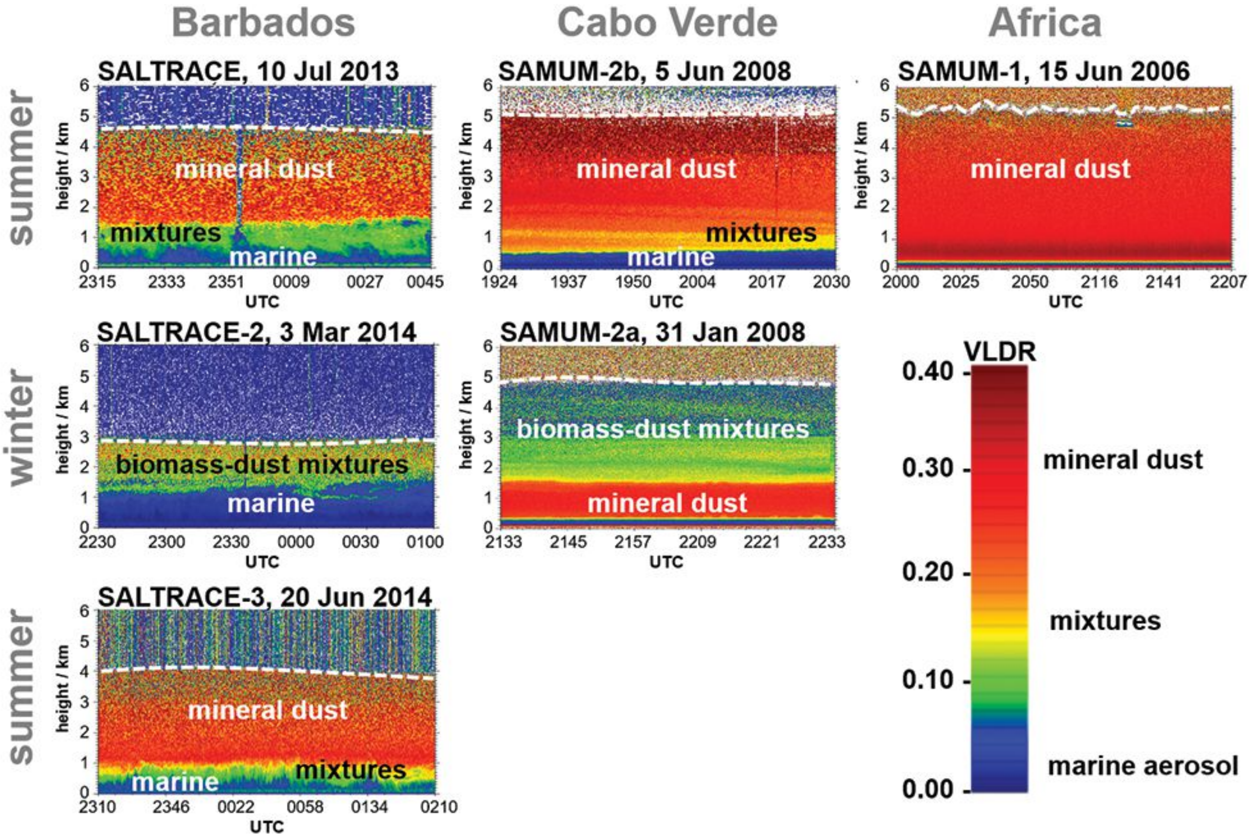

Fig. 7. Time–altitude cross sections of VLDR detected with the TROPOS lidar BERTHA at three different locations between Africa and the Caribbean (Ouarzazate, Morocco; Praia, Cabo Verde; and Barbados) in summer 2006, 2008, 2013, and 2014 and in winter 2008 and 2014. The aerosol extends from the ground to 3–5-km altitude. The top of the aerosol layers is indicated by the white dashed lines. Note: VLDR values in Morocco and Cabo Verde were measured at a wavelength of 710 nm, whereas the VLDR values in Barbados refer to 1,064 nm.

during the passage of Tropical Storm Chantal. The third example shows vertical profiles of lidar and in situ parameters for a case with high and low dust loads and discusses the SAL as a reservoir for CCN.

Modification of dust during transport across the Atlantic Ocean—A Lagrangian case study. One major objective of SALTRACE was to study the "aging" of dust during long-range transport and its impact on the radiation budget and cloud microphysical processes. This could be achieved by statistically comparing dust properties measured on the eastern Atlantic and later on the western Atlantic or by a Lagrangian experiment in which the same air mass is sampled multiple times on its trajectory as determined by means of meteorological models.

During SALTRACE we performed a Lagrangian experiment that studied dust in the Cabo Verde region and 5 days later in the western Atlantic. We started with a series of north–south tracks in the Cabo Verde area on 17 June 2013. Flight legs at four different altitudes between 1 and 5 km were performed between the islands of Sal and Santiago, a distance of 210 km, roughly perpendicular to the dust outflow from the African continent. Before and after the flight, we ran trajectory and dispersion simulations with the Hybrid Single-Particle Lagrangian Integrated Trajectory model (HYSPLIT) (Draxler and Hess 1998) to predict when the sampled air would arrive over Barbados. This was determined to be on 22 June 2013. In the Caribbean, we carried out two flights on 20 and 21 June 2013, prior to the arrival of the Lagrangian-selected air mass. We performed the Lagrangian flight on 22 June 2013 where we flew on a north–south track along 59.5°W (i.e., perpendicular to the direction of propagation of the dust layer

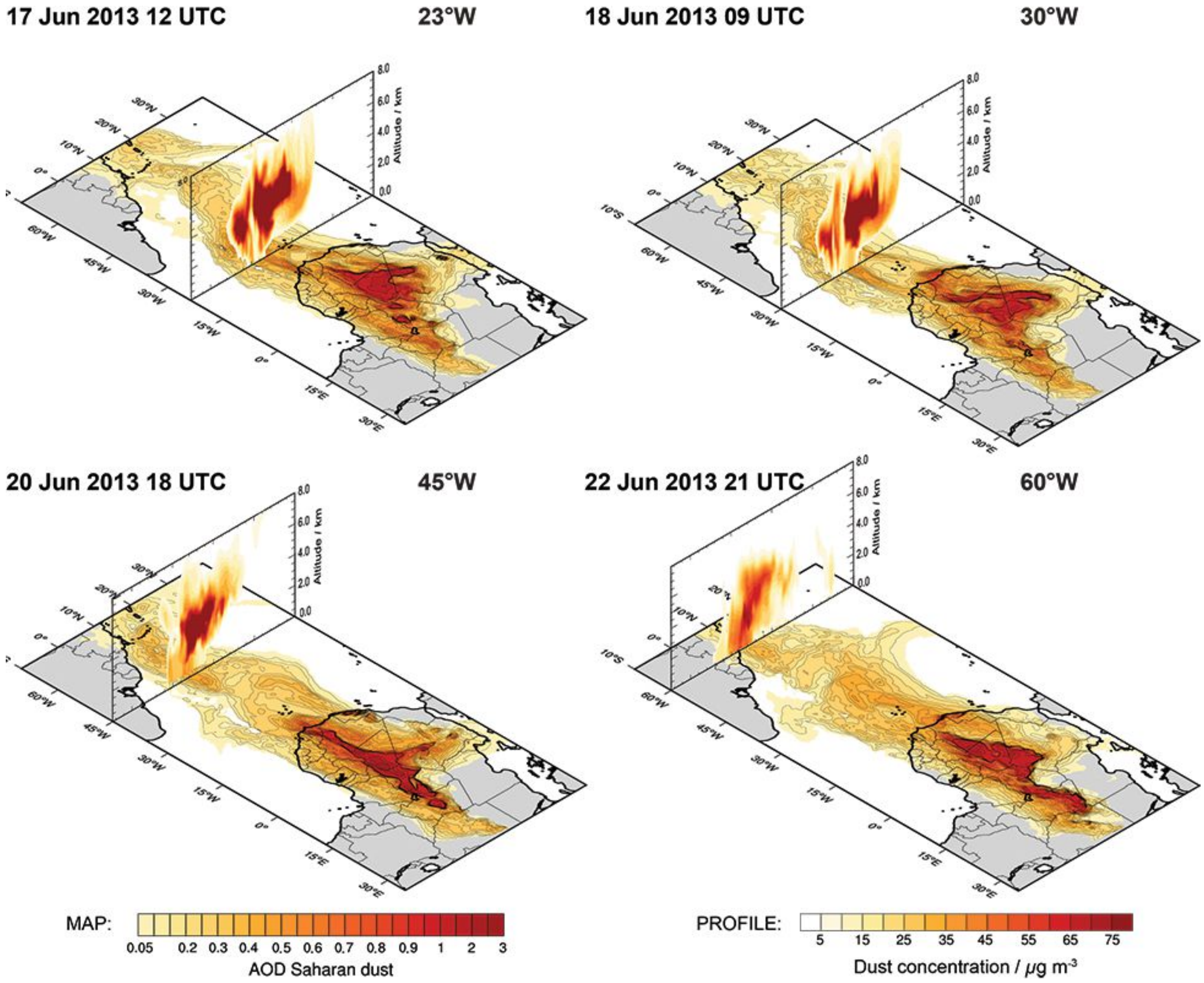

Fig. 8. COSMO-MUSCAT simulations showing the transatlantic dust transport for the Lagrangian dust sampling flights between 17 and 22 Jun 2013. Color-coded dust AOD maps are combined with longitude–altitude cross sections through the dust layer that show model dust mass concentrations.

from Africa to the Caribbean). The flight included several overpasses over Barbados at altitudes between 0.3 and 9 km and extended over a distance of ~470 km between 10.4° and 14.6°N. According to postcampaign analyses, the air mass sampled on 17 June 2013 at an altitude of 2.6 km in the Cabo Verde region was again sampled on 22 June 2013 over Barbados at an altitude of 2.3 km. It was above the typical scattered cloud layer extending from ~0.7 to 2 km on that day.

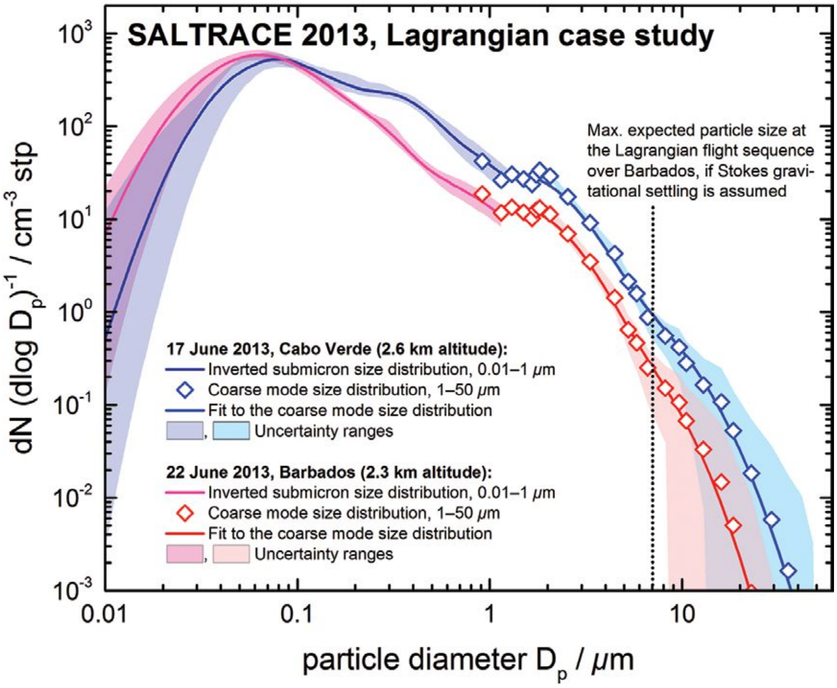

Fig. 9. Mineral dust size distribution detected with a combination of instruments before and after transatlantic transport: the size distribution between 0.01 and 1 μm was determined from the data of a CPC, a Grimm Sky OPC, and a UHSAS-A using a consistent Bayesian inversion procedure (Walser et al. 2017, manuscript submitted to *Atmos. Meas. Tech. Discuss.*); for the coarse mode above 1 μm, data points and uncertainty ranges from the CAS-DPOL spectrometer are shown. The air mass studied in the Cabo Verde region (blue symbols) on 17 Jun 2013 was sampled again 5 days later above Barbados (red symbols). According to Stokes gravitational settling, no particles larger than 7 μm should be present at an altitude of about 1.3 km below the SAL top (i.e., at the altitude where these measurements in Barbados were taken). Number concentrations are given for standard pressure and temperature conditions (1,013 hPa, 273 K).

The Lagrangian experiment relies on a certain degree of homogeneity of the sampled air mass—a precondition that is satisfied by the well-mixed SAL. For example, the variability of the particle number concentration in the Lagrangian leg over Cabo Verde was below ~10% in the coarse mode (0.5–50 μm) and around 2% in the size range between 5 nm and <~2.5 μm over distances of more than 170 km.

Figure 8 visualizes the airmass transport of the Lagrangian experiment on the basis of Consortium for Small-Scale Modeling Multiscale Chemistry Aerosol Transport Model (COSMO-MUSCAT) simulations. COSMO-MUSCAT is a regional dust model system that computes the size-resolved distribution of Saharan dust including radiative effects and feedbacks (Heinold et al. 2007, 2011). Simulations were run for the period April–July 2013 with 28-km horizontal grid spacing on a model domain that covers the Saharan Desert and the tropical Atlantic Ocean including the Caribbean. Combined with trajectory analysis, COSMO-MUSCAT shows the relationship between the sampling areas at Cabo Verde and Barbados. According to these simulations, the predominant number of trajectories launched over Cabo Verde arrived at Barbados within a 250-km radius within the 5-day transport time.

The four panels in Fig. 8 illustrate the location and extent of the dust layer sampled on both sides of the Atlantic in the Lagrangian experiment as it crosses the Atlantic Ocean. Color-coded dust AOD maps are combined with longitude–altitude cross sections through the dust layer, which show model dust mass concentrations on 17, 18, 20, and 22 June 2013. The position and timing of maps and cross sections exactly correspond to the course of a 7-day forward trajectory starting over Cabo Verde (15.5°N, 23.3°W) on 17 June 2013 and computed with COSMO wind fields. During transport, the modeled dust-layer depth decreases from about 5 (Cabo Verde) to 4 km (Barbados area) and about half of the dust mass is removed. AERONET measurements in Cabo Verde and Barbados confirm a decrease in the AOD (500 nm) by a factor of about 2 from 0.54 to 0.26 during the 5 days. Similar results were obtained from the long-range transport study carried out based on the airborne Doppler wind lidar retrievals and model results of Monitoring Atmospheric Composition and Climate (MACC), the global aerosol model from European Centre for Medium-Range Weather Forecasts (Chouza et al. 2016a). Although MACC was able to reproduce the general characteristics of the dust long-range transport process, important differences were observed in the dust vertical distribution and the African easterly jet intensity.

Figure 9 shows aerosol size distributions detected in Cabo Verde (blue symbols) at an altitude of 2.6 km and the corresponding measurements made 5 days later at an altitude of 2.3 km over Barbados (red symbols). The size distribution includes the total aerosol in the SAL and was detected with a combination of a condensation particle counter (CPC) and several optical particle counters (OPC). Detailed information about instruments used is given in Table ES1 in the supplemental material. Data from the CPC, the Grimm Sky OPC, and the Ultra Sensitivity Aerosol Spectrometer (UHSAS-A) were inverted with a consistent Bayesian inversion procedure and parameterized assuming three lognormal distributions following the method described following the method described in Walser et al. (2017, manuscript submitted to *Atmos. Meas. Tech. Discuss.*). The uncertainty range in the submicron size range reflects the uncertainty in the lognormal size distribution mode parameters. The supermicron size range was detected with a Cloud and Aerosol Spectrometer with Depolarization Detection (CAS-DPOL). The symbols show the mean values from the CAS-DPOL spectrometer, and the shaded areas indicate the standard deviation within the averaging interval. The complete size distribution (sub- and supermicron range) was parameterized with four lognormal distributions (solid lines).

Although in particular the coarse mode aerosol size range is associated with considerable uncertainties, changes are clearly visible in both total particle number concentration and number size distribution. With respect to particle number concentration in the size range between 100 nm and 50 μm, about 40% of all particles are "lost" during transatlantic transport. The number fraction of removed particles is size dependent and increases with increasing particles size. For example, in the size range between 1 and 10 μm about 60% of the particles are removed, whereas ~75% of the 10-μm particles, ~90% of the 20-μm and ~99% of the 30-μm particles are gone, suggesting that dry deposition is the dominating removal process at least during this case.

The detection of 10–30-μm particles in the Caribbean even after more than 4,000 km and 5 days of transport is unexpected. Although Maring et al. (2003) pointed out that Stokes gravitational settling overestimated the removal of particles smaller than 7.3 μm, they found that larger particles were effectively removed between Tenerife and Puerto Rico. In contrast, Denjean et al. (2016) found that the modal peak diameter of the volume size distribution remained unvaried from one side of the Atlantic Ocean to the other (i.e., Cabo Verde to Puerto Rico) suggesting that after 2–3 days from uplift gravitational settling is practically ineffective. Assuming a density of 2.6 g cm^{-3} for dust and a shape factor of 1.4 (Hinds 1999) to account for the nonspherical particle shape, which slows down the settling velocity, a particle with 20 (30)-μm in diameter descends 2.1 (4.6) km day^{-1}. This means that even if 20 (30)-μm particles had been at the top of the SAL at an altitude of 6–7 km over Cabo Verde, they should have been removed from the atmosphere within 3 (1.5) days. The Barbados measurements shown in Fig. 9 were performed at 2.3-km altitude above ground and about 1.3 km below the SAL top. Assuming SAL transport without vertical shear, and thus a Stokes settling distance of 1.3 km for this measurement, the expected maximum particle size would be about 7 μm. In contrast, 20% (10%) of the 20 (30) μm survived in the dust layer and were observed over Barbados after 5 days of transport (Fig. 8), a fact that may have important implications for the dust radiative effects and the ability of particles to act as INP. To understand the presence of these supermicron particles, Gasteiger et al. (2017) investigated particle settling in the SAL from an integrated model, lidar, and in situ perspective. Although not claiming that their simplified model describes processes during long-range transport in detail, their model suggests that daytime convective mixing within the SAL would allow a fraction of particles with diameters of 20 μm and larger to arrive in the Caribbean.

During SALTRACE, we sampled particles on board the Falcon for offline-chemical analyses. For the Lagrangian case, approximately 3,000 particles were collected. These were analyzed by scanning electron microscopy and energy-dispersive x-ray spectroscopy (EDX) for size and composition and by transmission electron microscopy and EDX for volatility and composition. Particles were classified according to the chemical composition as described in Kandler et al. (2009) with the exception of quartz being classified as silicate. Volatility was determined according to a method previously described (Kandler et al. 2011; Kristensen et al. 2016).

Figure 10 shows the aerosol composition and volatility state before and after transatlantic transport for the Lagrangian case. The general composition with comparatively low calcium contents in the supermicron fraction is in line with the mainly southern Saharan/Sahelian sources (Scheuvens et al. 2013). The change in composition at about 500-nm particle size after long-range transport is more pronounced than in the dust-influenced Cabo Verde boundary layer (Kandler et al. 2011; Lieke et al. 2011) but less distinct than observed by chemical and microphysical measurements over the African continent (Kaaden et al. 2009; Kandler et al. 2009; Müller et al. 2009; Weinzierl et al. 2009).

Comparing the chemical composition before and after transport reveals an increase in the number abundance of soluble sulfates—most ammonium- and sodium-dominated sulfates—for submicron particles; also, there is a slightly increased abundance of particles internally mixed between silicate and sulfate. This is corroborated by the fact that the abundance of silicate particles with detectable amounts of sulfate (~1%) increased from 2.5% to 4.3%. For supermicron particles, no considerable modification is visible, which is consistent with other recent observations in the Caribbean (Denjean et al. 2015). Also, the relative composition of the dust component with respect to different silicates (not shown) is indistinguishable before and after transport.

The volatility experiment for submicron particles reveals, in contrast, that there is an increase in both the amount of volatile material on the single particles and the abundance of totally volatile particles. The bottom panel of Fig. 10 shows the composition of the refractory residuals. Here, there is a clear increase in soot whereas dust decreases. Refractory material classified as "other" consists mainly of iron (probably oxides/hydroxides) and K-rich particles (perhaps

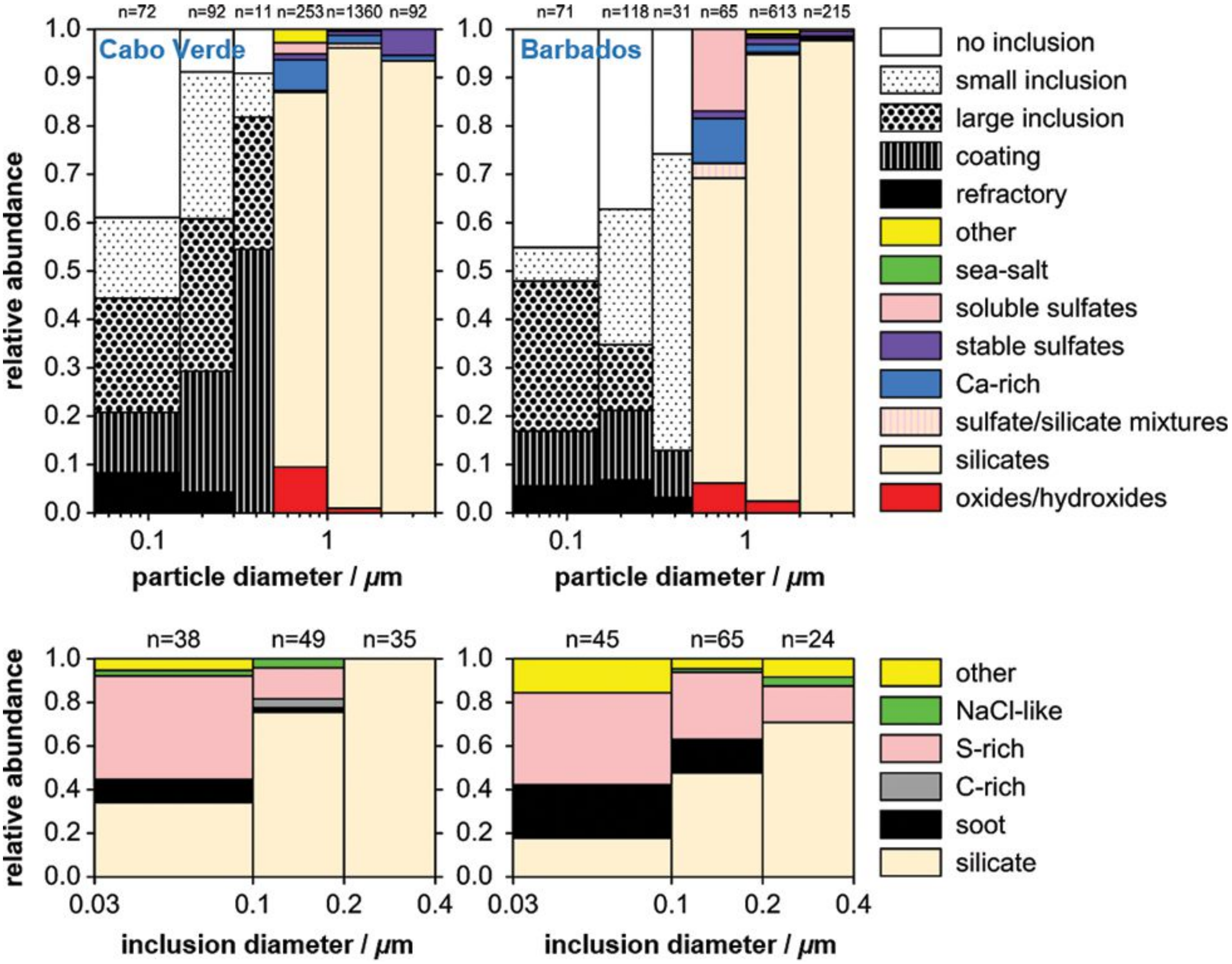

Fig. 10. Composition and volatility size distribution for the Lagrangian observations. The samples were collected (left) near Cabo Verde at 2.6-km altitude and (right) near Barbados at 2.3-km altitude. (top) Chemical particle groups are shown in color, and volatility observations are given in black and white ("small inclusion" referring to less than 30% of the particle volume, "large inclusion" to 30%–90%, and "coating" to more than 90% of the volume being refractory). (bottom) Composition of the refractory residuals with particle sizes given as projected area diameter. The numbers above the diagram are the particle counts for each bar; they cannot be considered as number size distribution.

biomass-burning material) (Lieke et al. 2011). The median volume fraction of volatile material internally mixed with soot is higher in transported aerosol (89% vs 79%). This volatile volume fraction for internally mixed dust particles does not change (7% vs 8%).

The passage of Tropical Storm Chantal and its impact on the Saharan air layer. During SALTRACE, we had the unique opportunity to perform extended aerosol measurements before, during, and after the passage of Tropical Storm Chantal, which evolved in an SAL environment. The SAL is attracting great interest because it is suspected to influence tropical cyclone activity (e.g., Dunion and Velden 2004; Evan et al. 2011). The observed modulation of the tropical Atlantic cyclone activity in the presence of the SAL has been attributed to various causes. Evan et al. (2011) link weak cyclone activity to surface cooling through the radiative effects of the dust particles in the SAL. Furthermore, dust particles acting as CCN and INP might influence the development and formation of precipitation in the convective clouds and thus impact on the cyclone development. Local vertical wind shear can be enhanced by the midlevel jet found in the SAL, thereby hindering cyclone development (Dunion and Velden 2004).

Figure 11 (top) shows a time series of VLDR and range corrected backscatter for the period between 8 and 11 July 2013 detected with the Ludwig-Maximilians-Universität (LMU) Portable Lidar System (POLIS) (Freudenthaler et al. 2016) together with a map of the Meteosat SAL-tracking satellite

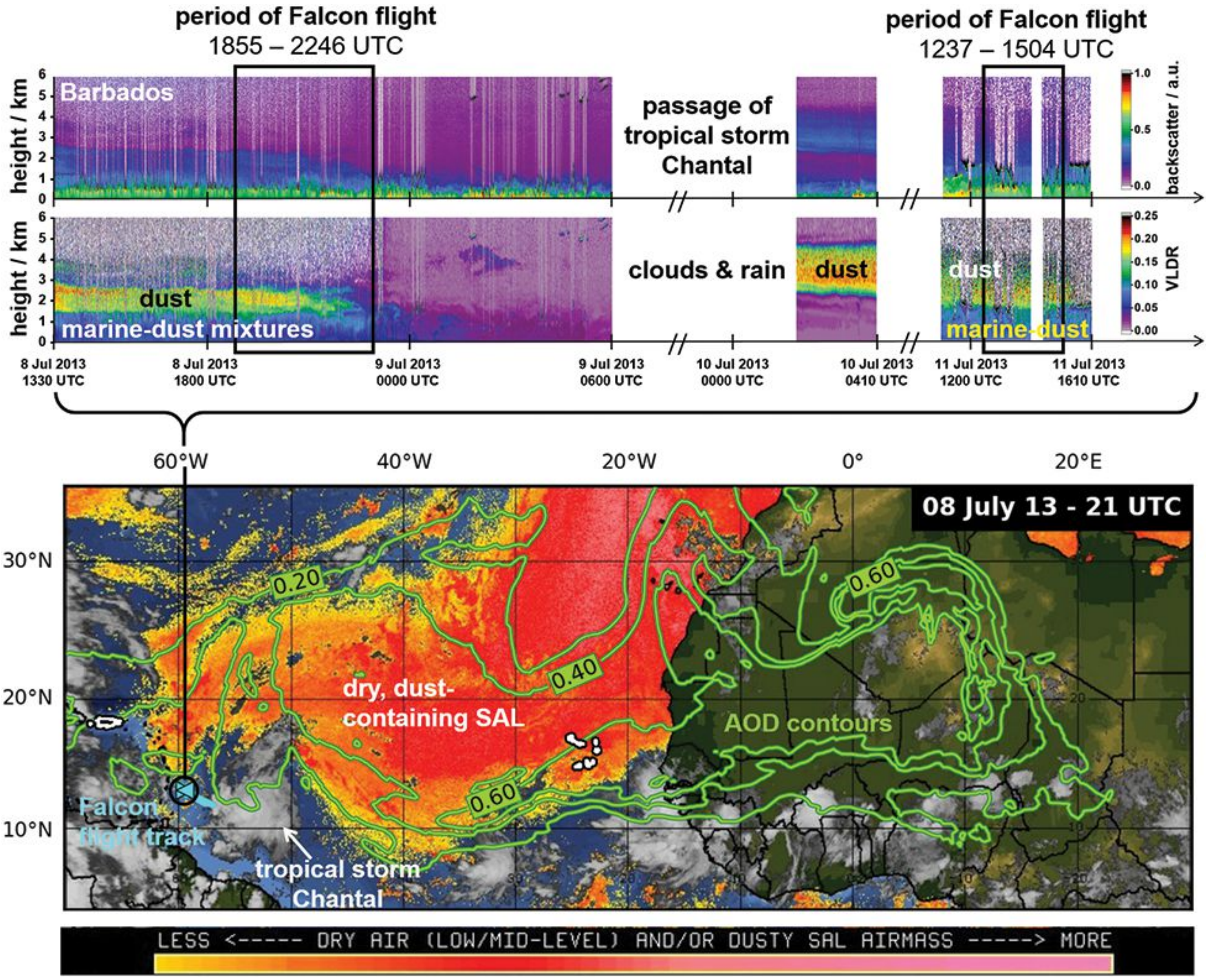

Fig. 11. (top) Measurements of VLDR (532 nm) and attenuated backscatter coefficient detected with the LMU lidar POLIS before, during, and after the passage of Tropical Storm Chantal, and on 11 Jul 2013 during the time of the first Falcon flight (Fig. 12). (bottom) Meteosat SAL-tracking satellite image (courtesy of the University of Wisconsin–Madison CIMSS) overlaid with contours of modeled dust AOD (500 nm, green contours) from the regional Saharan dust model COSMO-MUSCAT. The Falcon flight track is indicated in turquoise.

product, which we overlaid with contours of dust AOD from simulations with the regional dust model COSMO-MUSCAT. Both observations and regional dust simulations show that the passage of Chantal was associated with a reduced dust load in the Caribbean, which may largely be caused by mixing in clean air from farther south but also by wet removal of aerosols. This change in air mass is obvious from the SAL-tracking product (Fig. 11, bottom), while the analysis of dust model results including and without the storm event (not shown) reveals a minor role of wet deposition in the removal of dust. Vertical mixing was enhanced especially to the rear of the cyclone. Immediately after the passage of Chantal, changes in the dust properties were observed (Fig. 12) that might be linked to a change in the large-scale flow pattern over the tropical North Atlantic and West Africa, causing increased dust transport from southern Saharan and Sahelian dust sources. The dust layer was seen to extend to about 5 km, higher than the typically observed 4–5 km. Details about DSA over North Africa and transported dust reaching Barbados are given in Groß et al. (2015). Future investigations will focus on the interactions of Tropical Storm Chantal and dust transport, including sensitivity studies on dust radiative effects and feedbacks on atmospheric dynamics and sea surface temperature.

The SAL as a reservoir/source for CCN. Here we highlight the vertical distribution of the microphysical properties of mineral dust and its ability to act as CCN. Mineral particles may serve as CCN in liquid cloud droplet formation (Sullivan et al. 2009; Garimella et al. 2014), and as such they are likely to be of great importance over the tropical Atlantic (Twohy et al. 2009). The efficacy of dust particles to act as CCN increases significantly with particle size, but it is also influenced by the presence of coatings and

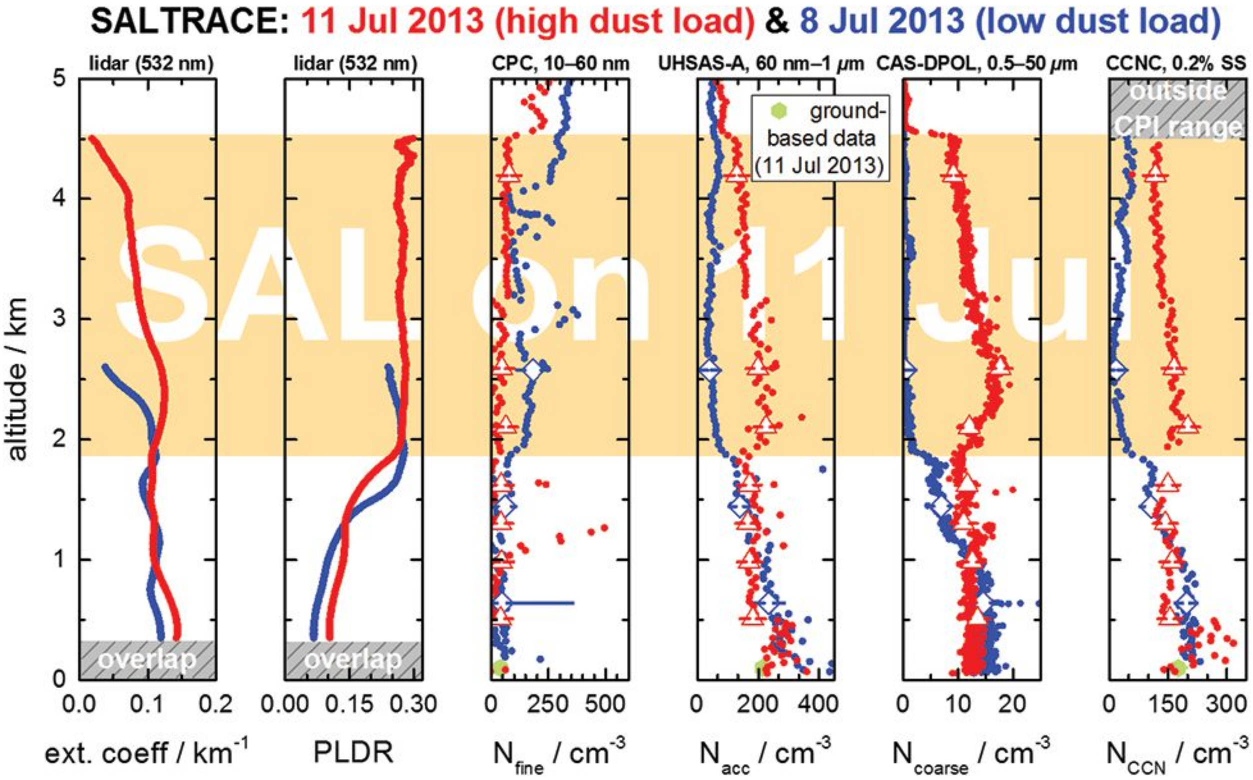

Fig. 12. Vertical profiles of extinction coefficient and PLDR detected with POLIS, aerosol number concentration detected with several instruments in different size classes, and CCN number concentration at 0.2% supersaturation (SS) for high (red) and low (blue) dust loads taken over Barbados on 8 and 11 Jul 2013 (see also Fig. 11 for the periods of the Falcon flights on those days). The corresponding ground-based measurements at Ragged Point are shown with green symbols. Data collected during sequences at constant altitude were averaged and are indicated with big symbols. The error bars indicate the 16th- and 84th-percentile values within the individual horizontal level. The gray-shaded areas sketch the overlap of the lidar and the range where the constant pressure inlet (CPI) of the CCN counter did no longer keep the CCNC at a constant pressure of 500 hPa. All data are given for ambient conditions.

the amount of (water soluble) coating material (e.g., Garimella et al. 2014). Pure mineral dust particles are hydrophobic, but if they are larger than ~0.4–0.8 μm they will act as CCN at atmospherically relevant supersaturations (Sullivan et al. 2009; Garimella et al. 2014). The addition of even minor amounts of water soluble material will increase the potential of dust particles to act as CCN (Sullivan et al. 2009). Furthermore, the addition of soluble material onto dust particles increases the water uptake at subsaturated conditions with respect to liquid water (Hatch et al. 2008) and, thus, influences their optical properties and the ability to scatter/absorb radiation.

Consequently, to assess the direct and indirect climate impacts from mineral particles, it is essential to investigate their mixing state and how that could change as the particles age in the atmosphere. Some studies indicate that processing of dust in the atmosphere leads to an addition of water soluble material (e.g., Perry et al. 2004; Begue et al. 2015). However, there have been only a few studies of the properties of aged African dust transported across the Atlantic. Denjean et al. (2015) investigated supermicron mineral dust particles sampled in Puerto Rico. They reported that up to 24% of the studied mineral dust particles were internally mixed with sulfate or chloride, while 3%–6% formed aggregates with sea salt particles. Only the latter group of mineral particles showed increased hygroscopic growth for relative humidity up to 94%.

Ground-based and airborne direct measurements of CCN concentrations were performed during SALTRACE. The potential of polarization lidar data to estimate vertical profiles of cloud-relevant aerosol parameters (CCN and INP number concentrations) was explored (Mamouri and Ansmann 2015). Furthermore, samples were collected for offline analysis of hygroscopic growth and ice nucleation ability.

Figure 12 contrasts vertical profiles of aerosol number concentration in different size classes together with the extinction coefficient measured with the ground-based lidar system from LMU Munich for days with high (11 July 2013) and low (8 July 2013) dust concentrations over Barbados. In addition, vertical profiles of PLDR enable us to distinguish the SAL pure dust layer that extends above about 1.5 (8 July) and 1.8 km (11 July) from the marine aerosol–dust mixture in the marine mixed layer. The particle number concentration in the fine mode (10–60 nm) seems to be depleted inside the SAL, while accumulation (60 nm–1 μm) and coarse modes (0.5–50 μm) are enhanced by a factor of more than 4 and 15, respectively, compared to free-tropospheric concentrations in these size ranges. The vertical profile of the CCN number concentration is correlated with accumulation and coarse mode number concentration. On the day with high dust loads, the CCN number concentration at altitudes of ~2–4 km is enhanced by a factor of about 5 compared to the day with the low dust load. Hence, it is likely that properties of clouds in the Caribbean formed at those altitudes are significantly influenced by long-range transported dust aerosol from northern Africa.

SUMMARY AND OUTLOOK.

Although it is generally accepted that mineral dust affects many climate processes, our understanding of long-range transported dust is limited by the fragmentary nature of past studies. The strategy of SALTRACE was to attain a large-scale picture of African dust transport across the Atlantic by linking ground-based and airborne measurements with remote sensing and modeling. Specific objectives were 1) to characterize the chemical, microphysical, and optical properties of "aged" dust in the Caribbean, 2) to quantify the impact of dust "aging" on the radiation budget and cloud microphysical processes, 3) to investigate the meteorological context of African dust transport into the Caribbean, and 4) to assess the roles of removal processes during transport.

The SALTRACE program in 2013/14, especially with the aircraft field experiment in June and July 2013, comprised by far the most extensive measurements ever performed to study long-range transported dust. To our knowledge, the Lagrangian in situ study that sampled coherent air masses separated by a distance of more than 4,000 km was unique and enables a detailed investigation of transport effects on dust properties.

The Lagrangian results were surprising in that they suggest that the removal rate of large supermicron particles is slower than expected and the chemical alterations to the particles are less pronounced than expected. The exact nature of these aging processes is unclear and more research will be needed. The SALTRACE dataset enables future studies to look in detail at changes of chemical, microphysical, and optical dust properties during transport and quantify their associated effects on radiation and clouds.

To place the SALTRACE measurements in a long-term context we related our measurements to the 50-yr Barbados dust record and found that the situation investigated during SALTRACE can be regarded as "normal" dust conditions. Thus, the SALTRACE dataset is well suited to constrain the Atlantic and

Caribbean dust properties and concentrations in models. Temporal trends of ground-based dust mass concentrations and AOD at Barbados agreed well with aircraft measurements indicating that 1) mineral dust makes a significant contribution to the AOD in the Caribbean, 2) dust transported at higher altitudes into the Caribbean is effectively mixed down into the boundary layer, and 3) that in general we can expect good comparability between ground-based, airborne, and remote sensing observations.

We carried out extensive measurements in Tropical Storm Chantal, which developed when dust concentrations were high over broad areas of the western Atlantic. Chantal passed through the Barbados region on 9 July 2013. Interestingly, by the time the storm overpassed our ground site on Barbados essentially all dust was gone, an observation that we attribute to enhanced advection of dust-free air from the south. The SAL-tracking product and modeled dust AOD in Fig. 11 clearly show this change in air mass associated with the passage of storm Chantal.

We collected numerous in situ and remote sensing profiles of dust properties, which we evaluated with respect to their ability to act as CCN. We found the CCN number concentration in the SAL to be highly enhanced (~up to a factor of 5) under conditions of high dust loads compared to low dust loads.

The SALTRACE data should yield new insights on the formation (and destruction) of the dust-bearing SAL and its impact on cloud evolution processes, the atmospheric radiation budget, and local meteorology. Ongoing analyses are expected to elucidate details on the processes occurring at the end of the atmospheric dust cycle as the SAL moved over the Caribbean.

Simultaneous Doppler lidar backscatter and wind measurements were conducted for the first time along the main Saharan dust transport path. This unique dataset not only provides the opportunity to investigate various features associated with this transport but also to test the ability of different global and regional models to simulate them. Ongoing regional modeling will use the rich dataset to address fundamental questions on Saharan dust transport: how export across the tropical Atlantic is influenced by the West African circulation, the role played by the different removal and mixing processes, and the impact of dust on radiative forcing and on the dynamics of the SAL. Regional dust simulations and trajectory analysis will be used to explore deposition processes, particle aging, and dust–cloud interactions.

The role of dust as CCN and INP and the associated impacts on weather needs further research. The next generation of mineral dust field experiments should focus on extended characterization of dust aerosol and include enhanced cloud observations (e.g., mixed-phase and ice clouds developing in dusty air layers) by combined in situ and remote sensing observations.

Finally, the long-term dust record from Barbados shows that large changes in transport have occurred and that these are clearly linked to climate in ways that we do not fully understand. In the coming decades we might expect continuing changes in global climate. However the projections for North Africa are highly uncertain and we cannot anticipate whether dust transport will increase or decrease (Seneviratne et al. 2012). Thus, it is important that dust transport out of Africa is carefully monitored in the coming years to better understand the controlling processes so as to develop better model projections of dust transport and the role of dust in a changing climate.

ACKNOWLEDGMENTS. The research leading to these results has received funding from the Helmholtz Association under Grant VH-NG-606 (Helmholtz-Hochschul-Nachwuchsforschergruppe AerCARE) and from the European Research Council under the European Community's Horizon 2020 research and innovation framework program/ERC Grant Agreement 640458 (A-LIFE). The SALTRACE campaign was mainly funded by the Helmholtz Association, DLR, TROPOS, and LMU. The SALTRACE flights in the Cabo Verde region were funded through the DLR-internal project VolcATS (Volcanic Ash Impact on the Air Transport System). We acknowledge funding from the LMU Munich's Institutional Strategy LMUexcellent within the framework of the German Excellence Initiative. The photometer calibration was supported by European Union's Horizon 2020 research and innovation program under Grant Agreement 654109 (ACTRIS-2). J. M. Prospero's research is supported by NSF Grant AGS-0962256. K. Kandler acknowledges financial support from the German Research Foundation (DFG, Grants KA 2280/2 and FOR 1525 INUIT). T. B. Kristensen thanks funding from the German Federal Ministry of Education and Research (BMBF) project 01LK1222B.

We thank the SALTRACE team and our local hosts for their support and the great collaboration. We are grateful to DLR flight experiments, in particular Andrea Hausold and Frank Probst; the pilots Stefan Grillenbeck, Michael Großrubatscher, Philipp Weber, Roland Welser; and the technical and sensor team from DLR flight operations for their great support during the preparation of SALTRACE and for the accomplishment of the research flights. Special thanks due to the certification team of CAS-DPOL for enabling us to fly this instrument on the Falcon. We are grateful to the following participants of the SALTRACE field experiment for their assistance before, during, and after the SALTRACE field phase: Reinhold Busen, Florian Dahlkötter, Daniel Fütterer, Markus Hartmann, Katharina Heimerl, André Klepel, Melanie Kujukovic, Christian Lemmerz, Anton Lex, Andreas Minikin, Engelbert Nagel, Stephan Rahm, Maximilian Rose, Meinhard Seefeldner, and Benjamin Witschas. Thanks are due to Andreas Dörnbrack, Robert Baumann, and Ingo Wenzel for preparing ECMWF and HYSPLIT trajectories and for their support with the weather forecast during SALTRACE. We thank Didier Tanré and LOA staff for their effort in establishing and maintaining Cabo Verde AERONET site and the Deutscher Wetterdienst (DWD) for good cooperation and support running the COSMO model and providing the required input data. We are grateful to the NASA CALIPSO team for providing CALIPSO data 3 h after downlink. Matthias Tesche kindly provided the SAMUM-1 and SAMUM-2 data in Fig. 8. We thank the University of Wisconsin–Madison CIMSS for providing the Meteosat SAL-layer tracking product.

SALTRACE would not have been possible without the excellent support from local authorities in Cabo Verde and Barbados including the Regional Security System (RSS), the Caribbean Institute for Meteorology and Hydrology (CIMH), and the Airport Authority GAIA (Grantley Adams International Airport Inc.), Barbados, who hosted us in their facilities and supported us to get clearances, which we gratefully acknowledge.

REFERENCES

Abdelkader, M., S. Metzger, R. E. Mamouri, M. Astitha, L. Barrie, Z. Levin, and J. Lelieveld, 2015: Dust–air pollution dynamics over the eastern Mediterranean. *Atmos. Chem. Phys.*, **15**, 9173–9189, doi:10.5194/acp-15-9173-2015.

Ansmann, A., and Coauthors, 2011: Saharan Mineral Dust Experiments SAMUM-1 and SAMUM-2: What have we learned? *Tellus*, **63B**, 403–429, doi:10.1111/j.1600-0889.2011.00555.x.

Atkinson, J. D., and Coauthors, 2013: The importance of feldspar for ice nucleation by mineral dust in mixed-phase clouds. *Nature*, **498**, 355–358, doi:10.1038/nature12278.

Balkanski, Y., M. Schulz, T. Claquin, and S. Guibert, 2007: Reevaluation of mineral aerosol radiative forcings suggests a better agreement with satellite and AERONET data. *Atmos. Chem. Phys.*, **7**, 81–95, doi:10.5194/acp-7-81-2007.

Begue, N., P. Tulet, J. Pelon, B. Aouizerats, A. Berger, and A. Schwarzenboeck, 2015: Aerosol processing and CCN formation of an intense Saharan dust plume during the EUCAARI 2008 campaign. *Atmos. Chem. Phys.*, **15**, 3497–3516, doi:10.5194/acp-15-3497-2015.

Brammer, A., and C. D. Thorncroft, 2015: Variability and evolution of African easterly wave structures and their relationship with tropical cyclogenesis over the eastern Atlantic. *Mon. Wea. Rev.*, **143**, 4975–4995, doi:10.1175/MWR-D-15-0106.1.

Braun, S. A., 2010: Reevaluating the role of the Saharan air layer in Atlantic tropical cyclogenesis and evolution. *Mon. Wea. Rev.*, **138**, 2007–2037, doi:10.1175/2009MWR3135.1.

Burton, S. P., and Coauthors, 2012: Aerosol classification using airborne High Spectral Resolution Lidar measurements—Methodology and examples. *Atmos. Meas. Tech.*, **5**, 73–98, doi:10.5194/amt-5-73-2012.

Carlson, T. N., and J. M. Prospero, 1972: The large-scale movement of Saharan air outbreaks over the northern equatorial Atlantic. *J. Appl. Meteor.*, **11**, 283–297, doi:10.1175/1520-0450(1972)011<0283:TLSMOS>2.0.CO;2.

Chouza, F., O. Reitebuch, S. Groß, S. Rahm, V. Freudenthaler, C. Toledano, and B. Weinzierl, 2015: Retrieval of aerosol backscatter and extinction from airborne coherent Doppler wind lidar measurements. *Atmos. Meas. Tech.*, **8**, 2909–2926, doi:10.5194/amt-8-2909-2015.

——, ——, A. Benedetti, and B. Weinzierl, 2016a: Saharan dust long-range transport across the Atlantic studied by an airborne Doppler wind lidar and the MACC model. *Atmos. Chem. Phys.*, **16**, 11 581–11 600, doi:10.5194/acp-16-11581-2016.

——, ——, M. Jähn, S. Rahm, and B. Weinzierl, 2016b: Vertical wind retrieved by airborne lidar and analysis of island induced gravity waves in combination with numerical models and in situ particle measurements. *Atmos. Chem. Phys.*, **16**, 4675–4692, doi:10.5194/acp-16-4675-2016.

Cotton, R. J., 2016: Ice in Clouds Experiment—Dust: A field campaign to study aerosol-cloud interactions. *Eighth Symp. on Aerosol–Cloud–Climate Interactions*, New Orleans, LA, Amer. Meteor. Soc., J5.3. [Available online at https://ams.confex.com/ams/96Annual/webprogram/Paper282066.html.]

Dahlkötter, F., and Coauthors, 2014: The Pagami Creek smoke plume after long-range transport to the upper troposphere over Europe—Aerosol properties and black carbon mixing state. *Atmos. Chem. Phys.*, **14**, 6111–6137, doi:10.5194/acp-14-6111-2014.

DeFlorio, M. J., I. D. Goodwin, D. R. Cayan, A. J. Miller, S. J. Ghan, D. W. Pierce, L. M. Russell, and B. Singh, 2016: Interannual modulation of subtropical Atlantic boreal summer dust variability by ENSO. *Climate Dyn.*, **46**, 585–599, doi:10.1007/s00382-015-2600-7.

Denjean, C., and Coauthors, 2015: Long-range transport across the Atlantic in summertime does not enhance the hygroscopicity of African mineral dust. *Geophys. Res. Lett.*, **42**, 7835–7843, doi:10.1002/2015GL065693.

——, and Coauthors, 2016: Size distribution and optical properties of mineral dust aerosols transported in the western Mediterranean. *Atmos. Chem. Phys.*, **16**, 1081–1104, doi:10.5194/acp-16-1081-2016.

Doherty, O. M., N. Riemer, and S. Hameed, 2008: Saharan mineral dust transport into the Caribbean: Observed atmospheric controls and trends. *J. Geophys. Res.*, **113**, D07211, doi:10.1029/2007JD009171.

Draxler, R. R., and G. D. Hess, 1998: An overview of the HYSPLIT_4 modeling system of trajectories, dispersion, and deposition. *Aust. Meteor. Mag.*, **47**, 295–308.

Dunion, J. P., and C. S. Velden, 2004: The impact of the Saharan air layer on Atlantic tropical cyclone activity. *Bull. Amer. Meteor. Soc.*, **85**, 353–365, doi:10.1175/BAMS-85-3-353.

Evan, A. T., A. K. Heidinger, and P. Knippertz, 2006: Analysis of winter dust activity off the coast of West Africa using a new 24-year over-water advanced very high resolution radiometer satellite dust climatology. *J. Geophys. Res.*, **111**, D12210, doi:10.1029/2005JD006336.

——, G. R. Foltz, D. X. Zhang, and D. J. Vimont, 2011: Influence of African dust on ocean–atmosphere variability in the tropical Atlantic. *Nat. Geosci.*, **4**, 762–765, doi:10.1038/ngeo1276.

——, C. Flamant, M. Gaetani, and F. Guichard, 2016: The past, present and future of African dust. *Nature*, **531**, 493–495, doi:10.1038/nature17149.

Fitzgerald, E., A. P. Ault, M. D. Zauscher, O. L. Mayol-Bracero, and K. A. Prather, 2015: Comparison of the mixing state of long-range transported Asian and African mineral dust. *Atmos. Environ.*, **115**, 19–25, doi:10.1016/j.atmosenv.2015.04.031.

Formenti, P., S. Caquineau, K. Desboeufs, A. Klaver, S. Chevaillier, E. Journet, and J. L. Rajot, 2014: Mapping the physico-chemical properties of mineral dust in western Africa: Mineralogical composition. *Atmos. Chem. Phys.*, **14**, 10 663–10 686, doi:10.5194/acp-14-10663-2014.

Freudenthaler, V., and Coauthors, 2009: Depolarization ratio profiling at several wavelengths in pure Saharan dust during SAMUM 2006. *Tellus*, **61B**, 165–179, doi:10.1111/j.1600-0889.2008.00396.x.

——, M. Seefeldner, S. Groß, and U. Wandinger, 2016: Accuracy of linear depolarisation ratios in clean air ranges measured with POLIS-6 at 355 and 532 NM. *EPJ Web Conf.*, **119**, 25013, doi:10.1051/epjconf/201611925013.

Garimella, S., Y. W. Huang, J. S. Seewald, and D. J. Cziczo, 2014: Cloud condensation nucleus activity comparison of dry- and wet-generated mineral dust aerosol: The significance of soluble material. *Atmos. Chem. Phys.*, **14**, 6003–6019, doi:10.5194/acp-14-6003-2014.

Gasteiger, J., S. Groß, B. Weinzierl, D. Sauer, and V. Freudenthaler, 2017: Particle settling and convective mixing in the Saharan Air Layer as seen from an integrated model, lidar, and in-situ perspective. *Atmos. Chem. Phys.*, **17**, 297–311, doi:10.5194/acp-17-297-2017.

Ginoux, P., J. M. Prospero, O. Torres, and M. Chin, 2004: Long-term simulation of global dust distribution with the GOCART model: Correlation with North Atlantic Oscillation. *J. Environ. Model. Software*, **19**, 113–128, doi:10.1016/S1364-8152(03)00114-2.

Gioda, A., O. L. Mayol-Bracero, F. N. Scatena, K. C. Weathers, V. L. Mateus, and W. H. McDowell, 2013: Chemical constituents in clouds and rainwater in the Puerto Rican rainforest: Potential sources and seasonal drivers. *Atmos. Environ.*, **68**, 208–220, doi:10.1016/j.atmosenv.2012.11.017.

Goudie, A. S., 2014: Desert dust and human health disorders. *Environ. Int.*, **63**, 101–113, doi:10.1016/j.envint.2013.10.011.

Groß, S., M. Tesche, V. Freudenthaler, C. Toledano, M. Wiegner, A. Ansmann, D. Althausen, and M. Seefeldner, 2011: Characterization of Saharan dust, marine aerosols and mixtures of biomass burning aerosols and dust by means of multi-wavelength depolarization and Raman measurements during SAMUM-2. *Tellus*, **63B**, 706–724, doi:10.1111/j.1600-0889.2011.00556.x.

——, M. Esselborn, B. Weinzierl, M. Wirth, A. Fix, and A. Petzold, 2013: Aerosol classification by airborne high spectral resolution lidar observations. *Atmos. Chem. Phys.*, **12**, 25 983–26 028, doi:10.5194/acpd-12-25983-2012.

——, V. Freudenthaler, K. Schepanski, C. Toledano, A. Schäfler, A. Ansmann, and B. Weinzierl, 2015: Optical properties of long-range transported Saharan dust over Barbados as measured by dual-wavelength depolarization Raman lidar measurements. *Atmos. Chem. Phys.*, **15**, 11 067–11 080, doi:10.5194/acp-15-11067-2015.

——, J. Gasteiger, V. Freudenthaler, T. Müller, D. Sauer, C. Toledano, and A. Ansmann, 2016: Saharan dust contribution to the Caribbean summertime boundary layer—A lidar study during SALTRACE. *Atmos. Chem. Phys.*, **16**, 11 535–11 546, doi:10.5194/acp-16-11535-2016.

Haarig, M., D. Althausen, A. Ansmann, A. Klepel, H. Baars, R. Engelmann, S. Groß, and V. Freudenthaler, 2016: Measurement of the linear depolarization ratio of aged dust at three wavelengths (355, 532 and 1064 nm) simultaneously over Barbados. *EPJ Web Conf.*, **119**, 18009, doi:10.1051/epjconf/201611918009.

Hankes, I., Z. Wang, G. Zhang, and C. Fritz, 2015: Merger of African easterly waves and formation of Cape Verde storms. *Quart. J. Roy. Meteor. Soc.*, **141**, 1306–1319, doi:10.1002/qj.2439.

Hatch, C. D., K. M. Gierlus, J. D. Schuttlefield, and V. H. Grassian, 2008: Water adsorption and cloud condensation nuclei activity of calcite and calcite coated with model humic and fulvic acids. *Atmos. Environ.*, **42**, 5672–5684, doi:10.1016/j.atmosenv.2008.03.005.

Haywood, J. M., and Coauthors, 2008: Overview of the dust and biomass-burning experiment and African Monsoon Multidisciplinary Analysis special observing period-0. *J. Geophys. Res.*, **113**, D00C17, doi:10.1029/2008JD010077.

——, and Coauthors, 2011: Motivation, rationale and key results from the GERBILS Saharan dust measurement campaign. *Quart. J. Roy. Meteor. Soc.*, **137**, 1106–1116, doi:10.1002/qj.797.

Heinold, B., J. Helmert, O. Hellmuth, R. Wolke, A. Ansmann, B. Marticorena, B. Laurent, and I. Tegen, 2007: Regional modeling of Saharan dust events using LM-MUSCAT: Model description and case studies. *J. Geophys. Res.*, **112**, D11204, doi:10.1029/2006JD007443.

——, and Coauthors, 2011: Regional modelling of Saharan dust and biomass-burning smoke. Part I: Model description and evaluation. *Tellus*, **63B**, 781–799, doi:10.1111/j.1600-0889.2011.00570.x.

Heintzenberg, J. O. S. T., 2009: The SAMUM-1 experiment over southern Morocco: Overview and introduction. *Tellus*, **61B**, 2–11, doi:10.1111/j.1600-0889.2008.00403.x.

Hinds, W. C., 1999: *Aerosol Technology: Properties, Behavior, and Measurement of Airborne Particles*. 2nd ed. Wiley, 504 pp.

Hoose, C., and O. Möhler, 2012: Heterogeneous ice nucleation on atmospheric aerosols: A review of results from laboratory experiments. *Atmos. Chem. Phys.*, **12**, 9817–9854, doi:10.5194/acp-12-9817-2012.

Huang, J. F., C. D. Zhang, and J. M. Prospero, 2010: African dust outbreaks: A satellite perspective of temporal and spatial variability over the tropical Atlantic Ocean. *J. Geophys. Res.*, **115**, D05202, doi:10.1029/2009JD012516.

Huneeus, N., and Coauthors, 2011: Global dust model intercomparison in AeroCom phase I. *Atmos. Chem. Phys.*, **11**, 7781–7816, doi:10.5194/acp-11-7781-2011.

IPCC, 2013: *Climate Change 2013: The Physical Science Basis*. Cambridge University Press, 1535 pp., doi:10.1017/CBO9781107415324.

Jähn, M., D. Muñoz-Esparza, F. Chouza, O. Reitebuch, O. Knoth, M. Haarig, and A. Ansmann, 2016: Investigations of boundary layer structure, cloud characteristics and vertical mixing of aerosols at Barbados with large eddy simulations. *Atmos. Chem. Phys.*, **16**, 651–674, doi:10.5194/acp-16-651-2016.

Jickells, T. D., and Coauthors, 2005: Global iron connections between desert dust, ocean biogeochemistry, and climate. *Science*, **308**, 67–71, doi:10.1126/science.1105959.

Jung, E., B. Albrecht, J. M. Prospero, H. H. Jonsson, and S. M. Kreidenweis, 2013: Vertical structure of aerosols, temperature, and moisture associated with an intense African dust event observed over the eastern Caribbean. *J. Geophys. Res. Atmos.*, **118**, 4623–4643, doi:10.1002/jgrd.50352.

Kaaden, N., and Coauthors, 2009: State of mixing, shape factor, number size distribution, and hygroscopic growth of the Saharan anthropogenic and mineral dust aerosol at Tinfou, Morocco. *Tellus*, **61B**, 51–63, doi:10.1111/j.1600-0889.2008.00388.x.

Kandler, K., and Coauthors, 2009: Size distribution, mass concentration, chemical and mineralogical composition and derived optical parameters of the boundary layer aerosol at Tinfou, Morocco, during SAMUM 2006. *Tellus*, **61B**, 32–50, doi:10.1111/j.1600-0889.2008.00385.x.

——, and Coauthors, 2011: Electron microscopy of particles collected at Praia, Cape Verde, during the Saharan Mineral Dust Experiment: Particle chemistry, shape, mixing state and complex refractive index. *Tellus*, **63B**, 475–496, doi:10.1111/j.1600-0889.2011.00550.x.

Kanitz, T., R. Engelmann, B. Heinold, H. Baars, A. Skupin, and A. Ansmann, 2014: Tracking the Saharan Air Layer with shipborne lidar across the tropical Atlantic. *Geophys. Res. Lett.*, **41**, 1044–1050, doi:10.1002/2013GL058780.

Karyampudi, V. M., and T. N. Carlson, 1988: Analysis and numerical simulations of the Saharan Air Layer and its effect on easterly wave disturbances. *J. Atmos. Sci.*, **45**, 3102–3136, doi:10.1175/1520-0469(1988)045<3102:AANSOT>2.0.CO;2.

Khan, B., G. Stenchikov, B. Weinzierl, S. Kalenderski, and S. Osipov, 2015: Dust plume formation in the free troposphere and aerosol size distribution during the Saharan Mineral Dust Experiment in North Africa. *Tellus*, **67B**, 27170, doi:10.3402/tellusb.v67.27170.

Kiladis, G. N., C. D. Thorncroft, and N. M. J. Hall, 2006: Three-dimensional structure and dynamics of African easterly waves. Part I: Observations. *J. Atmos. Sci.*, **63**, 2212–2230, doi:10.1175/JAS3741.1.

Knippertz, P., and M. C. Todd, 2010: The central west Saharan dust hot spot and its relation to African easterly waves and extratropical disturbances. *J. Geophys. Res.*, **115**, D12117, doi:10.1029/2009JD012819.

Kristensen, T. B., T. Müller, K. Kandler, N. Benker, M. Hartmann, J. M. Prospero, A. Wiedensohler, and F. Stratmann, 2016: Properties of cloud condensation nuclei (CCN) in the trade wind marine boundary layer of the western North Atlantic. *Atmos. Chem. Phys.*, **16**, 2675–2688, doi:10.5194/acp-16-2675-2016.

Kumar, P., I. N. Sokolik, and A. Nenes, 2011: Measurements of cloud condensation nuclei activity and droplet activation kinetics of fresh unprocessed regional dust samples and minerals. *Atmos. Chem. Phys.*, **11**, 3527–3541, doi:10.5194/acp-11-3527-2011.

Levin, Z., E. Ganor, and V. Gladstein, 1996: The effects of desert particles coated with sulfate on rain formation in the eastern Mediterranean. *J. Appl. Meteor.*, **35**, 1511–1523, doi:10.1175/1520-0450(1996)035<1511:TEODPC>2.0.CO;2.

Lieke, K., and Coauthors, 2011: Particle chemical properties in the vertical column based on aircraft observations in the vicinity of Cape Verde Islands. *Tellus*, **63B**, 497–511, doi:10.1111/j.1600-0889.2011.00553.x.

Liu, Z., and Coauthors, 2008: CALIPSO lidar observations of the optical properties of Saharan dust: A case study of long-range transport. *J. Geophys. Res.*, **113**, D07207, doi:10.1029/2007JD008878.

Maher, B. A., J. M. Prospero, D. Mackie, D. Gaiero, P. P. Hesse, and Y. Balkanski, 2010: Global connections between aeolian dust, climate and ocean biogeochemistry at the present day and at the last glacial maximum. *Earth-Sci. Rev.*, **99**, 61–97, doi:10.1016/j.earscirev.2009.12.001.

Mahowald, N., S. Albani, J. F. Kok, S. Engelstaeder, R. Scanza, D. S. Ward, and M. G. Flanner, 2014: The size distribution of desert dust aerosols and its impact on the Earth system. *Aeolian Res.*, **15**, 53–71, doi:10.1016/j.aeolia.2013.09.002.

Mamouri, R. E., and A. Ansmann, 2015: Estimated desert-dust ice nuclei profiles from polarization lidar: Methodology and case studies. *Atmos. Chem. Phys.*, **15**, 3463–3477, doi:10.5194/acp-15-3463-2015.

Maring, H., D. L. Savoie, M. A. Izaguirre, L. Custals, and J. S. Reid, 2003: Mineral dust aerosol size distribution change during atmospheric transport. *J. Geophys. Res.*, **108**, 8592, doi:10.1029/2002JD002536.

McConnell, C. L., and Coauthors, 2008: Seasonal variations of the physical and optical characteristics of Saharan dust: Results from the Dust Outflow and Deposition to the Ocean (DODO) experiment. *J. Geophys. Res.*, **113**, D14505, doi:10.1029/2007JD009606.

Morman, S. A., and G. S. Plumlee, 2014: Dust and human health. *Mineral Dust: A Key Player in the Earth System*, P. Knippertz and W. J.-B. Stuut, Eds., Springer Netherlands, 385–409.

Müller, D., and Coauthors, 2010: Mineral dust observed with AERONET Sun photometer, Raman lidar, and in situ instruments during SAMUM 2006: Shape-dependent particle properties. *J. Geophys. Res.*, **115**, D11207, doi:10.1029/2009JD012523.

Müller, T., A. Schladitz, N. Kaaden, and A. Wiedensohler, 2009: Spectral absorption coefficients and imaginary parts of refractive indices of Saharan dust during SAMUM-1. *Tellus*, **61B**, 79–95, doi:10.1111/j.1600-0889.2008.00399.x.

Myhre, G., and Coauthors, 2013: Anthropogenic and natural radiative forcing. *Climate Change 2013: The Physical Science Basis*, T. F. Stocker et al., Eds., Cambridge University Press, 659–740.

Nickovic, S., A. Vukovic, M. Vujadinovic, V. Djurdjevic, and G. Pejanovic, 2012: Technical Note: High-resolution mineralogical database of dust-productive soils for atmospheric dust modeling. *Atmos. Chem. Phys.*, **12**, 845–855, doi:10.5194/acp-12-845-2012.

Niedermeier, N., and Coauthors, 2014: Mass deposition fluxes of Saharan mineral dust to the tropical northeast Atlantic Ocean: An intercomparison of methods. *Atmos. Chem. Phys.*, **14**, 2245–2266, doi:10.5194/acp-14-2245-2014.

Nousiainen, T., and K. Kandler, 2015: Light scattering by atmospheric mineral dust particles. *Light Scattering Reviews 9: Light Scattering and Radiative Transfer*, A. A. Kokhanovsky, Ed., Springer Berlin Heidelberg, 3–52.

Otto, S., M. de Reus, T. Trautmann, A. Thomase, M. Wendisch, and S. Borrmann, 2007: Atmospheric radiative effects of an in-situ measured Saharan dust plume and the role of large particles. *Atmos. Chem. Phys.*, **7**, 4887–4903, doi:10.5194/acp-7-4887-2007.

Peng, M. S., B. Fu, T. Li, and D. E. Stevens, 2012: Developing versus nondeveloping disturbances for tropical cyclone formation. Part I: North Atlantic. *Mon. Wea. Rev.*, **140**, 1047–1066, doi:10.1175/2011MWR3617.1.

Perry, K. D., S. S. Cliff, and M. P. Jimenez-Cruz, 2004: Evidence for hygroscopic mineral dust particles from the Intercontinental Transport and Chemical Transformation Experiment. *J. Geophys. Res.*, **109**, D23S28, doi:10.1029/2004JD004979.

Pöschl, U., 2005: Atmospheric aerosols: Composition, transformation, climate and health effects. *Angew. Chem., Int. Ed.*, **44**, 7520–7540, doi:10.1002/anie.200501122.

Prospero, J. M., 1999: Long-range transport of mineral dust in the global atmosphere: Impact of African dust on the environment of the southeastern United

States. *Proc. Natl. Acad. Sci. USA*, **96**, 3396–3403, doi:10.1073/pnas.96.7.3396.

——, and T. N. Carlson, 1972: Vertical and areal distribution of Saharan dust over western equatorial north Atlantic Ocean. *J. Geophys. Res.*, **77**, 5255–5265, doi:10.1029/JC077i027p05255.

——, and P. J. Lamb, 2003: African droughts and dust transport to the Caribbean: Climate change implications. *Science*, **302**, 1024–1027, doi:10.1126/science.1089915.

——, E. Bonatti, C. Schubert, and T. N. Carlson, 1970: Dust in the Caribbean atmosphere traced to an African dust storm. *Earth Planet. Sci. Lett.*, **9**, 287–293, doi:10.1016/0012-821X(70)90039-7.

——, F. X. Collard, J. Molinie, and A. Jeannot, 2014: Characterizing the annual cycle of African dust transport to the Caribbean Basin and South America and its impact on the environment and air quality. *Global Biogeochem. Cycles*, **28**, 757–773, doi:10.1002/2013GB004802.

Raga, G. B., D. Baumgardner, and O. L. Mayol-Bracero, 2016: History of aerosol-cloud interactions derived from observations in mountaintop clouds in Puerto Rico. *Aerosol Air Qual. Res.*, **16**, 674–688, doi:10.4209/aaqr.2015.05.0359.

Redelsperger, J.-L., C. D. Thorncroft, A. Diedhiou, T. Lebel, D. J. Parker, and J. Polcher, 2006: African Monsoon Multidisciplinary Analysis: An international research project and field campaign. *Bull. Amer. Meteor. Soc.*, **87**, 1739–1746, doi:10.1175/BAMS-87-12-1739.

Reid, J. S., and Coauthors, 2003a: Comparison of size and morphological measurements of coarse mode dust particles from Africa. *J. Geophys. Res.*, **108**, 8593, doi:10.1029/2002JD002485.

——, and Coauthors, 2003b: Analysis of measurements of Saharan dust by airborne and ground-based remote sensing methods during the Puerto Rico Dust Experiment (PRIDE). *J. Geophys. Res.*, **108**, 8586, doi:10.1029/2002JD002493.

Ryder, C. L., and Coauthors, 2015: Advances in understanding mineral dust and boundary layer processes over the Sahara from Fennec aircraft observations. *Atmos. Chem. Phys.*, **15**, 8479–8520, doi:10.5194/acp-15-8479-2015.

Sassen, K., P. J. DeMott, J. M. Prospero, and M. R. Poellot, 2003: Saharan dust storms and indirect aerosol effects on clouds: CRYSTAL-FACE results. *Geophys. Res. Lett.*, **30**, 35–31, doi:10.1029/2003GL017371.

Schepanski, K., I. Tegen, B. Laurent, B. Heinold, and A. Macke, 2007: A new Saharan dust source activation frequency map derived from MSG-SEVIRI IR-channels. *Geophys. Res. Lett.*, **34**, 1–5, doi:10.1029/2007GL030168.

——, ——, M. C. Todd, B. Heinold, G. Bonisch, B. Laurent, and A. Macke, 2009: Meteorological processes forcing Saharan dust emission inferred from MSG-SEVIRI observations of subdaily dust source activation and numerical models. *J. Geophys. Res.*, **114**, D10201, doi:10.1029/2008JD010325.

——, ——, and A. Macke, 2012: Comparison of satellite based observations of Saharan dust source areas. *Remote Sens. Environ.*, **123**, 90–97, doi:10.1016/j.rse.2012.03.019.

Scheuvens, D., L. Schütz, K. Kandler, M. Ebert, and S. Weinbruch, 2013: Bulk composition of northern African dust and its source sediments—A compilation. *Earth-Sci. Rev.*, **116**, 170–194, doi:10.1016/j.earscirev.2012.08.005.

Schladitz, A., T. Müller, A. Massling, N. Kaaden, K. Kandler, and A. Wiedensohler, 2009: In situ measurements of optical properties at Tinfou (Morocco) during the Saharan Mineral Dust Experiment SAMUM 2006. *Tellus*, **61B**, 64–78, doi:10.1111/j.1600-0889.2008.00397.x.

Schütz, L., 1980: Long-range transport of desert dust with special emphasis on the Sahara. *Ann. N. Y. Acad. Sci.*, **338**, 515–532, doi:10.1111/j.1749-6632.1980.tb17144.x.

Seneviratne, S., and Coauthors, 2012: Changes in climate extremes and their impacts on the natural physical environment. *Managing the Risks of Extreme Events and Disasters to Advance Climate Change Adaptation*, C. B. Field et al., Eds., Cambridge University Press, 109–230.

Siebert, H., and Coauthors, 2013: The fine-scale structure of the trade wind cumuli over Barbados—An introduction to the CARRIBA project. *Atmos. Chem. Phys.*, **13**, 10 061–10 077, doi:10.5194/acp-13-10061-2013.

Smirnov, A., B. N. Holben, D. Savoie, J. M. Prospero, Y. J. Kaufman, D. Tanre, T. F. Eck, and I. Slutsker, 2000: Relationship between column aerosol optical thickness and in situ ground based dust concentrations over Barbados. *Geophys. Res. Lett.*, **27**, 1643–1646, doi:10.1029/1999GL011336.

Sokolik, I. N., and Coauthors, 2001: Introduction to special section: Outstanding problems in quantifying the radiative impacts of mineral dust. *J. Geophys. Res.*, **106**, 18 015–18 028, doi:10.1029/2000JD900498.

Spiegel, J. K., N. Buchmann, O. L. Mayol-Bracero, L. A. Cuadra-Rodriguez, C. J. Valle Díaz, K. A. Prather, S. Mertes, and W. Eugster, 2014: Do cloud properties in a Puerto Rican tropical montane cloud forest depend on occurrence of long-range transported African dust? *Pure Appl. Geophys.*, **171**, 2443–2459, doi:10.1007/s00024-014-0830-y.

Stevens, B., and G. Feingold, 2009: Untangling aerosol effects on clouds and precipitation in a buffered system. *Nature*, **461**, 607–613, doi:10.1038/nature08281.

——, and Coauthors, 2016: The Barbados Cloud Observatory: Anchoring investigations of clouds and circulation on the edge of the ITCZ. *Bull. Amer. Meteor. Soc.*, **97**, 787–801, doi:10.1175/BAMS-D-14-00247.1.

Sullivan, R. C., M. J. K. Moore, M. D. Petters, S. M. Kreidenweis, G. C. Roberts, and K. A. Prather, 2009: Effect of chemical mixing state on the hygroscopicity and cloud nucleation properties of calcium mineral dust particles. *Atmos. Chem. Phys.*, **9**, 3303–3316, doi:10.5194/acp-9-3303-2009.

Swap, R., M. Garstang, S. Greco, R. Talbot, and P. Kallberg, 1992: Saharan dust in the Amazon basin. *Tellus*, **44B**, 133–149, doi:10.1034/j.1600-0889.1992.t01-1-00005.x.

Tanré, D., and Coauthors, 2003: Measurement and modeling of the Saharan dust radiative impact: Overview of the Saharan Dust Experiment (SHADE). *J. Geophys. Res.*, **108**, 8574, doi:10.1029/2002JD003273.

Tegen, I., 2003: Modeling the mineral dust aerosol cycle in the climate system. *Quat. Sci. Rev.*, **22**, 1821–1834, doi:10.1016/S0277-3791(03)00163-X.

Tesche, M., A. Ansmann, D. Muller, D. Althausen, R. Engelmann, V. Freudenthaler, and S. Gross, 2009: Vertically resolved separation of dust and smoke over Cape Verde using multiwavelength Raman and polarization lidars during Saharan Mineral Dust Experiment 2008. *J. Geophys. Res.*, **114**, D13202, doi:10.1029/2009JD011862.

——, and Coauthors, 2011: Optical and microphysical properties of smoke over Cape Verde inferred from multiwavelength lidar measurements. *Tellus*, **63B**, 677–694, doi:10.1111/j.1600-0889.2011.00549.x.

Thorncroft, C. D., and M. Blackburn, 1999: Maintenance of the African easterly jet. *Quart. J. Roy. Meteor. Soc.*, **125**, 763–786, doi:10.1002/qj.49712555502.

Toledano, C., and Coauthors, 2011: Optical properties of aerosol mixtures derived from sun-sky radiometry during SAMUM-2. *Tellus*, **63B**, 635–648, doi:10.1111/j.1600-0889.2011.00573.x.

Twohy, C. H., and Coauthors, 2009: Saharan dust particles nucleate droplets in eastern Atlantic clouds. *Geophys. Res. Lett.*, **36**, L01807, doi:10.1029/2008GL035846.

Valle-Diaz, C. J., E. Torres-Delgado, S. M. Colon-Santos, T. Lee, J. L. Collett, W. H. McDowell, and O. L. Mayol-Bracero, 2016: Impact of long-range transported African dust on cloud water chemistry at a tropical montane cloud forest in northeastern Puerto Rico. *Aerosol Air Qual. Res.*, **16**, 653–664, doi:10.4209/aaqr.2015.05.0320.

Wang, C., S. Dong, A. T. Evan, G. R. Foltz, and S.-K. Lee, 2012: Multidecadal covariability of North Atlantic sea surface temperature, African dust, Sahel rainfall, and Atlantic hurricanes. *J. Climate*, **25**, 5404–5415, doi:10.1175/JCLI-D-11-00413.1.

Wang, W., A. T. Evan, C. Flamant, and C. Lavaysse, 2015: On the decadal scale correlation between African dust and Sahel rainfall: The role of Saharan heat low–forced winds. *Sci. Adv.*, **1**, e1500646, doi:10.1126/sciadv.1500646.

Washington, R., and Coauthors, 2012: Fennec—The Saharan climate system. *CLIVAR Exchanges*, No. 60, International CLIVAR Project Office, Southampton, United Kingdom, 31–32. [Available online at www.clivar.org/sites/default/files/documents/Exchanges60.pdf.]

Weinzierl, B., and Coauthors, 2009: Airborne measurements of dust layer properties, particle size distribution and mixing state of Saharan dust during SAMUM 2006. *Tellus*, **61B**, 96–117, doi:10.1111/j.1600-0889.2008.00392.x.

——, and Coauthors, 2011: Microphysical and optical properties of dust and tropical biomass burning aerosol layers in the Cape Verde region—An overview of the airborne in-situ and lidar measurements during SAMUM-2. *Tellus*, **63B**, 589–618, doi:10.1111/j.1600-0889.2011.00566.x.

——, and Coauthors, 2012: On the visibility of airborne volcanic ash and mineral dust from the pilot's perspective in flight. *Phys. Chem. Earth*, **45–46**, 87–102, doi:10.1016/j.pce.2012.04.003.

Wurzler, S., T. G. Reisin, and Z. Levin, 2000: Modification of mineral dust particles by cloud processing and subsequent effects on drop size distributions. *J. Geophys. Res.*, **105**, 4501–4512, doi:10.1029/1999JD900980.

Yu, H. B., and Coauthors, 2015: Quantification of trans-Atlantic dust transport from seven-year (2007–2013) record of CALIPSO lidar measurements. *Remote Sens. Environ.*, **159**, 232–249, doi:10.1016/j.rse.2014.12.010.

Zipser, E. J., and Coauthors, 2009: The Saharan Air Layer and the fate of African easterly waves. *Bull. Amer. Meteor. Soc.*, **90**, 1137–1156, doi:10.1175/2009BAMS2728.1.


READ
IT
ON
ANY
DEVICE
kobo

DIURNAL VARIATION OF TRMM/LIS LIGHTNING FLASH RADIANCES

Themistoklis Chronis and William J. Koshak

The diurnal variation of lightning imaging sensor flash radiance, in context with storm areal extent, is examined with special attention to the National Climate Assessment (NCA)

The diurnal variation of thunderstorm frequency has been documented since the early 1920s from Wilson (1921), Whipple (1929), and the famous Carnegie curve (Israel 1971; Wallace 1975; Williams and Heckman 1993), and more recently by regional (e.g., see Lopez and Holle 1986; Orville and Huffines 2001; Rudlosky and Fuelberg 2010; Chronis 2012; Nastos et al. 2013; Chronis et al. 2015b) and global ground-based lightning location networks (Lay et al. 2007; Hutchins et al. 2014).

In the late 1990s, the Lightning Imaging Sensor (LIS; Boccippio et al. 2000b; Koshak et al. 2000; Christian et al. 2003) on board the Tropical Rainfall Measuring Mission (TRMM) satellite revealed two important lightning-related facts. First, far more lightning occurs over land, and, second, the diurnal variation of the lightning flash count follows the sun (http://science.nasa.gov/science-news/science-at-nasa/1999/essd10jun99_2/). The regional and worldwide ground-based lightning observations of Pinto et al. (1996), Orville and Huffines (2001), Orville et al. (2011), Chronis (2012), Villarini and Smith (2013), Virts et al. (2013), Hutchins et al. (2014), and Holle (2014), along with the references therein, are consistent with these findings. In particular, these studies demonstrate that most lightning over land occurs in the afternoon, a phenomenon that is likely driven by the diurnal continental radiative forcing (Williams and Heckman 1993; Chen and Houze 1997; Williams and Stanfill 2002; Chronis et al. 2015b). Regional departures from this pattern of behavior are present when the nocturnal boundary layer plays a decisive role in the convective instability (Wallace 1975; Balling 1985; Easterling and Robinson 1985; Lopez and Holle 1986; Williams et al. 2000). For example, continental storms over the U.S. Great Plains exhibit a propensity for nocturnal lightning activity, in the presence of mesoscale convective systems (MCSs; MacGorman and Morgenstern 1998; Zajac and Rutledge 2001; Orville and Huffines 2001).

Conversely, the diurnal variation in oceanic lightning activity is less pronounced than the continental

AFFILIATIONS: Chronis—University of Alabama in Huntsville, Huntsville, Alabama; Koshak—NASA Marshall Space Flight Center, Huntsville, Alabama
CORRESPONDING AUTHOR: Themistoklis Chronis, themis.chronis@nsstc.uah.edu

The abstract for this article can be found in this issue, following the table of contents.
DOI:10.1175/BAMS-D-16-0041.1

In final form 13 November 2016

Publisher's Note: On 25 July 2017 this article was revised to correct the in-text citation for Stolzenburg and Marshall (1998).

activity (see Bailey et al. 2007), with preference for late night/early morning storms (e.g., see Orville and Huffines 2001; Lay et al. 2007; Hutchins et al. 2014). The mechanisms leading to this variation are discussed in detail in works by Chen and Houze (1997), Dai (2001), Yang and Smith (2006), Liu et al. (2008), and Nesbitt and Zipser (2003). Deviations from this typical oceanic behavior are noted where strong influences by land–sea-breeze circulation are at play (e.g., the Gulf of Mexico; Virts et al. 2015).

Surprisingly, the majority of studies have repeatedly addressed the diurnal response of the continental and oceanic lightning flash frequency (i.e., counts), overlooking other available lightning flash–related information. For instance, since 1998, LIS has been reporting a proxy for lightning flash energy [the "flash radiance data product," discussed in Koshak (2010), and which we indicate here by the symbol ε]. Despite that ε has proven valuable to advanced applications in atmospheric chemistry modeling (Koshak et al. 2014b), still very little is known in terms of its diurnal variation (Beirle et al. 2014).

Moreover, since the Carnegie curve offers insight into the state of the atmosphere's electrical circuit and coupling with the climate system (Williams et al. 1999; Williams 2005; Rycroft et al. 2008; Blakeslee et al. 2014), the diurnal variation of ε is likely also an important indicator of climate variation. That is, the raw lightning flash count alone is only one possible indicator of climate variation; however, given the variable lightning flash currents and channel lengths, the energy of a lightning flash can vary by many orders of magnitude, hence providing a more accurate picture of the interrelationship between lightning and climate. In addition, it is important to note that ε is directly linked to lightning nitrogen oxide (LNO_x) production, which in turn directly influences greenhouse gas, ozone concentration, and hence air quality and climate (Koshak et al. 2014a). Finally, since the variation in ε depends on the variation of the flash energetics, it provides direct insight into the microphysical and kinematical state of the thunder cell and its ability to separate charge. Therefore, any climate variations that change the characteristics of thunder cells will likely have an associated impact on the types and characteristics of the lightning produced, which in turn affects the statistics of the observed values of ε. Hence, one important intent of this work is to establish a baseline for the diurnal variation of ε across a global scale, with coverage across many diverse regions and seasons. This sets the stage for assessing changes in ε obtained from important follow-on space-based lightning imagers [namely, the future International Space Station Lightning Imaging Sensor (ISS/LIS; Blakeslee and Koshak 2016), and the Geostationary Operational Environmental Satellite-R (GOES-R, now *GOES-16*) Geostationary Lightning Mapper (GLM; Goodman et al. 2013)]. In particular, because diurnal variations in ε will be evaluated over the continental United States (CONUS) up to ~38°N, this work represents an important continuation of, and a unique contribution to, the National Climate Assessment (NCA) lightning–climate study given in Koshak et al. (2015).

This paper is organized as follows: The next section discusses the data and methodologies employed. Next, we provide the diurnal variation results and also examine additional possible influences or biases (e.g., geographical and seasonal effects, instrument detection biases, sample size biases). We then discuss these findings and explore a few candidate physical mechanisms that might be important in explaining the observed diurnal variations. Moreover, it is shown that the diurnal variation in ε is remarkably similar to the diurnal variation of the cloud-to-ground peak current over the United States. Finally, our conclusions are outlined.

DATA AND METHODS. LIS is a nadir-staring optical imager that employs a wide (~80° × 80°) field-of-view lens system that focuses the image on a high-speed 128 × 128 pixel-array charge-coupled device (CCD). LIS detects lightning during both the daytime and nighttime. During the daytime, the solar-lit cloud swamps the lightning signal. Hence, several filtering methods are employed to improve the signal-to-noise ratio in order to make the daytime detection of lightning possible. The first of these filtering methods is spatial filtering; that is, the CCD array size mentioned above coupled with the low-Earth orbital altitude of LIS results in a ~4×4 km^2 (nadir) to 6×6 km^2 (perimeter) pixel footprint that roughly matches a typical thunder-cell cloud-top size. That is, if a much larger pixel footprint were employed, the chance for swamping the signal with solar reflection from non-lightning-producing clouds would increase. Second, spectral filtering is used. The lens system contains a narrowband (~1 nm) interference filter that operates in the near-IR at 777.4 nm, a prominent oxygen emission multiplet within the lightning spectrum. Third, the LIS employs temporal filtering. A diffuse cloud-top lightning optical pulse is typically on the order of ~400-μs width at half maximum. Hence, the LIS employs a CCD frame time of ~2 ms, which was the technology capability at the time, and reasonably matches the lightning pulse width. Finally, the fourth filtering method for improving the signal-to-noise ratio is to subtract a running average of the LIS background radiance (denoted here by BG) at a pixel from the current pixel BG value. If this residual at a pixel exceeds a specified threshold, then an optical "event" is said to occur [here, pixel-level event is the vernacular used to define a component of the full optical flash emission; see Mach et al. (2007)]. The LIS Real Time Event Processor (RTEP) carries out this processing. Note that the BG exhibits large variations due to the diurnal solar zenith angle and, of course, also depends on cloud albedo. The instrument threshold settings are specified in accordance with the expected range in BG values; that is, higher BG values are associated with higher thresholds in order to minimize lightning detection false alarm rates due to photon shot noise (i.e., a type of electronic noise resulting from random temporal fluctuations of photos hitting an optical device). The reader is referred to Christian et al. (1989), Koshak et al. (2000), and Boccippio (2002) for more details and discussions of the LIS instrument characteristics summarized here.

The primary LIS data product that we shall investigate is the so-called flash radiance. Spatially adjacent optical events within a 2-ms frame define an optical "group." A 5.5-km spatial constraint and a 330-ms temporal constraint are employed to decide which groups belong to the same optical "flash" (Mach et al. 2007). The flash radiance data product ε is actually a spectral energy density (in J m^{-2} ster^{-1} μm^{-1}; i.e., the LIS instrument is integrated over the duration of the flash so that the time unit vanishes). We will, however, loosely keep referring to it in its common nomenclature as a flash radiance. Within the LIS processing algorithm, the value of ε is obtained in an expedient/convenient manner by simply summing up the individual event "radiances" within a flash. This "shortcut" approach means that the value of each flash radiance should technically be reduced by roughly a factor of $\Delta\omega/\Delta\Omega$ to give the true spectral energy density, where $\Delta\omega$ is the typical pixel field of view and $\Delta\Omega$ is the flash field of view, each subtended at the LIS; that is, the LIS flash radiance data product overestimates the true spectral energy density by approximately a factor of $\Delta\Omega/\Delta\omega$. However, we are not concerned about this technical nuance, since in this study we are just analyzing the relative changes in the quantity ε that itself is proportional to the intercepted spectral flash energy [in J m^{-2} μm^{-1}; see the appendix to Koshak (2010) for additional details].

Overall, this study compiled ~15 million lightning flashes detected from individual LIS orbits during a 13-yr period spanning from 2002 to 2014. Years prior to 2002 are excluded to avoid possible complications from the TRMM orbital boost that occurred during August 2001 (Liu et al. 2008), but 2015 was also excluded as a result of intermittent LIS operation before its final decommission.

Each flash is grouped into hourly bins of local solar time (LST). Note that LST is computed from each flash's longitude. All flashes are further grouped as being continental or oceanic based on a 5 km × 5 km landmask. The flash count in each 1-h LST bin is reported as the summation (i.e., total hourly flash count), whereas ε is reported as an hourly average. The analysis also examines the average BG values associated with each event in a flash, in order to determine if any instrument-threshold-related effects bias the diurnal variations of ε (see the section below on possible biases due to LIS threshold settings).

RESULTS. Figure 1a illustrates the continental and oceanic total flash count diurnal (in LST) variation in absolute units. Figure 1b reports the same as Fig. 1a but in relative units (i.e., normalized by the respective maximum, in percent). Figures 1a,b are in agreement with the discussion in the opening section of this paper in that they support the continental lightning's preference for the late afternoon (~1500–1700 LST). This diurnal behavior is well documented by a multitude of space-based or ground-based lightning observations (references herein). The oceanic flash count, when compared to the respective continental count in absolute units, exhibits little diurnal variability (Fig. 1a). However, when the count is plotted in relative units (i.e., as a percent of the maximum value), the oceanic lightning activity during the late night/early morning hours becomes much more evident (Fig. 1b) and lies in agreement with previously published results (as discussed in the introductory section of this paper).

We report on the continental and oceanic ε diurnal variations in absolute (Fig. 1c) and relative units (Fig. 1d). The first observation to be gleaned from Fig. 1c is that oceanic flashes exhibit larger ε values than the respective continental flashes. This oceanic–continental contrast in ε is documented by Boccippio et al. (2000a,b) and Beirle et al. (2014), and this analysis further confirms that the contrast exists throughout the entire course of the day (Figs. 1c,d). In addition to LIS's optical emission, the aforementioned continental–oceanic contrast in the cloud-to-ground lightning flash peak current has been documented by several authors (e.g., see Lyons et al. 1998; Orville and Huffines 2001; Hutchins et al. 2014; Cooray et al. 2014, and references therein) and more recently studied for its physical origin by Chronis et al. (2016).

A key finding of this study pertains to the continental and oceanic ε diurnal variations shown in

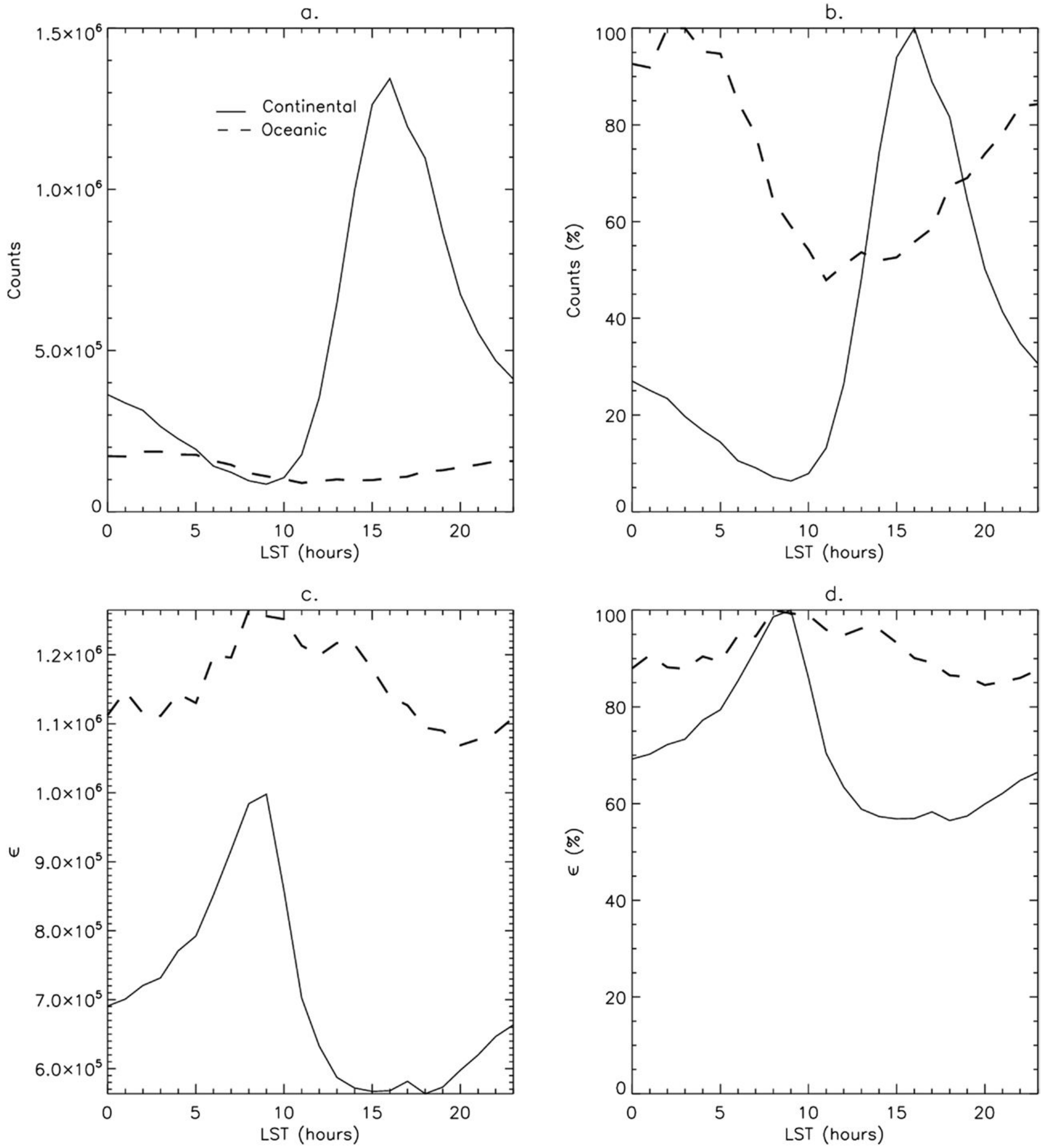

Fig. 1. (a) Total LST hourly continental (solid) and oceanic (dashed) flash counts in absolute units. (b) As in (a), but in relative units (%). (c) Continental (solid) and oceanic (dashed) ε in LST hourly averages. (d) As in (c), but for relative units. The *x* axis is shown in LST.

Figs. 1c,d. These exhibit a monotonic increase from ~2000 LST, reaching a maximum around 0900 LST, and a reduction thereafter (Fig. 1c). The continental ε has a broad minimum spanning between ~1500 and 1900 LST, whereas the oceanic ε gently decreases and does not reach a minimum until around 2000 LST (Fig. 1c). In terms of relative ε units (i.e., normalized by the respective ε maximum), the total continental diurnal variation is ~45% compared to ~15% for the oceanic (see Fig. 1d).

The current literature does not provide any background information in terms of the ε diurnal variation shown in Figs. 1c,d. The following subsections test whether the diurnal variations illustrated in Fig. 1 are due to any regional and/or seasonal effects or other statistical artifacts.

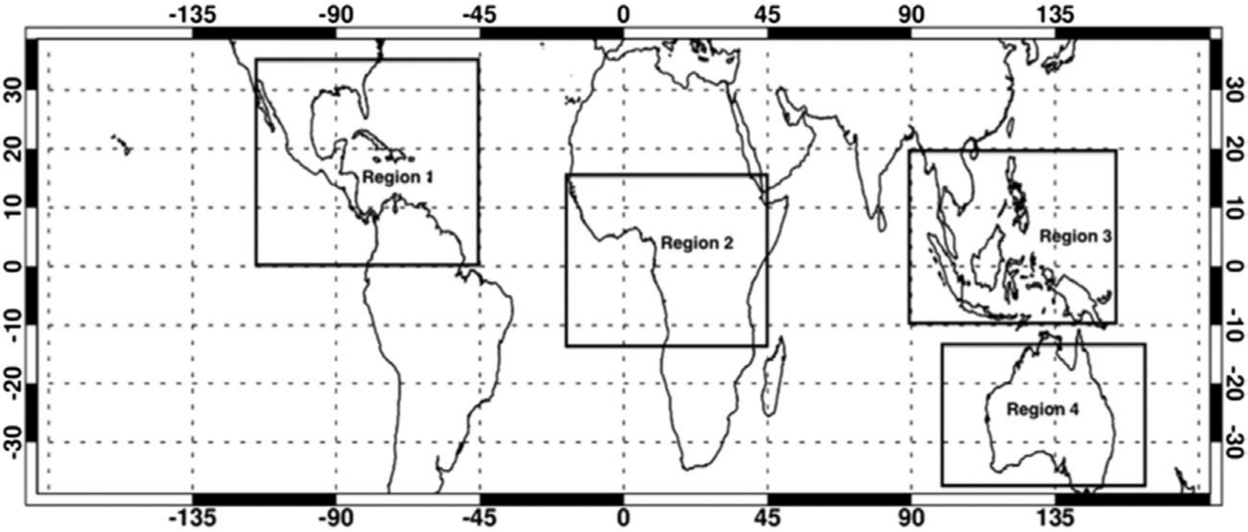

Fig. 2. Regions 1–4 for the regional parsed LIS dataset.

Sensitivity to regional and seasonal parsing. REGIONAL PARSING. The LIS global-scale (i.e., ~38°S–38°N) total flash counts and ε dataset employed in Fig. 1 are parsed into four regions (Fig. 2) encompassing part of the Americas (0°–35°N, 120°–45°W; region 1), Africa (15°S–15°N, 20°W–45°E; region 2), Southeast Asia (10°S–20°N, 90°–140°E; region 3), and Australia (35°–16°S, 100°–160°E; region 4). Note that for region 1 we have excluded latitudes south of ~0° to avoid possible effects from the South Atlantic anomaly (SSA; Buechler et al. 2012). For each of the four regions the same analysis that led to Fig. 1 is repeated.

As highlighted in Fig. 1a, all regions exhibit a total flash diurnal variation, typical of the so-called continental convective chimneys (see Williams and Satori 2004), with either a narrower (e.g., region 2) or broader (e.g., region 4) afternoon maximum (Fig. 3a). For regional differences in continental lightning activity differences, see Williams et al. (2002). The oceanic total flash counts of regions 1–4 (Fig. 3b) also closely follow the diurnal flash counts shown in Fig. 1a, in further agreement with the discussion in the opening section of this paper.

As far as the continental ε diurnal variation is concerned, all regions (Fig. 3c) exhibit an obvious consistency with the ε diurnal variation shown in Fig. 1c. In terms of the oceanic ε diurnal variation, regions 1, 3, and 4 (Fig. 3d) also highly agree with the findings in Fig. 1d (~0900 LST); however, region 2 (i.e., Africa) exhibits a diurnal ε maximum around 1300 LST that is approxiately four hours later than the typical 0900 LST result (Fig. 3d). Region 4 (i.e., Australia) exhibits the highest ε maximum for both continental and oceanic flashes (Figs. 3c,d). In contrast, region 2 (i.e., Africa) exhibits the lowest ε maximum for both continental and oceanic flashes (Figs. 3c,d).

SEASONAL PARSING. The original dataset employed in Fig. 1 is now parsed into the winter [December–February (DJF)], spring [March–May (MAM)], summer [June–August (JJA)], and fall [September–November (SON)] seasons and the diurnal variations of total flashes and ε are reported in Fig. 4.

As far as the continental/oceanic total flashes are concerned (Figs. 4a,b), we observe no deviation from the diurnal variation of the unparsed dataset (e.g., Figs. 1a,b). In terms of ε, all seasons consistently exhibit a continental ε diurnal maximum around 0900 LST and a broader minimum (~1500–1900 LST; Fig. 4c), in high agreement with the unparsed dataset (Fig. 1c). For the oceanic ε diurnal variation (Fig. 4d), all seasons exhibit a diurnal maximum (minimum) around 0900 LST (~2000 LST), also in line with the unparsed dataset shown in Fig. 1d. The winter (DJF) season demonstrates the highest ε values for continental and oceanic flashes.

Possible biases due to LIS threshold settings. As mentioned in the earlier section dealing with our data and methods, the LIS instrument threshold for lightning detection is set higher for larger BG values in order to minimize the false alarm rate due to photon shot noise. Therefore, it is important to determine if any ε diurnal increases (decreases) can be attributed to respective increases (decreases) in BG.

Figure 5a illustrates a bell-shaped diurnal BG variation, which simply confirms that the brightest cloud scenes occur at solar zenith (maximum BG values

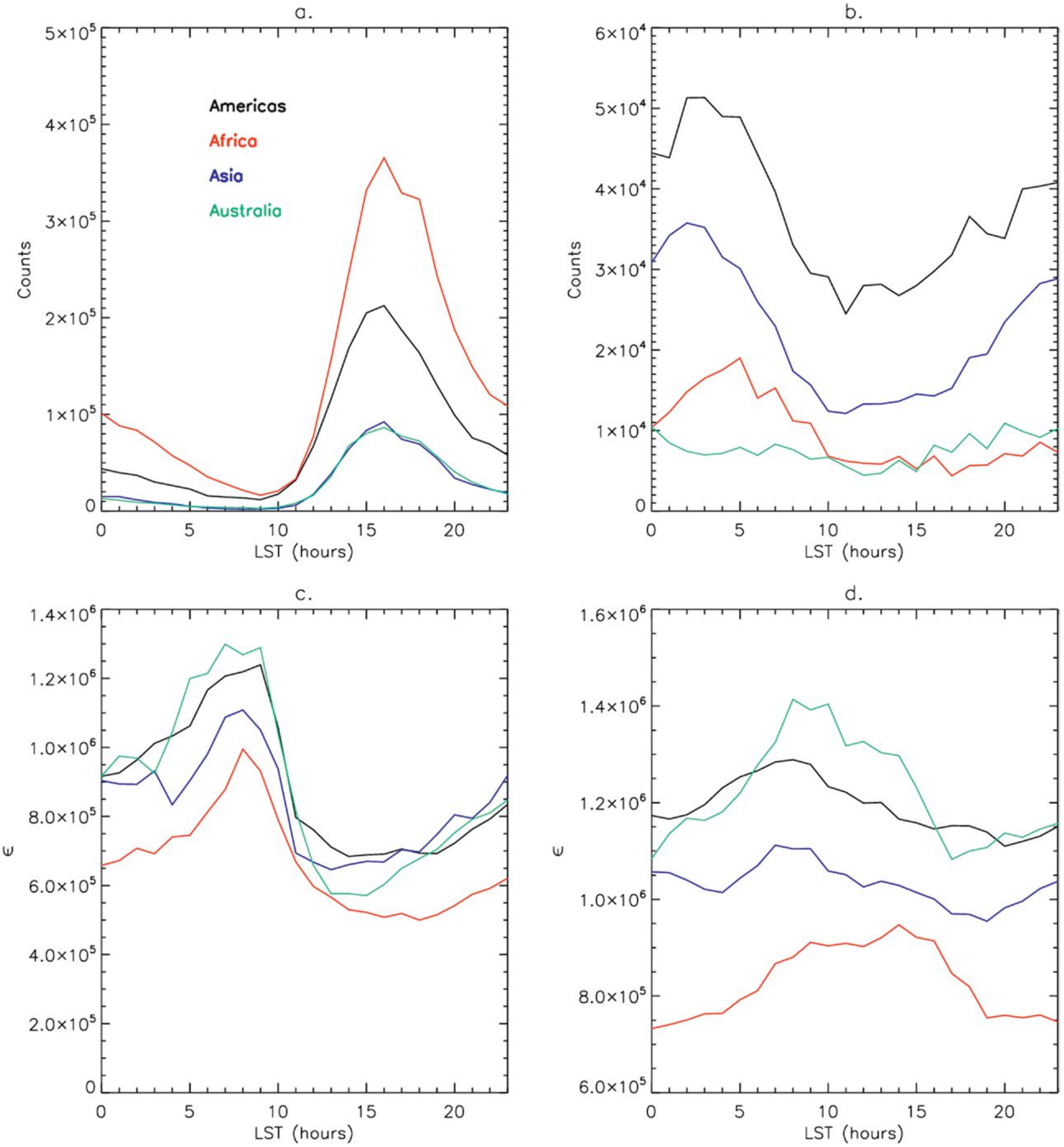

Fig. 3. As in Fig. 1, but the four selected regions for (a) continental and (b) oceanic flash counts in absolute units and (c) continental and (d) oceanic ε.

~1200 LST, both continental and oceanic BG). To facilitate the comparison, Fig. 5b is a copy of Fig. 1d, which showed the continental and oceanic ε diurnal variations. Figures 5c,d serve as the means of investigating whether a relationship/function between ε and BG can be established throughout daytime hours (i.e., BG > 0). Note that in Fig. 5 all variables are normalized by their respective maximum values and, hence, are reported as percentages.

The scatterplot in Fig. 5c between ε and BG exhibits three different trends: a positive linear trend from ~0500 to 0900 LST, a negative linear trend from 0900 to 1300 LST, and a rather invariant trend between ~1400 and 1800 LST. The term "invariant" refers to a statistically insignificant regression slope (i.e., ε = slope × BG, where the p value of the slope is greater than ~0.5 and thus statistically insignificant). Although both ε and BG increase from about 0400 to

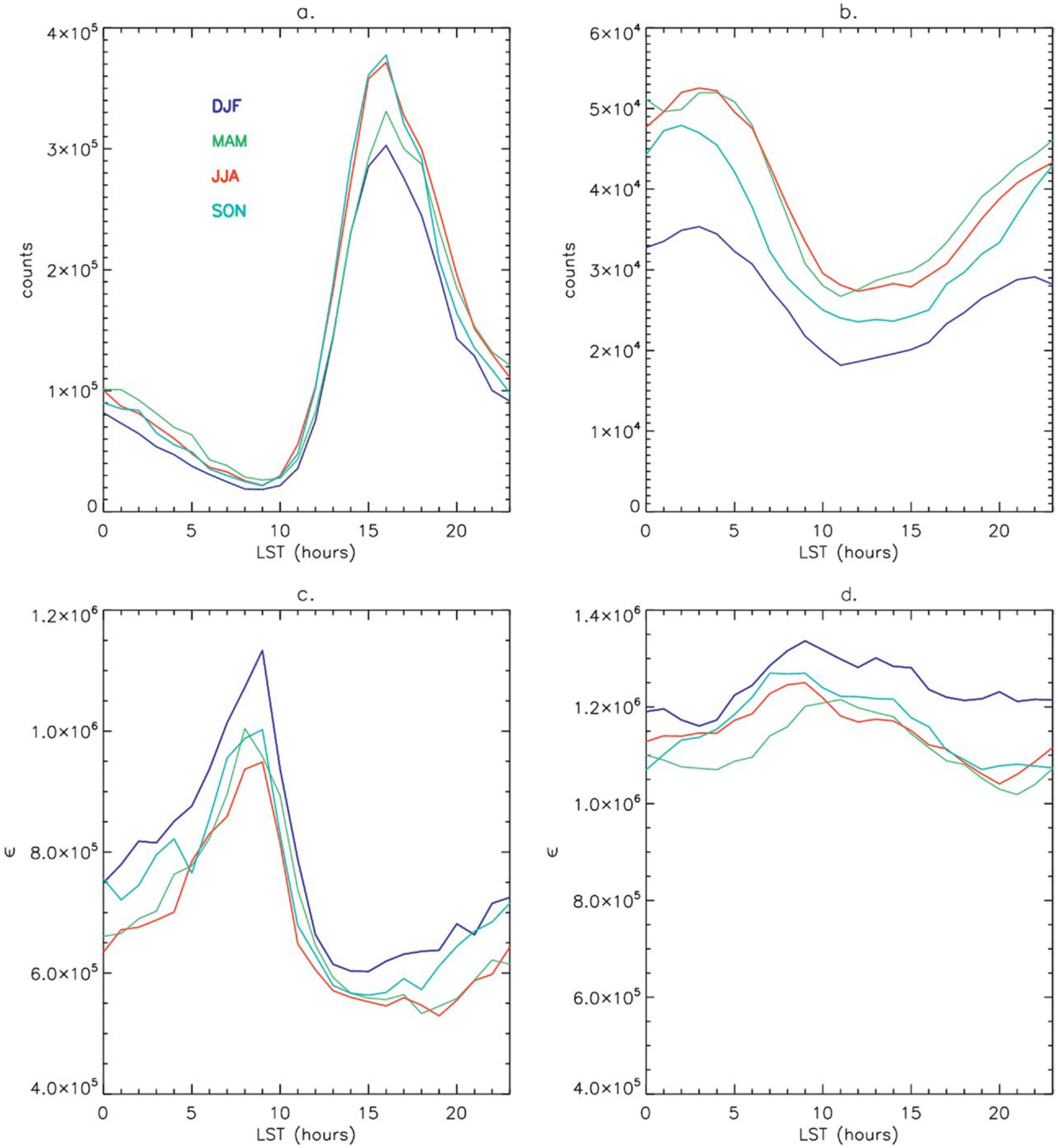

Fig. 4. As in Fig. 1, but the four seasons for (a) continental and (b) oceanic flash counts in absolute units and (c) continental and (d) oceanic ε.

0800 LST, ε decreases substantially, while BG continues increasing toward its peak. In addition, ε increases in the same manner prior to 0400 LST (i.e., before the BG values become greater than zero). In fact, ~20% of the continental ε diurnal variation occurs during nighttime hours (i.e., BG = 0; Fig. 5c). Therefore, the diurnal variation of ε appears to be a real (natural) variation and not an artifact of the LIS instrument thresholding methodology.

Interestingly, had we tested the same hypothesis for the oceanic ε, the findings in Fig. 5d would have indicated that 1) increasing BG values during ~0600–1100 LST relate to increasing ε values and 2) decreasing BG values during ~1300–1700 LST relate to decreasing ε values. In other words, had the oceanic ε been exclusively considered, the evidence would have suggested that the oceanic ε diurnal variation might be partly attributed to diurnal BG

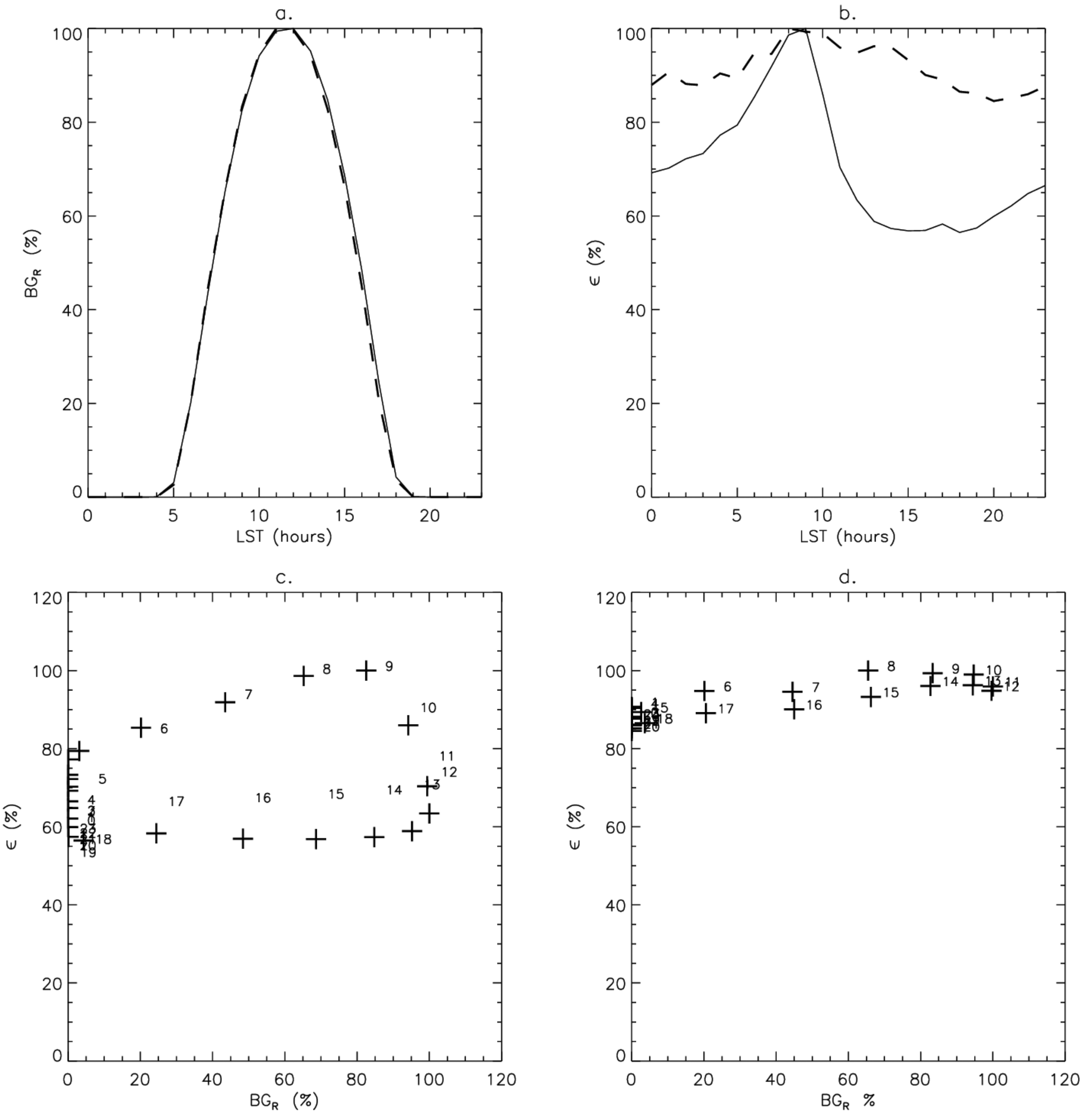

Fig. 5. Diurnal variation in relative units for continental (solid) and oceanic (dashed) (a) BGR and (b) ε. (c) Scatterplot showing continental hourly BGR (*x* axis) and ε (*y* axis) LST hourly averages in relative units. (d) As in (c), but for oceanic results.

biases. However, it would be unreasonable to suggest that such bias is selective for oceanic and not continental ε; hence, the linearity between the oceanic BG and ε diurnal time series observed in Fig. 5d is circumstantial. LIS decay through the several years of operation could further constitute a possible introduction of erroneous results; nonetheless, Buechler et al.'s (2012) deep convective cloud (DCC) analyses have demonstrated that the BG values have been stable during 1998–2010.

Possible sample-size-related biases. Another bias that could possibly introduce numerical artifacts is the sample size of the diurnal total flash count. For instance, a hypothesis could be framed around the fact that ε peaks during a diurnal period when the respective total flashes are minimum (~0900 LST; e.g., see Figs. 1a,c). To facilitate this comparison, we combine the diurnal total flash counts and ε averages into a single scatterplot, where the respective hourly bins are also annotated (Fig. 6). We observe that the total flashes are monotonically reduced between ~2100 and 0900 LST, reaching their minimum when ε is maximum (~0900 LST; Fig. 6a). Two statistical tests for significant differences in the ε means are performed (Student's and Wilcox). The results yield that the ε means at 2100 and 0900 LST are different at the 99.99% level (p value < 0.001). These statistical tests are repeated for intermediate diurnal periods (e.g., 2000 and 1000, 1900 and 1100 LST, and so forth) and in all cases the results also yielded significantly different ε means at the 99.99% level. Moreover, if the sampled total flash counts were biasing the diurnal ε variation, then this would also be evident in the oceanic ε results. However, from Fig. 6b we observe no consistent relationship between the two variables during any diurnal period.

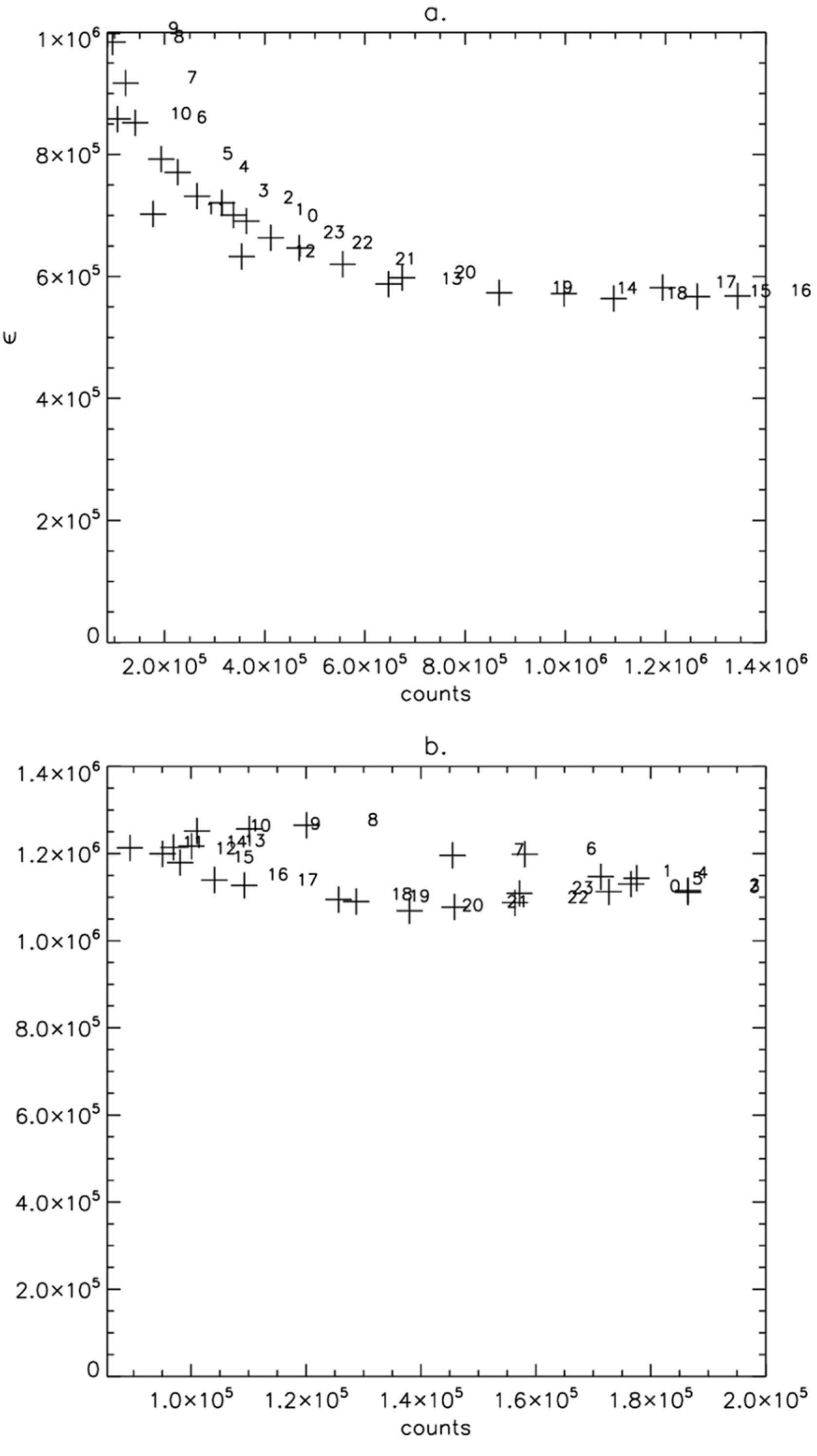

Fig. 6. (a) Scatterplot between continental LST hourly flash counts (*x* axis) and ε (*y* axis) LST hourly averages in absolute units. (b) As in (a), but for oceanic results.

DISCUSSION. An extensive part of the analysis (presented in the previous three subsections) was dedicated to examining the consistency of the results shown in Fig. 1. Even though the diurnal variation in ε was examined for 32 different cases (i.e., four regions, four seasons, and two surfaces: continental and oceanic), only the oceanic part of region 2 (Africa) has a diurnal maximum (~1200 LST) in ε that is somewhat of an outlier. Therefore, it would be fair to state that the diurnal variation in ε is regionally and seasonally robust but it is also free of significant biases related to the LIS threshold setting methodology, or sample size. Hence, the findings in this paper are significant because they reveal a real (i.e., natural) diurnal variation in a specific lightning flash characteristic (ε) that has not been previously documented, and which begs a preliminary physical explanation.

Relationship between ε and Ip. Works by Guo and Krider (1982), Idone and Orville (1985), and Gomes and Cooray (1998) found a linear relationship between the light intensity and the current *I* of laboratory-induced spark discharges. More recently, Wang et al. (2005) documented that current and light signals at the bottom of the rocket-triggered lightning channel exhibit a linear relationship along the rising portions of their waveforms (i.e., respective peaks). This relationship disappears and the light emission amplitude decreases much faster than the respective current (Wang et al. 2005). A relationship between lightning peak current and lightning strokes detected by the World Wide Lightning Location Network (WWLLN) has also been documented in Hutchins et al. (2012).

In light of the above-mentioned laboratory-demonstrated physical ties between ε [i.e., optical brightness of a flash; see the appendix to Koshak (2010)] and lightning current, the findings in the recent study by Chronis et al. (2015b) might further corroborate this relationship on a diurnal scale. The study was based on the National Lightning Detection Network (NLDN; Cummins et al. 1998; Cummins and Murphy 2009). Unlike spaceborne sensors, ground networks detect that the ground wave of the electromagnetic field radiated from the cloud-to-ground (CG) lightning flash. These peak radiation fields are positively correlated with the so-called first CG return stroke peak current (Ip, also shown in Hutchins et al. 2012). Chronis et al. (2015b) reported a consistent Ip quasi-sinusoidal diurnal (in LST) variation peaking around 0900 LST and attaining a minimum at ~1900–2000 LST over the CONUS for the period 2001–10. Although the values of Ip are not complicated by cloud optical

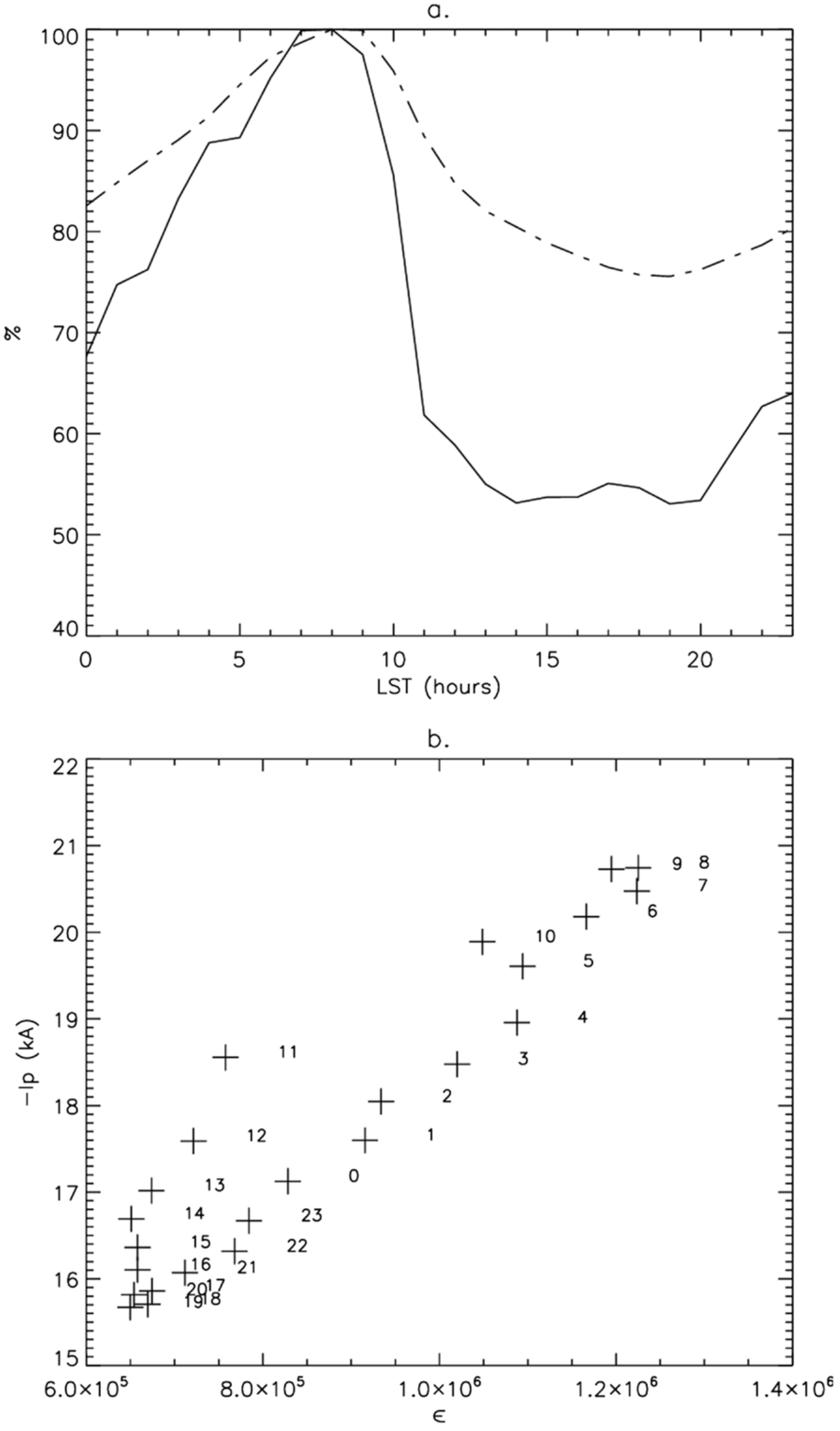

Fig. 7. (a) Diurnal variation in relative units between hourly ε (solid) and Ip (dashed) LST hourly averages over the CONUS. (b) Scatterplot showing results for the same variables.

thickness as is ε, the retrieval of Ip from measurements of radiated electric fields is affected by both modeling assumptions and measurement errors (Rachidi and Thottapillil 1993). For the purposes of Fig. 7 the diurnal variation in ε is recalculated for 30°–50°N, 120°–70°W (roughly the CONUS) from the unparsed LIS dataset. Despite the Ip and ε being retrieved from disparate observational platforms (i.e., ground-based versus spaceborne), Fig. 7 confirms the physical ties between Ip and ε on the diurnal scale. Figure 7b highlights a strong diurnal linearity (linear correlation coefficient ~0.8) between ε and Ip, but also temporal agreement in terms of the respective diurnal maxima and minima while their differences lie in their relative diurnal variation (Fig. 7a; ~25% vs 45%).

Given the regional limitation of the previous ε–Ip covariation study, we cannot assume that these diurnal similarities will be further evident on a global scale. For instance, Chronis et al. (2015b) did not compute the Ip diurnal variation over the oceans adjacent to the CONUS given the expected bias in Ip due to the reduction in the NLDN detection efficiency (Nag et al. 2011). Nevertheless, the previous comparison between ε versus Ip in Fig. 7, viewed in context with the findings in Fig. 6, has offered this study a distinct advantage that is discussed next.

Flash radiance ε in a capacitor model. A simple capacitor model can be invoked to provide some insight into the strong covariance found between ε and Ip (Fig. 7). The top plate of the capacitor represents the horizontal extent of the upper positive thundercloud charge ($+Q$) and the bottom plate the negative thundercloud charge ($-Q$). The area of each plate is A, and d is the vertical separation distance between the plates. The electric field E between the capacitor plates represents the vertical thundercloud electric field. The capacitance is given by $C = Q/V = \varepsilon_0 A/d$, where V is the voltage across the capacitor plates that represents the thundercloud electric potential between the charge centers (i.e., $V = Ed$) and ε_0, the permittivity of free space. Since the thundercloud is located above the conducting Earth, it is more realistic to envision the thundercloud capacitor to be sitting above a conducting plane rather than to just view the thundercloud as an isolated capacitor.

When this model improvement is made, the electrostatic boundary conditions are met by replacing the conducting plane with image plates (i.e., the standard method of images is invoked). Next, we take each plate to be a circular disk of radius a, with a constant charge density $\sigma = \pm Q/A = \pm Q/(\pi a^2)$ for the positive (top) and negative (bottom) plates, respectively. Hence, as the plate area increases, so too does Q in order for σ to remain constant. The electric potential due to one charged plate a distance z along the circular disk axis is given by $\sigma[(a^2 + z^2)^{1/2} - |z|]/(2\varepsilon_0)$. Carrying out the method of images for all four plates (i.e., the two real plates and the two image plates), one obtains by superposition the voltage across the capacitor V as

$$V = \frac{\sigma}{\varepsilon_0}\left[\sqrt{a^2 + d^2} - \sqrt{a^2 + \left(z_N + z_P\right)^2} + \frac{1}{2}\sqrt{a^2 + 4z_N^2} + \frac{1}{2}\sqrt{a^2 + 4z_P^2} - d - a\right],$$

where z_N and z_P are the altitude of the negative and positive charged plates, respectively, and hence $d = z_P - z_N$ (i.e., the thundercloud depth). Note that $V = \phi_N - \phi_P$, where ϕ_N is the electric potential of the negative plate with respect to the ground and ϕ_P is the potential of the positive plate with respect to the ground (again, each found from the method of images). Plots of ϕ_N, ϕ_P, V, and $E = V/d$ are provided in Fig. 8 as a function of increasing plate area (i.e., circular plate radius increasing from 10 to 2,000 m); the input values are $Q = 40$ C, $z_N = 7$ km, and $z_P = 10$ km.

The potential ϕ_N plays a fundamental role in setting a limit on Ip (Stolzenburg and Marshall 2008). Analytic models for CG lightning leaders involving long and thin conductors show that the charge per unit length λ along the CG leader channel as it extends to the ground is proportional to ϕ_N (Kasemir 1965; Mazur and Ruhnke 1998; Williams and Heckman 2012). The return stroke peak current Ip represents the neutralization of the deposited CG leader charge and is given by Ip = $\lambda \upsilon$, where υ is the return stroke speed. Hence, a larger magnitude of ϕ_N (or equivalently a larger magnitude of V; see Fig. 8) implies a larger magnitude of λ and, hence, a larger magnitude of Ip. Finally, the larger magnitude of Ip implies more channel brightness (i.e., larger ε). Therefore, these simple considerations lead to the expectation that Ip and ε should vary together, as is indeed found in Fig. 7.

EFFECT OF FLASH RATE.

Assuming that the thundercloud capacitor's geometrical characteristics are fixed (i.e., A and d are constant), it can be argued that frequent lightning discharges limit the growth of the electric field E, which in turn limits the value of the potential ϕ_N and thereby reduces the values of Ip and hence ε as discussed above. Hence, one would expect the flash rate and ε to have an inverse relationship. An important observation gleaned from Fig. 6a is that the total flash count and ε indeed follow an inverse relationship; however, it should be noted that this is true only during ~2200–0900 LST.

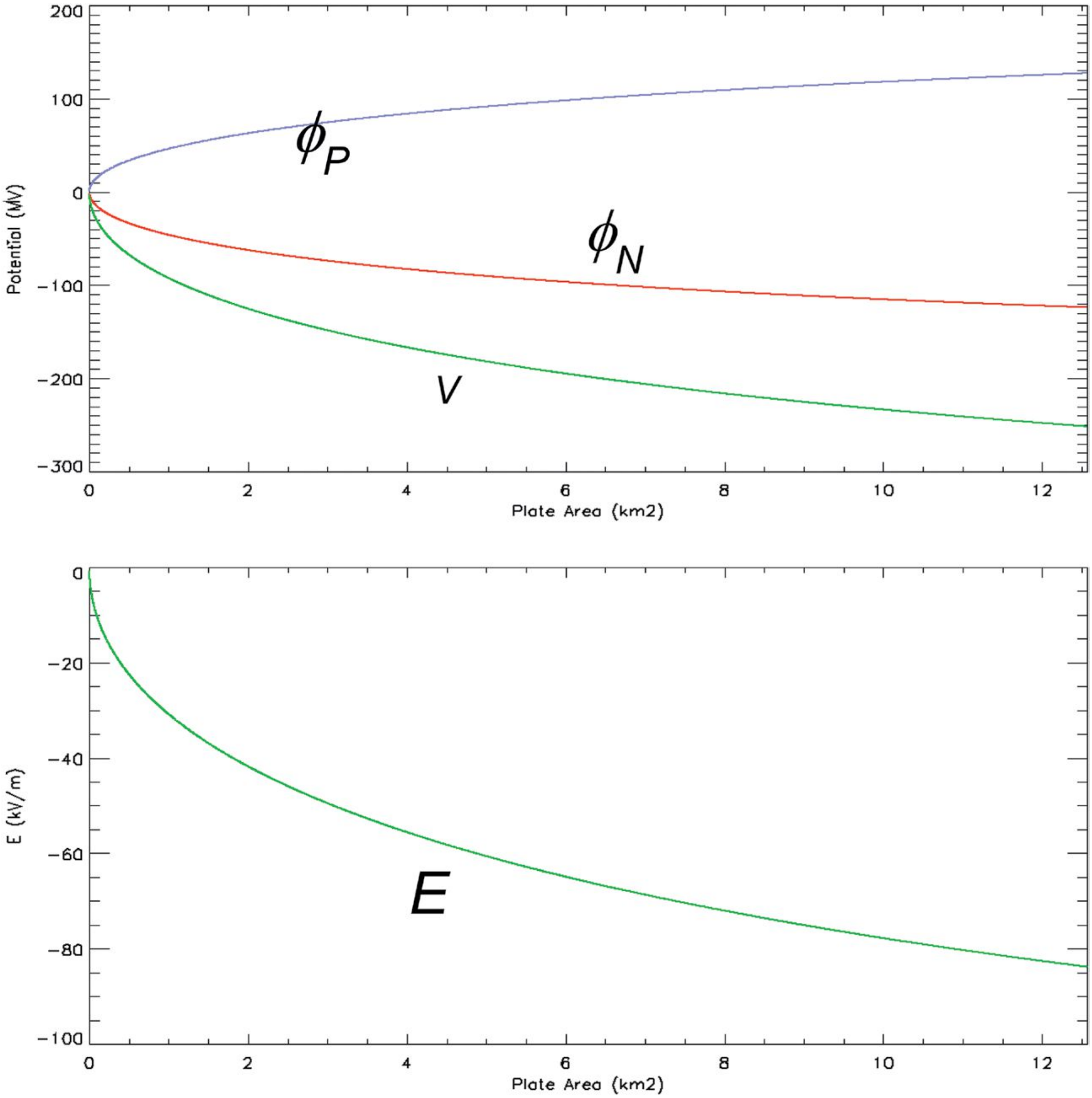

Fig. 8. The numeric results of a simple capacitor model for (top) ϕ_N (red), ϕ_P (blue), and V (green), and (bottom) $E = V/d$.

In contrast, this relationship is asymptotic during ~1600–2100 LST, a diurnal period during which the total flash count is reduced by almost 50% (Fig. 6a), while ε varies by less than ~3% (Figs. 1, 6a).

Oceanic flashes cast more doubt on a simple inverse relationship, in that Fig. 6b reveals that no relationship during any diurnal period can be established between the two variables (linear correlation coefficient ~0; Fig. 6b). Evidently, the collective results of Fig. 6 strongly advocate that the diurnal total flash count variation cannot unequivocally explain the respective ε variations throughout the entire 24-h day.

EFFECT OF STORM AREA. From the same capacitor model, a larger horizontal extent (i.e., larger capacitor plate area A) yields a larger Ip given σ is constant (see Fig. 8 and the associated discussion). The results presented by Nesbitt and Zipser (2003) are particularly useful for this examination for two reasons. The first is that their study compiled a database of the areal extent of storms observed from sensors on board the same satellite as LIS (TRMM). The second is that the Nesbitt and Zipser (2003) analysis also was performed as a function of LST (as done here). In particular, Nesbitt and Zipser (2003) documented the climatological

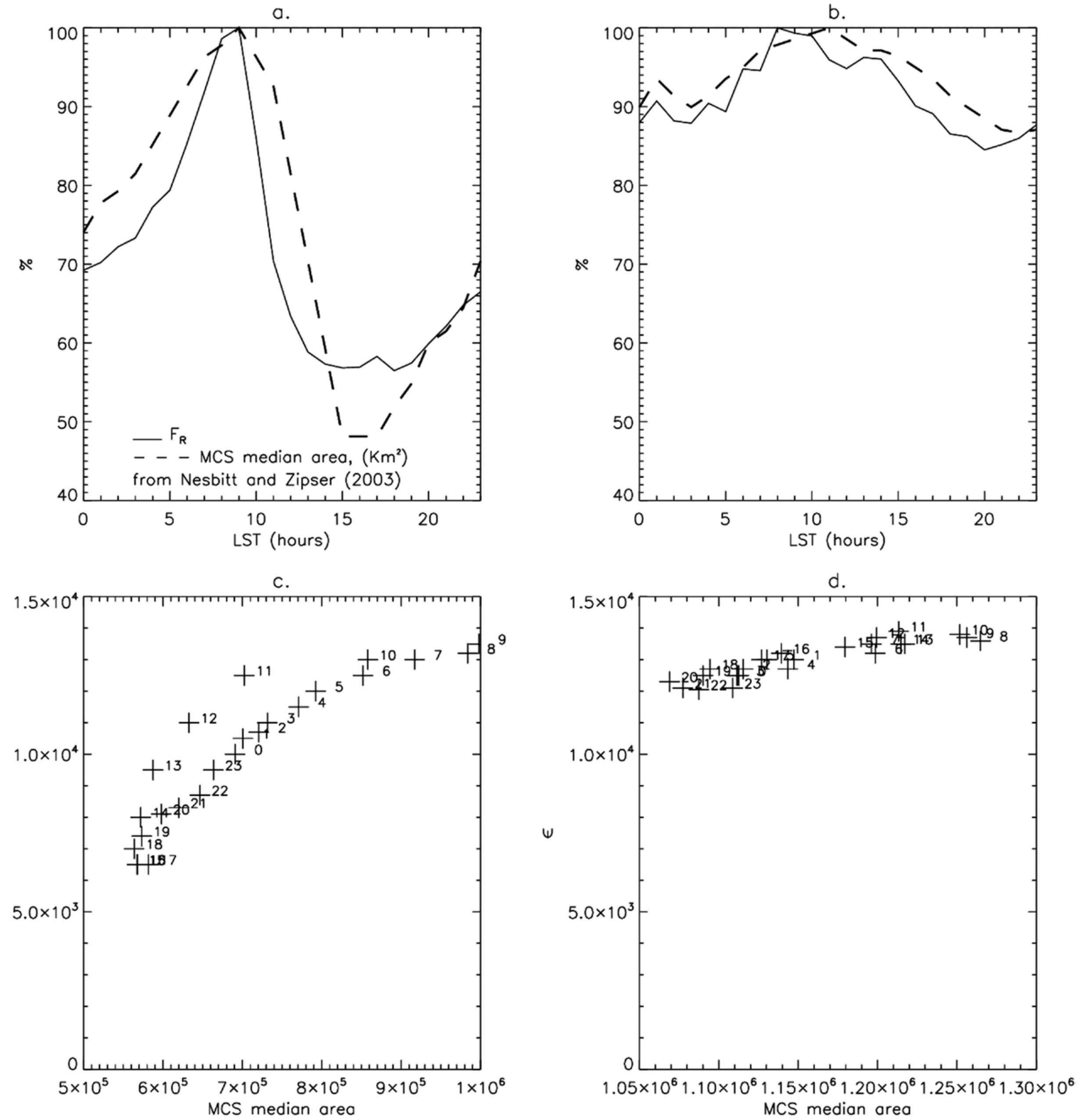

Fig. 9. (a) Diurnal variation in relative units for continental (solid) ε and MCS areal extent LST hourly averages. (b) As in (a), but for oceanic results. (c) Scatterplot showing differences between continental MCS areal extent and ε hourly averages in absolute units. (d) As in (c), but for oceanic results.

(December 1997–November 2000) diurnal precipitation features of convective storms as retrieved from TRMM's microwave ice scattering intensity and areal (i.e., horizontal) extent. The largest of the identified storm groups in their study were the MCSs. We deem that the MCS might be a key component in the observed ε diurnal variation for the following reasons. The MCSs have a unique dynamical organization that allows them to develop and propagate, even when the main source of atmospheric instability on a diurnal scale (i.e., the sun) is absent (see Houze 2004). The latter might provide clues relevant to the ε-increasing trend observed from the late night hours until ~0900 LST (see Figs. 1c,d). Moreover, the MCS areal extent diurnal variation exhibits a marked similarity with the continental and oceanic ε results shown in Figs. 1c,d (see Figs. 4, 5c in Nesbitt and Zipser 2003). In particular the diurnal area variations for both continental and oceanic MCSs exhibit a distinct maximum around 0900 LST followed by a decreasing trend, minimizing around 1500–1600 LST (continental) and ~2000 LST (oceanic). The mechanisms controlling the MCS maturity and decay diurnal phases are discussed in Nesbitt and Zipser (2003) and references therein. Figure 9 illustrates the diurnal variation of the MCS areal extent (from Figs. 4, 5c in Nesbitt and Zipser 2003) and the respective ε (i.e., from Figs. 1c,d) in relative (Figs. 9a,b) and absolute units (Figs. 9c,d). The noteworthy covariation between the two variables is not only evident from the linear correlation coefficient (~0.9; Figs. 8d, 9c) or the temporal coincidence between the respective diurnal maxima–minima, but also exemplified in terms of the relative diurnal variation. For instance, the continental MCS areal extent (~55%; Fig. 9a) and ε (~45%; Fig. 9a) relative diurnal variation are in close agreement, but in even closer agreement lie the respective oceanic values (~15%; Fig. 9b).

In light of the physical linkages between ε and A, as well as their diurnal similarity demonstrated in Fig. 9, the MCS areal extent hypothesis is certainly worth pondering as a preliminary physical explanation. Despite that not all the storms are MCSs, the processes that dictate the diurnal areal extent are not only restricted to the MCS storm type but also apply for smaller-scale storms. This is shown to be true for the continental storms in Nesbitt and Zipser (2003, see their Fig. 4c) and is also suggested in Chen and Houze (1997, see their Fig. 18 and references therein) as a more general characteristic diurnal storm evolution.

CONCLUSIONS. Since the Carnegie observations, lightning's diurnal variation has been established as one of its robust characteristics. However, during the past three decades, and despite the wealth of available lightning flash information, studies addressing variables other than flash counts are few and far between. Based on 13 years' worth of LIS observations, this study has revealed a previously overlooked, but very interesting, diurnal variation related to the flash radiance. The diurnal variation of the LIS flash radiance data product, ε, exhibits a consistent increase from late afternoon (~2000 LST) until ~0900 LST and a decreasing trend reaching a broader (continental) or narrower (oceanic) minimum spanning between 1500 and 1900 LST. The overall continental (oceanic) relative variation is ~45% (~15%).

The diurnal variation in ε was initially interrogated for regional and seasonal consistency as well as statistical biases. We found that the diurnal variation is consistent on seasonal, regional, and global scales, and does not appear to be associated with any artifacts (e.g., LIS threshold setting biases or sample size biases). In addition to documenting these novel findings and vetting potential biases, this study discussed some plausible arguments that might be important in explaining the findings herein. The physical ties and similarities to the Ip over the CONUS, but also the Ip's independence from cloud optical thickness, strengthens the hypothesis in favor of a physical mechanism that truly reflects the diurnal variations of flash energetics. Follow-on studies based on lightning energetics from, for example, the World Wide Lightning Location Network (Hutchins et al. 2012, 2013; Virts et al. 2013) or peak current from, for example, Vaisala's Global Lightning Dataset (Said et al. 2013) are expected to shed more light on the diurnal variations highlighted herein.

Moreover, using a simple electrical capacitor analog for a thundercloud (expanded to include a conducting plane Earth), it was shown that one should expect good covariance between ε and Ip, which is indeed what we found empirically (see Figs. 7, 8). Also, the diurnal variation of the total flash count (i.e., a limiting factor to E) explains to a certain extent the diurnal variation of ε over land; however, it does not explain the diurnal variation of ε over the ocean. Based on the same capacitance model, we further hypothesized that the thundercloud horizontal areal extent might explain the observed diurnal variation of ε (Fig. 9a). Data from previous studies support this hypothesis based on MCS storm types.

It is premature to give a final verdict for the exact causes of the diurnal variation in ε, but this paper has provided some important insights that are seemingly in line with simple modeling results and observations. Within this context this postulate can be questioned because of the uncertainties in the ε observations and diverse storm types, but also the employed oversimplifications of the thundercloud processes via a simple parallel plate capacitor model, which might disregard important but currently elusive mechanism(s) also contributing to the observed ε diurnal variation. Nevertheless, the findings herein raise various and important implications. Given the intimate relationship of lightning flash energetics and the production of nitrogen oxides (Koshak et al. 2014b), these results are pertinent to air quality modeling and atmospheric chemistry (e.g., Koshak et al. 2014a). In addition, the continental–oceanic, regional, and seasonal ε contrasts shown herein (see Figs. 1, 3, 4) could be examined from the viewpoint of a physical mechanism that regulates the flash energetics on a regional or seasonal scale across the convective spectrum, including flash radiance storm-scale observations and possible applications as a proxy for a storm's severity and updraft intensity (e.g., see Schultz et al. 2011; Chronis et al. 2015a). Within the context that flash radiance is an important component in modeling storms from a capacitor perspective, we argue that the findings herein might also raise additional implications for studies on the global electric circuit (Rycroft et al. 2008; Williams 2009; Chronis 2009; Hutchins et al. 2014; Blakeslee et al. 2014). We believe that the science community has just begun to understand how flash energetics can be studied independently but also in conjunction within the same framework as traditional lightning-related research. To this end, the GLM and ISS/LIS missions are expected to significantly augment the already available plethora of lightning flash observations and hence further explore several of the claims made by this contribution.

ACKNOWLEDGMENTS. This work was jointly supported under NASA Program Announcement NNH14ZDA001N-INCA (Climate Indicators and Data Products for Future National Climate Assessments; Dr. Jack Kaye and Dr. Lucia Tsaoussi, NASA Headquarters) and through a NOAA–NASA Interdepartmental Purchase Request Economy Act Order (NA15AANEG0143) for the NOAA GOES-R Geostationary Lightning Mapper Visiting Scientist Risk Reduction program under the guidance of Dr. Steve Goodman, senior (chief) scientist for the NOAA GOES-R Systems Program. The authors would also like to extend their appreciation to Mr. Dennis Buechler, Dr. Kenneth Cummins, and Dr. Rich Blakeslee for their insightful comments.

REFERENCES

Bailey, J. C., R. J. Blakeslee, D. E. Buechler, and H. J. Christian, 2007: Diurnal lightning distributions as observed by the Optical Transient Detector (OTD) and the Lightning Imaging Sensor (LIS). *Proceedings of the 13th International Conference on Atmospheric Electricity*, X. Qie and C. Sauders, Eds., Vol. II, ICAE, 657–660.

Balling, R. C., Jr., 1985: Warm season nocturnal precipitation in the Great Plains of the United States. *J. Climate Appl. Meteor.*, **24**, 1383–1387, doi:10.1175/1520-0450(1985)024<1383:WSNPIT>2.0.CO;2.

Beirle, S., W. Koshak, R. Blakeslee, and T. Wagner, 2014: Global patterns of lightning properties derived by OTD and LIS. *Nat. Hazards Earth Syst. Sci.*, **14**, 2715–2726, doi:10.5194/nhess-14-2715-2014.

Blakeslee, R. J., and W. J. Koshak, 2016: LIS on ISS: Expanded global coverage and enhanced applications, *The Earth Observer*, Vol. 28, No. 3, EOS Project Science Office, Greenbelt, MD, 4–14. [Available online at https://eospso.gsfc.nasa.gov/sites/default/files/eo_pdfs/May_June_2016_color%20508.pdf.]

——, D. M. Mach, M. G. Bateman, and J. C. Bailey, 2014: Seasonal variations in the lightning diurnal cycle and implications for the global electric circuit. *Atmos. Res.*, **135–136**, 228–243, doi:10.1016/j.atmosres.2012.09.023.

Boccippio, D. J., 2002: Lightning scaling relations revisited. *J. Atmos. Sci.*, **59**, 1086–1104, doi:10.1175/1520-0469(2002)059<1086:LSRR>2.0.CO;2.

——, and Coauthors, 2000a: The Optical Transient Detector (OTD): Instrument characteristics and cross-sensor validation. *J. Atmos. Oceanic Technol.*, **17**, 441–458, doi:10.1175/1520-0426(2000)017<0441:TOTDOI>2.0.CO;2.

——, S. J. Goodman, and S. Heckman, 2000b: Regional differences in tropical lightning distributions. *J. Appl. Meteor.*, **39**, 2231–2248, doi:10.1175/1520-0450(2001)040<2231:RDITLD>2.0.CO;2.

Buechler, D. E., W. J. Koshak, H. J. Christian, and S. J. Goodman, 2012: Assessing the performance of the Lightning Imaging Sensor (LIS) using Deep Convective Clouds. *Atmos. Res.*, **135–136**, 397–403, doi:10.1016/j.atmosres.2012.09.008.

Chen, S. S., and R. A. Houze Jr., 1997: Diurnal variation and life cycle of deep convective systems over the tropical Pacific warm pool. *Quart. J. Roy. Meteor. Soc.*, **123**, 357–388, doi:10.1002/qj.49712353806.

Christian, H. J., R. J. Blakeslee, and S. J. Goodman, 1989: The detection of lightning from geostationary orbit. *J. Geophys. Res.*, **94**, 13 329–13 337, doi:10.1029/JD094iD11p13329.

——, and Coauthors, 2003: Global frequency and distribution of lightning as observed from space by the Optical Transient Detector. *J. Geophys. Res.*, **108**, 4005, doi:10.1029/2002JD002347.

Chronis, T. G., 2009: Investigating possible links between incoming cosmic ray fluxes and lightning activity over United States. *J. Climate*, **22**, 5748–5754, doi:10.1175/2009JCLI2912.1.

——, 2012: Preliminary lightning observations over Greece. *J. Geophys. Res.*, **117**, D03113, doi:10.1029/2011JD017063.

——, D. Carey, C. J. Schultz, E. V. Schultz, K. M. Calhoun, and S. J. Goodman, 2015a: Exploring lightning jump characteristics. *Wea. Forecasting*, **30**, 23–37, doi:10.1175/WAF-D-14-00064.1.

——, K. Cummins, R. Said, W. Koshak, E. McCaul, E. R. Williams, G. T. Stano, and M. Grant, 2015b: Climatological diurnal variation of negative CG lightning peak current over the continental United States. *J. Geophys. Res. Atmos.*, **120**, 582–589, doi:10.1002/2014JD022547.

——, T. Lang, W. Koshak, R. Blakeslee, H. Christian, E. McCaul, and J. Bailey, 2015c: Diurnal characteristics of lightning flashes detected over the São Paulo

Lightning Mapping Array. *J. Geophys. Res. Atmos.*, **120**, 11 799–11 808, doi:10.1002/2015JD023960.

——, W. Koshak, and E. McCaul, 2016: Why do oceanic negative cloud-to-ground lightning exhibit larger peak current values? *J. Geophys. Res. Atmos.*, **121**, 4049–4068, doi:10.1002/2015JD024129.

Cooray, V., R. Jayaratne, and K. L. Cummins, 2014: On the peak amplitude of lightning return stroke currents striking the sea. *Atmos. Res.*, **149**, 372–376, doi:10.1016/j.atmosres.2013.07.012.

Cummins, K. L., and M. J. Murphy, 2009: An overview of lightning locating systems: History, techniques, and data uses, with an in-depth look at the U.S. NLDN. *IEEE Trans. Electromagn. Compat.*, **51**, 499–518, doi:10.1109/TEMC.2009.2023450.

——, E. P. Krider, and M. Malone, 1998: The U.S. National Detection Network and applications of cloud-to-ground lightning data by electric power utilities. *IEEE Trans. Electromagn. Compat.*, **40**, 465–480, doi:10.1109/15.736207.

Dai, A., 2001: Global precipitation and thunderstorm frequencies. Part II: Diurnal variations. *J. Climate*, **14**, 1112–1128, doi:10.1175/1520-0442(2001)014<1112:GPATFP>2.0.CO;2.

Easterling, D. R., and P. J. Robinson, 1985: The diurnal variation of thunderstorm activity in the United States. *J. Climate Appl. Meteor.*, **24**, 1048–1058, doi:10.1175/1520-0450(1985)024<1048:TDVOTA>2.0.CO;2.

Gomes, C., and V. Cooray, 1998: Correlation between the optical signatures and current waveforms of long sparks: Applications in lightning research. *J. Electrost.*, **43**, 267–274, doi:10.1016/S0304-3886(98)00008-4.

Goodman S., and Coauthors, 2013: The GOES-R Geostationary Lightning Mapper (GLM). *Atmos. Res.*, **125–126**, 34–49, doi:10.1016/j.atmosres.2013.01.006.

Guo, C., and E. P. Krider, 1982: The optical and radiation field signatures produced by lightning return strokes. *J. Geophys. Res.*, **87**, 8913–8922, doi:10.1029/JC087iC11p08913.

Holle, R. L., 2014: Diurnal variations of NLDN-reported cloud-to-ground lightning in the United States. *Mon. Wea. Rev.*, **142**, 1037–1052, doi:10.1175/MWR-D-13-00121.1.

Houze, R. A., Jr., 2004: Mesoscale convective systems. *Rev. Geophys.*, **42**, RG4003, doi:10.1029/2004RG000150.

Hutchins, M. L., R. H. Holzworth, C. J. Rodger, and J. B. Brundell, 2012: Far-field power of lightning strokes as measured by the World Wide Lightning Location Network. *J. Atmos. Oceanic Technol.*, **29**, 1102–1110, doi:10.1175/JTECH-D-11-00174.1.

——, ——, K. S. Virts, J. M. Wallace, and S. Heckman, 2013: Radiated VLF energy differences of land and oceanic lightning. *Geophys. Res. Lett.*, **40**, 2390–2394, doi:10.1002/grl.50406.

——, ——, and J. B. Brundell, 2014: Diurnal variation of the global electric circuit from clustered thunderstorms. *J. Geophys. Res. Space Phys.*, **119**, 620–629, doi:10.1002/2013JA019593.

Idone, V. P., and R. E. Orville, 1985: Correlated peak relative light intensity and peak current in triggered lightning subsequent return strokes. *J. Geophys. Res.*, **90**, 6159–6164, doi:10.1029/JD090iD04p06159.

Israel, H., 1971: *Fundamentals, Conductivity, and Ions.* Vol. 1, *Atmospheric Electricity*, Israel Program for Scientific Translations, 317 pp.

Kasemir, H. W., 1965: The thundercloud. *Problems of Atmospheric and Space Electricity*, S. C. Coroniti, Ed., Elsevier, 215–231.

Koshak, W. J., 2010: Optical characteristics of OTD flashes and the implications for flash-type discrimination. *J. Atmos. Oceanic Technol.*, **27**, 1822–1838, doi:10.1175/2010JTECHA1405.1.

——, M. F. Stewart, H. J. Christian, J. W. Bergstrom, J. M. Hall, and R. J. Solakiewicz, 2000: Laboratory calibration of the Optical Transient Detector and the Lightning Imaging Sensor. *J. Atmos. Oceanic Technol.*, **17**, 905–915, doi:10.1175/1520-0426(2000)017,0905:LCOTOT.2.0.CO;2.

——, H. S. Peterson, A. P. Biazar, M. Khan, and L. Wang, 2014a: The NASA Lightning Oxides Model (LNOM): Application to air quality modeling. *Atmos. Res.*, **135–136**, 363–369, doi:10.1016/j.atmosres.2012.12.015.

——, B. Vant-Hull, E. W. McCaul, and H. S. Peterson, 2014b: Variation of a lightning NOx indicator for national climate assessment. Preprints, *15th Int. Conf. on Atmospheric Electricity*, Norman, OK, IAMAS/IUGG. [Available online at www.nssl.noaa.gov/users/mansell/icae2014/preprints/Koshak_137.pdf.]

——, K. L. Cummins, D. E. Buechler, B. Vant-Hull, R. J. Blakeslee, E. R. Williams, and H. S. Peterson, 2015: Variability of CONUS lightning in 2003–12 and associated impacts. *J. Appl. Meteor. Climatol.*, **54**, 15–41, doi:10.1175/JAMC-D-14-0072.1.

Lay, E. H., A. R. Jacobson, R. H. Holzworth, C. J. Rodger, and R. L. Dowden, 2007: Local time variation in land/ocean lightning flash density as measured by the World Wide Lightning Location Network. *J. Geophys. Res.*, **112**, D13111, doi:10.1029/2006JD007944.

Liu, C., E. Zipser, D. Cecil, S. W. Nesbitt, and S. Sherwood, 2008: A cloud and precipitation feature database from nine years of TRMM observations. *J. Appl. Meteor. Climatol.*, **47**, 2712–2728, doi:10.1175/2008JAMC1890.1.

Lopez, R. E., and R. L. Holle, 1986: Diurnal and spatial variability of lightning activity in northeastern Colorado and central Florida during the summer.

Mon. Wea. Rev., **114**, 1288–1312, doi:10.1175/1520-0493(1986)114<1288:DASVOL>2.0.CO;2.

Lyons, W. A., M. Uliasz, and T. Nelson, 1998: Large peak current cloud-to-ground lightning flashes during the summer months in the contiguous United States. *Mon. Wea. Rev.*, **126**, 2217–2233, doi:10.1175/1520-0493(1998)126<2217:LPCCTG>2.0.CO;2.

MacGorman, D. R., and C. D. Morgenstern, 1998: Some characteristics of cloud-to-ground lightning in mesoscale convective systems. *J. Geophys. Res.*, **103**, 14 011–14 023, doi:10.1029/97JD03221.

Mach, D. M., H. J. Christian, R. J. Blakeslee, D. J. Boccippio, S. J. Goodman, and W. L. Boeck, 2007: Performance assessment of the optical transient detector and lightning imaging sensor. *J. Geophys. Res.*, **112**, D09210, doi:10.1029/2006JD007787.

Mazur, V., and L. H. Ruhnke, 1998: Model of electric charges in thunderstorms and associated lightning. *J. Geophys. Res.*, **103**, 23 299–23 308, doi:10.1029/98JD02120.

Nag, A., and Coauthors, 2011: Evaluation of U.S. National Lightning Detection Network performance characteristics using rocket-triggered lightning data acquired in 2004–2009. *J. Geophys. Res.*, **116**, D02123, doi:10.1029/2010JD014929.

Nastos, P. T., I. T. Matsangouras, and T.G. Chronis, 2013: Spatio-temporal analysis of lightning activity over Greece—Preliminary results derived from the recent state precision lightning network. *Atmos. Res.*, **144**, 207–217, doi:10.1016/j.atmosres.2013.10.021.

Nesbitt, S. W., and E. J. Zipser, 2003: The diurnal cycle of rainfall and convective intensity according to three years of TRMM measurements. *J. Climate*, **16**, 1456–1475, doi:10.1175/1520-0442-16.10.1456.

Orville, R. E., and G. R. Huffines, 2001: Cloud-to-ground lightning in the United States: NLDN results in the first decade, 1989–98. *Mon. Wea. Rev.*, **129**, 1179–1193, doi:10.1175/1520-0493(2001)129<1179:CTGLIT>2.0.CO;2.

——, ——, W. R. Burrows, and K. L. Cummins, 2011: The North American Lightning Detection Network (NALDN)—Analysis of flash data: 2001–09. *Mon. Wea. Rev.*, **139**, 1305–1322, doi:10.1175/2010MWR3452.1.

Pinto, O., Jr., R. B. B. Gin, I. R. C. A. Pinto, O. Mendes Jr., J. H. Diniz, and A. M. Carvalho, 1996: Cloud-to-ground lightning flash characteristics in southeastern Brazil for the 1992-1993 summer season. *J. Geophys. Res.*, **101**, 26 627–26 635, doi:10.1029/96JD01865.

Rachidi, F., and R. Thottapillil, 1993: Determination of lightning currents from far electromagnetic fields. *J. Geophys. Res.*, **98**, 18 315–18 321, doi:10.1029/93JD01616.

Rudlosky, S. D., and H. E. Fuelberg, 2010: Pre- and postupgrade distributions of NLDN reported cloud-to-ground lightning characteristics in the contiguous United States. *Mon. Wea. Rev.*, **138**, 3623–3633, doi:10.1175/2010MWR3283.1.

Rycroft, M. J., R. G. Harrison, K. A. Nicoll, and E. A. Mareev, 2008: An overview of Earth's global electric circuit and atmospheric conductivity. *Space Sci. Rev.*, **137**, 83–105, doi:10.1007/s11214-008-9368-6.

Said, R. K., M. B. Cohen, and U. S. Inan, 2013: Highly intense lightning over the oceans: Estimated peak currents from global GLD360 observations. *J. Geophys. Res. Atmos.*, **118**, 6905–6915, doi:10.1002/jgrd.50508.

Schultz, C. J., W. A. Petersen, and L. D. Carey, 2011: Lightning and severe weather: A comparison between total and cloud-to-ground lightning trends. *Wea. Forecasting*, **26**, 744–755, doi:10.1175/WAF-D-10-05026.1.

Stolzenburg, M., and T. C. Marshall, 1998: Charged precipitation and electric field in two thunderstorms. *J. Geophys. Res.*, **103**, 19 777–19 790, doi:10.1029/98JD01675.

Villarini, G., and J. A. Smith, 2013: Spatial and temporal variation of cloud-to-ground lightning over the continental U.S. during the period 1995–2010. *Atmos. Res.*, **124**, 137–148, doi:10.1016/j.atmosres.2012.12.017.

Virts, K. S., J. M. Wallace, M. L. Hutchins, and R. H. Holzworth, 2013: Highlights of a new ground-based, hourly global lightning climatology. *Bull. Amer. Meteor. Soc.*, **94**, 1381–1391, doi:10.1175/BAMS-D-12-00082.1.

——, ——, ——, and ——, 2015: Diurnal and seasonal lightning variability over the Gulf Stream and the Gulf of Mexico. *J. Atmos. Sci.*, **72**, 2657–2665, doi:10.1175/JAS-D-14-0233.1.

Wallace, J. M., 1975: Diurnal variations in precipitation and thunderstorm frequency over the conterminous United States. *Mon. Wea. Rev.*, **103**, 406–419, doi:10.1175/1520-0493(1975)103<0406:DVIPAT>2.0.CO;2.

Wang, D., N. Takagi, T. Watanabe, V. A. Rakov, M. A. Uman, K. J. Rambo, and M. V. Stapleton, 2005: A comparison of channel-base currents and optical signals for rocket-triggered lightning strokes. *Atmos. Res.*, **76**, 412–422, doi:10.1016/j.atmosres.2004.11.025.

Whipple, F., 1929: On the association of the diurnal variation of electric potential gradient in fine weather with the distribution of thunderstorms over the globe. *Quart. J. Roy. Meteor. Soc.*, **55**, 1–18, doi:10.1002/qj.49705522902.

Williams, E. R., 2005: Lightning and climate: A review. *Atmos. Res.*, **76**, 272–287, doi:10.1016/j.atmosres.2004.11.014.

——, 2009: The global electrical circuit: A review. *Atmos. Res.*, **91**, 140–152, doi:10.1016/j.atmosres.2008.05.018.

——, and S. J. Heckman, 1993: The local diurnal variation of cloud electrification and the global diurnal variation of negative charge on the Earth. *J. Geophys. Res.*, **98**, 5221, doi:10.1029/92JD02642.

——, and S. Stanfill, 2002: The physical origin of the land–ocean contrast in lightning activity. *C. R. Phys.*, **3**, 1277–1292, doi:10.1016/S1631-0705(02)01407-X.

——, and G. Satori, 2004: Lightning, thermodynamic and hydrological comparison of the two tropical continental chimneys. *J. Atmos. Sol.-Terr. Phys.*, **66**, 1213–1231, doi:10.1016/j.jastp.2004.05.015.

——, and S. Heckman, 2012: Polarity asymmetry in lightning leaders: The evolution of ideas on lightning behavior from strikes to aircraft. *Aerospace Lab Journal*, No. 5, ONERA, Paris, France, AL05–04. [Available online at www.aerospacelab-journal.org/sites/www.aerospacelab-journal.org/files/AL05-04_0.pdf.]

——, D. Rosenfeld, N. Madden, C. Labrada, J. Gerlach, and L. Atkinson, 1999: The role of boundary layer aerosol in the vertical development of precipitation and electrification: Another look at the contrast in lightning over land and over ocean. *Proc. 11th Int. Conf. on Atmospheric Electricity*, Guntersville, AL, IAMAS/IUGG, 754-757.

——, K. Rothkin, D. Stevenson, and D. Boccippio, 2000: Global lightning variations caused by changes in thunderstorm flash rate and by changes in the number of thunderstorms. *J. Appl. Meteor.*, **39**, 2223–2230, doi:10.1175/1520-0450(2001)040<2223:GLVCBC>2.0.CO;2.

——, and Coauthors, 2002: Contrasting convective regimes over the Amazon: Implications for cloud electrification. *J. Geophys. Res.*, **107**, 8082, doi:10.1029/2001JD000380.

Wilson, C. T. R., 1921: Investigations on lightning discharges and on the electric field of thunderstorms. *Philos. Trans. Roy. Soc. London*, **221A**, 73–115, doi:10.1098/rsta.1921.0003.

Yang, S., and E. A. Smith, 2006: Mechanisms for diurnal variability of global tropical rainfall observed from TRMM. *J. Climate*, **19**, 5190–5226, doi:10.1175/JCLI3883.1.

Zajac, B. A., and S. A. Rutledge, 2001: Cloud-to-ground lightning activity in the contiguous United States from 1995 to 1999. *Mon. Wea. Rev.*, **129**, 999–1019, doi:10.1175/1520-0493(2001)129<0999:CTGLAI>2.0.CO;2.

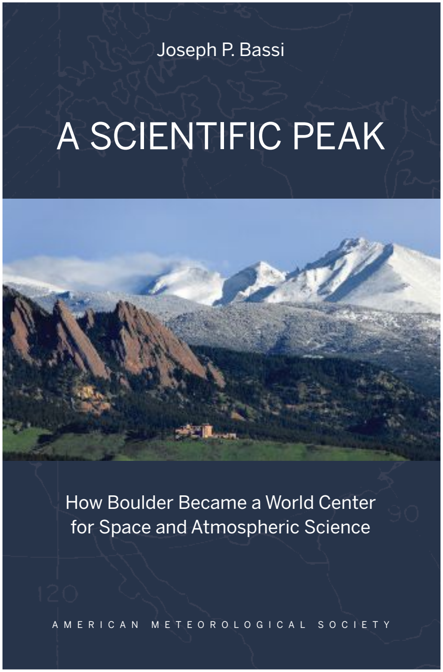

RECENT ADVANCES IN SATELLITE DATA RESCUE

Paul Poli, Dick P. Dee, Roger Saunders, Viju O. John, Peter Rayer, Jörg Schulz,
Kenneth Holmlund, Dorothee Coppens, Dieter Klaes, James E. Johnson, Asghar E. Esfandiari,
Irina V. Gerasimov, Emily B. Zamkoff, Atheer F. Al-Jazrawi, David Santek, Mirko Albani,
Pascal Brunel, Karsten Fennig, Marc Schröder, Shinya Kobayashi, Dieter Oertel,
Wolfgang Döhler, Dietrich Spänkuch, and Stephan Bojinski

Today's satellite data rescue activities uncover dormant records of our recent past and enable users to access, assess, and utilize early images and soundings for climate studies.

The Twenty-First Conference of the Parties (COP21) governing the United Nations Framework Convention on Climate Change (UNFCCC) saw the adoption in Paris in December 2015 of a global climate pact by representatives from 195 nations. The Paris agreement represents a historic milestone in terms of recognition by governments and the general public of the issues at stake. The Intergovernmental Panel on Climate Change (IPCC) Fifth Assessment Report states, "Warming of the climate system is unequivocal" (IPCC 2014a, p. 2). Several island states are already seeing the effects of climate change, confirming that "sea-level rise poses one of the most widely recognized climate change threats to low-lying coastal areas on islands and atolls" (IPCC 2014b, p. 1619). Better information on these and other impacts of climate change requires accurate and continuous measurements as laid out in the Global

AFFILIATIONS: Poli and Dee—European Centre for Medium-Range Weather Forecasts, Reading, United Kingdom; Saunders, John, and Rayer—Met Office, Exeter, United Kingdom; Schulz, Holmlund, Coppens, and Klaes—European Organisation for the Exploitation of Meteorological Satellites, Darmstadt, Germany; Johnson,* Esfandiari, Gerasimov,* Zamkoff,* and Al-Jazrawi*—Goddard Earth Sciences Data and Information Services Center, National Aeronautics and Space Administration Goddard Space Flight Center, Greenbelt, Maryland; Santek—Space Science and Engineering Center, University of Madison–Wisconsin, Madison, Wisconsin; Albani—European Space Agency, Frascati, Italy; Brunel—Météo-France, Lannion, France; Fennig and Schröder—Deutscher Wetterdienst, Offenbach, Germany; Kobayashi—Japan Meteorological Agency, Tokyo, Japan; Oertel—Akademie der Wissenschaften der Deutschen Demokratischen Republik, Berlin, Germany; Döhler and Spänkuch—Meteorologischer Dienst der DDR, and Meteorological Observatory Potsdam of the Deutscher Wetterdienst, Potsdam, Germany; Bojinski—World Meteorological Organization, Geneva, Switzerland

*** ADDITIONAL AFFILIATIONS:** Johnson, Esfandiari, and Gerasimov—ADNET Systems, Inc., Bethesda, Maryland; Zamkoff—Wyle Information Systems, LLC, Burlington, Massachusetts; Al-Jazrawi—Telophase Corp., Arlington, Virginia

CORRESPONDING AUTHOR: Paul Poli, paul.poli@shom.fr

The abstract for this article can be found in this issue, following the table of contents.

DOI:10.1175/BAMS-D-15-00194.1

A supplement to this article is available online (10.1175/ BAMS-D-15-00194.2).

In final form 7 November 2016

Climate Observing System (GCOS; GCOS 2010a) monitoring principles, originally adopted at the Fifth Conference of the Parties (COP5) in 1999. To construct useful multidecadal climate data records from those measurements, they must be combined with existing time series of past observations of the recent climate.

This goal has an impact on the planning of new observing systems (e.g., Leroy et al. 2008), imposing accuracy requirements that enable meaningful change detection times given the relative magnitudes of expected changes and natural variability. Space agencies have provided a strong response to the GCOS monitoring principles and the need for sustained climate data record (CDR) generation on essential climate variables (ECVs; Hollmann et al. 2013; Bojinski et al. 2014). The Committee on Earth Observation Satellites (CEOS)/Coordination Group for Meteorological Satellites (CGMS) Working Group on Climate (WGClimate) is currently addressing the realization of an architecture for climate monitoring from space (Dowell et al. 2013). Generating and interpreting climate records requires sustained research efforts as recognized by the World Climate Research Programme (WCRP) and the Committee on Space Research (COSPAR), which prepared a roadmap for observations in support of integrated Earth system science (Simmons et al. 2016).

This forward-looking view on observing systems for climate and long-term dataset generation supplements efforts to make optimal use of the great wealth of existing instrumental data records related to climate. Many potentially valuable in situ data records collected prior to the digital era remain largely inaccessible [see, e.g., Stickler et al. (2014) for a recent update]. The first photograph taken from space in 1946 by a rocket launched from New Mexico (Reichhardt 2006) also predates the digital era. However, since 1959, satellites have been launched for the purpose of observing the Earth's weather and climate (e.g., Suomi 1958; Kållberg et al. 2010). The early generations of satellite instruments during the 1960s and 1970s produced a wealth of data archived on magnetic tapes with high potential value for climate science. The term "data rescue" is often used to describe the laborious processes of locating, imaging, digitizing, and reformatting historical climate observations into a form that renders them useful for further analysis. Similar efforts are needed to rescue satellite data collected during the digital age. The early satellite records are especially valuable because they contain unique information about parameters and locations that have not otherwise been observed. As for historical in situ observations, the location of early satellite data records is not always known. The data may exist only on nonstandard and vulnerable media; documentation of instrument response and other metadata may be incomplete. These reasons, combined with the declining expertise about old instruments, highlight the urgency of satellite data rescue.

In the early 1990s, to realize the potential value of existing satellite records, the National Aeronautics and Space Administration (NASA) launched the Pathfinder datasets concept in response to the question of what can be done now to further global change research (Asrar and Dokken 1993). The number of datasets to be reprocessed then was limited to a few long series of measurements from the Advanced Very High-Resolution Radiometer (AVHRR), Television Infrared Observation Satellite (TIROS) Operational Vertical Sounder (TOVS), Geostationary Operational Environmental Satellite (GOES), Special Sensor Microwave Imager (SSM/I), Scanning Multispectral Microwave Radiometer (SMMR), and Land Remote Sensing Satellite (LANDSAT). The legacy of these sensors still extends to the present; some examples of the use of reprocessed Pathfinder data are presented below.

Today there are additional reasons to accelerate and expand the data rescue efforts initiated in the 1990s. Both the archive media and the pertinent expertise are fading fast. On the positive side, increasingly powerful computing facilities are now available that allow us to analyze these data faster than ever thought possible. General expertise about the use of satellite data has advanced a great deal since the launch of these early missions. In addition, new powerful tools and methods are available to assess the quality of the data. These factors taken together form the basis for the recent advances in satellite data rescue presented in this paper.

IMPROVED PRESERVATION AND DATA SERVICES FOR HISTORICAL RECORDS FROM SPACE. Unlike the early satellite programs, which did not address data recalibration and reprocessing, most space agencies today operate comprehensive data stewardship programs that include preservation of historical satellite data and provide substantial support for climate-related activities. Some agencies have developed complementary initiatives such as the Satellite Application Facility on Climate Monitoring (CM SAF; Schulz et al. 2009) attached to the European Organization for the Exploitation of Meteorological Satellites (EUMETSAT) and the Climate Change Initiative (CCI; Hollmann et al. 2013) sponsored by the European Space Agency (ESA). Their objectives include the generation of several fundamental CDR (FCDR) and thematic CDR (TCDR) to supplement those generated by the agencies themselves. Other examples are National Oceanic and Atmospheric Administration (NOAA)-sponsored FCDRs generated by Remote Sensing Systems (RSS; e.g., Wentz 2013) and the Center for Satellite Applications and Research (STAR; e.g., Zou and Wang 2011).

At the international level, coordination of satellite reprocessing activities is supported by the Sustained, Coordinated Processing of Environmental Satellite Data for Climate Monitoring (SCOPE-CM; Lattanzio et al. 2013). The primary objective of the Global Space-Based Intercalibration System (GSICS; Goldberg et al. 2011) is to coordinate intersatellite calibration of sensor data. Several efforts exist that attempt to harmonize practices; for example, the project Coordinating Earth Observation Data Validation for Re-Analysis for Climate Services (CORE-CLIMAX) reviewed available methodologies for validation of space-based CDR (Zeng et al. 2015).

Progress toward preservation of historical data from geostationary and polar-orbiting meteorological satellites has taken slightly different paths.

Geostationary satellites. The situation is well advanced for geostationary satellites back to the beginning of the 1980s (Knapp 2008), with SCOPE-CM coordinating various dedicated projects. Note, however, that current plans are missing historical records from the former Soviet Union and India, who have flown geostationary satellites for decades. They also do not address some of the earliest geostationary records. For example, from the United States, before the 1980s, the Applications Technology Satellite (ATS) series followed by the Synchronous Meteorological Satellite (SMS) predate the GOES series. The SMS data are being rescued from aging tapes at the Space Science and Engineering Center (SSEC) of University of Madison–Wisconsin. Figure 1 shows a photograph of such tapes and a sample series of four 5-min images held on tapes. The data rescued are served online (Table 1).

In Japan, most of the archive from the Geostationary Meteorological Satellite (GMS) has also been recovered from tapes and reprocessed for the year 1979 and from March 1987 to September 2009.

In Europe, most Meteosat data have already been reprocessed using current algorithms. A redesign of the entire processing chain is underway, so that novel algorithms can be applied to future reprocessing. Some of this effort is supported by Europe's Copernicus Climate Change Service (C3S), with a view to provide a background record for its series of Sentinel satellites that will continue the legacy of high-quality data records from space. However, satellite data rescue can still improve the Meteosat record; SSEC recently discovered a copy of the second year of data of the first Meteosat satellite (whose 2-yr original record

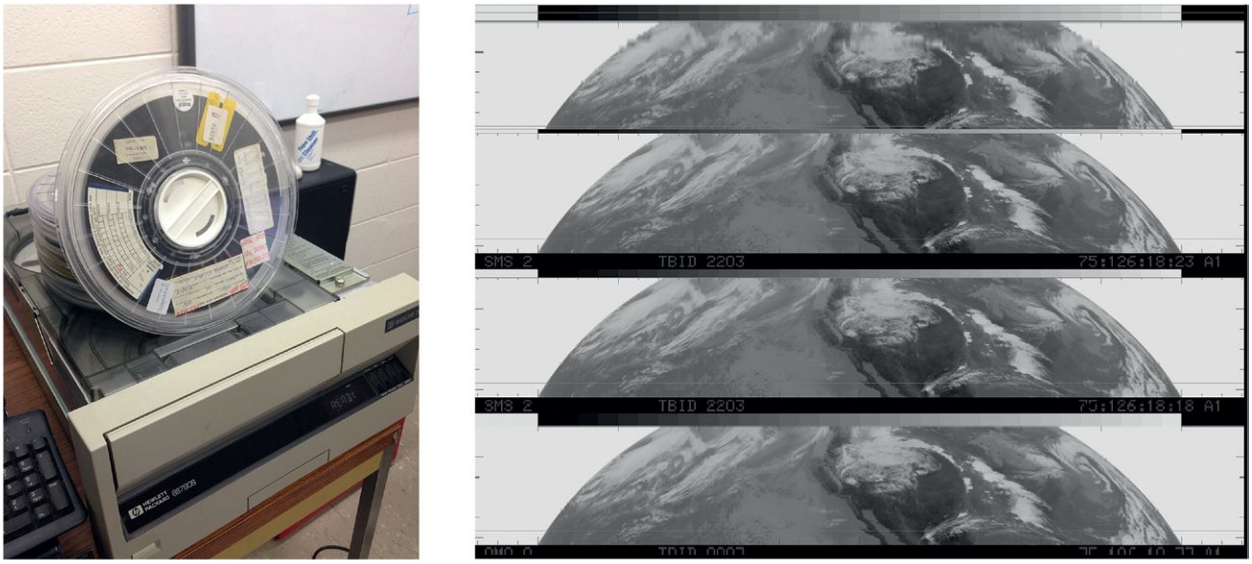

Fig. 1. (left) A nine-track tape, holding historical geostationary data, with the corresponding player underneath, at SSEC and (right) data extracted from the nine-track tapes: a series of four 5-min SMS-2 satellite images from 6 May 1975. Such images will help derive atmospheric motion vectors, with potential application to assimilation into global reanalyses.

Table 1. Radiance data rescued from aging media over the past few years.

Early U.S. geostationary imagers

- Visible and Infrared Spin Scan Radiometer (VISSR) on *SMS-1* and *SMS-2*, *GOES-1* to *GOES-7*
- Recovery complete for 1979–96; in progress for 1975–79
- www.ssec.wisc.edu/datacenter/archive.html

First European Geostationary Imager

- Meteosat Visible and Infrared Imager (MVIRI) on board *Meteosat-1* (launched 23 Nov 1977, retired 25 Nov 1979)
- Recovery in progress for Dec 1978–Nov 1979
- Data will become available online at http://navigator.eumetsat.int and www.ssec.wisc.edu/datacenter/archive.html

Radiometers on Nimbus: Data preserved by NASA

- High-Resolution Infrared Radiometer (HRIR), Medium Resolution Infrared Radiometer (MRIR), Temperature–Humidity Infrared Radiometer (THIR), Infrared Interferometer Spectrometer (IRIS), High Resolution Infrared Radiometer (HIRS) on *Nimbus-1* to *Nimbus-7*
- Recovery complete for 1964–85; search for Scanning Microwave Spectrometer (SCAMS) radiances still ongoing
- http://disc.sci.gsfc.nasa.gov/nimbus

Radiometers on Nimbus: Data preserved by University of Oxford

- Selective Chopper Radiometer (SCR) on *Nimbus-4* and *Nimbus-5*, Pressure Modulator Radiometer (PMR) on *Nimbus-6*, Stratospheric and Mesospheric Sounder (SAMS) on *Nimbus-7*
- Data available on disc at University of Oxford; copy made to ECMWF mass archive

Cameras on Nimbus

- Visible Camera on *Nimbus-1* to *Nimbus-4*
- Recovery complete for 1964, 1966, 1969, and 1970
- https://nsidc.org/data/nimbus/data-sets.html

Infrared SI-1 from former GDR, flown on Soviet Meteor satellites

- SI-1 on *Meteor-28* and *Meteor-29*
- Recovery complete for 1977 and 1979

had been declared lost because of tape decay despite several recovery attempts), and rescue work is underway in collaboration with EUMETSAT (Table 1).

Data recovery for polar-orbiting satellites. For polar-orbiting satellites, the largest agency with the longest records is undoubtedly NASA. Its Nimbus satellite program started in 1964 and collected Earth observations for over 30 yr. NASA now operates a data preservation program at the Goddard Earth Sciences (GES) Data and Information Services Center (DISC). Using novel technology patented by John Bordynuik Inc. (JBI), aging magnetic tapes are copied to new digital media by recovering the exact, original data bits and format. Access to data archived on the modern media is significantly improved, with data archive and transfer rates several orders of magnitude above those available when the data were first created. This makes it possible to serve entire mission datasets online for users to download. Open and fast data access enables researchers and users from many fields to investigate past cases or to search for correlation patterns with data in their own interest area.

The process of extracting data files from the Nimbus tapes brings about several problems. These include deviations of the data format from documentation, extra or missing label records, false end-of-file marks contained within data files, incorrect record length markers within files, corrupted or unreadable tapes, and bad data at the front or end of the old tapes. Reconciling duplicate files (primary tape vs backup) is another challenge. In addition, unlike current practice, file level metadata were nonexistent in the original Nimbus tapes other than as a listing of the number of files on the tape and vague date ranges, often written by hand on the tapes. This requires the data recovery teams to correctly understand the data format, that is, rely on the original documentation, in order to retrieve the true temporal and spatial extent as well as other ancillary information from the individual data files in the old original tapes.

In Europe, ESA leads a long-term data preservation (LTDP) program as part of its mandatory activities. This covers not only heritage data from ESA missions but also third-party missions available to ESA. The LTDP coordinates and optimizes European efforts in a cooperative framework. A recent example is the recovery of images from the oldest synthetic aperture radar (SAR), on *Seasat*, and on *ERS-1*. Comparing these data with the latest SAR generation on *Sentinel-1* shows in Fig. 2 the retreat of two large glaciers in southeast Greenland over a 36-yr period. This activity, part of the ESA LTDP, contributes to the ESA CCI. As this initiative moves forward, there is scope to improve the time series of several ECVs from such imagery data, such as continental ice sheets and sea ice.

Individual action. In addition to well-structured agency programs described thus far, foresight of individuals and research agencies has sometimes played key roles in satellite data preservation. Two such examples are given here. The first example involves four datasets of the British ancestry of sounding, which was developed at the University of Oxford.

Data from pressure-modulated infrared sounders [selective chopper radiometer (SCR) and pressure modulator radiometer (PMR); Table 1] and one limb-viewing infrared sounder [stratospheric and mesospheric sounder (SAMS)] were curated by a project funded by the U.K. Natural Environment Research Council. This project was visionary in its intention to keep raw mission data, whereas the prevailing approach at the time was to preserve geophysical retrievals. The discs holding the data were located in the library of the responsible institution, and a copy of the data was recently added to mass storage at the European Centre for Medium-Range Weather Forecasts (ECMWF). The data curation project included migrating them to a hardware-independent format [American Standard Code for Information Exchange (ASCII) files of hexadecimal characters] and providing a decoding software. This approach of converting records to a new data format was prevalent in the 1990s and applied not only to satellite data but other records, such as recovered from in situ. The norm now is to retain also the original data in their native format (or images), as allowed by the JBI technology.

A second example involves data collected by two infrared sounding Spectrometer Interferometer-1 (SI-1; Kempe et al. 1980) instruments flown on former Soviet meteorological polar-orbiting satellites (*Meteor-28* and *Meteor-29*). The SI-1 was an instrument (please see online supplement at http://dx.doi.org/10.1175/BAMS-D-15-00194.2) developed by the former Academy of Sciences of German Democratic Republic (GDR), in collaboration with the former Soviet Hydrometeorological Service (HYDROMET) and the former Meteorological Service of GDR (Spänkuch 1980). The data came to light thanks to a fortuitous meeting in Noordwijk (the Netherlands) at the end of 2013. Fortunately, the investigators who had worked on SI-1 in the late 1970s had preserved all (about 2000) original SI-1 spectra (between 6 and 25 μm). With support from EUMETSAT, the data were recovered and moved to a current data format. In addition, these SI-1 data were patiently quality controlled and georeferenced, and user documentation was drafted (Coppens et al. 2015).

RECOGNITION OF THE IMPORTANCE OF METADATA DESCRIBING HISTORICAL SATELLITE INSTRUMENTS.

High-level metadata: Inventories. Various inventories of Earth observation satellites have been made over the years (e.g., Houghton et al. 1986). For the initial purpose of reviewing capability and avoiding duplication in future satellite missions, the World Meteorological Organization (WMO) Space Programme has set up a database of metadata on past, present, and future satellite missions: the Observing Systems Capability Analysis and Review Tool (OSCAR; www.wmo-sat.info/oscar/). This facility, developed in coordination with CGMS and CEOS, has now evolved into a core element of WMO Integrated Global Observing System (WIGOS), covering also surface-based capabilities. These inventories help users identify past missions relevant to their topic of study.

Data lost? However, corresponding data records are not always readily available. There are even cases of

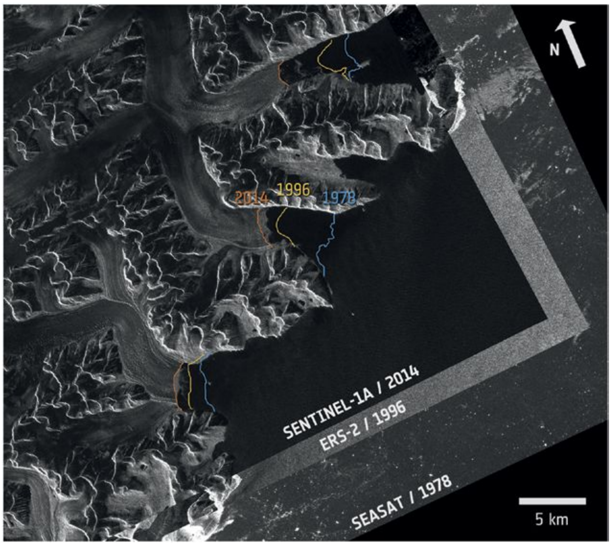

Fig. 2. Greenland glaciers retreat seen by three generations of radar missions. Radar scans from *Seasat* on 16 Aug 1978, *ERS-2* on 7 Aug 1996, and *Sentinel-1* on 20 Aug 2014 show glacier edges in southeast Greenland. Over the 36-yr period, the glaciers receded by about (top) 180 and (bottom) 61.5 m yr^{-1}. Such images help create long data records of glaciers and sea ice, with application to improve forcing datasets for climate models. (Credits: ESA and University of Rome La Sapienza.)

data records possibly lost forever. This includes some early geostationary satellites mentioned earlier. It also includes, for ozone, data from the backscatter ultraviolet (BUV) sensor on *Atmosphere Explorer-E* (Bhartia et al. 2013), which would patch a gap between *Nimbus-4* and *Nimbus-7* ozone-sensing UV instruments. Information gathered during the course of the present work indicates that the data were lost during transition from one mass archive system to another, as all unused data were discarded. Furthermore, infrared sounding data collected by the Special Sensor-H (SSH) instrument flown on four Defense Meteorological Satellite Program (DMSP) satellites appear to have been lost. So far, all attempts to locate these data have failed, but maybe the present paper will help jog memories.

Mission metadata. The preservation of mission metadata is somehow more challenging than the data themselves. Metadata are meant to include any knowledge or information present at the time the mission was operated. They are thus essential in order to use the data properly. Until recently, such information was not given the same attention as mission data. The situation has now improved with standards (e.g., GCOS 2010b) mandating management of algorithm theoretical basis documents, all supporting data, and data format definitions. Standards are emerging to qualify the system maturity (e.g., Bates and Privette 2012; John et al. 2014).

The knowledge accrued over the years, from laboratory measurements or field campaigns, was not always associated with the relevant mission, but their importance is now recognized to better exploit data a posteriori. Ancient instruments pose specific problems. For infrared radiometers, a key difficulty is determining precisely the instrument spectral response function. Such information, available at the time in digital form, has generally been lost and needs restoring from published charts or graphs. Recognizing this challenge, NASA and ESA have adopted specifications for preservation of data and documentation, and new systems are being developed as a result (e.g., Khayat et al. 2013; Albani et al. 2012).

GLOBAL REANALYSES

The scope of global reanalyses has expanded tremendously in recent years. From a niche activity—initially a few decades long and atmosphere only—reanalyses now include several components of the climate system and extend back in time by 100 yr or more (Dee et al. 2014; Compo et al. 2006). Assimilation of observations in a climate model generates a physically consistent set of gap-free gridded time series, with estimates of many essential climate variables. A reanalysis thus provides access to a massive amount of information contained in millions of weather reports from locations around the world in the form of comprehensive datasets that can be compared and sliced in any dimension. These datasets have many thousands of users (Gregow et al. 2015), who also request access to observations in a usable format. Historical in situ observations recovered by projects such as the European Union (EU) European Reanalysis of Global Climate Observations (ERA-CLIM; Dee et al. 2014), facilitated by the Atmospheric Circulation Reconstructions over the Earth initiative (ACRE; Allan et al. 2011), have now been used in several century-long reanalyses, such as the NOAA twentieth century reanalysis (20CR; Compo et al. 2011) and the ERA-20C (Poli et al. 2016). An outcome of ERA-CLIM was an inventory of early satellite missions of interest to global atmospheric reanalyses (see the supplement).

ADVANCES IN THE QUALITY ASSESSMENT OF HISTORICAL SATELLITE DATA RECORDS. Once data have been rescued from aging media, a first prerequisite before application in climate studies is a quality assessment. This can be done by comparison with similar observations at the same time. In the case of polar-orbiting satellites, instrument data can be compared from one instrument to the next by spatiotemporal matching (collocation) or using the simultaneous nadir overpass (SNO) technique as used by GSICS. As demonstrated for the High Resolution Infrared Radiometer (HIRS; Chen et al. 2013), calibration corrections obtained from present-day, highly calibrated instruments can then be propagated back in time to past instruments. This, however, requires an unbroken chain of radiometers. After 1979, the HIRS series has very few gaps between satellites [TIROS series N (TIROS-N), *NOAA-6* to *NOAA-19*, and MetOp]. Before 1979, the vertical temperature profile radiometer (VTPR) on *NOAA-2* to *NOAA-5* goes back to 1972. Before 1972, there are low-resolution and pressure-modulated sounders and imagers. However, the overlaps between instrument series are sometimes short and would largely benefit from the DMSP SSH data mentioned earlier. One may also use spatiotemporally complete NWP model datasets as a transfer standard.

Such datasets can be used as a comparison basis to assess historical satellite data quality. The evaluation of climate model simulations with observations requires long observational datasets, for example, as prepared by the Observations for Model Intercomparison Projects (Obs4MIPS; Teixeira et al. 2014). However, a reverse assessment of (potentially short) observation records can use model datasets as a reference. The latter need to be at subdaily temporal resolution and provide all the variables required to simulate the observations, typically temperature and humidity at various levels of the atmosphere. For this reason, such comparisons are more easily done with global reanalyses (see the sidebar on "Global reanalyses").

Mapping the three-dimensional state of the reanalyses into the observation space requires an observation operator. For radiances, EUMETSAT supports in Europe such developments through its Satellite Application Facility on Numerical Weather Prediction (NWP SAF) by enhancing capabilities of a fast radiative transfer model used in several present-day NWP systems and reanalysis systems [Radiative TOVS (RTTOV); Saunders et al. 1999].

One challenge consists of adjusting the fast radiative transfer model for a time period when trace gas concentrations in the atmosphere differed from present-day values, in some cases significantly. This requires new line-by-line radiative transfer computations as references. For instruments that are no longer operating (e.g., SCR and PMR), the task is more complex because their sensing principle is no longer applied on any current instrument, and so no observation operator was ever developed, and most investigators of the missions have already retired.

Early infrared sounders. An example of such quality assessment is shown here for the infrared interferometer spectrometer (IRIS) on *Nimbus-4*. Harries et al. (2001) already compared this data to present-day instruments, showing long-term changes in Earth's

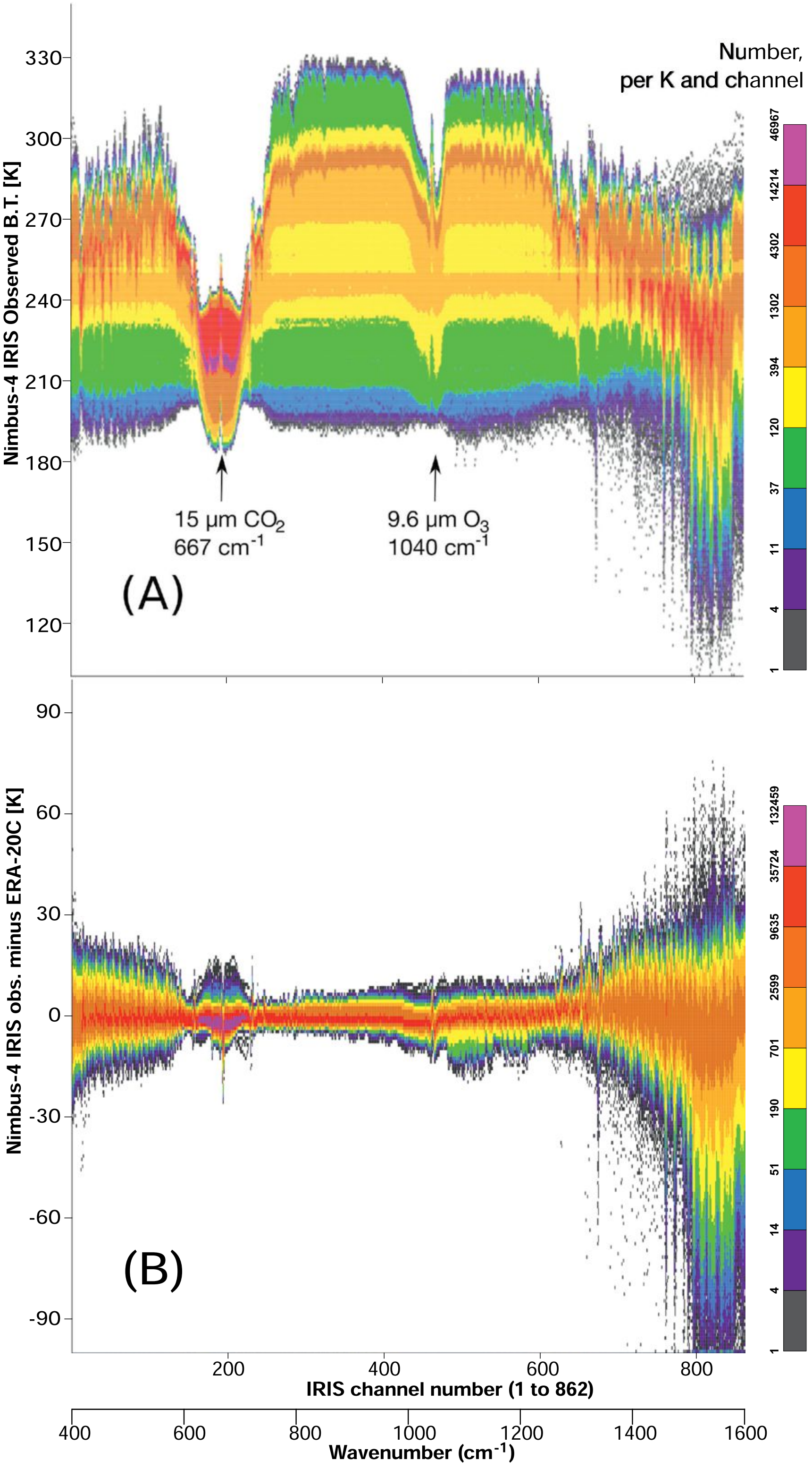

► **Fig. 3. (a) Spectra of *Nimbus-4* IRIS (Apr 1970–Jan 1971) brightness temperatures, quality controlled to retain only clear channels, and (b) departures with ERA-20C.**

atmosphere composition. With the additional help of instrument metadata in the newly recovered IRIS records (Table 1), advanced observation operators, and new reanalyses (all described earlier), it is now possible to produce closer comparisons between IRIS observations and models. Such comparisons also help quantify how accurately modern observation operators and reanalyses can represent the early satellite data variability in its various dimensions. For the spectral dimension, Fig. 3 shows the observed spectra of brightness temperatures, after applying the cloud detection scheme of McNally and Watts (2003) using the NWP SAF Aerosol and Cloud Detection Package for High Resolution Infrared Sounders. Applying the cloud detection restricts the comparison to clear-sky situations, as assumed in the radiative transfer calculations. In Fig. 3b, the differences with ECMWF twentieth century reanalysis (ERA-20C) represent the total sum of errors in the IRIS observations, the ERA-20C, the radiative transfer calculations, and the temporal and spatial mismatch between IRIS's 96-km pixel resolution and ERA-20C's 125-km horizontal and 3-hourly resolution. Note some errors may compensate and could be masked by such single-variable comparison. For the water vapor sounding channels (wavenumbers above 1200 $\mathrm{cm^{-1}}$ in Fig. 3) as well as temperature-sounding channels in the 15-μm carbon dioxide band (wavenumbers 600–750 $\mathrm{cm^{-1}}$), the negative mean differences between IRIS and ERA-20C suggest possibly suboptimal cloud detection. For the temperature-sounding channels the differences are under 1.5 K in standard deviation and about 1 K for the low-peaking and window channels. In addition to quantifying the total sum of errors, such comparisons enable a better understanding of the data quality and isolation of problematic time periods in the instrument record by comparing with mission metadata (Poli and Brunel 2016). The cloud detection could be further improved by using the imager data collected by *Nimbus-4* (now recovered; Table 1).

Another example of the data quality assessment is in the spatial domain. Maps enable identification of potential geolocation errors in the rescued satellite data (e.g., Poli et al. 2015) but also characterization of regional variations in reanalysis quality. For *Nimbus-6* HIRS-1, which predates the long series started in 1979 with TIROS-N, Fig. 4 shows the percentage of variance in observations for channel 5 (peaking in the mid- to upper troposphere) explained by ERA-20C over two periods (17–31 August 1975 and 31 January–3 March 1976, the only dates rescued so far). For a fair comparison with clear-sky calculations, the scenes are filtered to retain only pixels believed to be clear. In each 5° × 5° latitude–longitude box, the variance in the observations represents synoptic weather as well as seasonal changes between August and February and instrument noise. Where ERA-20C is able to represent the variations observed by the sounder, the variance explained is high. As expected, the results indicate that ERA-20C is able to represent the tropospheric temperature seasonal changes that dominate the variance over the southern and northern high latitudes. In northern (southern) midlatitudes, where the variance results from seasonal and synoptic signals, a fair (low) percentage of variance explained is found over well-observed (poorly observed) in situ land and ocean areas. These hemispheric differences reflect geographical differences in accuracy within ERA-20C (Poli et al. 2016). The low variance explained over the tropics is likely caused by ERA-20C assimilating only surface pressure and marine wind observations and the atmospheric model forced by monthly sea surface temperatures. Such comparison

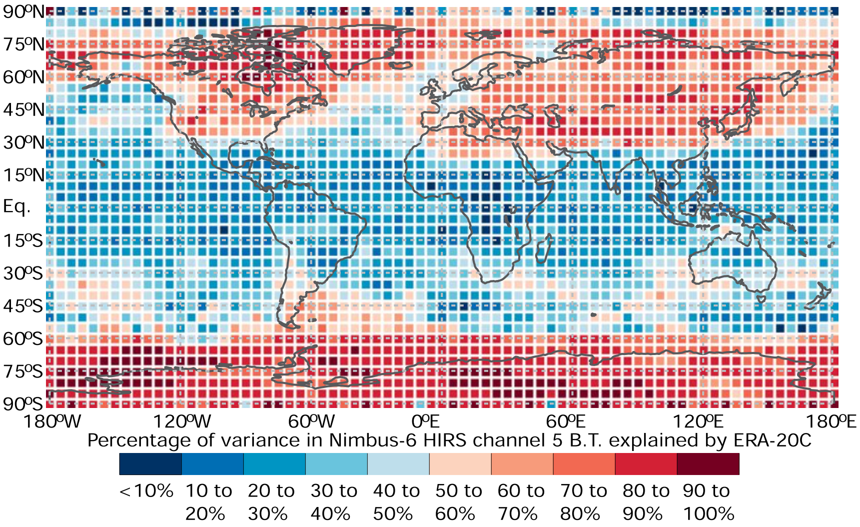

Fig. 4. Maps of percentage of variance in *Nimbus-6* HIRS-1 channel 5 (peaking in the mid- to upper troposphere) brightness temperature observations explained by ERA-20C, for scenes believed to be clear, by considering where observation minus ERA-20C differences for channel 8 (window) are between –1 and 2 K. Variances are computed within 5° × 5° latitude–longitude bin, for 17–31 Aug 1975 and 31 Jan–3 Mar 1976.

of observations with prior reanalyses helps prepare for the assimilation of HIRS-1 into future reanalyses.

Early microwave sensors for humidity. Continued measurements of humidity by microwave sensors have been available since SMMR on *Nimbus-7*. Its record was reprocessed two decades ago as part of the leading NASA Pathfinder datasets, and data are available online (Njoku 2003). Today the CM SAF is working to enhance the existing SMMR Pathfinder dataset by applying Climate and Forecast (CF) metadata conventions (http://cfconventions.org/) and by intercalibrating with SSM/I DMSP *F-8* for the channels that had similar characteristics. One aim is to achieve consistency with an existing FCDR of SSM/I and Special Sensor Microwave Imager/Sounder (SSM/IS) brightness temperatures (Fennig et al. 2015). After spectra and maps, another way to assess satellite data quality is to consider various types of weather conditions and reanalyses. Comparing a preliminary data sample produced by the CM SAF with ERA-20C indicates in Fig. 5 a satisfactory data quality for the 22-GHz, water vapor–sensitive SMMR channel, especially when only clear-sky scenes are considered. The match

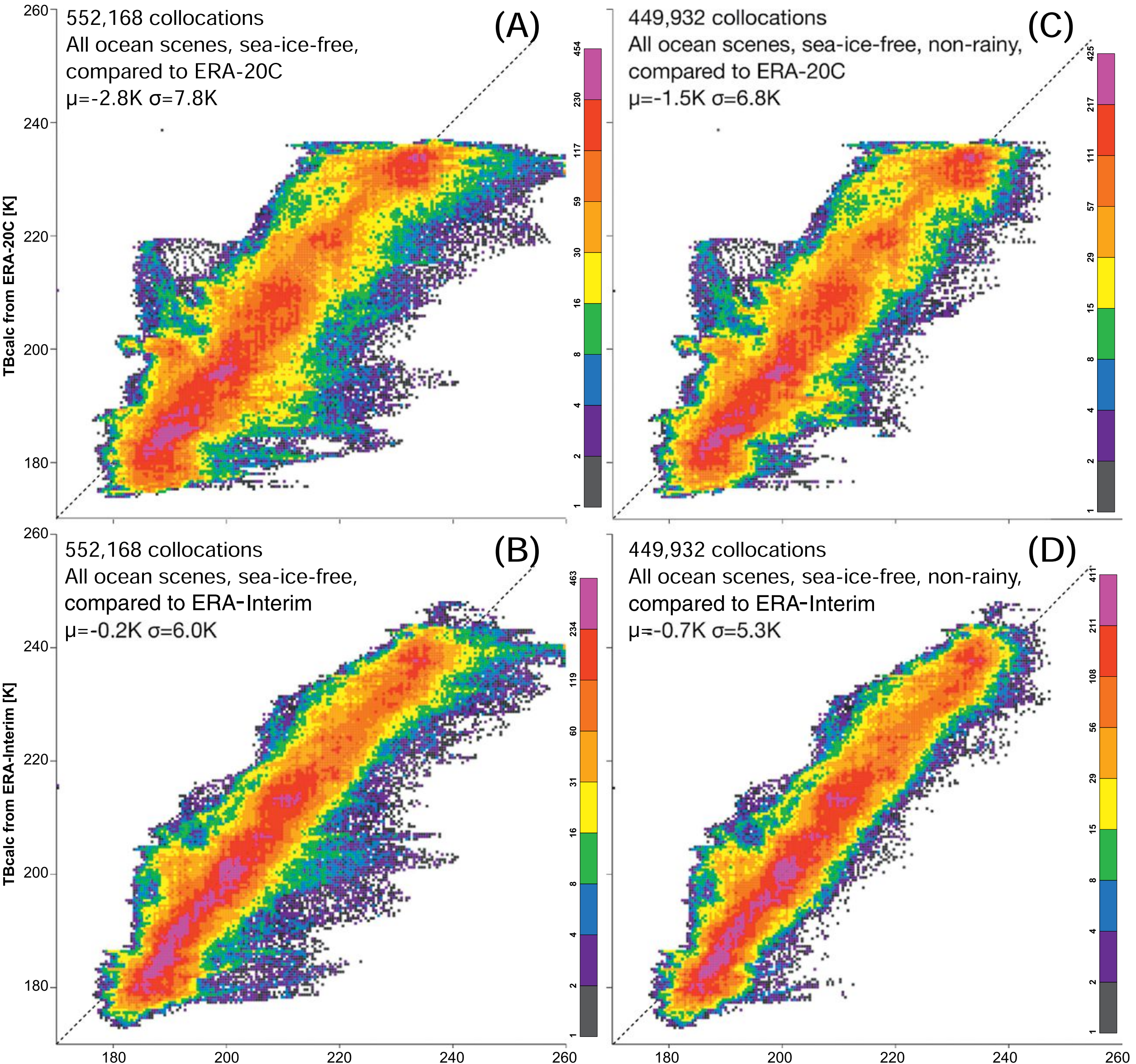

Colors show numbers of points per 0.5K x 0.5K. Average (μ) and standard deviation (σ) characterize TBcalc minus TBobs.

Fig. 5. Density scatterplots of observed brightness temperatures for *Nimbus*-7 SMMR channel 21V (horizontal axis) vs clear-sky radiative transfer calculations from reanalysis (vertical axis) for 26 Oct 1978. (a),(c) Comparisons to ERA-20C. (b),(d) Comparisons to ERA-Interim. (a),(b) All scenes and (c),(d) scenes believed to be rain free.

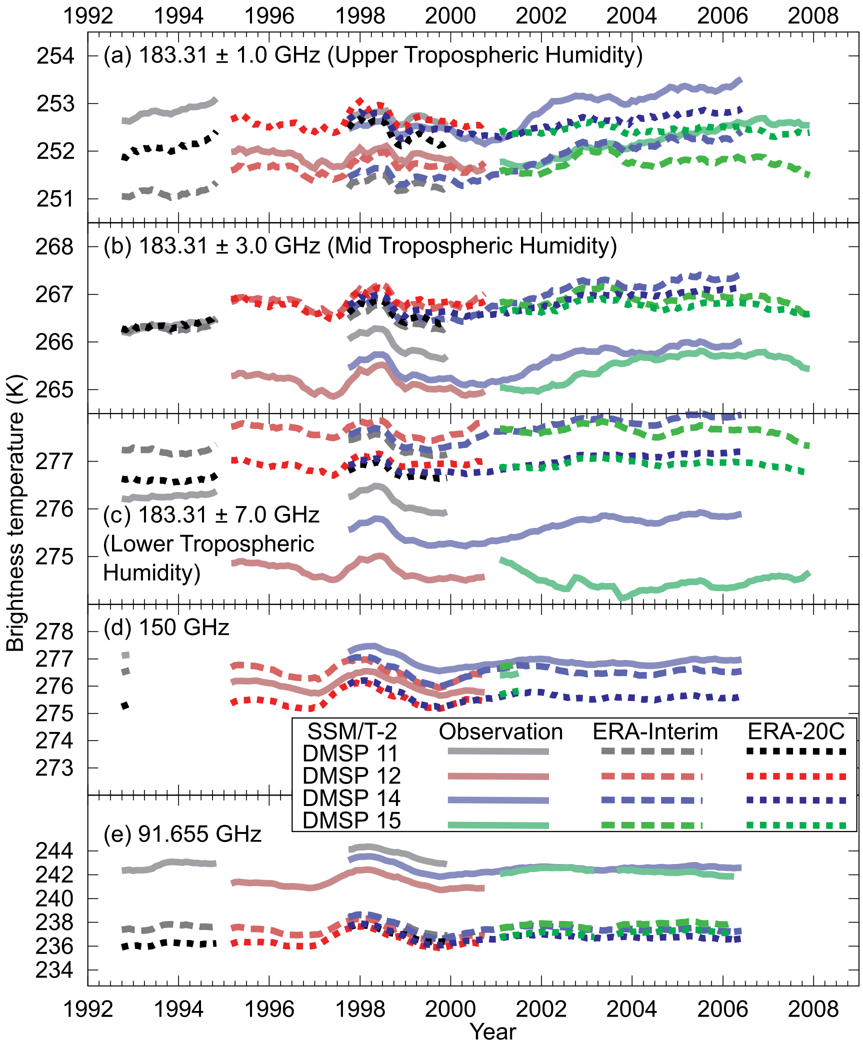

Fig. 6. Time series of brightness temperature data from SSM/T-2, and corresponding simulations from ERA-Interim and ERA-20C. Plots show 12-month running means for profiles averaged over the tropical ocean (30°N–30°S), using clear-sky data only.

is better for the ECMWF interim reanalysis (ERA-Interim; Dee et al. 2011), a reanalysis that assimilated a number of in situ and satellite data, than for ERA-20C, a reanalysis that only assimilated surface pressure and marine wind observations. The superior "instant accuracy" of a reanalysis that assimilates many more data sources compared to one that is restricted to only surface observations suggests a virtuous improvement; such assessments become more powerful as additional observations are assimilated into reanalyses and new observations are recovered from aging media.

Other instruments have been operating in the 183-GHz band, allowing for vertical sounding of water vapor, such as the Advanced Microwave Sounding Unit-B (AMSU-B), the Microwave Humidity Sounder (MHS), and the Advanced Technology Microwave Sounder (ATMS). Preceding them, the Special Sensor Microwave Water Vapor Profiler (SSM/T-2) series covers over 15 yr but has so far remained underused to study climatic variations of humidity (John et al. 2011). Assessing the quality of instrument data, by comparison with other datasets, is preparatory work for their exploitation in climate studies. With such a long record, one can also identify which model or reanalysis dataset tracks best the observed long-term variability. Figure 6 shows a time series of brightness temperature observations from SSM/T-2. Overlaid are simulations from ERA-Interim and ERA-20C. The long-term evolution of ERA-20C with respect to SSM/T-2 is more stable than ERA-Interim when projected into brightness temperature space. Kobayashi et al. (2015) give more details about lessons learned from this quality assessment of SSM/T-2 data.

APPLICATIONS IN CLIMATE STUDIES.

There are several applications to climate studies of the historical satellite data records recovered, tagged with metadata, and assessed by the aforementioned activities. Early observations from space, covering large regions that were largely inhabited at the time, are essential, along with recovered in situ observations, to help extend back in time our understanding of the climate and its changes with time.

Long time series of FCDR and TCDR. These enhancements can occur in several ways. One way is comparison with climate datasets for mutual validation. For example, the comparison to SSM/T-2 FCDR presented earlier enabled us to identify which of two reanalyses presented the more stable water cycle.

Another way is the direct application to retrievals to generate TCDRs and thereby improve ECV databases. The data can also be used as forcing to climate simulations. Such forcing datasets are largely derived from observations (e.g., Taylor et al. 2012). Rescuing early satellite data offers the potential to improve several forcing datasets. For example, in order to improve knowledge of past variations in sea ice concentration, the National Snow and Ice Data Center (NSIDC) has estimated North and South Pole sea ice edges from visible images collected by cameras on Nimbus satellites since the 1960s (Gallaher and Campbell 2014).

Assimilation into reanalyses. There is also the prospect of direct assimilation into reanalyses for all sounders that predate TIROS-N. It has been demonstrated that assimilation of a single sounder series such as VTPR can substantially improve the reanalysis quality in poorly observed areas such as the Southern Hemisphere (Uppala et al. 2005). Recovering as many additional sounders as possible prior to 1979 can potentially extend reanalysis quality further back in time.

There are additional benefits to aim for in a virtuous cycle of improvements initiated by reanalysis. Assimilation of satellite data not previously used may, at first, lead to discontinuities in reanalysis products. Usually, lessons are then learned that lead to improvements in aspects of data quality control and bias correction, assimilation methods, the atmospheric general circulation model, or the observation processing. A recent example is the mass and water balance improvement in Modern-Era Retrospective Analysis for Research and Applications, version 2 (MERRA-2), after assimilation of humidity-sensitive satellite data that had initially caused difficulties in the previous reanalysis (Takacs et al. 2016). As reanalyses become more accurate because of greater computing power, better models, and more observations, the errors in reconstructed time series decrease so that additional observations can be assimilated to further drive progress.

Interdisciplinary benefits. There are other applications that benefit from old satellite data thanks to intersatellite calibration bridging with continuous instrument data series. These benefits cut across several themes of Earth science because all sensors in space usually have some sensitivity to an unintended component of the Earth system (e.g., an atmospheric sensitivity for surface sensors or a surface sensitivity for atmospheric sounders).

A case in point is the satellite altimeter, as its data analysis requires wet atmospheric corrections to reduce a major source of uncertainty in resulting estimates of sea level rise (Ablain et al. 2009). The altimeters fly with radiometers in the 22-GHz frequency band in order to estimate total column water vapor. There would hence be benefits to oceanography in propagating backward the calibration of present-day, 22-GHz observations, now observed by state-of-the-art sensors of superior calibration, namely the SSMIS, ATMS, and Imaging/Sounding Microwave Radiometer–Improved (MTVZA-GY), which also observe the 183-GHz humidity sounding frequency. Furthermore, the committed future microwave imager (MWI) and microwave sounder (MWS) instruments on board the EUMETSAT Polar System Second Generation will continue these measurements until 2040. Knowing that remote sensing at these frequencies will continue for years to come and that sea level rise is one of the key factors of climate change, of potentially huge societal impact, this makes it more worthwhile to invest into producing a FCDR of 22- and 183-GHz measurements. Likewise, land surface estimates from early satellite records could benefit from improved atmospheric corrections, and sounder data could be better exploited through improved surface state knowledge via emissivity models.

Looking ahead. Over the past two decades, satellite data rescue complemented by reprocessing and mission continuity (e.g., National Academy of Sciences Engineering and Medicine 2015) have gained importance in satellite agencies' programs alongside new and innovative research missions. For data rescue, the difficulties reported in this paper include the loss of datasets, reconciliation of actual media contents with metadata available, deviation of the actual data format from expectations or documentation, and retiring expertise. These impediments could hinder satellite data rescue in years to come, if not dealt with urgently. The major anticipated benefit is the provision of longer "background" time series through climate simulations and reanalyses to help better exploit future series of Earth observation instruments in space and ensure continuity with records derived from past missions. We hope that this paper will encourage younger scientists to engage with the retiring generation of space scientists to pass on their knowledge and allow new insights to be gained from early satellite data.

ACKNOWLEDGMENTS. The Nimbus data used in this effort were acquired as part of the activities of NASA's Science Mission Directorate and are archived and distributed by the Goddard Earth Sciences (GES) Data and Information Services Center (DISC). The authors thank the following persons for enabling to locate data or metadata: Anthony McNally, Bob Wells, Clive Rodgers, Peter Bauer, Johannes Schmetz, W. Paul Menzel, Jerrold Robaidek, William L. Smith, and

Ronald Glumb. The work presented here was supported by the respective affiliation institutions of the authors as well as EU Grant Agreements 265229 (ERA-CLIM), 607029 (ERA-CLIM2), and 313085 (CORE-CLIMAX), and the EUMETSAT CM SAF visiting scientist program (CM_VS14_01). The authors would like to acknowledge Adrian Simmons for his comments that helped improve the manuscript.

REFERENCES

Ablain, M., A. Cazenave, G. Valladeau, and S. Guinehut, 2009: A new assessment of the error budget of global mean sea level rate estimated by satellite altimetry over 1993–2008. *Ocean Sci.*, **5**, 193–201, doi:10.5194/os-5-193-2009.

Albani, M., and Coauthors, 2012: Long term preservation of Earth observation space data: European LTDP common guidelines. LTDP Working Group Rep. GSCB-LTDP-EOPG-GD-09-0002 Issue 2.0, 48 pp. [Available online at https://earth.esa.int/documents/1656065/1681917/EuropeanLTDPCommonGuidelines_Issue2.0.pdf.]

Allan, R., P. Brohan, G. P. Compo, R. Stone, J. Luterbacher, and S. Brönnimann, 2011: The International Atmospheric Circulation Reconstructions over the Earth (ACRE) Initiative. *Bull. Amer. Meteor. Soc.*, **92**, 1421–1425, doi:10.1175/2011BAMS3218.1.

Asrar, G., and D. J. Dokken, Eds., 1993: *Earth Observing System (EOS) Reference Handbook*. NASA, 148 pp. [Available online at http://ntrs.nasa.gov/archive/nasa/casi.ntrs.nasa.gov/19930014548.pdf.]

Bates, J. J., and J. L. Privette, 2012: A maturity model for assessing the completeness of climate data records. *Eos, Trans. Amer. Geophys. Union*, **93**, 441, doi:10.1029/2012EO440006.

Bhartia, P. K., R. D. McPeters, L. E. Flynn, S. Taylor, N. A. Kramarova, S. Frith, B. Fisher, and M. DeLand, 2013: Solar Backscatter UV (SBUV) total ozone and profile algorithm. *Atmos. Meas. Tech.*, **6**, 2533–2548, doi:10.5194/amt-6-2533-2013.

Bojinski, S., M. Verstraete, T. C. Peterson, C. Richter, A. Simmons, and M. Zemp, 2014: The concept of essential climate variables in support of climate research, applications, and policy. *Bull. Amer. Meteor. Soc.*, **95**, 1431–1443, doi:10.1175/BAMS-D-13-00047.1.

Chen, R., C. Cao, and W. P. Menzel, 2013: Intersatellite calibration of NOAA HIRS CO_2 channels for climate studies. *J. Geophys. Res. Atmos.*, **118**, 5190–5203, doi:10.1002/jgrd.50447.

Compo, G. P., J. S. Whitaker, and P. D. Sardeshmukh, 2006: Feasibility of a 100-year reanalysis using only surface pressure data. *Bull. Amer. Meteor. Soc.*, **87**, 175–190, doi:10.1175/BAMS-87-2-175.

——, and Coauthors, 2011: The Twentieth Century Reanalysis Project. *Quart. J. Roy. Meteor. Soc.*, **137**, 1–28, doi:10.1002/qj.776.

Coppens, D., B. Theodore, W. Doehler, A. Damiano, D. Oertel, D. Klaes, J. Schmetz, and D. Spaenkuch, 2015: Exploitation of SI-1 data from *Meteor-28* and *29* spacecraft for climate purposes. *2015 EUMETSAT Meteorological Satellite Conf.*, Toulouse, France, EUMETSAT. [Available online at https://cimss.ssec.wisc.edu/itwg/itsc/itsc20/program/PDFs/30Oct/session7b/7p_07_coppens.pdf.]

Dee, D. P., and Coauthors, 2011: The ERA-Interim Reanalysis: Configuration and performance of the data assimilation system. *Quart. J. Roy. Meteor. Soc.*, **137**, 553–597, doi:10.1002/qj.828.

——, M. Balmaseda, G. Balsamo, R. Engelen, A. J. Simmons, and J.-N. Thépaut, 2014: Toward a consistent reanalysis of the climate system. *Bull. Amer. Meteor. Soc.*, **95**, 1235–1248, doi:10.1175/BAMS-D-13-00043.1.

Dowell, M., and Coauthors, 2013: Strategy towards an architecture for climate monitoring from space. CEOS, WMO, and CGMS Rep., 39 pp. [Available online at http://ceos.org/document_management/Working_Groups/WGClimate/WGClimate_Strategy-Towards-An-%20Architecture-For-Climate-Monitoring-From-Space_2013.pdf.]

Fennig, K., A. Andersson, and M. Schröder, 2015: Fundamental climate data record of SSM/I / SSMIS brightness temperatures. Satellite Application Facility on Climate Monitoring, accessed 20 Apr 2017, doi:10.5676/EUM_SAF_CM/FCDR_MWI/V002.

Gallaher, D., and G. Campbell, 2014: Nimbus ice edge points from Nimbus visible imagery L2, CSV. National Snow and Ice Data Center, Boulder, CO, digital media, doi:10.5067/NIMBUS/NmIcEdg2.

GCOS, 2010a: Implementation plan for the global observing system for climate in support of the UNFCCC (2010 update). GCOS Rep. 138, 186 pp. [Available online at www.wmo.int/pages/prog/gcos/Publications/gcos-138.pdf.]

——, 2010b: Guideline for the generation of datasets and products meeting GCOS requirements. GCOS Rep. 143, 12 pp. [Available online at www.wmo.int/pages/prog/gcos/Publications/gcos-143.pdf.]

Goldberg, M., and Coauthors, 2011: The Global Space-based Inter-Calibration System. *Bull. Amer. Meteor. Soc.*, **92**, 467–475, doi:10.1175/2010BAMS2967.1.

Gregow, H., and Coauthors, 2015: Worldwide survey of awareness and needs concerning reanalyses and respondents views on climate services. *Bull. Amer. Meteor. Soc.*, **97**, 1461–1473, doi:10.1175/BAMS-D-14-00271.1.

Harries, J. E., H. E. Brindley, P. J. Sagoo, and R. J. Bantges, 2001: Increases in greenhouse forcing inferred from the outgoing longwave radiation spectra of the Earth in 1970 and 1997. *Nature*, **410**, 355–357, doi:10.1038/35066553.

Hollmann, R., and Coauthors, 2013: The ESA climate change initiative: Satellite data records for essential climate variables. *Bull. Amer. Meteor. Soc.*, **94**, 1541–1552, doi:10.1175/BAMS-D-11-00254.1.

Houghton, J. T., F. W. Taylor, and C. D. Rodgers, 1986: *Remote Sounding of Atmospheres*. Cambridge University Press, 343 pp.

IPCC, 2014a: *Climate Change 2014: Synthesis Report Summary for Policymakers*. Cambridge University Press, 32 pp. [Available online at www.ipcc.ch/pdf/assessment-report/ar5/syr/AR5_SYR_FINAL_SPM.pdf.]

——, 2014b: *Climate Change 2014: Impacts, Adaptation, and Vulnerability. Part B: Regional Aspects*. Cambridge University Press, 688 pp. [Available online at www.ipcc.ch/pdf/assessment-report/ar5/wg2/WGIIAR5-PartB_FINAL.pdf.]

John, V. O., G. Holl, R. P. Allan, S. A. Buehler, D. E. Parker, and B. J. Soden, 2011: Clear-sky biases in satellite infrared estimates of upper tropospheric humidity and its trends. *J. Geophys. Res.*, **116**, D14108, doi:10.1029/2010JD015355.

——, R. Roebeling, and J. Schulz, 2014: CORE-CLIMAX system maturity matrix instruction manual. EUMETSAT Doc. CC/EUM/MAN/13/002 v4, 34 pp. [Available online at www.eumetsat.int/website/wcm/idc/idcplg?IdcService=GET_FILE&dDocName=PDF_CORE_CLIMAX_MANUAL&RevisionSelectionMethod=LatestReleased&Rendition=Web.]

Kållberg, P., S. Uppala, and A. Simmons, 2010: The real first weather satellite picture. *Weather*, **65**, 211–213, doi:10.1002/wea.652.

Kempe, V., D. Oertel, R. Schuster, H. Becker-Ross, and H. Jahn, 1980: Absolute IR-spectra from the measurement of Fourier-spectrometers aboard Meteor 25 and 28. *Acta Astronaut.*, **7**, 1403–1416, doi:10.1016/0094-5765(80)90015-6.

Khayat, M., S. Kempler, B. Deshong, I. Gerasimov, J. Johnson, E. Esfandiari, and M. Berganski, 2013: Implementing an open-source document preservation system at NASA GES-DISC. *2013 Fall Meeting*, San Francisco, CA, Amer. Geophys. Union, Abstract IN13A-1548. [Available online at http://disc.sci.gsfc.nasa.gov/additional/publications/year_2013/implement_open_source_preservation/.]

Knapp, K. R., 2008: Scientific data stewardship of International Satellite Cloud Climatology Project B1 global geostationary observations. *J. Appl. Remote Sens.*, **2**, 023548, doi:10.1117/1.3043461.

Kobayashi, S., P. Poli, and V. John, 2015: CM-SAF visiting scientist activity CM_VS14_01 report: Characterisation of SSM/T-2 radiances using ERA-Interim and other reanalyses. ERA Rep. 21, 37 pp. [Available online at www.ecmwf.int/sites/default/files/elibrary/2015/10518-cm-saf-visiting-scientist-activity-cmvs1401-report-characterisation-ssmt-2-radiances-using.pdf.]

Lattanzio, A., and Coauthors, 2013: Land surface albedo from geostationary satellites: A multiagency collaboration within SCOPE-CM. *Bull. Amer. Meteor. Soc.*, **94**, 205–214, doi:10.1175/BAMS-D-11-00230.1.

Leroy, S. S., J. G. Anderson, and G. Ohring, 2008: Climate signal detection times and constraints on climate benchmark accuracy requirements. *J. Climate*, **21**, 841–846, doi:10.1175/2007JCLI1946.1.

McNally, A. P., and P. D. Watts, 2003: A cloud detection algorithm for high-spectral-resolution infrared sounders. *Quart. J. Roy. Meteor. Soc.*, **129**, 3411–3423, doi:10.1256/qj.02.208.

National Academy of Sciences, Engineering, and Medicine, 2015: *Continuity of NASA Earth Observations from Space: A Value Framework*. National Academies Press, 105 pp.

Njoku, E. G., 2003: *Nimbus-7* SMMR Pathfinder brightness temperatures. National Snow and Ice Data Center, Boulder, CO, digital media. [Available online at http://nsidc.org/data/docs/daac/nsidc0036_smmr_pathfinder_tbs.gd.html.]

Poli, P., and P. Brunel, 2016: Meteorological satellite data rescue: Assessing radiances from *Nimbus-IV* IRIS (1970-1971) and *Nimbus-VI* HIRS (1975-1976). ERA Rep. 23, 59 pp. [Available online at www.ecmwf.int/sites/default/files/elibrary/2016/16338-meteorological-satellite-data-rescue-assessing-radiances-nimbus-iv-iris-1970-1971-and-nimbus.pdf.]

——, C. Peubey, K. Fennig, M. Schroeder, R. Roebelling, and A. Geer, 2015: Pre-assimilation feedback on a fundamental climate data record of brightness temperatures from special sensor microwave imagers: A step towards MIPs4Obs? ERA Rep. 19, 50 pp. [Available online at www.ecmwf.int/sites/default/files/elibrary/2015/11695-pre-assimilation-feedback-fundamental-climate-data-record-brightness-temperatures-special.pdf.]

——, and Coauthors, 2016: ERA-20C: An atmospheric reanalysis of the 20th century. *J. Climate*, **29**, 4083–4097, doi:10.1175/JCLI-D-15-0556.1.

Reichhardt, T., 2006: First photo from space. *Air and Space Magazine*, 24 October. [Available online at www.airspacemag.com/space/the-first-photo-from-space-13721411.]

Saunders, R. W., M. Matricardi, and P. Brunel, 1999: An improved fast radiative transfer model for assimilation of satellite radiance observations. *Quart. J. Roy. Meteor. Soc.*, **125**, 1407–1425, doi:10.1002/qj.1999.49712555615.

Schulz, J., and Coauthors, 2009: Operational climate monitoring from space: The EUMETSAT Satellite Application Facility on Climate Monitoring (CM-SAF). *Atmos. Chem. Phys.*, **9**, 1687–1709, doi:10.5194/acp-9-1687-2009.

Simmons, A., and Coauthors, 2016: Observation and integrated Earth-system science: A roadmap for 2016–25. *Adv. Space Res.*, **57**, 2037–2103, doi:10.1016/j.asr.2016.03.008.

Spänkuch, D., 1980: Arbeiten des Meteorologischen Dienstes der DDR auf dem Gebiet der indirekten Sondierung. *Z. Meteor.*, **30**, 205–214.

Stickler, A., and Coauthors, 2014: ERA-CLIM: Historical surface and upper-air data for future reanalyses. *Bull. Amer. Meteor. Soc.*, **95**, 1419–1430, doi:10.1175/BAMS-D-13-00147.1.

Suomi, V. E., 1958: The radiation balance of the Earth from a satellite. *Ann. IGY*, **I**, 331–340.

Takacs, L. L., M. Suarez, and R. Todling, 2016: Maintaining atmospheric mass and water balance within reanalysis. *Quart. J. Roy. Meteor. Soc.*, **142**, 1565–1573, doi:10.1002/qj.2763.

Taylor, K., R. Stouffer, and G. Meehl, 2012: An overview of CMIP5 and the experiment design. *Bull. Amer. Meteor. Soc.*, **93**, 485–498, doi:10.1175/BAMS-D-11-00094.1.

Teixeira, J., D. Waliser, R. Ferraro, P. Gleckler, T. Lee, and G. Potter, 2014: Satellite observations for CMIP5: The genesis of Obs4MIPs. *Bull. Amer. Meteor. Soc.*, **95**, 1329–1334, doi:10.1175/BAMS-D-12-00204.1.

Uppala, S. M., and Coauthors, 2005: The ERA-40 Re-Analysis. *Quart. J. Roy. Meteor. Soc.*, **131**, 2961–3012, doi:10.1256/qj.04.176.

Wentz, F. J., 2013: SSM/I version-7 calibration report. Remote Sensing Systems Tech. Rep. 011012, 46 pp.

Zeng, Y., and Coauthors, 2015: Analysis of current validation practices in Europe for space-based climate data records of essential climate variables. *Int. J. Appl. Earth Obs. Geoinf.*, **42**, 150–161, doi:10.1016/j.jag.2015.06.006.

Zou, C. Z., and W. H. Wang, 2011: Intersatellite calibration of AMSU-A observations for weather and climate applications. *J. Geophys. Res.*, **116**, D23113, doi:10.1029/2011JD016205.

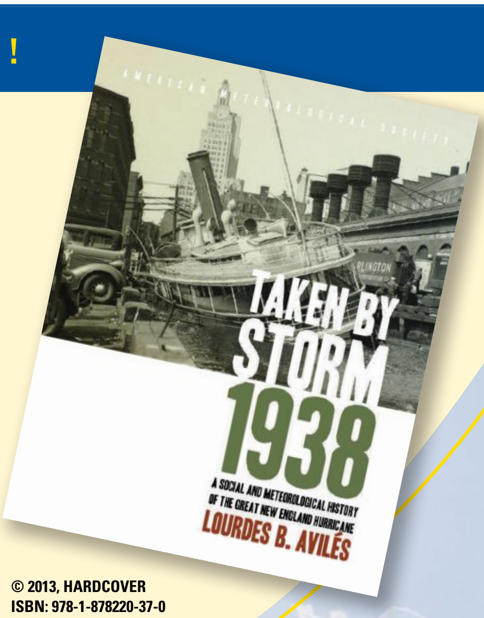

METHODS FOR COMPUTING THE BOILING TEMPERATURE OF WATER AT VARYING PRESSURES

Sam Miller

Four functions for computing boiling temperature are tested and the results are compared to data from the *CRC Handbook of Physics and Chemistry*.

Boiling has been described as a violent form of evaporation that occurs when the saturation (or equilibrium) vapor pressure is equal to the total atmospheric pressure (Glickman 2000). But atmospheric pressure varies with height (e.g., it is lower in Denver, Colorado, than it is in Miami, Florida), so the boiling temperature should also vary with height. It ought to be a simple matter to manipulate the known thermodynamic relationships to derive an equation describing the boiling point of water at a given atmospheric pressure. One such relation is the closed form of the Clausius–Clapeyron equation:

$$e_s = e_0 \exp\left[\frac{l_v}{R_v}\left(\frac{1}{T_0}-\frac{1}{T}\right)\right], \tag{1}$$

where e_s is the saturation vapor pressure (Pa), e_0 is the vapor pressure at the triple point of water (611.12 Pa), l_v is the latent heat of vaporization (equal to 2.5008×10^6 J kg^{-1} at 0°C, decreasing by about 10% as temperature increases to 100°C), R_v is the individual gas constant for vapor (461.2 J kg^{-1} K^{-1}), T_0 is the temperature at the triple point (273.16 K), and T is the temperature (K) (Miller 2015). This equation can be recast to show the relationship between total atmospheric pressure and the boiling temperature of water by

$$p_B = e_0 \exp\left[\frac{l_v}{R_v}\left(\frac{1}{T_0}-\frac{1}{T_B}\right)\right], \tag{2}$$

where p_B is the total atmospheric pressure at which the water is boiled (Pa) and T_B is the boiling temperature of water (K) at pressure p_B. By inverting this equation, we can then compute the boiling temperature at any given pressure. After about five steps, we arrive at

$$T_B = \frac{1}{\dfrac{1}{T_0} - \dfrac{R_v}{l_v}\ln\left(\dfrac{p_B}{e_0}\right)}. \tag{3}$$

There is a slight problem in using this expression to compute all boiling temperatures: l_v is *not* a constant (e.g., Court 1985; Henderson-Sellers 1984, 1985; Rogers and Yau 1989). It varies with temperature

AFFILIATION: Miller—Plymouth State University, Plymouth, New Hampshire
CORRESPONDING AUTHOR: Dr. Sam Miller, stmiller@plymouth.edu

The abstract for this article can be found in this issue, following the table of contents.
DOI:10.1175/BAMS-D-16-0174.1

In final form 29 November 2016

(in this case T_B), which implies that we would need to compute l_v before computing T_B. To do that, we need to know T_B first. There are numerical methods for closing this loop, but another method that yields results with a relatively small error is to simply use an average value of l_v in the known range of temperatures. The purposes and motivation of the research described in this paper were 1) to try three variations on the latent heat of vaporization (one a constant and two different functions of temperature) and apply these toward computing boiling temperature as a function of the total atmospheric pressure in the Clausius–Clapeyron equation and 2) to determine a direct function of total atmospheric pressure for computing boiling temperature. For the purposes of this research, the boiling temperatures listed in Lide (2006) were considered correct.

METHODS AND RESULTS. *Method 1: Constant l_v.* In the first method, the boiling temperature of water was computed for the pressures between mean sea level pressure (MSLP; 1,013.25 hPa) and the lower pressure (high elevation) limit shown on most skew *T*–log*p* diagrams (100 hPa) using (3) and the value of l_v at 50°C (2.3893×10^6 J kg^{-1}) from Table 1 (Tsonis 2007). This value of l_v was chosen for two reasons: 1) its corresponding temperature is midway between the known boiling temperatures at MSLP and at pressures near the top of the stratosphere and 2) doing so made it possible to determine the accuracy of the results when only a rough approximation of the parameter is used. The results are shown in Table 2.

Table 2 also shows boiling-point data taken from Lide (2006) and a summary of the differences between the boiling points computed from (3) and the boiling points taken from Lide (2006). Bias (column 5 of Table 2) was defined as computed value minus the Lide (2006) value. Accepting the values taken from Lide (2006) as "correct," the error values in column 6 of Table 2 were then computed by

$$\text{Error} = \text{abs}\left[\frac{(\text{Computed value})-(\text{Lide 2006 value})}{(\text{Lide 2006 value})}\right]\times 100\%, \qquad (4)$$

where the Lide (2006) values used in the denominator were first converted to the absolute scale.

These results indicate that, to within less than half a percentage point (mean error 0.33%) and about 1.15°C (mean bias), the Clausius–Clapeyron equation can be used to estimate the boiling point temperature of water in pressures typical of Earth's lower atmosphere, even when using a rough estimate of the value of the latent heat of vaporization.

TABLE 1. Latent heat of vaporization for water. Some values have been interpolated from available data (Tsonis 2007).

Temperature (°C)	l_v (10^6 J kg^{-1})
50	2.3893
45	2.3945
40	2.4062
35	2.4183
30	2.4300
25	2.4418
20	2.4535
15	2.4656
10	2.4774
5	2.4891
0	2.5008
−5	2.5128
−10	2.5247
−15	2.5366
−20	2.5494
−25	2.5622
−30	2.5749
−35	2.5890
−40	2.6030
−45	2.6189
−50	2.6348

TABLE 2. Comparison of boiling temperature values computed from the Clausius–Clapeyron equation with constant l_v (method 1) to values from Lide (2006). Elevations correspond to the *U.S. Standard Atmosphere* (NASA 1962, 1966, 1976).

Pressure (hPa)	Elevation (m)	Computed value (°C)	Lide (2006) value (°C)	Bias (°C)	Error (%)
1,013.25	0	100.76	100.00	0.76	0.20
1,000	111	100.41	99.63	0.78	0.21
900	988	97.59	96.71	0.88	0.24
800	1,947	94.49	93.51	0.98	0.27
700	3,010	91.04	89.96	1.08	0.30
600	4,203	87.14	85.95	1.19	0.33
500	5,570	82.63	81.34	1.29	0.36
400	7,180	77.26	75.88	1.38	0.40
300	9,157	70.57	69.11	1.46	0.43
200	11,766	61.56	60.07	1.49	0.45
100	15,787	47.22	45.82	1.40	0.44

Method 2: Linearly varying l_v. The second method used a linear function for l_v, and then used the computed value of l_v in (3) in an error-reduction loop to compute boiling temperature as a function of total atmospheric pressure. The linear function is

$$l_v = l_{v0} + l_{v1}T, \tag{5}$$

where l_v is the latent heat of vaporization at temperature T (J kg^{-1}), l_{v0} is its value at 0°C (2.5008×10^6 J kg^{-1}), l_{v1} is the slope of a linear function (−2,369), and T is the temperature (°C) (Miller 2015). This equation is described in greater detail in Rogers and Yau (1989). In this method, l_{v0} and l_{v1} were considered fixed constants, not variables to be determined. An error-reduction loop involving variable coefficients was employed in the third method, described below.

In the error-reduction loop for method 2, a first-guess temperature was used to estimate the value of l_v with (5), and the inverted Clausius–Clapeyron equation (3) was then used with the estimated l_v to compute the boiling temperature at a selected pressure. The resulting temperature was then substituted into the latent heat relationship (5), yielding an updated value of l_v, and the process was repeated. This was continued for each selected pressure level until the resulting boiling temperature from (3) and the guess temperature used for l_v in (5) were within 0.01°C. This method was used to compute boiling temperatures for the same pressures listed in Table 2, then compared to boiling point temperatures from Lide (2006). The results are shown in Table 3 and indicate a mean bias of about 6.45°C and a mean error of about 1.78% in the applicable range of pressures. Both of these are larger than the results described in Table 2. That is, by substituting this functional value of l_v for the fixed value (in an attempt to improve the prediction of boiling point temperature), the results got worse, not better.

Table 3. Comparison of boiling temperature values computed with linear-function l_v (method 2) to values from Lide (2006). Bias and error are as defined in text.

Pressure (hPa)	Computed value (°C)	Lide (2006) value (°C)	Bias (°C)	Error (%)
1,013.25	110.22	100.00	10.22	2.74
1,000	109.74	99.63	10.11	2.71
900	106.01	96.71	9.30	2.51
800	101.97	93.51	8.46	2.31
700	97.56	89.96	7.60	2.09
600	92.67	85.95	6.72	1.87
500	87.14	81.34	5.80	1.64
400	80.72	75.88	4.84	1.39
300	72.93	69.11	3.82	1.15
200	62.77	60.07	2.70	0.81
100	47.23	45.82	1.41	0.44

Method 3: Second-order polynomial function for l_v. The third method started with determining a new function for the latent heat of vaporization, by comparing the saturation vapor pressures derived from the Clausius–Clapeyron equation (which assumes temperature-dependent *variable* values of l_v) to the saturation vapor pressures derived for the same temperature using an advanced form of the equation (which assumes a *fixed* value of l_v, called l_{v0}):

$$e_s = e_0 \exp\left[\frac{l_{v0}}{R_v}\left(\frac{1}{T_0} - \frac{1}{T}\right) - \left(\frac{c - c_p^{\text{vapor}}}{R_v}\right)\ln\left(\frac{T}{T_0}\right) + T_0\left(\frac{1}{T_0} - \frac{1}{T}\right)\left(\frac{c - c_p^{\text{vapor}}}{R_v}\right)\right], \tag{6}$$

where e_0 is the reference pressure (611.12 Pa), l_{v0} is the latent heat of vaporization at 0°C (2.5008×10^6 J kg^{-1}), R_v is the individual gas constant for water vapor (461.2 J kg^{-1} K^{-1}), T_0 is the reference temperature at the triple point of water (273.16 K), T is the in situ temperature (K), c is the specific heat of liquid water at 0°C (4,215 J kg^{-1} K^{-1}), and c_p^{vapor} is the specific heat of water vapor at constant pressure (1,844.8 J kg^{-1} K^{-1}) (Miller 2015). Equation (6) can be derived analytically by referring to Rogers and Yau (1989), combining Eqs. (2.10) and (2.14) in their text, and integrating the result. It is also listed in Brock and Richardson (2001) in a slightly different form.

The values of l_v as a function of temperature between 0° and 100°C (in 1°C increments) were estimated by

- computing saturation vapor pressure with (1), which uses the temperature-dependent variable value of l_v, starting with a first-guess value of l_v;
- computing saturation vapor pressure with (6), which uses the fixed value of l_{v0}; and
- adjusting the variable value of l_v used in (1) to systematically minimize the difference between the two vapor pressures.

Henderson-Sellers (1984) derived a second-order function to compute l_v as a function of T. With this example in mind, a second-order polynomial ($R^2 \approx 1.0000$ and $\sigma = 49.11$ J kg^{-1}) was fitted to the results of the error-reduction calculations described above, taking the form

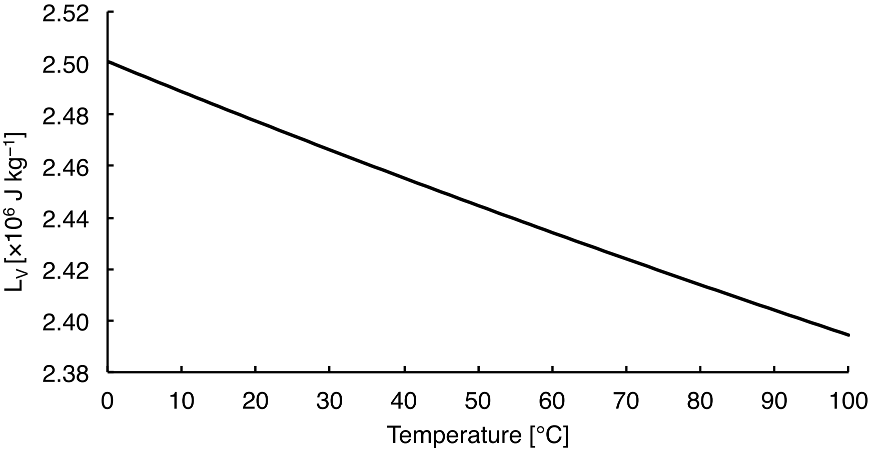

Fig. 1. Latent heat of vaporization as a function of temperature, computed by method 3.

$$l_v = l_{v0} + l_{v1}T + l_{v2}T^2, \qquad (7)$$

where l_v is the latent heat of vaporization (J kg^{-1}); l_{v0} is the new zeroth-order coefficient (2.5007 × 10^6), l_{v1} is the new first-order coefficient (–1,173.7723), l_{v2} is the second-order coefficient (1.1315), and T is the temperature (°C). [A first-order fit, similar to (5), yielded an R^2 of 0.9992.] Figure 1 shows the shape of the nearly linear function, and Table 4 summarizes the comparison between the computed values of l_v and those listed in Tsonis (2007). The mean bias between 0° and 50°C is 0.0309 × 10^6 (J kg^{-1}) (meaning the computed values are slightly high), and the mean error is 1.28%, indicating that (7) yields values of l_v that are probably serviceable for most meteorological applications (e.g., calculations of water vapor mixing ratio and integrated precipitable water). The rate of error growth in the available range of data suggests that the error at 100°C is about 5%, which is also probably sufficient for most meteorological applications.

From here, a second error-reduction loop was used to compute the boiling temperature as a function of pressure. In this loop, a first-guess temperature was used to compute the latent heat term using (7), and (3) was then used to compute the boiling temperature at a selected pressure. The resulting temperature was then substituted into the latent heat relationship (7), and the process was repeated. This was continued until the resulting boiling temperature from (3) and the guess temperature used for l_v in (7) were within 0.01°C. This method was used to compute boiling temperatures for pressures between 50 and 1,080 hPa, in 1-hPa increments. The results were stored in a file with two columns (one containing pressure and the other boiling temperature) and are plotted in Fig. 2.

Sample values of the boiling temperature computed with (7) in the error-reduction loop were compared to boiling point temperatures taken from Lide (2006), which is summarized in Table 5. The bias and error

Table 4. Comparison of l_v computed via (7) and those listed in Tsonis (2007).

Temperature (°C)	Computed l_v (10^6 J kg^{-1})	Tsonis (2007) l_v (10^6 J kg^{-1})	Bias (10^6 J kg^{-1})	Error (%)
100	2.3944			
95	2.3992			
90	2.4041			
85	2.4090			
80	2.4139			
75	2.4189			
70	2.4240			
65	2.4291			
60	2.4342			
55	2.4395			
50	2.4447	2.3893	0.0554	2.32
45	2.4500	2.3945	0.0555	2.32
40	2.4554	2.4062	0.0492	2.05
35	2.4608	2.4183	0.0546	2.27
30	2.4663	2.4300	0.0363	1.49
25	2.4719	2.4418	0.0301	1.23
20	2.4775	2.4535	0.0239	0.97
15	2.4832	2.4656	2.4656	0.71
10	2.4889	2.4774	0.0115	0.46
5	2.4948	2.4891	0.0057	0.23
0	2.5007	2.5008	–0.0001	0.004

values shown in columns 4 and 5 of Table 5 indicate the results are still warm relative to the Lide (2006) values, but to a smaller degree than the results of the calculations that used the fixed value of l_v (Table 2), and to a much lesser degree than the calculations using the linear-functional l_v (Table 3). The mean bias is 0.31°C, and the mean error in the range of pressures shown is 0.08%.

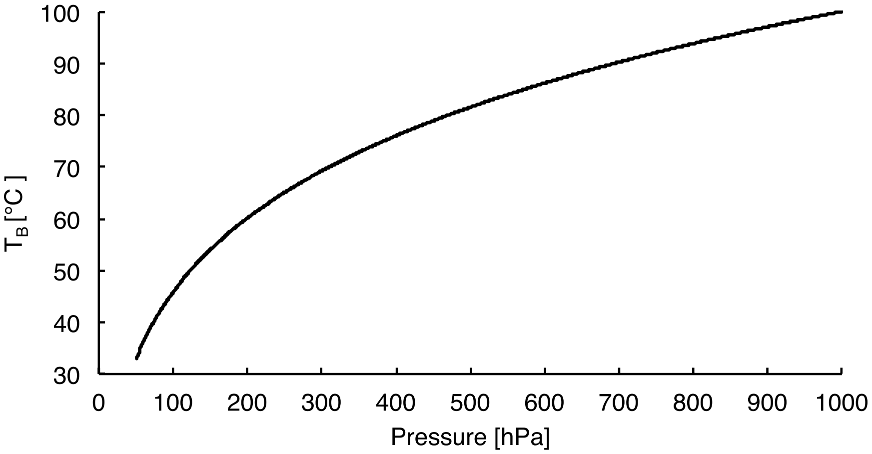

Fig. 2. Boiling temperature as a function of pressure, computed by method 3.

Method 4: Polynomial fits to method 3 results. The fourth and final method fitted a fifth-order polynomial, with $R^2 = 0.9998$ and $\sigma = 0.2377$°C, to the boiling pressure and temperature data in the file derived with the third method, using pressure as the independent variable and eliminating latent heat altogether:

$$T_B = a + bp_B + cp_B^2 + dp_B^3 + ep_B^4 + fp_B^5, \tag{8}$$

where T_B is the boiling temperature (°C), p_B is the pressure (hPa), and a–f are coefficients shown in Table 6. Lower-order polynomials yielded lower values of R^2, which is to be expected. A first-order fit yielded an R^2 value of 0.9236, and a second-order fit had a value of 0.9874. The fifth-order fit was judged a reasonable balance between quality of fit and usability, although additional work could certainly be done to fit higher-order polynomials. Different functions (a natural log function would be the logical choice) could also be tried in some future work.

Sample values of the boiling temperature computed with (8) were compared to boiling point temperatures taken from Lide (2006) and are summarized in Table 7. The bias and error values shown in columns 4 and 5 of Table 7 indicate this function is also slightly warm relative to the Lide (2006) values. The mean bias is 0.25°C, and the mean error in the range of pressures shown is 0.09%.

Table 5. Comparison of boiling temperature values computed with second-order function l_v (method 3) to values from Lide (2006).

Pressure (hPa)	Computed value (°C)	Lide (2006) value (°C)	Bias (°C)	Error (%)
1,013.25	100.50	100.00	0.50	0.13
1,000	100.12	99.63	0.49	0.13
900	97.16	96.71	0.45	0.12
800	93.92	93.51	0.41	0.11
700	90.32	89.96	0.36	0.10
600	86.27	85.95	0.32	0.09
500	81.61	81.34	0.27	0.08
400	76.10	75.88	0.22	0.06
300	69.28	69.11	0.17	0.05
200	60.19	60.07	0.12	0.04
100	45.87	45.82	0.05	0.02

SUMMARY AND CONCLUSIONS.

Boiling is an extreme form of evaporation that occurs when the saturation vapor pressure is equal to the total atmospheric pressure (Glickman 2000). The Clausius–Clapeyron equation (1) was recast to describe the boiling point (2) and solved for boiling temperature (3). Since one term in the equation is the latent heat of vaporization l_v, which is a function of temperature, one can either use an approximation of l_v to compute boiling temperature T_B at a given pressure P_B or use a temperature-dependent functional expression of l_v and proceed through an error-reduction loop. The purposes and motivation of

Table 6. Coefficients for fifth-order polynomial fit for boiling temperature as a function of pressure (method 4).

Coefficient	Value
a	20.682
b	0.3151
c	−0.000079207
d	1.1999×10^{-6}
e	-9.178×10^{-10}
f	2.7412×10^{-13}

this research were 1) to test one constant value and two temperature-dependent functional expressions for l_v in the Clausius–Clapeyron equation and 2) to derive a simple polynomial function, with atmospheric pressure as the independent variable, to compute boiling temperature. Values of boiling temperature as a function of pressure as reported in Lide (2006) were used as the standard by which all four methods were judged. Results are summarized in Table 8.

Table 7. Comparison of boiling temperature values computed with fifth-order polynomial (method 4) to values from Lide (2006).

Pressure (hPa)	Computed value (°C)	Lide (2006) value (°C)	Bias (°C)	Error (%)
1,013.25	100.34	100.00	0.34	0.09
1,000	99.93	99.63	0.30	0.08
900	97.12	96.71	0.41	0.11
800	94.08	93.51	0.57	0.16
700	90.41	89.96	0.45	0.12
600	86.14	85.95	0.19	0.05
500	81.41	81.34	0.07	0.02
400	76.10	75.88	0.22	0.06
300	69.56	69.11	0.44	0.13
200	60.24	60.07	0.17	0.05
100	45.38	45.82	−0.44	0.14

The first method used the value of l_v valid for 50°C and obtained results that were correct to within a mean error of 0.33% and a mean bias of 1.15°C for pressures typical of Earth's troposphere and lower stratosphere. The second method used the linear expression for l_v described by (5) (Rogers and Yau 1989), and the result was an even greater disagreement between computed values of T_B from (3) and those listed in Lide (2006), with a mean bias of about 6.45°C between MSLP and 100 hPa (indicating computed values of the boiling temperature were too warm) and a mean error of about 1.78%.

The third method began by deriving a new, second-order, temperature-dependent polynomial (7) for l_v. The new function for l_v yields a mean latent heat error of 1.28% between 0° and 50°C when compared to those listed in Tsonis (2007), and a probable error at 100°C of about 5%. An error-reduction loop was used to compute the boiling temperature as a function of pressure, wherein a first-guess temperature was used to compute the latent heat coefficient using the second-order polynomial shown in (7), and (3) was then used to compute the boiling temperature at a selected pressure. The resulting temperature from (3) was then substituted into the latent heat relationship (7), and the process was repeated until the resulting boiling temperature from (3) and the guess temperature used for l_v in (7) were within 0.01°C. This method was used to compute boiling temperatures for pressures between 50 and 1,080 hPa, in 1-hPa increments. This method for computing T_B showed a warm bias (mean value 0.31°C between MSLP and 100 hPa) compared to Lide (2006) and a mean error about 4 times smaller than those associated with computed values of T_B that used the constant value of l_v.

Table 8. Comparison of mean bias and error between MSLP and 100 hPa for methods tested to compute boiling temperature.

Method	Mean bias (°C)	Mean error (%)
1. Constant l_v in (3)	1.15	0.33
2. Linear l_v (5) in (3)	6.45	1.78
3. Second-order l_v (7) in (3)	0.31	0.08
4. Fifth-order polynomial in P_B (8)	0.25	0.09

The fourth method fitted a fifth-order polynomial (eliminating l_v and making P_B the sole independent variable) to the boiling temperatures resulting from the third method (8). The polynomial shows an R^2 value of 0.9998 and fit standard deviation of 0.2377°C. Computed values of T_B using the polynomial were associated with a mean bias of 0.25°C and a mean error of 0.09% when compared to Lide (2006).

ACKNOWLEDGMENTS. I wish to thank my colleagues R. Bruce Telfeyan, Don S. Harper III, and Stephen Augustyn, as well as three anonymous reviewers, for their valuable feedback. I would also like to thank my colleague Jason Cordeira for his assistance.

REFERENCES

Brock, F. V., and S. J. Richardson, 2001: *Meteorological Measurement Systems*. Oxford University Press, 290 pp.

Court, A., 1985: Comment on paper 'A new formula for latent heat of vaporization of water as a function of temperature', by B. Henderson-Sellers (1984, 110, 1186–1190). *Quart. J. Roy. Meteor. Soc.*, **112**, 283–284, doi:10.1002/qj.49711247117.

Glickman, T. S., Ed., 2000: *Glossary of Meteorology*. 2nd ed. Amer. Meteor. Soc., 855 pp. [Available online at http://glossary.ametsoc.org/.]

Henderson-Sellers, B., 1984: A new formula for latent heat of vaporization of water as a function of temperature. *Quart. J. Roy. Meteor. Soc.*, **110**, 1186–1190, doi:10.1002/qj.49711046626.

——, 1985: Reply to "Comment on paper 'A new formula for latent heat of vaporization of water as a function of temperature,' by B. Henderson-Sellers (1984, 110, 1186–1190)" by A. Court. *Quart. J. Roy. Meteor. Soc.*, **112**, 284.

Lide, D. R., Ed., 2006: *CRC Handbook of Chemistry and Physics*. 87th ed. CRC Press, 2608 pp.

Miller, S., 2015: *Applied Thermodynamics for Meteorologists*. Cambridge University Press, 385 pp.

NASA, 1962: *U.S. Standard Atmosphere, 1962*. U.S. Government Printing Office, 290 pp. [Available online at www.dtic.mil/cgi-bin/GetTRDoc?Location=U2&doc=GetTRDoc.pdf&AD=AD0659893.]

——, 1966: *U.S. Standard Atmosphere Supplements, 1966*. U.S. Government Printing Office, 300 pp. [Available online at www.dtic.mil/cgi-bin/GetTRDoc?Location=U2&doc=GetTRDoc.pdf&AD=AD0659543.]

——, 1976: *U.S. Standard Atmosphere, 1976*. U.S. Government Printing Office, 241 pp. [Available online at http://ntrs.nasa.gov/archive/nasa/casi.ntrs.nasa.gov/19770009539_1977009539.pdf.]

Rogers, R. R., and M. K. Yau, 1989: *A Short Course in Cloud Physics*. 3rd ed. Butterworth-Heinemann, 290 pp.

Tsonis, A. A., 2007: *An Introduction to Atmospheric Thermodynamics*. 2nd ed. Cambridge University Press, 187 pp.

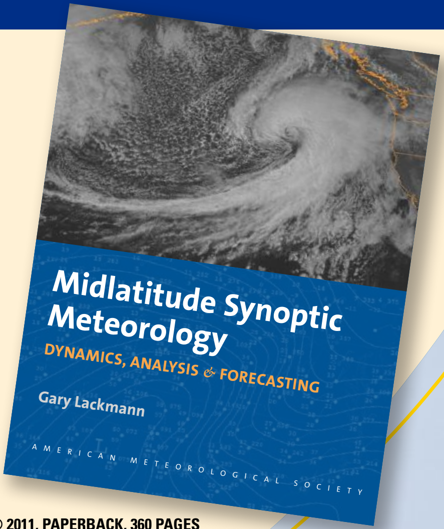

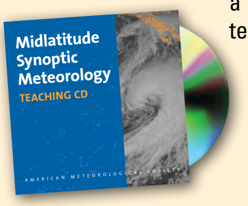

AMS titles now available as eBooks at springer.com

AMS BOOKS

RESEARCH APPLICATIONS HISTORY

www.ametsoc.org/amsbookstore

Springer

Scan to see
AMS eBook titles
at springer.com

Springer

HOME | MY SPRINGER | SUBJECTS | SERVICES | IMPRINTS & PUBLISHERS | ABOUT US

» New User
LOGIN

» American Meteorological Society

Home > Societies & Publishing Partners > American Meteorological Society

Search...
GO
Advanced Search

AMS BOOKS
RESEARCH APPLICATIONS HISTORY

American Meteorological Society

Promoting the development and dissemination of information and education on the atmospheric and related sciences.

AMERICAN METEOROLOGICAL SOCIETY

- About the American Meteorological Societ...
- Order print copies of AMS Books
- Booksellers seeking print copies of AMS ...
- For AMS Journals Online

American Meteorological Society eBooks

AMS Books grew out of a monograph publishing program related to the peer-reviewed journals published by the AMS and now encompasses a series of meteorological and historical monographs that reaches back five decades (formerly out-of-print volumes of which have been brought back on SpringerLink as eBooks) as well as a growing list of academic, policy, and general-interest books related to the atmospheric sciences.

Sort listing by: ○ Relevance ● Publication date ○ Title ○ Author ○ Copyright Year

Export to CSV

AMERICAN METEORLOGICAL SOCIETY EBOOKS

» Show all 11 results

Eloquent Science

A Practical Guide to Becoming a Better Writer, Speaker, and Atmospheric Scientist

Schultz, David

2009

Price from $45.00

Available Formats:

RESOURCES

Stay Informed

Receive notification of new releases from AMS Books

Submit a Book Proposal to the AMS

Download our book proposal guidelines

Become an AMS Member

Learn about the benefits of membership

CONNECT WITH THE AMERICAN METEOROLOGICAL SOCIETY

Like AMS on Facebook

Follow AMS on Twitter

AMERICAN METEOROLOGICAL SOCIETY

A COMPREHENSIVE DATABASE OF FLOOD EVENTS IN THE CONTIGUOUS UNITED STATES FROM 2002 TO 2013

XINYI SHEN, YIWEN MEI, AND EMMANOUIL N. ANAGNOSTOU

Data from thousands of U.S. Geological Survey (USGS) stream gauges and radar-rainfall estimates over the United States for a 12-yr period are used to retrieve over a half-million flood events and document their spatiotemporal precipitation and flow characteristics.

Flood events that appear as overflow from water bodies represent hydrological responses of basins to precipitation accumulation from storms. A comprehensive database of flood events is vital for studying this hydrological behavior at catchment scale and for analyzing the occurrence and impact of hydrological hazards, yet one is not available. Survey- and report-based flood catalogs are limited in terms of the number of recorded events (Adhikari et al. 2010; Calianno et al. 2013; Diakakis et al. 2012; Du et al. 2015; Gourley et al. 2010; Santos et al. 2015) and could be impractical in regions exhibiting less frequent weather hazards. Threshold-based approaches (Gourley et al. 2013) are restricted to gauging locations with available flood thresholds. Such thresholds are difficult to define across basins of different sizes because the term "overflow" varies with time and location. Existing databases, such as the Emergency Disasters Database (EM-DAT; www.emdat.be), the International Flood Network (IFNET; www.internationalfloodnetwork.org), the impact-categorized (United States) flash flood reports (Calianno et al. 2013), the European flash floods (Gaume et al. 2009), and a U.S. unified flash flood database (http://blog.nssl.noaa.gov/flash/database/) (Gourley et al. 2013) have primarily focused on flash floods or major floods noticeable by their impact. Consequently, records in these databases represent a subset of the different flood events that can cause hydrological hazards. Other recent flood databases have only recorded flow time series and/or annual peak values without identifying the flood events (Hall et al. 2015). Furthermore, although the timing and location of floods are available in some of the existing databases, the triggering precipitation characteristics are seldom archived.

In this study, we report the development of a new comprehensive database of flood events over the

AFFILIATIONS: SHEN, MEI, AND ANAGNOSTOU—Civil and Environmental Engineering Department, University of Connecticut, Storrs, Connecticut
CORRESPONDING AUTHOR: Prof. Emmanouil Anagnostou, manos@uconn.edu

The abstract for this article can be found in this issue, following the table of contents.
DOI:10.1175/BAMS-D-16-0125.1

In final form 12 October 2016

TABLE 1. Descriptors of a flood event record. Here "yyyy" stands for four digits of the year, "mmm" stands for three-letter abbreviation of the month, "dd" stands for two digits of the day, and "hh" stands for the two-digit hour.

Field code	Description	Definition	Unit
StartTimeP StartTimeF		Start date time of the triggering precipitation and flood event	yyyy/mmm/dd/hh
EndTimeP EndTimeF		Ending date time of the triggering precipitation and flood event	yyyy/mmm/dd/hh
Drainage area	Contributing area of the basin	Area of basin region delineated by the watershed algorithm	km^2
Perc	Percentage of the peak flow	The percentile of the peak flow in the entire flow series of the gauge	%
Pmean	Mean precipitation rate during the event	$P_{\text{mean}} = \frac{V_p}{A\tau_p} = \frac{\int^{\tau_p} p_A(t)\mathrm{d}t}{A\tau_p} = \frac{1}{A\tau_p}\int^{\tau_p} dt \iint^{\Omega} p(t,A')dA'$	mm h^{-1}
Peak	Peak flow	max [$q(t)$]	m^3 s^{-1}
Vq	Normalized flow volume	$V_q = \frac{\int^{\tau_q} q(t)\mathrm{d}t}{A}$	mm
Category	Correctness of volume and timing	3: $t_{\text{lag}} > 0$ and $R < 1$; 2: $R < 1$ and $t_{\text{lag}} \le 0$; 1: otherwise	—
BFI	Base flow index	$I_B = \frac{\int^{\tau_q}[q(t)-q_f(t)]\mathrm{d}t}{\int^{\tau_q} q(t)dt}$, where q_f stands for the fast flow	m^3 m^{-3}
R	Runoff coefficient	$R = \frac{\int^{\tau_q} q_f(t)\mathrm{d}t}{A \times V_p}$	m^3 m^{-3}
ETQ	Centroid of flow	$E\left\langle T_Q^N \right\rangle = \frac{\int^{\tau_q} t^N q(t)\mathrm{d}t}{A \times V_q}, N = 1$	h
VarTQ	Spreadness of flow	$Var\left\langle T_Q \right\rangle = E\left\langle T_Q^2 \right\rangle - E^2\left\langle T_Q \right\rangle$	h^2
ETR	Centroid of precipitation	$E\left\langle T_R^N \right\rangle = \frac{\int^{\tau_p} t^N p_A(t)dt}{A \times V_p}, N = 1$	h
VarTR	Spreadness of precipitation	$Var\left\langle T_R \right\rangle = E\left\langle T_R^2 \right\rangle - E^2\left\langle T_R \right\rangle$	h^2
ELs	Mean water travel distance	$E\left\langle L_S T_R \right\rangle = \frac{\iint^{\Omega} L_S \int^{\tau_p} p(t,A')tdtdA'}{A \times V_p}$	m
VarLs	Variance of water travel distance	$Var\left\langle L_S \right\rangle = E\left\langle L_S^2 \right\rangle - E^2\left\langle L_S \right\rangle$	m^2
CovTrLs	Covariance of precipitation and water travel distance	$Cov\left\langle L_S, T_R \right\rangle = E\left\langle L_S T_R \right\rangle - E\left\langle L_S \right\rangle E\left\langle T_R \right\rangle$ where $E\left\langle L_S T_R \right\rangle = \frac{\iint^{\Omega} L_S \int^{\tau_p} p(t,A')tdtdA'}{A \times V_p}$	m h

contiguous United States (CONUS), identified from precipitation and flow records using the characteristic points method (CPM) (Mei and Anagnostou 2015). Besides being fully automatic because of its physical basis, CPM requires only flow and rainfall time series and does not depend on user-defined thresholds or calibration. Furthermore, using the available information on triggering basin-average precipitation, we have computed multiple descriptors (summarized in Table 1) for each event, including runoff coefficient, base flow index, and first- and second-order moments of both precipitation and flow (Zoccatelli et al. 2011)—parameters that do not exist in current flooding catalogs. These descriptors broaden the applicability of this database to varying flood studies, including hydrological modeling (Jayakrishnan et al. 2005; Park and Markus 2014; Shen et al. 2016a), flood risk analyses (Apel et al. 2009), and geomorphological and geophysical impact analyses (Costa 1987; Xu et al. 2004).

DATA AND METHODOLOGY. We used CPM as the kernel identifier of the flood events. In this study we introduced minor modifications to the method to improve the significance of events and the completeness of associated precipitation. The two input datasets to the CPM were the U.S. Geological Survey (USGS) stream flows (IF) and the National Stage IV multisensor precipitation analyses (Stage IV) products (Klazura and Imy 1993). We used multiscale flow direction (FDR) and accumulation (FAC) maps (Lehner et al. 2006; Wu et al. 2011) to segment basin regions and calculate the spatial moments of precipitation. The computational steps (also depicted in Fig. 1) were as follows:

1) The USGS flow time series at intervals from 1 min to 1 h was offset from the local time zone to coordinated universal time (UTC) and then accumulated to hourly to match the Stage IV–based basin-average precipitation time series.
2) The flow time series from step 1 was input to the CPM to perform the base flow separation and then the flood event identification by matching necessary characteristics of an event. Identified events with a peak value below the 80th percentile of the entire flow series were considered insignificant and filtered out.
3) Stage IV precipitation fields were used to generate basin-average precipitation time series. The basin region was segmented using the traditional watershed algorithm, requiring an FDR map and the location of the basin outlet. To balance the computation and accuracy, FDR maps of variable resolution (30′, 1/16°, or 1/8°) are selected, based on the drainage area. For this study, we selected a coarser resolution when the basin had more than 1,000 grid cells at the resolution. Before the segmentation, gauge locations were snapped into the river network. We searched the grid by matching the drainage area (accompanied by the gauge information provided by USGS) to the FAC (which equals to the drainage area) within three pixels' distance from the gauge location.
4) The original rainfall association module of the CPM (Mei and Anagnostou 2015) was modified

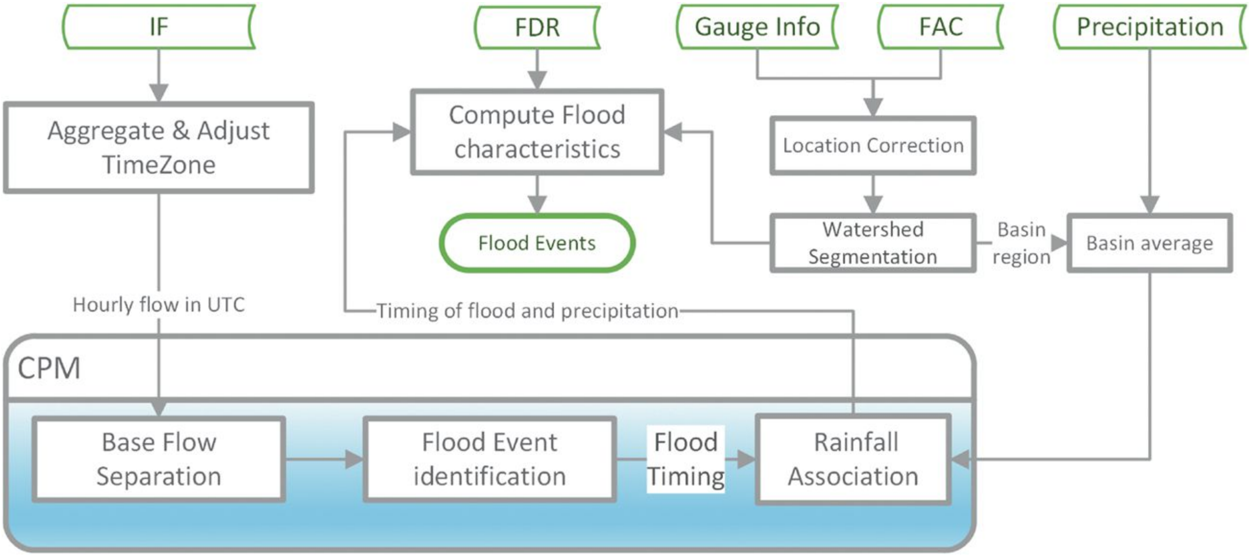

Fig. 1. Flowchart of flood events extraction for each USGS gauge data record.

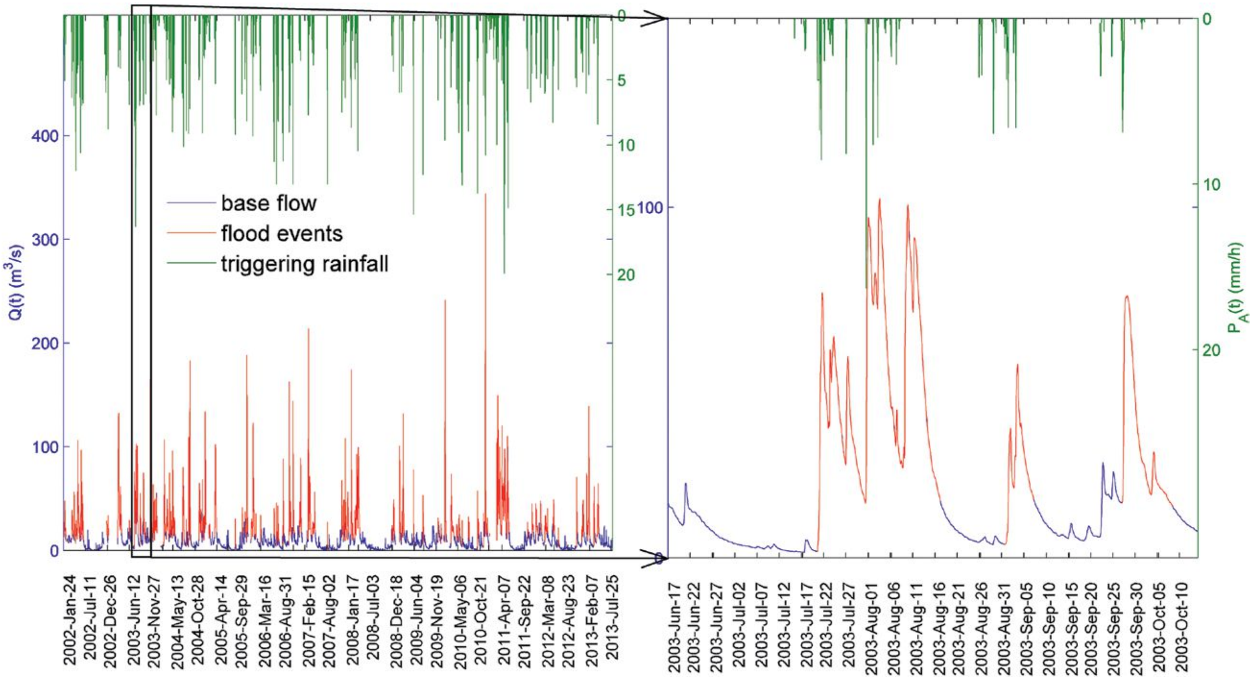

FIG. 2. Extracted flood hydrographs on the flow measurements of gauge USGS03007800; $P_A(t)$ is the basin-averaged precipitation defined in Table 1.

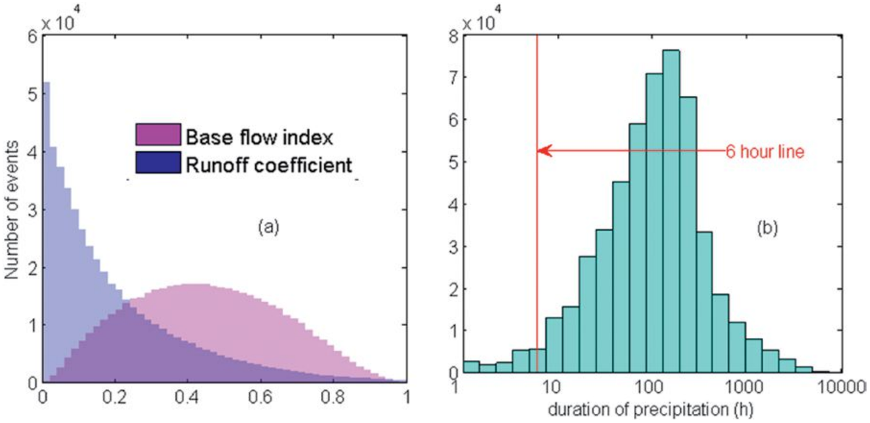

FIG. 3. Distribution of flood event characteristics from the database: (a) base flow index and runoff coefficient and (b) duration of triggering precipitation.

to improve the accuracy of the start time of triggering precipitation. Specifically, when CPM could not find a sufficient precipitation amount to associate to a given flood event, we tripled the value of the drainage area–derived searching period [L_{SP}; Eq. (6) in Mei and Anagnostou (2015)] to identify the triggering precipitation. The start time of precipitation was defined as the latest time, t_{pb}, in the basin-average precipitation time series for which precipitation accumulation between t_{pb} and the start time of the flood, t_{fb}, is at least twice the total basin outflow accumulation of the flood event.

5) Based on the event precipitation and flow time series we calculated multiple descriptors of the flood event, listed in Table 1.

RESULTS. We extracted 542,092 flood events from January 2002 to August 2013, applying the above procedure to flow records from 6,301 USGS hydrometric stations in the CONUS area. We discarded 762 stations whose records were incomplete, which contained back flow, or whose locations we could not snap to streams on the geographical map. Users can mine this database using different criteria—for example, peak value exceeding the 95th percentile of the peak flow record, duration, by defining drainage area ranges, and so on. Figure 2 provides an example of extracted flood events in USGS gauge 03007800, while Fig. 3 gives the overall distributions of selected flood characteristics.

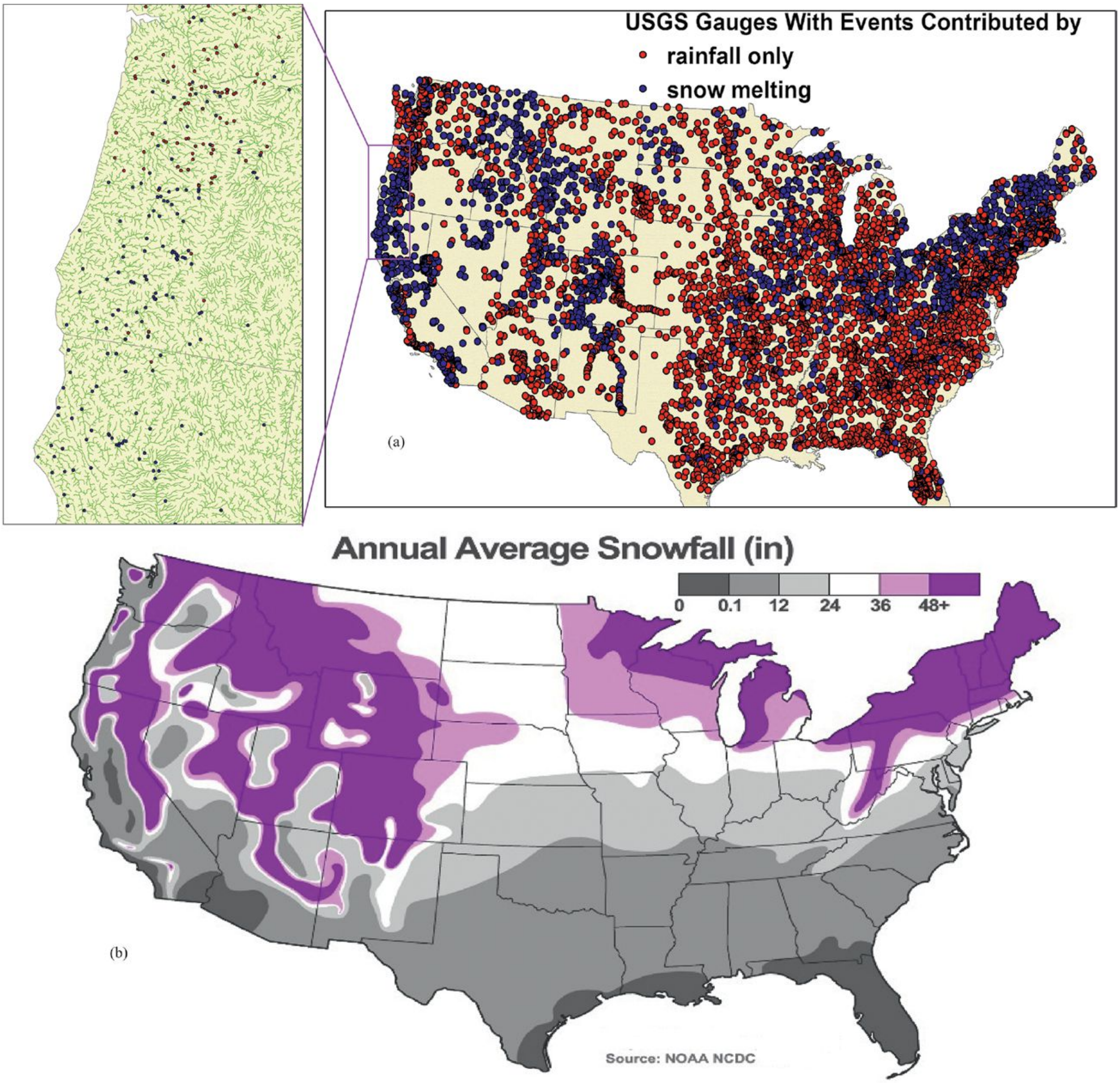
USGS Gauges With Events Contributed by

Annual Average Snowfall (in)

Source: NOAA NCDC

Fig. 4. Basins with floods to which melting snow contributed: (a) gauges of flood events with snowmelt contributions inferred from the derived database and (b) average annual snowfall [source: National Oceanic and Atmospheric Administration (NOAA)/National Climatic Data Center (NCDC)].

In Fig. 3a, the number of events is shown to decrease exponentially as a function of the runoff coefficient and to have a nearly parabolic distribution against the base flow index, with the maximal occurrence at 0.42. Figure 3b shows the duration distribution of triggering precipitation, with a median of 212.7 h. Precipitation lasting less than 6 h triggered 15,218 events, which are thus classified as flash floods (www.srh.noaa.gov/mrx/hydro/flooddef.php). Limited by the spatiotemporal resolution (4 km, hourly) of the Stage IV data, very short duration flash floods (lasting a few hours) associated with small-scale basins are not represented well by the spatial precipitation moments in this database.

Categorization of events facilitates different levels of flood studies. We categorized all events in our database into three classes by evaluating the runoff coefficient R, and the lag between the start time of flow and that of triggering precipitation, t_{lag}, of each event. If the matched precipitation provided enough fast flow (i.e., $R < 1$), and the causal relationship between triggering precipitation and flood event held (i.e., $t_{lag} > 0$), we labeled the event as category 3; if only the first condition was satisfied, we labeled it as category 2; if neither condition held, we labeled it as category 1. The timing error in category 2 and both the volume and timing errors in category 1 came from snowmelt contribution and/or data error. For studies at quantitative, qualitative, and basic levels, we correspondingly recommend using events of only category 3, categories 2 and 3, and all categories, as demonstrated below.

In Fig. 4a, rivers where melting snow makes a significant contribution to floods are identified by evaluating the *R* value of events in category 1. If *R* is greater than 1.2, it indicates a shortage of at least 20% of associated precipitation. The shortage may come from the fact that the snowmelt contribution was not considered in the CPM or due to error in the precipitation data. To moderate this ambiguity, we highlighted the gauges that had such events in at least one in 5 years of the available data record. By comparing with Fig. 4b, we note that the spatial pattern of USGS gauge locations with events affected by snow melting was in agreement with that of the annual snowfall. It should be noted that the snowfall locations and snowmelt-affected flows are expected to exhibit spatial and temporal lags, depending on the basin sizes and river lengths. A characteristic example is snowmelt-affected stream gauge records in the coastal areas of California and the central and southern plains that exhibit spatial lags relative to the snowfall locations.

Figure 5 analyzes the dependence of flood event characteristics on basin morphometry. As stated by Costa (1987), the number of flood events greatly reduces as a function of drainage area *A* and drainage density D_d and flood peak tends to increase as a function of elongation ratio R_e. Figures 5a and 5b show the histogram of the annual number of events with respect to *A* and D_d, respectively, using events in all categories and of peak value greater than the 90th percentile of the time series. Although mean annual count of events varies among gauges of similar *A* because of the different climate conditions, *A* has a negative correlation to the mean annual count of flood events. We have not, however, observed a declining trend of this count with D_d in Fig. 5b. A possible explanation is that *A* dominates D_d in reducing the probability of flood events. To verify this, Fig. 5c illustrates the count dependence on both factors. For the drainage area bin between 25 and 300 km^2, we observe a nearly monotonically declining trend of count with D_d. Other bins do not exhibit such clear trends, since they have limited dynamic range of D_d values. The count is reduced greatly with the drainage area in a similar D_d condition. Note that basins of total channel length shorter than 1 km or drainage area less than 24 km^2 are not included in Figs. 5b and 5c, owing to resolution limitations in the 1-km geomorphological maps. To evaluate the flood peak dependence on the elongation ratio among basins of varying sizes, peak flow rate in m^3 s^{-1} was normalized by the drainage area to be converted to mm h^{-1}. Figure 5d exhibits the peak flow rate dependence on mean precipitation and R_e. At the same level of precipitation, peak flow increases monotonically with R_e. Generally, the peak flow rate should increase with mean precipitation, as shown by most parts of Fig. 5d. The events maximal column of P_{mean} (31–313 mm h^{-1}) is not exhibited in Fig. 5d because event samples of this high precipitation level are not adequate to be statistically representative.

We used events from category 3, where snowmelt contribution and data error are relatively small, to validate the predictability of flood concentration time and spreadness from the spatial moments of precipitation. Considering that precipitation spatial moments were computed from the 4-km Stage IV data, we ruled out basins smaller than 100 km^2 for the subsequent analysis to maintain the accuracy of precipitation spatial moments. According to the geomorphological instantaneous unit hydrograph (GIUH) theory (Rigon et al. 2016; Zoccatelli et al. 2011), the centroid and spreadness of a flood event can be predicted by precipitation moments using:

$$E\langle T_q \rangle = E\langle T_R \rangle + E\langle T_S \rangle = E\langle T_R \rangle + \frac{E\langle L_S \rangle}{v} \quad (1)$$

and

$$\begin{aligned} Var\langle T_Q \rangle &= Var\langle T_R \rangle + Var\langle T_S \rangle + 2Cov\langle T_S, T_R \rangle \quad (2) \\ &= Var\langle T_R \rangle + \frac{Var\langle L_S \rangle}{v^2} + 2\frac{Cov\langle L_S, T_R \rangle}{v}, \end{aligned}$$

where *v* is the effective traveling velocity of a water parcel and other variables are formulated in Table 1; E<·>, Var<·>, and Cov<·,·> stand for the expectation, variance, and covariance, respectively, of a random variable or variables. Variables TQ, TR, and LS denote the flow concentration time, runoff generation time, and travel distance, respectively. Variables used in Table 1 are described as follows: p(t, A′) represents the precipitation field, with t denoting the time and A′ denoting the location; *A* and t_{lag} stand for drainage area and time lag between the start time of a flood event and the triggering precipitation. Variables τ_q and τ_p are the duration of a flood event and its triggering precipitation, respectively. For a given gauged basin, event-dependent velocity υ is obtained by solving Eq. (1) using training events. Then the solved υ is fit by Eq. (3) to include dependences on the mean precipitation and spreadness:

$$\frac{1}{v} = a + b\frac{\sqrt{Var\langle T_R\rangle}}{P_{mean}}, \qquad (3)$$

where a and b are basin-specific coefficients that depend on geomorphological and geophysical characteristics, and P_{mean} is defined in the fifth row of Table 1. Equation (3) indicates that heavier precipitation and narrower spreadness generate a higher energy-gradient line of flow that results in greater water traveling velocity. The predicted $E\langle T_Q\rangle$ and $\mathrm{Var}\langle T_Q\rangle$ against observations for all gauged basins are plotted in Figs. 6a–d. We note a minor underestimation, but otherwise a strong agreement, for the $E\langle T_Q\rangle$ predictions; the performance of $\mathrm{Var}\langle T_Q\rangle$ predictions

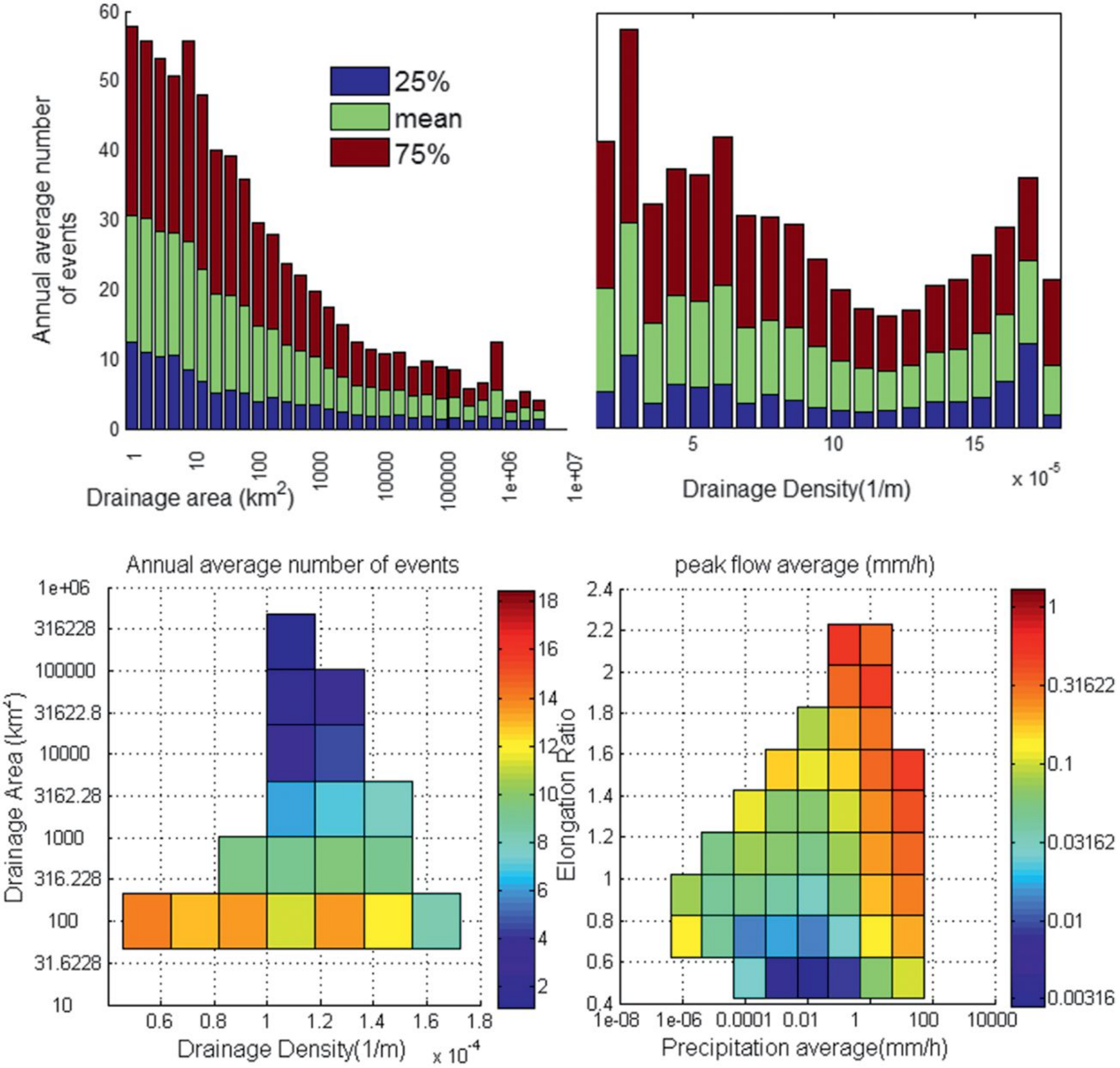

Fig. 5. Dependence of flood event characteristics on geomorphological factors: annual average number of events vs (a) drainage area and (b) drainage density, (c) annual number of events vs both drainage area and drainage density, and (d) normalized peak flow vs elongation ratio and normalized precipitation. In (a) and (b), the 25th and 75th percentiles and mean values are outlined, while in (c) and (d) the mean values of gauges/events are rendered to each bin.

is worse, particularly in basins exceeding 1,000 km^2. The agreement is also depicted in the density plots of predicted versus observed Pearson correlation coefficients shown in Figs. 6e and 6f and in the normalized root-mean-square difference (NRMSD) shown in Figs. 6g and 6h. We have observed good predictability of the flood concentration time and correlation of flood spreadness, by/to the precipitation spatial moments, respectively. It is noted, however, that simplified assumptions that equalize total precipitation to the direct runoff while ignoring the effect of interception, evapotranspiration and infiltration, and the velocity difference between the surface flow and interflow between the hill slope and channel can contribute to error in predicting the flood spreadness (Rigon et al. 2016; Zoccatelli et al. 2011).

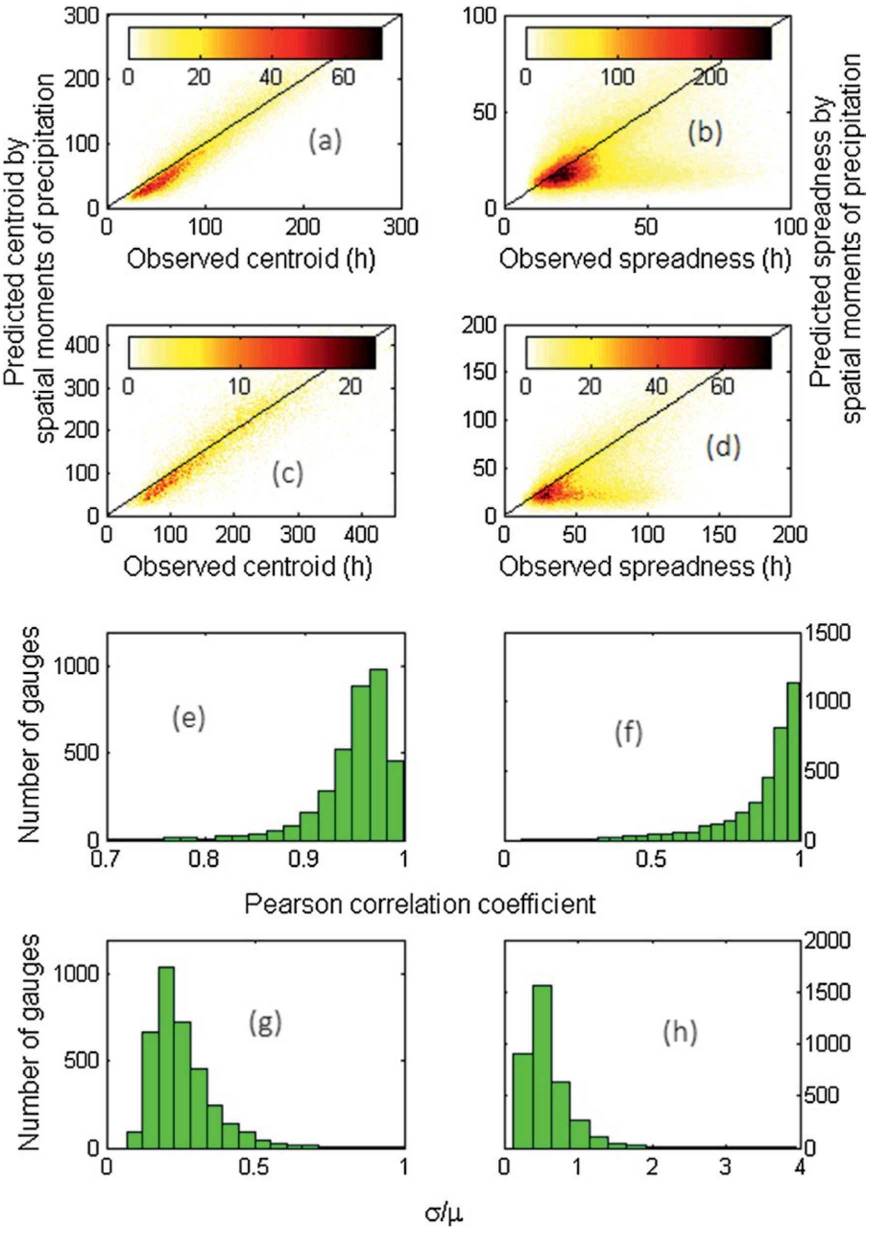

FIG. 6. Predictability of (left) centroid and (right) spreadness of flood events from spatial moments of precipitation: (a),(b) two-dimensional intensity maps (number of events) of predicted and observed flood centroid and spreadness hourly grid values in basins with drainage area below 1,000 km^2; (c),(d) as in (a),(b), but for basins with drainage area greater than 1,000 km^2; (e),(f) density plots of the Pearson correlation coefficients of predicted vs observed flood centroid and spreadness values; (g),(h) as in (e),(f), but for NRMSD.

SUMMARY. This article described a newly derived flood events database for the CONUS area. This database, containing the most flood events and descriptors, is more comprehensive than currently available flood event datasets. A unique aspect of it is the association of the flood events to the triggering precipitation characteristics. Correlation of flood event concentration time and spreadness to the precipitation spatial moments and evaluation of the initial influence of melting snow on floods consolidates the quality of the database and demonstrates its potential for supporting GIUH applications and flood vulnerability investigations, among many other studies. The article also showed the dependence of the number of flood events and flow peak values on geomorphological characteristics. The confirmation and refinement of existing dependences reveals the possibility of discovering and evaluating more elaborate and multivariant statistical relationships between flood characteristics and basin geomorphological factors.

A limitation of this database primarily comes from the use of Stage IV precipitation data available at hourly intervals and 4-km spatial resolution. Therefore, short-duration (1–4 h) and localized flood events that do not exhibit the complete set of flood characteristics defined in the CPM are not identifiable. Furthermore, the precipitation spatial moments in small watersheds (areas < 100 km^2) are less accurate owing to the spatial resolution (~16 km^2) of the precipitation dataset.

This database, which is available to the research community (http://ucwater.engr.uconn.edu/fedb/), can support a number of flood modeling and vulnerability analysis studies. We also expect it to be used jointly with distributed basin morphometric datasets (Shen et al. 2016b) to extend the skills mentioned above to ungauged basins (e.g., predicting the *a* and *b* parameters by geomorphological and geophysical features) or with infrastructure and socioeconomic datasets to assess social impacts of floods. We expect to update the database annually over the CONUS area based on newly released USGS streamflow and Stage IV precipitation records. Furthermore, extension of this database to earlier years, incorporation of finer-resolution precipitation analysis, and extension of its coverage globally based on Earth observation datasets are among our future research directions.

ACKNOWLEDGMENTS. The study was supported by the Connecticut Institute for Resilience and Climate Adaptation (CIRCA). The USGS instantaneous flow data from before October 2007 were shared by Dr. Zachery Flamig at the University of Oklahoma via http://flash.ou.edu/USGS/, and the records from after October 2007 were downloaded via http://waterdata.usgs.gov/nwis, the USGS National Water Information System (NWISWeb). The National Stage IV QPE product was downloaded via www.emc.ncep.noaa.gov/mmb/ylin/pcpanl/stage4/, hosted by the National Centers for Environmental Prediction (NCEP), NOAA. This paper was edited by Dr. Lisa Ferraro Parmelee, manager of LFP Editorial Enterprises LLC. The dataset can be downloaded from http://ucwater.engr.uconn.edu/fedb.

REFERENCES

Adhikari, P., Y. Hong, K. R. Douglas, D. B. Kirschbaum, J. Gourley, R. Adler, and G. R. Brakenridge, 2010: A digitized global flood inventory (1998–2008): Compilation and preliminary results. *Nat. Hazards*, **55**, 405–422, doi:10.1007/s11069-010-9537-2.

Apel, H., G. Aronica, H. Kreibich, and A. Thieken, 2009: Flood risk analyses—How detailed do we need to be? *Nat. Hazards*, **49**, 79–98, doi:10.1007/s11069-008-9277-8.

Calianno, M., I. Ruin, and J. J. Gourley, 2013: Supplementing flash flood reports with impact classifications. *J. Hydrol.*, **477**, 1–16, doi:10.1016/j.jhydrol.2012.09.036.

Costa, J. E., 1987: Hydraulics and basin morphometry of the largest flash floods in the conterminous United States. *J. Hydrol.*, **93**, 313–338, doi:10.1016/0022-1694(87)90102-8.

Diakakis, M., S. Mavroulis, and G. Deligiannakis, 2012: Floods in Greece, a statistical and spatial approach. *Nat. Hazards*, **62**, 485–500, doi:10.1007/s11069-012-0090-z.

Du, S., H. Gu, J. Wen, K. Chen, and A. Van Rompaey, 2015: Detecting flood variations in Shanghai over 1949–2009 with Mann-Kendall tests and a newspaper-based database. *Water*, **7**, 1808–1824, doi:10.3390/w7051808.

Gaume, E., and Coauthors, 2009: A compilation of data on European flash floods. *J. Hydrol.*, **367**, 70–78, doi:10.1016/j.jhydrol.2008.12.028.

Gourley, J. J., J. M. Erlingis, T. M. Smith, K. L. Ortega, and Y. Hong, 2010: Remote collection and analysis of witness reports on flash floods. *J. Hydrol.*, **394**, 53–62, doi:10.1016/j.jhydrol.2010.05.042.

——, and Coauthors, 2013: A unified flash flood database across the United States. *Bull. Amer. Meteor. Soc.*, **94**, 799–805, doi:10.1175/BAMS-D-12-00198.1.

Hall, J., and Coauthors, 2015: A European flood database: Facilitating comprehensive flood research beyond administrative boundaries. *Proc. Int. Assoc. Hydrol. Sci.*, **370**, 89–95, doi:10.5194/piahs-370-89-2015.

Jayakrishnan, R., R. Srinivasan, C. Santhi, and J. Arnold, 2005: Advances in the application of the SWAT model for water resources management. *Hydrol. Processes*, **19**, 749–762, doi:10.1002/hyp.5624.

Klazura, G. E., and D. A. Imy, 1993: A description of the initial set of analysis products available from the NEXRAD WSR-88D system. *Bull. Amer. Meteor. Soc.*, **74**, 1293–1311, doi:10.1175/1520-0477(1993)074<1293:ADOTIS>2.0.CO;2.

Lehner, B., K. Verdin, and A. Jarvis, 2006: HydroSHEDS technical documentation, version 1.0. U.S. World Wildlife Fund, 27 pp. [Available online at https://hydrosheds.cr.usgs.gov/HydroSHEDS_TechDoc_v10.doc.]

Mei, Y., and E. N. Anagnostou, 2015: A hydrograph separation method based on information from rainfall and runoff records. *J. Hydrol.*, **523**, 636–649, doi:10.1016/j.jhydrol.2015.01.083.

Park, D., and M. Markus, 2014: Analysis of a changing hydrologic flood regime using the Variable

Infiltration Capacity model. *J. Hydrol.*, **515**, 267–280, doi:10.1016/j.jhydrol.2014.05.004.

Rigon, R., M. Bancheri, G. Formetta, and A. de Lavenne, 2016: The geomorphological unit hydrograph from a historical-critical perspective. *Earth Surf. Processes Landforms*, **47**, 27–37, doi:10.1002/esp.3855.

Santos, M., J. Santos, and M. Fragoso, 2015: Historical damaging flood records for 1871–2011 in Northern Portugal and underlying atmospheric forcings. *J. Hydrol.*, **530**, 591–603, doi:10.1016/j.jhydrol.2015.10.011.

Shen, X., Y. Hong, K. Zhang, H. Li, and Z. Hao, 2016a: Refining a distributed linear reservoir routing method to improve performance of the CREST model. *J. Hydrol. Eng.*, **22**, doi:10.1061/(ASCE)HE.1943-5584.0001442.

——, H. J. Vergara, E. I. Nikolopoulos, E. N. Anagnostou, Y. Hong, Z. Hao, K. Zhang, and K. Mao, 2016b: GDBC: A tool for generating global-scale distributed basin morphometry. *Environ. Modell. Software*, **83**, 212–223, doi:10.1016/j.envsoft.2016.05.012.

Wu, H., J. S. Kimball, N. Mantua, and J. Stanford, 2011: Automated upscaling of river networks for macroscale hydrological modeling. *Water Resour. Res.*, **47**, W03517, doi:10.1029/2009WR008871.

Xu, Y.-G., B. He, S.-L. Chung, M. A. Menzies, and F. A. Frey, 2004: Geologic, geochemical, and geophysical consequences of plume involvement in the Emeishan flood-basalt province. *Geology*, **32**, 917–920, doi:10.1130/G20602.1.

Zoccatelli, D., M. Borga, A. Viglione, G. Chirico, and G. Blöschl, 2011: Spatial moments of catchment rainfall: Rainfall spatial organisation, basin morphology, and flood response. *Hydrol. Earth Syst. Sci.*, **15**, 3767–3783, doi:10.5194/hess-15-3767-2011.

CLIMATE OBSERVATIONS, CLIMATE MODELING, AND CLIMATE SERVICES

Chris Hewitt, Carlo Buontempo, Paula Newton, Francisco Doblas-Reyes,
Kerstin Jochumsen, and Detlef Quadfasel

Recognizing that there are significant risks and opportunities for society arising from changes in the climate, the European Climate Observations, Modeling and Services (ECOMS) initiative was formed in 2012. ECOMS has ensured close cooperation across climate-related projects in Europe and beyond, and has identified priorities for climate modeling and climate services.

ECOMS is led by three major European projects: European Provision of Regional Impacts Assessments on Seasonal and Decadal Timescales (EUPORIAS), Seasonal-to-Decadal Climate Prediction for the Improvement of European Climate Services (SPECS), and the North Atlantic Climate (NACLIM). The end of this four-year-long program was marked with an international conference. The conference presented and reviewed scientific advances, discussed what the next scientific advances will be, and made recommendations for priorities in the field of climate science for climate services for societal benefit.

AFFILIATIONS: Hewitt and Newton—Met Office, Exeter, United Kingdom; Buontempo—ECMWF, Reading, United Kingdom; Doblas-Reyes—Barcelona Supercomputing Center, Barcelona, Spain; Jochumsen and Quadfasel—University of Hamburg, Hamburg, Germany
CORRESPONDING AUTHOR: Dr. Chris Hewitt, chris.hewitt@metoffice.gov.uk

DOI:10.1175/BAMS-D-17-0012.1

In final form 12 January 2017

INTERNATIONAL CONFERENCE ON CLIMATE SCIENCE AND CLIMATE SERVICES

What:	Two hundred invited participants, including speakers and panelists from leading research institutions, international organizations, the European Commission, the Intergovernmental Panel on Climate Change (IPCC), the World Meteorological Organization (WMO), and the World Climate Research Programme (WCRP), discussed advances in climate science and climate services to benefit society.
When:	5–7 October 2016
Where:	Met Office, Exeter, United Kingdom

OVERVIEW. The conference began with overview presentations to set the scene. Several speakers stressed the importance of climate science in the Intergovernmental Panel on Climate Change (IPCC) process, and the United Nations Framework Convention on Climate Change's (UNFCCC) 2015 Paris Agreement.

Funding bodies provide significant investments for climate research, observations, and climate services. The European Commission (EC) has invested billions of euros into climate-related research. Previous EC funding programs have focused on developing excellent science, which is still recognized as essential, but current programs place more emphasis on innovation, economic growth, and harnessing knowledge to provide effective solutions. The EC, through its Copernicus program for European Earth observations, is developing a climate change service to pull through research and development to operational services giving access to information for monitoring and predicting climate change to support adaptation and mitigation. Climate science is an essential component.

The Met Office's chief scientist (conference host) discussed scientific challenges: "we know that we are taking the planet into uncharted territory and our work is not yet done." The Paris Agreement was "the end of the beginning and now the real work can start." Can scientists provide society with information about what climate variations and changes may occur, where and with what implications? Central to this is our ability to understand and predict climate extremes at sufficient resolution, and to develop the tools, based on credible high-resolution models and large ensemble simulations, for assessing the impacts and the envelope of risks.

The UN's World Meteorological Organization and the Global Framework for Climate Services (GFCS) are instrumental in coordinating actions worldwide. The GFCS is developing a Climate Services Information System to provide data and products to assist in decision-making. Of concern is sustaining observing networks and resolving large differences between observational datasets. The GFCS is undertaking pilot studies in eight countries to develop and use climate services effectively.

The IPCC comprehensively, objectively, openly, and transparently assesses the scientific and technical information. Scientific challenges for their next (Sixth) Assessment Report include assessing past and future regional changes, particularly for extreme events, such as droughts and trends in Arctic sea ice, and improving near-term predictions on multiannual time scales.

The World Climate Research Programme (WCRP) aims to determine the predictability of climate and the effects of human activities on climate. The Paris Agreement was reached in large part because of the knowledge provided by the scientific community. The focus of research now must evolve from "making the case" for anthropogenic climate change to the development and dissemination of regional information to minimize risks and build resilience. A smart end-to-end information system is needed that integrates knowledge from different disciplines to provide climate services to meet societal needs.

OCEAN OBSERVATIONS. Ocean observations in NACLIM (www.naclim.eu) focused on the North Atlantic Ocean, which is one of the most important drivers for global ocean circulation and its variability on time scales beyond the interannual. Global climate variability is, to a large extent, triggered by changes in the North Atlantic sea surface state. By monitoring relevant ocean parameters, such as sea surface temperature, sea ice distributions, and heat fluxes, the observational program in NACLIM provided a reference basis for numerical models for climate predictions and economic impact studies.

Key results presented included a new climate record of Arctic and Antarctic ice surface temperatures, covering high-latitude seas, sea ice, and ice cap surface temperatures based on satellite infrared measurements. Additionally, ocean volume flux time series were extended and are now able to address interannual variability. Flux correction in coarse-resolution climate models was found to be valuable for reducing the model biases, and initializing models with the upper Arctic stratification was identified as being essential for the predictive skill of models regarding both the freshwater storage and sea ice volume. Simulating these two parameters is important for realistically stratifying the North Atlantic Ocean.

CLIMATE PREDICTIONS. This discussion focused on the SPECS project (www.specs-fp7.eu) and collaborations between scientists during SPECS and EUPORIAS. The collaboration usefully illustrated the scientific challenges posed by the development of climate services.

A large number of climate model experiments and analyses of climate data have been undertaken and are available via the public SPECS data repository as part of the Earth System Grid Federation (ESGF), through numerous scientific publications, and as factsheets on the SPECS website. The factsheets provide entry-level information about the technical and scientific aspects of climate prediction, something previously lacking. They were driven by questions raised by the EUPORIAS partners and users and will be built upon by some WCRP initiatives. The climate prediction experiments showed that climate prediction is both an initial-value and a boundary-forced problem, and stronger links should be built between the climate prediction, weather forecasting, and climate change communities. The experiments suggested that observational uncertainty should be taken into account in a more formal way.

The importance of process-based forecast quality assessments was shown, along with examples that used climate extremes in sea ice extent, ocean thermodynamics, and land surface variables. These cases demonstrated that no single forecast system is perfect. Instead, forecast systems are complementary in representing climate phenomena differently. Multisystem predictions, including dynamical and statistical–empirical systems, are needed to provide reliable and accurate climate information. Traceable postprocessing that includes downscaling and bias adjustment is fundamental to maximizing the benefits of forecast information. However, postprocessing cannot replace the benefits produced by improving the models and forecast systems to address problems like forecast initial shock and drift.

Central to SPECS has been the public release of information and solutions. While the data produced are publicly available using a standard created by the SPECS project, a range of functions has been created and provided using the open-source language R, along with associated training.

CLIMATE SERVICES. Presentations and discussions about climate services, particularly from the EUPORIAS project (www.euporias.eu), emphasized the importance of close engagement between the developers of a climate service and the intended users, ideally to "coproduce" the service. An extensive analysis of users in Europe has been conducted by the EUPORIAS project, including 80 in-depth interviews and an online survey. The analysis highlighted some of the perceived barriers to the use of climate predictions in Europe, such as the reliability and accuracy of the forecasts, usable information, relevance, and accessibility of the information.

The importance of regional information in climate impact studies was discussed. An example shown was in the Alps, where the climate change trend from global model projections is the opposite of that found in regional model projections. Downscaling global seasonal predictions to finer spatial resolution using a dynamical climate model for a region covering the Great Horn of Africa was also shown. Although the large-scale signal was not deteriorated by the downscaling, there is no evidence that the downscaling had a positive impact on the skill of the predictions for this region.

Tools to analyze, postprocess, bias correct, and downscale climate prediction data have been developed and discussions emphasized that having good and open access to data and tools is a prerequisite for the development of an effective climate service community.

Climate impact modeling was discussed, with examples shown for hydrological models simulating seasonal river flow in Europe (often with more skill than the skill shown for precipitation in Europe), and variations in crop yields and river flows under a changing climate.

The session finished with a discussion of the challenges of presenting the confidence level associated with climate predictions. Users appear to prefer graphical representations that they are familiar with even when the objective understanding, as measured in a decision laboratory experiment, is lower than for other kinds of representations.

FORWARD LOOK. Major scientific developments have been made, including developing and delivering useful services based on the science, but there is still a long way to go. The conference identified gaps in knowledge and highlighted several potential priorities categorized below as observations, resolution, predictions, and user engagement. The conference noted that the move toward developing climate services for societal benefit must not be at the expense of the development of the underlying science that underpins such services.

Observations. There is continued need to improve observational records and ensure that observational activities are sustained, with benefits for evaluating models, assessing baselines, and monitoring the climate. The conference highlighted significant differences between observational datasets, with some datasets not capturing variability well.

Resolution. Global climate model resolution needs to be increased dramatically to reduce biases in models and to understand and predict climate extremes. This requires new forms of collaboration in the community, and the software, tools, and hardware necessary to support this also need to be developed. Much higher computing power is required, along with a substantially larger base of technical specialists to develop better models capturing the processes and resolution sufficiently.

Predictions. Predictions of the climate for the coming months and years have enormous potential for assisting a wide range of decision-makers. While forecasts for the coming weeks and seasons are operational, the multiannual time scale is largely a research activity. There is an urgent need to better understand users' needs, and to develop and disseminate the forecasts to address such needs. Case studies demonstrating benefits would facilitate progress. However, assessing the value of climate services is complicated, often because decisions are rarely based solely on climate information. There are challenges in communicating uncertainty, but users should be aware that forecasts are probabilistic and that the reliability of those probabilities should be verified. Failing to properly communicate the uncertainty can have consequences, as a false sense of certainty can lead to maladaptive decision-making and a loss of trust in forecast providers.

User engagement. The services are often inadequate for users' decisions. The underpinning scientific capability and knowledge should not be oversold (nor undersold) and strengths and limitations must be articulated. Many users struggle to understand or use climate model output. Reasons include technical challenges, data formats, irrelevant variables, inadequate uncertainty estimations, and errors in the data; so how can climate predictions be more useful and useable for users? Multidisciplinary teams will help, along with improvements to information systems, improvements to engagement with users, and developing the capacities and capabilities of both the providers and the users. Good communicators and translators are needed to bridge from the science through the services to better inform decisions, but also to feed back the user requirements to the scientists to develop different models and forecasts. Strong collaborations are now starting to develop between researchers, service providers, and end users, and these efforts have the potential to be highly beneficial to both the climate science community and society at large.

The above priorities, and other outcomes, from the conference will be taken forward in a larger follow-on to ECOMS. Called Climateurope (www.climateurope.eu), this activity is creating a managed network that includes climate science communities, funding bodies, providers, and users to coordinate and support the knowledge base (primarily in Europe, but extending globally as far as possible) and to enable better management of climate-related risks and opportunities.

ACKNOWLEDGMENTS. The EUPORIAS, SPECS, and NACLIM projects were funded by the Seventh Framework Programme of the European Commission (GA308291, GA308378, and GA308299, respectively) and supported this conference. We thank Natalie Garrett, Guillaume Gastineau, Joe Daron, Mar Rodriguez, Jane Strachan, Michel Déqué, and Tim Stockdale, who took notes during the conference that have been useful reminders for writing this account. We thank Bernd Eggen, Helen Fox, Nicola Golding, Sarah Gooding, Chenbo Guo, Nick Hopkins, Alison Lee, Felicity Liggins, and Mathew Menary who helped organize the conference.

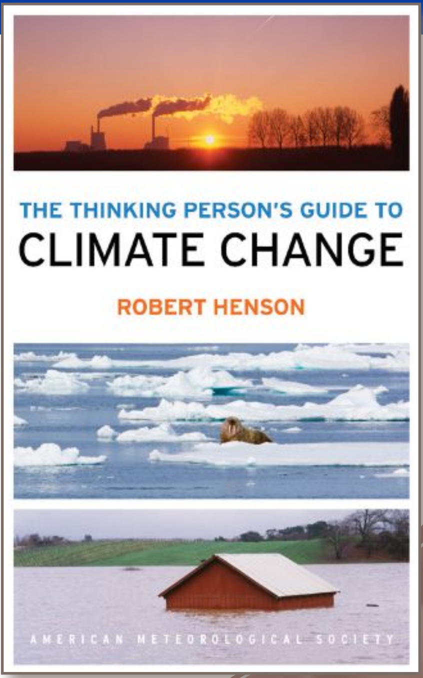

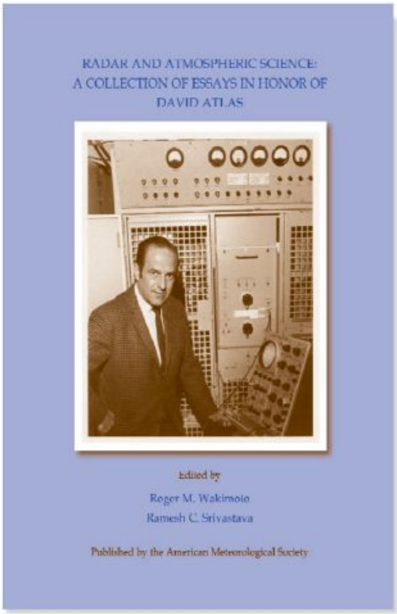

RADAR AND ATMOSPHERIC SCIENCE:
A COLLECTION OF ESSAYS IN HONOR OF
DAVID ATLAS

Edited by

Roger M. Wakimoto
Ramesh C. Srivastava

Published by the American Meteorological Society

AMS BOOKS

RESEARCH ◆ APPLICATIONS ◆ HISTORY

AMS MEMBERS GET FREE

CLIMATE

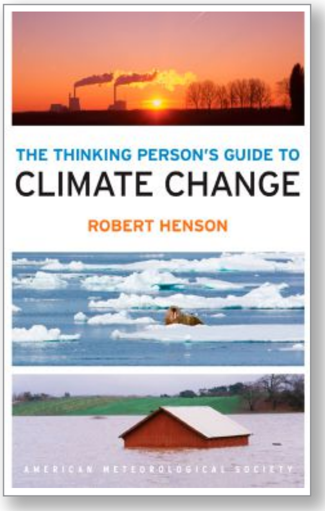

The Thinking Person's Guide to Climate Change

ROBERT HENSON

This fully updated and expanded revision of The *Rough Guide to Climate Change* combines years of data with recent research. It is the most comprehensive overview of climate science, acknowledging controversies but standing strong in its stance that the climate is changing—and something needs to be done.

© 2014, PAPERBACK, 520 PAGES,
ISBN: 978-1-935704-73-7
LIST $30 MEMBER $20

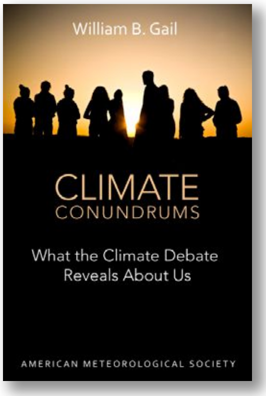

Climate Conundrums:

What the Climate Debate Reveals about Us

WILLIAM B. GAIL

This is a journey through how we think, individually and collectively, about humanity's relationship with nature, and more. Can we make nature better? Could science and religion reconcile? Gail's insights on such issues help us better understand who we are and find a way forward.

© 2014, PAPERBACK, 240 PAGES,
ISBN: 978-1-935704-74-4 LIST $30 MEMBER $20

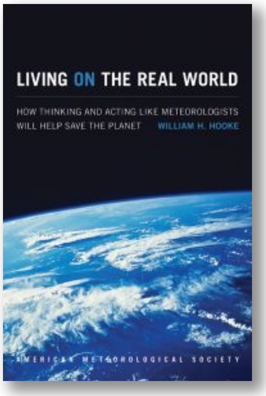

Living on the Real World:

How Thinking and Acting Like Meteorologists Will Help Save the Planet

WILLIAM H. HOOKE

Meteorologists focus on small bits of information while using frequent collaboration to make decisions. With climate change a reality, William H. Hooke suggests we look to the way meteorologists operate as a model for how we can solve the 21st century's most urgent environmental problems.

© 2014, PAPERBACK, 272 PAGES, ISBN 978-1-935704-56-0 LIST $30 MEMBER $22

GUIDES

An Observer's Guide to Clouds and Weather:

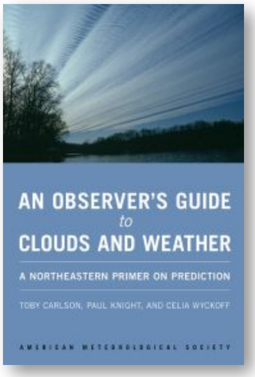

A Northeastern Primer on Prediction

TOBY CARLSON, PAUL KNIGHT, AND CELIA WYCKOFF

With help from Penn State experts, start at the beginning and go deep. This primer, intended for both serious enthusiasts and new meteorology students, will leave you with both refined observation skills and an understanding of the complex science behind the weather: the ingredients for making reliable predictions of your own. It connects fundamental meteorological concepts with the processes that shape weather patterns, and will make an expert of any dedicated reader.

© 2014, PAPERBACK, 210 PAGES,
ISBN: 978-1-935704-58-4 LIST $30 MEMBER $20

Eloquent Science:

A Practical Guide to Becoming a Better Writer, Speaker, and Atmospheric Scientist

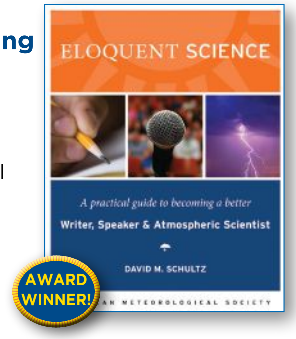

DAVID M. SCHULTZ

The ultimate communications manual for undergraduate and graduate students as well as researchers in the atmospheric sciences and their intersecting disciplines.

© 2009, PAPERBACK, 440 PAGES,
ISBN 978-1-878220-91-2

LIST $45 MEMBER $30

TEXTBOOK

Midlatitude Synoptic Meteorology:

Dynamics, Analysis, and Forecasting

GARY LACKMANN

This textbook links theoretical concepts to modern technology, facilitating meaningful application of concepts, theories, and techniques using real data.

©2011, PAPERBACK, 360 PAGES,
ISBN 978-1-878220-10-3
LIST $100 MEMBER $75 STUDENT MEMB. $65

Midlatitude Synoptic Meteorology Teaching CD

More than 1,000 PowerPoint Slides.

© 2013, CD, ISBN 978-1-878220-27-1 LIST $100 MEMBER $75

To order: bookstore.ametsoc.org, 617-226-3998, or use the order form in this magazine

SHIPPING + DISCOUNTS AT BOOKSTORE.AMETSOC.ORG

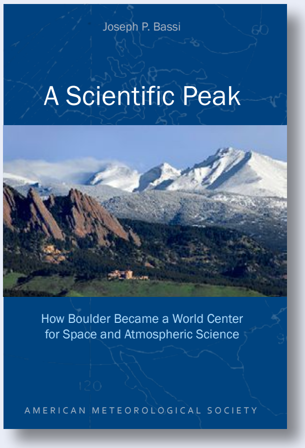

A Scientific Peak:

How Boulder Became a World Center for Space and Atmospheric Science

JOSEPH P. BASSI

How did big science come to Boulder, Colorado? Joe Bassi introduces us to the characters, including Harvard sun–Earth researcher Walter Orr Roberts, and the unexpected brew of politics, passion, and sheer luck that during the Cold War era transformed this "Scientific Siberia" to home of NCAR and NOAA.

© 2015, PAPERBACK, 264 PAGES, ISBN: 978-1-935704-85-0
LIST PRICE: $35.00 **MEMBER PRICE: $25.00**

METEOROLOGICAL MONOGRAPH SERIES

AMS Meteorological Monographs Vols. 1–55 (1947–2010) are available via Springer at springer.com/ams, with select volumes available in print via AMS at bookstore.ametsoc.org. Starting in 2016 with Vol. 56, new monographs will be open access, available via the AMS Journals Online site.

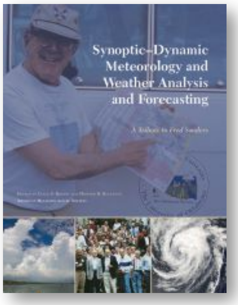

Synoptic–Dynamic Meteorology and Weather Analysis and Forecasting:

A Tribute to Fred Sanders

EDITED BY LANCE F. BOSART AND HOWARD B. BLUESTEIN

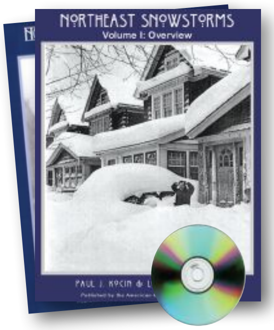

Northeast Snowstorms

(Volume I: Overview, Volume II: The Cases)

PAUL J. KOCIN AND LOUIS W. UCCELLINI

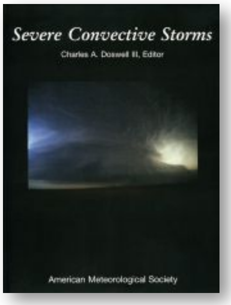

Severe Convective Storms

EDITED BY CHARLES A. DOSWELL III

Booksellers, groups, or for examination copies:
The University of Chicago Press:
1-800-621-2736 (US & Canada)
773-702-7000 (all others)
custserv@press.uchicago.edu

HISTORY

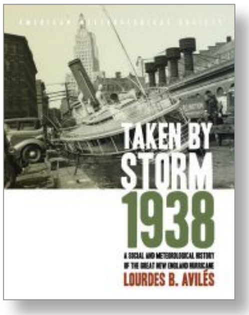

Taken by Storm, 1938:

A Social and Meteorological History of the Great New England Hurricane

LOURDES B. AVILÉS

The science behind the 1938 Hurricane, which hit New England unannounced, is presented here for the first time along with new data that sheds light on the motivations of the Weather Bureau forecasters. This compelling history successfully weaves science, historical accounts, and social analyses to create a comprehensive picture of the most powerful and devastating hurricane to hit New England to date.

© 2013, HARDCOVER, 288 PAGES, ISBN: 978-1-878220-37-0
LIST $40 **MEMBER $30**

Father Benito Viñes:

The 19th-Century Life and Contributions of a Cuban Hurricane Observer and Scientist

LUIS E. RAMOS GUADALUPE
TRANSLATED BY OSWALDO GARCIA

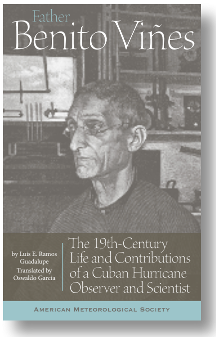

Before Doppler radar and weather broadcasts, Spanish Jesuit Benito Viñes (1837–1893) spent decades observing the skies at Belen Observatory in colonial Cuba. Nicknamed "the Hurricane Priest," Viñes taught the public about the weather and developed the first network of weather observation stations in the Caribbean, groundwork for the hurricane warning systems we use today.

© 2014, PAPERBACK, 172 PAGES
ISBN: 978-1-935704-62-1 **LIST $20** **MEMBER $16**

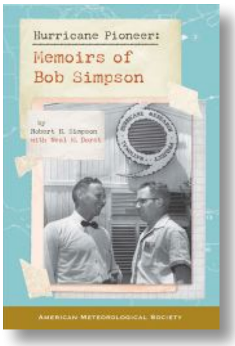

Hurricane Pioneer:

Memoirs of Bob Simpson

ROBERT H. SIMPSON AND NEAL DORST

In 1951, Bob Simpson rode a plane into a hurricane—just one of the many pioneering exploits you'll find in these memoirs. Bob and his wife Joanne are meteorological icons: Bob was the first director of the National Hurricane Research Project and a director of the National Hurricane Center. He helped to create the Saffir–Simpson Hurricane Scale; the public knows well his Categories 1–5. Proceeds from this book help support the AMS's K. Vic Ooyama Scholarship Fund.

© 2015, PAPERBACK, 156 PAGES
ISBN: 978-1-935704-75-1 **LIST $25** **MEMBER $20**

LOOKING FOR AN EXPERT?

LOOK TO AMS!

AMS announces the launch of our new online directory of **Weather and Climate Service Providers.**

This new online directory replaces the former BAMS Professional Directory and lists an array of weather and climate service providers. You can find the new directory under the **“Find an Expert”** link from the AMS home page.

It’s easier than ever for the weather, water, and climate community and the general public to search for organizations and individuals offering these important services.

Learn more at www.ametsoc.org

NEW!

Weather & Climate Service Providers Directory

AMERICAN METEOROLOGICAL SOCIETY 1919

AMS

American Meteorological Society

www.ametsoc.org

45 BEACON

LETTER FROM HEADQUARTERS

CONTRIBUTORS

I was looking recently at the annual reports from several other scientific societies. I always enjoy seeing how those organizations choose to summarize a year's worth of activities and accomplishments into just a few colorful and engaging pages. AMS creates its own annual report, of course, with the same goal of letting people see the impressive range of initiatives and their success over the past year. The 2016 Annual Report is available on the AMS website (along with the reports from prior years) at www.ametsoc.org/ams/index.cfm/about-ams/ams-annual-reports/.

As I was coming to the end of one of the reports from a related scientific society, I suddenly realized that nearly all of them shared a common feature that is not reproduced in the AMS annual report—a list of people who have made financial contributions to their society in the past year. AMS has traditionally included the list of contributors in the Secretary–Treasurer's Report that is published in *BAMS* each year. This practice predates the separate AMS Annual Report, providing a nice level of continuity over many years. It is an impressive list each year, and those financial donations are truly critical to the success of many programs carried out by the Society.

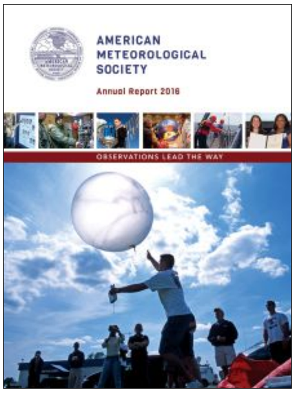

While the AMS Annual Report is nearly unique by not including the list of those financial donors, perhaps its most striking feature is one that I have seen in no other society's annual report—a listing of all the volunteers who served the Society over the course of the past year. Even using small type, this listing dominates the AMS Annual Report each year, accounting for more than half the pages. This list represents those of you who contribute your time and talent to AMS, and without those incredibly generous contributions, very little of the Society's work would get done.

I encourage you to go to the AMS Annual Report and at least scan the listing of well over a thousand volunteers who contributed to the success of AMS last year. And if you are not on that list, consider volunteering in some way in the future so that you, too, can be a contributor to that success. The "Get Involved" link at the top of every web page provides more information on how to become more active in the Society.

Keith L. Seitter, CCM
Executive Director

Water and the Coasts: Opportunity, Vulnerability, and Risk Management

[Editor's note: This column and AMS Policy Program memo is adapted from an AMS Policy Program study of the same name. The full study is available at www.ametsoc.org/studies*.]*

Water is simultaneously a resource and a threat. It is centrally important to every aspect of socioeconomic well-being, and water becomes a hazard when there is too much, too little, or if the quality is poor. The opportunities and challenges posed by water are especially acute at the coasts, which are both major resources and often highly vulnerable to extreme events. Coastal communities are also particularly sensitive to changes in land use, population distributions, and climate.

A recent AMS Policy Program study on water and the coasts identified seven ways to advance coastal risk management: 1) provide actionable information; 2) prepare and empower information users; 3) create decision support products and services that harness scientific advances for societal benefit; 4) build strong partnerships among stakeholders, practitioners, and information providers; 5) develop the next generation workforce; 6) align roles and responsibilities; and 7) recognize linkages and potential leverage.

PROVIDE ACTIONABLE INFORMATION (OBSERVATIONS, SCIENCE, AND FORECASTS). Observational infrastructure; science (research, data assimilation, and models); and computational capabilities determine the accuracy of weather and water forecasts and provide the foundational information needed for risk management. Forecasts of water quantity and quality are most useful when they account for all sources of water (e.g., precipitation, tides, waves, sea level, and storm surge) and factors that affect water's behavior (e.g., land use and infrastructure).

Efforts to fill in observational gaps near the coasts and to improve the interoperability of different modeling approaches (e.g., river forecast, wave, ice, estuarine hydrodynamic, and storm surge models) have great potential to improve informational resources. Greater understanding of the linkages among the physical climate system, biological resources, and socioeconomic well-being would facilitate decision making and is possible through improved integration of physical, natural, and social sciences.

PREPARE AND EMPOWER INFORMATION USERS. When equipped to use information effectively, stakeholders, emergency managers, policymakers, the media, and the public make better decisions. We recognize coastal vulnerabilities, effectively weigh options for risk management, and know how to respond when confronting hazards. However, influxes of people and turnover among coastal populations ensure that efforts to prepare and empower information users must be ongoing. Similarly, long periods of time between high-impact events lead to complacency and require strategies for ensuring that people know how to respond when hazards arise.

Formal education (pre-K through college and graduate training) and informal outreach to groups and individuals can help communities take up and use information effectively. These efforts will be most useful when grounded in insights from social sciences, particularly research on how to engage effectively (e.g., with stakeholders, emergency managers and other practitioners, information users, policymakers, the media, and the public) and to enhance risk communication.

CREATE SERVICES & DECISION SUPPORT PRODUCTS THAT HARNESS SCIENTIFIC ADVANCES FOR SOCIETAL BENEFIT. Products and services that are accessible and tailored to specific user needs are easier to integrate into risk management decisions. Big data and data analytics offer new opportunities to create decision support products and enhanced risk management services. Data accessibility and ease-of-use among information providers and users improves the uptake and use of information.

BUILD STRONG PARTNERSHIPS AMONG INFORMATION PROVIDERS, USERS, AND STAKEHOLDERS. There is a need for strong, sustained networks of connected partners working together across federal agencies and among local, regional, and federal organizations and stakeholders. Institutionalizing key relationships can overcome the risk of turnover within agencies and among experts and service providers. Efforts to manage risks and water resources have the best chance of success when stakeholders understand differing perspectives and work to identify shared values that can be advanced together.

DEVELOP THE NEXT GENERATION WORKFORCE. Improving risk management over time will depend on providing scientists and practitioners with the knowledge, skills, and abilities (KSAs) needed most. Expertise in probabilistic modeling; stakeholder engagement; risk communication; integrated risk assessment; data analytics; and the integration of the physical, natural, and social sciences, among other KSAs, are likely to be particularly useful in the future.

ALIGN ROLES AND RESPONSIBILITIES. Conflicts arise among users who are separated across local, state, and federal jurisdictions. Suboptimal allocations of resources can occur when decision-making responsibilities are narrowly focused, and efforts to deal with a problem at one scale can create new problems at other locations or scales. This creates a need for aligning responsibilities and jurisdictions, and setting the appropriate spatial scales for management. Regional and national coordination is needed for issues that exceed local jurisdictions.

Federal roles with respect to water resource management may include setting of standards; identifying best practices; providing a repository of case studies and/or lessons learned; helping to ensure and enhance public goods; regulation; and the provision of resources to local and regional efforts. Federal efforts that apply to diverse local communities have greater chance of widespread adoption and success.

Determining public, private, and academic roles; adapting those roles as needs and capabilities shift over time; and facilitating collaboration among the public, private, and academic sectors will be critical for enhancing risk assessment and management efforts.

RECOGNIZE LINKAGES AND POTENTIAL LEVERAGE. Efforts to address coastal vulnerabilities can, at times, contribute to other priorities. Coastal risk management projects that achieve multiple goals may be more appealing to local communities and policymakers. For example, green infrastructure to mitigate coastal flooding may also provide fisheries habitat and recreational assets. The United States can both learn from other countries and share our resources and information with other countries (e.g., identify common needs, case studies, and lessons learned).

—PAUL HIGGINS, AMS POLICY PROGRAM DIRECTOR

ABOUT OUR MEMBERS

Doug Hill, chief meteorologist at WJLA ABC7 in Washington, D.C., will be retiring in September after 33 years on the air. Hill came to Washington in 1984 and was a meteorologist for the CBS affiliate WUSA Channel 9 for 16 years. He worked alongside D.C. weather broadcasters Gordon Barnes and Topper Shutt, now the chief meteorologist at WUSA.

In 2000, Hill moved from WUSA to WJLA to become its chief meteorologist. During his tenure, WJLA's weather team expanded to eight meteorologists, broadcasting weather segments not only on Channel 7 but also on News Channel 8 and, for several years, on the radio station WTOP.

Hill's career path to weather broadcasting was unconventional. After attending Towson University, he joined the U.S. Air Force and then became a patrol and public information officer in the Prince George's County Police Department for six years. He was good on television, and was encouraged to apply for TV broadcasting jobs.

After his first job as a weathercaster in Richmond, he spent four-and-a-half years in Detroit before coming to Washington. Once he retires, Hill said, he plans to devote his energy to his family and church. As of mid-May, Hill's successor had not yet been named.

DONALD RAY JOHNSON
1930–2017

Donald Ray Johnson—atmospheric scientist, educator, and mentor to scores of students and scientists of all ages—died on April 13, 2017. Don will be remembered for his passion for science and education, his commitment to his students, and his devotion to his family.

Don was born on April 1, 1930 in McPherson, Kansas, in a hospital about 25 miles from his parents' farm near Inman, Kansas. His parents, Anton Rudolf Johnson and Ethel Marie (Bergstrom) Johnson, operated a 160-acre farm. As a child, Don enjoyed taking care of the animals and helping his parents with the many farm chores. One of his earliest memories on the farm was fishing with his grandfather, Isaac Bergstrom, who lived with them. According to Don in a 2007 interview with Steve Erickson, "He spoiled me. He would do the dishes and, of course, in the summertime he loved to fish. He was too old to work on the farm, so we would walk down to the river about a half a mile away in the afternoon two or three times a week to fish. Then we would come home, clean the fish, and have fish for breakfast."

By the age of 14, Don could work and drive a tractor as well as anybody. At that time there was a high demand for hired farm help because of labor shortages during World War II. So at 14 and 15, Don drove a John Deere tractor to plow fields and pull a combine to harvest wheat. He spent 10–14 hours a day working during the summer and fall except on Sunday or rainy days. Every morning he started milking the cows by hand at 5:30 a.m. in order to leave for high school by 7:30.

The Johnson family farmed with horses until 1940, when Don was 10 and they got their first tractor. Don learned to ride bareback and occasionally helped neighbors to drive a herd of cattle 12 miles from the winter feed lots to summer pastures. When he was 12, his father fixed up a buggy that had been stored in the barn so that Don was able to travel the countryside by buggy or by horseback. Don's experiences on the Kansas farm were authentic and rich as he became an accomplished farmhand and rancher. He could have easily taken over the farm from his father.

But Don had another dream: to become a scientist, and especially a teacher. From his earliest days, education was extremely important to Don, and he credits his parents for his love of teaching. In his 2007 interview, he stated, "Since my parents only were able to complete grade school with no opportunities for high school, the guiding principle of my parents was to acquire all the education for which one has opportunities. I was probably meant to be a teacher along the way."

Don's formal education started with Alpha Grade School, District 39, which was a half-mile from his home. When he started first grade in 1936, Alpha was a one-room country school with just over 20 pupils. After finishing his own work, he would eavesdrop on the older students as they learned their more advanced lessons. In a sign of things to come, Don graduated from eighth grade in 1944 with the highest score on the final countywide exam of all the 300 students in McPherson County.

Although he was generally private about it, religion was also an important factor in Don's and his family's lives. His early childhood church was the New Andover Lutheran Church about two miles away from the farm, where he was buried with full military honors on April 22, 2017. His religion and family teaching resulted in a strong sense of ethics and values that served as a sturdy foundation for Don's entire personal and professional lives.

Don went to Inman Rural High School, commuting about 11 miles on muddy or gravel roads in a Model A Ford, usually with four or five neighbor's children. He did well in all his classes and especially liked math and science. When he was a senior, a neighboring school board asked him to teach at one of the nearby country schools as soon as he finished high school. But Don was determined to continue his education, and in 1948 he began his studies at Bethany Lutheran College in Lindsborg, Kansas, with the help of a tuition scholarship.

It was here, under the wise tutelage of mathematics teacher Anna Marm, that he fell in love with mathematics. In his 2007 interview, Don noted that Professor Marm would say, "If you learn your mathematics, you can do anything you want to do." Don also majored in chemistry and minored in physics and education. Because of poor crops on the farm during his junior and senior year, Don worked 25 hours a week at a local filling station in order to support himself and finish college.

By 1950, the Korean War was raging. Don had a deferment from the draft to go to Kansas State, where he had been admitted for graduate studies in chemistry. But one day near the end of his senior year, Marm handed him a notice from the air force about a meteorology program at the University of Washington. Don applied, was accepted, and received a direct commission as a second lieutenant in the air force, and started his meteorology education after his graduation from Bethany College in 1952 with a B.S. degree in mathematics. In early September, Don entered active duty in the Air Force Reserves at Camp Attebury, Indiana. Shortly afterward he moved to the University of Washington, where he received a B.S. in meteorology a year later.

In August 1952, Don met Dorothea Marie Christiansen through mutual friends at an exhibition game of the New York Giants football team in St. Peter, Minnesota. A year later, on August 26, 1953, they married at Bethesda Lutheran Church in South St. Paul, Minnesota.

Donald Ray Johnson with his wife, Dorothea.

Immediately after they were married, the air force assigned Don to Germany, and they spent the following three years in Europe, at Sembach Air Force Base in Germany and Chambley Air Force Base in France. Don was now a meteorologist, getting valuable practical experience in weather analysis and forecasting, briefing military pilots before they took off from the base.

Don and Dorothea enjoyed Europe and visited most of the western European countries while there. Travel was rewarding to Don, and until he became ill late in his life, he traveled extensively. He reached every continent except Antarctica, including multiple visits to China, Australia, Europe, Mexico, Brazil, Argentina, and Uruguay—all for meetings, collaborations, and interactions with scientists.

After their stay in Europe, Don and Dorothea moved to Oklahoma in 1957 and Don spent two years as a forecaster at Tinker Air Force Base. In 1959, he applied to graduate school at the University of Wisconsin, Madison, and was accepted. Thus Don left active military service at age 29. He was proud of his military service and credited his experiences with learning how to deal with people as well as developing a strong appreciation for the practical side of atmospheric sciences.

Don studied under Lyle Horn at Wisconsin and received in Ph.D. in meteorology in 1965. His Ph.D. research was flying a net radiometer on a radiosonde to measure the net infrared radiation at night. He was appointed assistant professor at Wisconsin in 1964 and full professor in 1970. From 1977 to 1999 he served as associate director of the Space Science and Engineering Center at Wisconsin, working closely during this time with the "father of satellite meteorology," Professor and Director Vern Suomi (1915–1995). After he retired from teaching in 1994, Don was honored with the title of emeritus professor.

In the academic year 1968–69, Don visited the Department of Meteorology at Penn State University, where he worked with his friend and colleague John Dutton on the theory of available potential energy in the framework of isentropic coordinates. From the time of publication of their seminal monograph, *The Theory of Available Potential Energy and a Variational Approach to Atmospheric Energetics*, Don and isentropic coordinates became synonymous in the minds of many.

But his work was much more than simply using isentropic coordinates in analyses and numerical models. His research was elegant in the sense that it was based on a thorough understanding of classical mathematics, physics, and thermodynamics, following such great scientists as George Hadley (1685–1768), William Ferrel (1817–1891), Sir Napier Shaw (1854–1945), Constantin Carathéodory (1873–1950), Eric Eady (1915–1966), Edward Lorenz (1917–2008), and others. His vision of the atmosphere as a four-dimensional system constantly striving to reach equilibrium in the presence of ever-changing radiational heating and cooling in an isentropic framework was revolutionary and created a new way of thinking about Earth's atmosphere.

In the late 1960s and early 1970s, Don and John Dutton developed exact equations for the available potential energy of Earth's atmosphere, extending the work of Lorenz and others who used approximate equations in isobaric coordinates. In his later work, Don used exact forms of the entropy and angular momentum equations to describe the structure and evolution of global and synoptic-scale circulation patterns while ensuring strict conservation principles. The isentropic framework pervades much of Don's work throughout his career because this quasi-Lagrangian coordinate system enables unique mathematical and physical insights. Furthermore, use of isentropic coordinates in numerical models enables simulation and prediction of adiabatic flows and transports with little or no numerical truncation errors. He also applied these theoretical approaches and related entropy, energy, and angular momentum conservation principles to the First Global Atmospheric Research Project (GARP) Global Experiment (FGGE) and Global Weather Experiment (GWE) data to describe the equator-to-polar extent of the Hadley circulation and embedded Ferrel cells. These studies have provided a holistic view of the general circulation that is dynamically and energetically consistent. His 1989 monograph, *The Forcing and Maintenance of Global Monsoonal Circulations: An Isentropic Analysis*, was a masterpiece, showing how isentropic coordinates simply and elegantly revealed the patterns of summer and winter monsoonal flows.

Don also made seminal contributions to the development and understanding of climate models. His 1997 *Journal of Climate* article "General coldness of climate models and the second law: Implications for modeling the Earth system," shows why almost all climate models exhibit a cold bias. His analysis described how the nonconservation of energy that should be conserved under adiabatic flow leads to artificial sources and sinks, which in turn lead to cold biases in climate models based on sigma, pressure, and height coordinates. This paper is just one of many that illustrates Don's scholarship and rigor in pursuing deep understanding of, and mathematical basis for, atmospheric behavior.

Don, his students, and research group also developed creative and unique models of climate, fronts, jet streaks, and cyclones. He developed novel diagnostic and verification techniques that reveal how well models conserve quantities, such as equivalent potential temperature (moist entropy), and thus provide metrics to quantitatively assess the models' ability to correctly simulate reversible thermodynamic flows. Under Don's leadership, his Wisconsin research group developed an innovative global climate model in hybrid isentropic–sigma coordinates, a model that shows much better conservation features of moist entropy, energy, potential vorticity, and chemical constituents than other models. Working closely with National Centers for Environmental Prediction (NCEP) and other NOAA scientists, he transferred these capabilities to the development of operational and research numerical models run today by the National Weather Service and NOAA's Earth System Research Laboratory in Boulder, Colorado.

Don was passionate about his work and could launch into a full lecture, without notes, at a moment's notice at any time and any place. A typical example from his many lectures of this type is the following excerpt from his speech at the AMS symposium in his honor (*Professor Donald R. Johnson—A Named Symposium of the American Meteorological Society: Atlanta, February 2014*. The Penny University Press, 131 pp.):

> In the tropics, all quasi-horizontal motion realized from thermodynamic forcing is synonymous with ageostrophic motion because the geostrophic adjustment time scale is essentially infinite relative to the diurnal heating by solar radiation and moist convection. Thus in the absence of a quasi-static geostrophic mode of mass transport, the meridional and ascending branches of the isentropic and isobaric zonally-averaged mass transport, as determined in their respective coordinate systems, are essentially equivalent in the sense that no distinction develops, since the ageostrophic transport constitutes the total transport. However in polar and extratropical latitudes where the geostrophic adjustment time scale is on the order of several hours and substantially less than the diurnal cycle and, even more significantly, much less than the life time of the coupled poleward and equatorward meridional mass transport within cyclonic/anticyclonic circulations of several days to a week, geostrophy with cyclonic curvature and gradient balance prevails as the primary mode for the mass circulation as well as the transport of atmospheric properties.

Don was unusual in that he made major contributions to three broad areas of atmospheric science. He was a world-class scientist in the strict academic sense, publishing more than 85 journal papers, six book chapters, and two monographs. He contributed much to the community he loved through service and leadership activities in scientific societies and university consortia. He served as president of AMS in 1992 and was awarded the Charles Franklin Brooks Award in 1998 and the AMS Teaching Excellence Award in 2005. He was made an Honorary Member of AMS in 2016. Don was a Fellow of AMS and the American Association for the Advancement of Science, and was a member of the UCAR Board of Trustees from 1991 to 1997. He served as chief scientist for NCEP from 2001 to 2005, where he worked with operationally oriented scientists on problems of global numerical weather prediction.

But he placed an equal, or even greater, weight on education and mentoring, guiding 26 Ph.D. graduates and 31 M.S. graduates. Don was an excellent writer and a formidable editor. None of his students escaped page after page of red ink as Don carefully read each draft of their theses. His writing was sharp, clear, accurate, and precise, and he expected his students to write in the same unambiguous ways. Yet his criticism was always kind and constructive, and after the initial shock at all the crimson, we learned to welcome his insightful editing. As Steven Silberberg wrote, "What made him superlative as our mentor was how he blended his talents with his students to subtly and profoundly develop each student's ability in a way that inspired us to reach a level far beyond what we thought we were capable of."

Don was awarded the AMS 2005 Teaching Excellence Award in large part because of the impact he had on his students, many who then became leaders within the research, academic, and operational communities.

As director of the Division of Earth Sciences, Universities Space Research Association from 1994 to 2005, Don led an effort to develop a university-level multidisciplinary Earth system science curriculum. With NASA support, Don partnered with many universities to create a next generation of science, technology, engineering, and mathematics (STEM) education courses. The more than 130 courses have reached well over 100,000 undergraduate students, and most continue to be taught in one form or another around the world. For this effort, Don was recognized by AGU with their 2010 Excellence in Geophysical Education Award.

Perhaps the best way to celebrate Donald R. Johnson's life is to quote from his concluding remarks at his 2014 symposium: "I will end this introduction here, hoping that it has conveyed the continuing excitement of my long-term efforts to understand the fascinating and complex behavior of Earth's atmosphere from the basic principles of physics, thermodynamics, and mathematics. I have enjoyed my voyage in these studies and relished my association with my students, colleagues at the University of Wisconsin, and from around the world. All of these have contributed greatly to my understanding of the atmosphere and to my satisfaction as a teacher and mentor."

Don became the scientist and teacher he imagined he would become while growing up on the family farm in Kansas, emphasizing near the end that his career was built on the "lifeblood of students that professors enjoy." As former students of Donald R. Johnson, we felt his joy every step of the way and carry it with us even today.

Don is survived by his beloved wife of 64 years, Dorothea; sons, Mark and Bryan: and daughter, Christine.

—Richard A. Anthes, Louis W. Uccellini, and John R. Stremikis

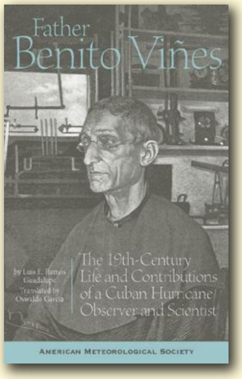

RALPH CICERONE
1943–2017

What can you say to truly honor someone as multifaceted as Ralph Cicerone? He was a world-renowned atmospheric scientist who spent his career bringing scientists together to address pressing societal issues and working to educate the public and decision-makers, all with the goal of making new discoveries and finding policies that would benefit both people and the planet. He dedicated his life to understanding the impact of humans on the environment and working to minimize that impact. He was a leader and a mentor to many.

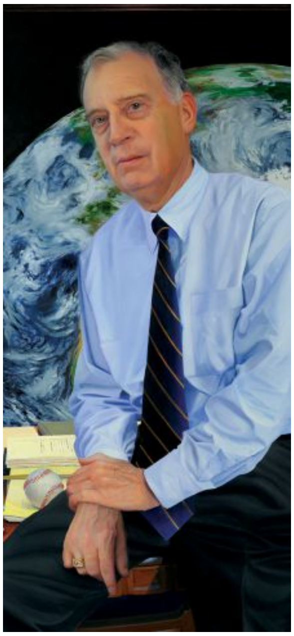
Ralph Cicerone

In the 1970s, he and atmospheric chemist Richard Stolarski showed that chlorine could deplete stratospheric ozone, work that was cited in the 1995 Nobel Prize in Chemistry awarded to Paul Crutzen, Mario Molina, and F. Sherwood Rowland. This important atmospheric chemistry research led to an understanding of the role of chlorofluorocarbons (CFCs) in destroying the ozone layer, and led to the adoption of the 1987 Montreal Protocol, a global treaty that banned CFCs and other ozone-depleting substances.

In 1989, after positions at Scripps Institution of Oceanography and as director of the Atmospheric Chemistry Division at the National Center for Atmospheric Research, Cicerone moved to the University of California, Irvine (UCI), to found the Earth System Science Department. This interdisciplinary department was the first of its kind in the country and soon gained international prominence for its work advancing fundamental understanding of how the atmosphere, land, and oceans interact as a system, and how the Earth can change on time scales of a human lifetime.

Cicerone quickly rose through the ranks at UCI, from chair of Earth system science, to dean of physical sciences, eventually serving as the fourth chancellor of the university. While at Irvine, he was a leader in promoting gender equity among faculty, demonstrating that a department with a significant number of female faculty could rise to the top of national and international rankings. As a first-generation college student himself, Cicerone understood the life-changing value of education and called access to a university education a basic American value. With Ralph at the helm, UCI became a leader in improving economic mobility for low-income students.

In 2005, Cicerone was elected as the 21st president of the National Academy of Sciences (NAS). His election was well timed. During a period when science was increasingly politicized, his steady voice of reason and emphasis on evidence supported a civil and respectful dialogue between scientists, policymakers, and politicians. Under Ralph's leadership, the academies produced a comprehensive set of reports on climate change and possible responses, *America's Climate Choices*, in 2011. Other key accomplishments that occurred under his leadership were a 2008 book titled *Science, Education, and Creationism*, a public-oriented summary of the evidence for evolution; the restoration and modernization of the 1924 NAS building in Washington, D.C.; the 2013 establishment of the $500 million Gulf Research Program following the Deepwater Horizon explosion and oil spill; and an international summit on gene editing in 2016. During his presidency, Ralph again turned his attention to gender equity, putting in place new processes to help identify and elect worthy female candidates to membership in NAS.

Throughout his career, Cicerone had the rare ability to see both the forest and the trees. He could drill down to the crux of a problem, breaking it down into manageable components while simultaneously keeping in mind the broader context.

One cannot talk about the life of Ralph Cicerone without

IN MEMORIAM

EDWIN BOYD
1916–2017

KEN CAMPANA
1941–2017

TOM JOHNSTON
1971–2017

CHUCK LEITH
1923–2016

CONNOR VERNON
1953–2017

talking about baseball. As an undergraduate at the Massachusetts Institute of Technology, he served as captain of the baseball team. His love of baseball led to one of his accomplishments as chancellor of UCI: bringing baseball back to the campus as an officially recognized sport. The UCI ballfield was officially renamed Cicerone Field in 2009 to honor Ralph.

Most people knew about his scientific achievements. Ralph was a model scientist, but also a model human. Those of us who were lucky enough to know him personally knew Ralph as a kind and generous man with a subtle sense of humor. We miss him but keep him in our thoughts as a role model.

—Maggie Walser and Chris Elfring

BOB BAXTER

1954–2017

Bob Baxter spent 40 years in the meteorological and air pollution research field. He was responsible for the evaluation of the air quality–related analyses on numerous environmental studies related to space launch activities. These analyses included air quality impact, global climate change, ozone depletion, reentry of space debris, and visibility degradation due to rocket exhaust plumes. He was actively involved with the Environmental Protection Agency (EPA) in development of guidance for the use of remote sensors in collection of meteorological data, and served as a faculty member at multiday workshops on quality assurance in the operation and evaluation of data from remote and in-situ instrumentation.

After graduating from San Jose State University with a B.S. in meteorology in 1977, Bob joined AeroVironment, Inc. While at AeroVironment, he specialized in the development and application of unique measurement methodologies, including remote upper-air meteorological measurements and real-time tracer analyzers. In addition, he developed an interest in quality assurance of air quality and meteorological measurements that persisted throughout his career. In 1986, he led the establishment of a Santa Barbara office for quality assurance support to the Santa Barbara County Air Pollution Control District. He also developed auditing procedures and quality assurance standards lab and managed several large auditing contracts for clients such as the National Park Service and the California Air Resources Board.

In 1991, Bob moved to Parsons Corporation, where he continued to manage and direct projects for government and industry relating to ambient air issues, meteorological and air quality data collection, and quality assurance in measurement programs. While at Parsons, he again managed several large regional air monitoring efforts and quality assurance auditing contracts. Beginning in 1993, Bob teamed with the Meteorological Standards Institute, participating as faculty staff in several workshops on quality assurance and quality control of upper-air and surface meteorological measurements, as well as surface air quality measurements. Based on his experience obtained through these efforts, he became a major contributor for revisions to the EPA meteorological guidance and the release of the document, *Meteorological Monitoring Guidance for Regulatory Modeling Applications*, published in 2000.

Bob Baxter

In 1994, he received his Certified Consulting Meteorologist (CCM) certification (#531) from AMS. His involvement in AMS continued through his career, including participation as a CCM board member from 2004 through 2009. In addition to AMS, Bob was a longtime member of the Air and Waste Management Association and the American Society for Test and Materials.

In 2002, Bob moved to Technical & Business Systems, Inc. (T&B Systems), building upon his growing expertise in innovative air quality sampling techniques, remote sensing, and quality assurance. In 2010, he became co-owner of T&B Systems. Most recently, Bob had been enthusiastically pursuing the use of off-the-shelf unmanned aerial vehicles to make above-surface air quality and meteorological measurements. This effort embodies much of what was key to Bob's professional life: his love of meteorology, his excitement and enthusiasm in developing new measurement techniques, and an insistence on quality measurements.

—David Bush

[Editor's Note: The following post is adapted from William Hooke's blog, Living on the Real World (www.livingontherealworld.org/). Hooke is the former director of the AMS Policy Program and currently a senior policy fellow.]

Before Leaving the Topic of "Defensiveness" For Good…

Originally posted on April 21, 2017

…One last, brief set of thoughts for scientists on the eve of tomorrow's March for Science and Earth Day.

This post is triggered by an article by Tim Requarth in *Slate* (a tip of the hat to Fred Carr, a former AMS president, who caught the article and forwarded the link along). The article focuses on scientists' obsessive infatuation with the knowledge-deficit approach to argument–that "if the public knew what we know about __________ (fill in the blank; climate change is a popular choice here), they wouldn't be thinking what they're thinking or doing what they're doing…"

Mr. Requarth's article merits reading (and re-reading) in its entirety, but a brief excerpt:

> Many scientists hope that by doing a better job of explaining science, they can move the needle toward scientific consensus on politically charged issues. As recent studies from Michigan State University found, scientists' top reason for engaging the public is to inform and **defend** *[emphasis added]* science from misinformation.
>
> It's an admirable goal, but almost certainly destined to fail. This is because the way most scientists think about science communication—that just explaining the real science better will help—is plain wrong. In fact, it's so wrong that it may have the opposite effect of what they're trying to achieve…

Mr. Requarth cites and summarizes Dan Kahan's[1] research, choosing this bottom line:

> The takeaway is clear: Increasing science literacy alone won't change minds. In fact, well-meaning attempts by scientists to inform the public might even backfire. Presenting facts that conflict with an individual's worldview, it turns out, can cause people to dig in further. Psychologists, aptly, dubbed this the "backfire effect."

He then concludes:

> There's a certain irony that scientists, of all people, know so little about, well, the science of science communication…

Randy Olson captures this same set of ideas in his remarkable book, *Don't Be Such a Scientist: Talking Substance in an Age of Style*. He speaks in (often earthy) language about the importance of appealing to the gut rather than the head. A considerably longer read, but still worth your time.

…

You could argue that little in all this is actually new—that the ancient Greek rhetoricians already saw it this way, two thousand years or so ago, offering variants on this message:

First win the audience; then win the argument.

So enjoy Saturday's March for Science: outdoors in spring weather, with friends, part of a huge crowd, looking and laughing at clever placards and great tee-shirts, feeding off the energy of the group, tweeting and messaging—what's not to like? But try your best throughout the day to keep your talk pro-science and positive, not political and negative. And when the march is over, reflect on the serious business ahead for science. We have to win the hearts and minds of the audience—political leaders and the public—before winning any argument. In a word, we have to (respectfully) court them.

The bad news? After digging ourselves in a hole for the past few decades on contentious issues ranging from vaccination to climate change by acting in full-scold mode, such courtship will take a while.

The good news? "Giving the facts," as we've done for years, but now with an admixture of courtship thrown in? (Using the five languages of love) Acts of service? Gifts? Words of affirmation? Quality time? Physical touch (maybe a bit problematic; let's replace that with face-to-face)? All that not only promises to be more effective; it looks to be a lot more fun.

---

[1] Mr. Kahan has so much wisdom to offer, I didn't want to pick and choose. Follow this link and make your own selection of starting point: www.google.com/?client=safari&channel=mac_bm#channel=mac_bm&q=dan+kahan

AMS BOOKS: HISTORY • CLIMATE • WEATHER

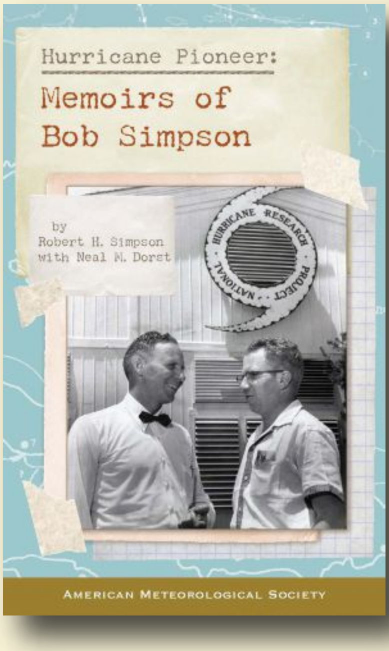

HURRICANE PIONEER

Memoirs of Bob Simpson

Robert H. Simpson with Neal M. Dorst

In 1951, Bob Simpson rode a plane directly into the wall of a hurricane—just one of his many pioneering explorations. This autobiography of the first director of the National Hurricane Research Project and co-creator of the Saffir-Simpson Hurricane Scale starts with childhood remem-mbrance and ends in first-hand account of a revolutionary

© 2014, PAPERBACK
ISBN: 978-1-935704-75-1
LIST $30 MEMBER $20

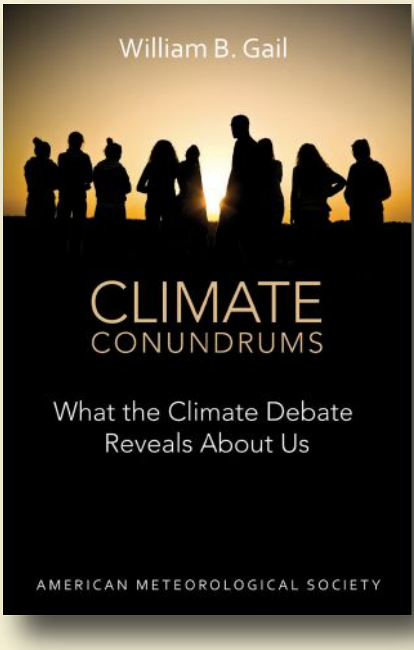

CLIMATE CONUNDRUMS

What the Climate Debate Reveals About Us

William B. Gail

This is a journey through how we think, individually and collectively, derived from the climate change debate. With wit and wisdom, Gail explores several questions: Can we make nature better? Could science and religion reconcile? Insights from such issues can help us better understand who we are and help

© 2014, PAPERBACK
ISBN: 978-1-935704-74-4
LIST $30 MEMBER $20

Browse online at
ametsoc.org/bookstore

FREE SHIPPING
for AMS Members!

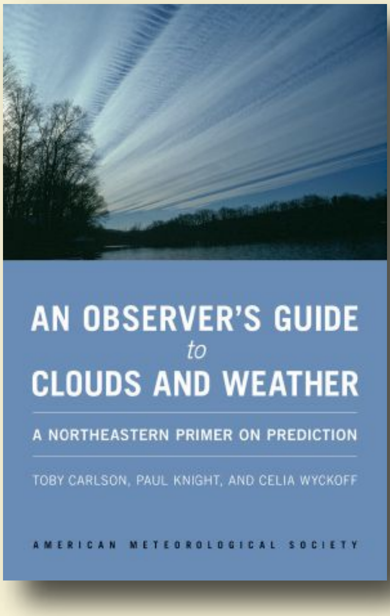

AN OBSERVER'S GUIDE TO CLOUDS AND WEATHER

A Northeast Primer on Prediction

Toby Carlson, Paul Knight, and Celia Wyckoff

With help from Penn State experts, start at the beginning and go deep. This primer for enthusiasts and new students alike will leave you with both refined observation skills and an understanding of the complex science behind the weather: the ingredients for making reliable predictions of your own.

© 2014, PAPERBACK
ISBN: 978-1-935704-58-4
LIST $35 MEMBER $20

AMS BOOKS

AMS Books are available to groups and booksellers, and desk copies may be obtained, through our distributor The University of Chicago Press: 1-800-621-2736 or custserv@press.uchicago.edu.

STUDENT PRESENTATION AWARDS

A number of conferences present awards recognizing outstanding student contributions to the atmospheric, oceanic, and related sciences. Listed here are students who received awards for their oral or poster presentations given at the 97th AMS Annual Meeting, 22–26 January 2017 in Seattle, Washington.

The AMS extends its congratulations to the students honored below and wishes them success in their careers.

Lance Bosart Symposium

Student Poster Presentations

Patrick Duran University at Albany, SUNY	The Tropopause Structure of Hurricanes Nadine (2012) and Patricia (2015)
James Russell North Carolina State University	African Easterly Waves and Tropical Cyclogenesis

Robert A. Houze Jr. Symposium

Student Poster Presentations

Jason Endries Appalachian State University	1st Place	Vertical Structure and Character of Precipitation in the Tropical High Andes of Bolivia and Southern Peru
Yongxian Pei Florida International University	2nd Place	Shear-motion Combined Effects on Tropical Cyclone Low-wavenumber Precipitation Asymmetry

Severe Local Storms Symposium

Student Poster Presentations

Paul W. Miller University of Georgia	1st Place	A Climatology of Weakly Forced and Pulse Thunderstorms in the Southeast United States
Erik R. Nielsen Colorado State University	2nd Place	An Updated U.S. Geographic Distribution of Concurrent, Collocated Tornado and Flash Flood Events and Look at Those Observed during the First Year of VORTEX-SE
Lawrence Wolfgang Hanft University of Nebraska	3rd Place	An Observational Study of High Theta-E Airmasses

33rd Conference on Environmental Information Processing Technologies (EIPT)

Student Oral Presentations

Benjamin Toms University of Oklahoma	1st Place	Development of a Novel Road Ice Detection and Road Closure System: Modeling, Observations and Risk Communication
Andrew Byrd University of Oklahoma	2nd Place	Weather Observations With a Cylindrical Polarimetric Phased Array Radar

Student Poster Presentation

Taylor Faires University of Oklahoma	1st Place	Developing a Tornado Debris Signature Algorithm

31st Conference on Hydrology

Student Oral Presentations

Karl Lapo University of Washington	1st Place	Testing Turbulence Schemes in Land Models During Stable Conditions
Sebastian Los Utah State University	2nd Place	Intermittent Water Vapor Exchanges and Their Role in Vineyard Evapotranspiration

Student Poster Presentations

Mary Forrester Colorado School of Mines	1st Place	Diagnosing Ecohydrologic and Atmospheric Feedbacks from Beetle-Induced Tree Mortality with a Coupled Atmosphere–Hydrology Model
William Hahn University of Wisconsin	2nd Place	Examining Shallow Snowfall Cases by Using Ground-Based Cloud Radars

29th Conference on Climate Variability and Change

Oral Presentations

Natalie Thomas University of Maryland	Seasonality in the Secular Warming of the Northern Continents
Xiaojuan Liu University of Washington	What Determines the Meridional Heat Transport? Insights from Varying Rotation Rate Experiments

Poster Presentation

Nirupam Karmakar Indian Institute of Science	A Study of the Relationship Between the Intraseasonal Variability and Extreme Rainfall Events in the Indian Summer Monsoon Rainfall in a GCM
Zoe A Brooke Zibton University of Wisconsin	Link Between CERES Radiative Energy Flux and Southern Hemisphere Jet Stream Variability

28th Conference on Weather Analysis and Forecasting

Student Oral Presentations

Rosimar Rios-Berrios University at Albany, SUNY	1st Place	A Multi-Case Perspective on Tropical Cyclone Intensification under Moderate Vertical Wind Shear
Christopher McCray McGill University	2nd Place	A Surface Dynamic and Thermodynamic Analysis of Long-Duration Freezing Rain Events
William Currier University of Washington	3rd Place	Using OLYMPEX High Elevation Measurements to Evaluate Predicted Frozen Precipitation by both PRISM and WRF (4/3 km) in the Olympic Mountains during WY 2015 and 2016

Student Poster Presentations

Leah Campbell University of Utah	1st Place	Mechanisms Contributing to the Tug Hill Lake-Effect Precipitation Maximum during OWLeS IOP2b
Sara Ganetis Stony Brook University, SUNY	2nd Place	Environmental Conditions Associated with Different Snow Band Structures within Northeast U.S. Winter Storms
Aaron Updike Valparaiso University	3rd Place	Characterizing and Predicting Along-Coast and Diurnal Marine Stratus Variability on the U.S. West Coast

24th Conference on Numerical Weather Prediction

Student Oral Presentations

Elizabeth Smith University of Oklahoma	1st Place	The Great Plains Low-Level Jet During PECAN: Initial Comparisons of Profiling Observations with WRF Model Predictions
Erik Nielsen Colorado State University	2nd Place	Observations of Extreme Short-Term Precipitation Associated with Supercells and Mesovortices
Alexander Jacques University of Utah	3rd Place	Detection of Mesoscale Pressure Perturbations with Five Minute Gridded Analyses

Student Poster Presentations

Thomas Gowan University of Utah	1st Place	Overview of the NCAR High-Resolution (3-km) Ensemble and Validation of Its Quantitative Precipitation Forecasts Over Complex Terrain in the Western US
Yongqiang Sun Pennsylvania State University	2nd Place	Contributions of Moist Convection and Internal Gravity Waves to Building the Atmospheric "-5/3" Kinetic Energy Spectra
Jessica McDonald NOAA/SPC/Hollings	3rd Place	Insights into Predicting Tornado Development Using NEWS-e Vorticity Forecasts

21st Conference on Integrated Observing and Assimilation Systems for the Atmosphere, Oceans, and Land Surface

Best Student Presentations

Tse-Chun Chen University of Maryland	Efficient Estimation of the Impact of Observing Systems using EFSO
Xu Lu University of Oklahoma	Impact of Issues of Vortex Initialization and HWRF Model Errors on Hurricane Inner Core Data Assimilation and Intensity Prediction

18th Conference on Aviation, Range, and Aerospace Meteorology

Best Student Presentations

Corey G. Amiot University of Alabama	Using C-band Dual-Polarization Radar Signatures to Improve Convective Wind Forecasting at Cape Canaveral Air Force Station and NASA Kennedy Space Center
Emily A. Ranquist University of Colorado	Exploring the Range of Weather Impacts on UAS Operations

16th Annual AMS Student Conference

Outstanding Student Conference Poster Awards

Alicia C. Camacho SUNY, Port Jefferson Station, NY	Representation of the Extratropical Cyclone Wind Field and Warm Conveyor Belt in Climate and Weather Models
Michelle A. Dovil NCAS, Washington, D.C.	How Minorities Use Social Media During Weather Related Crises: Results of a U.S. National Weather Survey
Keon Gibson UCAR, Crown Point, IN	Investigating the Sources of Inaccuracy in a Geonor Precipitation Gauge
Nicholas S. Grondin University of South Alabama	Comparing Temperature Data from USA Mesonet Stations and Automatic Surface Observing Stations across the Northern Gulf Coast
Carrie E. Lang SUNY Geneseo	Lake-to-Lake Connection Influence on Lake-effect Snowfall Totals
Gina Li Virginia Polytechnic Institute	A Novel Web Application to Analyze and Visualize Extreme Heat Events
Chris Lunger City College of New York	Investigation of Convective Storms during the Caribbean Mid-Summer Drought
Robert Prestley Pennsylvania State University	An Analysis of Social Media Services at NWS Louisville to Enhance Forecast Operations and High-Impact Weather Event Decision Support
Benjamin Tucker University of Maryland	Determination of Planetary Boundary Layer Heights From Doppler Wind Lidar Measurements
Kristofer S. Tuftedal Iowa State University	Radar Detection of Tornadogenesis
Usaama A. Van CREST, New York, NY	Applications of Remote Sensing and In-Situ Measurements for Studying Lateral Carbon Fluxes Between Tidal Marshes and Connected Estuarine Waters
Luke M. Western University of Bristol, UK	Decision Theory Based Classification of Atmospheric Hazards

15th Conference on Artificial and Computational Intelligence and Its Applications to the Environmental Sciences

Presenatation Awards

Sebastian Josef University of Innsbruck	1st Place	Forecasting Low-Visibility Conditions at Vienna Airport with Tree-Based Statistical Models
Costa Christopoulos Massachusetts Institute of Technology	2nd Place	Evaluation of Machine Learning Techniques for Precipitation Type Forecasting
Ryan A. Lagerquist University of Oklahoma	3rd Place	Using Machine Learning to Predict Straight-line Convective Wind Hazards Throughout the Continental United States

14th Conference on Polar Meteorology and Oceanography

Oral Presentations

Christina McCluskey Colorado State University	1st Place	Ice Nucleating Particles over Oceans to High Latitudes
Megan Jones Ohio State University	2nd Place	An Exceptional Summer during the South Pole Race of 1911–1912

Poster Presentations

Pyxie Star Evergreen State College	1st Place	Validation of Satellite-Based Measurements of Precipitable Water Vapor at Various Arctic Stations
Richard Wilson Jones University of East Anglia	2nd Place	Evaluating Reanalysis Products in the Amundsen Sea Embayment, Antarctica

13th Symposium of the Urban Environment

Outstanding Oral Presentations

Lento Manickathan ETZH	Conjugate Vegetation Model for Evaluating Evapotranspirative Cooling in Urban Environment
Luis Ortiz City College of New York	Urban Impacts on New York City Weather During a Heat Wave

Excellent Oral Presentation

Michael A. Allen University of Western Ontario	A Climatology of Urban Surface Heat Islands Derived from Hemispherical Radiometric Surface Temperatures

Outstanding Poster Presentations

Erin B. Wetherley University of California	Urban Composition and Surface Temperature at Multiple Scales Using Airborne Spectroscopic and Thermal Imaging
Alexandria J. Herdt Texas Tech University	Urban Microclimate Monitoring in Seoul, Korea: Fine Scale Summer Heating along the Cheonggye Stream Renewal Project

Excellent Poster Presentations

Guangdong Duan City University of Hong Kong	Mixing of a Passive Scalar in an Urban-Street Canyon
Jiajun Gu Cornell University	Intercomparison of Three Source Estimation Methods in a Building Downwash Environment: Applicability, Limitations and Research Needs

Best Poster Presentations

Toshiya Yoshida Kyoto University	Influences of Complex Roughness over an Actual Urban Area on Turbulent Flows as Revealed by Large-Eddy Simulations
Anamika Shreevastava Purdue University	Incorporation of Urban Form and Function for Improved Correlation Between Land Use Types and Land Surface Temperatures

13th Annual Symposium on New Generation Operational Environmental Satellite Systems

Best Student Oral Presentation

Jason Apke University of Alabama in Huntsville	Analysis of Relationships in Deep Convection between Super Rapid Scan Geostationary Satellite Derived Cloud Top Outflow, Updrafts and Total Lightning

Best Student Poster Presentation

Yi Wang Texas A&M University	Assessing the Effect of Satellite Viewing Geometry on Retrieved Ice Cloud Particle Surface Roughness Using MISR Satellite Observations

12th Symposium on Societal Applications: Policy, Research and Practice

At Large

Brianna Pagan Loyola Marymount University	1st Place	Does Near Term Climate Change Risk Represent a 'Yard Sale' for the US Ski Industry?
Sage Lincoln National Oceanic and Atmospheric Administration	2nd Place	Drought, Growth, and Climate Adaptation: A Case Study of Water Management in Las Vegas
Aisha C. Reed Haynes George Mason University	3rd Place	An Investigation of the Relationship between Vulnerable Populations and Hazard Casualties in Warning Dissemination Coverage Gaps

Oral Presentation

Minh Duc Phan East Carolina University	1st Place	Weather on the Go: An Assessment of Smartphone Mobile Weather Applications Use among College Students
Jennifer A. Spinney University of Western Ontario	Honorable Mention	The Canadian Weather Prediction Process: The Complication of Notification in Toronto, Ontario

Poster Presentations

Ilyza Lustig Yale University	1st Place	Economic Evaluation of Local Damages and Coastal Protection Strategies in the Face of SLR: A Case Study from New York's Hudson Valley
D. Graham Andrews National Center for Atmospheric Research	Honorable Mention	Emerging Decadal Climate Information: What's the Potential for Flood Risk Management?

Ninth Symposium on Aerosol–Cloud–Climate Interactions

Best Student Oral Presentations

Michael Diamond University of Washington	Entrainment and Mixing of Biomass Burning Aerosol into the Namibian Stratocumulus Cloud Deck
Alyson Douglas University of Wisconsin	Quantifying and Decomposing the Shortwave Indirect Effect into the Twomey and Cloud Lifetime Components
Thea Schiebel Institute of Technology Karlsruhe, Germany	Contribution of Soil Organic Matter to the Ice Nucleation Activity of Arable Soil Dust Aerosol Particles

Best Student Poster Presentations

Siddhant Gupta University of Illinois	Spatio-Temporal Variability in Cloud Microphysical Properties over the South-East Atlantic
Johannes Mohrmann University of Washington	Meteorological and Microphysical Controls on the Stratocumulus to Cumulus Transition
Kuan-Ting O University of Washington	Ultra-Clean Layers (UCLs) and Low Albedo Clouds (gray clouds) in the Marine Boundary Layer—CSET Aircraft Data, 2-D Bin Spectral Cloud Parcel Model, Large Eddy Simulation and Satellite Observations from CALIPSO, MODIS and COSMIC

Eighth Conference on the Meteorological Application of Lightning Data

Student Oral Presentations

Tyler Kranz University of Arizona	1st Place	Thunderstorm and Terrain Interactions over the Grand Canyon Region
Retha Matthee Mecikalski University of Alabama	2nd Place	Lightning Characteristics Relative to Radar, Altitude and Temperature for a Multicell, MCS and Supercell over Northern Alabama

Student Poster Presentations

Thomas Philippe Lavigne Texas A&M	1st Place	Relationship Between the Global Electric Circuit and Electrified Cloud Parameters at Diurnal, Seasonal and Interannual Timescales
Brody Fuchs Colorado State University	2nd Place	Relationships Between Storm Microphysics, Dynamics, and Charge Structure

Eighth Conference on Environment and Health

Best Student Oral Presentations

Morgan Gorris University of Michigan	The Spatiotemporal Relationship between Climate and Valley Fever in the Southwestern United States
Paul Chakalian Arizona State University	Determining Social Mechanisms of Extreme Heat Vulnerability in Phoenix, Arizona
Jane Baldwin Princeton University	Quantifying the Risk of Compound Heat Wave Events

Eighth Conference on Weather, Climate, Water and the New Energy Economy

Oral Presentations

Jessica M. Tomaszewski University of Colorado	1st Place	Do Wind Turbines Pose Roll Hazards to Light Aircraft?
Elliot I. Simon DTU Wind Energy (Risø)	2nd Place	Lidars Lifted: The Østerild Balconies Experiment
Joseph C.Y. Lee University of Colorado	3rd Place	Improvements in Wind Power Forecasts through Use of the WRF Wind Farm Parameterization Evaluated with Meteorological and Turbine Power Data

Seventh Conference on Transition of Research to Operations

Oral Presentations

Brooke Hagenhoff University of North Dakota	1st Place	A Regime Based Climatological Assessment of WRF Simulated Deep Convection and Associated Precipitation
Cameron J. Nixon Valparaiso University	2nd Place	Forecasting Left-Moving Supercells Using an Ensemble Data Assimilation System

Poster Presentations

Katie A. Wilson University of Oklahoma	1st Place	An Instantaneous Self-Assessment of Forecaster Cognitive Workload
Makenzie Krocak University of Oklahoma	2nd Place	Establishing a Baseline: What We Know about Tornado Warning Reception, Comprehension and Response

Fifth Symposium on Prediction of the Madden–Julian Oscillation: Processes, Prediction and Impact

Best Student Oral Presentation

Stephanie S. Rushley University of Washington	Examining Changes to the Madden–Julian Oscillation in a Warmer Climate Using CMIP5 Models

Best Student Poster Presentation

Rachel Colleen Sodowsky Rosenstiel School of Marine and Atmospheric Science	Large-Scale and Convective Characteristics of the ITCZ and MJO Initiation Over the Indian Ocean

Third Symposium on High Performance Computing for Weather, Water, and Climate

Student Oral Presentations

Negin Sobhani National Center for Atmospheric Research	1st Place	Performance Analysis and Optimization of the Weather Research and Forecasting Model (WRF) Advection Schemes
Steven Brus University of Notre Dame	2nd Place	Efficiency Gains in Coastal Ocean Modeling Through High-order Solution Algorithms

THE LIFE CYCLES OF EXTRATROPICAL CYCLONES

Edited by Melvyn A. Shapiro and Sigbjørn Grønås

Containing expanded versions of the invited papers presented at the International Symposium on the Life Cycles of Extratropical Cyclones, held in Bergen, Norway, 27 June–1 July 1994, this monograph will be of interest to historians of meteorology, researchers, and forecasters. The symposium coincided with the 75th anniversary of the introduction of Jack Bjerknes's frontal-cyclone model presented in his seminal article, "On the Structure of Moving Cyclones." The monograph's content ranges from a historical overview of extratropical cyclone research and forecasting from the early eighteenth century into the mid-twentieth century, to a presentations and reviews of contemporary research on the theory, observations, analysis, diagnosis, and prediction of extratropical cyclones. The material is appropriate for teaching courses in advanced undergraduate and graduate meteorology.

CALENDAR OF MEETINGS

The Call for Papers and Calendar sections list conferences, symposia, and workshops that are of potential interest to AMS members. **Complete information about events listed in the calendar can be found on the meetings page of the AMS website, www.ametsoc.org. New additions to the calendar are highlighted.**

To list an event in the calendar, please submit the event name, dates, location, and deadlines for abstracts, manuscripts, and preregistration to amsmtgs@ametsoc.org. For a submission to appear in a given issue, it must be submitted at least eight weeks prior to the month of publication (that is, to appear in the March *Bulletin,* the submission must be received by 1 January).

AMS MEETINGS

2017

JULY

17th Conference on Mesoscale Processes, 24–28 July, San Diego, California
Abstract deadline: 30 March 2017
Preregistration deadline: 14 June 2017
Manuscript deadline: 22 August 2017
Initial announcement published: Oct. 2016

29th Conference on Climate Variability and Change/24th Conference on Probability and Statistics/16th Conference on Artificial Intelligence, 28–29 July, Baltimore, Maryland
Abstract deadline: 21 March 2017
Preregistration deadline: 15 June 2017
Manuscript deadline: 28 August 2017
Initial announcement published: Nov. 2016

AUGUST

2017 Summer Community Meeting, 2–3 August, Madison, Wisconsin
Preregistration deadline: 17 June 2017
Initial announcement published: TBD

AMS Short Course on Differential Reflectivity Calibration, 27 August, Chicago, Illinois
Preregistration deadline: 21 July 2017
Initial announcement published: July 2017

AMS Short Course on Open Source Radar, 27 August, Chicago, Illinois
Preregistration deadline: 21 July 2017
Initial announcement published: July 2017

AMS Short Course on Millimeter Wavelength Radars: Engineering, Theory, and Science Applications, 27 August, Chicago, Illinois
Preregistration deadline: 21 July 2017
Initial announcement published: July 2017

AMS Short Course on Phased Array Antennas for Weather Radar Applications, 27 August, Chicago, Illinois
Preregistration deadline: 21 July 2017
Initial announcement published: July 2017

AMS Short Course on Spaceborne Radar: Data, Retrievals, and Validation, 27 August, Chicago, Illinois
Preregistration deadline: 21 July 2017
Initial announcement published: July 2017

SEPTEMBER

38th Conference on Radar Meteorology, 28 August–1 September, Chicago, Illinois
Abstract deadline: 11 May 2017
Preregistration deadline: 21 July 2017
Manuscript deadline: 15 September 2017
Initial announcement published: Aug. 2016

2018

JANUARY

***David J. Raymond Symposium, 11 January, Austin, Texas**
Session topic proposal deadline: 1 May 2017
Abstract deadline: 1 August 2017
Preregistration deadline: 1 December 2017
Manuscript deadline: 11 February 2018
Initial announcement published: Feb. 2017

***Robert T. Ryan Symposium, 8 January, Austin, Texas**
Session topic proposal deadline: 1 May 2017
Abstract deadline: 1 August 2017
Preregistration deadline: 1 December 2017
Manuscript deadline: 11 February 2018
Initial announcement published: Feb. 2017

***Peter J. Webster Symposium, 9 January, Austin, Texas**
Session topic proposal deadline: 1 May 2017
Abstract deadline: 1 August 2017
Preregistration deadline: 1 December 2017
Manuscript deadline: 11 February 2018
Initial announcement published: Feb. 2017

***46th Conference on Broadcast Meteorology, 7–10 January, Austin, Texas**
Session topic proposal deadline: 1 May 2017
Abstract deadline: 1 August 2017
Preregistration deadline: 1 December 2017
Manuscript deadline: 11 February 2018
Initial announcement published: Feb. 2017

***34th Conference on Environmental Information Processing Technologies, 7–11 January, Austin, Texas**
Session topic proposal deadline: 1 May 2017
Abstract deadline: 1 August 2017
Preregistration deadline: 1 December 2017
Manuscript deadline: 11 February 2018
Initial announcement published: Feb. 2017

---

*An exhibit program will be held at this meeting.

***32nd Conference on Hydrology, 7–11 January, Austin, Texas**
Session topic proposal deadline: 1 May 2017
Abstract deadline: 1 August 2017
Preregistration deadline: 1 December 2017
Manuscript deadline: 11 February 2018
Initial announcement published: March 2017

***31st Conference on Climate Variability and Change, 7–11 January, Austin, Texas**
Session topic proposal deadline: 1 May 2017
Abstract deadline: 1 August 2017
Preregistration deadline: 1 December 2017
Manuscript deadline: 11 February 2018
Initial announcement published: April 2017

***27th Symposium on Education, 7–11 January, Austin, Texas**
Session topic proposal deadline: 1 May 2017
Abstract deadline: 1 August 2017
Preregistration deadline: 1 December 2017
Manuscript deadline: 11 February 2018
Initial announcement published: April 2017

***25th Conference on Probability and Statistics in the Atmospheric Sciences, 7–11 January, Austin, Texas**
Session topic proposal deadline: 1 May 2017
Abstract deadline: 1 August 2017
Preregistration deadline: 1 December 2017
Manuscript deadline: 11 February 2018
Initial announcement published: March 2017

***22nd Conference on Integrated Observing and Assimilation Systems for the Atmosphere, Oceans, and Land Surface (IOAS-AOLS), 7–11 January, Austin, Texas**
Session topic proposal deadline: 1 May 2017
Abstract deadline: 1 August 2017
Preregistration deadline: 1 December 2017
Manuscript deadline: 11 February 2018
Initial announcement published: Feb. 2017

***22nd Conference on Satellite Meteorology and Oceanography, 7–11 January, Austin, Texas**
Session topic proposal deadline: 1 May 2017
Abstract deadline: 1 August 2017
Preregistration deadline: 1 December 2017
Manuscript deadline: 11 February 2018
Initial announcement published: March 2017

***21st Conference of Atmospheric Science Librarians International, 7–11 January, Austin, Texas**
Session topic proposal deadline: 1 May 2017
Abstract deadline: 1 August 2017
Preregistration deadline: 1 December 2017
Manuscript deadline: 11 February 2018
Initial announcement published: July 2017

***21st Conference on Planned and Inadvertent Weather Modification, 7–11 January, Austin, Texas**
Session topic proposal deadline: 1 May 2017
Abstract deadline: 1 August 2017
Preregistration deadline: 1 December 2017
Manuscript deadline: 11 February 2018
Initial announcement published: Feb. 2017

***20th Conference on Atmospheric Chemistry, 7–11 January, Austin, Texas**
Session topic proposal deadline: 1 May 2017
Abstract deadline: 1 August 2017
Preregistration deadline: 1 December 2017
Manuscript deadline: 11 February 2018
Initial announcement published: March 2017

***20th Joint Conference on the Applications of Air Pollution Meteorology with the A&WMA, 7–11 January, Austin, Texas**
Session topic proposal deadline: 1 May 2017
Abstract deadline: 1 August 2017
Preregistration deadline: 1 December 2017
Manuscript deadline: 11 February 2018
Initial announcement published: Feb. 2017

***19th Symposium on Meteorological Observation and Instrumentation, 7–11 January, Austin, Texas**
Session topic proposal deadline: 1 May 2017
Abstract deadline: 1 August 2017
Preregistration deadline: 1 December 2017
Manuscript deadline: 11 February 2018
Initial announcement published: April 2017

***17th Conference on Artificial and Computational Intelligence and its Applications to the Environmental Sciences, 7–11 January, Austin, Texas**
Session topic proposal deadline: 1 May 2017
Abstract deadline: 1 August 2017
Preregistration deadline: 1 December 2017
Manuscript deadline: 11 February 2018
Initial announcement published: April 2017

17th Annual AMS Student Conference, 6–7 January, Austin
Abstract deadline: 2 October 2017
Preregistration deadline: 15 December 2017
Initial announcement published: March 2017

***16th Symposium on the Coastal Environment, 7–11 January, Austin, Texas**
Session topic proposal deadline: 1 May 2017
Abstract deadline: 1 August 2017
Preregistration deadline: 1 December 2017
Manuscript deadline: 11 February 2018
Initial announcement published: July 2017

***16th History Symposium, 7–11 January, Austin, Texas**
Session topic proposal deadline: 1 May 2017
Abstract deadline: 1 August 2017
Preregistration deadline: 1 December 2017
Manuscript deadline: 11 February 2018
Initial announcement published: May 2017

***15th Conference on Space Weather, 7–11 January, Austin, Texas**
Session topic proposal deadline: 1 May 2017
Abstract deadline: 1 August 2017
Preregistration deadline: 1 December 2017
Manuscript deadline: 11 February 2018
Initial announcement published: Feb. 2017

---

*An exhibit program will be held at this meeting.

***14th Annual Symposium on New Generation Operational Environmental Satellite Systems, 7–11 January, Austin, Texas**
Session topic proposal deadline: 1 May 2017
Abstract deadline: 1 August 2017
Preregistration deadline: 1 December 2017
Manuscript deadline: 11 February 2018
Initial announcement published: March 2017

***14IMPACTS: Major Weather Events and Impacts of 2017, 7–11 January, Austin, Texas**
Session topic proposal deadline: 1 May 2017
Abstract deadline: 1 August 2017
Preregistration deadline: 1 December 2017
Manuscript deadline: 11 February 2018
Initial announcement published: Feb. 2017

***13th Symposium on Societal Applications: Policy, Research and Practice, 7–11 January, Austin, Texas**
Session topic proposal deadline: 1 May 2017
Abstract deadline: 1 August 2017
Preregistration deadline: 1 December 2017
Manuscript deadline: 11 February 2018
Initial announcement published: Feb. 2017

***10th Symposium on Aerosol–Cloud–Climate Interactions, 7–11 January, Austin, Texas**
Session topic proposal deadline: 1 May 2017
Abstract deadline: 1 August 2017
Preregistration deadline: 1 December 2017
Manuscript deadline: 11 February 2018
Initial announcement published: April 2017

***Ninth Conference on Weather, Climate, and the New Energy Economy, 7–11 January, Austin, Texas**
Session topic proposal deadline: 1 May 2017
Abstract deadline: 1 August 2017
Preregistration deadline: 1 December 2017
Manuscript deadline: 11 February 2018
Initial announcement published: March 2017

***Ninth Conference on Environment and Health, 7–11 January, Austin, Texas**
Session topic proposal deadline: 1 May 2017
Abstract deadline: 1 August 2017
Preregistration deadline: 1 December 2017
Manuscript deadline: 11 February 2018
Initial announcement published: Feb. 2017

***Eighth Conference on Transition of Research to Operations, 7–11 January, Austin, Texas**
Session topic proposal deadline: 1 May 2017
Abstract deadline: 1 August 2017
Preregistration deadline: 1 December 2017
Manuscript deadline: 11 February 2018
Initial announcement published: Feb. 2017

***Eighth Symposium on Advances in Modeling and Analysis Using Python, 7–11 January, Austin, Texas**
Session topic proposal deadline: 1 May 2017
Abstract deadline: 1 August 2017
Preregistration deadline: 1 December 2017
Manuscript deadline: 11 February 2018
Initial announcement published: Feb. 2017

***Sixth Symposium on the Weather, Water, and Climate Enterprise, 7–11 January, Austin, Texas**
Session topic proposal deadline: 1 May 2017
Abstract deadline: 1 August 2017
Preregistration deadline: 1 December 2017
Manuscript deadline: 11 February 2018
Initial announcement published: Feb. 2017

***Sixth Symposium on Building a Weather-Ready Nation: Enhancing Our Nation's Readiness, Responsiveness, and Resilience to High Impact Weather Events, 7–11 January, Austin, Texas**
Session topic proposal deadline: 1 May 2017
Abstract deadline: 1 August 2017
Preregistration deadline: 1 December 2017
Manuscript deadline: 11 February 2018
Initial announcement published: March 2017

***Sixth AMS Symposium on the Joint Center for Satellite Data Assimilation (JCSDA), 7–11 January, Austin, Texas**
Session topic proposal deadline: 1 May 2017
Abstract deadline: 1 August 2017
Preregistration deadline: 1 December 2017
Manuscript deadline: 11 February 2018
Initial announcement published: Feb. 2017

***Sixth Symposium on Prediction of the Madden–Julian Oscillation and Sub-Seasonal Monsoon Variability, 7–11 January, Austin, Texas**
Session topic proposal deadline: 1 May 2017
Abstract deadline: 1 August 2017
Preregistration deadline: 1 December 2017
Manuscript deadline: 11 February 2018
Initial announcement published: March 2017

***Sixth Aviation, Range, and Aerospace Meteorology Special Symposium, 7–11 January, Austin, Texas**
Session topic proposal deadline: 1 May 2017
Abstract deadline: 1 August 2017
Preregistration deadline: 1 December 2017
Manuscript deadline: 11 February 2018
Initial announcement published: Feb. 2017

Sixth AMS Conference for Early Career Professionals, 7 January, Austin, Texas
Preregistration deadline: 15 December 2017
Initial announcement published: July 2017

***Fourth Symposium on High Performance Computing for Weather, Water, and Climate, 7–11 January, Austin, Texas**
Session topic proposal deadline: 1 May 2017
Abstract deadline: 1 August 2017
Preregistration deadline: 1 December 2017
Manuscript deadline: 11 February 2018
Initial announcement published: Feb. 2017

***Third Symposium on U.S.–International Partnerships, 7–11 January, Austin, Texas**
Session topic proposal deadline: 1 May 2017
Abstract deadline: 1 August 2017
Preregistration deadline: 1 December 2017
Manuscript deadline: 11 February 2018
Initial announcement published: July 2017

---

*An exhibit program will be held at this meeting.

*Third Symposium on Multiscale Predictability: Data-model Integration and Uncertainty Quantification for Climate and Earth System Monitoring and Prediction, 7–11 January, Austin, Texas

Session topic proposal deadline: 1 May 2017
Abstract deadline: 1 August 2017
Preregistration deadline: 1 December 2017
Manuscript deadline: 11 February 2018
Initial announcement published: July 2017

*Special Symposium on Impact-Based Decision Support Services, 7–11 January, Austin, Texas

Session topic proposal deadline: 1 May 2017
Abstract deadline: 1 August 2017
Preregistration deadline: 1 December 2017
Manuscript deadline: 11 February 2018
Initial announcement published: Feb. 2017

*Conference on Earth Observing SmallSats, 7–11 January, Austin, Texas

Session topic proposal deadline: 1 May 2017
Abstract deadline: 1 August 2017
Preregistration deadline: 1 December 2017
Manuscript deadline: 11 February 2018
Initial announcement published: Feb. 2017

*Plains Elevated Convection at Night (PECAN) Symposium, 7–11 January, Austin, Texas

Abstract deadline: 1 August 2017
Preregistration deadline: 1 December 2017
Manuscript deadline: 11 February 2018
Initial announcement published: TBD

FEBRUARY

12th International Conference on Southern Hemisphere Meteorology and Oceanography/Australian Meteorological and Oceanographic Society Annual Meeting, 5–9 February, Sydney, Australia

Session topic proposal deadline: 30 April 2017
Abstract deadline: 31 August 2017
Preregistration deadline: 30 August 2017
Initial announcement published: May 2017

APRIL

33rd Conference on Hurricanes and Tropical Meteorology, 16–20 April, Ponte Vedra Beach, Florida

Abstract deadline: 16 October 2017
Preregistration deadline: 6 March 2018
Manuscript deadline: 17 May 2018
Initial announcement published: May 2017

JUNE

18th Conference on Mountain Meteorology, 25–29 June, Santa Fe, New Mexico

Abstract deadline: 16 February 2018
Preregistration deadline: 14 May 2018
Manuscript deadline: 29 July 2018
Initial announcement published: July 2017

MEETINGS OF INTEREST

2017

JULY

Conference on Regional Sea-Level Changes and Coastal Impacts, 10–14 July, New York, New York

AUGUST

37th International Association for Hydro-Environment Engineering and Research (IAHR) World Congress, 13–18 August, Kuala Lumpur, Malaysia

254th American Chemical Society National Meeting: Symposium on Atmospheric Fate and Transport of Pesticide Emissions, 20–24 August, Washington, D.C.

10th International Carbon Dioxide Conference, 21–25 August, Interlaken, Switzerland

IAPSO-IAMAS-IAGA Joint Assembly, 27 August–1 September 2017, Cape Town, South Africa

Fourth International Conference on Earth System Modelling (4ICESM), 28 August–1 September, Hamburg, Germany

SEPTEMBER

ICB2017L 21st International Congress of Biometeorology, 3–7 September, Durham, Great Britain

EMS Annual Meeting 2017, 4–8 September, Dublin, Ireland

International Data Assimilation Symposium, 11–15 September, Florianopolis, Brazil

OCTOBER

Geological Society of America Annual Meeting 2017, 22–25 October, Seattle, WA

NOAA's 42nd Climate Diagnostics and Prediction Workshop, 23–26 October, Norman, Oklahoma

NOVEMBER

Northeast Regional Operational Workshop XVIII, 1–2 November, Albany, New York

Habitable Worlds 2017: A System Science Workshop, 13–17 November, Laramie, Wyoming

Sixth International Workshop on Monsoons (IWM-6), 13–17 November, Singapore

2018

APRIL

2018 IEEE Radar Conference, 23–27 April, Oklahoma City, Oklahoma

---

*An exhibit program will be held at this meeting.

EYEWITNESS

EVOLUTION OF THE ATMOSPHERIC SCIENCES

by ROBERT G. FLEAGLE

Eyewitness: Evolution of the Atmospheric Sciences describes how the atmospheric sciences were transformed in the span of the author's professional career from its origins in primitive weather forecasting to its current focus on numerical modeling of environmental change. It describes the author's observations of persons, events, and institutions beginning with graduate study during the Second World War and moving on to continuing expansion of the atmospheric sciences and technologies, through development of a major university department, development of new scientific and professional institutions, and to the role that the science of the atmosphere now plays in climate change and other issues of social and political policy.

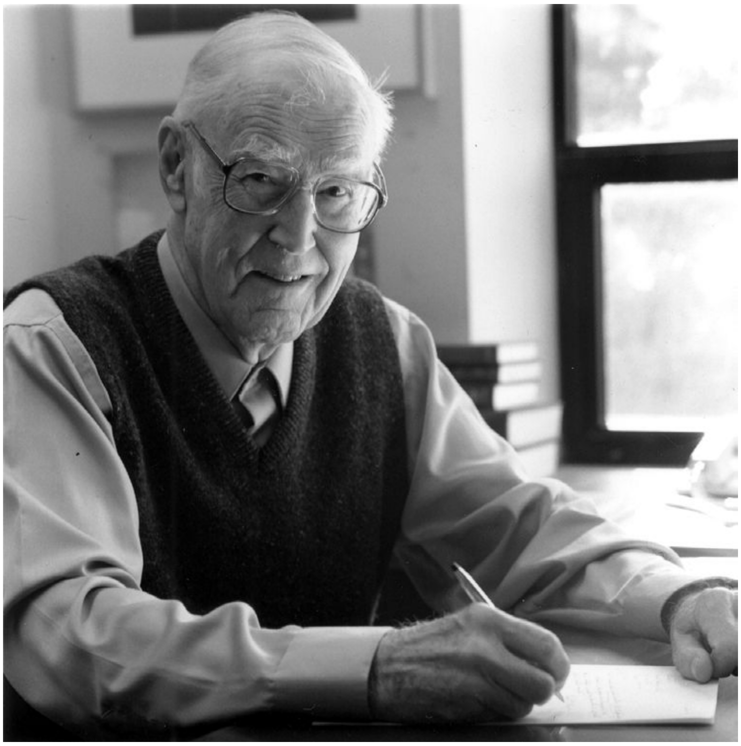

Photo ©Kathy Sauber/University of Washington

EYEWITNESS: EVOLUTION OF THE ATMOSPHERIC SCIENCES

ISBN 1-878220-39-X, 129 pp., hardbound, $75 list/$55 member.

Order online: www.ametsoc.org/amsbookstore
or see the order form at the back of this issue.

ABOUT THE AUTHOR

Robert G. Fleagle earned degrees in physics and meteorology at The Johns Hopkins University and New York University and began his professional career in 1948 at the University of Washington (UW). His research has focused on the structure of midlatitude cyclones, the physics and structure of the surface boundary layer, and processes of air–sea interaction. He is the author of about 100 papers published in scientific journals and of books on atmospheric physics and global environmental change. Applications of science to social and political policy have been important motivations for his career and have occupied his attention increasingly as the decades passed.

Fleagle participated at close range in the beginnings and growth of a major university department and of the University Corporation for Atmospheric Research (UCAR). In 1963 and 1964 he served as a staff specialist in the Office of Science and Technology, Executive Office of the President, and in 1977–78 he served as consultant to the National Oceanic and Atmospheric Administration. He has held many administrative posts including chairman of the UW Department of Atmospheric Sciences (1967–77), chairman of the National Academy of Sciences Committee on Atmospheric Sciences (1969–73),

CALL FOR PAPERS

ANNOUNCEMENT

AMS Short Course on Differential Reflectivity Calibration, 27 August 2017, Chicago, Illinois

The AMS Short Course on Differential Reflectivity Calibration will be held on 27 August 2017, preceding the 38th AMS Radar Meteorology Conference in Chicago, Illinois. Preliminary programs, registration, hotel, and general information are posted on the AMS website (www.ametsoc.org/ams/index.cfm/meetings-events/ams-meetings/38th-conference-on-radar-meteorology/).

Even though the quantity Zdr was first introduced to the radar meteorology community more than 40 years ago by Seliga and Bringi, the calibration of Zdr continues to be a topic of research, an issue for most radars, and a quantity whose temporal stability is poorly documented and inadequately understood. Gathering data in light rain is perhaps the most accepted technique for Zdr calibration. However, such precipitation events can be uncommon for a radar site and most operational radars have a mission to document the weather and not execute calibration scans, thus making detailed calibration studies difficult.

Estimates of Zdr bias can be made by several techniques: 1) vertical pointing data, 2) engineering calibration, 3) crosspolar power technique, and 4) using external targets such precipitation and Bragg scatter. This short course describes the details of these methods and applies them to data from the National Center for Atmospheric Research (NCAR) S-Pol radar to illustrate the concepts. S-Pol data are used to document the drift of the Zdr bias from fine time resolution measurements (less than 10-minute intervals) over extended periods of time (hours and days). The gathered data allows for an identification of the radar components that cause the Zdr bias to drift. An important aspect covered is the Zdr bias drift cause by temperature change of the antenna.

Calibration and data quality experts give presentation about their experiences with NEXRAD and the DWD (German Weather Service) radars. Techniques that are used for Zdr calibration are described, illustrated with data, and discussed.

The goal of the course is to educate the student as to the methods, principles, issues, and signal processing techniques required for accurately estimating Zdr bias and its uncertainty. The course is aimed at students, engineers and scientists who desire to know the details of Zdr calibration and how to apply the techniques to their radars and data.

The course consists of presentations by four radar calibration experts. Power points will be made available to the students. Solar calibration scans are discussed in detail and the signal processing program (in C++) will be given to the students. A remote live demonstration of S-Pol Zdr calibration will be shown.

A luncheon will be provided during the short course. For more information please contact John Hubbert (email: hubbert@ucar.edu). (7/17)

ANNOUNCEMENT

AMS Short Course on Open Source Radar, 27 August 2017, Chicago, Illinois

The AMS Short Course on Open Source Radar will be held on 27 August 2017 preceding the 38th AMS Radar Meteorology Conference in Chicago, Illinois. Preliminary programs, registration, hotel, and general information are posted on the AMS website (www.ametsoc.org/ams/index.cfm/meetings-events/ams-meetings/38th-conference-on-radar-meteorology/).

Open source software (OSS) is a fundamental building block contributing to the process of open science. Recently, radar OSS packages have emerged that facilitate research and development, drive operational national and regional infrastructure, build community, and accelerate pushing the overall state of the art forward. Examples of such packages are the Py-ART (Python ARM Radar Toolkit), ARTView, BALTRAD, wradlib, and LROSE.

This course will introduce participants to OSS tools for working with weather radar data that use the Python programming language. The objective of this course is to present the amazing results that can be archived with open source community development process, in which different individuals and organizations contribute together to a project and provide the results to the community. These tools are collected and made available in the form of a turnkey open radar virtual machine. The course will consist of the following parts:

- introduction to open science concepts and collaborative methods;
- the Python programming language and the Jupyter notebook;
- introduction to Py-ART, concepts, and hands-on notebooks;
- introduction to BALTRAD, concepts, and hands-on notebooks;
- introduction and demo of LROSE;
- introduction to the development of a graphical user interface for radar data (i.e., ARTView);
- intermediate usage including retrievals and manipulation of data using Py-ART and other Python radar applications.

A luncheon will be provided during the short course. Basic knowledge of radar and scientific programming are required. Knowledge of Python is beneficial but not necessary. Using your own laptop with at least 2 GB of memory and 1 GB of free space will be essential for the course. Software and Jupyter notebooks need to be preinstalled by participants prior to the course; instructions for preparation will be emailed in advance. For additional information, please contact Gamma Anderson (email: gamaanderson92@gmail.com). (7/17)

ANNOUNCEMENT

AMS Short Course on Millimeter Wavelength Radars: Engineering, Theory, and Science Applications, 27 August 2017, Chicago, Illinois

The AMS Short Course on Millimeter Wavelength Radars: Engineering, Theory and Science Applications will be held on 27 August 2017, preceding the 38th Conference on Radar Meteorology in Chicago, Illinois. Preliminary programs, registration, hotel, and general information are posted on the AMS website (www.ametsoc.org).

Millimeter wave radars have been used by the research community for over two decades to study clouds. Historically, the research community has used vertically pointing profiling radars. Recently, there has been an increase in the number of millimeter wave radars deployed around the world. These radars use a variety of configurations that include both scanning and zenith profiling capabilities. In addition to providing spatial mapping of the clouds, many radars have capabilities such as dual-frequency or dual-polarization. Millimeter wave radar systems have significantly different requirements and challenges when compared to traditional weather radars.

The objective of this short course is to introduce millimeter wave radar systems and applications. The course will cover the fundamental principles of radars as applied to millimeter wavelengths, their applications, and techniques for data processing. The lectures will use data from the U.S. Department of Energy's ARM radars to highlight the concepts and applications. In addition, software tools shall be used for a hands-on session to interact with the radar data.

A luncheon will not be provided during the short course. Computers, laptops or internet access will not be provided for this course. For additional information, please contact Nitin Bharadwaj (email: nitin@pnnl.gov). (7/17)

ANNOUNCEMENT

AMS Short Course on Phased Array Antennas for Weather Radar Applications, 27 August 2017, Chicago, Illinois

The AMS Short Course on Phased Array Antennas for Weather Radar Applications will be held on 27 August 2017, preceding the 38th AMS Conference on Radar Metrology. Preliminary programs, registration, hotel, and general information are posted on the AMS website (www.ametsoc.org).

Phased array antennas (PAAs) are becoming increasingly prevalent for weather radar applications. PAAs offer significant advantages over traditional antenna approaches, but come with higher complexity. Numerous interrelated design variables are typically optimized to achieve the requisite performance at minimum cost. This course will address the key design considerations for phased array hardware so that weather experts have a greater understanding of their capabilities and tradeoffs. The goal is to be in a better position to make recommendations and assessments in the future regarding their usage and requirements.

This four module course is focused on providing a technical background on phased array antennas for weather radar for the non-antenna expert. The first module will review the fundamental background and mathematics for phased array antenna and radar operation. The second module will discuss key requirements for phased array antennas, and how the requirements impact the hardware design and cost. This will include an overview of advanced architectures such as multi-beam, digital, and dual-polarized antennas that are planned for future weather radar systems. The third module will provide details of phased array capabilities and tasking for weather observation and will include a survey of recent systems emerging from academia and industry. Finally, the last module will be an interactive exercise where the attendees will be provided with a PC and will work in groups to perform the initial trade studies for a phased array antenna design, including operating frequency selection, antenna size, power, and physical architecture for a phased array to meet a weather radar sensing mission at the lowest cost.

The course format is a half day (4 hours) consisting of lectures and a design exercise at the end. For additional information, please contact Mark Leifer (email: mleifer@ball.com) or Matt Little (email: mlittle@ball.com). 7/17)

ANNOUNCEMENT

AMS Short Course on Spaceborne Radar: Data, Retrievals, and Validation, 27 August 2017, Chicago, Illinois

There is a lack of tools and trained scientists who are able to use open source data tools to use, understand, validate, and apply retrievals to spaceborne radar measurements. In this course, we will describe spaceborne radar hardware, uncertainties in the measurements, and potential applications and use open source software tools to access, process, and retrieve geophysical information (microphysical, cloud structure, and precipitation climatologies), and uncertainties from spaceborne radar measurements at W, Ku, and Ka bands.

The objective of this course is to familiarize students with data from current and future spaceborne radar measurements from TRMM, CloudSat, GPM, and future missions such as EarthCare. Participants will bring their own computers for a hands-on open source tutorial. Open-source cloud-based virtual machines, with Python code contained within Jupyter notebooks, will be used for lab practical exercises.

The outcomes for this course include:

- understanding of the measurements provided by spaceborne radar retrievals and their uncertainties;
- understanding of the theory of spaceborne radar measurements and geophysical retrievals based upon the measurements;
- use of open source software to read, process, and visualize spaceborne radar measurements.

Students will be required to do some but not a lot of coding during the project, and most code will be provided as a reference. However, students will be exposed to state of the art techniques for analyzing spaceborne radar data. The course format consists of lectures and three interactive laboratory assignments that can be completed any time during or following the conference. A box lunch will be provided during the short course. Internet access will be available or required for this course. Please bring a laptop computer to the course for online exercises. For more information, please contact Steve Nesbitt (tel.: 217-244-3740; email: snesbitt@illinois.edu). (7/17)

CALL FOR PAPERS

27th Symposium on Education, 8–10 January, Austin, Texas

The 27th Symposium on Education will highlight outstanding papers, posters, and activities highlighting education and outreach, with a focus on broader impacts. Presentations by this year's pre-college and university teaching award recipients will be included in the program. A special Education Town Hall meeting will take place Tuesday evening immediately following the late afternoon session.

The theme for the 2018 AMS Annual Meeting, "Transforming communication in the weather, water, and climate enterprise—Focusing on challenges facing our sciences," highlights the need for fundamental communication and information to address our most pressing needs, including those in education and outreach. As appropriate, we encourage authors to incorporate and discuss the best methods to communicate information as well as communication-related examples in their presentation and poster abstracts.

For the 2018 meeting, the symposium is soliciting papers and posters on all aspects of university, K–12, formal, and informal education. This year, we welcome the submission of abstracts for sessions with the

2018 AMS ANNUAL MEETING CALL FOR PAPERS

7–11 January 2018, Austin, Texas

The 2018 AMS Annual Meeting theme is "Transforming communication in the weather, water, and climate enterprise—Focusing on challenges facing our sciences." For the full description of the theme, please visit the AMS 2018 Annual Meeting webpage (https://annual.ametsoc.org/). Preliminary programs, registration, hotel, and general information will also be posted on the AMS website in late September 2017.

Beginning with the 2018 Annual Meeting, a link will be available for those that would like to propose a session topic. This link will be posted to the Annual Meeting webpage in the early spring. The deadline for proposals is 1 May 2017.

The abstract submission portal will open on 15 May 2017. Authors will be able to submit abstracts to topics that are a combination the listing from the call for papers as well as those that have been proposed from our community. The deadline for abstract submissions is 1 August 2017 (https://ams.confex.com/ams/). The $95 fee includes the submission of your abstract, the posting of your extended abstract, and the uploading and recording of your presentation, which will be archived on the AMS website. Authors of accepted presentations will be notified via e-mail by late September 2017.

All extended abstracts are to be submitted electronically and will be available online. Instructions for formatting extended abstracts will be posted on the AMS website. Authors have the option to submit extended abstracts (up to 10 MB) electronically by 27 February 2018. All abstracts, extended abstracts, and presentations will be available on the AMS website at no cost. Annual Meeting calls for papers are noted with green headers in this section.

following themes, including submissions for jointly sponsored sessions:

- pre-college education initiatives;
- university education initiatives;
- outreach and broader impacts;
- innovative teaching strategies in university instruction on atmospheric dynamics;
- using alternative presentation formats to inform your audience
- effective strategies for increasing minority participation in the atmospheric sciences;
    - This session seeks projects that demonstrate innovative and transformative strategies and best practices to solve the lack of inclusion of diverse groups, including minority students in the atmospheric sciences. It seeks methodologies for attracting, recruiting, and retaining diverse ethnicities and projects that demonstrate practices that increase participation, access, awareness, and interest of underrepresented minorities.
- building tomorrow's atmospheric science workforce
    - We are particularly interested in research to understand workforce trends in our field as well as presentations of how we should best prepare students and postdocs for tomorrow's atmospheric science careers.
- active learning demonstrations from the atmospheric sciences
    - Research shows that students benefit from active learning strategies in the classroom. In this session we request proposals for demonstrations of successful activities that attendees could use in their own teaching. Demonstrations should be active: that is, the audience members should be called on to participate in them or a video should be shown of students performing the activity. Demonstrations should take no more than 13 minutes and be accompanied by a handout outlining the activity for participants to take home. Each demonstrator will have 2 minutes at the start of the session to introduce their activity, the grade/educational level it is aimed at, and the learning context that their activity fits into. Demonstrators will then simultaneously present through the rest of the session in a share-a-thon format, with attendees free to move between tables/activities. We ask that abstracts briefly outline the activity and learning objective, educational level the activity is aimed at, and any requests for demonstration space (e.g. video screen, table, large open space).
- research relevant to the teaching and learning of atmospheric science
    - Discipline-based research in atmospheric science education is a fairly new field. To encourage discussion and support growth in this area, we welcome preliminary research reports with a 7-minute presentation/7-minute discussion format where audience feedback can be solicited, as well as more polished education findings using the traditional 11-minute talk/3-minute question format.
- television meteorologists as educators (themed joint session with 46th Conference on Broadcast Meteorology)
    - Television meteorologists not only deliver weather forecasts and information but in many cases are called upon as trusted sources to educate their audience on a wide variety of atmospheric and more general science issues. In this session, we explore the universe of methods and topics—from blogs to podcasts and from tsunamis to climate—whereby weathercasters become educators.
- scientific communication [joint session with 34th Conference on Environmental Information Processing Technologies (EIPT)]
    - A broad invitation to submit papers related to all aspects of science communication.
- poster session (open for all education, outreach, and broader impacts topics)

For additional information please contact the program chairpersons, Diane Stanitski (diane.stanitski@noaa.gov) and Jeffrey Yuhas (jayuhas@mac.com). (4/17; 7/17)

CALL FOR PAPERS

21st Conference of Atmospheric Science Librarians International, 10–11 January, Austin, Texas

This is an invitation for joining Atmospheric Science Librarians International (ASLI) and to submit an abstract for consideration for presentations on any aspect of the conference theme and address various aspects for delivering ICE—information, communication, and education—through collections, resources, instruction, delivery, and dissemination of data, information, and knowledge.

The AMS describes the 2018 Meeting theme on communication as "a dynamic, powerful, and essential part of the weather, climate, and water enterprise. Successful communication requires active engagement—not only thinking about what, when, where, how, why, and to whom we speak but also carefully listening to better understand and respond appropriately. Every day we communicate to share and generate ideas, exchange information, inform the public, and create an understanding and awareness of our sciences. And we do this with the goal of benefitting society within an ever-changing backdrop of policy, technology, and knowledge."

The dynamic role that libraries play in this process is evidenced by the AMS recognizing the importance their mission to "generate ideas, exchange information, inform the public, and create an understanding and awareness of our sciences," because this is the very same mission of the libraries and librarians supporting that "ever-changing backdrop of policy, technology, and knowledge," because we inform, communicate, and educate. This provides librarians with a dynamic and robust challenge as we develop collections, user services, library research and instruction, and the ever-increasing importance of utilizing new social media, as effective tools of communication, networking, and outreach, not only among librarians, but more importantly across disciplines, lines of work, and for public engagement. ASLI is seeking librarians, educators, and communicators for answers to critical questions:

- What are technical and practical opportunities for improving communication by librarians in their work environments and examples of "best practices" and new methods of communication?
- How can libraries and librarians improve community-wide understanding, engagement, and information and knowledge exchanges for and among stakeholders (especially policy-makers and the public) using their services?
- What are the opportunities for librarians to enhance existing or develop new strategies for effective communication "across generations, languages, cultures," and among government, academic, and commercial sectors"? (AMS) ASLI strengthened by employing outreach strategies to recruit new members, keeping current members engaged, and responding to members' needs through surveys and discussions. Its annual meeting provides a major focal point and forum developments, discussions, and presentations. Join ASLI in this endeavor, and with this ASLI's invitation for papers addressing any of the above topics.

All attendees for the 21st Conference of Atmospheric Science Librarians International (ASLI) must register and wear a badge. This year, ASLI Conference attendees should register in advance through the AMS website until 1 December 2017. Registrations received between 2 December 2017 and the conference dates will be charged $75. For those registering onsite, registration will take place at the AMS Annual Meeting registration desk. Registration for the ASLI Conference does Not include registration for other 98th AMS Annual Meeting events, but ASLI Conference registrants are encouraged to visit the exhibits.

ASLI will again join the Environmental Information Processing Technologies (EIPT) group in planning & hosting a joint program, and is seeking contributions on the following topics:

- software engineering;
- data management and communication;
- advances in observations, modeling and new media technologies;
- mobile computing for communicating weather information;
- data visualization;
- satellite technologies;
- radar technologies;
- road weather observations;
- AWIPS;
- research to operations and quasi-operational systems.

Another area for consideration is the very useful and popular part of previous programs, the "technology tools and tips" session. This is a brief description or "lightening round" of any tool or innovation you are using, and if you can describe your experiences with the technology in around 3-5 minutes, we would love to hear from you. Talks on technology failures and lessons learned from experience are especially welcome, as are proposals from students using innovative strategies around information.

Please submit your abstract electronically to the ASLI program chairperson, Fred Stoss (email: climatefred@gmail.com), Librarian in the Science and Engineering Information Center at the SUNY University at Buffalo, by 1 August 2017. Submissions should include full contact information for the presenter(s), a title, and a brief abstract of less than 250 words. In most cases presentations are 10 minutes with 5 minutes for questions. For additional information please contact the ASLI program chairperson Fred Stoss (email: climatefred@gmail.com; tel: 585-305-2223). (7/17)

CALL FOR PAPERS

16th Symposium on the Coastal Environment, 7–11 January 2018, Austin, Texas

The 16th Symposium on the Coastal Environment is sponsored by the American Meteorological Society and organized by the AMS Committee on Coastal Environment. The theme for the 2018 AMS Annual Meeting is "Transforming communication in the weather, water, and climate enterprise—Focusing on challenges facing our sciences". Communication is an essential part of the weather, climate, and water enterprise. Significant challenges remain in communicating emergency actions simply, expressing probabilistic/uncertainty information clearly, honing our predictive skills, and perfecting our data collection and analysis techniques. These issues are brought into sharp focus in coastal regions: with steadily expanding human activity in this increasingly vulnerable region, clear and accurate communication of weather-related hazards and uncertainty is becoming increasingly important. The 16th Symposium on the Coastal Environment will explore the various challenges and opportunities in the communication of weather in the coastal zones of the world. Session topics include the following:

- air pollution in the coastal environment (joint session);
- big data in the coastal environment (joint session);
- high-performance computing applications in the coastal zone (joint session);
- regional and coastal hydrodynamic model coupling: (a) storm surge and coastal hazards, (b) hydrological impacts, (c) biogeochemical impacts (joint session);
- creating and communicating medium- to seasonal and long-term forecasts in the coastal environment
- novel observational techniques for the coastal environment: (a) drones, remote sensing, and regional networks and (b) data assimilation and management;
- communicating scientific uncertainty in the coastal environment;
- case studies.

For additional information please contact the program chairpersons, Mona Behl (email: mbehl@uga.edu) and Michael DeFlorio (email: mike.deflorio@gmail.com). (7/17)

CALL FOR PAPERS

15th Conference on Space Weather, 7–11 January 2018, Austin, Texas

The 15th Conference on Space Weather is sponsored by the American Meteorological Society and organized by the AMS Committee on Space. The theme for the 2018 AMS Annual Meeting is “Transforming communication in the weather, water, and climate enterprise—Focusing on challenges facing our sciences.” Communication is a dynamic, powerful, and essential part of the weather, climate, and water enterprise. Successful communication requires active engagement—not only thinking about what, when, where, how, why, and to whom we speak but also carefully listening to better understand and respond appropriately. Following this theme, the Conference on Space Weather will solicit papers on the following topics:

- next steps in space weather research and forecasting;
- shifting paradigms: communicating space weather through social and broadcast media;
- results from the great American solar eclipse;
- impact of space weather on communication;
- major scientific challenges in space weather;
- observational platforms for space weather.

For additional information please contact the program chairpersons, Richard Behnke (email: behnke.richard@yahoo.com) or Michael Wiltberger (email: wiltbemj@ucar.edu). (2/17; r7/17)

CALL FOR PAPERS

Sixth Symposium on the Madden–Julian Oscillation and Sub-Seasonal Monsoon Variability, 7–11 January 2018, Austin, Texas

The Sixth Symposium on the Madden–Julian Oscillation and Sub-Seasonal Monsoon Variability is sponsored by the American Meteorological Society and organized by the AMS Committee on Tropical Meteorology and Tropical Cyclones. Presentations are solicited on studies of the intraseasonal variability related to the Madden–Julian oscillation (MJO), the boreal summer intraseasonal oscillation (BSISO), the Asian–Australian monsoons, and their impacts on weather and climate throughout the world. Papers related to recent or upcoming field experiments, including DYNAMO, YMC, PISTON, and CAMP2Ex, are also encouraged.

Proposed topics for this conference include the following:

- theoretical studies of the MJO dynamics and physics;
- observational analysis of MJO onset and propagation;
- modeling studies of the MJO and associated multi-scale processes;
- propagation of the MJO through the Maritime Continent;
- tropical–extratropical interactions associated with the MJO;
- observations of sub-seasonal variability in the South Asian–Australian monsoon;
- interactions between the MJO and monsoon precipitation;
- observations, theory, modeling, and prediction of boreal summer monsoon sub-seasonal variability;
- air–sea interaction in the MJO;
- sub-seasonal tropical variability under changing climate;
- identifying and predicting the MJO;
- MJO modulation of extreme weather events;
- societal impacts of the MJO, including in agricultural and energy sectors.

This conference will also host the Bernhard Haurwitz Lecture by George Kiladis to honor his contributions to observational studies of tropical–extratropical wave dynamics. Student abstract submissions are especially encouraged. Cash awards for the top two oral and poster presentations will be given. Students, if they wish to participate, should indicate their eligibility for a student award when they submit their abstracts.

For additional information, please contact the program chairs, Ángel Adames (email: angel.adames-corraliza@noaa.gov), Xianan Jiang (email: xianan@ucla.edu), Scott Powell (email: spowell@atmos.colostate.edu), or Justin Stachnik (email: stachnik@ku.edu). (3/17; r7/17)

CALL FOR PAPERS

Sixth Annual AMS Conference for Early Career Professionals, 7 January 2018, Austin, Texas

The Sixth Annual AMS Conference for Early Career Professionals is organized by the AMS Board for Early Career Professionals and sponsored by the American Meteorological Society. Learning does not stop after college. After a four-year bachelors program, early career members of AMS enter a world of multiple opportunities, including graduate school and a competitive job market. In addition, a new set of life skills are brought upon early careers, such as time management, negotiation, and work life balance. The Board for Early Career Professionals is aimed to assist both graduate students and early career professionals in this transition, providing tips and tricks to succeed in the weather, water and climate enterprise.

The Sixth Annual AMS Conference for Early Career Professionals serves as a gateway for graduate students and early careers to connect and network with other members, boards, and committees of AMS. The conference comprises a mix of speakers, panelists, and group discussions. Several networking opportunities throughout the conference encourage communication with both other young professional attendees and invited early, mid, and late career professionals involved in AMS. A special networking event will held early Sunday evening for only those that register for the conference.

Sessions will cover a variety of topics that are of interest to early career professionals. Some include communication techniques, tips and tricks to stay relevant in the workforce, and skillsets not taught in college. Interactive small group discussions, led by professionals in the field, will focus on a variety of career skills, issues, and choices that affect early career professionals. Attendees will have an opportunity to hear about how they can benefit from or be a part of AMS boards and committees, and will be able to network with representatives within the AMS. A joint session with the 17th Annual AMS Student Conference will focus on developing skills needed by both early career professionals and graduate students.

Other early career events will take place during the week, including the Eighth Annual AMS Reception for Early Career Professionals, joint sessions specifically highlighting early career research, social media use, and roadmaps to Certified Consulting Meteorologist (CCM) and Certified Broadcast Meteorologist (CBM) accreditation, a town hall meeting, and a student and early career speed networking event. Up-to-date information on the Early Career Professionals Conference can be found on Facebook (search "AMS Early Career Professionals") and Twitter (@AMSEarlyCareer).

Please note that there is a separate registration fee to attend this conference: visit the AMS 2018 Annual Meeting website for more details.

For additional information, please contact the conference chairpersons Chris Schultz (e-mail: christopher.j.schultz@nasa.gov), Matt Lacke (e-mail: matt.lacke@jcdh.org), Samantha Tushaus (email: sam.tushaus@gmail.com), or Jared Rennie (e-mail: jared@cicsnc.org). (7/17)

STUDENT TRAVEL GRANTS

Student Travel Grants are available for senior undergraduate and graduate students to attend AMS meetings held in the United States and Canada. The travel grants are available only to members, including student members, of the AMS.

AMS recognizes the considerable benefit that students can gain from attending conferences even if they are not presenting a paper there, and AMS wants to encourage interactions between students and other conference attendees. To this end, travel grants will be awarded to a student who is not presenting a paper at the conference.

Students who are presenting papers and potentially in need of travel support should inquire of the program chair whether any funds will be available for this purpose.

For more information and to complete an application form, please visit the AMS website at www.ametsoc.org.

CALL FOR PAPERS

Third Symposium on U.S.–International Partnerships, 7–11 January 2018, Austin, Texas

The Third Symposium on US-International Partnerships is sponsored by the American Meteorological Society. Proposed topics for this conference include the following:

- implementation of "Weather-Ready Nations:" case studies from planning and implementation beyond the United States;
- successes, opportunities, and challenges in disaster risk reduction in the Americas: building on the diverse dialogues on disasters occurring in the Americas in 2016;
- successes, opportunities, and challenges in weather, water and climate-related communication across national borders;
- bilateral cooperation in weather, water and climate: lessons learned in cross-cultural communication;
- challenges in communication of developing country NMHS priorities with funding partners: exploring methodologies for coordination (proposed invited panels).

For additional information please contact co-chairs, Michael Ferrari (email: michael.ferrari@weather.com), Renee Leduc Clarke (email: renee@narayanstrategy.com), or Stephen Zebiak (email: steve@iri.columbia.edu). (7/17)

CALL FOR PAPERS

Third Symposium on Multiscale Predictability: Data–Model Integration and Uncertainty Quantification for Climate and Earth System Monitoring and Prediction, 8–9 January 2018, Austin, Texas

The Third Symposium on Multiscale Predictability is sponsored by the American Meteorological Society. With ever-increasing computing resources, climate and Earth system models have seen considerable improvements over the years through the use of increasingly fine resolutions with more accurate physics. Increasingly advanced modeling and data assimilation techniques traditionally used for weather prediction are implemented to facilitate greater data–model integration and uncertainty quantification for climate and earth system monitoring and prediction.

Through a mix of invited and contributed presentations, this special 2-day symposium solicits papers on the recent progress and challenges on data–model integration and uncertainty quantification for various climate and Earth system processes beyond weather phenomena, including, but not limited to, atmospheric composition and chemistry, biogeochemistry, hydrology, ocean, cryosphere, land surface, ecosystem, and the interaction and coupling among various processes. Particular emphasis will be given to the use of advanced modeling and data assimilation techniques to understand both the practical and intrinsic aspects of multiscale predictability of Earth and climate systems. Practical predictability refers to the current capability of a modeling system under best practice given state-of-the-art models with state-of-the-art initial and boundary conditions. Intrinsic predictability refers to the limit of prediction at different temporal and spatial scales given nearly perfect initial conditions and nearly perfect models.

For additional information please contact co-chairs, Professor Fuqing Zhang, Penn State University (tel.: 814-865-0470; email: fzhang@psu.edu) and Professor Kerry Emanuel, MIT (tel.: 617-253-2462; email: emanuel@mit.edu). (7/17)

CALL FOR PAPERS

Special Symposium on Plains Elevated Convection at Night (PECAN), 8–9 January 2018, Austin, Texas

The Special Symposium on Plains Elevated Convection at Night (PECAN) is sponsored by the American Meteorological Society.

Papers that discuss research from the Plains Elevated Convection At Night (PECAN) field campaign, concluded in July 2015, are solicited. Designed as a multi-agency project (NSF, NOAA, NASA, DOE) PECAN was set to advance the understanding of continental, nocturnal, warm-season precipitation. PECAN was focused on nocturnal convection in conditions over the Southern Great Plains with a stable boundary layer (SBL), a nocturnal low-level jet (NLLJ), and frequent bores and other wave motions. A major part of PECAN was to study how elevated convection forms and evolves at night. As a result, a substantial amount of effort was spent in understanding mesoscale convective systems (MCSs) and associated outflows that frequently trigger bores and secondary convection. An extensive array of instrumentation was deployed during PECAN. This multi-sensor suite of instrumentation is expected to lead to new and exciting science. Papers in all aspects of the core PECAN experiment: MCSs, bres, convective initiation, low-level jets, and any related modeling and instrumentation are solicited. It is anticipated that the Symposium will have a full day of presentations and an extensive poster session. It is anticipated that time for a discussion to discuss future PECAN focused meetings will be reserved..

For additional information please contact the program chairperson, Belay B. Demoz (email: bdemoz@umbc.edu) or Tammy Weckwerth (email: tammy@ucar.edu) (7/17)

CALL FOR PAPERS

18th Conference on Mountain Meteorology, 25–29 June 2018, Santa Fe, New Mexico

The 18th Conference on Mountain Meteorology, sponsored by the American Meteorological Society (AMS) and organized by the AMS Committee on Mountain Meteorology will be held at La Fonda on the Plaza in Santa Fe, New Mexico (https://www.lafondasantafe.com/). Preliminary programs, registration, hotel, and general information will be posted on the AMS website (http://www.ametsoc.org) in early April 2018.

The program committee for this conference seeks contributions on all aspects of mountain meteorology, including but not limited to the following:

- stable and convective orographic precipitation;
- boundary layers and turbulence in complex terrain;
- diurnal mountain winds and cold-air pools;
- mountain waves and terrain induced windstorms;
- barrier jets and cold-air damming;
- numerical weather prediction, data assimilation, and forecasting in complex terrain;
- applications of mountain meteorology (e.g., air quality, fire dynamics, and wind resource assessment);
- mountain climate and hydrology;
- biosphere–atmosphere interactions in complex terrain;
- new or emerging topics in mountain meteorology;
- preliminary results from recent field campaigns.

There will also be a special session in honor of Dr. Jim Steenburgh. The Committee on Mountain Meteorology encourages abstract submissions from students: Awards will be given to the best student oral and poster presentations at the conference. Students must indicate that they wish to be included in the competition when submitting an abstract. Two student travel awards will also be available to help supplement travel expenses. Please contact the conference chairpersons or refer to the AMS website for further details regarding eligibility and how to apply.

Please submit your abstract electronically via the AMS website by 16 February 2018; see the website for instructions. An abstract fee of $95 (payable by credit card or purchase order) is charged at the time of submission (refundable only if abstract is not accepted). The abstract fee includes the submission of your abstract, the posting of your extended abstract, and the uploading and recording of your presentation that will be archived on the AMS website.

Authors of accepted presentations will be notified via e-mail by early April 2018. Instructions for formatting extended abstracts will be posted on the AMS website. Extended manuscripts (file size up to 3 MB) must be submitted electronically by 29 July 2018. All abstracts, extended abstracts, and presentations will be made available on the AMS website.

For further information, please contact the program co-chairs: David Kingsmill (email: david.kingsmill@colorado.edu) or Mimi Hughes (email: mimi.hughes@noaa.gov). (7/17)

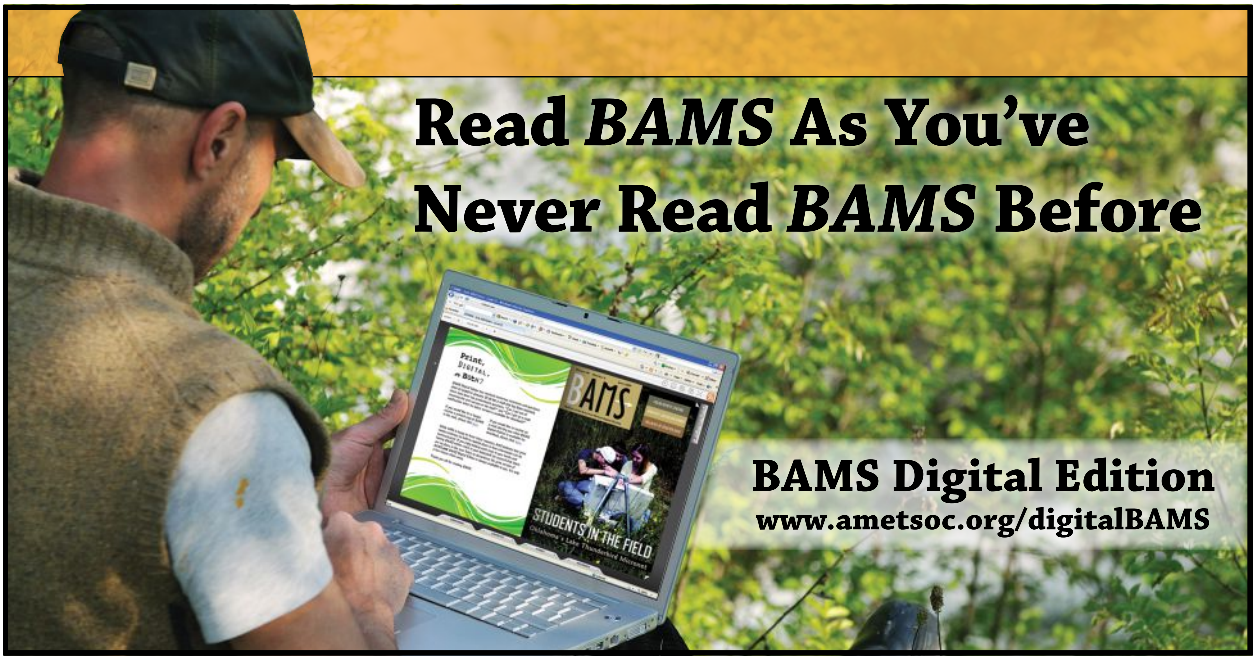

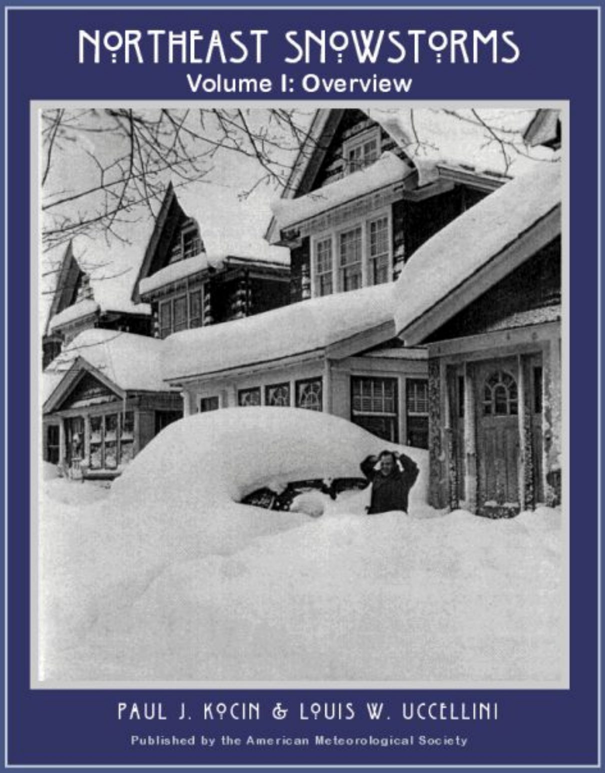

NOMINATION SUBMISSIONS

The Council of the American Meteorological Society invites members of the AMS to submit nominations for the Society Awards, Lecturers, Named Symposia, Fellows, Honorary members, and nominees for elective Officers and Councilors of the Society.

Information regarding awards, including award descriptions, listings of previous recipients, and the process for submitting nominations are on the AMS website www.ametsoc.org/awards.

Note: Deadlines differ and some nominations must be submitted on a specific form vs. electronic submission which is available on the AMS website or by request from Headquarters.

2018 AWARDS COMMITTEES

Each committee or commission listed below has the responsibility to select and submit to the Council the names of individuals nominated for the Society's awards listed. The name(s) of individual(s) nominated, a two-page cv, a bibliography of no more than three pages, and three supporting letters should be electronically submitted before **1 May 2018** for the awards that follow, unless stated otherwise. The nominees for awards remain on the committee's active list for three years.

ATMOSPHERIC RESEARCH AWARDS COMMITTEE

The Carl-Gustaf Rossby Research Medal
The Jule G. Charney Award
The Verner E. Suomi Award*
The Remote Sensing Prize (biennial)
The Clarence Leroy Meisinger Award
The Henry G. Houghton Award

OCEANOGRAPHIC RESEARCH AWARDS COMMITTEE

The Sverdrup Gold Medal
The Henry Stommel Research Award
The Verner E. Suomi Award*
The Nicholas P. Fofonoff Award

HYDROLOGIC RESEARCH AWARDS COMMITTEE

Hydrologic Sciences Medal

AWARDS OVERSIGHT COMMITTEE

The Charles Franklin Brooks Award for Outstanding Services to the Society
The Cleveland Abbe Award for Distinguished Service to the Atmospheric Sciences by an Individual
The Joanne Simpson Mentorship Award
The Award for Outstanding Services to Meteorology by a Corporation
Special Awards

EDUCATION AND HUMAN RESOURCES COMMISSION

The Louis J. Battan Author's Award (Adult and K–12)
The Charles E. Anderson Award
The Edward N. Lorenz Teaching Excellence Award
Distinguished Science Journalism in the Atmospheric and Related Sciences

PROFESSIONAL AFFAIRS COMMISSION

Outstanding Contribution to the Advance of Applied Meteorology
Award for Broadcast Meteorology
Award for Excellence in Science Reporting by a Broadcast Meteorologist
The Henry T. Harrison Award for Outstanding Contributions by a Consulting Meteorologist

WEATHER AND CLIMATE ENTERPRISE COMMISSION

The Kenneth C. Spengler Award

LOCAL CHAPTER AFFAIRS COMMITTEE

Local Chapter of the Year Award
(nomination form available online at www.ametsoc.org/amschaps/index.html.)

---

* Recommended by the Atmospheric Research Awards Committee in even-numbered years and by the Oceanographic Research Awards Committee in odd-numbered years.

2018 AWARDS COMMITTEES

SCIENTIFIC AND TECHNOLOGICAL ACTIVITIES COMMISSION

The Charles L. Mitchell Award
The Award for Exceptional Specific Prediction
The Francis W. Reichelderfer Award
The Helmut E. Landsberg Award
The Award for Outstanding Achievement in Biometeorology

- **LECTURERS**
  Robert E. Horton Lecturer in Hydrology
  Bernhard Haurwitz Memorial Lecturer
  Walter Orr Roberts Lecturer

- **PAPER**
  Banner I. Miller

- **STUDENT PAPERS**
  Robert Leviton Student Prize
  Max A. Eaton Student Prize
  Spiros G. Geotis Student Prize
  Peter V. Hobbs Student Prize

- **NAMED SYMPOSIA**
  Section E, of the Policy, Guidelines, and Procedures for Awards and Lectureships provides the Policy on Named Conferences/Symposia and Special Issues of AMS Journals *(full policy description available at www.ametsoc.org/awards):*

> Recognition of scientists in the fields served by the AMS, living or deceased, in the form of a named conference or symposium or a named special issue of one of the Society's journals is an honor reserved for only the most outstanding of our colleagues. It should be awarded only to those individuals who are completing a career, or who have recently died having completed a career, of significant achievements in their field and whose contributions would make them worthy of consideration for Honorary Member of the AMS…

2018 FELLOWS COMMITTEE

The Committee's function is to submit to the Council the names of individuals for election to Fellow.

> Article III, Section 6, of the AMS Constitution provides that those eligible for election to Fellow shall have made outstanding contributions to the atmospheric or related oceanic or hydrologic sciences or their applications during a substantial period of years. The nominees for Fellow must be a member of the Society and remain on the committee's active list for three years.

A nomination letter and three supporting letters should be electronically submitted before 1 May 2018. A list of Fellows and the process for submitting nominations are on the AMS website (www.ametsoc.org/awards).

NOMINATING COMMITTEE

The Committee's function is to submit to the Council the names of individuals for 1) the office of President-Elect for a term of one year starting at the close of the Annual Meeting and 2) four positions on the Council for a term of three years starting at the close of the Annual Meeting.

As per Article VI of the AMS Constitution, formal nominations by petition may be submitted to the Secretary-Treasurer by 1 July. In addition, the AMS Nominating Committee welcomes recommendations from the membership of candidates for office, which will be considered as the slate is prepared. Such recommendations will be most helpful if they are sent to the Nominating Committee nominating-committee@ametsoc.org by the end of December and are in the form of a 1-page letter describing the proposed candidate's background and qualifications. Questions about the nomination process should also be addressed to the Nominating Committee.

HONORARY MEMBERS

Article III, Section 5, of the AMS Constitution provides that Honorary Members shall be persons of acknowledged preeminence in the atmospheric or related oceanic or hydrologic sciences, either through their own contributions to the sciences or their application or through furtherance of the advance of those sciences in some other way. They shall be exempt from all dues and assessments. The nominees for Honorary member remain on an active list for three years.

Deadline: 1 June 2018; a form and list of Honorary Members is available at www.ametsoc.org/awards.

CORPORATION AND INSTITUTIONAL MEMBERS

Membership in the American Meteorological Society does not imply AMS endorsement of an organization's products or services.

SUSTAINING MEMBERS

Aerospace Corporation
Ball Aerospace & Technologies Corporation
Harris Corporation
Lockheed Martin Corporation
Northrop Grumman Corporation
University Corporation for Atmospheric Research
Vaisala, Inc.
Weather Services International, Inc.

REGULAR MEMBERS

AccuWeather, Inc.
Aerospace & Marine International Corporation
Atmospheric and Environmental Research, Inc.
Atmospheric Science Technology, LLC
Atmospheric Technology Services Company, LLC
Baron Services, Inc.
Botswana Meteorological Services
Campbell Scientific, Inc.
Centuria Corporation
CSIRO Marine and Atmospheric Research
Davis Instruments Corporation
Earth Networks
EKO Instruments Company, Ltd.
ERT, Inc.
Furuno USA
Global Science & Technology, Inc.
Global Weather Corporation
I. M. Systems Group
Johns Hopkins University, Applied Physics Laboratory
Kipp & Zonen USA Inc.
Meteorological Service of New Zealand Ltd.
Meteorological Technology International
METER
Murray & Trettel, Inc.
NRG Systems, Inc.
Orbital ATK, Inc.
Panasonic Weather Solutions
Pelmorex Media Inc.
R. M. Young Company
Radiometrics Corporation
Raytheon Company
Republic of Korea Air Force, Headquarters
Riverside Technology, inc.
Royal Netherlands Meteorological Institute
Schneider Electric Weather
Science Applications International Corporation
Science Systems and Applications, Inc.
Scintec AG
SeaSpace Corporation
SGT, Inc.
Sonalysts, Inc.
SpectraSensors, Inc.
St. Louis University, Dept. of Earth & Atmospheric Sciences
The Weather Channel Television Network
U.S Department of Energy, Office of Science
Unisys Corporation
University of Alabama in Huntsville,Earth System Science Ctr
University of Colorado Libraries
University of Illinois, Department of Atmospheric Sciences
University of Oklahoma, School of Meteorology
University of Wisconsin - Madison, SSEC
Vieux & Associates, Inc.
Weather Decision Support Systems, International
Weather Modification, Inc.

SMALL BUSINESS MEMBERS

Climadata Corporation
EWR Weather Radar Systems
Forecastic Productions
Geonor, Inc.
National Council of Industrial Meteorologists
National Weather Service Employees Organization
Remtech, Inc.
WeatherSTEM, Inc.
Yankee Environment Systems, Inc.

PUBLICATIONS MEMBERS

Abdus Salam International Centre for Theoretical Physics
ARPA FVG, Osservatorio Meteorologico Regionale
Bureau of Meteorology
Civil Aeronautics Administration, MOTC
CNR
Colorado State University Libraries
Columbia University
Dartmouth College Baker Library
Desert Research Institute
Deutscher Wetterdienst
Embry Riddle Aeronautical University
Environment Canada Library, Downsview
EUMETSAT Library
Faculty of Geo-Information Science and Earth Observation - University of Twente
Finnish Meteorological Institute

For questions relating to corporation and institutional membership, please contact Maria Sarantopoulos at AMS Headquarters—telephone: 617-227-2426, x3912; fax: 617-742-8718; e-mail: msarantopoulos@ametsoc.org; or write to American Meteorological Society, Attn: Maria Sarantopoulos, 45 Beacon St., Boston, MA 02108-3693.

CORPORATION AND INSTITUTIONAL MEMBERS

Florida International University Library
Geophysical Institute/International Arctic Research Center
Harvard University, Gordon McKay and Blue Hill Libraries
Hong Kong Observatory Library
Indian Institute of Technology Bhubaneswar
Indian Institute of Tropical Meteorology
India Meteorological Department
Indiana University Library
Irish Meteorological Service
Japan Weather Association
Los Alamos National Laboratory
Lyndon State College, Samuel Read Hall Library
MBL/WHOI Library
Meteo-France
MeteoSwiss
Meteorologisk institutt
Millersville University, Department of Earth Sciences
MIT, Lincoln Laboratory
National Centers for Environmental Information
National Environment Agency
National Weather Center Library
Naval Postgraduate School, Dudley Knox Library
New York University
NOAA - GLERL Library
NOAA AOML Library
NOAA Central Library
NOAA Seattle Library
North Carolina State University Hunt Library
Pennsylvania State University, Paterno Library
South African Weather Service
Swedish Meteorological & Hydrological Institute
U.K. National Meteorological Library
U.S. Army Corps of Engineers, Library - ERDC
U.S. Department of Commerce, Boulder Labs Library
U.S. EPA Main Library
Universitatsbibliothek Innsbruck
Universitatsbibliothek Trier
University Centre in Svalbard
University of Copenhagen, Niels Bohr Institute Library
University of Delaware Library
University of Frankfurt Library
University of Hawaii at Manoa, Library
University of Maryland, McKeldin Library
University of Melbourne, Baillieu Library
University of Nebraska-Lincoln Libraries
University of New South Wales Library
University of North Carolina, Ramsey Library
University of North Dakota, Chester Fritz Library
University of Northern Colorado, Michener Library
University of Washington Libraries
WeatherPredict Consulting Inc.
Weizmann Institute of Science
Yale University, Center for Science & Social Science Info

Color indicates new or reinstated member

FELLOWSHIP AND SCHOLARSHIP SPONSORS

FELLOWSHIPS
AMS Giving Program
DOE, Atmospheric System Research
Lockheed Martin Corporation*
NASA Earth Science
NOAA's Climate Program Office
NOAA's National Weather Service

FRESHMAN AND UNDERGRADUATE SCHOLARSHIPS
Baron Services Inc.
Earth Networks
CLS America, Inc.
Harris Corporation
Lockheed Martin MS2
Naval Weather Service Association
Raytheon Company
R. M. Young Company
SAIC, Center for Atmospheric Physics
Science and Technology Corporation
Stinger Ghaffarian Technologies
Vaisala, Inc.
Jerome Namias Memorial Endowed Scholarship
Edgar J. Saltsman Endowed Scholarship
Bernard Vonnegut and Vincent Schaefer Endowed Scholarship
Percival D. Wark and Clara B. (Mackey) Wark Endowed Scholarship

MINORITY SCHOLARSHIPS
AMS Giving Program

SENIOR SCHOLARSHIPS
AMS 75th Anniversary Endowed Scholarship
Bhanwar Lal Bahethi Scholarship
Om and Saraswati Bahethi Scholarship
Saraswati (Sara) Bahethi Scholarship
Werner A. Baum Undergraduate Endowed Scholarship
Loren W. Crow Memorial Scholarship
The Dr. Robert Fraser Scholarship
Karen Hauschild Friday Endowed Scholarship
Bob Glahn Endowed Scholarship in Statistical Meteorology
The Jerry C. Glover Scholarship
Dr. Pedro Grau Undergraduate Scholarship
Richard and Helen Hagemeyer Scholarship
John R. Hope Endowed Scholarship in Atmospheric Sciences
David S. Johnson Endowed Scholarship
Larry R. Johnson Scholarship
Dr. Yoram Kaufman Scholarship
Carl W. Kreitzberg Endowed Scholarship
Ethan and Allan Murphy Endowed Memorial Scholarship
The Naval Weather Service Association Scholarship Award
K. Vic Ooyama Endowed Scholarship
The Orville Family Endowed Scholarship in Meteorology
The Ken Reeves Scholarship
Michael J. Roberts, Jr. Scholarship
Guillermo Salazar Rodriguez Undergraduate Scholarship
Mark J. Schroeder Endowed Scholarship in Meteorology

---

*Corporate Patron

INDEX TO ADVERTISERS

ONLINE CAREER CENTER

The AMS Online Career Center may be accessed through the AMS website at www.ametsoc.org/careercenter/index.html. In addition to posting positions, advertisers may search and view job seekers' résumés.

Job Posting Rates:
$375 (30-day posting)

$1593.75 (5 pack of jobs) Usable for 30-day job postings. Buy 5 job posting credits at a 15% discounted rate. These credits may be used at anytime during the next 12 months.

$3000 (10 pack of jobs) Usable for 30-day job postings. Buy 10 job-posting credits at a 20% discounted rate. These credits may be used at anytime during the next 12 months.

$3375 (12 pack of jobs) Usable for 30-day job postings or a continual 12-month posting. Buy 12 job-posting credits at a 25% discounted rate. These credits may be used at anytime during the next 12 months.

Advertisers may upload a company logo free of charge.

Résumés: View complete resumes for free! If you find any candidates you are interested in, submit your interest to them. If the candidate is interested in your opportunity, we connect you for just $20.00. If the candidate is not interested, you pay nothing!

AMS Corporation Member Discounts: Active AMS Corporation Members (small business, regular, or sustaining) receive a 25% discount when posting a position. Contact Kelly G. Savoie (ksavoie@ametsoc.org) to receive a coupon code. To receive the discount, the code must be entered when you post a position. The discount code is non-transferable.

AMS Member Benefit: AMS Members will be given 14-days advance access to a job listing. A member-only symbol will appear next to the posting. After 14 days, the job posting is open to all.

Submission of Ads: Advertisers must create an online account and submit ad text through the AMS Career Center site. Ad text may be entered at any time.

Payment Information: Prepayment is required by credit card or valid purchase order.

Contact Information: If you have questions, please contact Customer Service at 888-575-WORK (9675) (inside U.S.) or 860-440-0635 (outside U.S.).

ADVERTISING POLICY

The AMS will accept tasteful and accurate advertisements for products and services of professional interest to AMS members from organizations that are actively involved in the atmospheric and related sciences. The AMS also accepts advertising from organizations that have an interest in the atmospheric and related sciences and services, but are not actively involved in them. These organizations may promote their contributions to AMS activities and other good works, but may not directly promote products or services. The AMS reserves the right to refuse advertising that does not meet these criteria. Acceptance of advertising does not constitute the Society's endorsement of the product or service being advertised.

SYNOPTICS AMS Community Snapshots

AMS held the 23rd annual Maury Project two-week summer workshop for K-12 educators at the U.S. Naval Academy in Annapolis, Maryland. Clockwise from upper left: Maury teachers collected critters in the Chesapeake Bay, sampled waters, surveyed the beach, and deployed a CTD instrument (conductivity-temperature-depth). The Maury Project and its Project ATMOSPHERE counterpart have provided content and leadership training for 1,065 K-12 educators.

Call for photos: BAMS is looking for community snapshots from AMS members. Send to Rachel Thomas-Medwid at rthomas@ametsoc.org. Please include identifying information.